

Next Generation of Magneto-Dielectric

Antennas and Optimum Flux Channels

by

Tara Yousefi

A Dissertation Presented in Partial Fulfillment
of the Requirements for the Degree
Doctor of Philosophy

Approved August 2017 by the
Graduate Supervisory Committee:

Rodolfo Diaz, Chair

Douglas Cochran

Stephen Goodnick

George Pan

ARIZONA STATE UNIVERSITY

December 2017

ABSTRACT

There is an ever-growing need for broadband conformal antennas to not only reduce the number of antennas utilized to cover a broad range of frequencies (VHF-UHF) but also to reduce visual and RF signatures associated with communication systems. In many applications antennas need to be very close to low-impedance mediums or embedded inside low-impedance mediums. However, for conventional metal and dielectric antennas to operate efficiently in such environments either a very narrow bandwidth must be tolerated, or enough loss added to expand the bandwidth, or they must be placed one quarter of a wavelength above the conducting surface. The latter is not always possible since in the HF through low UHF bands, critical to Military and Security functions, this quarter-wavelength requirement would result in impractically large antennas.

Despite an error based on a false assumption in the 1950's, which had severely underestimated the efficiency of magneto-dielectric antennas, recently demonstrated magnetic-antennas have been shown to exhibit extraordinary efficiency in conformal applications. Whereas conventional metal-and-dielectric antennas carrying radiating *electric* currents suffer a significant disadvantage when placed conformal to the conducting surface of a platform, because they induce opposing image currents in the surface, magnetic-antennas carrying magnetic radiating currents have no such limitation. Their magnetic currents produce co-linear image currents in electrically conducting surfaces.

However, the permeable antennas built to date have not yet attained the wide bandwidth expected because the magnetic-flux-channels carrying the wave have not been designed to guide the wave near the speed of light at all frequencies. Instead, they tend to lose the wave by a leaky fast-wave mechanism at low frequencies or they over-bind a slow-wave at high frequencies. In this dissertation, we have studied magnetic antennas in detail and presented the design approach and apparatus required to implement a flux-channel carrying the magnetic current wave near the speed of light over a very broad frequency range which also makes the design of a frequency independent antenna (spiral) possible. We will learn how to construct extremely thin conformal antennas, frequency-independent permeable antennas, and even micron-sized antennas that can be embedded inside the brain without damaging the tissue.

ACKNOWLEDGMENTS

“But though the professed aim of all scientific work is to unravel the secrets of nature, it has another effect, not less valuable, on the mind of the worker. It leaves him in possession of methods which nothing but scientific work could have led him to invent.”

James Clerk Maxwell

My deepest gratitude goes to my advisor and mentor, Professor Rodolfo Diaz, who has guided me through my education, has taught me that before we can learn, we need to learn how to learn, and for pushing me to go farther than I ever thought I could go. None of this was possible without his guidance, encouragement, and insight.

I would like to express my appreciation for the valuable input of my committee, Professor Douglas Cochran, Professor Stephen Goodnick, and Professor George Pan who contributed to many discussions that helped to shape this project.

I am very thankful to my parents for their selflessness to encourage me to follow my dreams even though it meant sacrificing the chance to meet for all these years.

I am fully indebted to my amazing husband, Amir, for his support in every way possible and for his patience for every time I broke my promise to be down from the study in just five more minutes.

TABLE OF CONTENTS

	Page
LIST OF TABLES	x
LIST OF FIGURES	xi
CHAPTER	
INTRODUCTION	1
WHY THE MAGNETIC LOSS TANGENT IS NOT A RELEVANT CONSTRIANT FOR PERMEABLE CONFORMAL ANTENNAS	13
2.1 Introduction	13
2.2 Closed Form Model of an Electrically Small Permeable Dipole	17
2.3 The Material Selection Rule	26
2.4 Experimental Verification.....	36
2.5 Proof That a Conformal Magnetic Antenna Always Beats a Conformal Metal Antenna	40
2.6 Summary and Conclusions	47
A WIDEBAND MULTIMODE PERMEABLE CONFORMAL ANTENNA THINNER THAN $\lambda/75$ USING ADVANCED FERROMAGNETIC LAMINATE COMPOSITE MATERIALS	50
3.1 Introduction	50
3.2 The Gain-Bandwidth Problem.....	53
3.3 The Closed-Form Design of the Antenna	54
3.4 Full-Wave Model of the Antenna.....	57
3.5 Experimental Results	59
3.6 Conclusion.....	63

CHAPTER	Page
A FIRST ORDER MODEL OF THE MULTIPLE-FEED TOROIDAL MAGNETO-DIELECTRIC ANTENNA	65
4.1 Introduction	65
4.2 Wideband Impedance Model of the Conventional Loop Antenna.....	71
4.3 Deriving the Model for Quadrant Fed Metal Loop Antennas	78
4.4 Deriving the Model for a Quadrant Fed Mode 0	81
4.5 Deriving the Model for a Quadrant Fed Mode 1	85
4.6 Models for Quadrant Fed Dielectric Antennas	90
4.7 Models for Quadrant Fed Permeable Antennas	92
4.8 Comparison to Previous Results.....	94
4.9 The Input Impedance and the Effect of a Realistic Feed Loop	99
4.10 The Effect of the Realistic Metal Loop Feed and HFSS Confirmation	102
4.11 Conclusion.....	105
PARALLEL SOLENOID FEED FOR DIPOLE AND MONOPOLE MAGNETIC ANTENNAS.....	107
5.1 Introduction	107
5.2 Parallel Solenoid Feed for Linear Magnetic Current Dipole Antenna.....	110
5.3 Parallel Solenoid Feed for the Monopole Mode of a Magnetic Current Loop.....	117
5.4 Parallel Solenoid Feed for the Dipole Mode of a Magnetic Current Loop..	124
5.5 Using the Parallel Solenoid Feed as a Tuning Aid to Achieve a Good VSWR.....	127

CHAPTER	Page
5.6 Conclusion.....	134
DEMONSTRATION OF THE EFFECT OF THE PARALLEL SOLENOID FEED ON A MAGNETIC ARCHIMEDEAN SPIRAL ANTENNA.....	
6.1 Introduction	136
6.2 Basic Archimedean Spiral with One Feed at the Center	138
6.3 The Effect of Using a Solenoid Feed with Multiple Grounded Loops	149
6.4 Final Antenna Geometry and Results.....	153
6.5 Archimedean Spiral Antenna Built Using CZN Laminates Instead of NiZn Tiles.....	157
6.6 Conclusion.....	159
Comprehensive Study on Metalized Magnetic Flux Channel Antenna	
7.1 Introduction	161
7.2 Theory of the infinite magneto dielectric rod.....	169
7.2.1 Phase and amplitude plots of the magnetic current of the MD rod	169
7.2.2 Using Savitzky-Golay filters to smooth data and obtaining α and β plots for MD rod	172
7.2.3 Radiated power of the antenna obtained from the Poynting vector	183
7.2.4 Finding the location of bandwidth edge of the rod on α and β plots.....	191
7.2.5 Obtaining the total power dissipated in the antenna using the induced EMF method.....	196
7.3 Theory of the Magneto dielectric open trough.....	199
7.3.1 Magneto dielectric open trough with different cross sections.....	207

CHAPTER	Page
7.3.2 Using Savitzky-Golay filters to smooth data and obtaining α and β plots for MD open trough	212
7.3.3 The effect of the open trough's aspect ratio on the bandwidth and cutoff frequency using the β plots or the velocity plots	215
7.3.4 Calculating the radiated power of the magneto dielectric open trough.....	219
7.4 Theory of the magneto-dielectric trough with a slit.....	222
7.4.1 Obtaining the β plots for MD slitted trough and the radiated power using the Poynting vector	227
7.5 Comparison of the MD rod, MD open trough, and the MD slitted trough ..	230
7.5.1 Comparing the MD rod and the square open trough with the same volume.....	230
7.5.2 Comparison of a MD open trough to the magneto-dielectric rod with both the same volume and the same cutoff frequency	231
7.6 Conclusion.....	253
DISPERSION FEATURES OF THE OPEN TROUGH AND SLITTED TROUGH IN BOTH BOUND-WAVE AND LEAKY-WAVE REGIONS	256
8.1 Introduction	256
8.2 Transverse resonance solution to the trough	264
8.2.1 The leaky wave regime solution using successive approximation.....	266
8.2.2 Guided wave regime solution using successive approximation.....	271
8.2.3 Simplified successive approximation method.....	275

CHAPTER	Page
8.2.4 Transverse resonance equation solution using unconstrained minimization routine	280
8.3 Comparing the transverse resonance method to the Greens function method and to full wave simulation	282
8.4 Application of transverse resonance method to a slitted trough.....	293
8.5 Full wave simulation results of the slitted trough	306
8.6 Application of transverse resonance method to dispersive permeable material.....	307
8.7 Full wave simulation results of the trough and the slitted trough filled with metal walls	313
8.8 Conclusion.....	318
OPTIMAL PERMEABLE ANTENNA FLUX CHANNELS FOR CONFORMAL APPLICATIONS SUMMARY AND DESIGN GUIDELINES	320
9.1 Introduction	320
9.2 The generalized admittance surface	322
9.3 Enforcing anisotropy in the materials of construction.....	333
9.4 Exploiting the frequency dependent dispersion of realistic permeable materials.....	344
9.5 Conclusion.....	347
REFERENCES	350
APPENDIX	
A. OTHER INTERESTING APPLICATIONS OF MAGNETIC ANTENNAS: PUSHING THE LIMITS OF RADIO FREQUENCY (RF) NEURONAL TELEMETRY	356

APPENDIX	Page
B. DETAILS AND CALCULATIONS ON THE THEORY OF THE INFINITE MAGNETO DIELECTRIC ROD.....	400

LIST OF TABLES

Table	Page
2-1 Typical Hesitivities of Microwave Materials	29
4-1 Summary of Quadrant Fed Metal Loop Antenna Models	89
5-1 Duality Between the Electric and Magnetic Dipole.	108
6-1 Values of Powers for Each Antenna.	152
A-1 Radiation Resistance, Material Resistance, Efficiency and Input Impedance at Resonance of Electrical Loop and Magnetic Dipole Antennas	364

LIST OF FIGURES

Figure	Page
1-1 (a) Conformal Permeable Antenna Showing That the Current and the Image Current Are Constructive. (b) Metal Antenna Close to a Ground Plane Showing Destructive Image Current (c) Metal Antenna Having a Large Distance From the Ground Plane in Order to Have a Constructive Image Current.	2
1-2 (a) Body Wearable Magnetic Belt Antenna [2] (b) Micron Size Magnetic Antenna Embedded Inside the Brain for Neuronal Telemetry.	3
1-3 (a) 1.5” Thick Magnetic Dipole on Top of an HUMVEE Instead of a 6 Foot Whip Antenna [2] (b) Magnetic Spiral Antenna Built Out of Ferrite Tiles (c) Extremely Thin Magnetic Conformal Antenna Mountable on an Airplane.	4
2-1 Dielectric Dipole Model Based on Schelkunoff’s Model of Electrically Small Metallic Antennas, Including the Dielectric Material’s Impedance.	19
2-2 Circuit Model for the Magneto-Dielectric Dipole Antenna	21
2-3 Contours of Radiation Efficiency: Using Equation (7) Versus μ' and μ'' (a) and Versus μ' and $\tan(\delta)$ (b). The Three Regions Indicate Region of High Material Loss, Moderate Material Loss And Low Material Loss. For Comparison, Contours of Radiation Efficiency Using Equation (8) Versus μ' and $\tan(\delta)$ Are Shown in (c). ..	25
2-4 (a) A Single Debye Susceptibility Function (b) A Single Lorentz Susceptibility Function	27
2-5 Magnetic Conductivity of the (a) Debye and (b) Lorentz Examples	28

Figure	Page
2-6 Simulated Antenna: A Half Cylinder Dipole Conformal to A Metal Ground Plane Fed By 8 Loop Feeds	32
2-7 Four Hypothetical Lorentz Materials with Very Different Loss Tangents (a) Have Magnetic Conductivities (b) That Reach the Same Peak. The Fullwave Simulated Results for The Radiation Efficiency from All Four Materials (c) Are on Top Of Each Other (Dashed Curves) And Almost Identical to The Closed Form Prediction from Equation (19) (Solid Curve).....	35
2-8 (a) NiZn Absorber Tiles from Fair Rite Show a Debye-Like Permeability, (b) Test Article Shown Is a Dipole Mounted on An Aluminum Carrier Plane. (c) Measured Realized Gain and HFSS Simulated Results Are Very Close. (d) The HFSS Computed Radiation Efficiency Closely Agrees with Equation (7), But Is Dramatically Different from The Conventional Equation (8).	38
2-9 Installation on The Roof of A HUMVEE Highlights the Difference in Size Between the Antenna and A Conventional Whip (a). Gain of The Permeable Dipole (Red) Is Comparable or Better Than That of The Whip (b).	39
2-10 The Magnetic Current Distribution Attained by a Distributed Feeding Network on a $\mu = 40$ Dipole From 10MHz Through 120MHz is Nearly Triangular.	41
2-11 The Impedance of The Modeled Antenna, (a) Imaginary Part and (b) Real Part, Can be Approximated with a Closed-Form Circuit Model (Magenta Curve with Symbols) That Improves on Sebastian's [12] Original (Green) to Agree with the HFSS Simulations (Red).....	42

Figure	Page
2-12 A metal dipole constrained to operate in the same conformal volume as the simulated magnetic antenna has an input impedance that can be derived from its microstrip-like geometry.....	42
2-13 Comparison of the Real (a) and Imaginary (b) parts of the input impedance of the two antennas.....	43
2-14 Match Bandwidth From 10MHz to 300MHz For the Permeable Antenna (Red) Exceeds That of Two Versions of the Metal Antenna (a). Similarly, the Efficiency Bandwidth Product of the Permeable Antenna Exceeds That of the Metal Antenna (b).....	46
3-1 (a) Theoretical Model of the Permeable Toroid, (b) Detail of a Quadrant in the Simulation, (c) Schematic of the Feed Circuit , (d) a Photograph of the Antenna. .	52
3-2 Derivation of the Closed-Form Model For the Dipole Mode (Mode 1) of the Permeable Antenna.	56
3-3 The Full-Wave Calculated Radiation Efficiency (a) and Mismatch Loss (b) of the Manufactured Demonstrator in Mode 1 Differ From the Ideal Closed-Form Expectation.	59
3-4 Measured Mode-Former Loss and Full-Wave Computed Mismatch Loss Relative to a 200Ω System Impedance.	60
3-5 Measured (Dashed) and Calculated (Solid) Antenna Efficiency: Mode 0 in Blue, Mode 1 in Red.....	61
3-6 Measured Gain Blue=M0, Red=M1.	61

Figure	Page
3-7 Measured Antenna Patterns at 0° (Red) and 45° (Blue) Azimuth Versus Elevation For (a) Mode 1 and (b) Mode 0 at 300MHz.	63
4-1 Simple Mode-Former (a) For Feeding the Toroidal Four-Port Antenna (b) and Generating a Vertically Polarized Mode 0 and a Rotating Mode 1 [28].	69
4-2 Two Biconical Transmission Lines Having the Same Impedance with Different Cone and Tilt Angles.....	72
4-3 Loop Antenna Built from Several Sections of Biconical Vee Antennas.....	73
4-4 Darlington Form Model of the Loop Antenna.....	76
4-5 Evolution of the Quadrant Fed Mode 0 Model.....	81
4-6 The Loop Is Divided into a Large Number of Sections of Lengths 2ρ (Left). Then the First Segment Is Replaced by a Small Bicone as a Feed (Right).....	82
4-7 Effective Complex Inductance Versus Frequency.	84
4-8 Evolution of the Quadrant Fed Mode 1 Model.....	86
4-9 Effective Complex Capacitance Versus Frequency	87
4-10 Darlington Form Model of the Quadrant Fed Mode1.	90
4-11 Equivalent Circuit for Mode 0 of the Permeable Antenna	93
4-12 Equivalent Circuit for Mode 1 of the Permeable Antenna	94
4-13 Permeability of the CZN Laminate Material	98
4-14 Original Closed-Form Efficiency Expressions (Red Curve), Results from the Derivation in This Report (Blue Curve), Dashed Line Shows 1λ Perimeter.....	98

Figure	Page
4-15 Original Closed-Form Efficiency Expression for a Linear Dipole (Red Curve), Results From the Derivation in This Report (Blue Curve), Dashed Line Shows 1λ Perimeter.....	99
4-16 Schematic of One Quadrant in Mode 1 of the Permeable Antenna Fed at the Top Midpoint of Each Quadrant Instead of at the Ground Plane.....	102
4-17 Mode 1 Active Input Impedance at the Feed Loop Based on the Closed Form Equations (Solid) and Based on an HFSS Simulation (Dashed).	104
4-18 Mode 0 Active Input Impedance at the Feed Loop Based on the Closed Form Equations (Solid) And Based on an HFSS Simulation (Dashed).	104
5-1 Electric Dipole and the Magnetic Dipole.	109
5-2 Magnetic Dipole with Feed Loop.....	109
5-3 Magnetic Dipole Antenna Fed with Multiple Electric Loop Feeds.....	110
5-4 (a) Parallel Solenoid Fed Antenna Structure and (b) Is a Closeup View Close to the Feed Port of the Same. (c) Parallel Solenoid Fed Dipole Antenna with Fewer Turns.	112
5-5 (a) Comparison of Peak Realized Gain (b) S11 of Different Antenna Structures Considered. Note That for the Three Feed Case, the Active S11 at the Individual Port Is Plotted.....	113
5-6 Comparison of the Magnetic Current Distribution of the Different Antenna Configurations for the Frequencies 50, 110, 190 and 290 MHz.....	114

Figure	Page
5-7 3D Polar Plot of Total Gain at Different Frequencies for the Parallel Solenoid Feed Magnetic Current Dipole Antenna.....	115
5-8 Current Distribution Along the Dipole Length for the Single Feed Loop Case.....	116
5-9 Current Distribution Along the Dipole Length With a Solenoid Having Loops Spaced 3cm Apart.....	116
5-10 Monopole Mode of a Magnetic Current Loop with 4 Feed Loops.....	117
5-11 Monopole Mode of a Magnetic Current Loop with 4 Feed Loops and a Solenoid Cage With 16 Bars.....	118
5-12 Side View of a Quarter of the Designed Circular Antenna.....	120
5-13 Top View of a Quarter of the Designed Circular Antenna.....	121
5-14 Peak Gain of the Monopole Mode with 4 Feed Loops (Red 40 Bars, Blue 16 Bars, Black No Cage).....	122
5-15 Realized Gain of the Monopole Mode with 4 Feed Loops (Red 40 Bars, Blue 16 Bars, Black No Cage).	122
5-16 Return Loss (S11) of the Monopole Mode with 4 Feed Loops(Red 40 Bars, Blue 16 Bars, Black No Cage).	123
5-17 Pattern Versus Theta of the Monopole Mode with 4 Feed Loops(Red 40 Bars, Blue 16 Bars, Black No Cage) at 420 MHz and Phi=0 Degrees.....	124
5-18 Peak Gain of the Dipole Mode with 4 Feed Loops (Red 40 Bars, Blue 16 Bars, Black No Cage).....	125

Figure	Page
5-19 Realized Gain of the Dipole Mode with 4 Feed Loops (Red 40 Bars, Blue 16 Bars, Black No Cage).....	126
5-20 Pattern Versus Theta of the Dipole Mode with 4 Feed Loops (Red 40 Bars, Blue 16 Bars, Black No Cage) at 420 MHz and Phi=45 Degrees.....	126
5-21 Peak Gain of the Dipole Mode with Different Spacing Between the Wires of the Transmission Line (Red 0.05 Inch , Blue 0.02 Inch, Green 0.25inch).	127
5-22 Quadrant of the Toroidal Magnetic Antenna with 4 Feed Loops and a 16 Bar Solenoid (a) Side View (b) Top View.	128
5-23 (a) Peak Gain and (b) S11 of the Mentioned Antenna Normalized to a 50 Ohm System Impedance.	129
5-24 (a) Input Impedance (b) Smith Chart Mentioned Antenna Normalized to a 50 Ohm System Impedance.	129
5-25 (a) Antenna S11 (b) Smith Chart (c) Input Impedance of the Mentioned Antenna Normalized to a 200 Ohm System Impedance.	130
5-26 Quadrant of the Toroidal Magnetic Antenna with 4 Feed Loops and a 24 Bar Solenoid (a) Side View (b) Top View.	131
5-27 (a) Peak Gain and (b) S11 of the Mentioned Antenna Normalized to a 50 Ohm System Impedance.	132
5-28 (a) Input Impedance and (b) Smith Chart of the Mentioned Antenna Normalized to a 50 Ohm System Impedance.	133

Figure	Page
5-29 (a) Antenna S11 (b) Smith Chart of the Mentioned Antenna Normalized to a 200 Ohm System Impedance.	134
6-1 Currents on a Spiral Antenna Near the Feed Tend to Cancel Each Other as Seen from the Far Field	138
6-2 Currents on a Spiral Antenna at the Active Region.....	139
6-3 Smallest and Largest Active Region Supported by a General Spiral Antenna.	140
6-4 Smallest and Largest Active Region Supported by Our Specific Antenna Delimit Its Operational Band to Between 95 MHz and 315 MHz.....	141
6-5 (a) Frequency Dependence of the Permeability of Nizn Tiles (b) Basic Model of a Ferrite Archimedean Spiral Antenna with Only One Feed at the Center.	142
6-4 (a) Efficiency of the Single Loop Fed Spiral Antenna (b) Peak Gain of the Single Loop Fed Spiral Antenna, and the Impedance of the Basic Ferrite Archimedean Spiral Antenna.	143
6-5 Impedance of the Single Loop Fed Spiral Antenna.....	143
6-6 Impedance of the Single Fed Spiral Antenna.	144
6-7 A Few Integration Paths and a Table of the Distance of the Paths From the Center For the Single Loop Fed Spiral Antenna.....	145
6-8 Integral Versus Frequency for Different Lines for the Single Loop Fed Spiral Antenna.....	146
6-9 Value Of $E \cdot dl$ Versus Distance from the Feed.....	146

Figure	Page
6-10 A Few Integration Paths and a Table of the Distance of the Paths From the Center for the 4 Loop Solenoid Fed Spiral Antenna.	147
6-11 Integral Versus Frequency for Different Lines for the 4 Loop Solenoid Fed Spiral Antenna.....	148
6-12 Plots of $Im = E \cdot dl$ for (a) Spiral Antenna with One Feed Loop at the Center (b) the Solenoid Fed Spiral Antenna With 4 Loops to Ground. Showing an Increase In Im at the Position of the Loop.	149
6-13 Changes in Peak Gain When We Change the Number of Loops to Ground From 4 Loops to 30 Loops and Comparing the Results to the Case Without the Solenoid and the Case of the 8 Loop Structure Touching the Ferrite.	150
6-14 (a) Magnetic Spiral Antenna Without any Solenoid Feed, (b) Magnetic Spiral Antenna With an 8 Loop Solenoid Touching the Ferrite and, (c) the Solenoid Fed Spiral Antenna With 30 Loops to Ground, (d) the Impedance of Each of the Antennas (e) the Gain of the Antennas.	151
6-15 Model and Dimension of the Final Design of the Magnetic Spiral Antenna.	153
6-16 (a) Photograph of the First Version of the Spiral Fed by a 4-Loop Parallel Solenoid (b) HFSS Models of the Same Structure With 4 Loops and 30 Loops and the Measured and Simulated Gain (c) Input Impedance and Smith Chart Representation	154
6-17 S11 of the Spiral Antenna Showing a Very Good Match After Only A 2:1 Transformer.....	155

Figure	Page
6-18 Gain θ Pattern at f=95MHz at $\varphi = 0$ and $\varphi = 90$ Degrees	155
6-19 Gain θ Pattern at f=235MHz at $\varphi = 0$ and $\varphi = 90$ Degrees.	156
6-20 Plot of the Efficiency of the Final Parallel Solenoid Fed Antenna, the Theoretical Efficiency of an Archimedean Antenna with a Height of 18mms, and the Spiral Fed with a Single Loop and the Antenna When the Solenoid Is Touching the Surface.	157
6-21 Model of the Spiral Antenna Using CZN Laminates. The Different Regions, Due to the Anisotropic Material, Are Shown in Green and Blue.	158
6-22 Peak Gain of the Ferrite Tile Antenna (Purple) and the CZN Laminate Antenna(Blue).	159
7-1 (a) Magneto Dielectric Archimedean Spiral and a (b) MD Toroid Fed with a Multiloop Solenoid Feed.....	162
7-2 The Generalized Magneto Dielectric Trough Antenna	163
7-3 Spiral Antenna with a 4 Loop Solenoid Feed.....	164
7-4 Comparison of the Gain of a Spiral Antenna Using Different Number of Loops in the Solenoid Feed.....	165
7-5 Different Views of the Magnetic Trough Spiral Antenna	166
7-6 (a) Peak Gain (b) Efficiency of the Spiral Antenna with the Solenoid and with the Trough.....	166
7-7 Amplitude (a) and Phase (b) of the Current as a Function of the Distance From the Feed Multiplied by the Wavelength (z/λ) for a Magneto-Dielectric Rod With a 2	

Figure	Page
<p>Inch Radius and a Material with $\mu = 80$ And $\epsilon = 2$. Frequencies Go From 30 MHz to 170 MHz In 20 MHz Steps. The Star Symbol Shows the Current Wave Approaching the Light Line.....</p>	169
<p>7-8 Amplitude (a) and Phase (b) of the Current as a Function of the Distance From the Feed Multiplied by the Wavelength (z/λ) For a Magneto-Dielectric Rod with a 2 Inch Radius and a Material with $\mu = 80$ and $\epsilon = 2$. Frequencies Go From 190 MHz to 330 MHz in 20 MHz Steps. The Star Symbol Shows the Current Wave Approaching the Light Line. The Blue Arrows Shows the Current Wave Going from One Mode to Another Mode and the Red Arrow Shows the Plateau That's the Indication of the New Mode Starting to Appear.....</p>	170
<p>7-9 Amplitude (a) and Phase (b) of the Current as a Function of the Distance From the Feed Multiplied by the Wavelength (z/λ) for a Magneto-Dielectric Rod with a 2 Inch Radius and a Material with $\mu = 80$ And $\epsilon = 2$. Frequencies Go from 350 MHz to 490 MHz in 20 MHz Steps.....</p>	172
<p>7-10 Amplitude of the Current as a Function of the Distance from the Feed Divided by the Wavelength (z/λ) for a Magneto-Dielectric Rod with a 2 Inch Radius and a Material with $\mu = 80$ and $\epsilon = 2$. Frequencies Go from 30 MHz to 170 MHz in 20 MHz Steps.....</p>	173
<p>7-11 Demonstration of Least-Squares Smoothing by Locally Fitting a Second-Degree Polynomial (Solid Line) to Five Input Samples. Blue Dots Show the Input Samples,</p>	

Figure	Page
Red Circles Show the Smoothed Output Sample, and Green X's Show the Effective Impulse Response Samples (Weighting Constants).	174
7-12 Showing the Steps of Obtaining the Slope of the Amplitude of a 2" Magneto Dielectric Rod.	176
7-13 Slope of the Current Amplitude of a 2" Magneto Dielectric Rod or the α -Plot in Nepers Per Wavelength.....	177
7-14 Showing the Steps of Obtaining the Slope of the Phase of a 2" Magneto Dielectric Rod.....	178
7-15 Slope of the Current Phase of a 2" Magneto Dielectric Rod or the β -Plot in Radians Per Wavelength.....	179
7-16 Current Phase and Amplitude Plots of Rod with Different Radii	180
7-17 Current Phase and Amplitude Plots of the 1.6" Rod at Higher Frequencies and Passing the Light-Line	181
7-18 Current Phase and Amplitude Plots of the 1.6" Rod at Higher Frequencies and Passing the Light-Line	182
7-19 Phase Velocity Plot for the 1.6" Rod at Higher Frequencies and Passing the Light-Line	183
7-20 Infinite Magneto Dielectric Rod.....	184
7-21 Radiated Power of a Magneto Dielectric Rod with $r=2''$ and $\mu = 80$ with the 0.5db Bandwidth Edges and Relative Bandwidths Shown in the Figure	186

Figure	Page
7-22 Phase Plots of a Magneto Dielectric Rod With $r=2''$ and $\mu = 80$ Showing the Onset Frequency of Each Mode.....	187
7-23 Radiated Power of a Magneto Dielectric Rod with $r=1.6''$ and $\mu = 80$ with the 0.5db Bandwidth Edges and Relative Bandwidths Shown in the Figure	188
7-24 Phase Plots of Magneto Dielectric Rod with $r=1.6''$ and $\mu = 80$ Showing the Onset Frequency of Each Mode.....	188
7-25 Comparing the Rod with the Larger Cross Section to the Rod with Smaller Cross Section Shows That, as Expected, They Have Almost the Same Bandwidth.....	189
7-26 Radiated Power of a Magneto Dielectric Rod with $r=2''$ and $\mu = 80$ and the Location of the 0.5db Bandwidth Edge on the α and β Plots	192
7-27 Location of the 0.5dB Bandwidth Edge on the Wave Velocity Plot	193
7-28 Radiated Power of a Magneto Dielectric Rod with $r=1.6''$ and $\mu = 80$ and the Location of the 0.5db Bandwidth Edge on the α and β Plots	194
7-29 Location of the 0.5dB Bandwidth Edge on the Wave Velocity Plot	195
7-30 Radiated Power of a Magneto Dielectric Rod with $r=2.4''$ and $\mu = 80$	195
7-31 Location of the 0.5dB Bandwidth Edge on the Wave Velocity Plot and the β Plot	196
7-32 Radiated Power and Total Power of a PMC Rod with Different Radii.....	198
7-33 Radiated Power and Total Power of a Magneto Dielectric Rod. The Difference Between Them Is the Power Lost into Surface Waves.....	199
7-34 Magneto Dielectric Open Trough with the Fields Shown.....	200

Figure	Page
7-35 Magneto Dielectric Open Trough with the Fields Shown.....	202
7-36 A 2” by 2” Magneto Dielectric Open Trough with $\mu = 80$	205
7-37 Amplitude and Phase of the Current Wave as a Function of Distance from Feed for a 2” by 2” Trough Filled with $\mu = 80$ and $\epsilon = 2$, from 30 MHz to 170MHz.....	205
7-38 Amplitude (Top) and Phase (Bottom) of the Current Wave as a Function of Distance from Feed for a 2” by 2” Trough Filled with $\mu = 80$ and $\epsilon = 2$, from 190 MHz to 330MHz	206
7-39 Amplitude and Phase of the Current Wave as a Function of Distance from Feed for a 2” by 2” Trough Filled with $\mu = 80$ and $\epsilon = 2$, from 190 MHz to 330MHz.....	207
7-40 Geometry of 4” by 1” Depth Open Trough Filled with a Material with $\mu = 80$, $\epsilon = 2$	208
7-41 Amplitude (a) and Phase (b) of the Current as a Function of the Distance from the Feed Multiplied by the Wavelength (z/λ) for a Magneto-Dielectric Shallow Open Trough with a 4 Inch by 1 Inch Cross-Section and a Material with $\mu = 80$ and $\epsilon = 2$. Frequencies Go from 30 MHz to 170 MHz in 20 MHz Steps. The Star Symbol Shows the Current Wave Does Not Reach the Light-Line.....	209
7-42 Geometry of a 1” Width by 4” Depth Deep Open Trough Filled with a Material with $\mu = 80$ and $\epsilon = 2$	210
7-43 Amplitude (a) and Phase (b) of the Current as a Function of the Distance from the Feed Multiplied by the Wavelength (z/λ) for a Magneto-Dielectric Deep Open Trough with a 1 Inch by 4 Inch Cross-Section and a Material with $\mu = 80$ and	

Figure	Page
$\epsilon = 2$. Frequencies Go from 30 MHz to 170 MHz in 20 MHz Steps. The Star Symbol Shows the Current Wave Reaches the Light Line and Goes to Another Mode Similar to What Happened for the High Frequency Magneto Dielectric Rod.	211
7-44 Amplitude of the Current as a Function of the Distance from the Feed Divided by the Wavelength (z/λ) for a Magneto-Dielectric 2" \times 2" Open Trough and a Material with $\mu = 80$ and $\epsilon = 2$ and for Very Small Values of (z/λ). Frequencies Go From 30 MHz to 170 MHz in 20 MHz Steps.	212
7-45 Amplitude of the Current for Very Small Values of (z/λ) for the 2" \times 2" Open Trough. Solid Lines Show the Low Pass Filtered Data and the Dotted Lines Show the Linear Fit. Frequencies Go From 30 MHz to 170 MHz in 20 MHz Steps.	213
7-46 The Slope of the Amplitude Decay or the α Plot of a Magneto-Dielectric Rod with a 1.6 Inch Radius and a Material with $\mu = 80$ and $\epsilon = 2$ Extended to Higher Frequencies	213
7-47 Phase of the Current as a Function of the Distance from the Feed Divided by the Wavelength (z/λ) for a Magneto-Dielectric 2" \times 2" Open Trough and a Material with $\mu = 80$ and $\epsilon = 2$ and for Very Small Values of (z/λ). Frequencies Go From 30 MHz to 170 MHz in 20 MHz Steps.....	214
7-48 The Slope of the Phase Plot or the β Plot of a Magneto-Dielectric 2" \times 2" Open Trough and a Material with $\mu = 80$ and $\epsilon = 2$	215
7-49 (a) β Plots of Three Structures (b) the Wave Velocity of Three Structures	217

Figure	Page
7-50 Inverse of the Slope of the β Plots Versus Aspect Ratio.....	218
7-51 The Open Trough and the Rod Having the Same Cross Section Area and the Same Cutoff Frequency	220
7-52 (a) Open Trough with 3.8" \times 1.053" Cross Section (b) α Plot of the Structures (c) β Plots of the Structures (d) the Wave Velocity of the Structure.....	221
7-53 (a) Radiated Power of a Magneto Dielectric Rod with $r=1.6''$ and $\mu = 80$ (b) Radiated Power of a 3.8" \times 1.053" Magneto Dielectric Open Trough with $\mu = 80$	222
7-54 Geometry of the Magneto Dielectric Slitted Trough.....	223
7-55 The Normalized Admittance Seen from the Opening of the Slit Looking Inside the Material	223
7-56 Phase and Amplitude Plots of the Slitted Trough with Different Slit widths.....	227
7-57 Magneto Dielectric Slitted Trough with Given Dimensions	228
7-58 β Plot Which Has Been Obtained from the Phase Plots of the 2'' by 2'' Slitted Trough.....	229
7-59 Radiated Power of the 2 by 2 Slitted Trough Showing That the Peak of the Radiated Power Happens Close to the Onset Frequency	229
7-60 The Slope of the Phase Plot or the β Plot of the Magneto-Dielectric Rod (Left) and the 2" \times 2" Open Trough (Right) Both Having a Material with $\mu = 80$ and $\epsilon = 2$	230

Figure	Page
7-61 The Wave Velocity of the MD Rod and Trough Normalized to the Speed of Light	231
7-62 Wide Trough and Rod Having the Same Volume and the Same Cutoff Frequency	232
7-63 Unwrapped Phase of the Current as a Function of the Distance from the Feed Divided by the Wavelength (z/λ) for a Magneto-Dielectric Wide Trough (Left) and a Rod with a 1.6 Inch Radius (Right) Both Having a Material with $\mu = 80$ and $\epsilon = 2$. Frequencies Go from 30 MHz to 270 MHz in 20 MHz Steps.....	232
7-64 Phase of Both Structures Versus (z/λ) on the Same Figure for Frequencies from 110 MHz to 270 MHz.	233
7-65 Amplitude of the Current as a Function of the Distance from the Feed Divided by the Wavelength (z/λ) for a Magneto-Dielectric Wide Trough (Left) and a Rod with a 1.6 Inch Radius (Right) Both Having a Material with $\mu = 80$ and $\epsilon = 2$. Frequencies Go from 30 MHz to 270 MHz in 20 MHz Steps.	234
7-66 (a) Trough and Rod with the Same Volume and the Same Cutoff (b) α Plot of Both Structures (Blue Shows the Rod and Green Shows the Trough) and (c) the β Plots of Both Structures (d) the Wave Velocity of Both Structures.....	235
7-67 Phase Plots of (a) Trough with the Same Volume as the Previous Figure and Half the Permeability (b) Rod with the Same Volume as the Previous Figure and Half the Permeability	236

Figure	Page
7-68 (a) Trough and Rod with the Same Volume and the Same Cutoff (b) α Plot of Both Structures (Blue Shows the Rod and Green Shows the Trough) and (c) the β Plots of Both Structures (d) the Wave Velocity of Both Structures.....	237
7-69 (a) β Plots of Both Structures with the Same Volume as the Previous Figures and $\mu = 20$ (b) the Wave Velocity of Both Structures with the Same Volume as the Previous Figures and $\mu = 20$	238
7-70 (a) β Plots of Both Structures with the Same Volume as the Previous Figures and $\mu = 20$ (b) the Wave Velocity of Both Structures with the Same Volume as the Previous Figures and $\mu = 20$	238
7-71 Phase Plots of (a) Trough with 12.8 Inch Squared Cross Section and $\mu = 25$ (b) Rod with the Same Volume as the Previous Figure $\mu = 80$	239
7-72 Phase Plots of the Trough with 12.8 Inch Squared Cross Section and $\mu = 25$ Rod with the Same Volume as the Previous Figure and $\mu = 80$ Plotted in the Same Figure. We Can See They Are Overlapping the Colored Lines Show the Trough and the Dashed Black Lines Show the Rod.....	240
7-73 (a) β Plots of the Rod and the Trough Having the Same Permeability \times Volume (b) the Wave Velocity of the Rod and the Trough Having the Same Permeability \times Volume.....	241
7-74 Normalized Bandwidth vs Aspect Ratio of the Trough and Fitted Line	242
7-75 Flow Chart Showing Our Choices in Designing the Rod and the Open Trough Antenna.....	243

Figure	Page
7-76 Structures Having the Same Volume (Cross-Section) , and the Same Cutoff Frequency But Different Values of Permeability \times Cross Section	245
7-77 (a) β Plots of Four Structures (b) the Wave Velocity of Four Structures.....	247
7-78 Structures Having the Same Volume (Cross-Section) , and the Same Cutoff Frequency But Different Values of Permeability \times Cross Section	248
7-79 (a) β Plots of Three Structures (b) the Wave Velocity of Four Structures	249
7-80 β Plots of and Wave Velocity Plot of the Open Trough and the Slitted Trough with Same Onset Frequency	250
7-81 β Plots of and Wave Velocity Plot of the Open Trough and the Slitted Trough Showing Enhanced Radiation Bandwidth	251
7-82 Three Permeable Channels with the Same Onset Frequency and Same Permeability Times Cross Section Product.....	251
7-83 Radiated Power Versus Frequency of the Permeable Channels of Figure 7-82 Showing the Enhanced Bandwidth Available with the Slitted Trough Structure..	252
7-84 Complete Flowchart of Choices Given with the Trough and the Slitted Trough...	253
8-1 An Open Trough with Isotropic Permeable Material	257
8-2 Difference Between the Electric Field in a Trough and an Open Flux Channel	259
8-3 (a) Cross Section of the Partially Dielectric-Loaded Millimeter-Wave Antenna (b) Dispersion Plot Over a Very Wide Frequency Range for the Structure Shown in 8-3	
(a) When $a = 2.20$ mm, $a' = 1.00$ mm, $b = 1.59$ mm, $d = 0.10$ mm, and $e, = 2.56.261$	

Figure	Page
8-4 Normalized Phase Constant of Circular Dielectric Rod Waveguide. The Dielectric Constant and Radius of the Rod Were Assumed to Be 5.0 and 5.0 mm, Respectively. [34]	262
8-5 (a)Front View (b) Sideview (c) Equivalent Circuit	264
8-6 Real and Imaginary Parts of k_z for a 1'' by 1'' Open Trough Using the Transverse Resonance Method.....	279
8-7 Velocity Normalized to the Speed of Light Versus Free-Space Wavenumber	279
8-8 Real and Imaginary Parts of k_z Obtained from Optimization and from the Approximation Method.....	281
8-9 Values of $\text{Re}(k_x0)$ and $\text{Im}(k_x0)$ That Results in the Minimum of the Transverse Resonance Equation.....	282
8-10 Open Trough Geometry Filled with a Permeable Material	283
8-11 Open Trough Structure Simulation in HFSS Showing the Integration Paths to Obtain the Magnetic Current	284
8-12 β Plot Obtained from Three Different Methods for a 3.8'' by 1.053'' Open Trough with $\mu = 80, \epsilon = 2$	285
8-13 α Plot Obtained Three Different Methods for a 3.8'' by 1.053'' Open Trough with $\mu = 80$ and $\epsilon = 2$	285
8-14 β Plots of a 1''by1'' Trough with $\mu = 40$ and $\epsilon = 3.2$ Using HFSS and Transverse Resonance Method.....	287
8-15 β_{x0}/β_0 Plots of a 1.053'' by 8.3'' Trough with $\mu = 80$ and $\epsilon = 2$	288

Figure	Page
8-16 β_{xmed}/β_{med} Plots of a 1.053" by 8.3" Trough with $\mu = 80$ and $\varepsilon = 2$	288
8-17 Plot of kz/k_0 and the First and Second Derivative Showing That the Zero Crossing of the Second Derivative Can Be Used as an Approximate Measure of Defining the Minimum Frequency of Accountability of the Transverse Resonance Method	289
8-18 β_{x0}/β_0 Plots of a 1" by 1" Trough with $\mu = 40$ and $\varepsilon = 3.2$	290
8-19 β_{xmed}/β_{med} Plots of a 1" by 1" Trough with $\mu = 40$ and $\varepsilon = 3.2$	290
8-20 Plot of the Second Derivative of a kz/k_0 of 1" by 1" Trough with $\mu = 40$ and $\varepsilon = 3.2$ Showing That the Zero Crossing of the Second Derivative Can Be Used as an Approximate Measure of Defining the Minimum Frequency of Accountability of the Transverse Resonance Method	291
8-21 Two Open Trough Structures with Different Permeabilities and Cross Sections While Having the Same Cross Section Area Times the Permeability.	292
8-22 Beta Plots of the Two Geometries with the Same $\mu \cdot vol$ Showing That the Rules Found Before Holds in the Transverse Resonance Method for Frequencies Higher Than the Reliable Frequency	292
8-23 Geometry of the Slitted Trough Where the Slit Adds a Capacitance Term	293
8-24 Inverse Velocity ($\beta/2\pi$) Plot for a 1.053" by 3.8" Open Trough with $\mu = 40$, $\varepsilon = 3.2$ Shown in Red and the Same Plot for a 0.67" by 3.8" Slitted Trough with the Same Material and a 0.335" Slit Shown in Black.....	302

Figure	Page
8-25 α Plot for a 1.053” by 3.8” Open Trough with $\mu = 40$, $\varepsilon = 3.2$ Shown in Red and the Same Plot for a 0.67” by 3.8” Slitted Trough with the Same Material and a 0.335” Slit Shown in Black.....	303
8-26 Inverse Velocity ($\beta/2\pi$) Plot for a 1.053” by 3.8” Open Trough with $\mu = 40$, $\varepsilon = 3.2$ Shown in Red and the Same Plot for a 0.67” By 3.8” Slitted Trough with the Same Material and A 0.335”Slit Shown In Black and the Same Plot for a 0.67” by 5.972” Slitted Trough with the Same Material and a 0.595” Slit Shown in Magenta.....	304
8-27 A Plot for a 1.053” by 3.8” Open Trough with $\mu = 40$, $\varepsilon = 3.2$ Shown in Red and the Same Plot For a 0.67” by 3.8” Slitted Trough with the Same Material and A 0.335” Slit Shown in Black and the Same Plot for a 0.67” by 5.972” Slitted Trough With the Same Material and a 0.595” Slit Shown in Magenta	305
8-28 Geometry of a 5”by 0.8” Slitted Trough Simulated in HFSS and Showing the Integration Lines	306
8-29 β Plots of a 5”by 0.8” Slitted Trough Obtained Using Fullwave HFSS Simulation and Transverse Resonance Method	307
8-30 Inverse Velocity ($\beta/2\pi$) Plot for a 1.053” by 3.8” Open Trough with $\mu = 40$, $\varepsilon = 3.2$ Shown in Black and Inverse Velocity ($\beta/2\pi$) Plot for the Same Dimensions and CZN Material Filling.....	309

Figure	Page
8-31 Inverse Velocity ($\beta/2\pi$) Plot for a 1.053” by 3.8” Open Trough with $\mu = 40$, $\epsilon = 3.2$ Shown in Black and Inverse Velocity ($\beta/2\pi$) Plot for the Same Dimensions and CZN Material Snoeked to 0.75GHz.....	311
8-32 Inverse Velocity ($\beta/2\pi$) Plot for a 1.053” by 3.8” Open Trough with $\mu = 40$, $\epsilon = 3.2$ Shown in Black and Inverse Velocity ($\beta/2\pi$) Plot for the Same Dimensions and CZN Material Snoeked to 0.5GHz.....	312
8-33 Inverse Velocity ($\beta/2\pi$) Plot for a 1.053” by 3.8” Open Trough with $\mu = 40$, $\epsilon = 3.2$ Shown in Black and Inverse Velocity ($\beta/2\pi$) Plot for the Same Dimensions and CZN Material Snoeked to 0.375GHz.....	313
8-34 Geometry of a 1.053”by 3.8” Open Trough Simulated in HFSS with Added Vertical Metal Walls Touching the Ground	315
8-35 Geometry of a 1.053”by 3.8” Open Trough Simulated in HFSS with Added Vertical Metal Walls and a 1mm Gap from Ground	315
8-36 β Plots of a 1.053”by 3.8” Open Trough with Homogenous Material, with Added Walls Touching the Ground and with Added Walls with a Gap to Ground	316
8-37 Magnitude of the Magnetic Current Versus Distance from Feed in Wavelengths for the Case of the Open Trough with Walls and the Case of the Open Trough without Walls Showing the Mode Filtering Effect of the Vertical Walls.....	317
9-1 (a) Open and Slitted Troughs Containing the Same Amount of Material of Relative Permeability 40 (b) Phase Velocity of Both Troughs Showing the Slope of the	

Figure	Page
Slitted Trough's Curve Is Much Shallower Than That for the Conventional Trough (c) Radiated Power Versus Frequency for Both Troughs	324
9-2 Example of a Frequency Selective Surface	325
9-3 Half of a Permeable Dipole Placed on a Conducting Surface, Fed by a Coaxial Transmission Line at its Center Loop.....	326
9-4 Geometry of an Antenna Consisting of a Permeable Material Surrounded by a Rectangular Metal Enclosure with a Slit at the Top	326
9-5 Front View, Top View, and Equivalent Circuit of Inductive Strips which Are Infinitely Extended Plane Grating Formed by Metallic Strips of Zero Thickness with Edges Parallel to the Electric Field and the Plane Wave in Free Space Incident at Angle θ [35]	327
9-6 (a) Transmission Line Model of the Nearly Pure Capacitance of the Slitted Plane (b) Parallel Solenoid Modeled as a Shunt Inductor-Capacitor (LC) Series Circuit	328
9-7 (a) Photograph of the First Version of the Spiral Fed by a 4-Loop Parallel Solenoid (b) HFSS Models of the Same Structure with 4 Loops and 30 Loops and the Measured and Simulated Gain (c) Input Impedance and Smith Chart Representation	330
9-8 (a) HFSS Models of the 30 Loop Spiral in a Trough Geometry (b) Comparison Between the Peak Gain of the Spiral on Ground and the Spiral in the Trough Geometry (c) S11 of the Trough Spiral and the Smith Chart Representation Showing a Very Large Operational Bandwidth from 50 MHz to 550 MHz	331

Figure	Page
9-9 (a) Ferromagnetic Artificial Materials Resulting from Alternating Thin Metal Films with Thin Insulating (b) Composite Material Used as a Substrate	334
9-10 (a) Laminate Material Blocking the Flow of the Eddy Currents (b) Solid Ferromagnetic Material Allowing the Eddy Current to Flow.....	336
9-11 (a) TE01 Mode Fields Shown for the Case of Laminate Plate Parallel to the Ground Plane (b) Fields Shown for the Case of Laminate Plate Perpendicular to the Ground Plane.....	337
9-12 TEM Parasitic Mode Shown in the Horizontal and Vertical Laminates Showing that the Vertical Laminate Structure Has a Built-in Mode Filter Against This Traveling TEM Wave Mode. The Red “Arrow Points” Indicate the Desired Magnetic Field (Magnetic Current).....	339
9-13 TE01 Rectangular Mode for Horizontal and Vertical Laminates Showing That the Horizontal Laminates Short Out This Desired Electric Field.....	340
9-14 Trough Geometry with the Vertical Metal Plates Showing That the Vertical Metal Plates Suppress the Side to Side Propagation of the Higher Order TE21 Mode ...	342
9-15 Flow Graph of the Design Procedure of the Optimum Flux Channel	349
A-1: Electric Dipole Carrying an Alternating Electric Current and Its Electromagnetic Dual Which Is the Magnetic Dipole (in This Case Modeled as Rods).....	362
A-2. Relative Permeability (Left, Unitless) and Corresponding Heaviside Magnetic Conductivity (Right, in Ohms/Meter) of a Typical High Frequency Ferromagnetic Material ($\mu_{\text{initial}} = 450$).....	364

Figure	Page
A- 3. A Schematic of a Network with Two Accessible Terminals.....	372
A-4. Two General Types of Antennas. (a) Dipole Antenna (b)Loop Antenna.....	373
A-5. Sketch of the Idealized Antennas Considered in This Analysis. (a)Electric Dipole Antenna (b)Magnetic Dipole Antenna.....	374
A- 6. The Fields of the Electric Dipole Antenna, Magnetic Dipole Antenna and the Loop Antenna Normalized to the Fields on Their Surface Is Plotted in the Same Figure as the Induced Current in Each of These Antennas Normalized to the Source Current. The Distance Between the Antennas Has Been Change from 5mm to 40 mm with 5mm Steps. The Normalized Fields of the Three Different Antennas are the Same But Using a Pair of Magnetic Dipole Antennas Results in a Four Order of Magnitude Improvement in the Mutual Coupling, Eight Order of Magnitude Improvement on Power Transfer, When Compared to the Conventional Electric Dipoles and Loops.	384
A-7. Top View of the FDTD Domain Used to Analyze Two Coupled Micro-Antennas	393
A-8. Time Domain History of the Interaction Between the Antennas When the First One Is Excited by an Impulse. (a) Current in the Source Antennas Where Blue Shows the Electric Dipole and Red Shows the Magnetic Dipole. (b) Current in the Second Antennas Where Blue Shows the Electric Dipole and Red Shows the Magnetic Dipole.....	395
A-9. Frequency Domain Induced Current on the Second Antenna	396

Figure	Page
B-1 Infinite Magneto Dielectric Rod Showing the Current Band at the Origin	401
B-2 A Plot of the Real Part of $-K_{1x}/xK_{0x}$	407
B-3 A Plot of the Imaginary Part of $-K_{1x}/xK_{0x}$	407
B-4 A Plot of k_{p0a} Versus Normalized k_z	408
B-5 Plot of the Common Term Before the Pole Appears for $k_z > k_0$ at 30 MHz, 110MHz, and 170MHz	410
B-6 Plot of the Common Term After the Pole Appears for $k_z > k_0$ at 210 MHz, 300 MHz, and 350MHz	411
B-7 Plots of the Common Term at 188MHz, 210MHz, 300 MHz, and 350 MHz, After Adding Some Loss and Changing μ_r from 80 to $80-j0.1$, to See the Appearance of the Surface Wave Pole and Its Behavior at Higher Frequencies	414

CHAPTER 1

INTRODUCTION

“It is of great advantage to the student of any subject to read the original memoirs on that subject, for science is always most completely assimilated when it is in the nascent state.”

James Clerk Maxwell

There is an ever growing need for broadband conformal antennas to not only reduce the number of antennas utilized to cover a broad range of frequencies (VHF & UHF) but also to reduce the visual and RF signatures associated with communication and radar systems. The general understanding of an antenna is a device, usually metal, that is used to transmit or receive signals. In metal antennas, the wave's electric field is attached to the surface of the wire and the wave is sufficiently bound to be guided close to the speed of light. When the wave reaches the end of the antenna, let's say a metal dipole, it will reflect partially and radiate substantially. In penetrable antennas, meaning dielectric or magnetic antennas, there are two different mechanisms of radiation. If the cross section of the penetrable material is large enough, the wave can actually be trapped inside the material as a slow wave. In that case when the trapped wave reaches the end of the structure it is strongly reflected and radiates weakly. However if the cross section of the penetrable material is not large enough to trap the wave then the wave is weakly bound and therefore the wave leaks as it moves along the length of the structure. The wave that reaches to the end of the antenna radiates similar to the metal antenna.

Previously used conformal metallic antennas have narrow bandwidth and low efficiency because their radiation source is an electric current. Since these antennas are mounted on a conducting ground plane, the electric current parallel to the surface fights the opposing image current caused by the mentioned ground plane. But if instead of the electric current, the primary source of radiation is a magnetic current, as in the case of antennas with very high permeabilities, then by mounting these antennas on a conducting ground plane there will be no loss of gain or efficiency. The radiating magnetic current of these antennas, which we call true magnetic ($\mu_r \gg 1, \epsilon_r > 1$) antennas, will be aided by the image current produced by the metallic ground plane.

As seen in the figure, the image of the magnetic current in the permeable antenna does not oppose the radiation magnetic current since they point in the same direction however the image of the electric current in the metal antenna opposes the radiating electric current unless the distance between the metal antenna and metal ground plane is so large that the antenna is no longer considered conformal

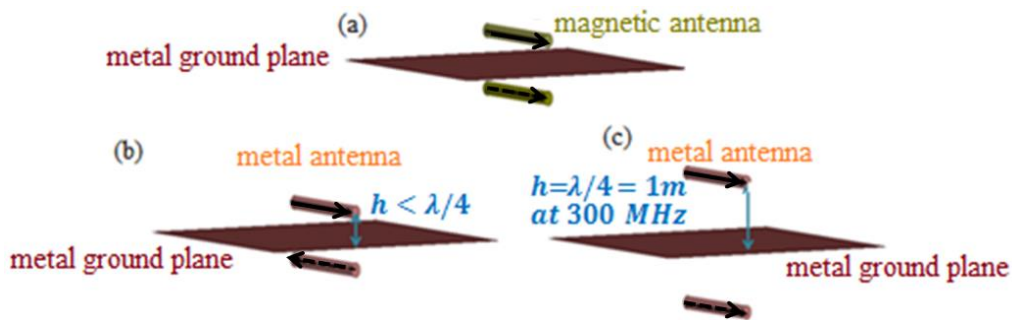


Fig. 1-1 (a) Conformal Permeable Antenna Showing That the Current and the Image Current Are Constructive. (b) Metal Antenna Close to a Ground Plane Showing Destructive Image Current (c) Metal Antenna Having a Large Distance From the Ground Plane in Order to Have a Constructive Image Current.

The importance of permeable antennas ($\mu_r > \epsilon_r$) is that they can outperform metal (and dielectric) antennas in low impedance environments such as conformal to a metal surface, adjacent or inside the human body, immersed in water, or inside the earth.

Since the human body is a low impedance material, permeable antennas, as small as tens of microns, can be used inside the body (brain) [1] and achieve up to 80dB higher gain than metal alternatives. They can also be placed close to the body and be used as a belt antenna therefore eliminating the need for carrying standard tall whip antennas while having a better performance [2] .

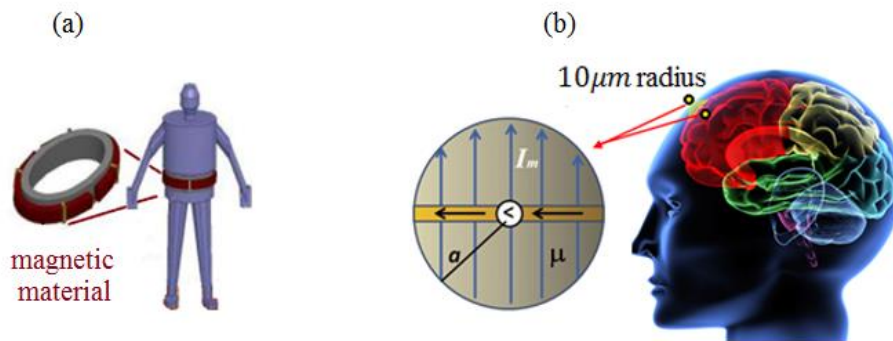


Fig. 1-2 (a) Body Wearable Magnetic Belt Antenna [2] (b) Micron Size Magnetic Antenna Embedded Inside the Brain for Neuronal Telemetry.

Most importantly, permeable antennas can be placed in close contact with a metal ground plane without degradation of performance which solves the problem of electrically small conformal communication. This means that permeable antennas can be placed on top of HUMVEEs instead of very long whip antennas. They can be mounted on airplanes and they can be used to build very wideband spirals with high gain.

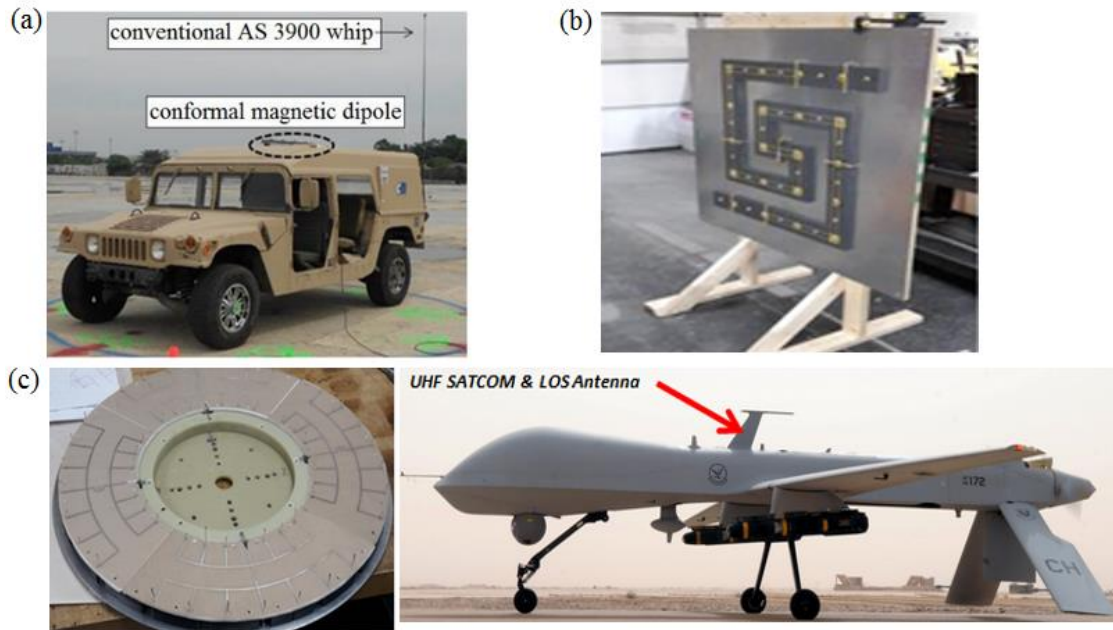


Fig. 1-3 (a) 1.5” Thick Magnetic Dipole on Top of an HUMVEE Instead of a 6 Foot Whip Antenna [2] (b) Magnetic Spiral Antenna Built Out of Ferrite Tiles (c) Extremely Thin Magnetic Conformal Antenna Mountable on an Airplane.

When a “high impedance” magneto-dielectric material is used as an antenna, it can be thought of as a magnetic conductor carrying magnetic currents through the dB/dt term in Maxwell’s curl equations.

The question that needs to be answered at this point is: Why have magnetic antennas not been extensively used before? As pointed out by Sebastian [2], the reason is based on a wrong assumption by Rumsey and DeVore [3, 4] that led to the misconception that the radiation efficiency of antennas would be reduced by the loss tangent of the permeable material. We will prove that the loss tangent does not necessarily cause a reduction in the antenna efficiency and by knowing this fact we will demonstrate different instances of permeable antennas ranging from conformal antennas mounted on

vehicles and airplanes to spirals and in vivo antennas. Novel feeding techniques will be presented and the optimum magnetic flux channel will be introduced and studied in detail as the next generation of magneto-dielectric antennas. The dissertation covers all these subjects in 9 chapters and an extensive appendix. An abstract of the chapters are as follows.

In chapter 2, the subject is introduced by first summarizing the work of Sebastian [2] where magnetodielectric antennas were modeled in closed form by using Schelkunoff's electrically-small-antenna models. Including realistic dispersive permeabilities, common in magnetic materials, in the model he showed that the radiation efficiency of permeable antennas is predominantly a function of the volume of the permeable material and the peak Heaviside magnetic conductivity in its permeability spectrum. Sebastian's model is then expanded by obtaining a first approximation to the input impedance of linear magneto-dielectric dipoles with the aid of fullwave simulations (using ANSYS HFSS). Using this model of the input impedance it is then possible to compare like-to-like a conformal magnetodielectric dipole and a conformal metal dipole constrained to fit within the same volume on the surface of a conducting ground plane.

Using as an example a 1 meter long antenna operating from HF to VHF, it is proven that the magnetodielectric antenna attains an Efficiency Bandwidth Product (EBWP) at least 10dB higher than the corresponding metal antenna over the band. Then, using the Best-Yaghjian formalism it is shown that these antennas are easier to match and can attain wider bandwidths than equivalent conformal metal antennas.

In chapter 3, a conformal permeable toroidal antenna operating in both a vertically polarized monopole mode and circularly polarized (CP) dipole mode in the UHF frequency range is designed based on the principles of magneto-dielectric radiators elucidated in chapter 2. The permeable material for this antenna is a new advanced ferromagnetic laminate composite material whose high impedance and anisotropic properties support the desired radiation via magnetic currents. Given the measured dispersive permeability of the material and the desired Gain, a radiation efficiency equation heuristically based on the linear dipole equation from chapter 2 was used to determine the approximate toroid diameter and cross section. Thereafter using fullwave tools (ANSYS HFSS) the dimensions of the antenna were fine tuned to maximize the Peak Gain while minimizing is ripple over the band.

The final manufactured antenna is less than 0.5 m in diameter and less than 2 cm thick. Its performance was verified in an antenna chamber by our customer (JEM Engineering) by feeding it with a simple mode former using commercially available components. Including the imperfections of the feed network and the performance of the simple matching scheme, the antenna is shown to operate from 200MHz to 500MHz with an input match of better than -10dB, CP dipole realized gain as high as +2dBi and monopole mode vertically polarized gain as high as -1 dBi.

The success with this antenna demonstrator provided empirical proof that these magnetodielectric antennas indeed constitute a new family of high Gain and wide bandwidth antennas with a huge potential impact in wireless communication in the difficult long wavelength frequencies ranging from HF through UHF. These frequencies

are of importance both to Defense applications and City and State safety and security applications since these bands of frequency are also used by Fire and Police Departments.

However, to fully exploit this potential requires the ability to design these antennas from first principles. Design by repeated fullwave simulation is not acceptable, not even when such “design” is carried out by using a (super) computer with brute force optimization. In such an approach, there is no way to know whether the solution obtained is indeed the best solution or just a local minimum found by the optimizer within the bounds of the rules it was given. The rules must be derived first. Therefore there was a clear need to develop a complete analytic theory of these antennas that could be reduced to practical rational design rules that the engineer can use to create the magnetodielectric antenna solution for the given application.

Chapter 4 is then the demonstration that we now have a solid foundation for the new field of *Magnetodielectric Antenna Theory and Design*. In this chapter, a model of the input impedance of the toroidal permeable antenna, which is the dual of the conventional metal loop antenna, is derived, starting from Schelkunoff’s transmission line description of the loop antenna instead of the electrically-small-limit model. This antenna, as seen in chapter 3, operates in both the monopole mode and circularly polarized dipole mode and is constructed from a torus of high permeability material.

Since the ultimate goal of having an antenna’s input impedance model is to enable the derivation of its best matching network; the input impedance is expressed in its widest band most general form as a frequency independent resistor terminating a reactive network which is called the Darlington form. Because such a circuit mimics closely the

input impedance of the dipole modes of the spherical mode expansion, it is a much better model of the antennas as we go beyond the electrically small limit. The feed loop contribution is explicitly accounted for and the closed-form equation results are compared with fullwave simulations of a typical toroidal antenna operating in both monopole and circularly polarized dipole mode showing excellent agreement well beyond the electrically small limit.

As briefly mentioned in the initial paragraph of this Introduction, permeable materials do not necessarily bind the electromagnetic wave the way a metal wire or surface does. Therefore to “force” these conformal magnetodielectric antennas to behave as near-perfect duals of metal antennas in free space, the way the permeable flux channel contains the B-field needs to be engineered. As a minimum, based on Sebastian’s original guidelines, this is guaranteed in the initial design by selecting the size of the cross section of the channel such that the onset of the lowest order guided (and radiating) mode (TE₀₁) within the magnetodielectric material occurs inside the band of operation not too far below its upper edge. If the onset occurs too low in the band, the waves can become too strongly trapped in the material at the high frequencies and will not radiate. If the onset is set too high, then the wave leaks out of the material at the low frequencies and the effective length of the antenna is much smaller than its physical length. Peak performance is obtained when the magnetic current inside the antenna uses the full length of the antenna over the whole frequency band. That is, we want to maintain the magnetic flux contained within the flux channel at all frequencies without trapping it into a slow wave.

As Sebastian showed, an engineering trade-off that accomplished this to a degree is to feed the antenna with multiple loops. However multiple independent feeds then require a feed network (under the antenna ground plane) that distributes the energy from the source's desired one feed point to the several loops. A better solution is the novel distributed feed network we call the parallel solenoid.

Chapter 5, introduces this new kind of electric feed configuration for permeable antennas that maintains the magnetic current as uniform as possible inside the flux channel while being fed at only one point and incurring none of the deleterious phase delay effects that occur when a ferrite rod is fed by a conventional solenoid winding.

The importance of the feed network for magnetic antennas is explained in detail and it is mentioned how this feed configuration can overcome the problems of conventional feeds. We will see in this chapter that it was using this structure that enabled the toroidal antenna of chapter 3 to attain its maximum bandwidth and peak Gain. This proposed solenoid feed will enhance the performance of any permeable antenna that needs a flux binding mechanism. At the same time, the mentioned novel feed can be used as an impedance tuning mechanism to achieve the particular impedance bandwidth goals of the design.

A key property of the parallel solenoid feed is that it helps bind the magnetic flux to the permeable channel at the low frequencies (preventing leakage) while at the same time allowing efficient radiation at the high frequencies. This happens because the parallel solenoid is itself a frequency dependent structure that can be used to play-off against the frequency dependence of the channel (its surface wave onset properties) to

obtain a nearly-uniform amplitude traveling current along the channel over the broadest possible frequency band. The acid test for this claim is to design a magnetodielectric traveling wave antenna. The most severe test of all is to design a frequency independent magnetodielectric antenna, namely a spiral, because it is known that the ultrawideband performance of spirals hinges on them carrying a uniform amplitude traveling wave near the speed of light over the entire band.

In chapter 6, we demonstrate a magnetic Archimedean spiral antenna as another example of a permeable conformal wideband antenna and show the useful feature of the parallel solenoid feed for this specific antenna. It is shown that a wideband and high gain spiral antenna can be designed and built with NiZn absorber tiles as long as a flux binding mechanism is present. It is proven in this chapter that by adding the parallel solenoid feed to the magnetic spiral antenna we could get high gain and efficiency, frequency independent behavior resulting in a very good VSWR, and a good axial ratio, with a bandwidth of 11:1 (only limited by the dimensions of the spiral).

The key role of the propagation properties of the magnetic flux channel is then addressed in Chapter 7 where again the goal is to derive an analytic model with design rules that the engineer can use to design traveling wave antennas and therefore extend the theory to the most general types of magnetodielectric antennas needed in practical applications. This development is the first step into achieving the optimum permeable flux channel for all magnetodielectric antennas. The metallized trough channel is introduced as the natural evolution of the previous work.

The ultimate goal in designing magnetic antennas is to have an antenna that can be absolutely conformal to the aerodynamically designed outer mold-line of its platform while maximizing the strength of the magnetic current in the flux channel and at the same time pulling the guided wave at the TE₀₁ onset towards the surface of the channel over the widest possible frequency range ensuring propagation of the wave near the speed of light. These goals are accomplished by using the trough and the slitted trough. Source excitation, flux binding, tailoring of the frequency response of the guiding surface are attained while the structures becomes completely conformal to any surface. A fullwave analytic Green function formulation for the trough is developed and used for this study in this chapter.

In chapter 8, the optimum flux channel is studied further by focusing on its omega-beta diagram. The leaky wave and guided wave regimes of these antennas are demonstrated. Two additional methods of obtaining the dispersion diagrams are presented and it will be shown that the transverse resonance method is a very fast and easy method to obtain the dispersion diagram and it is accurate in the frequency range where it is needed: around the onset frequency. An estimate is derived of the minimum frequency that the TRM method can be trusted to yield correct data on the leaky wave behavior of the channel. Below that frequency, we can either use a fullwave simulation to obtain the results or use the Green's function method. This chapter will give a full understanding of the dispersion diagram of flux channel structures in order to come up with a methodology and proper tools for designing an optimum flux channel

Chapter 9 serves as a detailed discussion leading to a design flow graph to obtain the optimum flux channel based on all the studies on how the geometry and the material properties can be used to flatten the $\omega - \beta$ diagram about onset to obtain the maximum operating bandwidth. The previous chapters had given us hints all along of what was required to design the optimum flux channel: These are now discussed explicitly: using a change in the cross section geometry of the channel, adding the slit, the role of the parallel solenoid, using a material with certain properties that would make the antenna resemble a PEC antenna, or even adding vertical metal walls to the material to artificially cause anisotropy. This chapter contains a full discussion and a summary of all these methodologies and gives full design guidelines for an optimum flux channel.

As a detailed appendix we demonstrate a very interesting application of the magnetic antennas which is the ability to use micron sized magnetic antennas for radio frequency neuronal telemetry. It is shown that magnetic antennas are the solution to not overheating the brain tissue and having very low SAR levels. We will see that true magnetic antennas combine the best characteristics of dipoles and loops and by calculating the coupling between identical magnetic antennas inside a model of the body medium we show an increase in the power transfer of up to 8 orders of magnitude higher than could be realized with the loops and dipoles, making the microscopic RF in-vivo transmitting antenna possible.

CHAPTER 2

WHY THE MAGNETIC LOSS TANGENT IS NOT A RELEVANT CONSTRIANT FOR PERMEABLE CONFORMAL ANTENNAS

*“No amount of experimentation can ever prove me
right; a single experiment can prove me wrong.”*

Albert Einstein

2.1 Introduction

An error based on a false assumption in the 1950’s, and perpetuated through re-derivation in the 1970’s, has hindered the modern use of the “ferrite rod” antenna family under the expectation that someday lower loss magnetic materials might be developed. Nevertheless, within the last five years several investigators have included ferrite materials in fullwave simulations of antennas [5, 6] and have observed unexpected levels of efficiency. The purpose of this chapter is to disseminate to the antenna engineering community at large the explanation for those results and to provide the foundation for the general theory of such magneto-dielectric antennas, specifically when such antennas are applied as conformal antennas or as antennas immersed within low impedance media [1, 7] (e.g. under seawater or inside the human body.)

This chapter is based on our paper: Tara Yousefi, Tom Sebastian and Rodolfo E. Diaz, "Why the Magnetic Loss Tangent Is Not a Relevant Constraint for Permeable Conformal Antennas," *IEEE Trans. Ant. Propag.*, vol. 64, no. 7, pp. 2784-2796, 2016.

In addition, in this chapter we introduce the subject of magneto-dielectric antennas by summarizing the work of Sebastian [2]. In the referenced dissertation magnetodielectric antennas were modeled in closed form by using Schelkunoff's electrically-small-antenna models. These models included realistic dispersive permeabilities and showed that the radiation efficiency of permeable antennas is predominantly a function of the volume of the permeable material and the peak Heaviside magnetic conductivity in its permeability spectrum. We will see this in detail in this chapter and a comparison of a conformal magnetodielectric dipole and a conformal metal dipole constrained to fit within the same volume on the surface of a conducting ground plane will be presented which can also be found in the referenced dissertation [2].

This latter point, the application to antennas conformal to a conducting surface, is key to this discussion; particularly when the efficiency of a permeable antenna is compared to that of an equivalent metallic antenna constrained to operate in the same conformal volume.

Starting from Schelkunoff's [8] electrically small antenna model, where the Inductance, Capacitance, and Radiation Resistance of the external electromagnetic fields of the antenna are represented by circuit elements, a closed-form model for a penetrable material antenna (i.e. not made from a conductor but from a dielectric) is obtained by accounting for the internal electromagnetic fields as an additional impedance placed in series with the external one. A similar technique has been applied before by R. W. P. King to model resistive dipoles [9]. The resulting circuit model of the input impedance of this dielectric antenna is then used to derive the circuit model for the input impedance of

its dual, the permeable rod antenna. The form of the circuit is such that the radiation efficiency can be derived immediately in closed form in terms of the geometric parameters of the antenna and its dispersive (frequency dependent) permeability.

The first important result arises from comparing this efficiency to that obtained by Rumsey [3] and DeVore [4] for the ferrite dipole. It is seen that because Rumsey assumed a priori the requirement for low loss ($\mu'' \ll \mu'$) his resulting efficiency equation obtains a term in the denominator of the form $\mu''/|\mu'|^2$ which then leads to the conclusion that the only way to maximize efficiency by reducing this term is to minimize μ'' , that is, reduce the loss tangent. By contrast, the correct efficiency equation derived under no a priori assumption has in the denominator the term $\mu''/\{|\mu'|^2 + |\mu''|^2\}$. Immediately we see that another way to minimize this term is to have a very large μ'' , that is, very large loss tangents would obviously also lead to high efficiency. This is not surprising since, taking the argument to the limit, a Perfect Magnetic Conductor (PMC) is as lossless as a Perfect Electric Conductor (PEC.)

Section 2.2 is concluded by showing a plot of efficiency contours versus the real and imaginary parts of the permeability for a given antenna at a given frequency to show that large useful regions of the complex permeability plane have remained unexplored to date in the search for antenna materials simply because of the long-standing misconception caused by an unwarranted assumption back in the 1950's.

In Section 2.3 the efficiency equation from Section 2.2 is further simplified by acknowledging that all permeable materials are lossy because they are dispersive, and that dispersion must satisfy the Kramers-Krönig [10, 11] relations. Therefore, considering

the two prototypical physically realizable materials, the Debye relaxation and the Lorentz resonance, the frequency dependence of the term $\mu''/\{|\mu'|^2 + |\mu''|^2\}$ is explicitly evaluated. The result is a startling simplification that shows this frequency dependent function reduces to a constant of the material times the frequency. And this constant of the material contains Snoek's [12] Product, well-known among permeable material experts as a fundamental constant that characterizes families of materials.

A consequence of this result is the “material selection rule” that, given the geometric constraints on the antenna (occupied volume) and the desired radiation efficiency, reveals the family of materials (Snoek's product) that will meet the requirements. Conversely, given a material, the dimensions of the antenna required to attain a given radiation efficiency are determined. These results, derived in the electrically small limit are actually valid up to moderate dimensions (over a wavelength) as shown by fullwave simulations. A further consequence of these results is that since the efficiency is fixed by the material family, the engineer is free to choose which specific member of the family to use for the application; and the obvious choice that attains maximum bandwidth is the member that exhibits the highest μ'' in the band of use. Fullwave simulations also verify these results.

The phenomena that arise when the antenna is no longer electrically small, and especially when the interior of the antenna can support surface waves, are discussed in the reference dissertation [2] but are not addressed in this paper and left for a future communication. For many applications, such effects are not relevant because the presence of material loss tends to push the electromagnetic fields to the exterior of the

material as frequency increases and thus the trapping of waves is avoided by judicious choice of the material.

In Section 2.4 the application of these antennas to the problem of electrically small conformal communication antennas is specifically addressed. Because the radiating currents of these antennas are the magnetic polarization currents in the material, these antennas are true duals of conventional electric current antennas. They can be placed in intimate contact with a metal ground plane or immersed in a low impedance medium without degradation of performance. Experimental results from recent publications validating the theory derived here are discussed.

In Section 2.5 we compare the Efficiency Bandwidth Product (EBWP) of conformal permeable antennas to that of metal antennas constrained to the same conformal volume. It is shown that the EBWP of the magnetic antennas can far exceed that of the metal antennas when the loss in the materials (permeable materials and copper) are considered. The reason for this result is the extreme degradation of the Radiation Resistance of electric current antennas tangent and proximate to a metal ground-plane due to the induced opposing images. For the same reason, the Match Bandwidth of the magnetic antennas is much larger, not because they are lossy but because their Radiation Resistance is unaffected by the ground-plane.

2.2 Closed Form Model of an Electrically Small Permeable Dipole

According to Schelkunoff [8], in the electrically small limit, the input reactance of a dipole antenna can be derived from quasi-electrostatic and quasi-magnetostatic

considerations. Combining those with the Radiation Resistance of an elementary dipole (triangular current distribution) we obtain the classic model of a small (metallic) cylindrical dipole antenna as a series LCR circuit. The circuit parameters are given in equations (2-1).

$$C_{an} = \frac{\pi\epsilon_0 \frac{l}{2}}{\ln\left(\frac{l/2}{\rho}\right)} \quad (2-1a)$$

$$L_{an} = \frac{\mu_0 \frac{l}{2}}{3\pi} \ln\left(\frac{l/2}{\rho}\right) \quad (2-1b)$$

$$R_{rad} = 20\pi^2 \left(\frac{l}{\lambda}\right)^2 = 5(kl)^2 \quad (2-1c)$$

Equations (2-1) denote the external radiation impedance of the antenna; external in the sense that all the fields of concern are outside the metal constituting the dipole.

If now the current flowing in this circuit is not flowing over the surface of a PEC cylinder but flowing through a penetrable dielectric cylinder (as conduction current, displacement current, or both) then to the same degree of approximation we can derive the internal impedance by assuming the electric flux density (d) is constant through the cylindrical rod so that the associated B field is purely azimuthal and given by the familiar expression for the B-field inside a current carrying wire. Thus, there are an additional Capacitance and Inductance in series given by equations (2-2a) and (2-2b), such that the internal material impedance to be added in series to the external radiation impedance is given by equation (2-2c). And therefore, the input impedance of an electrically small dielectric dipole is given by equation (2-2d).

$$C_{diel} = \frac{\epsilon_0(\epsilon_r - 1)\pi\rho^2}{l} \quad (2-2a)$$

$$L_{diel} = \frac{\mu_0(\mu_r - 1)l}{8\pi} \quad (2-2b)$$

$$Z_{mat_d} = j\omega L_{diel} + \frac{1}{j\omega C_{diel}} \quad (2-2c)$$

$$Z_{in_diel}^e = Z_{mat_d} + j\omega L_{an} + \frac{1}{j\omega C_{an}} + R_{rad} \quad (2-2d)$$

The resulting circuit model is shown in Fig. 2-1. The constitutive properties are understood to be complex and frequency dependent ($\epsilon'(\omega) - j\epsilon''(\omega)$; $\mu'(\omega) - j\mu''(\omega)$)

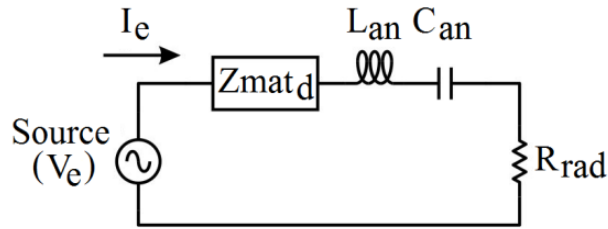


Fig. 2-1 Dielectric Dipole Model Based on Schelkunoff's Model of Electrically Small Metallic Antennas, Including the Dielectric Material's Impedance.

King and Wu used a similar argument to derive the properties of resistive antennas [9]. Having the input impedance in Ohms of a dielectric antenna it is straightforward to derive the dual magnetic input impedance in Mhos of the permeable antenna. This magnetic input impedance is what would be seen by a magnetic voltage source, V_m (in Amperes) driving a magnetic current, I_m (in Volts) into the antenna and it is obtained by invoking the duality of Maxwell's equations as suggested in equation (2-3). (When

applying duality, superscript m denotes a magnetic quantity while superscript e denotes the conventional electric quantity.)

$$Z_{in_perm}^m(1/\Omega) = \frac{V_m}{I_m} = \frac{Z_{in_diel}^e(\Omega)}{\eta_0^2} \Big|_{swap \ \varepsilon_r \leftrightarrow \mu_r} \quad (2-3)$$

The permeable dipole is fed by driving electric current through a loop at its center. In that case the magnetic voltage V_m is the current in the loop I_e , and the magnetic current I_m is the Voltage at the feed of the loop so that the magnetic input impedance is just the conventional Input Admittance seen at the feed of the loop which is the inverse of the impedance of its dual: the corresponding dielectric dipole. This is given by equation (2-4).

$$Y_{in_perm}^e(1/\Omega) = \frac{Z_{in_diel}^e(\Omega)}{\eta_0^2} \Big|_{swap \ \varepsilon_r \leftrightarrow \mu_r} \quad (2-4)$$

Immediately we obtain all the elements of the circuit model for the permeable antenna term by term as shown in equations (2-5). Since for the dielectric dipole all the elements were in series, for the permeable dipole, its dual, they appear in shunt.

$$Y_{mat} = \frac{Z_{mat}}{\eta_0^2} \Big|_{swap \ \varepsilon_r \leftrightarrow \mu_r} \quad (2-5a)$$

$$L_{MD} = \frac{C_{an}}{\eta_0^2} = \frac{\mu_0 \pi l / 2}{\ln\left(\frac{l/2}{\rho}\right)} \quad (2-5b)$$

$$C_{MD} = \frac{L_{an}}{\eta_0^2} = \frac{\epsilon_0 \pi l}{6\pi} \ln\left(\frac{l/2}{\rho}\right) \quad (2-5c)$$

$$G_{rad} = \frac{R_{rad}}{\eta_0^2} = \frac{20\Omega(kl)^2}{\eta_0^2} \quad (2-5d)$$

The subscript “MD” denotes this is a magneto-dielectric dipole. The end result is that now we have a circuit model for the loop-fed permeable dipole as shown in Fig. 2-2, under the assumption that the magnetic (polarization) current is uniform within the cylindrical rod’s cross section. (No skin effect is being assumed, although as reference [2] shows it can be added to the model.)

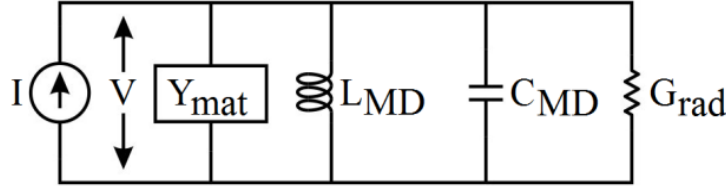


Fig. 2-2 Circuit Model for the Magneto-Dielectric Dipole Antenna

As shown in reference [2], the material admittance for the magneto-dielectric dipole takes the form shown in equations (2-6).

$$Y_{mat} = G_{mat} + jB_{mat} \quad (2-6a)$$

$$G_{mat} = \frac{1}{\frac{\omega \mu_0 \pi \rho^2}{l} \frac{\mu''}{|\mu_r - 1|^2}} + \frac{\omega \epsilon_0 \epsilon'' l}{8\pi} \quad (2-6b)$$

$$B_{mat} = -\frac{1}{\omega \frac{\mu_0 \pi \rho^2}{l} \frac{|\mu_r - 1|^2}{\mu' - 1}} + \frac{\omega \epsilon_0 (\epsilon' - 1) l}{8\pi} \quad (2-6c)$$

At this point it is trivial to calculate the Radiation efficiency because the radiation conductance, G_{rad} , is in parallel with the loss conductance, G_{mat} , terms involving ϵ'' and μ'' . It follows that the efficiency is given by equation (2-7).. Here we show the final expression in which for the sake of simplicity we ignore the dielectric loss.

$$e_{MD} = \frac{1}{1 + \frac{\mu''(\omega)}{(\mu'(\omega) - 1)^2 + (\mu''(\omega))^2} \frac{6}{\left(\frac{\rho}{l}\right)^2 (kl)^3}} \quad (2-7)$$

Comparing the result of equation (7) with Rumsey's and DeVore's results [3, 4] in equation (2-8), we see a significant difference. Because both Rumsey and DeVore assumed from the outset that the material had to be low loss, they made the approximation $\mu' \gg \mu''$ and the μ''^2 term in the denominator never appeared.

$$e_{Rumsey} = \frac{1}{1 + \frac{\mu''(\omega)}{(\mu'(\omega))^2} \frac{6}{\left(\frac{\rho}{l}\right)^2 (kl)^3}} \quad (2-8)$$

The missing term completely changes the conclusions drawn for this efficiency equation. It is at once apparent that the limit $\mu'' \rightarrow \infty$ of the PMC is included in equation (2-7) and is as expected 100% efficient.

Because of the duality of Maxwell's equations, the result in equation (2-7) for a permeable dipole is identical to its dual for a dielectric dipole, obtained by simply swapping μ for ε . However, dielectric dipoles are seldom ever considered (except perhaps as a corollary to the cited work of Wu and King [9]) because, for electric dipole antennas, metals are freely available. (After all, for a metal $\varepsilon'' \gg \varepsilon'$, and the radiation efficiency tends to 100%.)

Of course, for the metal case, a more accurate evaluation requires taking into account the skin depth effect. Since such an effect is second order for the permeable materials of interest we have omitted it even though it is contained in [2].)

Two important points that are not being addressed in the above development are the following:

(i) It should be clear that in this discussion we are not addressing penetrable antennas that are internally electrically large, as in the case of a dielectric resonator antenna. The theory and practice for such antennas is well understood; and it is obvious that if a significant amount of energy is to reside within a resonator then the imaginary part of the constitutive parameter must be much smaller than the real part to avoid wasting energy.

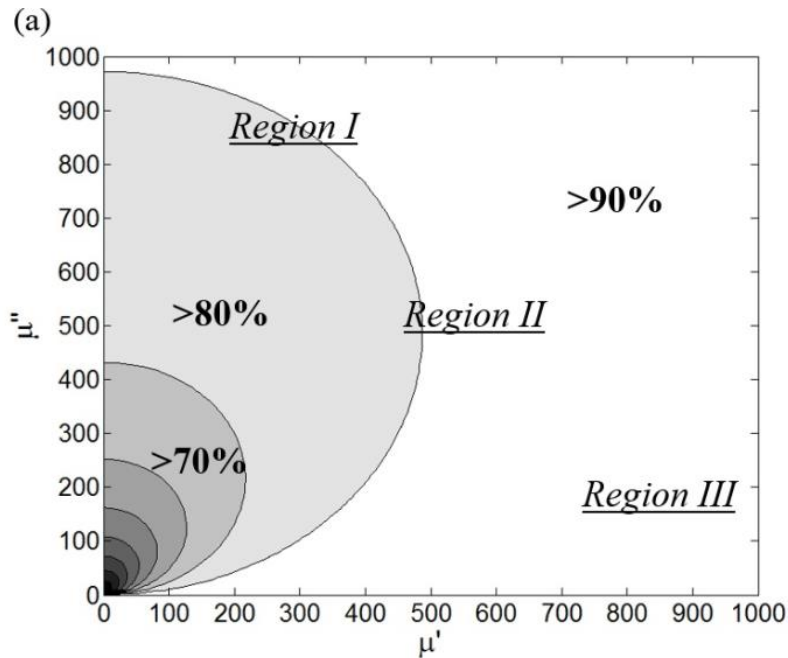
(ii) We have discussed a complete duality between dielectric and permeable antennas as the only means of creating true magnetic current radiators. The nonexistence of magnetically conducting media (because of the absence of freely moving magnetic monopoles) precludes enforcing strict duality to metal antennas at all frequencies.

To emphasize what the difference between equations (2-7) and (2-8) means regarding the choice of materials available to the engineer, we show in Fig.2-3 contours of the radiation efficiency for a 0.6m long dipole, 0.0254m radius¹, at 250MHz. The conventional wisdom that permeable materials must have a low loss tangent to be used in antennas structures, has been forcing engineers to look for materials in a low loss region, named Region III shown in Fig.2-3. But as shown in Fig.2-3(a) and Fig.2-3(b) a greater than 90% efficiency is possible with materials of moderate (Region II) and high (Region I) loss (μ'').

¹ Whenever possible, standard metric units have been used for showing antenna dimensions. However on occasion metric and English unit are both used since dimensions given by costumers have been in English units and we have not changed the costumer design specifications.

By comparing Fig.2-3(b) to Fig.2-3(c) it can be seen that Rumsey's and DeVore's equations show a very small region of efficiencies higher than 80% while the results obtained from our equations show that these efficiencies can be obtained over a much greater region of the μ' and μ'' space and at high loss tangents.

The physical reason for these results is the fact that the presence of loss in the material, forces the electromagnetic fields to the outside of the material, thus reducing the amount of power dissipated inside, but still providing a surface that tends to bind the wave and guide it along the length of the dipole to radiate the signal. Whereas the results of Fig. 2-3 are given for one specific antenna geometry at one specific frequency, equation (2-7) can be cast in a truly universal form applicable to all physically realizable permeable materials. This is the subject of Section III.



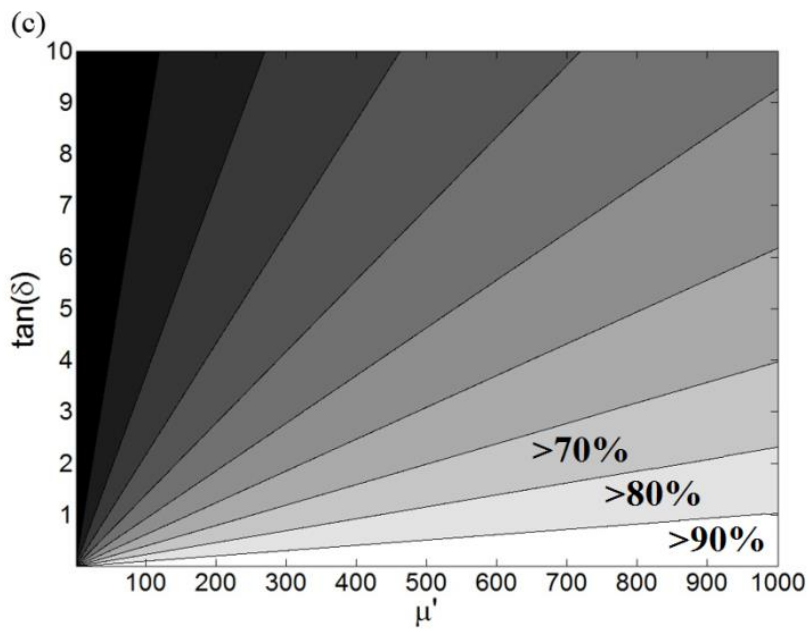
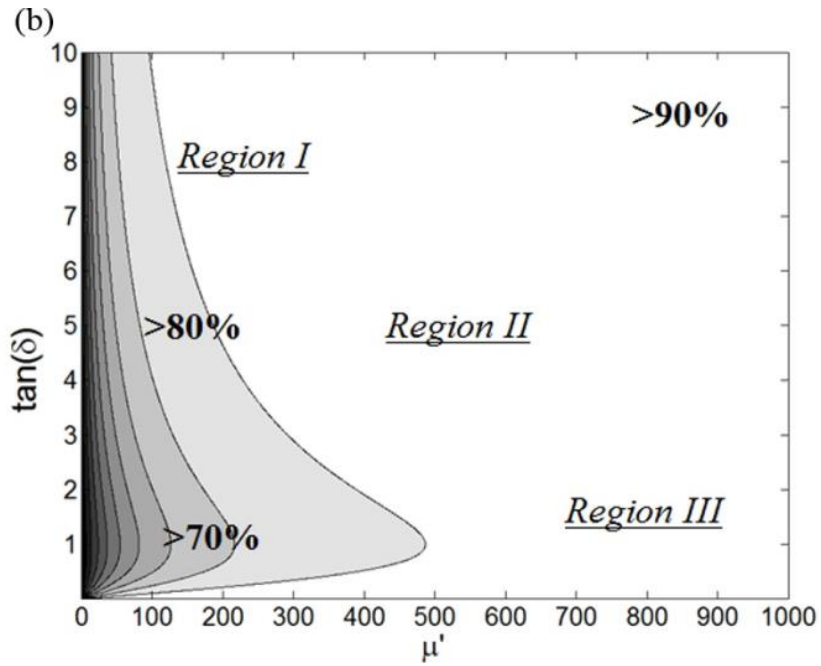


Fig. 2-3 Contours of Radiation Efficiency: Using Equation (7) Versus μ' and μ'' (a) and Versus μ' and $\tan(\delta)$ (b). The Three Regions Indicate Region of High Material Loss, Moderate Material Loss And Low Material Loss. For Comparison, Contours of Radiation Efficiency Using Equation (8) Versus μ' and $\tan(\delta)$ Are Shown in (c).

2.3 The Material Selection Rule

Because almost all realistic materials of interest for antenna applications obey the requirements of causality, linearity, passivity, and energy conservation, the frequency dependent permeability and permittivity must be analytic functions of a very precise nature that obey the Kramers-Krönig relations [10, 11]. Two classic examples of analytic functions that obey these relations, and are observed in the susceptibility spectra of ferromagnetic and ferrimagnetic materials, are a Debye function and a Lorentz function (equations (2-9), where $\mu_r = 1 + \chi$).

$$\text{Debye} \quad \chi_{Debye} = \frac{\chi_{DC}}{1 + j \frac{\omega}{\omega_0}} \quad (2-9a)$$

$$\text{Lorentz} \quad \chi_{Lor} = \frac{\chi_{DC}}{1 + j \frac{\omega}{\omega_0} \alpha - \left(\frac{\omega}{\omega_0}\right)^2} \quad (2-9b)$$

In these, ' χ_{DC} ' is the DC susceptibility, ' ω_0 ' is the relaxation frequency (or resonance frequency) and ' α ' in the Lorentz function is the damping factor

An example of these two susceptibility functions is given in Fig.2-4 with $\chi_{DC} = 75$, $\omega_0 = 2\pi(1.6GHz)$ and $\alpha = 0.8$ for the Lorentz function.

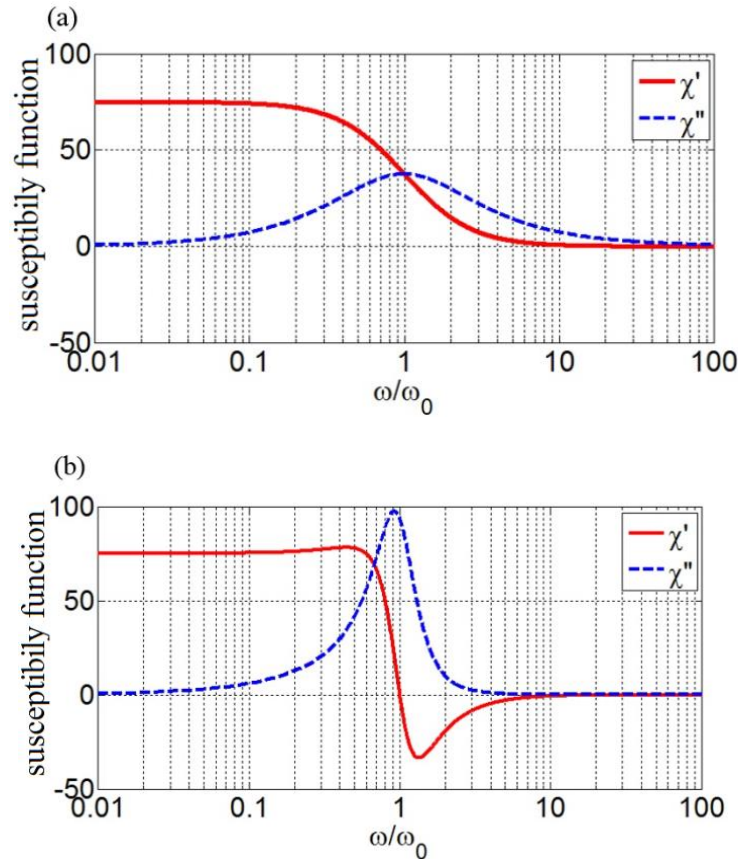


Fig. 2-4 (a) A Single Debye Susceptibility Function (b) A Single Lorentz Susceptibility Function

Because the susceptibility spectra of all permeable materials are in principle composed of a finite sum of these functions, we consider the two simplest cases, a material defined by a single Debye function and a material defined by a single Lorentz. The lessons learned can then be extended after that to the most general case.

The first point to be made is that the loss in frequency dependent permeable materials, due to the imaginary part of the permeability, is indistinguishable from the loss that would occur if the materials possessed magnetic conductivity. That is, since Heaviside defined the magnetic conductivity measured in ohms/meter as $\sigma_m = \omega\mu_0\mu''$, in complete analogy to the relationship between electric conductivity and ϵ'' , all the

results of metallic and dielectric antennas have their dual in permeable antennas as long as we never address the DC limit. (Since the experimental absence of magnetic monopoles precludes the existence of magnetic conductivity at $\omega=0$.)

We can then make use of the analytic conductivity function to understand the dispersion of the material as was done by Grant for dielectrics [13] . The real parts of the complex magnetic conductivity of the two materials of Fig. 2-4 are shown in Fig. 2-5.

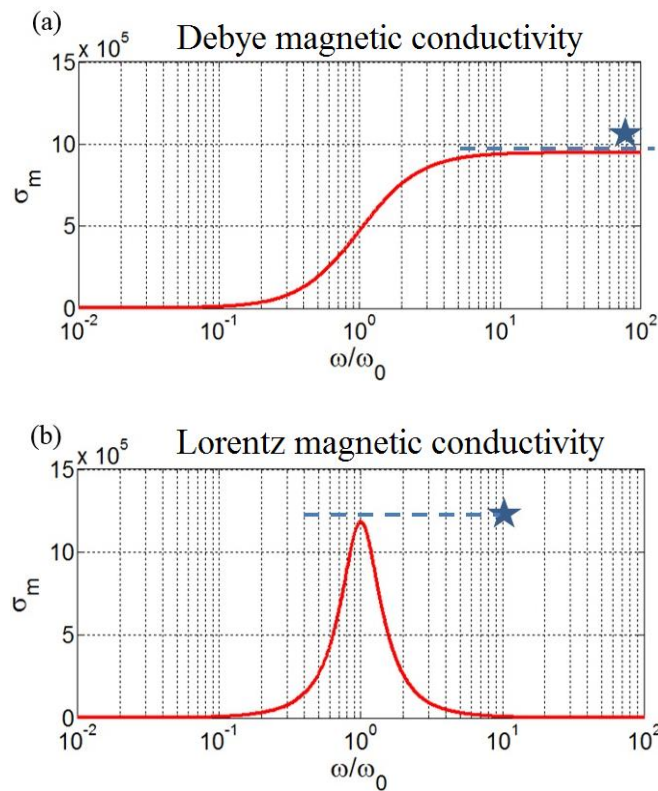


Fig. 2-5 Magnetic Conductivity of the (a) Debye and (b) Lorentz Examples

The star marker represents the ‘maximum magnetic conductivity’ in both the Debye and Lorentz curve. For a Debye equation, this maximum value is twice the magnetic conductivity at the relaxation frequency i.e. $2\sigma_m(\omega_0)$ and for the Lorentz

function, this value is equal to the magnetic conductivity at resonance i.e. $\sigma_m(\omega_0)$. We have given the term “hesitivity” (h_m) to this maximum conductivity and it is easy to show that it has a form given by equations (2-10) and (2-11) .

$$h_m(Debye) = 2\sigma_m(\omega_0) = \omega_0\mu_0(\mu_{DC} - 1) \quad (2-10)$$

$$h_m(Lorentz) = \sigma_m(\omega_0) = \frac{\omega_0\mu_0(\mu_{DC} - 1)}{\alpha} \quad (2-11)$$

We point out immediately that the hesitivity is proportional to the Snoek’s Product ($\omega_0\mu_0(\mu_{DC} - 1)$) [12] and therefore is also a fundamental quantity that characterizes families of magnetic materials. Materials that belong to the same family have the same hesitivity. For Debye materials, hesitivity and Snoek Product is identical. Table 1 shows typical Hesitivities of some magnetic material families.

Table 2-1 Typical Hesitivities of Microwave Materials

Material	h_m (Ω/m)
Air	0
Bulk NiZn ferrite	30,000
Co ₂ Z Hexaferrite (aligned)	280,000
CoFeSiB ferromagnetic metal alloy	2,175,000
CoZrNb ferromagnetic metal alloy	5,000,000

Now, in the efficiency equation (2-7) for a permeable dipole, the complex permeability appears in the very specific functional form of equation (2-12).

$$f(\mu) = \frac{\mu''(\omega)}{|\mu_r(\omega) - 1|^2} = \frac{\mu(\omega)''}{(\mu'(\omega) - 1)^2 + (\mu''(\omega))^2} \quad (2-12)$$

Let, $\mu' - 1 = \chi' = x$ and $\mu'' = \chi'' = y$. Therefore,

$$f(\mu) = \frac{y}{x^2 + y^2} \quad \text{or} \quad (2-13a)$$

$$x^2 + \left(y - \frac{1}{2f(\mu)}\right)^2 = \left(\frac{1}{2f(\mu)}\right)^2 \quad (2-13b)$$

The latter is the equation of a circle with center at $(0, 1/[2f(\mu)])$ and radius $'1/[2f(\mu)]'$.

For the Debye susceptibility function, the real and imaginary parts of the function can be separated as in equations (2-14).

$$\chi'_{Debye} = x = \frac{\chi_{DC}}{1 + \left(\frac{\omega}{\omega_0}\right)^2} \quad (2-14a)$$

$$\chi''_{Debye} = y = \frac{\chi_{DC} \left(\frac{\omega}{\omega_0}\right)}{1 + \left(\frac{\omega}{\omega_0}\right)^2} \quad (2-14b)$$

And it follows that,

$$y = x \left(\frac{\omega}{\omega_0}\right) \quad (2-15)$$

Substituting (2-14), (2-15) and (2-12) into (2-13b), we get equation (2-16a) that is immediately solved to give equation (2-16b).

$$x^2 \left[1 + \left(\frac{\omega}{\omega_0} \right)^2 \right] - x \frac{1}{f(\mu)} \left(\frac{\omega}{\omega_0} \right) = 0 \quad (2-16a)$$

$$x = \frac{\frac{1}{f(\mu)} \left(\frac{\omega}{\omega_0} \right)}{1 + \left(\frac{\omega}{\omega_0} \right)^2} \quad (2-16b)$$

Comparing (2-16b) and (2-9a) we get:

$$\chi_{DC} = \frac{1}{f(\mu)} \left(\frac{\omega}{\omega_0} \right) \quad \text{or} \quad \omega_0 \chi_{DC} = \frac{\omega}{f(\mu)} \quad (2-17)$$

Finally, since the hesitivity of a single Debye material is defined in (10a) as $h_m(Debye) = \omega_0 \mu_0 (\mu_{DC} - 1)$, it follows that the function $f(\mu)$ has a very simple interpretation:

$$f(\mu) = \frac{\omega \mu_0}{h_m(Debye)} \quad (2-18a)$$

$$f(\mu) = \frac{\omega \mu_0}{h_m(Debye)} = \frac{\omega \mu_0}{h_m(Lorentz)} = \frac{\omega \mu_0}{h_m} \quad (2-18b)$$

Similarly, if we consider the single Lorentz material, the same derivation leads exactly to the same equation.

Substituting this result into the radiation efficiency equation for the magneto-dielectric dipole we obtain equation (2-19).

$$e_{MD_dipole} = \frac{1}{1 + \frac{\omega \mu_0}{h_m} \frac{6}{\left(\frac{\rho}{l} \right)^2 (k_0 l)^3}} \quad \text{or} \quad (2-19a)$$

$$e_{MD_dipole} = \frac{1}{1 + \frac{\eta_0^2}{(20\Omega) h_m Vol_d k_0^2}} \quad (2-19b)$$

Therefore, the efficiency of a cylindrical magneto-dielectric dipole carrying a uniform magnetic current through its cross section and, at worst, the triangular distribution along its length (as expected for small dipoles) is uniquely determined by a single material parameter, its hesitivity, and its volume. (Of course, to simplify this discussion we have assumed the permeable material is also a “good” dielectric with no excess dielectric loss or conductivity, a reasonable assumption since there are many such materials available to the engineer in the MHz to GHz range.)

These results can be readily verified using the Ansys HFSS fullwave electromagnetic solver. Fig.2-6 shows the candidate antenna: a half cylinder dipole conformal to a metal ground plane, of length 1 m and radius 0.0127 m. The dipole is fed by 8 loop feeds in phase to maximize the uniformity of magnetic current along its length.

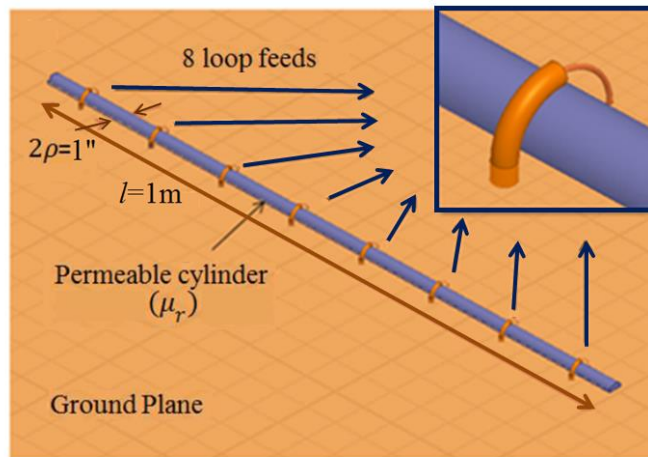


Fig. 2-6 Simulated Antenna: A Half Cylinder Dipole Conformal to A Metal Ground Plane Fed By 8 Loop Feeds

In Fig. 2-7(a) four hypothetical Lorentz materials are considered as materials of construction for this dipole, with very different loss tangent in the 30MHz to 300MHz range: ranging from a material with magnetic loss tangent equal to 1 at 100MHz (brown solid (μ') and dashed (μ'') curves) to the material represented by the solid black (μ') and dashed black (μ'') curves, with a worst-case loss tangent of 0.06 at 300MHz.

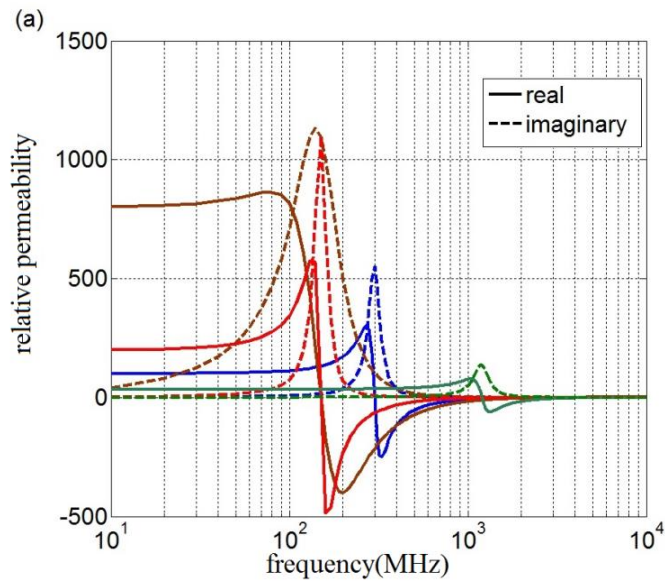
As shown in Fig. 2-7(b) all these materials have the same peak magnetic conductivity. Equal hesitivity implies by equation (2-19) that if they are used to construct the same linear dipole carrying the same current distribution they must all exhibit the same radiation efficiency. The calculated Radiation efficiency is then shown in Fig. 2-7(c). The fullwave simulated result from all four materials are on top of each other (dashed curves) and almost identical to the closed form prediction from equation (2-19).

The purpose of the multiple feeds in the linear dipole of Fig. 2-6 is to maintain the magnetic flux channeled inside the dipole and thus ensure a magnetic current along its length that has at worst the triangular distribution expected of electrically small dipoles (see Fig. 2-10, as an example).

As is well known from magnetostatics, the aspect ratio of a permeable object affects whether or not the magnetic flux injected by a current loop stays inside the object or leaks out to the surrounding space. Whereas a single loop-feed creates a nearly uniform flux inside a sphere of any permeability, to maintain a uniform flux within a high aspect ratio prolate spheroid, only fed by a single loop, requires that spheroid to have an extremely large permeability. The multiple feeds in the linear dipole of Fig. 2-6 thus play the same role as the windings of a solenoid do in magnetostatics, ensuring the flux is as

contained as possible regardless of the permeability of the cylindrical rod. This ensures that the magnetic current along its length that has at worst the triangular distribution expected of electrically small dipoles (see Fig. 2-10, as an example).

We emphasize that the efficiency equation derived under the assumption of an electrically small antenna works extremely well throughout this frequency range, even at 300MHz (with less than 0.5dB deviation) where the dipole is one wavelength long and clearly not electrically small. (The dipole of Fig. 2-6, 1m long, is indeed electrically small at 30 MHz and under.)



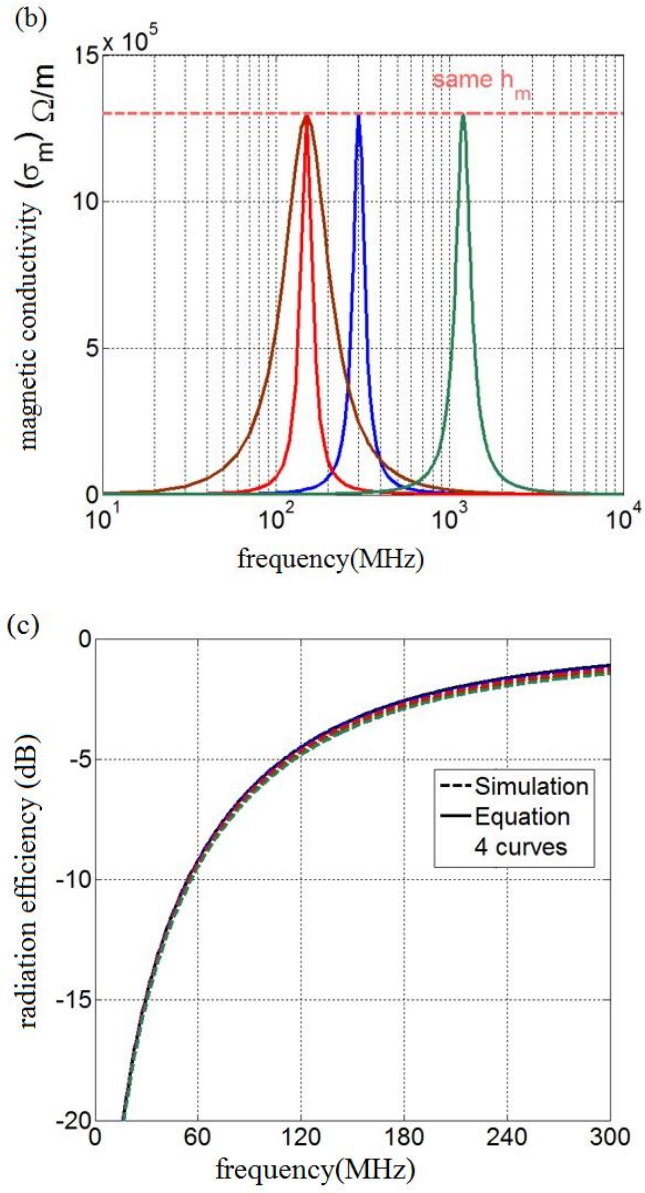


Fig. 2-7 Four Hypothetical Lorentz Materials with Very Different Loss Tangents (a) Have Magnetic Conductivities (b) That Reach the Same Peak. The Fullwave Simulated Results for The Radiation Efficiency from All Four Materials (c) Are on Top Of Each Other (Dashed Curves) And Almost Identical to The Closed Form Prediction from Equation (19) (Solid Curve).

As shown in [2] the same calculation done with Debye materials of equal hesitivity achieves similar success, with the maximum deviation at 300MHz being of the order of 1 dB. Therefore equation (2-19) constitutes a material selection rule:

Given a volume constraint for the permeable antenna and a desired efficiency at a given frequency, the hesitivity (and therefore the material family) is determined. Conversely, given an available material family (hesitivity), the volume required to attain a given efficiency at a prescribed frequency is likewise determined. There is no need for blind optimization or random attempts at using a variety of materials; the closed-form of equation (2-19) tells us all we need to know to begin the antenna design.

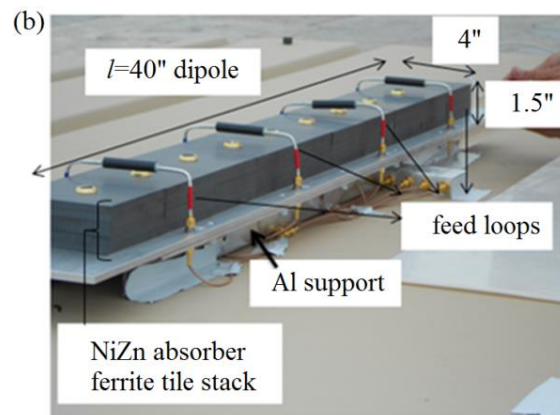
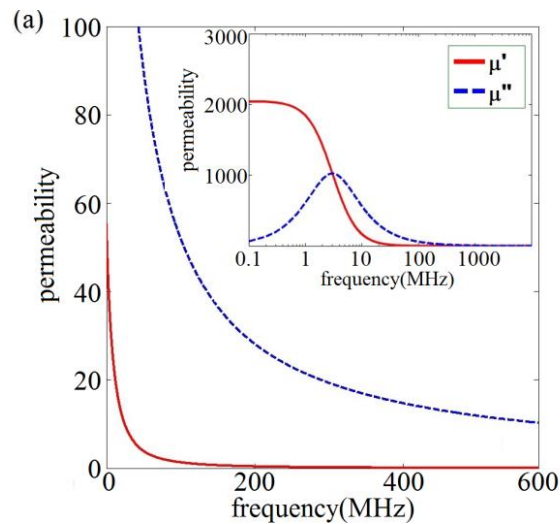
2.4 Experimental Verification

Antennas designed according to this prescription have been reported in [14-15]. Fig. 2-8 extracts the salient results from the first. Fig. 2-8(a) is a plot of the measured permeability of the commercially available NiZn absorber tiles from Fair Rite, exhibiting a Debye-like behavior. (Similar material is sold by Ferroxcube Corporation).

The inset shows the full spectrum but the plot focuses on the VHF to UHF frequency range. Clearly throughout this range the loss tangent of the material is much greater than 1. Fig. 2-8(b) shows a photograph of the test article: a 40 inch long dipole, 4 inches wide and 1.5 inches thick, mounted on an Aluminum carrier plane and then the antenna was mounted on a larger ground plane (or as shown in Fig. 2-9 on the roof of a HUMVEE.) In this case four feed loops were used to maximize the uniformity of the magnetic current. All four loops were combined directly and fed by a 50 ohm system.

Fig. 2-8(c) shows the excellent agreement between the measured realized Gain (Gain including the mismatch loss because no matching network was used for the dipole) and the HFSS simulated result. Finally, Fig. 2-8(d) shows the HFSS computed radiation efficiency compared to the prediction from the closed-form equation and for comparison what would have been expected from the old equation derived by Rumsey and DeVore.

The almost 20dB difference between the old expected efficiency and the true efficiency explains why these antennas have not been actively explored until now. The fact that no attempt to match the antenna was made can be used to highlight the excellent natural Gain Bandwidth product that these antennas exhibit in conformal applications.



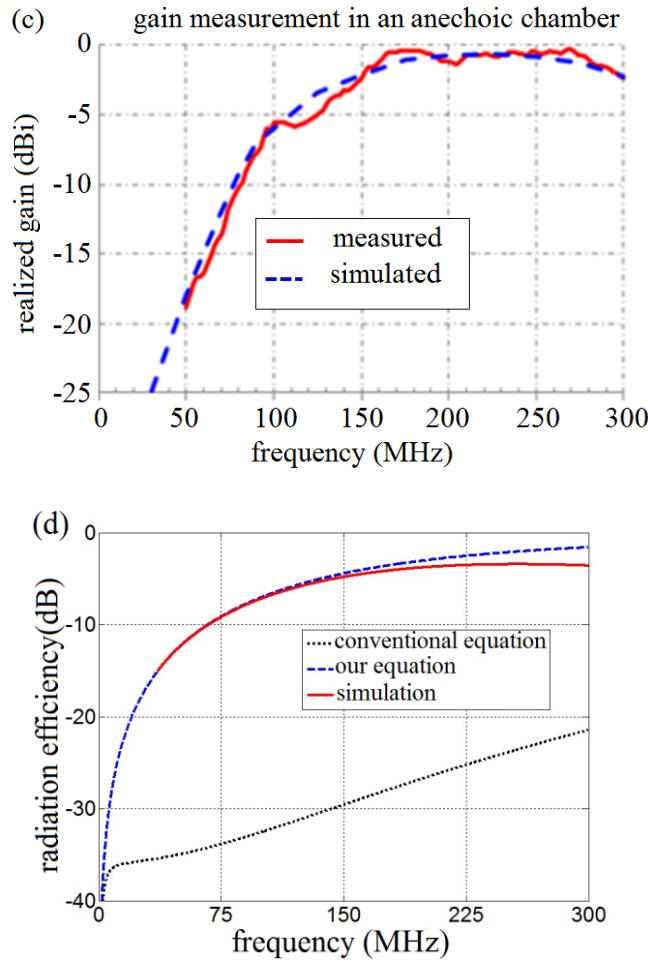


Fig. 2-8 (a) NiZn Absorber Tiles from Fair Rite Show a Debye-Like Permeability, (b) Test Article Shown Is a Dipole Mounted on An Aluminum Carrier Plane. (c) Measured Realized Gain and HFSS Simulated Results Are Very Close. (d) The HFSS Computed Radiation Efficiency Closely Agrees with Equation (7), But Is Dramatically Different from The Conventional Equation (8).

As Fig. 2-9 shows, when the antenna was placed on the roof of a HUMVEE and compared on the same open range to a standard 9 foot whip antenna, the Gain is approximately equal or better than that of the whip in the 30MHz to 88MHz range. Both antennas exhibit the same ground bounce null around 110MHz and then the magnetic

dipole continues to operate above that, whereas the whip is not tuned to work above 100MHz.

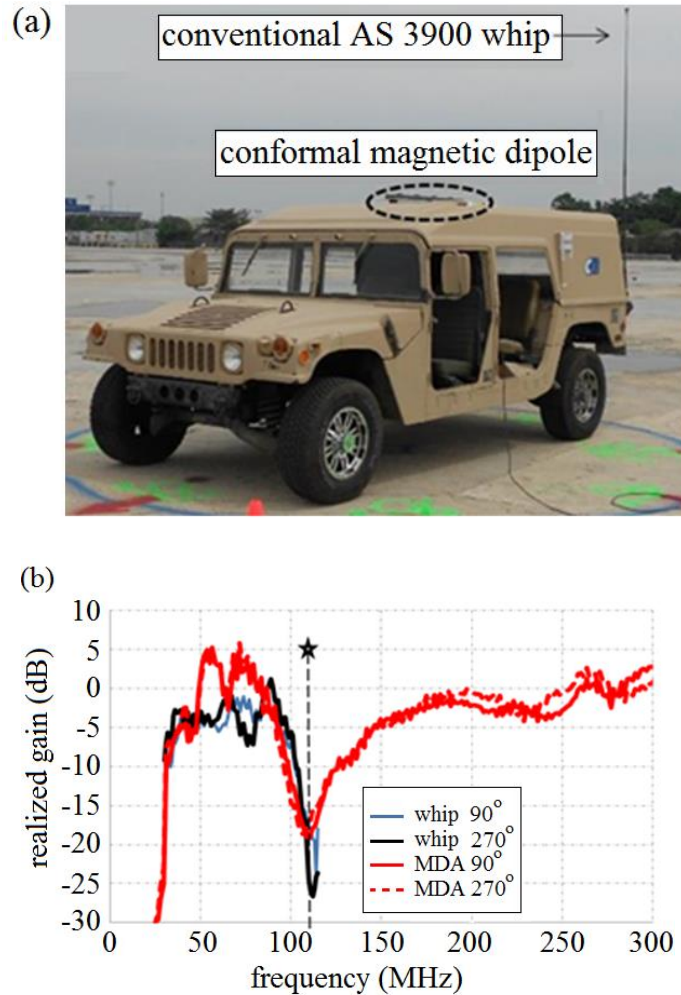


Fig. 2-9 Installation on The Roof of A HUMVEE Highlights the Difference in Size Between the Antenna and A Conventional Whip (a). Gain of The Permeable Dipole (Red) Is Comparable or Better Than That of The Whip (b).

The results attainable using high performance Lorentz-like materials, as with the ferromagnetic laminate material used in reference [14], will be discussed in a follow-on

paper. The final issue to be addressed for these antennas is the input impedance and the question of whether they are harder or easier to match than conventional antennas.

It should be obvious that these antennas are indicated for those problems requiring a conformal antenna solution, for instance on airborne platforms where blade antennas add undesirable weight and drag to the aircraft. In such cases a metal (and dielectric) conformal antenna suffers from anti-linear images that dramatically reduce its radiation resistance.

Not only do the images reduce the practical gain of metal antennas, they also reduce their efficiency to such a degree that the moderate loss experienced by permeable antennas is negligible by comparison. We address this point in Section V, again starting from the electrically small limit because that is where the greatest problem exists, namely at VHF and below where conventional antennas can become inordinately large.

2.5 Proof That a Conformal Magnetic Antenna Always Beats a Conformal Metal Antenna

Using fullwave (HFSS) simulations of a combined-multi-loop fed linear dipole 39" long, 3.15" wide, 1" thick, a closed-form circuit model of the input impedance was derived. Fig. 2-10 illustrates the nearly triangular magnetic current distribution attained by the feeding structure from 10MHz through 120MHz even though the maximum permeability of the core material is only a moderate 40 (the CZN laminate used in [14]).

Because the impedance model derived in Section II above (based on [2]) does not include the effects of the realistic distributed feed structure, with its inevitable parasitics,

we use the HFSS result to obtain a slightly modified circuit model that comes closer to matching the simulated results.

The plots in Fig. 2-11(a) and Fig. 2-11(b) show that the modified circuit model exactly matches the reactance but deviates slightly in the resistance term. The latter is shown on a logarithmic scale since it changes by two orders of magnitude over the frequency range of concern: 10 MHz to 100 MHz.

Now, we can compare this impedance model to that of a conventional metal antenna in exactly the same conformal volume: a metal strip dipole 39" long, 3.15" wide, 1" above the same ground plane.

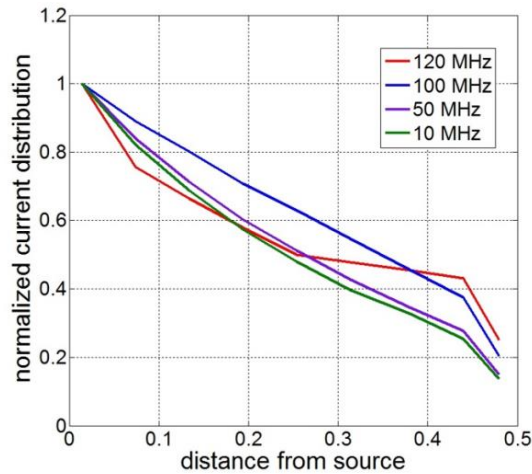


Fig. 2-10 The Magnetic Current Distribution Attained by a Distributed Feeding Network on a $\mu = 40$ Dipole From 10MHz Through 120MHz is Nearly Triangular.

The reactance of the metal antenna can be approximated by that of a center series-fed air substrate microstrip (68Ω impedance) open circuited at both ends (Fig. 2-12), whereas the radiation resistance is the free space value for the strip dipole degraded by the image factor $\sin^2 kh$, with $h = 1"$

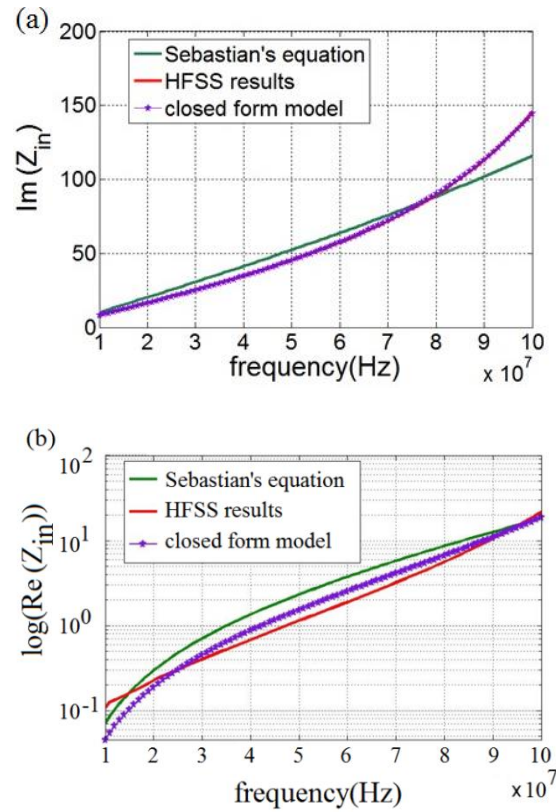


Fig. 2-11 The Impedance of The Modeled Antenna, (a) Imaginary Part and (b) Real Part, Can be Approximated with a Closed-Form Circuit Model (Magenta Curve with Symbols) That Improves on Sebastian's [12] Original (Green) to Agree with the HFSS Simulations (Red).

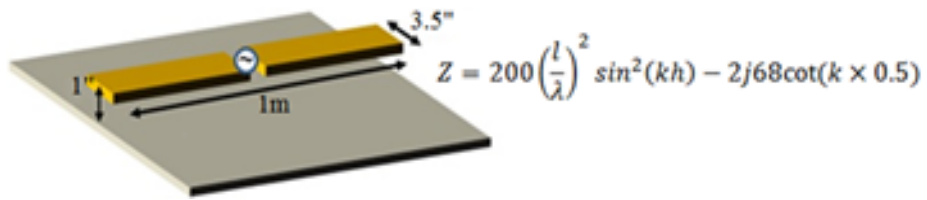


Fig. 2-12 A metal dipole constrained to operate in the same conformal volume as the simulated magnetic antenna has an input impedance that can be derived from its microstrip-like geometry.

As Fig. 2-13(a) shows, the metal dipole's radiation resistance (blue) is over two orders of magnitude lower than the permeable dipole's (red) due to the ground plane image effect. The reactance in Fig. 2-13(b) (blue) is capacitive and though it looks worse

in a linear plot as in the figure, if we were to plot it as an absolute value in a logarithmic scale relative to a 100Ω system impedance it is really not worse than that of the permeable dipole.

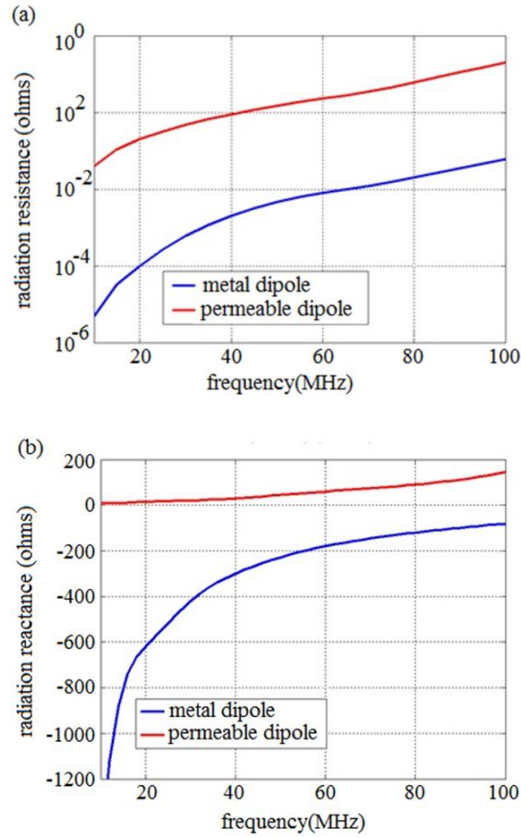


Fig. 2-13 Comparison of the Real (a) and Imaginary (b) parts of the input impedance of the two antennas.

The extremely low radiation resistance of the metal conformal dipole implies that its Gain-Bandwidth Product (GBWP) is extremely small. And this is the fundamental problem with conformal metal antennas. Using the definition that $BW \sim 1/Q$, we can estimate the bandwidth of the conformal metal dipole to be given by equation (2-20):

$$fBW_{microstrip\ dipole} \approx \frac{R}{X} = \frac{200 \left(\frac{l}{\lambda}\right)^2 \sin^2(kt)}{136 \cot(kl/2)} \quad (2-20)$$

It is true that the electrical distance to ground seen by the metal antenna could be increased to $\lambda/4$ by using a high permittivity substrate or if desired an artificial magnetic conductor (AMC). However, even if doing so increases its radiation resistance to its free space value, this only happens over a very narrow band of frequencies. This follows because a physically thin grounded substrate ($t \ll \lambda_0$) can only increase the gain of a proximate antenna when its reflection coefficient ranges from $\Gamma = -j$ to $\Gamma = +j$. Thus the fractional bandwidth over which an AMC operates is known to be given by equation (2-21) below, and can only be increased by the presence of true permeability [15].

$$fBW_{AMC} = \frac{\Delta\omega}{\omega_0} = 2\pi\mu_r \frac{t}{\lambda_0} \quad (2-21)$$

But the AMC bandwidth calculated from equation (2-21) is not the final bandwidth of the conformal antenna because no attempt at including the effect of the stored near-field energy around the antenna has been made.

A detailed examination of this point is beyond the scope of this chapter. The literature on conformal antennas over AMCs shows very different bandwidths being reported by different investigators, and in many cases the efficiency of the antennas is not reported, making it hard to assess the final GBWP attained.

Nevertheless, when the AMC is much larger than the antenna so that the bandwidth measured is indeed that of the antenna, as modified by the AMC, the bandwidth is actually consistent with our equation (2-20), this is the case of [16]. However, when the antenna (typically a patch) is positioned over a finite-sized AMC such that it is the combination of antenna plus finite AMC, held in free space, that radiate

(that is in the absence of any other nearby ground planes) then the bandwidth is much larger. This is the case of reference [17]. Then there are the cases where the bandwidths calculated from both equations (2-20) and (2-21) are close to each other. In that case the effects are confounded as in [18].

Since in the present discussion we are concerned with conformal antennas operating at low communication frequencies, involving long wavelengths (e.g. 10 m) and since we know that for an AMC to work as a ground plane it must be significantly larger than the antenna and larger than $4\lambda^2$ [18], the case of the AMC is not germane.

Having closed-form impedance models for both antennas we can use the Best-Yaghjian [19] Match Bandwidth equation (equation (2-22)) to determine the fractional bandwidth (FBW) that would result from matching each antenna at every frequency of its band. Though this formulation does not tell us how to affect that match, its consistency with the Bode-Fano criterion allows us to use it as a formal comparison of the ability to match antennas to a given VSWR criterion.

$$Q_{Ant}(\omega_0) = \frac{\omega_0}{2R_{in}(\omega_0)} |Z'_{in}(\omega_0)| \quad (2-22a)$$

$$fBW(\omega_0) = \frac{2\sqrt{\beta}}{Q(\omega_0)} \quad (2-22b)$$

$$\text{where } \beta = \frac{|\Gamma|^2}{1 - |\Gamma|^2} \quad (2-22c)$$

Consider a 2.5:1 VSWR bandwidth requirement. This corresponds to $|\Gamma| = 0.429$, so that $\beta = 0.226$. The resulting match bandwidths from 10MHz to 300MHz are

shown in Fig. 2-14(a) for the permeable antenna (red) and for two versions of the metal antenna: one open at both ends (blue), one shorted at both ends (black).

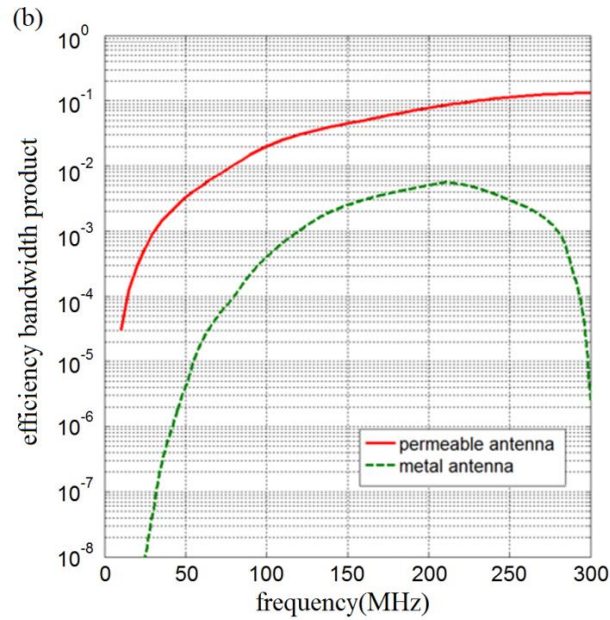
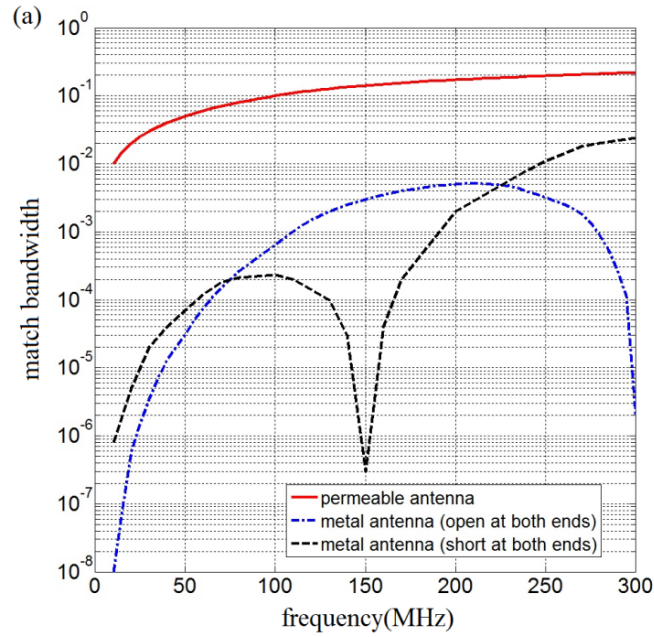


Fig. 2-14 Match Bandwidth From 10MHz to 300MHz For the Permeable Antenna (Red) Exceeds That of Two Versions of the Metal Antenna (a). Similarly, the Efficiency Bandwidth Product of the Permeable Antenna Exceeds That of the Metal Antenna (b).

Because the permeable core of the permeable antenna is lossy, a more fair comparison of the two antennas is the Efficiency Bandwidth product (EBWP). Therefore, the BW calculated must be multiplied by the radiation efficiency. But on this account the metal antenna also suffers because its radiation resistance is so small that the surface resistance of its metal actually competes with it.

Assuming Copper, the surface resistance of a 1 meter long, 3.15 inch wide antenna can be calculated. The result is then the EBWP plots of Fig. 2-14b.

The permeable dipole has an EBWP that is at worst 12 dB greater than the metal conformal antenna and this advantage rises to more than 50dB in the low HF range.

These results prove that, in the indicated conformal antenna application, the permeable antenna is indeed easier to match than an equivalent metal-and-dielectric conformal antenna, and that in terms of realizable Gain Bandwidth Product the permeable antenna (using commercially available material) has a 10dB to 50dB advantage over any equivalent metal antenna over the same frequency range of interest.

2.6 Summary and Conclusions

A radiation efficiency equation for permeable dipole antennas has been derived in closed form in terms of the geometric parameters of the antenna and its dispersive permeability. By comparing the efficiency of a ferrite dipole obtained from the derived efficiency equation with Rumsey and DeVore's results we see a significant difference. Contrary to the traditional misconception, the radiation efficiency of conformal antennas

constructed from dispersive (lossy) ferromagnetic and ferrimagnetic materials is not necessarily reduced by the loss tangent of the permeable material.

We find that both low loss permeable materials and permeable materials with very large μ'' , that is, with very large loss tangents, can achieve high efficiencies. Therefore the magnetic loss tangent is not the relevant parameter that determines the efficiency of these antennas.

By using examples of dispersive permeability (as either a Debye-like or Lorentz-like response) it has been demonstrated that the most important material parameter controlling the radiation efficiency is not the instantaneous loss tangent but the peak value of the Heaviside magnetic conductivity which is proportional to the well-known Snoek's product.

A material selection rule has been proposed which states that given the geometric constraints on the antenna and the desired radiation efficiency there is a family of materials given by Snoek's product that will meet the requirements. Also, given a material, the dimensions of the antenna required to attain a given radiation efficiency are determined.

Furthermore, since the efficiency is fixed by the material family, the engineer is free to choose which specific member of the family to use for the application; and the obvious choice that attains maximum bandwidth is the member that exhibits the highest μ'' in the band of use.

It has been shown in theory and with experimental results that these permeable antennas can be placed in close contact with a metal ground plane without degradation of

performance which solves the problem of electrically small conformal communication. Furthermore, it has also been shown that the EBWP of the magnetic antennas and their match bandwidth can far exceed that of the metal antennas when the loss in the permeable materials and metals are considered.

Using the example of a 1 meter long antenna operating from HF to VHF and proving that the magnetodielectric antenna attains an Efficiency Bandwidth Product (EBWP) at least 10dB higher than the corresponding metal antenna over the band and furthermore showing that these antennas are easier to match and can attain wider bandwidths than equivalent conformal metal antennas by using the Best-Yaghjian formalism will obviously lead to an interest in designing different antennas with more fascinating properties.

An example of this antenna will be proposed in the next chapter which is an extremely thin, very wideband conformal antenna that can support both the UHF Line of Sight (LOS) and the UHF SATCOM functions for a wide range of airborne and terrestrial applications

CHAPTER 3

A WIDEBAND MULTIMODE PERMEABLE CONFORMAL ANTENNA THINNER THAN $\lambda/75$ USING ADVANCED FERROMAGNETIC LAMINATE COMPOSITE MATERIALS

“When you change the way you look at things, the things you look at change.”

Max Planck

3.1 Introduction

In the previous chapter the principles of magneto-dielectric radiators have been explained in detail. By using the principles of chapter 2 and using new advanced ferromagnetic laminate composite material we have designed an extremely thin conformal toroidal magneto dielectric antenna, having an instantaneous bandwidth that spans the range from 200 MHz through 400 MHz and is able to support both the UHF Line of Sight (LOS) and the UHF SATCOM functions for a wide range of airborne and terrestrial applications. For the LOS function the antenna produces an azimuthally omnidirectional, vertically polarized, antenna pattern (null towards zenith) whereas the SATCOM function requires a circular polarization (CP) beam with boresight at zenith.

This chapter is based on our paper: T. Yousefi, R. Diaz, C. Daniel and D. Aukland, "A Wideband Multimode Permeable Conformal Antenna thinner than $\lambda/75$ using advanced ferromagnetic laminate composite materials," *IEEE AWPL Special Cluster on Conformal Antennas and Arrays from New Advanced Materials*. vol. 15. pp. 1931-1934. 2016.

The high impedance and anisotropic properties of the new advanced materials supports the desired radiation via magnetic currents and since the measured dispersive permeability of the material and the desired Gain is given and the radiation efficiency equation based on the linear dipole equation from chapter 2 is known, the approximate toroid diameter and cross section of the toroid was calculated and using fullwave simulation (ANSYS HFSS) [20], the dimensions of the antenna were fine tuned to maximize the Peak Gain while minimizing is ripple over the band.

To absolutely minimize the thickness of a conventional metal antenna in a conformal form factor, high impedance permeable substrates are usually, high impedance permeable substrates are usually considered mandatory. However, it only takes a moment's consideration of the volume equivalence principle to realize that extremely shallow metal radiating structures backed by a permeable substrate over a ground plane radiate mostly through the magnetic currents dB/dt of the substrate. It follows then that the most economical way of using the permeable material is to shape it into the radiating element. This goal has been reached by using a new advanced high permeability anisotropic ferromagnetic laminate as the permeable material of construction.

Cobalt-Zirconium-Niobium (CoZrNb) ferromagnetic alloy deposited onto $12 \mu m$ thick polyimide film by St. Gobain, S.A. is cut into the final desired thickness and wound onto a dielectric tape reel. The result is a conformal toroidal magnetic flux channel antenna meeting the above requirements, designed based on the theory of magneto-dielectric radiators [2, 14] and fed by four quadrant feeds.

The theory of these magneto-dielectric or magnetic-flux channel antennas, and initial demonstration of their unexpectedly high efficiency and peak gain, have been described in recent publications [14, 21]. Control of the feeds' amplitudes and phases with a mode-former enables the excitation of a monopole mode (all feed currents in the same direction, mode 0) as well as in x and y horizontal dipole modes for CP operation. Fig. 3-1(a) shows the idealized geometry from which the closed-form design equations are obtained. Fig. 3-1(b) shows the ANSYS HFSS model [20] of one quadrant, highlighting the laminated nature of the permeable core and the distributed quadrant feed. Fig. 3-1(c) is a schematic illustration of the feed network and Fig. 3-1(d) is a photograph of the assembled test prototype.

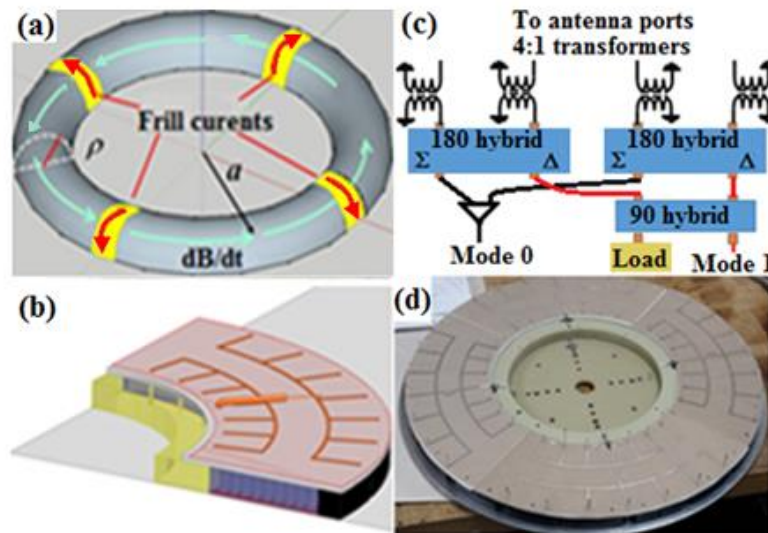


Fig. 3-1 (a) Theoretical Model of the Permeable Toroid, (b) Detail of a Quadrant in the Simulation, (c) Schematic of the Feed Circuit , (d) a Photograph of the Antenna.

In Section 3.2 we briefly discuss the physical limits that prevent conformal metal antennas from ever reaching the kinds of instantaneous bandwidths that these permeable

antennas can attain. The key result is that the material loss penalty associated with realistic permeable materials is practically insignificant when compared with the loss of Gain Bandwidth Product (GBWP) suffered by realistic conformal metal antennas.

Following the same procedure as Sebastian [2], a closed-form model of the input impedance of this antenna can be derived from first principles. This model enables us to design the baseline geometry of the antenna and select the materials of construction based on the requirements.

This approach is illustrated by focusing on the CP dipole mode for SATCOM in Section 3.3. Then, to account for the realistic details of the antenna construction and for the higher order phenomena not included in the closed-form model, a fullwave computational electromagnetics (CEM) model is created using ANSYS HFSS. The results are discussed in Section 3.4. In Section 3.5, we then compare the performance predicted by the antenna model with the performance measured in an anechoic chamber. It is shown that by including the measured imperfections of the mode forming feed network, the model and experiment agree quite closely.

3.2 The Gain-Bandwidth Problem

Because the presence of a ground-plane in intimate proximity to a permeable antenna does not affect its GBWP, the input impedance of a conformal magnetic flux channel antenna is functionally similar to the impedance of a conventional metal antenna in free space. The constraining parameter, when these antennas are electrically small, is the intrinsic radiation bandwidth of the antenna which has the well-known Fano-Chu limit of $(ka)^3$, where a is the radius of the circumscribing sphere and k is the

propagation constant in free space. For planar antenna geometries, this result is lower by about at least 6dB.

However, a conformal metal antenna parallel to a ground plane (e.g. a patch [22]) at a height, t , has its radiation resistance reduced by the factor $\sin^2(kt)$. It follows that the GBWP of a metal conformal antenna is reduced at least by this same factor and is worse if the close proximity of the metal antenna to its image increases the stored near field reactive energy per cycle. Now consider a conformal antenna required to operate at 300MHz constrained to a maximum diameter of 0.5 m and no taller than 2.5 cm. Since the perimeter of the antenna is already more than a wavelength long, the intrinsic fractional bandwidth of the antenna is at least 100%. However, if it is a metal conformal antenna the factor $\sin^2(kt) = 0.025$ would bring the actual fractional bandwidth to the order of 2.5%, 26 times smaller (-14dB) than the 66% required to cover the band from 200MHz to 400MHz instantaneously.

This disadvantage in bandwidth can only be remedied by adding -14dB loss. By contrast, as will be shown below, the theoretical radiation efficiency of a practical permeable conformal antenna (that by definition already has at least 100% bandwidth) is only -2dB. As would be expected, this disadvantage of metal conformal antennas when compared to permeable ones gets catastrophic as the frequency is dropped to the VHF and below.

3.3 The Closed-Form Design of the Antenna

For the sake of conciseness, we limit the discussion of the closed form model to Mode 1; knowing that the steps for Mode 0 are identical. Following [2] we begin with the

metal antenna model of the desired permeable antenna. In this case it is a loop antenna fed at the centers of four quadrants to create, for instance, a y-directed dipole as suggested in Fig. 3-2(a). Following Schelkunoff's method [8] the series inductance and shunt capacitance representing the external near fields are derived in closed form by integrating the distributed inductance and capacitance of the principal wave under the assumed terminating conditions. The result is the external inductance of the quadrant (L_{Q_M1}) in series with the external capacitance (C_{Q_M1}). When the antenna is not a metal but a dielectric, the flux it carries is no longer only the conduction current but includes the displacement current through the dielectric. Associated with this internal flux are additional electric and magnetic fields inside the dielectric. By integrating over their stored energy, we obtain the internal impedance of the antenna and this results in the series terms L_{int} and C_{int} . From the far field power radiated by the current distribution, the total radiation resistance follows, and therefrom the quadrants contribution, $R_{rad_Q_M1}$.

Finally, following Schelkunoff [23] we cast the total circuit into Darlington form by finding the coupling inductor, L_P , that turns the modal radiation resistor, R , into the calculated radiation resistance, $R_{rad_Q_M1}$, of the antenna. The result is a closed form circuit model of the dielectric, quadrant-fed Mode 1 antenna, $Z_{inp_ε}$ (Fig. 3-2(b)). To obtain the circuit model of the permeable antenna fed by an ideal frill-loop-current, simply swap $μ ↔ ε$ throughout, and obtain the input admittance by $Y_{inp_μ} = Z_{inp_ε} / η_0^2$, where $η_0$ is the impedance of free space. Given the effective relative permeability of the magnetic laminate, $μ_{int}$. (Fig. 3-2(c)) and its effective permittivity, $ε_{int} ≈ 3$, Fig.3-2(d)

shows the final closed form circuit model of the permeable antenna. Each of the circuit elements can be recognized as the dual inverse of the elements in Fig.3-2(b) and the full details of the derivation of this circuit are left for Chapter 4.

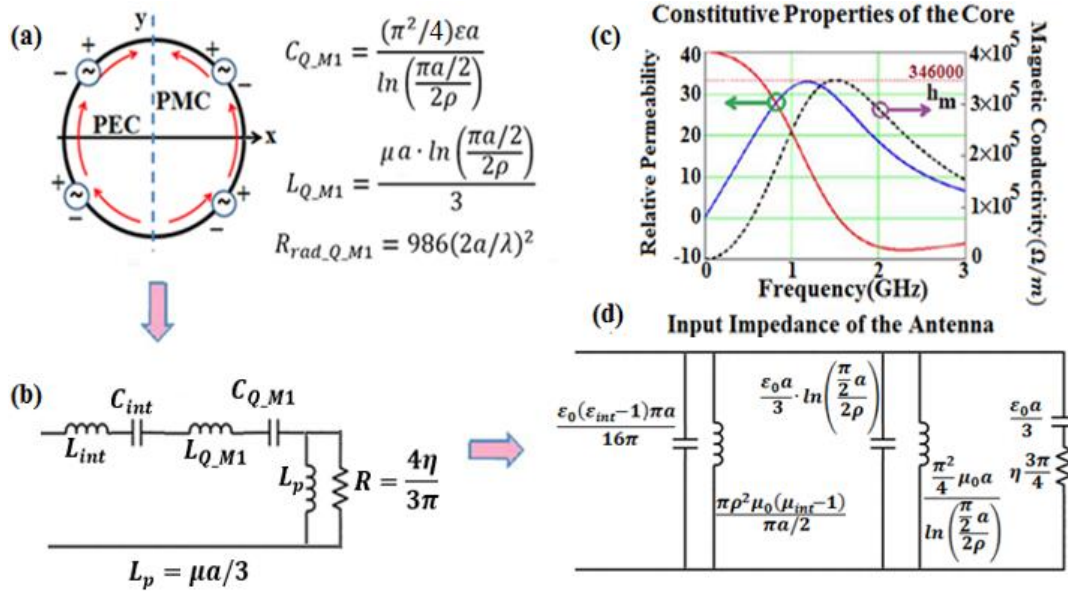


Fig. 3-2 Derivation of the Closed-Form Model For the Dipole Mode (Mode 1) of the Permeable Antenna.

The radiation efficiency of the antenna follows immediately by dividing the real part of the admittance of the rightmost series RC circuit in Fig. 3-2(d) by the real part of the total input admittance. After some algebra, as in [2], the result simplifies to equation (3-1), where the volume of the antenna, Vol , and the peak magnetic conductivity in the spectrum of the antenna (Fig. 3-2(c)), termed the hesitivity, h_m , are the dominant factors that determine the antenna efficiency.

$$eff_{M1} = \frac{1}{1 + \frac{\eta \cdot 12\pi}{Vol \cdot h_m} \left\{ (0.785a)^2 + \left(\frac{1}{k_0} \right)^2 \right\}} \quad (3-1)$$

3.4 Full-Wave Model of the Antenna

The manufactured article shown in Fig. 3-1(b) was simulated using ANSYS HFSS. For this demonstrator, a trivial way to match the antenna to a “better than 2:1 VSWR” requirement, is to feed the antenna with a mode former that creates the desired rotating CP beam with peak at zenith. As is well known, a mode former consisting of 180 and 90 degree hybrids will dump the mismatched power into its “hidden” loads. Therefore, all we have to do is transform the impedance at the quadrant ports of the antenna from the 50 ohm standard of the mode former ports to the natural locus of the mode 1 impedance. This locus is approximately 200 ohms.

Therefore, 4:1 MACOM MABAES0031 E-Series RF 4:1 Flux Coupled Transformers were connected between the coax ports and the quadrant loop feeds. The in-house built mode-former operated from 220MHz to 420MHz with a worst case 20 degree deviation from the ideal 90 degree rotation from quadrant to quadrant and a worst case 1dB imbalance in amplitude. As expected the S_{11} at the input of the mode former is much better than -10dB throughout the band. However, the dumped mismatch loss will appear now in the efficiency measured in the antenna chamber.

The most important insight gained from the fullwave model is the identification of the non-idealities to be expected in the measurement. These include artefacts resulting from the method of construction of the antenna, such as the presence of excess dielectrics used as a hub and capture ring that keep the wound-up laminated ferromagnetic material core in place. The next most important non-idealities are the higher order wave

phenomena supported by the ferromagnetic core (the flux channel) when its cross section is comparable to the wavelength.

For instance, the corrugated ground-plane formed by the 1.7cm thick and 7.6 cm wide laminated core material can carry a slow guided TM wave in the transverse direction that can be excited by the feed loop. The phase delay introduced by this slow wave plus the distance to ground turns the intended short circuit connection to ground into an open, partly interrupting the feed current. This perturbation extends from 261 MHz through 349 MHz, at which point the surface impedance of the corrugated plane is no longer inductive. Since this is a feed point effect the loss in efficiency occurs for both Modes.

The second higher order effect is the onset of TE_{01} surface wave guidance by the magneto-dielectric core itself. Since the laminates in the anisotropic core are perpendicular to ground, this occurs when the internal electrical thickness of the core is a quarter wave, that is, when $f_{TE_{01}} = c_0 / (4 \cdot 0.017 \sqrt{40 \cdot 3})$, approximately 404MHz. Above that frequency, a significant part of the input power gets dumped into trapped waves instead of radiation. As shown in Fig. 3-3, it is precisely in this frequency range that the antenna performance deviates from the closed-form model. Even though mode filtering techniques could be implemented into the flux channel design to reduce these effects the important point of this effort was to demonstrate that these permeable antennas lead to extremely thin useful multimode, multifunction wideband antennas.

3.5 Experimental Results

The antenna efficiency measured in the anechoic chamber referenced to the input port of the mode former includes: the radiation efficiency, the mismatch loss, the transformer insertion loss, and the mode former loss.

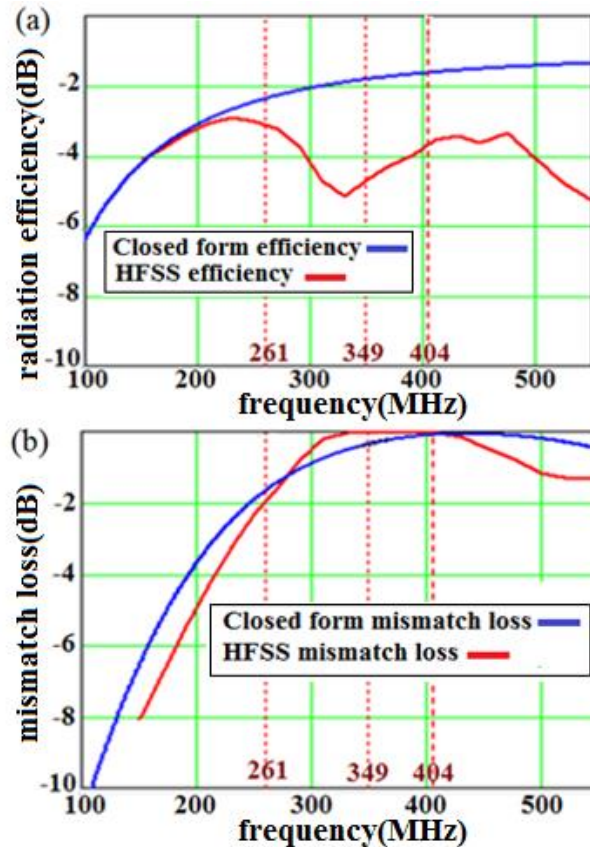


Fig. 3-3 The Full-Wave Calculated Radiation Efficiency (a) and Mismatch Loss (b) of the Manufactured Demonstrator in Mode 1 Differ From the Ideal Closed-Form Expectation.

The mismatch loss is $10\log(1 - |S_{11}|^2)$, and the closed form result follows from the circuit model's $Y_{inp-\mu}$ relative to the 200Ω system impedance (from the 4:1 transformers.) The mode-former loss is the deviation of the 4-way amplitude split and

phase progression from the ideal for the given mode. This was measured for both the monopole (M_0) and the CP dipole (M_1) modes. This data is shown in Fig. 3-4.

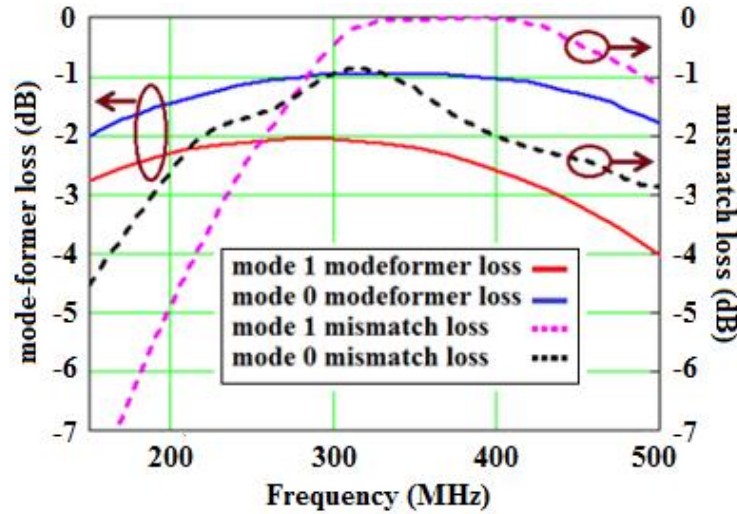


Fig. 3-4 Measured Mode-Former Loss and Full-Wave Computed Mismatch Loss Relative to a 200Ω System Impedance.

Because off-the-shelf hybrids were used to construct the mode-former for the demonstrator, the hidden loads were not accessible to measure the mismatch loss. However, the full-wave simulation can be used to gauge it, and it is also shown in Fig. 3-4. In principle, the mode-former loss is an “avoidable” imperfection. Very high quality and extremely broadband mode-formers can be made in this frequency range using lumped elements [24]. Fig. 3-5 compares the measured antenna efficiency shown in dashed curves (M_0 in blue, M_1 in red) with the expected efficiency based on: the full-wave data from Fig. 3-3, the mode former loss measured, and the manufacturer’s insertion loss specifications for the transformer. Given the other possible sources of

variation between experiment and model the agreement is quite good. Fig. 3-6 shows the maximum Gain measured in the anechoic chamber for both modes.

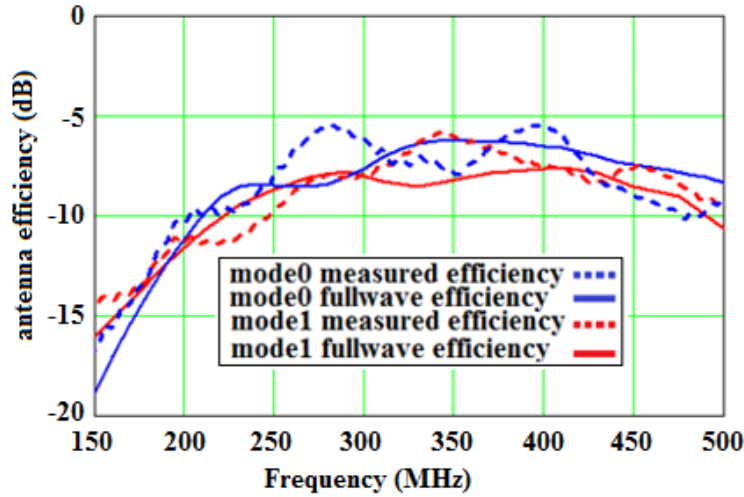


Fig. 3-5 Measured (Dashed) and Calculated (Solid) Antenna Efficiency: Mode 0 in Blue, Mode 1 in Red.

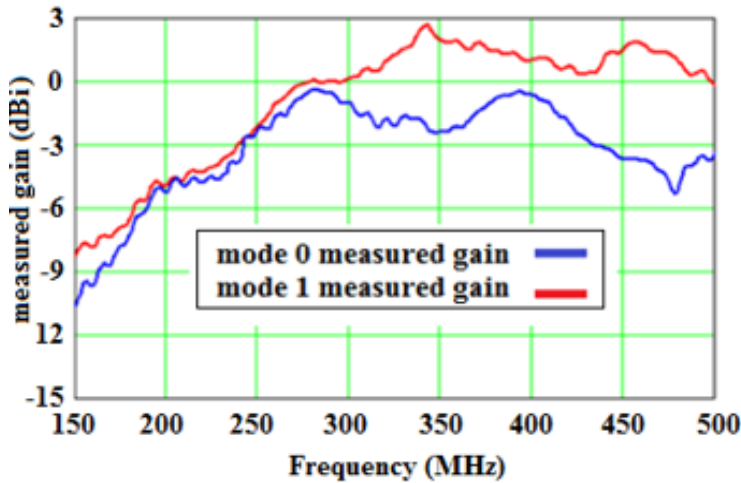


Fig. 3-6 Measured Gain Blue= M_0 , Red= M_1 .

The CP dipole M_1 (in red) readily attains +2dBi of Gain in the band of operation in spite of all the imperfections because the antenna directivity (measured and fullwave computed) reaches 9.5dB at 450MHz. The gain in M_0 is about -3dB lower because its better mode-former loss is offset by worse mismatch loss and, as the antenna patterns

show, the greater “spillover” of its vertically polarized pattern does not allow a significant increase of Directivity as frequency goes up.

Although both modes operate within the same 200 MHz to 500 MHz frequency range, they are used for completely different functions, and therefore have to meet different requirements. For instance, the gain required of M_1 from 245 MHz to 380 MHz, lies in the +2 dBi to +4 dBi range. Fixing the imperfections, we have noted, would make this goal attainable. However, the typical gain required of M_0 is of the order of 0 dBi. Implementing a dedicated matching network for this mode would also lead to meeting that specification. It is because of the multifunction purpose of this antenna that the difference in gain between the two modes is not a relevant performance parameter.

Because what matters for these applications is the capability of the antenna to meet the GBWP requirements of the various functions within the overall frequency band, we have reported the efficiency in dB and not percent. Although the 10% to 25% (-10 dB to -6 dB) efficiency seen in Fig. 3-5 may seem low, we have already pointed out that any competing conformal metal antenna, constrained to fit within the same 1.7 cm thick profile would suffer a -14dB penalty to its GBWP.

Finally, Fig. 3-7 shows the measured antenna patterns at 300MHz for both mode 1 (left) and mode 0 (right). The good azimuthal symmetry maintained by the quadrant feed is seen in the similarity between the 0 degree and 45 degree azimuth beams.

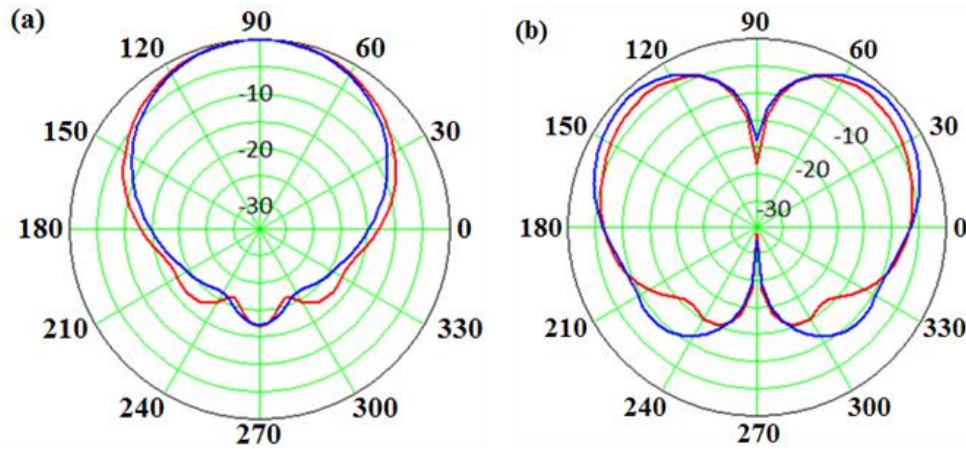


Fig. 3-7 Measured Antenna Patterns at 0° (Red) and 45° (Blue) Azimuth Versus Elevation For (a) Mode 1 and (b) Mode 0 at 300MHz.

3.6 Conclusion

A permeable toroidal magnetic flux channel antenna has been designed and manufactured that is less than 2 cm thick ($\lambda/75$ at 200MHz) and has a 43 cm outer diameter. The antenna has been fed by a simple mode-former and is designed to operate from 200 MHz to 400MHz and attains a measured gain ranging from -3dBi to +2dBi through at least 500MHz. The performance of the manufactured antenna has been verified in an antenna chapter which shows the design specifications have been met and including the imperfections it can operate from 200MHz to 500MHz with an input match of better than -10dB, CP dipole realized gain as high as +2dBi and monopole mode vertically polarized gain as high as -1 dBi. If high performance tailor-made components (transformers and hybrids) were used, an additional +2dB increase in gain is plausible.

The successful results of this antenna prove that conformal magneto dielectric antennas can indeed open a new window to designing high gain and very wideband antennas that can be very thin. This is crucial for wireless communication in the difficult

long wavelength frequencies ranging from HF through UH which are important frequencies for many applications ranging from defense applications to city and state safety and security applications since these bands of frequency are also used by Fire and Police Departments.

Since these antennas are very useful and no other conformal antenna with the same thickness can compete in terms of efficiency, it would be very helpful to have the ability to design these antennas from first principles. In many cases antenna design procedures depend on some trial and error and repetitive tuning using fullwave simulation which we don't find acceptable, not even when such "design" is carried out by using a (super) computer with brute force optimization. We avoid the confusion of not knowing whether the solution obtained by optimization is indeed the best solution or just a local minimum found by the optimizer within the bounds of the rules it was given by developing a complete analytic theory of these antennas.

In the next chapter, the complete analytic theory of these conformal magneto dielectric antennas is presented and a practical rational design rules which be provided that the engineer can use to create the magnetodielectric antenna solution for the given application.

CHAPTER 4

A FIRST ORDER MODEL OF THE MULTIPLE-FEED TOROIDAL MAGNETO-DIELECTRIC ANTENNA

“The equations at which we arrive must be such that a person of any nation, by substituting the numerical values of the quantities as measured by his own national units, would obtain a true result.”

James Clerk Maxwell

4.1 Introduction

Several recent papers have addressed the unexpectedly high Efficiency-Bandwidth Product (EBWP) of conformal antennas constructed from existing realistic (dispersive, lossy) magneto-dielectric materials (such as ferromagnetic metal films and ferrites) [14, 25, 26] . The reason for this apparently extraordinary behavior lies in an unwarranted assumption that was made by the early investigators of the ferrite rod dipole. Because they assumed the permeable material had to have low loss ($\mu'' \ll \mu'$) their calculated efficiency equation was automatically restricted to that limit [2, 27] . Since then most antenna engineers have assumed permeable antennas would not work until very low loss magnetic materials were invented. This has been shown not to be the case.

This chapter is based on our paper: Tara Yousefi, Rodolfo E. Diaz, “A First Order Model of the Multiply-Fed Toroidal Magneto-Dielectric Antenna”, *IEEE Antennas and Propagation*, accepted.

As we had seen in the previous chapter the toroidal magnetic antenna, constructed from a high permeability (and low permittivity) dispersive material and used as an electrically thin conformal antenna, exhibits a radiation efficiency up to two orders of magnitude higher than metal conformal antennas constrained to the same volume [28]. We had also mentioned in chapter 3, the need for a solid foundation for the new field of *Magnetodielectric Antenna Theory and Design* and the importance of understanding these antennas instead of blind trial and error and depending on full wave simulators and optimizers for an optimum design.

In this chapter, a model of the input impedance of the toroidal permeable antenna, which is the dual of the conventional metal loop antenna, is derived, starting from Schelkunoff's transmission line description of the loop antenna instead of the electrically-small-limit model. This antenna, as seen in chapter 3, operates in both the monopole mode and circularly polarized dipole mode and is constructed from a torus of high permeability material. We had also seen in the previous chapter that this specific magneto dielectric antenna is one of the many instances of permeable antennas all having an advantage over metal (and dielectric) antennas in low impedance environments, such as: conformal to a metal surface, adjacent or inside the human body, immersed in water, or inside the earth. Thus, their applications range from HF communications, through body wearable and implantable RF networks [1], to, possibly, subsurface communication and imaging.

The most important feature of the representation described in this chapter is that since the ultimate goal of having an antenna's input impedance model is to enable the

derivation of its best matching network; the input impedance is expressed in its widest band most general form as a frequency independent resistor terminating a reactive network which is called the Darlington form.

Our goal in this chapter is to put these results in a unified context by developing the Impedance model of these antennas in closed form, following Schelkunoff's principal wave model of electrically small to moderate-sized (larger than 1λ) antennas [8, 23]. The resulting theory yields straight-forward expressions for the input impedance and for the radiation efficiency, giving the engineer rules of thumb for designing these antennas.

The conformal toroidal magneto-dielectric antenna is used as the exemplar in this development because of its versatility as a wideband, multi-function conformal antenna.

As is well known in the practice of mono-pulse systems, whenever an antenna aperture can radiate multiple linearly independent beams, that antenna can serve a variety of functions beyond the capabilities of omnidirectional single mode antennas. Combination of the multiple beams can be used in direction finding systems or in MIMO communication schemes to exploit multipath.

The multiple-feed toroidal antenna, subject of this paper, has been built and demonstrated, as detailed in references [14] and [28]. As stated in [28] our particular toroidal antenna was designed to meet the different functions required by different communication bands of interest in the UHF range: In the band from 225 MHz to 512 MHz terrestrial line-of-sight communication (LOSCOM) requires a vertically polarized antenna with peak gain near the horizon. Conventional systems meet this requirement using vertical whip antennas which have to be approximately 1 to 2 feet tall to operate

efficiently at the low end of the band. By feeding all four ports of our toroidal antenna in phase, the antenna radiates in Mode 0, the vertically polarized monopole mode, with a null to zenith and a maximum towards the horizon, and it is only 0.7 inches tall.

For communication to satellites in the 245 MHz to 380 MHz band (SATCOM MUOS), encompassing both Transmit and Receive bands, the need is for a CP radiator with main beam to zenith. In that case feeding the four ports of the antenna with a rotating phase of 90 degrees from port to port results in a CP main beam towards zenith, Mode 1.

That is, as is the case with the well-known four-arm sinuous antenna, appropriate excitation of the four ports can produce an x-polarized linear dipole or a y-polarized linear dipole and these can be combined by the feed network into a rotating CP dipole. Because conventional four arm sinuous antennas by default feed opposite arms with 180 degree phase shift their feed network is simpler, consisting of two selectable 90 degree hybrids (one for RHCP one for LHCP), but as a consequence they only have access to Mode 1. Because we also want the vertically polarized Mode 0, we use all four ports and implement a full four ports mode-former as is the standard practice with four-arm spiral antennas (see for instance [29].)

Note that a conventional four-arm (metal) sinuous antenna could not replace the permeable toroidal antenna discussed here for the Mode 1 function because the thickness constraint of 0.7 inches would place its radiating elements a distance of $h = \lambda/50$ from ground, thus incurring a severe bandwidth reduction (of -19dB) because of the image factor $\sin^2(kh)$ [27].

Fig. 4-1a below illustrates the simplest mode-former that gives access to the desired modes constructed using off-the-shelf power dividers and hybrids. As explained in reference [29] custom-made integrated mode-formers using stripline components on a single circuit board can attain bandwidths in excess of 10:1. Fig. 4-1b is a photograph of the subject antenna.

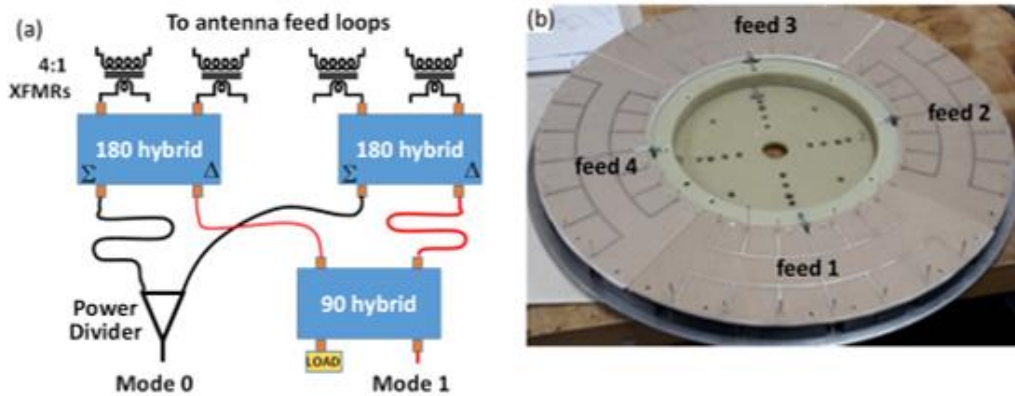


Fig. 4-1 Simple Mode-Former (a) For Feeding the Toroidal Four-Port Antenna (b) and Generating a Vertically Polarized Mode 0 and a Rotating Mode 1 [28].

Significance and impact:

- i. Considering that there is no fundamental theory for magneto-dielectric antennas, the first significant contribution is the development of the theory with everything it entails, including rules of thumb and closed form expressions. Using the models given in this work, small to moderate sized magneto-dielectric antennas can now be designed from first principles, with no need for a full wave electromagnetic simulator with an optimizer for the design.

- ii. These permeable conformal antennas have been proven to have much higher efficiency compared to metal and dielectric antennas constrained to the same conformal volumes, they are easier to match, and can attain wider bandwidths than equivalent conformal metal antennas.
- iii. They should also excel in other important low impedance environments such as in proximity or inside the human body and sub-surface applications.

In Section 2 we discuss Schelkunoff's loop antenna model based on biconical transmission lines and we express the input impedance of the loop in Darlington form which has a frequency independent resistor terminating a reactive network. Such a model is valid beyond the electrically small limit with the important consequence that it leads to the correct self-resonance frequency of the loop and a radiation resistance that does not always stay as ω^4 .

In section 3 we obtain a wideband impedance model of the quadrant fed toroidal metal antenna for both Mode 0 and Mode 1, as a prelude for the development of the impedance model for dielectric and, ultimately, permeable antennas. For Mode 0, which has the most similarity to the loop, we divide half of the loop into a large number of small (differential) segments and use the transmission line model, to obtain the impedance circuit model. As expected, the result is equivalent to simply moving the short circuit of the loop model of section II from $\varphi = \pi$ to the two walls at $\varphi = 0$ and $\varphi = \pi/2$. The same is done for Mode 1 and, the input impedance is obtained.

In section 4, the "electric" case of the penetrable antenna, the dielectric antenna, is derived from that of the metal antenna of section III by inserting the material properties

into that model. Thus, we obtain a wideband impedance model for dielectric quadrant-fed antennas.

In section 5, by using the concept of duality and the results of section IV, we obtain an impedance model for quadrant-fed permeable antennas working in both Mode 1 and Mode 0.

Section 6 compares the results obtained from the new wideband impedance model and the results previously derived, showing that this model works much better when we move farther from the small antenna limit.

Finally, in section 7, the feed loop contribution is explicitly accounted for and the results are compared with fullwave simulations [20] of a typical antenna operating in both Mode 0 and Mode1, demonstrating very good agreement.

4.2 Wideband Impedance Model of the Conventional Loop Antenna

Schelkunoff's model of the principal wave carried by a curved two-wire antenna is based on the principal wave impedance of the biconical antenna of arbitrary angle between the cones (biconical Vee antenna) [8] . It can be shown that for two diverging wires whose radii are a_1 and a_2 while d is the distance between the corresponding elements of the wires, the wave impedance can be written as:

$$K = \frac{\eta}{\pi} \ln \left[\frac{d}{\sqrt{a_1 \times a_2}} \right] \quad (4-1)$$

If the cones have the same radius, $a_1 = a_2 = \rho$ at a distance of d this becomes:

$$K = \frac{\eta}{\pi} \ln \left[\frac{d}{\rho} \right] \quad (4-2)$$

This means that the two biconical transmission lines shown in Fig. 4-2 have the same impedance although their cone angles and tilt angles are different.

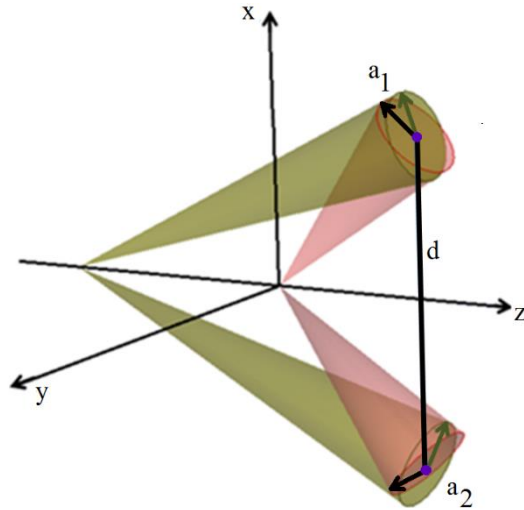


Fig. 4-2 Two Biconical Transmission Lines Having the Same Impedance with Different Cone and Tilt Angles.

As an example of Schelkunoff's method, consider the loop antenna of Fig. 4-3. We can imagine building the loop out of many sections of biconical Vee antennas, however for clarity we have only shown 4 sections in Fig.4-3. Thus, for the four sections in the figure, from the feed to the first 45 degrees of arc we can imagine a biconical Vee of 135 degree cone separation angle (the red dashed outline, where we have omitted the symmetric side of the structure for clarity). Then from that point on to 90 degrees of arc we can imagine another section of a biconical Vee antenna and so on.

In Fig. 4-3 we have used the cascade of biconical transmission lines starting at the feed as an illustration because it makes the role of the feed in starting the principal wave

clear. We then have chosen to draw those transmission lines with symmetry about the midplane at the center of the loop because the symmetric modes of excitation of this antenna are of interest and therefore we will have a mirror symmetry plane in the middle. Regardless of the representation, as Schelkunoff himself points out, the local principal wave impedance is the same whether we think of the infinitesimal sections as sections of biconical lines or as sections of parallel wire lines; this is why he uses as the physical parameters of the line the local cross sectional radius and the center to center separation between the wires, instead of the angles of the cones.

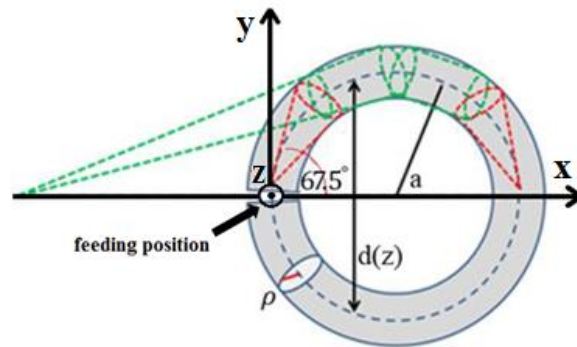


Fig. 4-3 Loop Antenna Built from Several Sections of Biconical Vee Antennas.

Before proceeding with the derivation, it is important to make another point about Schelkunoff's derivation. Although it is traditionally assumed to imply thin wire antennas, his baseline model is the biconical transmission line; that means that he is not strictly limited to physically thin wires. The key point in his work is the assumption that the principal wave dominates the performance, and so there should be no significant phase shift around the circumference of the wire. Therefore, as long as there is not a considerable phase shift around the circumference, this model should work very well for not-physically-thin (fatter) antennas.

The proof that this method works for “fatter” cross sections can be seen in section VII where the modeled antenna is a rather fat toroid of 7 inch radius with a mean cross sectional diameter of 2.24 inches which is about a third of the radius and as can be seen later in the paper, the agreement with the model is excellent.

However, if there is a considerable phase shift around the circumference of the wire, not only is Schelkunoff’s basic assumption invalidated, our model would also fail on another account: because then the magneto-dielectric rod would trap the wave. So indeed, we are staying by definition and practical choice of the cross-section dimensions, and overall size of the antenna versus wavelength, within the spirit of the thin wire limit.

The principal wave’s impedance of each section is given by equation (3), ($x=0$ is the origin, at the feed.)

$$K(x) = \frac{\eta}{\pi} \ln \left[\frac{d(x)}{\rho(x)} \right] \quad (4-3)$$

With the inductance per unit length and capacitance per unit length given by equations (4).

$$\hat{L} = \frac{\mu_0}{\pi} \ln \left[\frac{d(x)}{\rho(x)} \right], \hat{C} = \frac{\pi \epsilon_0}{\ln \left[\frac{d(x)}{\rho(x)} \right]} \quad (4-4)$$

If we assume that the sections shown in Fig. 4-3 are very small, then a sum of the inductance per unit length would be analogous to integrating the inductance per unit

length and should result in the same value that Schelkunoff gives for the self –inductance. Assuming that each quarter of the loop has been divided into N sections, with basic mathematical manipulations we can write:

$$L_{total} = 2 \cdot \frac{2\pi a}{4N} \cdot \sum_{i=1}^N \frac{\mu_0}{\pi} \ln \left[\frac{2a \cdot \sin \left(i \frac{\pi}{2N} \right)}{\rho(x)} \right] \quad (4-5a)$$

$$L_{total} = \frac{\mu_0 a}{N} \cdot \ln \left(\left(\frac{2a}{\rho} \right)^N \left(\frac{\sqrt{N}}{2^{N-1}} \right) \right) \quad (4-5b)$$

For large values of N, we reach the limit:

$$L_{total} = \mu_0 a \cdot \ln \left[\frac{a}{\rho} \right] \quad (4-6)$$

This is the procedure used by Schelkunoff to obtain the self-inductance and the shunt Capacitance of the small metal loop of constant wire diameter as given in equations (7).

$$L_{loop} = \mu_0 a \cdot \ln \left[\frac{a}{\rho} \right], C_{loop} = \frac{\pi^2 \varepsilon_0 a}{3 \cdot \ln \left[\frac{a}{\rho} \right]} \quad (4-7)$$

From the far field radiation integral, we also know the radiation resistance of the electrically small loop, given by $R_{rad} = 20 \cdot \pi^2 (k_0 a)^4$. If we stop at this point and write the circuit model of the loop as the parallel combination of L and C from equation (7), the

anti-resonance frequency, when the short at the end of the loop opposite the feed is reflected as an open at the input, is off by 10% from the expected $\pi a = \lambda_0/4$.

$$f_0 = \frac{1}{2\pi\sqrt{LC}} = 0.55 \frac{c_0}{2\pi a} \rightarrow \pi a = \frac{\lambda_0}{3.6} \quad (4-8)$$

This inconsistency is remedied by writing the circuit model in Darlington form. According to Darlington [30], any two-port LCR network can be realized as a two-port LC network terminated in a frequency independent resistor. Schelkunoff obtains such a model for the impedance of a small dipole by enforcing its similarity to the impedance of the lowest order TM spherical mode [23].

Following the same reasoning we look for a model of the form illustrated in Fig.4-4, where L must be L_{loop} and we expect C to be close to C_{loop} while C_s should be smaller than C and of the right value to turn the constant radiation conductance G into the calculated Rrad; that is, to make

$$Re(Z_{loop}(\omega \rightarrow 0)) = 20 \cdot \pi^2 (k_0 a)^4 \quad (4-9)$$

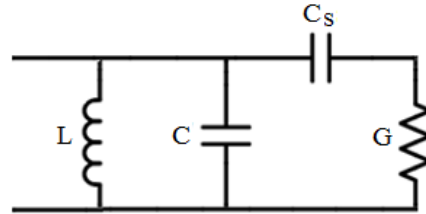


Fig. 4-4 Darlington Form Model of the Loop Antenna.

The circuit is shown in its tank form (parallel connection) because according to Schelkunoff [8], antennas should be classified in terms of whether they are a pole or a zero of the impedance function at DC, and the loop is a zero. From the lowest TE spherical mode we require G to be a constant, independent of the thinness factor of the loop, $\ln(a/\rho)$.

$$G = \frac{1}{\eta} \frac{2}{3\pi} \quad (4-10)$$

It is easy to show that C_s must be of the form shown in equation (4-11) in order to obtain a Radiation resistance that is indeed independent of the cross section (thinness) of the antenna, where g is a constant to be determined.

$$C_s = g \frac{\epsilon a}{\ln\left(\frac{a}{\rho}\right)} \quad (4-11)$$

From the given circuit, we obtain the admittance of the loop

$$Y_{loop}(\omega) = \left(\frac{1}{G} + \frac{1}{j\omega C_s}\right)^{-1} + \frac{1}{j\omega L} + j\omega C \quad (4-12)$$

So that the real part of the input impedance of the loop is

$$\begin{aligned} & Re(Z_{loop}(\omega)) \\ &= \frac{\omega^4 L^2 C_s^2 G}{(G - \omega^2 L C G - \omega^2 L C_s G)^2 + (\omega C_s - \omega^3 L C C_s)^2} \end{aligned} \quad (4-13)$$

For small ω , we only keep the term G^2 in the denominator resulting in equation (4-14):

$$Re(Z_{loop}(\omega \rightarrow 0)) = \frac{\omega^4 L^2 C_s^2 G}{G^2} = \frac{\omega^4 L^2 C_s^2}{G} \quad (4-14)$$

Substituting L and C_s from equations (4-7) and (4-11) yields:

$$Re(Z_{loop}(\omega \rightarrow 0)) = \frac{(\omega^2 \mu_0 a g \epsilon_0 a)^2}{G} \quad (4-15)$$

Given the value of G from equation (4-10), this results in equation (4-9) if $g = 1/3$.

With $C = C_{loop}$, $L = L_{loop}$ and C_s as derived, the anti-resonance of the circuit of Fig. 4-4 lies within 1% of the expected $\pi a = \lambda_0/4$.

4.3 Deriving the Model for Quadrant Fed Metal Loop Antennas

In Schelkunoff's original model a single feed is assumed for the loop. In our case we have more than one feed; but the procedure is the same. For Mode 0, the job of the multiple feeds is to maintain the current along the perimeter of the loop as uniform as possible. For Mode 1, the multiple feeds are used to excite a $\cos(\varphi)$ dependence of the current along the perimeter.

Since we are about to follow the same procedure illustrated with Schelkunoff's single-feed loop in Section II, it bears outlining the whole procedure and its logic before proceeding with the details:

When we start with Schelkunoff's model, the cascade of transmission lines leads to an inescapable frequency dependent input impedance that for the dipole mode is capacitive at the low end whereas for the loop mode it is inductive. By going to the DC limit, we are forced to select that Capacitance or that Inductance as the value given by the

model. Then, still following Schelkunoff, we know that the dipole mode is a pole of the impedance function and as such we expect it to have an inductance in series with the DC Capacitance. The resonance seen in the input impedance forces the choice of that inductance by the requirement $\omega_{res} = 1/\sqrt{LC}$; again, this choice is inescapable. The same thing happens with the loop mode: it must be a zero of the impedance function and therefore it must have a capacitor in parallel with it. The resonance seen in the impedance function determines that Capacitance.

Then to complete the model we need to add the radiation resistance for the dipole mode and the radiation conductance for the loop mode. Since we eventually will have multiple feed points, the current carried on the antenna can be guaranteed to stay close to the ideal distribution (this is the same trick employed by the clover-leaf antenna loop): the loop mode can be assumed to have a uniform azimuthal current whereas the dipole mode can be assumed to have the cosine distribution. (Of course, we would expect that when the individual center-fed quadrants of the antenna approach a wavelength in length, this assumption would break down. That means four feed points are not enough to expect the antenna to function up to when it is four wavelengths in circumference. For the 17-inch diameter antenna used as an example here that occurs above 800MHz.) Given the reasonable assumption of the ideal current distribution, the radiation resistance is calculated by the far field integration approach and again we have a result forced upon us by the principal wave model.

However, at this point there is an interesting problem. If as customary we were to place the frequency dependent radiation resistance in series with the series LC of the

dipole mode, we find that the resonance of the antenna does not occur at the frequency it is supposed to occur at ($2\pi a = \lambda$ for Mode 1.) Similarly, for the loop mode, the frequency dependent radiation conductance also results in the loop's tank resonance occurring off the expected frequency ($\pi a = \lambda/4$ for a single-feed loop). The cause of this problem is the frequency dependence of the radiation resistance.

Therefore, we turn to Schelkunoff's *Advanced Antenna Theory* [23] where he points out that the correct circuit models of these fundamental antennas are not the electrically small models (series LCR and shunt LCG) but rather the circuit models that closely represent the lowest order spherical TM and TE wave modes. Those are given in Darlington form, where the radiation loss is represented by a fixed resistance (a known factor of the impedance of free space) that is connected to the rest of the circuit by a coupling element. When we adopt that form for the antenna's modes of concern the value of the coupling elements is forced upon us by having to replicate the radiation resistance calculated from the far field integral.

At every turn, following Schelkunoff's method forces upon us the choice of all the circuit elements. The happy result at the end is that indeed now the antenna resonates at the expected frequencies.

In the following section, we outline the steps described above in detail; and to maximize clarity we do it for one particular cross section of the antenna, so that the various circuit elements have actual units of Farads and Henries, and so forth. When this analysis is repeated for a large number of toroidal radii and cross sections, it turns out that the fundamental LC circuit elements can always be written down in expressions

similar to those derived by Schelkunoff for electrically small antennas, involving factors of the radius of the toroid, and logarithms of the ratio of the radius to its cross section. We give those closed-form expressions in the text.

4.4 Deriving the Model for a Quadrant Fed Mode 0

The Mode 0 case can be viewed as an evolution of the single feed loop as suggested in Fig. 4-5. Instead of a symmetry PEC at $\varphi = \pi$, we now have two walls spanning a quadrant (at $\varphi = 0$ and $\varphi = \pi/2$ in the figure.) Therefore, to zeroth order we expect the quadrant series inductance to be one fourth of that of the singly fed loop and the quadrant shunt capacitance to also be one fourth of the shunt capacitance of the singly fed loop. This would lead automatically to an anti-resonance frequency that is 4 times higher than that of the single loop.

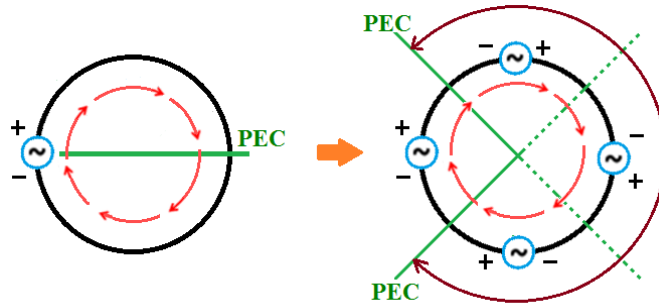


Fig. 4-5 Evolution of the Quadrant Fed Mode 0 Model.

For reasons that will become apparent presently, we first solve the case of PEC boundaries at $\varphi = \pm\pi/2$. We divide the half circle into many sections of length 2ρ as shown in Fig.4-6.

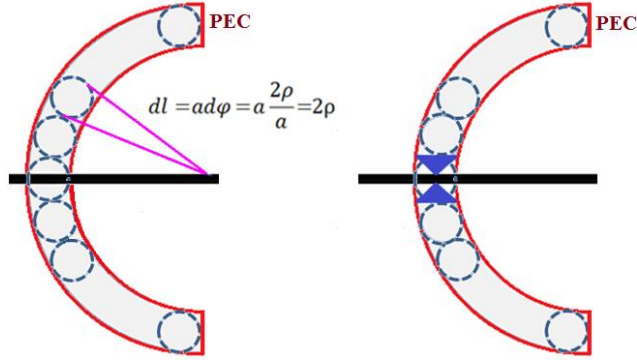


Fig. 4-6 The Loop Is Divided into a Large Number of Sections of Lengths 2ρ (Left). Then the First Segment Is Replaced by a Small Bicone as a Feed (Right).

As shown, the first section is replaced by a bicone with top diameter of 2ρ and length ρ . The impedance of this section, having an internal half angle of $\pi/4$ is:

$$Z_0 = 120 \cdot \ln \left(\cot \left(\frac{\pi}{8} \right) \right) \quad (4-16)$$

The next segment is a “two wire” line of wire diameter 2ρ and center to center separation 4ρ with impedance of Z_1 :

$$Z_1 = 120 \cdot \cosh^{-1} \left(\frac{4\rho}{2\rho} \right) \quad (4-17)$$

And the total number of sections in the quadrant will be:

$$N = \text{round} \left[\frac{\left[\frac{\pi}{2} a - 2\rho \right]}{2\rho} \right] \quad (4-18)$$

For example assuming $a=7$ inches, and $\rho = 0.05$ inch, Then the number of sections needed is:

$$N = \text{round} \left[\frac{\left[\frac{\pi}{2} \cdot 7 - 0.05 \right]}{2 \cdot 0.05} \right] = 109 \quad (4-19)$$

The above dimensions have been chosen because Schelkunoff's various approximations are all equivalent for the case of high fineness antennas (thin wires). Once we demonstrate this works, we can extend it to the thicker cross sections common to magneto-dielectric antennas.

The impedance of each section is

$$Z_n = 120 \cdot \cosh^{-1} \left(\frac{2a \cdot \sin \left(n \cdot \frac{2\rho}{a} \right)}{2\rho} \right) \quad (4-20)$$

Such that the transmission line cascade ranges for the bicone feed of 105 ohms to a last segment of 676 ohms. The impedance seen at the input of the last section is a short circuit:

$$Z_{in_N} = jZ_n \tan(k_0 \cdot 2\rho) \quad (4-21)$$

Then the input impedance of each of the sections follows:

$$\begin{aligned} Z_{in_m} \\ = Z_{N+1-m} \frac{Z_{in_{m-1}} \cos(2k_0\rho) + jZ_{N+1-m} \sin(2k_0\rho)}{Z_{N+1-m} \cos(2k_0\rho) + jZ_{in_{m-1}} \sin(2k_0\rho)} \end{aligned} \quad (4-22)$$

So that the input impedance seen at the feed is

$$Z_{in} = Z_0 \frac{Z_{in_N} \cos(2k_0\rho) + jZ_0 \sin(2k_0\rho)}{Z_0 \cos(2k_0\rho) + jZ_{in_N} \sin(2k_0\rho)} \quad (4-23)$$

From this result, the inductance lumped circuit element is obtained by evaluating the effective complex inductance, $L_{eff} = Z_{in}/j\omega$, at zero frequency (DC.) A plot of the effective complex inductance is shown in Fig.4-7 (solid line curves). A closed form

expression, L_{app} , that is within 1% of the DC limit is denoted by the constant dashed line and shown in equation (4-24); not surprisingly, half of equation (4-6).

$$L_{app} = L_{halfM0} = \frac{\mu a}{2} \cdot \ln \left[\frac{a}{\rho} \right] \quad (4-24)$$

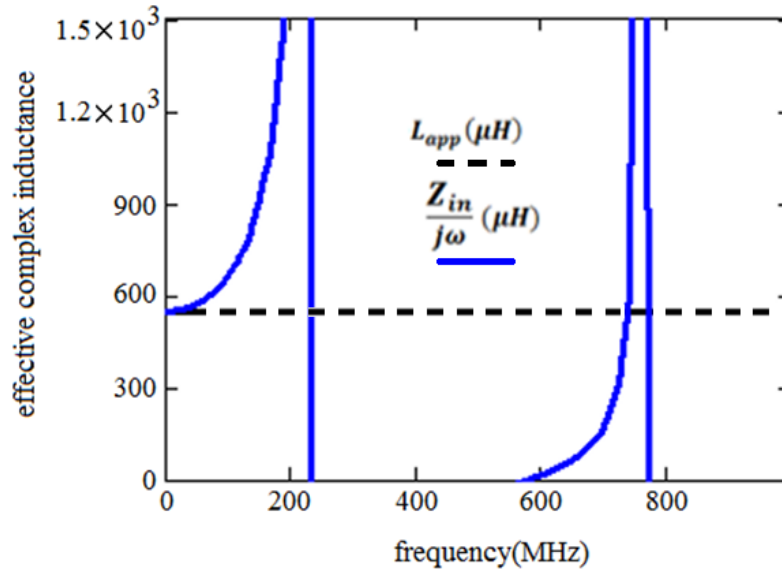


Fig. 4-7 Effective Complex Inductance Versus Frequency.

It follows that for the quadrant-fed case, invoking the PEC symmetry plane at $\varphi = 0$ gives equations (4-25) for the inductance and shunt capacitance, of the circuit.

$$L_{Q_M0} = \frac{\mu a}{4} \cdot \ln \left[\frac{a}{\rho} \right], C_{Q_M0} = \frac{\pi^2 \epsilon a}{12 \cdot \ln \left[\frac{a}{\rho} \right]} \quad (4-25)$$

Given that one quadrant radiates a quarter of the power.

$$R_{rad_Q_M0} = 5 \cdot \pi^2 (ka)^4 \quad (4-26)$$

Setting:

$$G = 4 \cdot \frac{1}{\eta} \frac{2}{3\pi} \text{ and } C_s = g \frac{\epsilon a}{\ln\left(\frac{a}{\rho}\right)} \quad (4-27)$$

The same procedure yields $g = 4/3$ to obtain the Radiation resistance and recovering the expected resonant frequency. The equivalent circuit model for Mode 0 is the same as that in Fig.4-4 except that the circuit parameters are now those given by equations (4-25) through (4-27).

4.5 Deriving the Model for a Quadrant Fed Mode 1

The evolution of the Mode 1 model is suggested in Fig. 4-8. Similar to Mode 0, the active impedance at one feed is obtained by solving the half loop but this time it is terminated on a PMC symmetry plane.

The reason that the PEC and PMC planes have been chosen as seen is that this is precisely the symmetry required to create the Mode 1 and Mode 0 aligned with the conventional Cartesian axes, Mode 0 being a z polarized monopole mode, while Mode 1 consists of x-polarized and y-polarized planar dipole modes. This forces the input impedance to be calculated at the mid- point between the symmetry planes. However this can be easily handled with a displaced impedance when required as done below using the asymmetric feed technique.

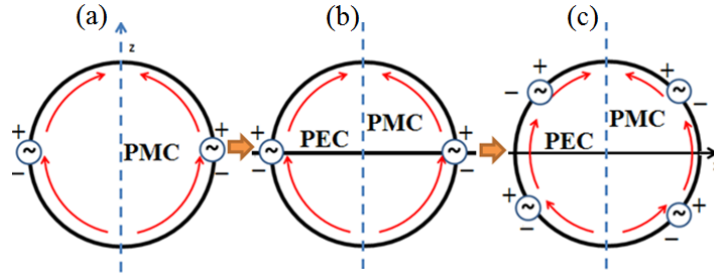


Fig. 4-8 Evolution of the Quadrant Fed Mode 1 Model.

As before, we divide the half circle into a number of sections of lengths 2ρ and replace the first section with a bicone with top diameter of 2ρ and length ρ . The rest of the procedure is identical to that for Mode 0 except in this case the cascade of transmission lines terminates on an open circuit instead of a short circuit. That is, the only difference is the impedance of the last section:

$$Z_{in_{N-OC}} = -jZ_n \cot(k \cdot 2\rho) \quad (4-28)$$

In this case, the shunt capacitance lumped circuit element is obtained by evaluating the effective complex Capacitance corresponding to the input admittance, $C_{eff} = Y_{in}/j\omega$, at zero frequency (DC); where Y_{in} is the inverse of Z_{in} . A plot of the effective complex capacitance is shown in Fig.4-9 (solid line curves) and a closed form expression, C_{app} , that is within 1% of the DC limit is denoted by the constant dashed line.

$$C_{app} = \frac{\pi \epsilon_0 \left(\frac{\pi a}{2}\right)}{\ln\left(\frac{\frac{\pi}{2} a}{2\rho}\right)} \quad (4-29)$$

The next step is to find the inductance which can be done by using the observed series resonance at 297.3 MHz.

In this example, we conclude the series inductance is 0.173 micro-Henries a quantity closely approximated by the closed-form expression:

$$L_{app} = \frac{\mu_0 \left(\frac{\pi a}{2}\right) \ln\left(\frac{\frac{\pi}{2} a}{2\rho}\right)}{3\pi} \quad (4-30)$$

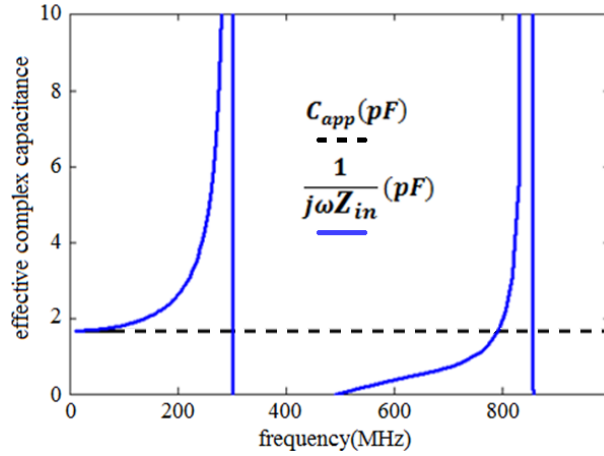


Fig. 4-9 Effective Complex Capacitance Versus Frequency

Calculating the Radiation resistance of the full Mode 1 current distribution by integrating the far field radiated power, referenced to the total current flowing across the $y=0$ plane we obtain, $R_{rad} = 493(2a/\lambda)^2$.

For an antenna that is halved with a PMC wall, the impedance is doubled meaning that the impedance of the half antenna will be $R_{rad-half-M1} = 2 \times 493(2a/\lambda)^2$

In the thin wire limit, we expect the resonance to occur when

$$\frac{\pi}{2} a = \frac{\lambda}{4} \quad (4-32)$$

We have so far obtained the zeroth order model of the case shown in Fig. 4-8 (a). The series connection of the above L, C and R_{rad} resonates 10% higher than equation (4-32). Remembering that we had a similar problem with the simple loop model, and that it

was remedied by the Darlington form of the circuit, we proceed for now as is and will check to see if the result recovers the expected resonance at the end.

To model a quadrant, we slice the loop of Fig. 4-8(a) with a PEC symmetry plane and the impedance of a quadrant, fed against the PEC plane, is simply half of that of the half section:

$$Z_{Q_PEC_M1} = \frac{Z_{halfM1}}{2} \quad (4-33)$$

In dividing the source impedance in half we then divide the Radiation resistance in half recovering:

$$R_{rad_Q_PEC} = 493 \left(\frac{2a}{\lambda} \right)^2 \quad (4-34)$$

But the quadrant of the Mode 1 antenna is fed at the center of the quadrant as suggested in Fig.4-8(c). Then it follows, by the rules of the asymmetrically fed antenna (or sleeve-fed monopole) that the impedance at the displaced feed-point must deliver the same total power as the original base feed. Since the current at the mid quadrant point for Mode 1 must have the value $\cos(\pi/4) = 0.707$ relative to the value at the base, $I_{midQ}^2 Z_{midQ} = I_{base}^2 Z_{base}$ leads to the impedance being multiplied by a factor of 2 : $Z_{Q_M1} = 2 \cdot Z_{Q_PEC_M1}$.

In summary, the Mode 1 quadrant circuit elements are:

$$C_{Qc} = \frac{1}{2} \cdot \frac{\frac{\pi^2}{2} \epsilon a}{\ln\left(\frac{\frac{\pi}{2} a}{2\rho}\right)}, L_{Qc} = 2 \cdot \frac{\mu \frac{a}{2} \ln\left(\frac{\frac{\pi}{2} a}{2\rho}\right)}{3} \quad (4-35)$$

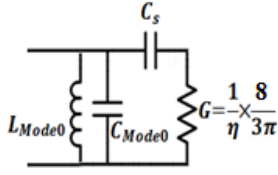
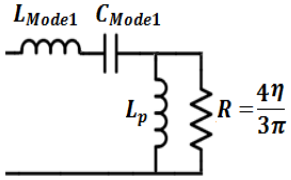
$$R_{rad_Qc} = 2 \cdot 493 \left(\frac{2a}{\lambda} \right)^2 \quad (4-36)$$

Where the subscript Qc stands for a quadrant center fed. To obtain the Darlington form we assume a circuit consistent with the lowest order TM mode as shown in Fig.4-10, where we have multiplied the TM Resistance by **2** to account for the factor of 2 from the quadrant feed. The result is that $L = L_{Qc}$, $C = C_{Qc}$ and following the same kind of procedure outlined in equations (9) through (15), we determine the coupling inductor:

$$L_p = \frac{\mu a}{3} \quad (4-37)$$

And the resonance is now exactly at $(\pi/2)a = \lambda/4$ as desired. Table 4-1 summarizes the Mode 0 and Mode 1 quadrant-fed metal loop antenna circuit models.

Table 4-1 Summary of Quadrant Fed Metal Loop Antenna Models

	
$L_{M0} = \frac{\mu a}{4} \cdot \ln \left[\frac{a}{\rho} \right]$	$L_{M1} = \frac{\mu a}{3} \cdot \ln \left(\frac{\frac{\pi}{2} a}{2\rho} \right)$
$C_{M0} = \frac{\pi^2 \varepsilon a}{12 \cdot \ln \left[\frac{a}{\rho} \right]}$	$C_{M1} = \frac{\frac{\pi^2}{4} \varepsilon a}{\ln \left(\frac{\frac{\pi}{2} a}{2\rho} \right)}$
$C_s = \frac{4}{3} \frac{\varepsilon a}{\ln \left(\frac{a}{\rho} \right)}$	$L_p = \mu a / 3$

It should be noted that the radiation resistor and the radiation conductor in these models differs from Schelkunoff's TM and TE models by the effect of the quadrant feed. In the case of mode 0 it is a factor of 4 because the loop has been cut out into 4 sections and in the case of mode 1 it is a factor of 2 because the feed is located at the 45 degree line.

The fact that the circuit elements that couple the antenna to free space (L_p , C_s) in the above Darlington models do not alter the value of the near field inductance of the antenna models means that we can immediately insert the material properties into these models the way Sebastian did in his dissertation [2].

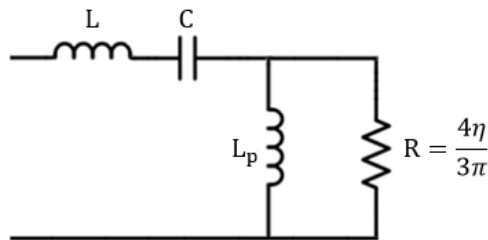


Fig. 4-10 Darlington Form Model of the Quadrant Fed Mode1.

4.6 Models for Quadrant Fed Dielectric Antennas

Even though both Mode 0 and Mode 1 are quadrants of the same antenna, the interior impedance added in series to the inductance is not the same for both Modes. The impedance consists of a quadrant's worth of dielectric with an excess internal inductance per unit length. When the flux is uniform inside the quadrant, as in Mode 0, we immediately write for a length of arc of $\pi a/2$:

$$L_{int_{M0}} = \frac{\mu_0 \mu_{int} \pi a}{16\pi}; C_{int_{M0}} = \frac{\pi \rho^2 \varepsilon_0 \varepsilon_{int}}{\frac{\pi a}{2}} \quad (4-38)$$

$$\therefore Z_{int_{M0}} = j\omega \frac{\mu_0 \mu_{int} \pi a}{16\pi} + \frac{1}{j\omega \frac{\pi \rho^2 \varepsilon_0 \varepsilon_{int}}{\frac{\pi a}{2}}} \quad (4-39)$$

However, for the $\cos(\varphi)$ flux occurring in the quadrant of Mode 1, the internal energy integral is halved, therefore if the feed were at the symmetric (PEC) base point we would have:

$$L_{int_{M1}} = \frac{\mu_0 \mu_{int} \pi a}{32\pi}; C_{int_{M1}} = \frac{\pi \rho^2 \varepsilon_0 \varepsilon_{int}}{\pi a}; \quad (4-40a)$$

$$\therefore Z_{int_{M1_basePEC}} = j\omega \frac{\mu_0 \mu_{int} \pi a}{32\pi} + \frac{1}{j\omega \frac{\pi \rho^2 \varepsilon_0 \varepsilon_{int}}{\pi a}} \quad (4-40b)$$

However, feeding Mode 1 at the mid quadrant point does not feed it at the peak current. Therefore, this internal impedance is also transformed by the factor of 2.

$$Z_{int_{M1}} = j\omega \frac{\mu_0 \mu_{int} \pi a}{16\pi} + \frac{1}{j\omega \frac{\pi \rho^2 \varepsilon_0 \varepsilon_{int}}{\pi a/2}} \quad (4-41)$$

The fundamental assumption when we insert the material internal impedance into the circuit is that all the flux in the antenna goes through the material. This means that the internal impedances just derived are placed in series in front of both circuits obtained above. Therefore, for Mode 0:

$$Z_{\varepsilon_{M0}} = \frac{j\omega \mu_0 (\mu_{int} - 1) \pi a}{16\pi} + \frac{1}{j\omega \frac{\pi \rho^2 \varepsilon_0 (\varepsilon_{int} - 1)}{\frac{\pi}{2} a}} \quad (4-42)$$

$$+ \frac{1}{\frac{1}{j\omega \frac{\mu_0 a}{4} \ln\left[\frac{a}{\rho}\right]} + \frac{j\omega \pi^2 \varepsilon_0 a}{12 \cdot \ln\left[\frac{a}{\rho}\right]} + \frac{1}{\frac{1}{j\omega \frac{4}{3} \frac{\varepsilon_0 a}{\ln\left(\frac{a}{\rho}\right)}} + \eta \frac{3\pi}{8}}}$$

For Mode 1 we have:

$$Z_{\varepsilon_{M1}} = j\omega \frac{\mu_0(\mu_{int} - 1)\pi a}{16\pi} + \frac{1}{j\omega \frac{\pi \rho^2 \varepsilon_0 (\varepsilon_{int} - 1)}{\pi a/2}} + \frac{j\omega \mu_0 a}{3} \cdot \ln\left(\frac{\frac{\pi}{2} a}{2\rho}\right) + \frac{1}{\frac{j\omega \frac{\pi^2}{4} \varepsilon_0 a}{\ln\left(\frac{\frac{\pi}{2} a}{2\rho}\right)}} + \frac{1}{\frac{3}{j\omega \mu_0 a} + \frac{1}{\eta} \frac{3\pi}{4}} \quad (4-43)$$

The annotation subscript ε reminds the reader that these are the penetrable antenna models for dielectric antennas.

4.7 Models for Quadrant Fed Permeable Antennas

Following Sebastian [2], to enforce duality we swap all μ for ε and vice versa and the Impedances above become the Admittances seen by an ideal uniform frill current strip at the feed. So, for Mode 0 of the permeable antenna we will obtain equation 44, corresponding to the circuit of Fig. 4-11.

$$\begin{aligned}
Y_{\mu_{M0}} &= j\omega \frac{\epsilon_0(\epsilon_{int} - 1)\pi a}{16\pi} + \frac{1}{j\omega \frac{\pi \rho^2 \mu_0 (\mu_{int} - 1)}{\frac{\pi}{2} a}} \\
&+ \frac{1}{\frac{1}{j\omega \frac{\epsilon_0 a}{4} \cdot \ln\left[\frac{a}{\rho}\right]} + j\omega \frac{\pi^2 \mu_0 a}{12 \cdot \ln\left[\frac{a}{\rho}\right]} + \frac{1}{j\omega \frac{4}{3} \frac{\mu_0 a}{\ln\left(\frac{a}{\rho}\right)} + \frac{1}{\eta} \frac{3\pi}{8}}}
\end{aligned} \tag{4-44}$$

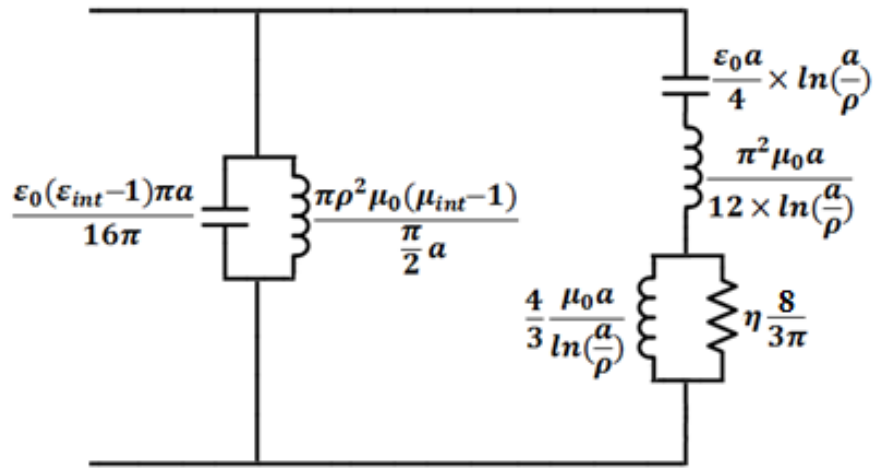


Fig. 4-11 Equivalent Circuit for Mode 0 of the Permeable Antenna

For Mode 1 of the permeable antenna we obtain:

$$Y_{\mu_{M1}} = j\omega \frac{\epsilon_0(\epsilon_{int} - 1)\pi a}{16\pi} + \frac{1}{j\omega \frac{\pi \rho^2 \mu_0 (\mu_{int} - 1)}{\frac{\pi a}{2}}} \tag{4-45}$$

$$+ \frac{j\omega\epsilon_0 a}{3} \cdot \ln\left(\frac{\pi a}{2\rho}\right) + \frac{1}{\frac{j\omega \frac{\pi^2}{4} \mu_0 a}{\ln\left(\frac{\pi a}{2\rho}\right)}} + \frac{1}{\frac{3}{j\omega\epsilon_0 a} + \eta \frac{3\pi}{4}}$$

The circuit is shown in Fig.4-12

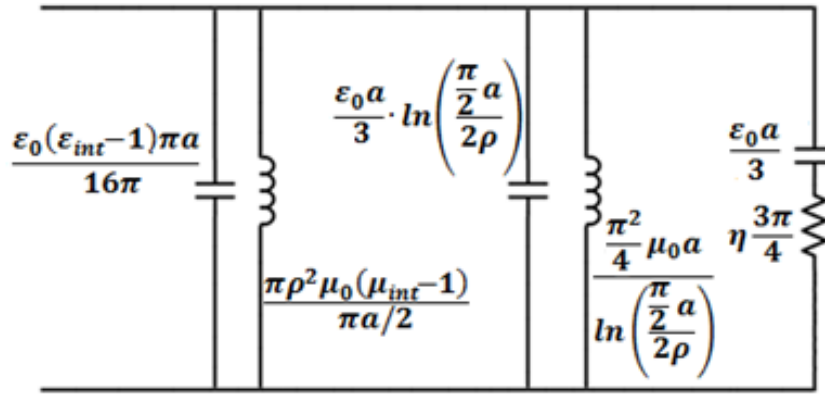


Fig. 4-12 Equivalent Circuit for Mode 1 of the Permeable Antenna

4.8 Comparison to Previous Results

The key result of the models originally derived by Sebastian is the closed-form determination of the efficiency as a function of frequency. Sebastian gives [2] :

$$eff_{loop} = \frac{1}{1 + \frac{12}{\pi \left(\frac{\rho}{a}\right)^2 (ka)^5 \left(\frac{\mu''}{[\mu' - 1]^2 + \mu''^2} \right) + \frac{3\epsilon''}{2\pi(ka)^3}} \quad (4-46)$$

$$\begin{aligned}
& eff_{dipole} \\
& = \frac{1}{1 + \frac{6}{\left(\frac{\rho}{a}\right)^2 (kl)^3 \left(\frac{\mu''}{[\mu' - 1]^2 + \mu''^2} \right) + \frac{3\varepsilon''}{4(kl)}}} \quad (4-47)
\end{aligned}$$

The main difference between those derivations and the ones in this report is the explicit representation of the radiation resistance or conductance in Darlington form. This form yields results exactly like the low frequency, electrically small limit approximation of the radiation terms but has the advantage of deviating realistically from that result at high frequencies, precisely when the antenna is no longer electrically small. The Darlington form correctly approximates to first order the coupling of the antennas to the lowest order spherical wave dipole modes.

This is important because, while the electrically small radiation resistance of a dipole increases as ω^2 , in reality we know this increase cannot go on forever, so that the efficiency expressions of equations (4-46) and (4-47) were overstating the efficiency at the high end, by tending to 100% efficiency.

The efficiency of the antennas is derived directly from the above circuits as the ratio of the Radiation Conductance to the total Conductance which includes the loss conductance due to the material loss in the permeability of the material, μ_{int} . (For simplicity, we have ignored the dielectric loss term which can always be included if needed.)

$$eff = \frac{Re(Y_{rad})}{Re(Y_{loss}) + Re(Y_{rad})} = \frac{G_{rad}}{G_{loss} + G_{rad}} \quad (4-48)$$

The Mode 1 circuit model, it is the simplest case. It should behave like Sebastian's linear dipole model.

$$eff_{M1} = \frac{Re \left[\frac{1}{\frac{3}{j\omega\epsilon_0 a} + \eta \frac{3\pi}{4}} \right]}{Re \left[\frac{1}{j\omega \frac{\pi\rho^2\mu_0(\mu_r - 1)}{\frac{\pi a}{2}}} \right] + Re \left[\frac{1}{\frac{3}{j\omega\epsilon_0 a} + \eta \frac{3\pi}{4}} \right]} \quad (4-49)$$

$$eff_{M1} = \frac{1}{1 + \left[\frac{3\pi}{8ka \left(\frac{\rho}{a}\right)^2} + \frac{1.89}{(ka)^3 \left(\frac{\rho}{a}\right)^2} \right] \left(\frac{\mu''}{[\mu' - 1]^2 + \mu''^2} \right)} \quad (4-50)$$

To compare with Sebastian's original closed form expressions, recall that those derivations used the frequency dependent Radiation Resistance form instead of the Darlington form of the circuit. Therefore, to recover that approximation all we have to do is go to the low frequency limit. This means that in the denominator of the last expression we would simply ignore the first term in the square bracket when compared to the second. The resulting form is identical to Sebastian's result in equation (4-47).

Similarly, the efficiency for Mode 0 is given by the ratio of the conductances, the real parts of the admittances:

$$\begin{aligned}
Y_{rad} = & \left[\frac{1}{\frac{1}{j\omega \frac{4}{3} \frac{\mu_0 a}{\ln\left(\frac{a}{\rho}\right)} + \frac{3\pi}{8\eta}} + \frac{j\omega \frac{\pi}{12} \mu_0 a}{\ln\left(\frac{a}{\rho}\right)}} \right. \\
& \left. + \frac{1}{j\omega \varepsilon_0 \frac{a}{4} \ln\left(\frac{a}{\rho}\right)} \right]^{-1} \quad (4-51) \\
Y_{loss} = & \frac{1}{j\omega \frac{\pi \rho^2 \mu_0 (\mu_r - 1)}{\frac{\pi a}{2}}}
\end{aligned}$$

Inserting these expressions into equation (4-48) results in an expression for the efficiency of mode 0.

To illustrate the difference the Darlington form of the circuits makes, we select a test case: a toroid of mean radius 7 inches (inner radius 5.5 inches, outer radius 8.5 inches) and mean cross sectional radius of 1.129 inches (a rectangular cross section of width = 3 inches and thickness = 0.667" plus its image), assuming the CZN laminate material of the antenna in [3] with the permeability shown in Fig.4-13 and a relative permittivity of 3.25.

Fig.4-14, shows the Sebastian result for the loop as the red curve and the results from the derivation in this report for Mode 0 as the blue curve. Fig. 4-15 shows the corresponding results for Mode 1. Mode 0 peaks at about -0.1dB efficiency. The old loop model overstated the efficiency by almost 2.5dB in the 100 MHz range. Mode 1 now

tapers off at the high end to about -1dB efficiency instead of approaching 0dB asymptotically.

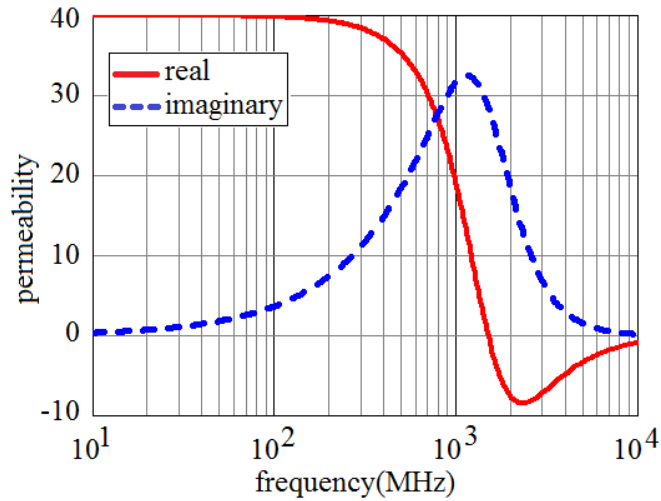


Fig. 4-13 Permeability of the CZN Laminate Material

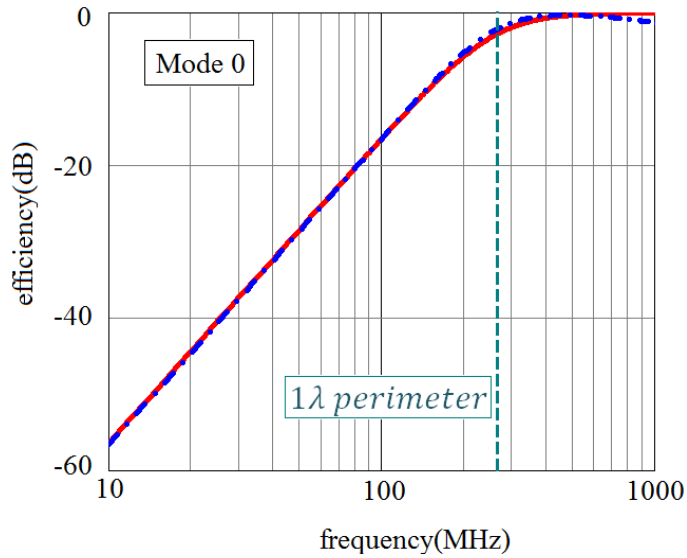


Fig. 4-14 Original Closed-Form Efficiency Expressions (Red Curve), Results from the Derivation in This Report (Blue Curve), Dashed Line Shows 1λ Perimeter.

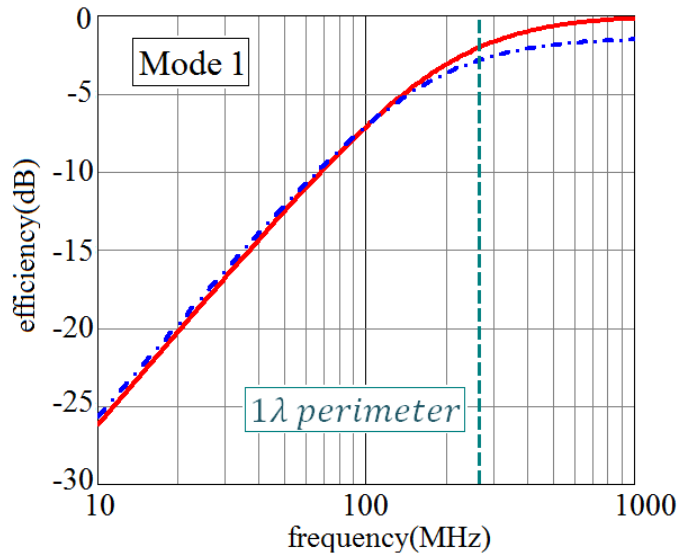


Fig. 4-15 Original Closed-Form Efficiency Expression for a Linear Dipole (Red Curve), Results From the Derivation in This Report (Blue Curve), Dashed Line Shows 1λ Perimeter.

Comparing Fig. 4-14 and 4-15 we see that the dipole (Mode 1) is much more efficient than the loop (Mode 0) at the low end, as expected, but the efficiencies cross over when the antenna circumference exceeds one wavelength. In this case for the 7 inch mean radius antenna the above curves show this happening at 360 MHz.

4.9 The Input Impedance and the Effect of a Realistic Feed Loop

The circuits derived in the previous sections yield the active impedance seen at the quadrant feed under the assumption that a uniform current band excites the toroid at the feed position. This is implicit in the method of derivation when we use duality. It is akin to the assumption of a perfect Delta Voltage generator or “magnetic current band” being used to drive metal antennas. Now, we know from experience, and Schelkunoff’s discussion of the feed gap problem of metal antennas [8], that a realistic feed differs from

the ideal in the excess capacitance of the feed region. Schelkunoff recommends tapering the feed region down as a biconical transmission line and then if this section is long enough and the antenna thin enough, the gap capacitance becomes a negligible contribution.

This works with metal antennas because the series impedance of metal is always almost zero, so that “necking down” the antenna at the feed does not really block the flux injected by the source generator. Unfortunately, in the case of permeable materials, any reduction of cross section results in an increase in Reluctance of the local flux path that could force the magnetic current to exit the antenna at that point. Therefore such an approach must be evaluated carefully, preferably in a fullwave simulation, before implementing it.

Without any such modification, the analog to the excess capacitance at the feed in a metal antenna is the excess self-impedance of the metal loop used to drive the exciting current around the permeable flux channel. The consequences of this additional impedance are now examined.

The antenna input impedance we have calculated must be related to the inductance seen by the feed loop simply by

$$L_{loopfeed} = \frac{Z}{j\omega} \quad (4-52)$$

By definition, we have the correct answer for Z and L, in the case of an idealized frill current. However, we note that this inductance is proportional to the susceptance of the “core” material ($\mu - 1$). Therefore, we are missing the part of the inductance that the loop must see when the material vanishes, that is, the pure self-inductance of the loop in

free space, L_{loop_0} . A full model of the transition from the inductance being dominated by the core to the inductance being that of the empty loop, as a function of μ is beyond the scope of this paper. However, since the permeable core term appears in terms of the susceptance, we should be able to approximate the total inductance seen by the loop by equation (4-53).

$$L_{loopfeed} = \frac{Z}{j\omega} + L_{loop_0} \quad (4-53)$$

In addition, we have another term that the frill current does not give us. Because by definition the frill current is assumed to be purely circuital, azimuthally constant, and electrically small, it develops no shunt capacitance; but we know that all realistic loops have such a shunt capacitance. Therefore, for a permeable toroidal antenna in free space fed at the quadrants, the true input impedance seen at the loop feed is the parallel combination of:

$$L_{loopfeed_{M0,M1}} = \mu_0 a_{wire} \cdot \ln \left[\frac{a_{wire}}{\rho_{wire}} \right] + \frac{Z_{M0,M1}}{j\omega} ; \quad (4-54)$$

$$C_{loopfeed} = \frac{\pi^2 \epsilon a_{wire}}{3 \cdot \ln \left[\frac{a_{wire}}{\rho_{wire}} \right]}$$

Since normal practice is to use these permeable antennas as conformal antennas, flush on a ground plane, we really have half a structure fed by half a feed loop. But when we do this, again normal practice dictates that symmetry be maximized by not putting the feed at the point where the coax loop breaks through the ground but rather at the top midpoint of the permeable core as shown in Fig.4-16, pushing any parasitic resonances of the feed region as high in frequency as possible.

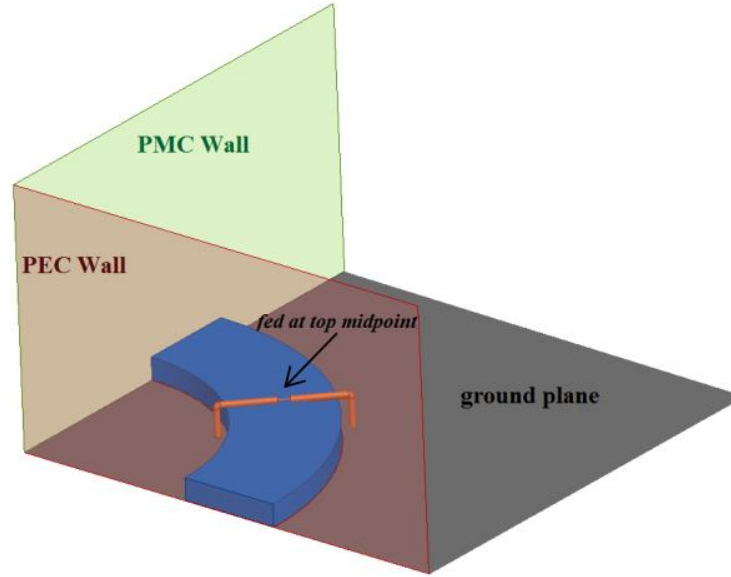


Fig. 4-16 Schematic of One Quadrant in Mode 1 of the Permeable Antenna Fed at the Top Midpoint of Each Quadrant Instead of at the Ground Plane.

From the discussion on the Mode 0 loop we immediately know that for the conformal antenna fed at the top midpoint of the core, against the short circuit at the ground plane, the input impedance at the feed loop must then be:

$$L_{loopconf_{M0,M1}} = \frac{\mu_0 a_{wire}}{2} \cdot \ln \left[\frac{a_{wire}}{\rho_{wire}} \right] + \frac{Z_{M0,M1}}{j\omega 2} ;$$

$$C_{loopconf} = \frac{\pi^2 \epsilon a_{wire}}{6 \cdot \ln \left[\frac{a_{wire}}{\rho_{wire}} \right]}$$
(4-55)

4.10 The Effect of the Realistic Metal Loop Feed and HFSS Confirmation

Consider an antenna constructed using the ferromagnetic metal laminate (the material of Fig. 4-13) in the form of a half-toroid on ground, 0.667” thick and inner and outer radii 5.5” and 8.5”. This is equivalent to a mean toroid cross sectional radius

(including the image) of 29mm. For antennas constructed from such metal laminates, the cross section of the feed-loop is always made larger than the permeable core cross section to prevent the core material from shorting out or capacitively “loading down” the feed-loop. Thus, we assume a metal feed-loop of radius $a_{wire} = 36mm$ and of cross sectional radius corresponding to a 0.141” coaxial cable, $\rho_{wire} = 1.79mm$.

This clearance between the feed-loop metal and the core means that, of the loop area, only the fraction $(29/35)^2 = 0.687$ is filled with the permeable material; and so the antenna impedance contribution to the loop inductance must be derated by this factor. Additionally, even though the permittivity of the magneto-dielectric material is assumed to be 3.25, the effective permittivity inside the feed-loop is closer to 2.1 because, again, the loop area is larger than the cross section of the material (inserting air gaps in series with the loop’s shunt capacitance.) After these corrections, equations (4-55) give the expected input impedance in closed-form. For comparison, one quadrant of this half toroid on ground was modeled and simulated using HFSS as shown in Fig. 16. The results for both Modes 1 and 0 are shown in Figures 4-17 and 4-18.

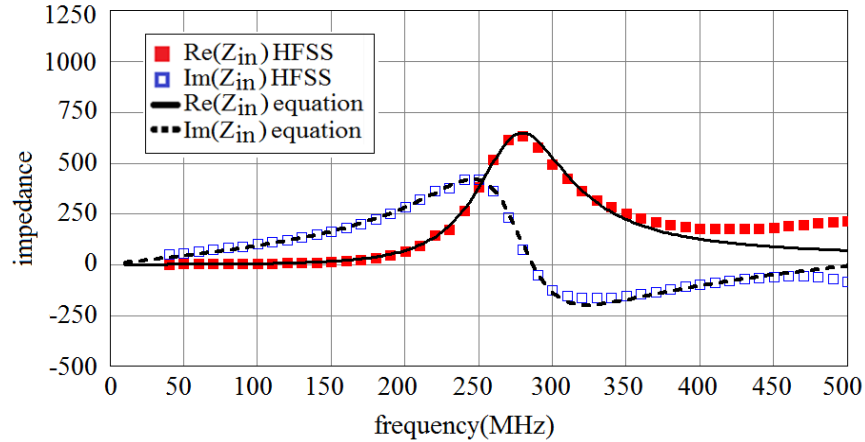


Fig. 4-17 Mode 1 Active Input Impedance at the Feed Loop Based on the Closed Form Equations (Solid) and Based on an HFSS Simulation (Dashed).

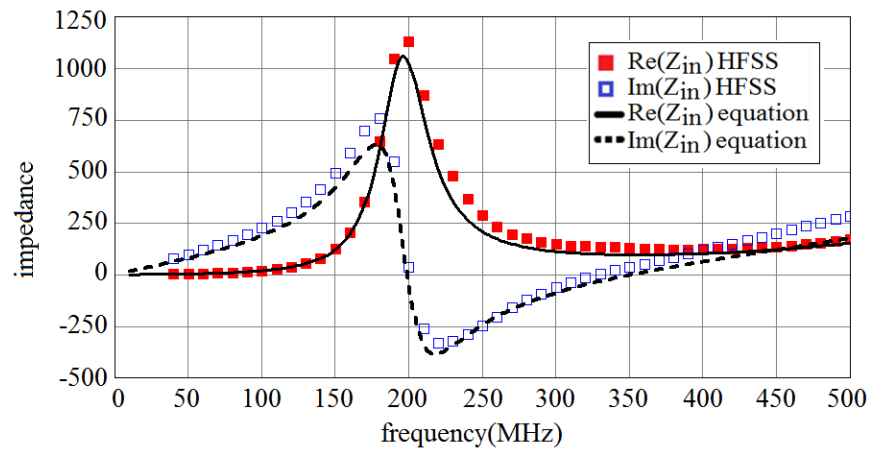


Fig. 4-18 Mode 0 Active Input Impedance at the Feed Loop Based on the Closed Form Equations (Solid) And Based on an HFSS Simulation (Dashed).

The agreement is quite good all the way through the first anti-resonance, especially recognizing that this antenna is one wavelength in circumference at 269 MHz. Clearly, the model derived here, using the Darlington form to explicitly represent the coupling of the antennas to free space (as Schelkunoff did), is not limited to the electrically small limit domain.

The differences seen in the figures are either the result of second order corrections not taken into account in the model, or the result of the onset of guided wave phenomena (as evidenced by the HFSS result distortions beginning at 400MHz in Mode 1). Referring back to the circuit models we can see that the low frequency behavior of mode 1 is dominated by the external radiation inductance. However, the behavior of mode 0 is dominated by the internal inductance which is due to the material. Consequently mode 0 is much more susceptible to imperfect containment of the flux in the flux channel (that is, invalidation of the assumption of uniform current distribution) which may be the reason for the slightly greater disagreement between HFSS and the closed form model seen in mode 0.

4.11 Conclusion

A model of the input impedance of the toroidal permeable antenna operating in both a vertically polarized monopole Mode 0 and linearly polarized dipole Mode 1 has been derived, starting from Schelkunoff's transmission line description of the loop antenna instead of the electrically small limit model, and expressing the result in Darlington form. In particular, the impedance model for realistic conformal antennas fed at four points around the circumference, and including realistic loop-feed effects, has been compared to fullwave simulations.

The results show that the closed-form model is valid well beyond the electrically small limit. Using this exemplar, we have demonstrated that there is a straight-forward theory of magneto-dielectric antennas that is just as accessible as the classical theory of

metal antennas. However, we had seen in many instances of magneto dielectric antennas that there was a metal cage like structure present. The reason for the presence of this structure is that as mentioned in the introduction of this dissertation, permeable materials do not completely bind the wave therefore a flux binding mechanism is needed. An optimum flux binding mechanism needs to ensure that the magnetic current inside the antenna uses the full length of the antenna over the whole frequency band and the magnetic flux is contained within the flux channel at all frequencies without trapping it into a slow wave.

As shown in the referenced dissertation [2] and repeated in the upcoming chapter, an engineering trade-off that accomplished this to a degree is to feed the antenna with multiple loops. However multiple independent feeds then require a complicated feed network located under the antenna ground plane that distributes the energy from the source's desired one feed point to the several loops. A better and novel distributed feed network solution which we call the parallel solenoid is explained in detail in the next chapter.

CHAPTER 5
PARALLEL SOLENOID FEED FOR DIPOLE AND MONOPOLE MAGNETIC
ANTENNAS

*“Once we accept our limits, we go beyond them.”
Albert Einstein*

5.1 Introduction

In the previous chapter we have seen that the toroidal magnetic antenna is able to attain high gain and a large bandwidth, however these properties can only be obtained by using a proper flux binding mechanism like the parallel solenoid feed structure that maintains the magnetic current as uniform as possible inside the flux channel while being fed at only one point and incurring none of the deleterious phase delay effects that occur when a ferrite rod is fed by a conventional solenoid winding. If the toroidal antenna in the previous chapter did not have this feed mechanism, the wave would have not been bound inside the material and the high gain and large bandwidth goals would have not been met.

In this chapter, we introduce this new kind of electric feed configuration used for permeable antennas. This feed configuration overcomes the problems of conventional solenoid feeds and the better performing multiple parallel loop feed system by optimizing the magnetic current distribution and the input impedance of such antennas.

This chapter is based on our published patent: R. Diaz, T. Yousefi, T. Sebastian, S. Clavijo, “New Parallel Solenoid Feed Structure for True Magnetic Antennas”, Patent number: US 20160365642 A1, filed on January 2015, Published

It therefore can be used to improve broad band matching of broad band antennas or as specific tuning aid for narrower band applications.

The permeable dipole antenna is the electromagnetic dual of the dielectric dipole [2]. Duality between the ideal electric and magnetic dipoles is summarized in table 5-1.

Table 5-1 Duality Between the Electric and Magnetic Dipole.

Electric dipole	Magnetic dipole
Electric voltage feed	Magnetic voltage feed
carrying an electric current ' I_e '	carrying magnetic current ' I_m '
PEC feed line	PMC feed line
Electric input impedance(ohms)	Magnetic input impedance(mhos) equal to Electric input impedance(ohms)/ η_0^2

The figure below shows the electric dipole and the magnetic dipole. Strict duality requires that since the electrical electric dipole has perfect electric conductor (PEC) feed lines and an electric voltage source load (V_e), the magnetic dipole should have perfect magnetic conductor (PMC) feed lines and a magnetic voltage source (V_m)

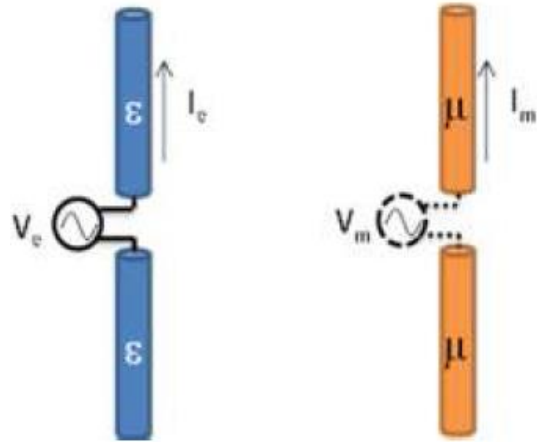


Fig. 5-1 Electric Dipole and the Magnetic Dipole.

Since we don't have PMC feed lines and magnetic voltage sources, we use a PEC feed loop to feed the magnetic dipole. This configuration is shown in the figure below.

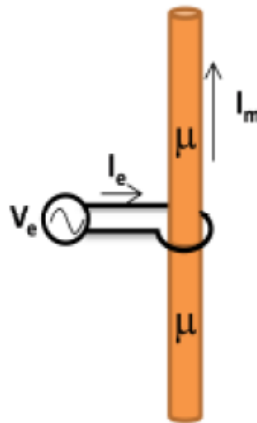


Fig. 5-2 Magnetic Dipole with Feed Loop.

The fundamental magnetic conductor dipole can be fed by an electrically small current loop or many loops in the shape of a solenoid. The problem with the conventional solenoid feed is the significant phase delay it creates as we move away from the feed center which can cause destructive interference. The multi-loop parallel feed will eventually involve a complicated feed network and usually requires an elaborate

matching circuit. The new feed, named the parallel solenoid, utilizes just a single feed point for the linear magnetic current dipole antenna which eliminates the need for complicated matching circuits. In the case of the toroidal magnetic antenna multiple feed points are desirable for multi-mode operation but, still, within each section of the antenna, it is desirable to maintain the magnetic current as uniform as possible. Thus, each section is fed with a parallel solenoid. The multiple feed with the proper solenoid has a superior performance than the multiple feed without the solenoids.

In addition to the solenoid improving the Gain performance of the antennas it can also be used to fine tune the antenna's input impedance. We will show that the solenoid design (namely, the number of grounded loops and the distance between the twin lines) can be used to achieve a very good VSWR for Mode 1 of the Toroidal antenna with only a 4:1 transformer as matching circuit.

5.2 Parallel Solenoid Feed for Linear Magnetic Current Dipole Antenna

As a first example to show the effect of the solenoid feed, we start our analysis with a permeable magnetic dipole antenna that is 1m long, 0.25" tall and 2.5" wide as shown in Fig.5-3. The permeable material used is Bekaert's CZN laminates.

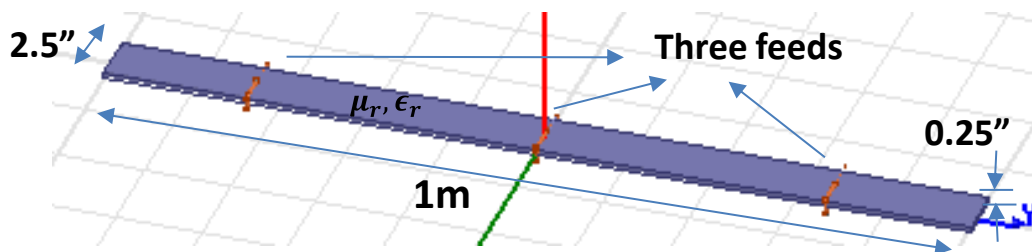


Fig. 5-3 Magnetic Dipole Antenna Fed with Multiple Electric Loop Feeds

Traditionally, ferrite rod antennas have been fed with a solenoid of many turns. The problem with such a configuration, especially at high frequencies, is that since the feed current wire is wound on the ferrite, there is a considerable amount of phase delay as we go further away from the feed source point. Therefore, the excited magnetic currents in the magneto-dielectric material eventually become out of phase and can cancel each other. This is the main reason why a parallel feed configuration of multiple feed loops might be required.

The problem with multiple feeds is the need for a feed network consisting of splitters and/or hybrids. The more components used in an antenna the more loss is incurred and the greater the chance for mismatch due to component tolerances.

Fig. 5-4 shows the proposed parallel solenoid feed on the linear dipole. In this feed, instead of winding just one conductor, which is the center conductor in a coax feed, in series as in a regular solenoid, the inner and outer conductor of the coax feed is stretched to the ends of the material in the form of a two-wire transmission line with grounded shorting pins at regular intervals. This configuration solves the considerable phase delay of the conventional solenoid because the principal wave feeding all the loops travels along the two-wire line nearly at the speed of light .

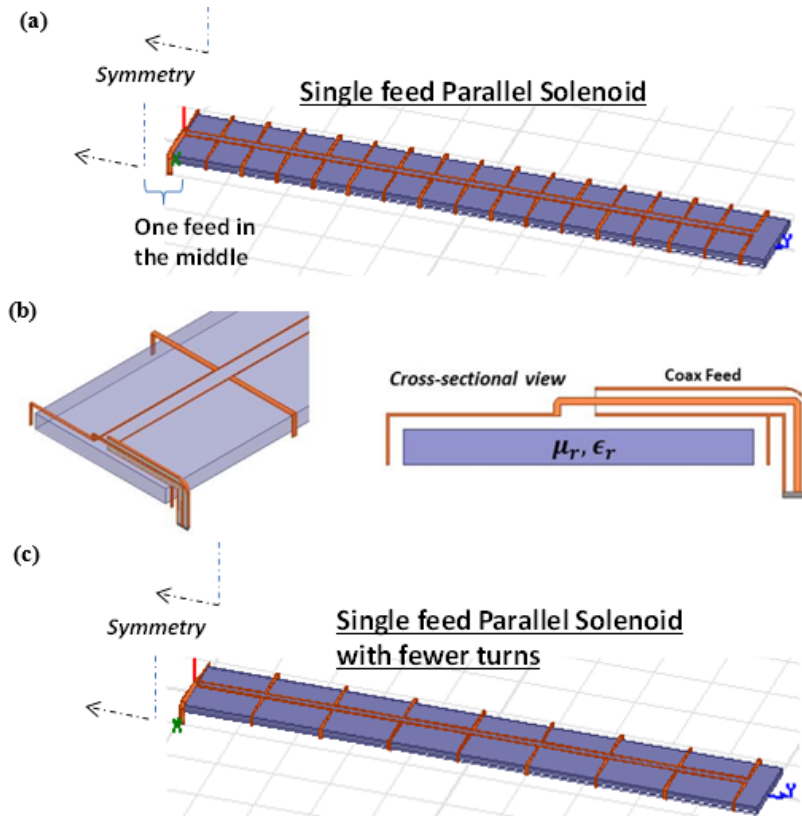
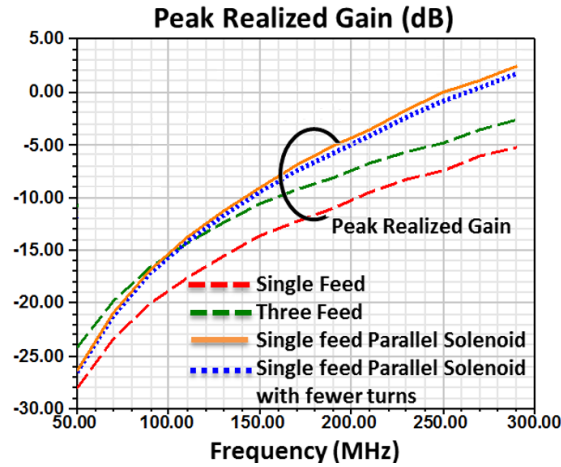


Fig. 5-4 (a) Parallel Solenoid Fed Antenna Structure and (b) Is a Closeup View Close to the Feed Port of the Same. (c) Parallel Solenoid Fed Dipole Antenna with Fewer Turns.

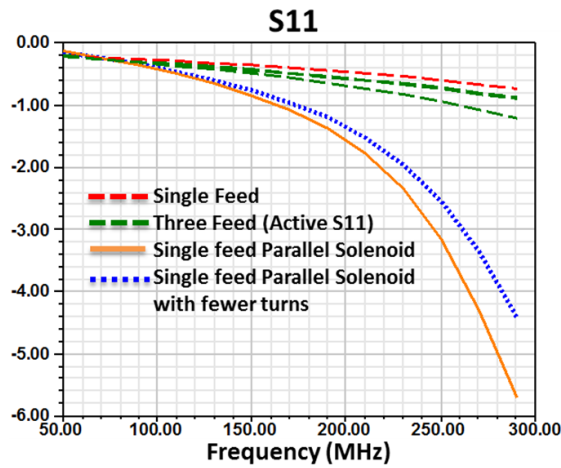
The configuration in Fig.5-4 (a) is compared with a single loop fed antenna having a feed at the center and with a three parallel loop fed antenna (as in Fig.5-3). A fourth case is the parallel solenoid fed antenna with fewer turns as shown in Fig.5-4 (c).

The comparison of peak realized gain is shown in Fig.5-5 (a) and the comparison of S11 is shown in Fig.5-5 (b). As expected, the peak realized gain of the single feed which is the red curve is the lowest because its magnetic current is least uniform. It can be seen that adding two additional feed loops improves the peak realized gain which is shown by the green curve. It can also be seen that the realized gain over the whole band simulated is considerably better for the case of the parallel solenoid. The S11 of the

antenna using the proposed feed method is also the best among the three cases. Therefore, without any additional matching circuit, the single loop fed parallel solenoid is superior to the single loop fed and three feed antenna in performance. The reduction in the number of grounding pins of the parallel solenoid has little effect on its gain performance in this case but it can be important since too many bars can cause over binding of the current.



(a)



(b)

Fig. 5-5 (a) Comparison of Peak Realized Gain (b) S11 of Different Antenna Structures Considered. Note That for the Three Feed Case, the Active S11 at the Individual Port Is Plotted.

In order to study the reason of this improvement in performance, the magnetic current distribution in the dipole has been plotted in Fig.5-6 for the three cases of one feed, three feeds, and a parallel solenoid with one feed.

By looking at the results, it is obvious that the parallel solenoid feed which is shown by blue curves draws more magnetic current than the other two cases at every frequency close to the feed. Also, the current distribution is considerable more uniform than the single feed case. Therefore, the resulting gain and peak realized gain is considerably higher.

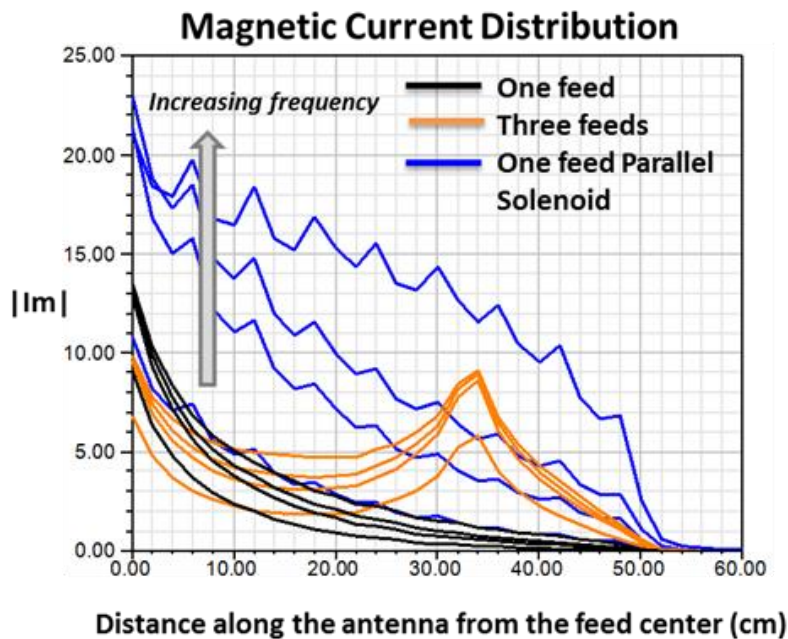


Fig. 5-6 Comparison of the Magnetic Current Distribution of the Different Antenna Configurations for the Frequencies 50, 110, 190 and 290 MHz.

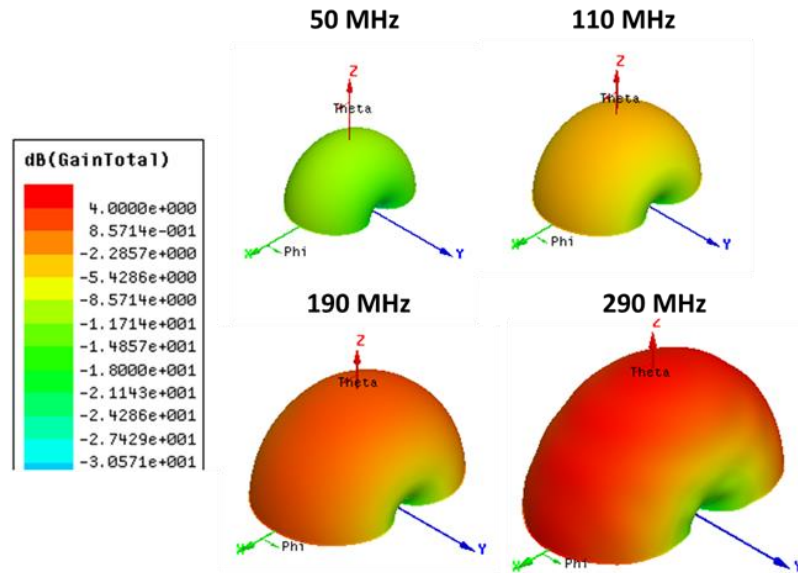


Fig. 5-7 3D Polar Plot of Total Gain at Different Frequencies for the Parallel Solenoid Feed Magnetic Current Dipole Antenna.

Fig.5-7 shows the 3D polar plot of the total Gain of the parallel solenoid feed magnetic current dipole. As expected, the dipole pattern has the donut shape with the antenna aligned along the y-axis.

To emphasize the pay-off of using a parallel solenoid to obtain a nearly ideal magnetic current distribution through the antenna we consider the case of a 1m linear dipole fed with only one loop and vary the dipole's permeability. The magnetic current distribution along the dipole length for the single feed loop case is shown in Fig.5-8. In order to attain a triangular current distribution (the prototypical current distribution of electrically small dipoles), we need to have a permeability as high as 300. We can see that for lower permeabilities the current decays “exponentially” from the feed; the flux leaks out.

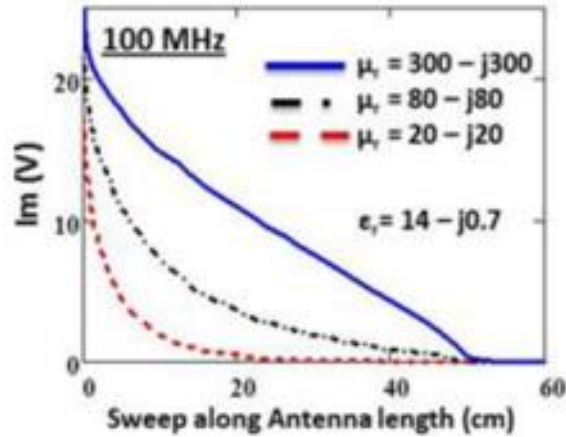


Fig. 5-8 Current Distribution Along the Dipole Length for the Single Feed Loop Case.

By contrast in Fig.5-9 we have plotted the normalized current distribution at different frequencies versus the distance from the source for a $\mu = 40$ laminate material with a parallel solenoid having loops spaced 3cm apart. All of them are essentially triangular current distributions. It can be seen that by using $\mu = 40$ laminate material and the mentioned parallel solenoid we can have a triangular current distribution down to 10MHz which clearly proves that the solenoid contains the magnetic current.

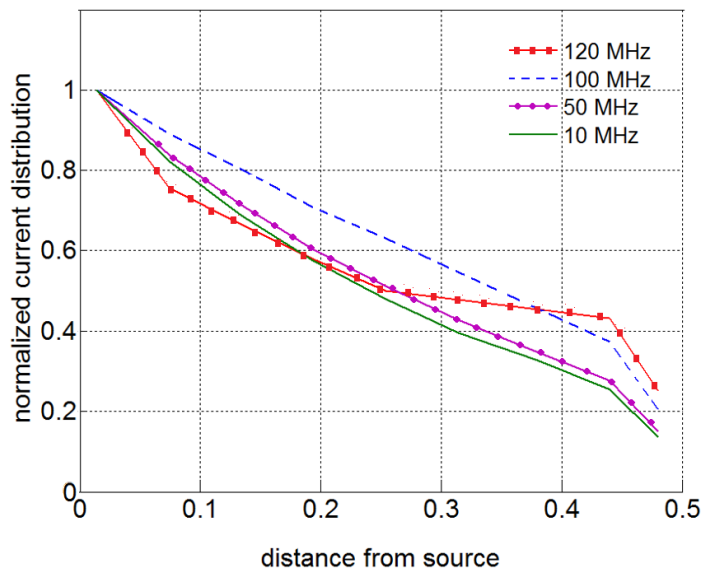


Fig. 5-9 Current Distribution Along the Dipole Length With a Solenoid Having Loops Spaced 3cm Apart.

5.3 Parallel Solenoid Feed for the Monopole Mode of a Magnetic Current Loop

The effect of the solenoid feed on antenna performance has been studied for the linear magnetic dipole and it was found that the cage helps the electromagnetic wave to stay within the magnetic material. In the case of the toroidal magnetic antenna intended to be used beyond the electrically small limit, we have to make sure that no higher order modes are excited around the circumference. This is accomplished by feeding the antenna at multiple points around the circumference. In broad terms, the upper frequency limit of performance of the antenna is multiplied by the number of symmetrically disposed feeds. The conventional approach which is shown below, injects the magnetic current at four feed points to suppress the excitation of higher order modes.

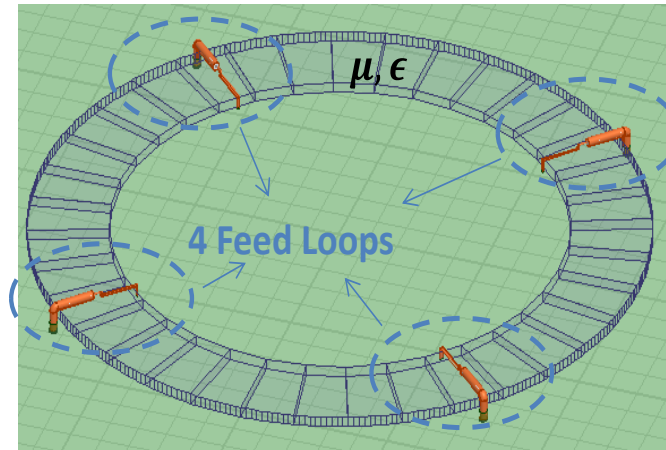


Fig. 5-10 Monopole Mode of a Magnetic Current Loop with 4 Feed Loops.

The proposed parallel solenoid as shown below, also uses multiple feeds but the cage distributes the feed current over wider feed regions of the loop, preventing flux leakage and ensuring that all the material available contributes to radiation. As shown in the figure the multiple loops are connected to each other by a curved two-wire

transmission line. The width of the transmission line conductors and the separation between them and the width of the loops are all adjustable parameters.

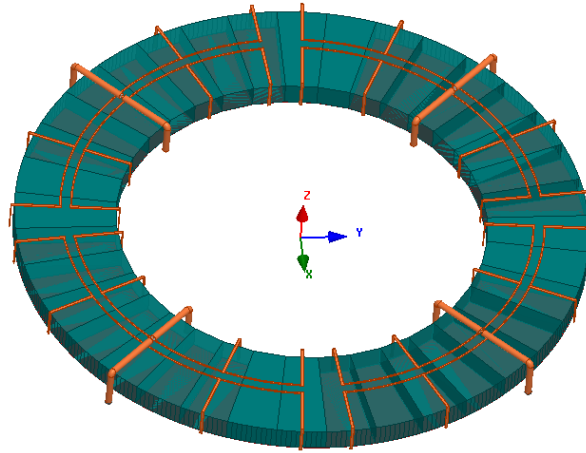


Fig. 5-11 Monopole Mode of a Magnetic Current Loop with 4 Feed Loops and a Solenoid Cage With 16 Bars.

The spacing and dimensions of the bars depends on the specific design but a good rule of thumb is to make the space between them equal to the mean cross-sectional diameter of the magnetic antenna. The mean cross-sectional radius is defined as the square root of the area including the image in the ground plane, divided by π . Thus, for a magnetic antenna which is 2.5 inches wide and 0.25 inches thick and is mounted on a ground plane, the effective area is 2.5×0.5 inches squared and the mean radius is 1.12 inches. Therefore, the nominal spacing of the bars should be of the order of 2.24 inches \pm 50%.

This rule of thumb is based on magnetostatics considerations. If there were no permeable material, that is, if we had an “air core”, then a distance of one core radius between loops would keep the flux uniform, as we know from the Helmholtz coils principle.

However, since all useful permeable cores have a permeability greater than 1.0 this minimum distance can be increased. If the permeability of the magnetic antenna material is very high its bars can be spaced farther apart since the material presents an extremely low reluctance path for the flux and becomes the flux's preferred channel. On the other hand, if it is very low they will need to be placed closer together because the higher reluctance allows leakage of the flux into the surrounding space.

Well known rules for the calculation of leakage flux in conventional magnetic circuits can be used to advantage to make these determinations. However, since the goal of feeding the antenna with the parallel solenoid is not only to maintain a uniform magnetic current through the antenna but also to enable broad band operation by exploiting the large Gain Bandwidth product intrinsic to these antennas, other considerations come into play beside magnetostatics. Specifically, at higher frequencies the surface wave guidance onset frequency appropriate to the material's cross section is approached [2] . At that point and above wave effects such as phase delay become more important. Therefore, in practice the magnetostatics rule of thumb is used to begin the design and then the final design of the solenoid is performed using full physics (fullwave) solutions of the particular antenna design. Figures 5-12 and 5-13 show the dimensions of a quarter of the designed toroidal antenna.

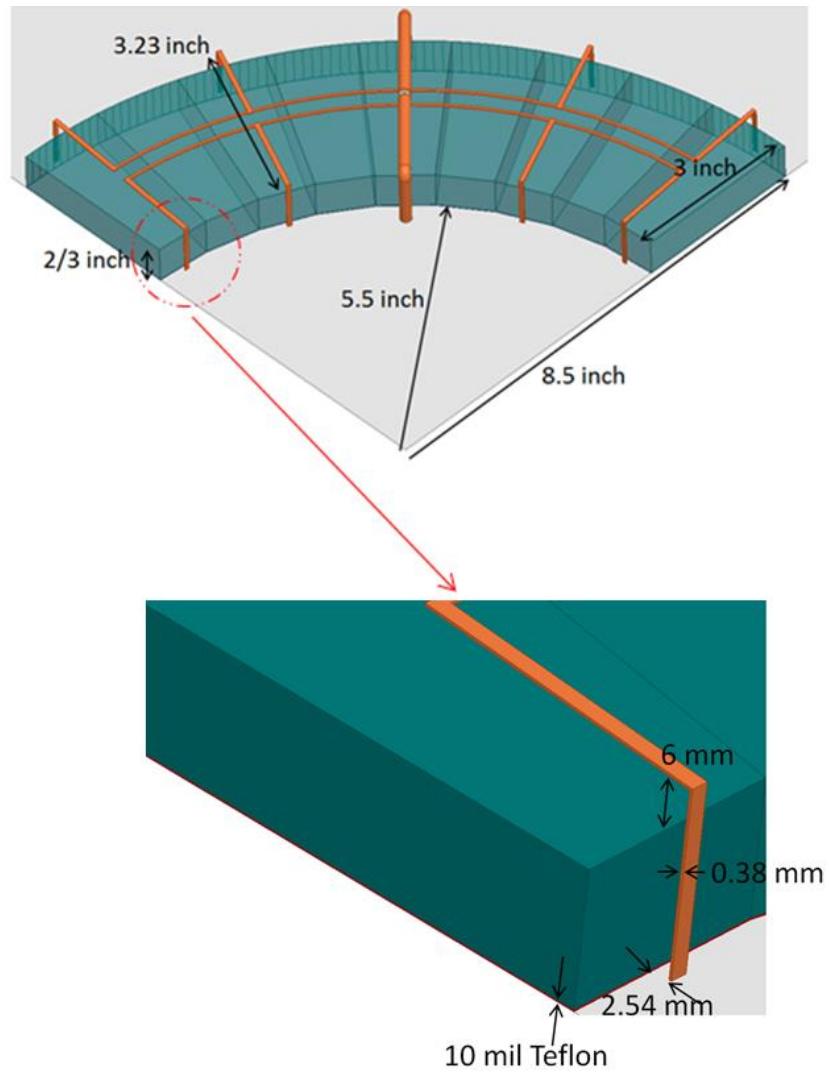


Fig. 5-12 Side View of a Quarter of the Designed Circular Antenna.

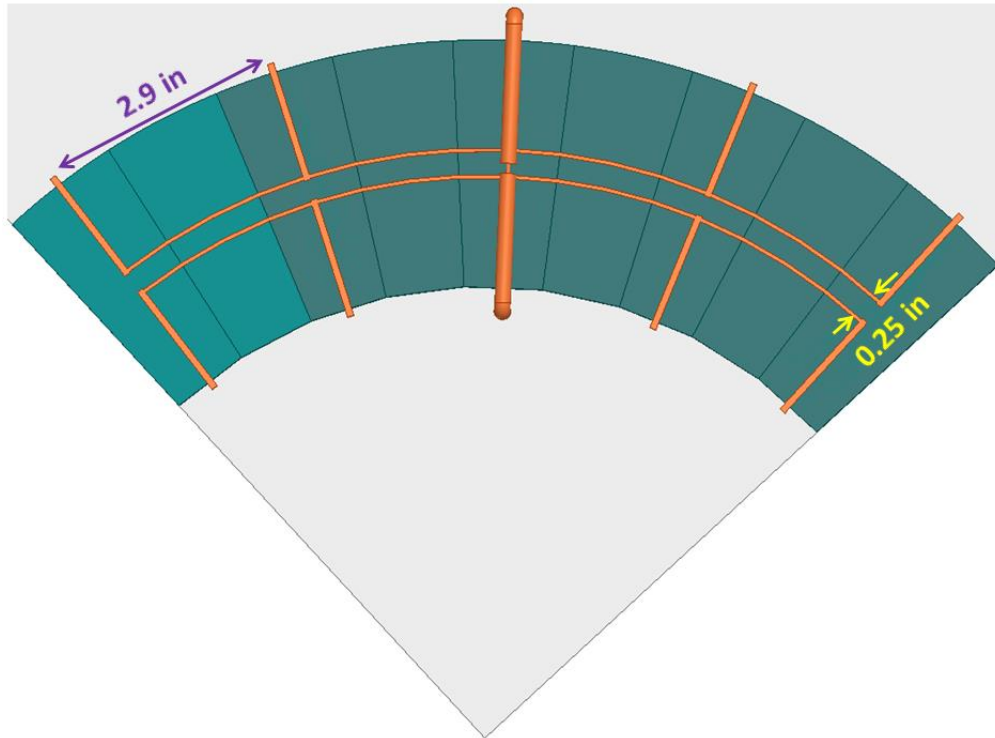


Fig. 5-13 Top View of a Quarter of the Designed Circular Antenna.

Beside the number of bars in the solenoid feed, the width of the transmission line conductors connecting the bars, and the separation between them are adjustable parameters. As shown in Fig.5-14 the peak gain of the parallel solenoid cage with 16 or 40 bars is higher than the antenna without the parallel solenoid. Fig.5-15 shows that in order to obtain the highest realized gain in a desired frequency band we can use the number of bars as a design parameter and in this case 16 bars results in the highest realized gain. We surmise that forty bars “over bind” the magnetic current wave, trapping the energy in the material at the high frequencies.

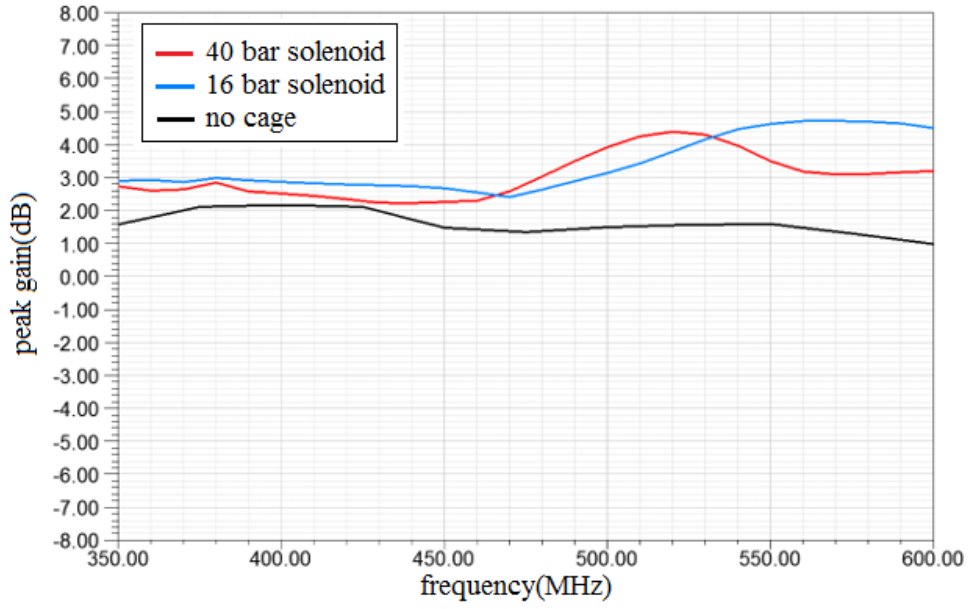


Fig. 5-14 Peak Gain of the Monopole Mode with 4 Feed Loops (Red 40 Bars, Blue 16 Bars, Black No Cage).

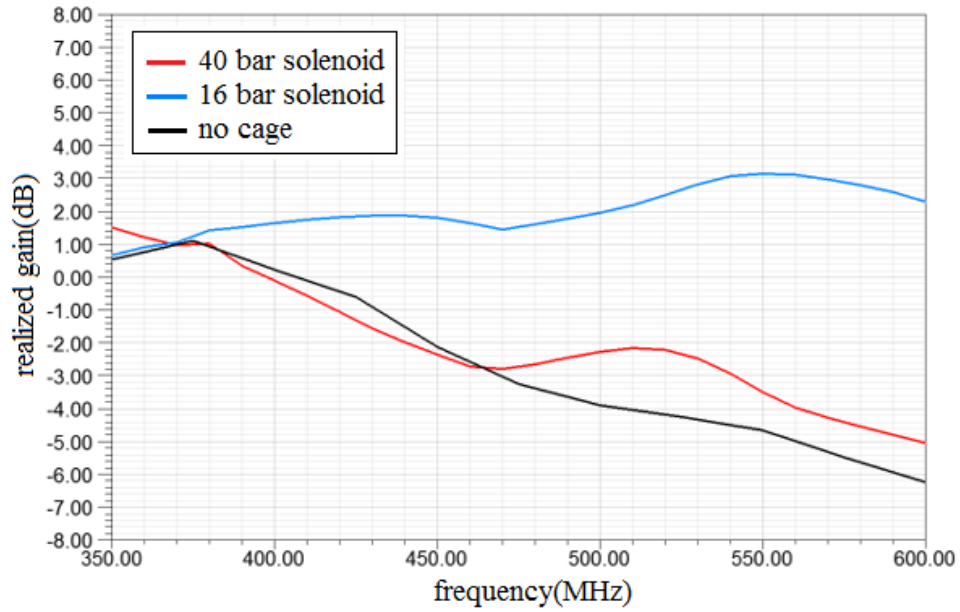


Fig. 5-15 Realized Gain of the Monopole Mode with 4 Feed Loops (Red 40 Bars, Blue 16 Bars, Black No Cage).

The figures below show the return loss for the three different cases which shows how the number of bars can be used as a tuning aid to achieve a better return loss.

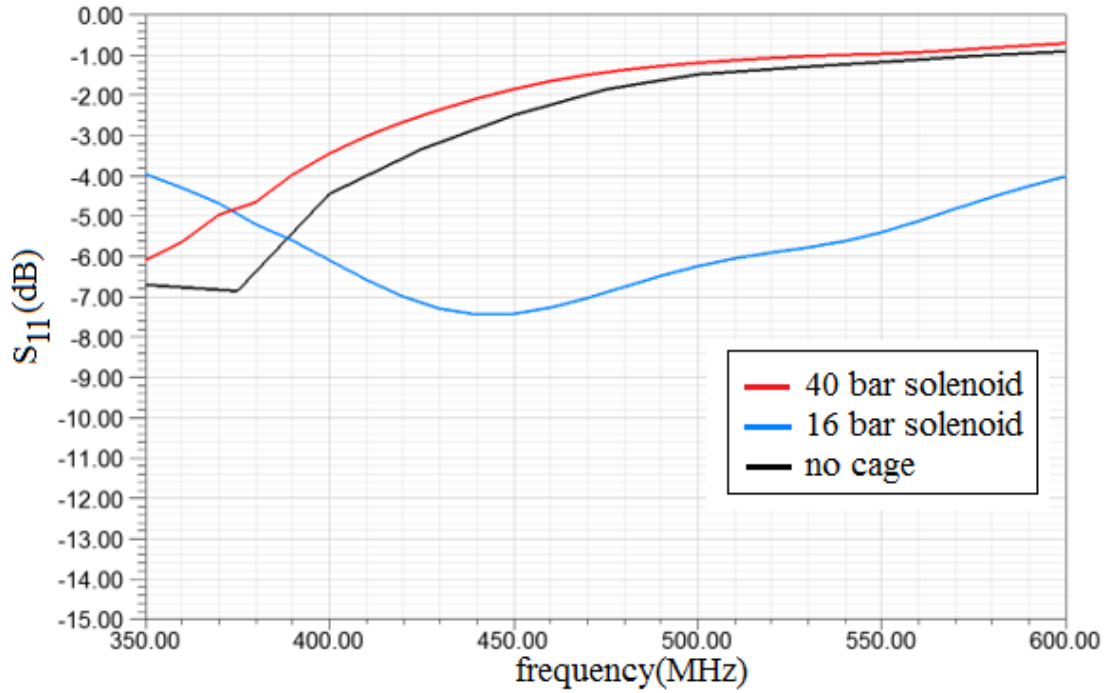


Fig. 5-16 Return Loss (S_{11}) of the Monopole Mode with 4 Feed Loops (Red 40 Bars, Blue 16 Bars, Black No Cage).

The patterns of the three different cases have also been plotted below.

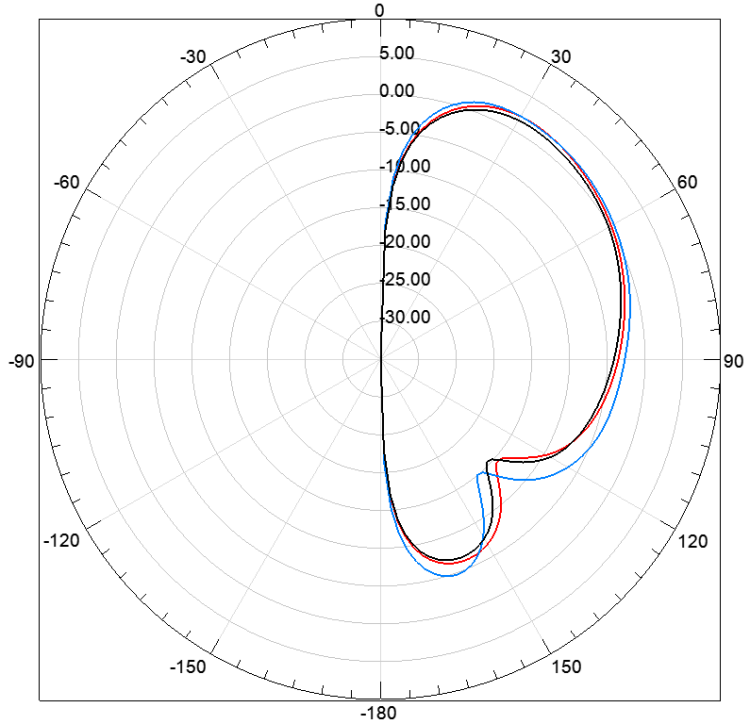


Fig. 5-17 Pattern Versus Theta of the Monopole Mode with 4 Feed Loops(Red 40 Bars, Blue 16 Bars, Black No Cage) at 420 MHz and Phi=0 Degrees.

5.4 Parallel Solenoid Feed for the Dipole Mode of a Magnetic Current Loop

The same reasoning can be followed for the dipole mode of a magnetic current toroidal antenna, and the peak gain, realized gain, and the patterns have been plotted. As shown below we can conclude that the peak gain and the realized gain of the 16 bar configuration is higher than the other two alternatives. Again, the number of bars and the width of the different parts of the cage can be used as peak gain and realized gain tuning parameters as stated for the monopole mode. Clearly, for this multi-mode antenna the best parallel solenoid design is obtained by an engineering trade-off between the benefits afforded each mode and the corresponding specifications that they must meet.

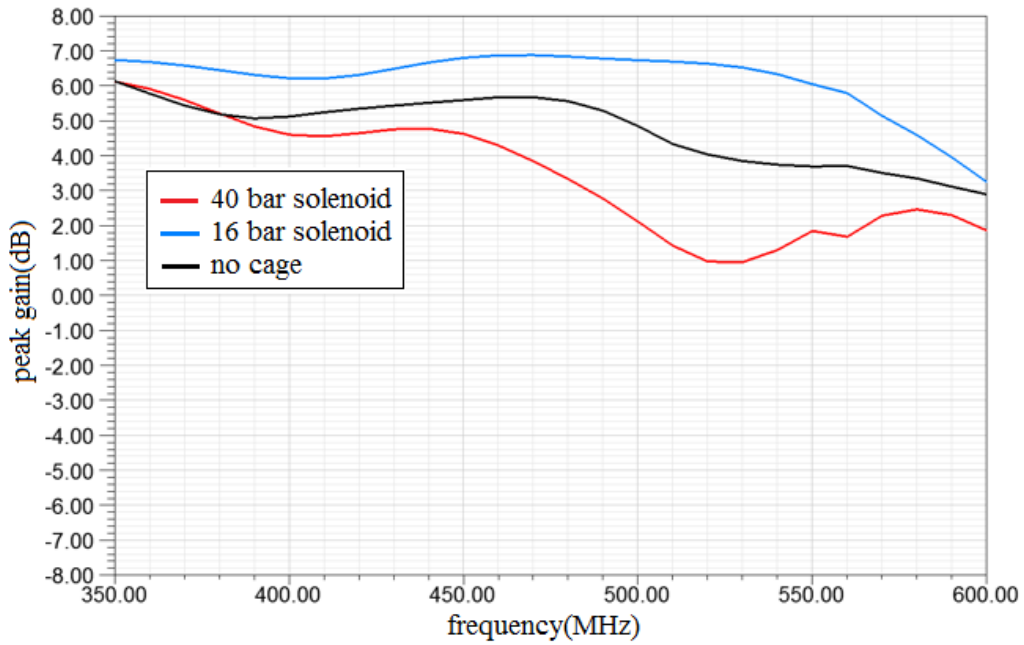


Fig. 5-18 Peak Gain of the Dipole Mode with 4 Feed Loops (Red 40 Bars, Blue 16 Bars, Black No Cage).

The following figure also shows that the realized gain achieved by using the parallel solenoid is higher than the configuration with only 4 feed loops.

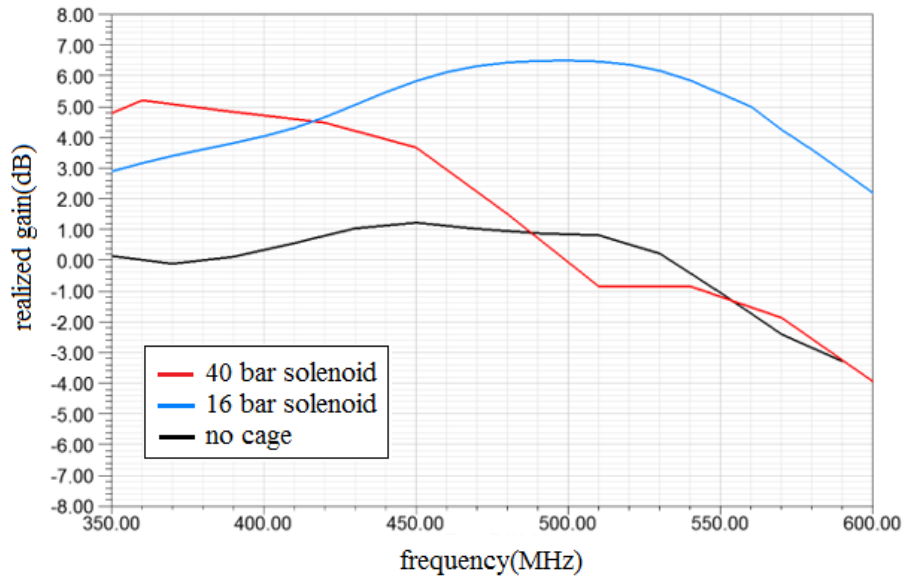


Fig. 5-19 Realized Gain of the Dipole Mode with 4 Feed Loops (Red 40 Bars, Blue 16 Bars, Black No Cage).

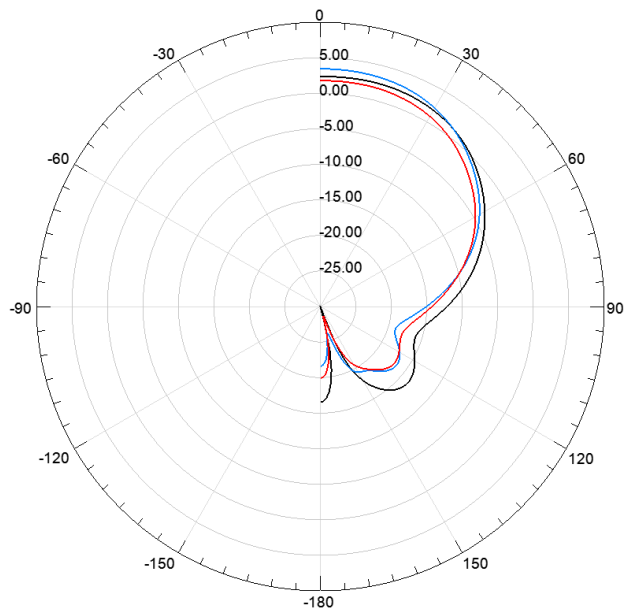


Fig. 5-20 Pattern Versus Theta of the Dipole Mode with 4 Feed Loops (Red 40 Bars, Blue 16 Bars, Black No Cage) at 420 MHz and Phi=45 Degrees.

As an example to show how we can use different parameters as tuning aids for desired frequency bands, the gap between the transmission lines connecting the bars has been used as a tuning parameter. It can be seen that we can obtain an optimum value for the gap to get a higher peak gain.

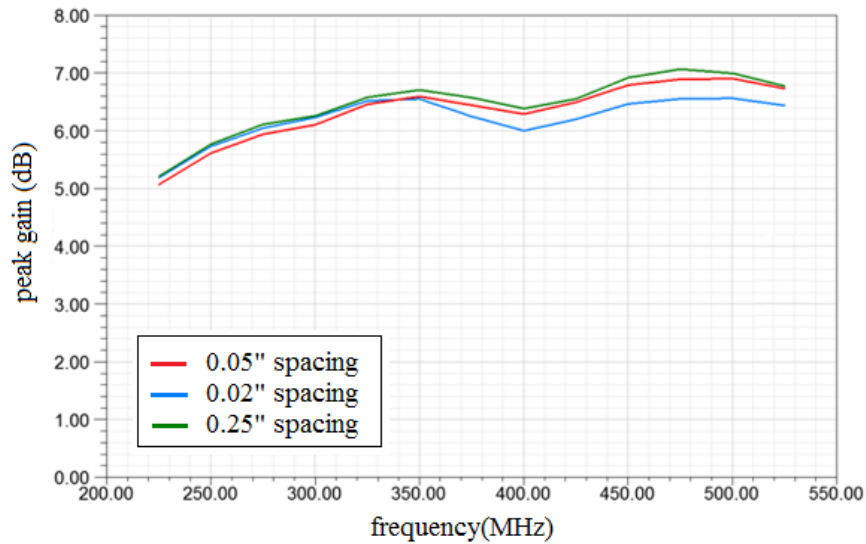


Fig. 5-21 Peak Gain of the Dipole Mode with Different Spacing Between the Wires of the Transmission Line (Red 0.05 Inch , Blue 0.02 Inch, Green 0.25inch).

5.5 Using the Parallel Solenoid Feed as a Tuning Aid to Achieve a Good VSWR

In previous sections, we have introduced the parallel solenoid feed as a new way to feed true magnetic antennas. It will be shown that not only does the solenoid contain the magnetic current inside the magnetic material, as seen in previous sections, but also the width of the transmission line conductors and the separation between them and the width and number of the loops can be adjusted for each specific design.

Specifically, we will see how changing the number of bars and the distance between the twin lines can result in a very good VSWR for mode 1 with only a 4:1 transformer and without needing any complex matching circuit.

True magnetic antennas have high gain and a broad bandwidth. However, in order to have a good realized gain, the antenna needs to have a good VSWR. Many matching schemes can be used, with some of them involving many inductive and capacitive circuit elements which would add to the complexity of the structure.

Fig. 5-22. Shows the side and top views of a quadrant of the toroidal magnetic antenna. As seen in the figure, the full antenna has 4 feed loops and a solenoid with 16 bars to the ground.

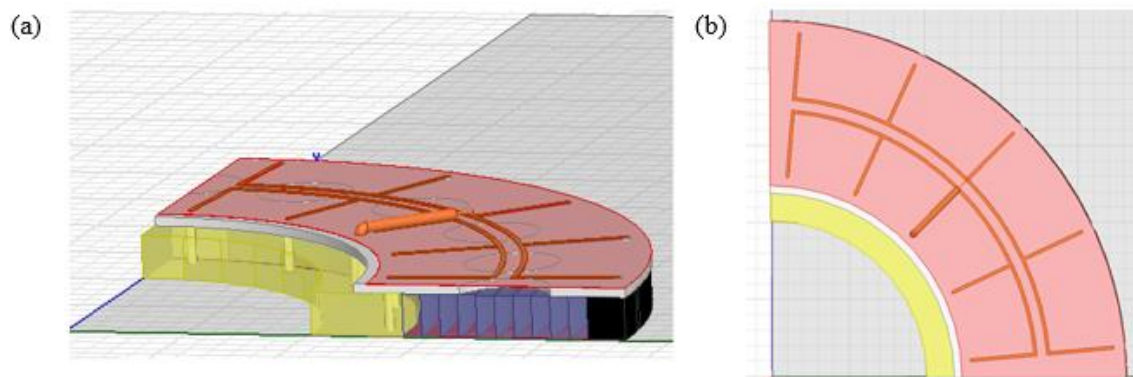


Fig. 5-22 Quadrant of the Toroidal Magnetic Antenna with 4 Feed Loops and a 16 Bar Solenoid (a) Side View (b) Top View.

The peak gain and S11 of the antenna, normalized to a 50 ohm impedance, with 4 feed loops and a solenoid with 16 bars is shown in Fig.5-23. The important frequency range for this mode in the envisioned application is the range from 280 MHz to 400 MHz, and we see that the VSWR needs improving.

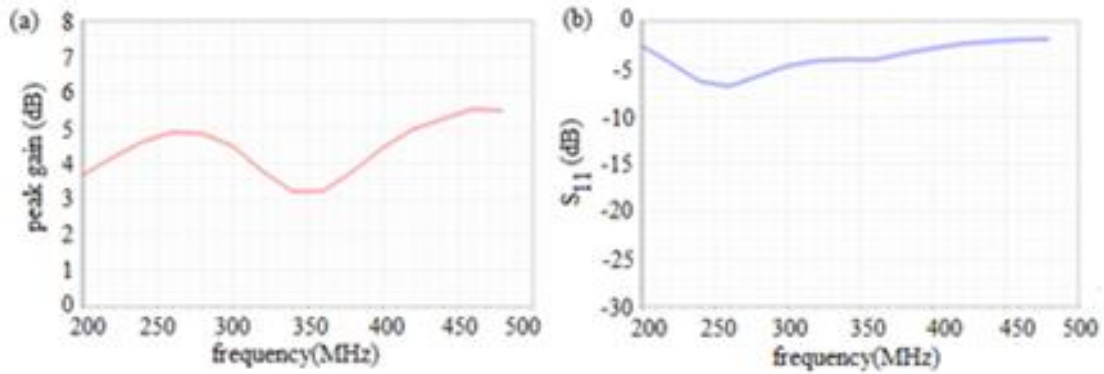


Fig. 5-23 (a) Peak Gain and (b) S₁₁ of the Mentioned Antenna Normalized to a 50 Ohm System Impedance.

In order to start a matching approach, we should first look at the impedance of the antenna through both the real and imaginary parts of the impedance and the smith chart. Fig5-24 shows the input impedance and smith chart normalized to a 50 ohms system impedance. It can be understood from Fig5-24(b) that we would probably need a complex matching system.

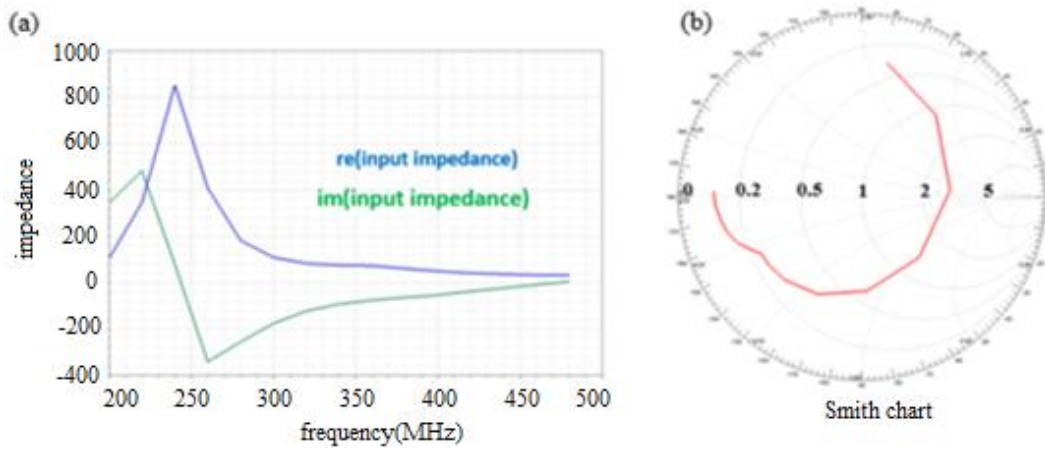


Fig. 5-24 (a) Input Impedance (b) Smith Chart Mentioned Antenna Normalized to a 50 Ohm System Impedance.

We can see in Fig5-25 that changing the reference impedance from 50 ohms to other impedances for example 200 ohm does not improve the VSWR therefore a simple transformer cannot help in this case.

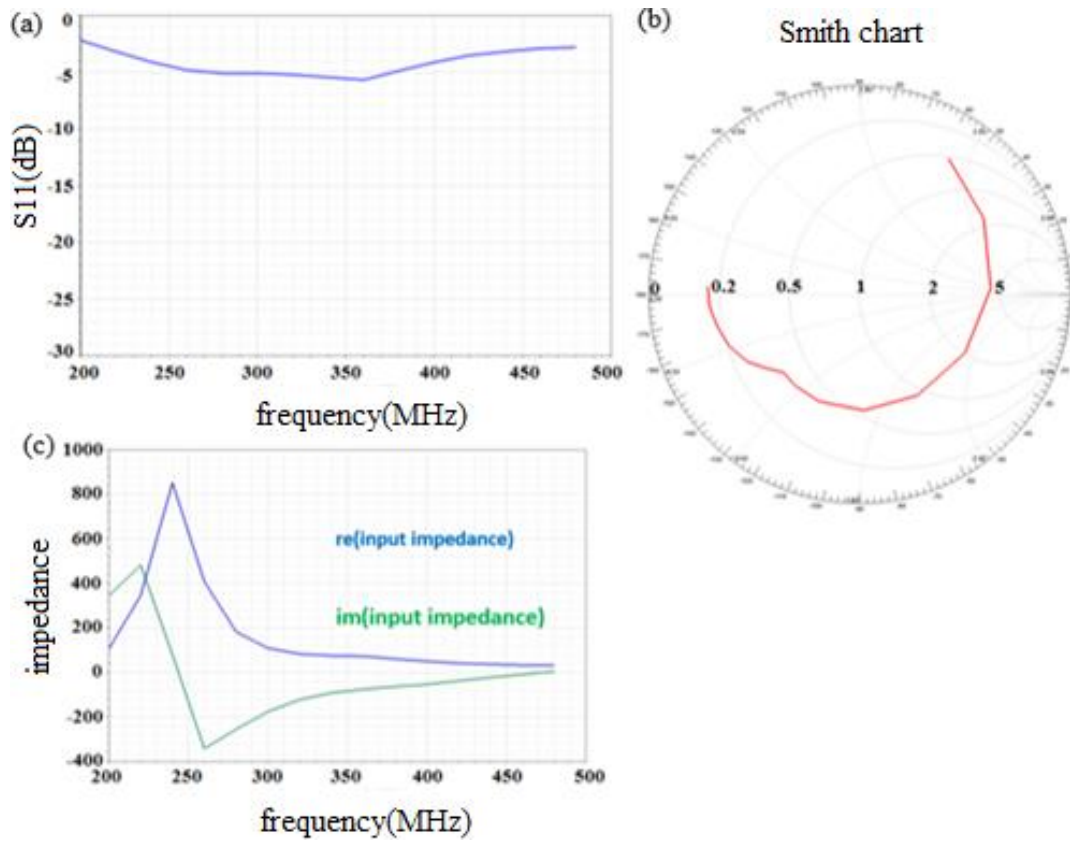


Fig. 5-25 (a) Antenna S_{11} (b) Smith Chart (c) Input Impedance of the Mentioned Antenna Normalized to a 200 Ohm System Impedance.

Redesigning the solenoid structure can give us a practical way to achieve a wideband match for the toroidal antenna without needing a complex matching system. The solenoid of the new antenna configuration has more bars and the gap between the curved twin line is bigger than the previous antenna structure.

Fig5-26 shows the side view and top view of a quadrant of the toroidal magnetic antenna with 4 feed loops, 24 bars to the ground, and a bigger distance between the curved twin lines than the previous structure.

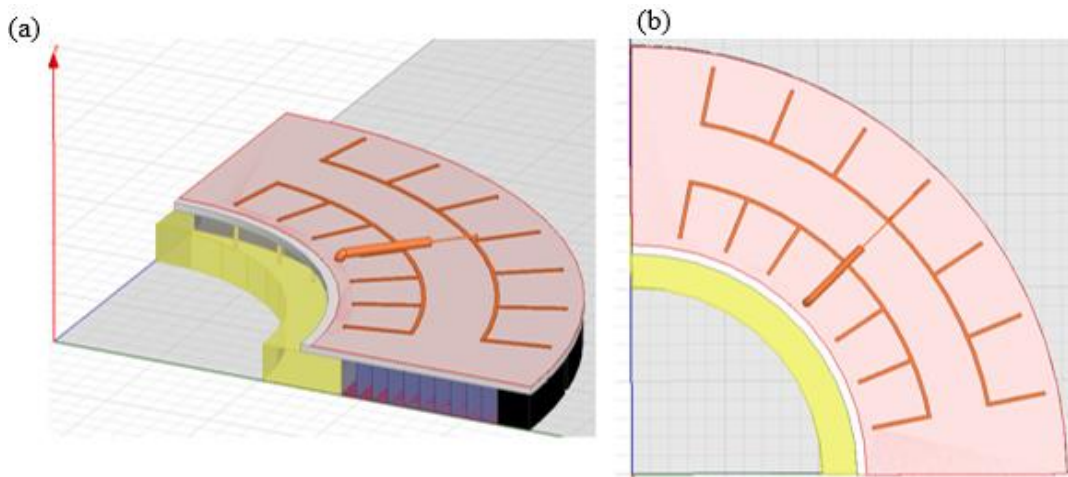


Fig. 5-26 Quadrant of the Toroidal Magnetic Antenna with 4 Feed Loops and a 24 Bar Solenoid (a) Side View (b) Top View.

The peak gain and S11 of the antenna with 4 feed loops and a solenoid with 24 bars is shown in Fig.5-27 and we see that the VSWR (normalized to a 50 ohm system impedance) does not show any improvement compared to the previous geometry. We will see later that the VSWR of this geometry will have a considerable improvement when normalized to a 200 ohm system impedance.

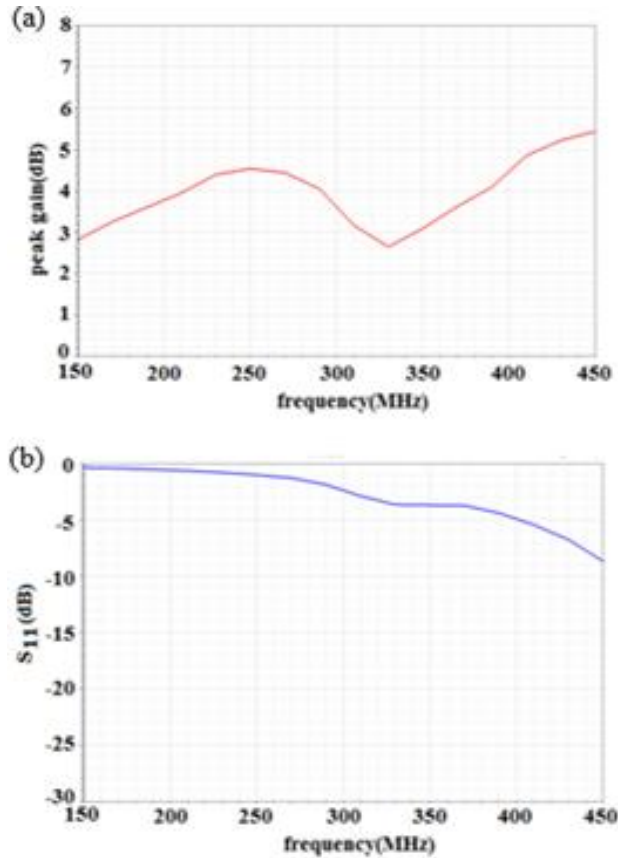


Fig. 5-27 (a) Peak Gain and (b) S11 of the Mentioned Antenna Normalized to a 50 Ohm System Impedance.

In order to see the impedance behavior of the new antenna configuration we again look at both the impedance of the antenna and the smith chart. Fig. 5-28 shows the input impedance and smith chart normalized to a 50 ohms system impedance. Although the reflection coefficient plotted in the smith chart in Fig.5-28 (b) is not located at the center of the smith chart, which is shown as an undesirable VSWR in Fig 5-27 (b), we can see that it is centered at the 250 ohm location in the smith chart. As shown in Fig 5-29(b) if we use a 200 ohm system impedance (a 4:1 transformer) we can move the reflection

coefficient to the center of the smith chart meaning that we will have a good wideband match.

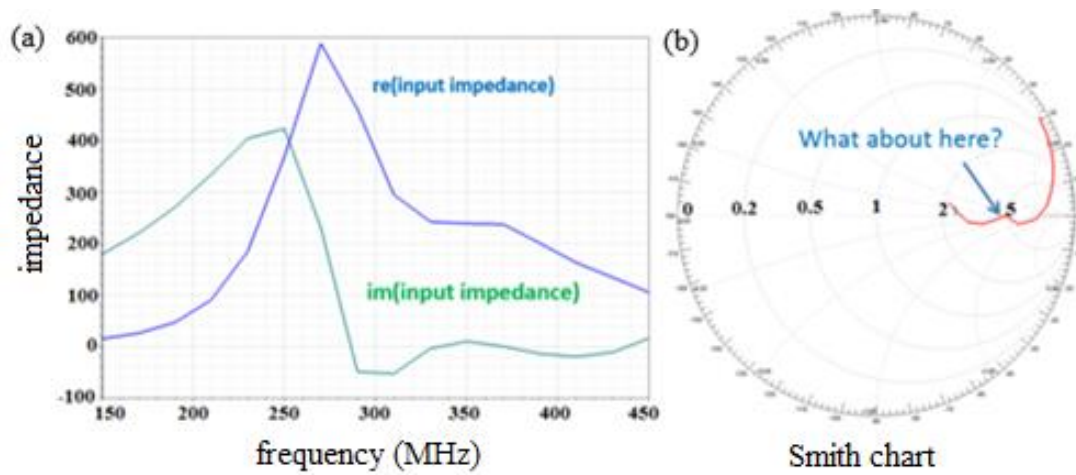


Fig. 5-28 (a) Input Impedance and (b) Smith Chart of the Mentioned Antenna Normalized to a 50 Ohm System Impedance.

In Fig. 5-29, the S11 of the new antenna configuration and the smith chart can be seen normalized to a 200 ohm system impedance which shows a good VSWR with only a 4:1 transformer needed, proving that tuning the solenoid structure can be used to achieve good VSWR in the desired frequency range from 280 MHz to 400 MHz.

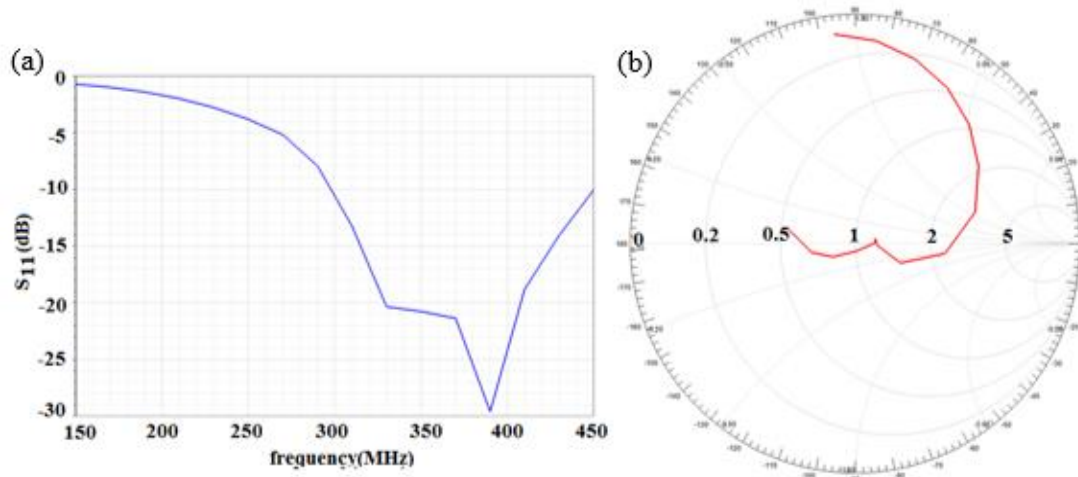


Fig. 5-29 (a) Antenna S_{11} (b) Smith Chart of the Mentioned Antenna Normalized to a 200 Ohm System Impedance.

5.6 Conclusion

In this chapter, it has been shown that using the proposed parallel solenoid feed system for permeable antennas eliminates the significant phase delay problem of conventional solenoids and the complex feeding circuit required for multiple feed loops.

In antennas such as toroidal magnetic antennas, using the proposed solenoid feed will enhance the performance of the antenna by maintaining the flux inside the antenna which results in higher peak gain and higher realized gain. Although the superior performance of the parallel solenoid feed system has been shown by some antenna examples, it is not limited to the mentioned antennas. Any type of antenna that needs to have a contained flux can benefit from a properly designed solenoid feed. Any true magnetic antenna using permeable magnetic material and having magnetic current in a permeable channel can have its current distribution tailored and its efficiency optimized by the use of a parallel solenoid. Once the baseline rules of thumb are used to begin the

design, the antenna engineer can use full wave simulation software like HFSS or CST to fine tune the solenoid parameters for their particular antenna. The key goal is to determine the number of bars needed to maintain the flux at low frequencies while allowing the wave to radiate easily at high frequencies.

Additionally, this new proposed feed structure can be used as a tuning mechanism to achieve specific input impedance design goals. In a specific example, changing the number of grounded bars and the distance between the curved twin lines in the solenoid, we achieved a very good VSWR with only a 4:1 transformer.

Up to this point in the dissertation we have seen that the parallel solenoid feed helps to bind the magnetic flux to the permeable channel at lower frequencies, preventing leakage, while at the same time not over binding the flux and allowing an efficient radiation at higher frequencies. The reason the parallel solenoid is able to do this is that it is a frequency dependent structure and therefore can manipulate the frequency dependent behavior of the channel itself so it can carry a nearly uniform amplitude magnetic current wave.

The ultimate test in the applicability of the parallel solenoid structure would be to use it in a frequency independent magneto dielectric antenna, for example a spiral, since we know that the ultra-wideband performance of the spiral is dependent on the current channel carrying a uniform amplitude traveling wave near the speed of light over the entire large bandwidth. This is the topic of the next chapter and we will demonstrate the importance of the parallel solenoid feed structure on a magneto-dielectric Archimedean spiral antenna and prove the crucial importance of the flux binding structure.

CHAPTER 6

DEMONSTRATION OF THE EFFECT OF THE PARALLEL SOLENOID FEED ON A MAGNETIC ARCHIMEDEAN SPIRAL ANTENNA

*“The human mind always makes progress, but it is
a progress in spirals.”*

Madame de Stael

6.1 Introduction

As mentioned in the previous chapter, the parallel solenoid feed is a new kind of electric feed configuration for permeable antennas and it is crucial to their performance because all realistic magneto dielectric antennas need a flux binding mechanism. In this chapter, we show that this feed mechanism can pass the ultimate test which is flux binding for a frequency independent magneto dielectric antenna for the specific example of an Archimedean spiral. In previous chapters, we have shown for the toroidal magnetic antenna that in addition to the solenoid overcoming the problems of conventional feeds it can be used as a tuning aid to obtain desirable input impedance properties. At the same time, the antenna performance is enhanced by maintaining the flux inside the material which results in higher peak gain and higher realized gain.

This chapter is based on our published patent: R. Diaz, T. Yousefi, T. Sebastian, S. Clavijo, “New Parallel Solenoid Feed Structure for True Magnetic Antennas”, Patent number: US 20160365642 A1, filed on January 2015, Published

The magnetic antenna presented in this chapter is a spiral antenna. We demonstrate the design and simulation of a magnetic spiral antenna built with 123 NiZn tiles each with a 4inch \times 4inch cross section and 6mm thickness. Similar to the previously designed toroidal magnetic antenna, this magnetic antenna also needs a proper flux channel to prevent the flux from escaping the magnetic material. Our goal is to design a spiral antenna with high gain, frequency independent impedance behavior, and a circular polarization; and we will show how the parallel solenoid feed is necessary to obtain the desirable antenna properties.

In section 2 we will start with the theory of spiral antennas and how it would affect the design of the proposed magnetic antenna in terms of the spiral active region. As a baseline the Archimedean spiral with one feed at the center using the ferrite tiles will be demonstrated.

Section 3 shows how using a solenoid feed helps with both increasing the gain and achieving a frequency independent behavior. In this section we will also compare three different magnetic spiral antenna geometries which are the magnetic spiral antenna without any solenoid feed, the same antenna with an 8 loop solenoid touching the ferrite, and the final design which is the parallel solenoid fed antenna with 30 loops to ground. The comparison shows the benefit of the solenoid feed and the importance of having a small gap between the solenoid and the ferrite surface. In this section, we will see how crucial the parallel solenoid feed is.

In section 4, the final antenna geometry and results are shown and the radiation patterns show the circular polarization. We have also shown that the antenna has a good

efficiency in the frequency range of operation defined by the smallest and largest active region. It is also shown that using the CZN Ferromagnetic metal laminates to build the antenna instead of the NiZn tiles would result in a significant increase in gain and efficiency which is the result of much higher Hestivity of the laminates.

6.2 Basic Archimedean Spiral with One Feed at the Center

In order to get an idea of how the parallel solenoid works for the case of the spiral antenna and why it is necessary; we have to first understand how the spiral antenna works. A spiral antenna is a frequency independent antenna by nature. The figure below shows the current on a two wire spiral antenna. If the wavelength is very large as is the case shown in the figure, we can see the current amplitude in the first half wavelength which is a sine function. If we make the wave length too long it will look like we have a bent two wire transmission line that where ever we have a current, right next to it we have an opposing current and an observer at the far field would not expect radiation to occur.

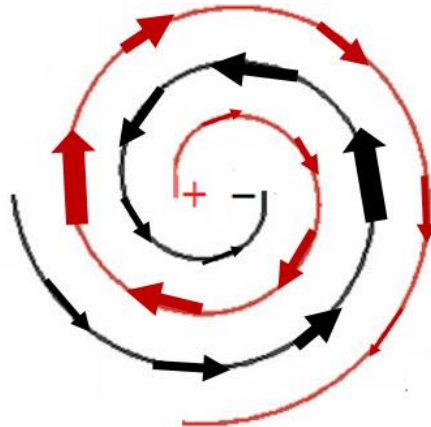


Fig. 6-1 Currents on a Spiral Antenna Near the Feed Tend to Cancel Each Other as Seen from the Far Field

However, if we go far enough we will reach a point over which the wave on the wire undergoes a 180 degree phase shift as the wire physically sweeps zero degrees to π . We will get to a point on the spiral that the currents on adjacent arms on the spiral are pointing in the same direction and the currents on the other side are also pointing in the same direction. Thus a far field observer will not see any radiation coming from the origin but he will see a region (a band) that seems to be the source of all the radiation. The circle seen in Fig.6-2 is called the active region and in that region we seem to have all the radiation sources for the specific frequency in which $2\pi R = \lambda$

The reason that this structure is frequency independent is that at all frequencies; if the spiral is big enough, we will have an active region for that frequency. The region appears for high frequencies near the origin and for the lower frequencies far from the origin.

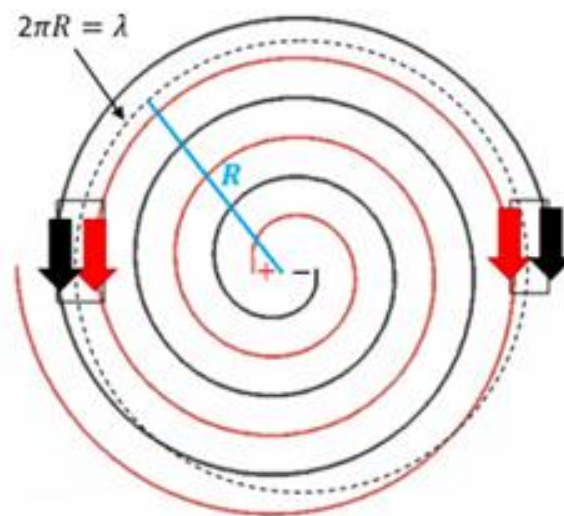


Fig. 6-2 Currents on a Spiral Antenna at the Active Region.

If in addition to the scaling property, the structure is also self-complementary then absolute frequency independence of the impedance is guaranteed. Since we are limiting the dimension of the antenna, we will have a minimum frequency that the antenna could work in defined by the outer radius of the spiral and a maximum defined by the smallest turn near the center. Fig.6-3 shows the smallest and largest active region expected for a general spiral antenna and Fig.6-4 shows the smallest and largest active region expected for the Archimedean spiral built using 4 inch square ferrite tiles. The largest active region which defines the low end is approximately when the outer perimeter is 1 lambda which in this case is at 95MHz (purple circle). The high end has to start around the red circle since the central three tiles would be just a linear dipole. This is about 0.95m in perimeter or 315MHz. This behavior will show itself as a drop in efficiency and gain after 315 MHz .

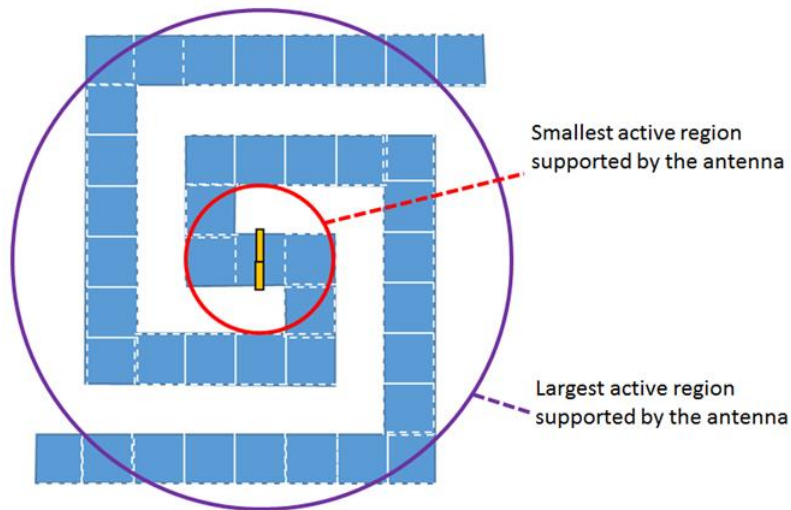


Fig. 6-3 Smallest and Largest Active Region Supported by a General Spiral Antenna.

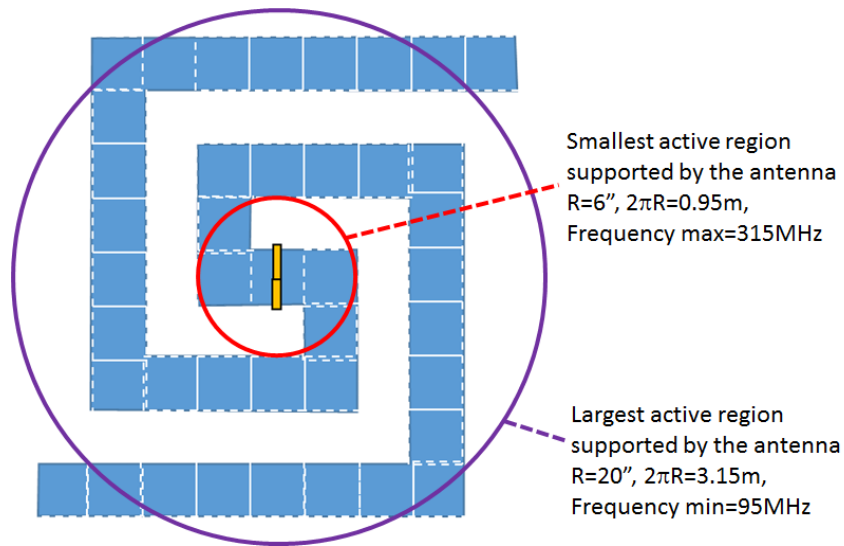


Fig. 6-4 Smallest and Largest Active Region Supported by Our Specific Antenna Delimit Its Operational Band to Between 95 MHz and 315 MHz

The Archimedean spiral suggested in Fig. 6-3 was designed using 123 NiZn tiles each with a 4inch \times 4inch cross section and 6mm thickness and the unit tile highlighted in Fig. 6-4(b) consists of three tiles stacked on top of each other resulting in 18mms total height of the spiral. The spiral shown in Fig.6-4(b) has been fed with one feed loop at the center of the antenna. The permeability of the material is that shown in Fig.6-4(a) with a μ_{DC} of the order of 2500 and a relaxation frequency of about 3MHz.

At this point we expect the flux to leak in the VHF frequency range and higher since the permeability drops in that frequency range and we only have one feed at the center. As we have guessed at this point and the results will prove later, the parallel solenoid feed is necessary to keep the flux inside the magnetic spiral.

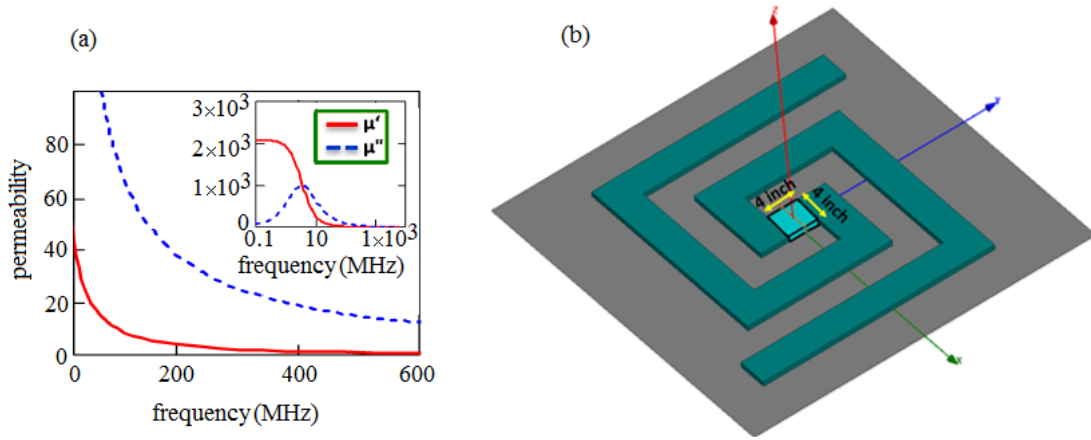
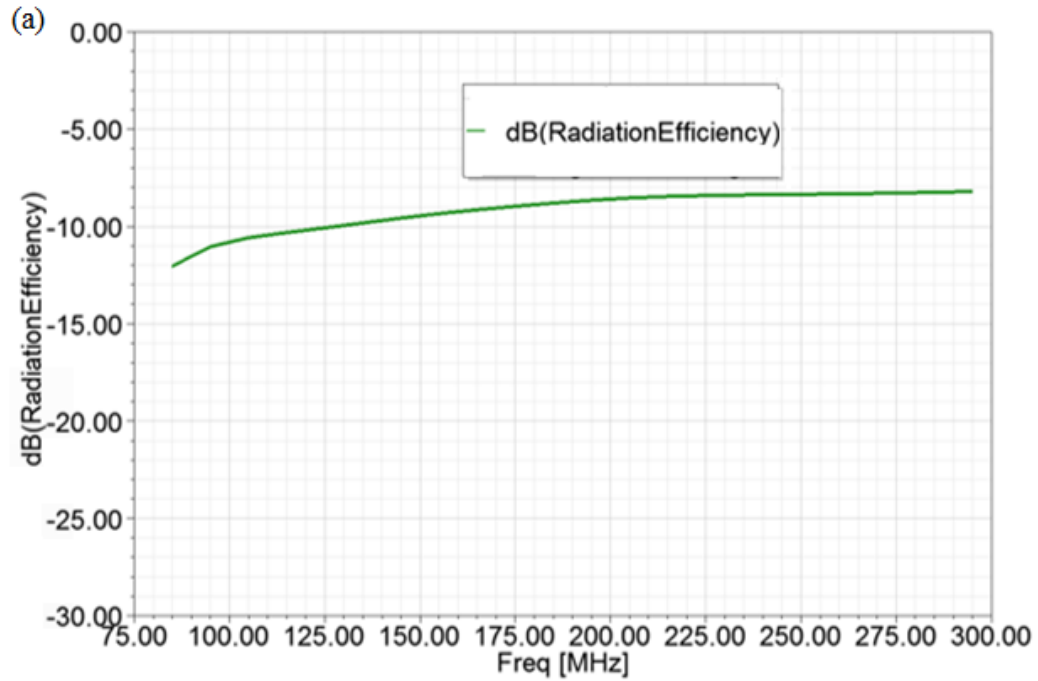


Fig. 6-5 (a) Frequency Dependence of the Permeability of Nizn Tiles (b) Basic Model of a Ferrite Archimedean Spiral Antenna with Only One Feed at the Center.

The efficiency, gain, and the impedance of the basic ferrite Archimedean spiral antenna are shown in Fig.6-6 (a) Fig 6-6(b) and Fig. 6-7.



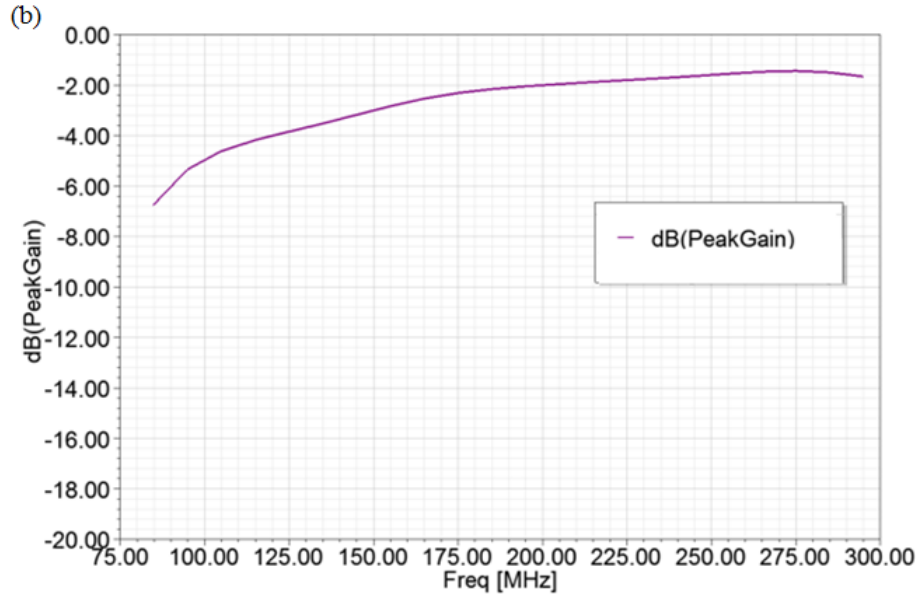


Fig. 6-4 (a) Efficiency of the Single Loop Fed Spiral Antenna (b) Peak Gain of the Single Loop Fed Spiral Antenna, and the Impedance of the Basic Ferrite Archimedean Spiral Antenna.

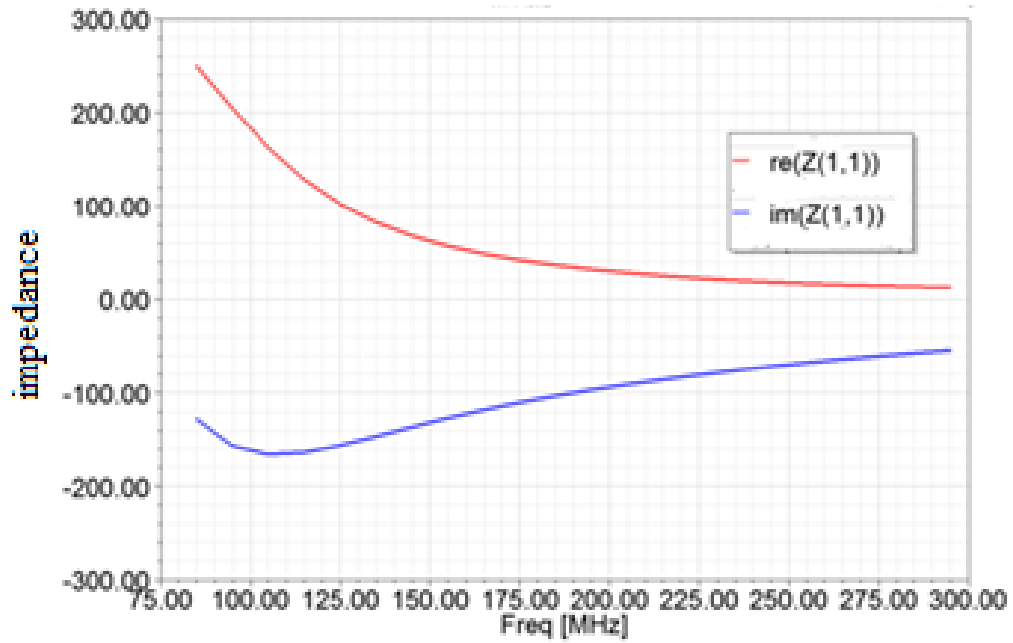


Fig. 6-5 Impedance of the Single Loop Fed Spiral Antenna

Fig.6-7 shows that the impedance response is not frequency independent which we already expected since there is no way to keep the flux from leaking from the structure. A plot of the $\oint E \cdot dl$ along the structure which is the magnetic current I_m can clearly show if this is the case.

In order to do this, we will use HFSS field calculator as follows. We define integration paths as shown by the black loop in Fig.6-7. The distance from feed is defined as the length of the path from feed to the integration path as shown by the yellow arrow. After calculating the integral along a number of integration paths we can plot $\oint E \cdot dl$ as a function of distance from the feed point.

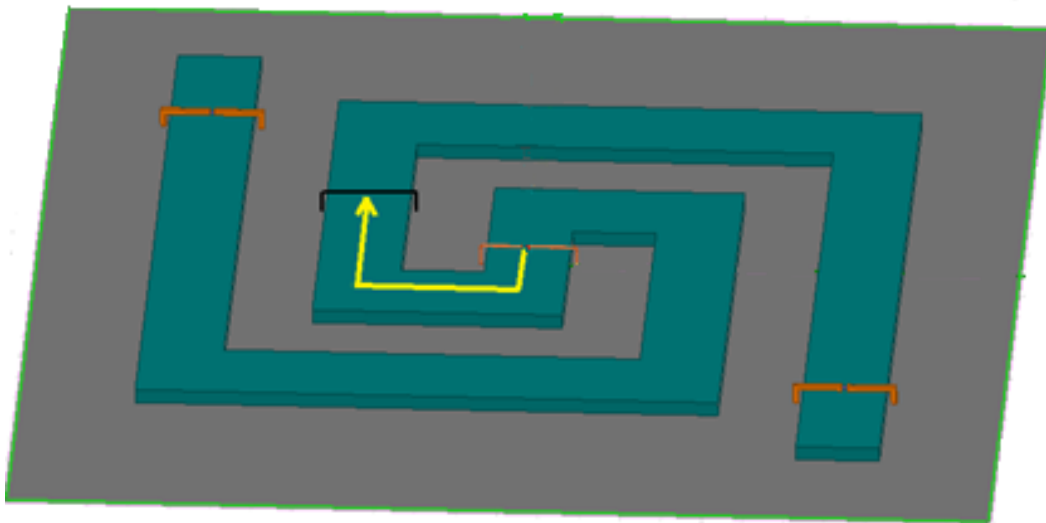


Fig. 6-6 Impedance of the Single Fed Spiral Antenna.

A few integration paths and a table of the distance of the paths from the center can be seen in Fig.6-8 and the numbering of the lines is as shown in the HFSS model below.

line	Distance from feed(mm)
1	25.8
2	50.8
3	154.4
5	244.4
6	355.6
10	555.6
13	771.6
14	841.6
19	1191.6
20	1261.6
23	1546.4
26	1801.4

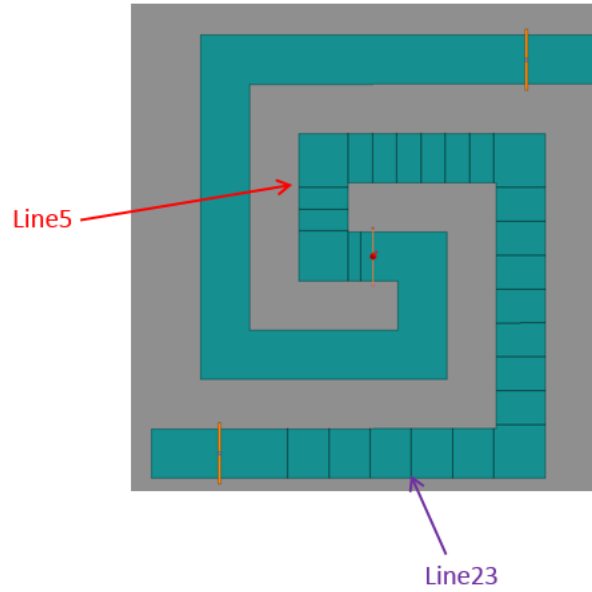


Fig. 6-7 A Few Integration Paths and a Table of the Distance of the Paths From the Center For the Single Loop Fed Spiral Antenna.

By having the integration data, we can plot the integral versus frequency for different lines as seen in Fig. 6-10. We can see that as we get further from the feed, the flux escapes therefore similar to other magnetic antennas, using the parallel solenoid is necessary.

We have also plotted $\oint E \cdot dl$ versus distance from the feed at three different frequencies as seen in Fig. 6-11.

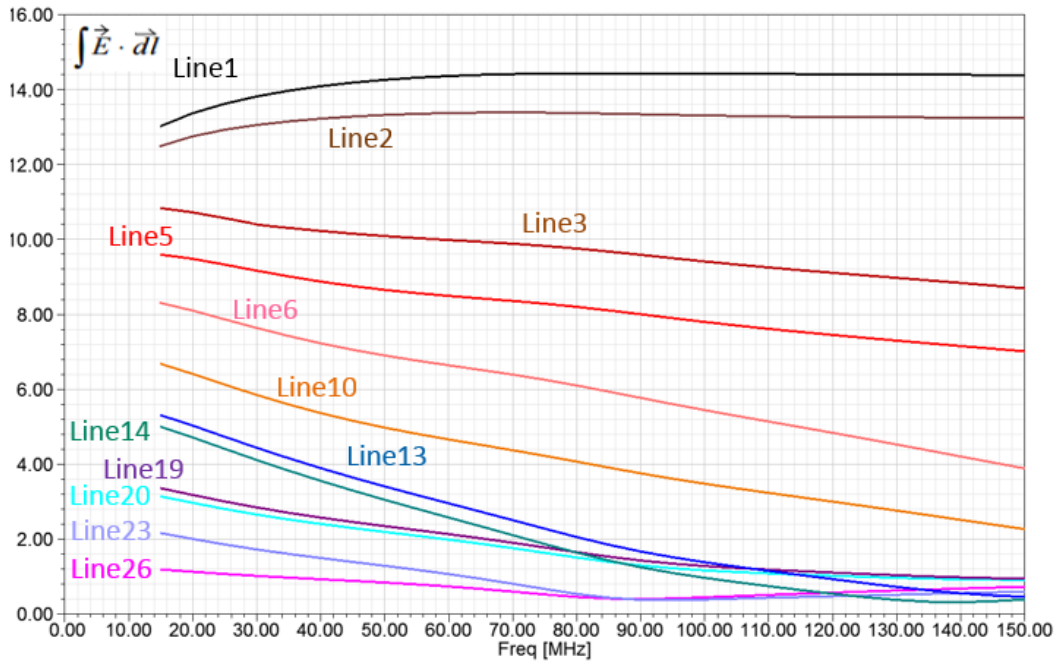


Fig. 6-8 Integral Versus Frequency for Different Lines for the Single Loop Fed Spiral Antenna.

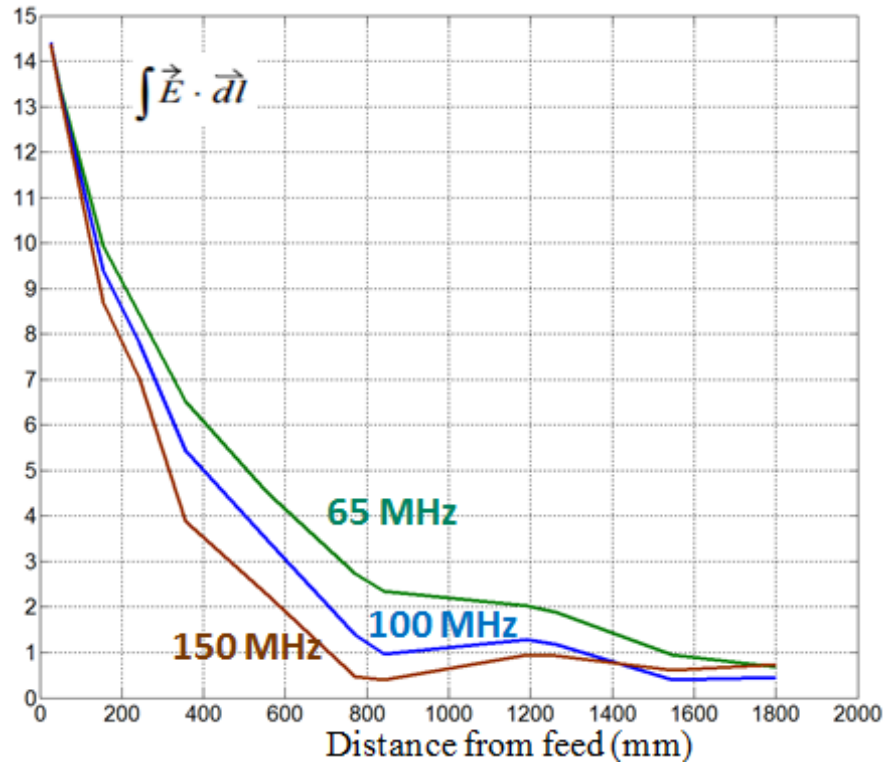


Fig. 6-9 Value Of $\oint E \cdot dl$ Versus Distance from the Feed

The previous figure also shows that there is no mechanism to keep the flux inside the material. Therefore, the next logical step would be adding a solenoid feed with loops to ground as seen below. First, we start with a solenoid feed with only 4 loops to ground. The lines shown in black are integration paths and numbering of the lines is similar to what we had before and in this structure, there is a 3mm distance between the solenoid and the ferrite. The integration lines (paths) have a 1mm distance from the ferrite which makes them identical to the paths for the previous case (without the solenoid).

A few integration paths and a table of the integration values can be seen In Fig. 6-12 below.

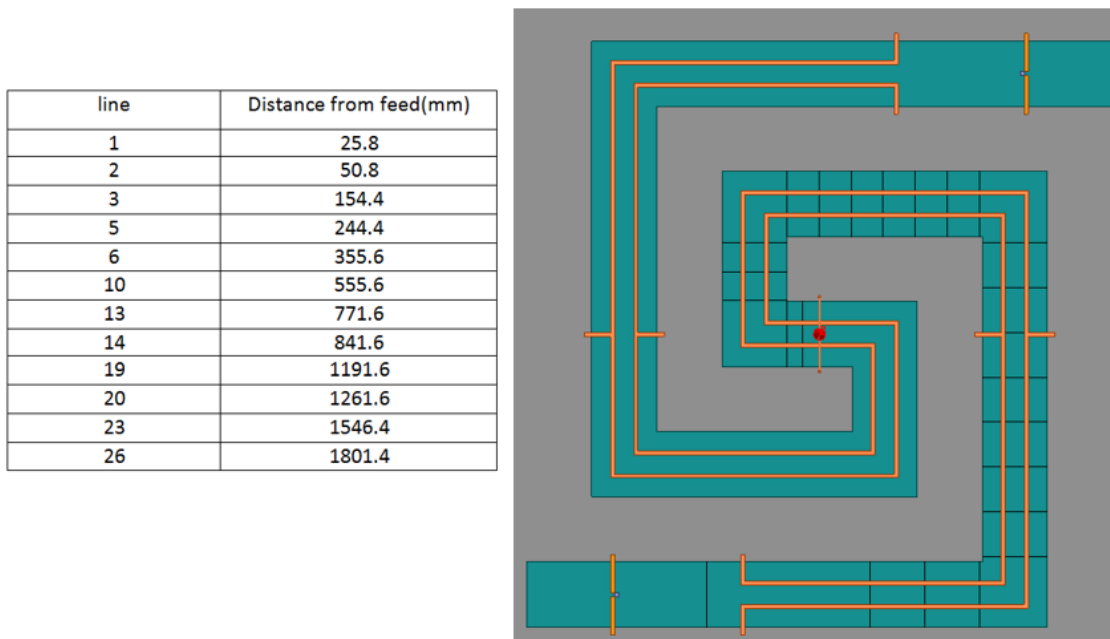


Fig. 6-10 A Few Integration Paths and a Table of the Distance of the Paths From the Center for the 4 Loop Solenoid Fed Spiral Antenna.

The integral versus frequency for different lines is shown in Fig. 6-13. It can be seen that a line that is farther from the feed, does not necessarily have lower flux at all frequencies which is the effect of adding the solenoid.

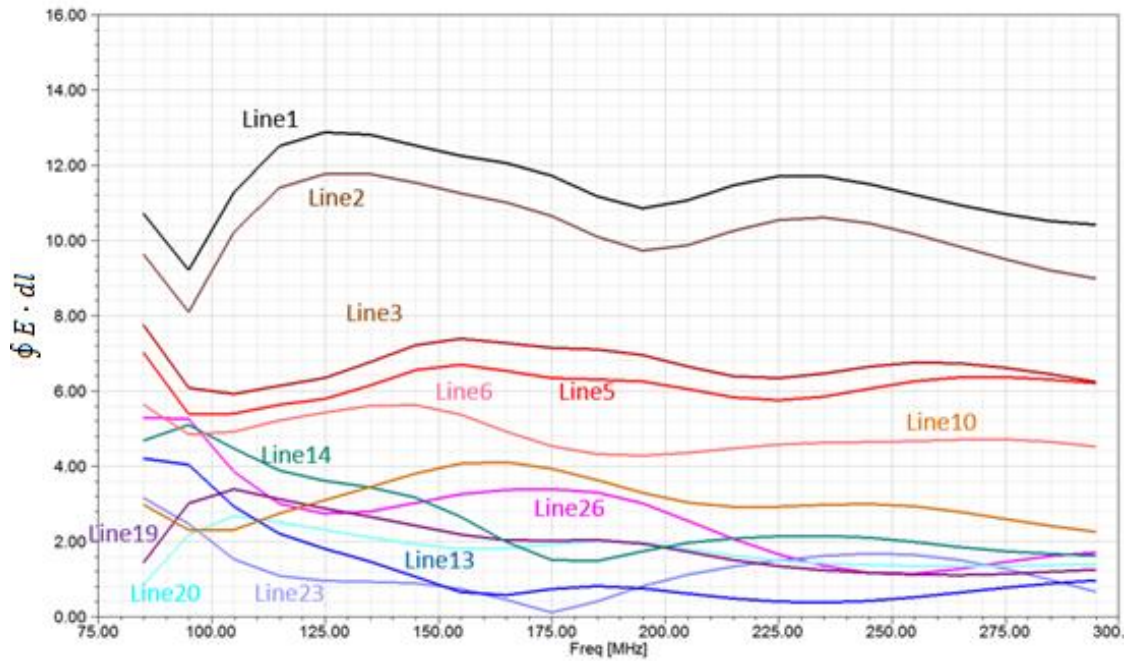


Fig. 6-11 Integral Versus Frequency for Different Lines for the 4 Loop Solenoid Fed Spiral Antenna

This means that there is a mechanism that is trying to keep the flux inside the material. A plot of the $\oint E \cdot dl$ versus distance from the feed at a few frequencies similar to what had been done in Fig.6-11 will help to see this more clearly. In order to compare these two cases, we have shown the flux versus distance of the two cases side by side. It can be seen that at the position of the loop to ground we have an increase in the flux. Therefore, in the next section we will study the effect of adding more grounded loops to the solenoid.

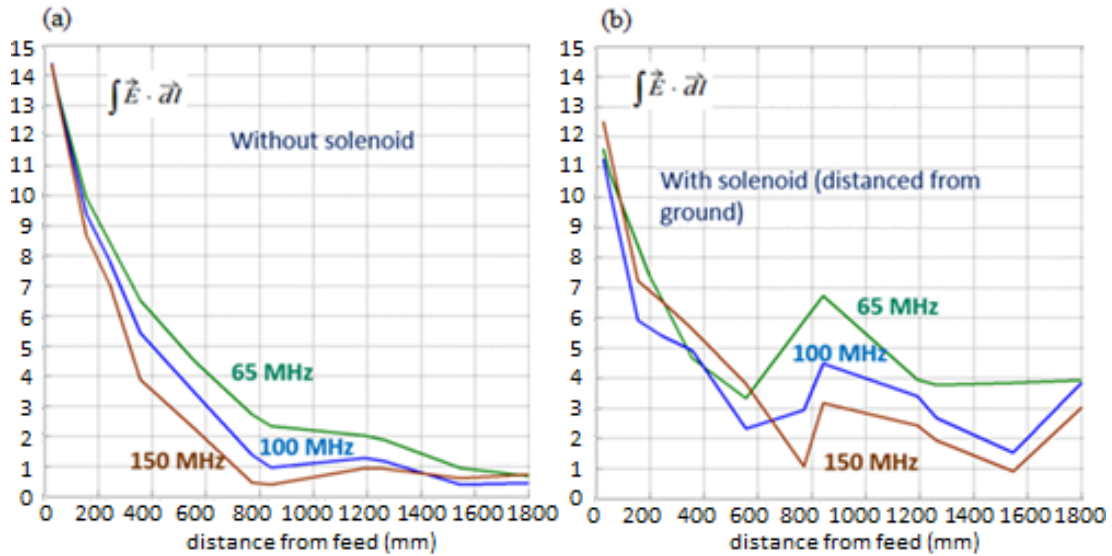


Fig. 6-12 Plots of $I_m = \int E \cdot dl$ for (a) Spiral Antenna with One Feed Loop at the Center (b) the Solenoid Fed Spiral Antenna With 4 Loops to Ground. Showing an Increase In I_m at the Position of the Loop.

6.3 The Effect of Using a Solenoid Feed with Multiple Grounded Loops

In the previous section, we saw that adding four grounded loops and using a solenoid feed begins to help maintain the flux in the material. Therefore, we will study the effect of adding even more loops to ground. Our goal is to achieve a high gain while having impedance that is frequency independent since the impedance shown in Fig. 6-7 is not. We will also show that the solenoid should be spaced a small distance from the ferrite surface to minimize near field loss and then we will show that adding the number of loops will result in smoother impedance and a higher gain and efficiency.

The figure below shows how the peak gain changes with adding more and more loops. It should be noted that as the red plot shows, when the solenoid feed is touching

the ferrite we have a significant loss. Therefore, in all other cases, which are named as distanced, we have a 3mm gap between the solenoid feed and the ferrite.

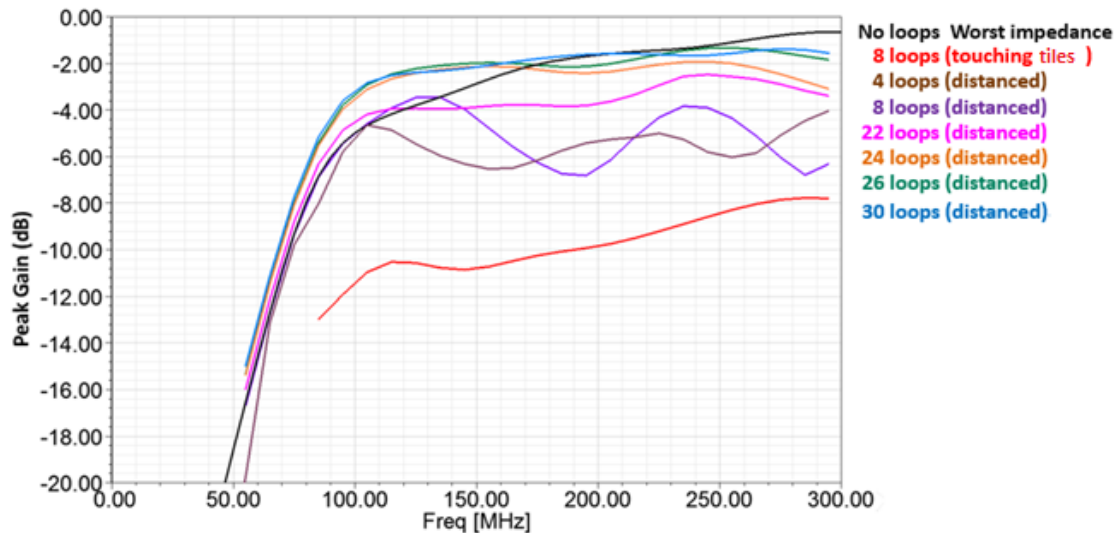


Fig. 6-13 Changes in Peak Gain When We Change the Number of Loops to Ground From 4 Loops to 30 Loops and Comparing the Results to the Case Without the Solenoid and the Case of the 8 Loop Structure Touching the Ferrite.

The comparisons between the gains show that adding the loops will increase the gain but another important factor is the impedance behavior. Fig. 6-14 (a) and (b), below show two different cases. The first case is the magnetic spiral antenna without any solenoid feed and the second case is the solenoid fed antenna with 30 loops to ground. The impedance of each of these antennas has been plotted in Fig. 6-14(c) and the gain is plotted in Fig.6-16(d). We see that the antenna with the 30 loop solenoid has both high gain and nearly frequency independent impedance.

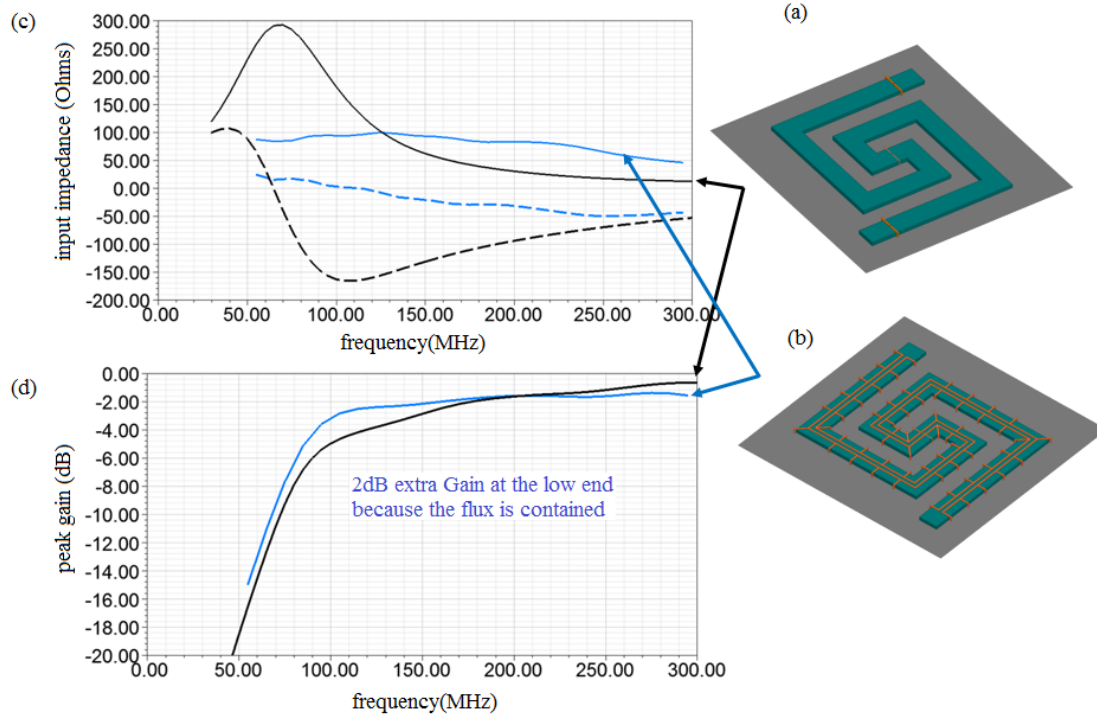


Fig. 6-14 (a) Magnetic Spiral Antenna Without any Solenoid Feed, (b) Magnetic Spiral Antenna With an 8 Loop Solenoid Touching the Ferrite and, (c) the Solenoid Fed Spiral Antenna With 30 Loops to Ground, (d) the Impedance of Each of the Antennas (e) the Gain of the Antennas.

At this point a comparison between the reflected power, the radiated power, and the lost power of the three mentioned antennas would be useful. These powers are defined as seen in equations below and can be calculated from the data obtained from HFSS.

$$P_{radiated} = efficiency \times (1 - |\Gamma|^2) \quad (6-1)$$

$$P_{reflected} = |\Gamma|^2 \quad (6-2)$$

$$P_{lost} = P_{accepted} - P_{radiated} \quad (6-3)$$

$$P_{lost} = (1 - |\Gamma|^2) - efficiency \times (1 - |\Gamma|^2) \quad (6-4)$$

The table below shows the values of these powers for each antenna

Table 6-1 Values of Powers for Each Antenna.

Results at 250 MHz	$P_{reflected}$	$P_{radiated}$	P_{lost}
Antenna with no solenoid	62%	6%	32%
8 loop antenna	8%	2%	90%
30 loop antenna	15%	16%	69%

We can see that the final antenna (Antenna with 30 loops to ground) has the most power radiated which again shows the importance of the solenoid feed. The reason that the power lost in the case with no solenoid seems to be low is that most of the power is already reflected which means frequency dependent behavior and bad VSWR. The low reflected power of the final antenna shows a good match.

It should be noted that the NiZn ferrite tiles being used for this antenna are sold as RF absorber tiles for Electromagnetic Compatibility (EMC) anechoic chambers. As the permeability spectrum shows in Figure 6-4 the permeability at 250MHz is predominantly imaginary. Thus, losing input power is not a surprise, the surprise is that only 69% of the power is lost and that Gain approaching 0dB CP can be attained.

6.4 Final Antenna Geometry and Results

The figure below shows the final antenna geometry with the dimensions. The distance between the vertical rods and the ferrite is 6mm and the distance between the horizontal rods and the ferrite is 3mm. The solenoid consists of 30 loops to ground and there is no resistor termination for the low end is needed.

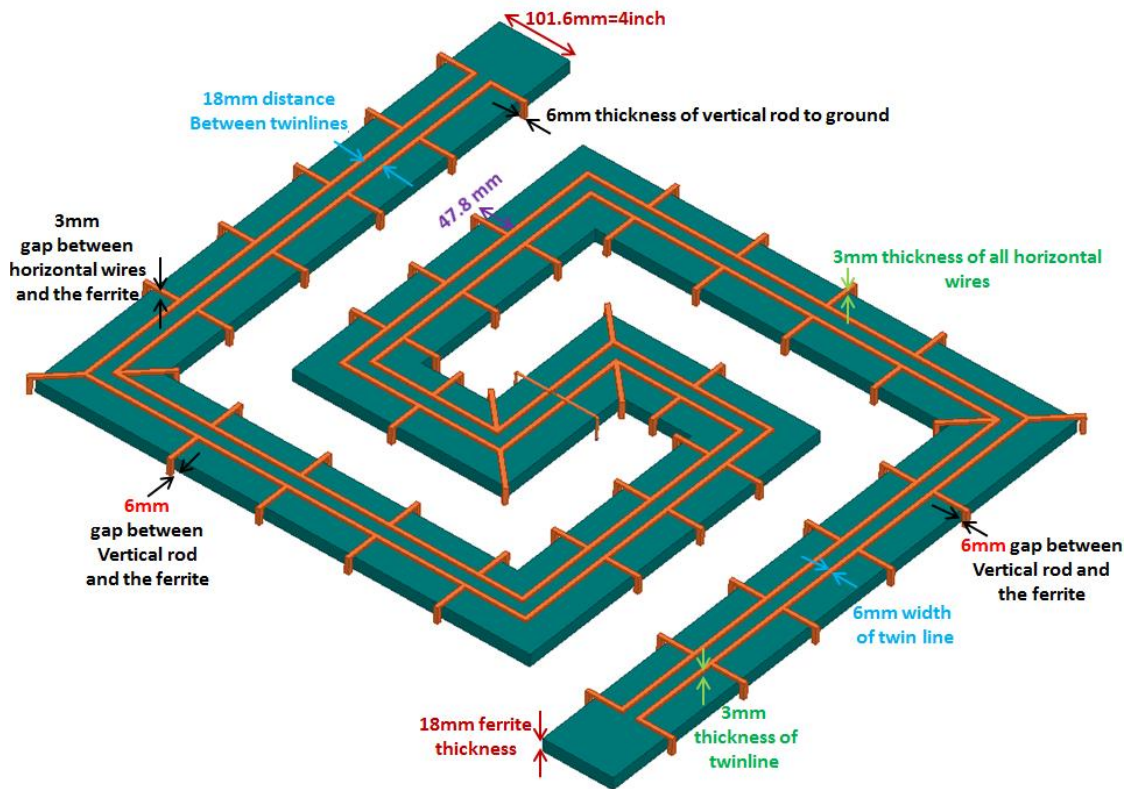


Fig. 6-15 Model and Dimension of the Final Design of the Magnetic Spiral Antenna.

To put in perspective the contribution of the parallel solenoid Fig. 6-18 compares the original 4 loop design to the final design. The figure shows that the measured performance matched the computational simulations within the expected measurement and fabrication uncertainties (middle top). The next iteration of the parallel solenoid is shown in the lower CAD figure and its performance in the second plot in the middle. The

design with 30 loops to ground increases the Gain by up to 4dB and smooths out the performance over the band. As the input impedance plots at the bottom show the input impedance is indeed slowly varying with frequency and easily matched to a 50 ohm standard microwave system by simply using a 2:1 transformer.

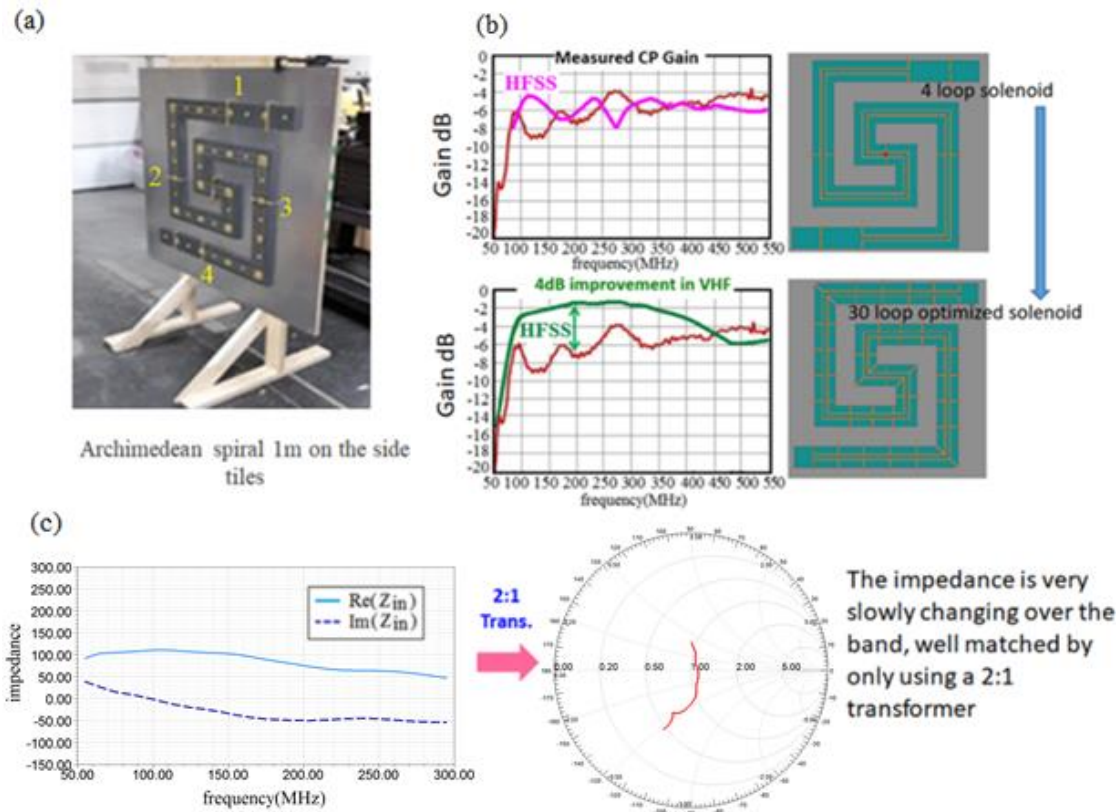


Fig. 6-16(a) Photograph of the First Version of the Spiral Fed by a 4-Loop Parallel Solenoid (b) HFSS Models of the Same Structure With 4 Loops and 30 Loops and the Measured and Simulated Gain (c) Input Impedance and Smith Chart Representation

In the following plot, the S_{11} of the structure can be seen after the 2:1 transformer which shows a 11:1 VSWR bandwidth

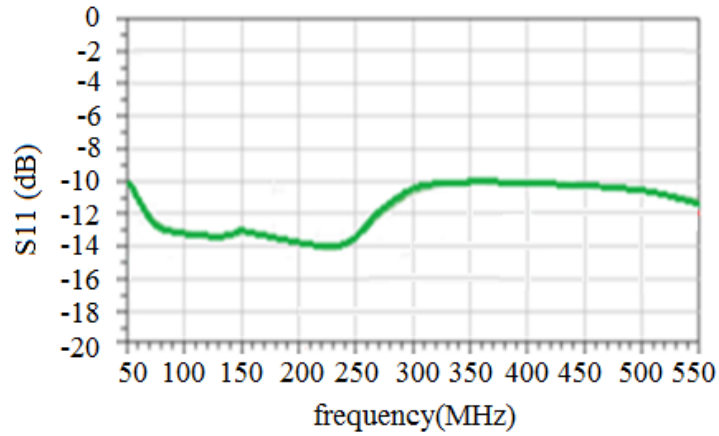


Fig. 6-17 S11 of the Spiral Antenna Showing a Very Good Match After Only A 2:1 Transformer

In order to see if the antenna has a circular polarization we will plot the antenna pattern in a lower and a higher frequency. We see that we have a very good circular polarization in lower frequencies and the axial ratio get worse as we go to higher frequency. Fig. 6-20 shows the Gain_θ pattern at $f=95\text{MHz}$ at $\varphi = 0$ and $\varphi = 90$ and Fig. 6-21 shows the Gain_θ pattern at $f=235\text{MHz}$ at $\varphi = 0$ and $\varphi = 90$

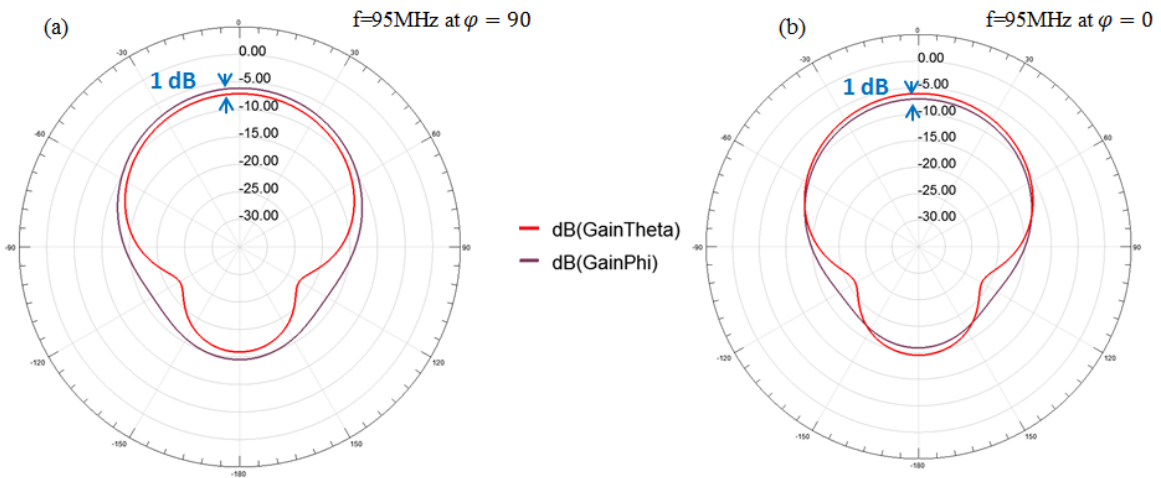


Fig. 6-18 Gain_θ Pattern at $f=95\text{MHz}$ at $\varphi = 0$ and $\varphi = 90$ Degrees

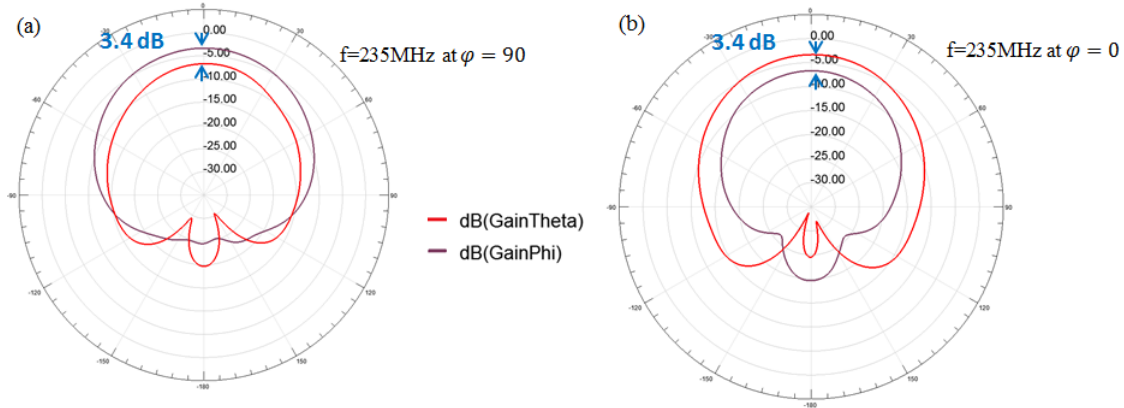


Fig. 6-19 Gain_θ Pattern at $f=235\text{MHz}$ at $\varphi = 0$ and $\varphi = 90$ Degrees.

Fig. 6-22 shows the efficiency of the final parallel solenoid fed antenna, the theoretical efficiency of an Archimedean antenna with a height of 18mms and the spiral fed with a single loop and the antenna when the solenoid is touching the surface of the ferrite. The center fed spiral has high efficiency but is not frequency independent and the case of the solenoid touching the ferrite has a frequency independent behavior but has low efficiency. It can be seen that the final antenna design has both high gain and a frequency independent behavior within its expected band of operation (95MHz to 315MHz) and more.

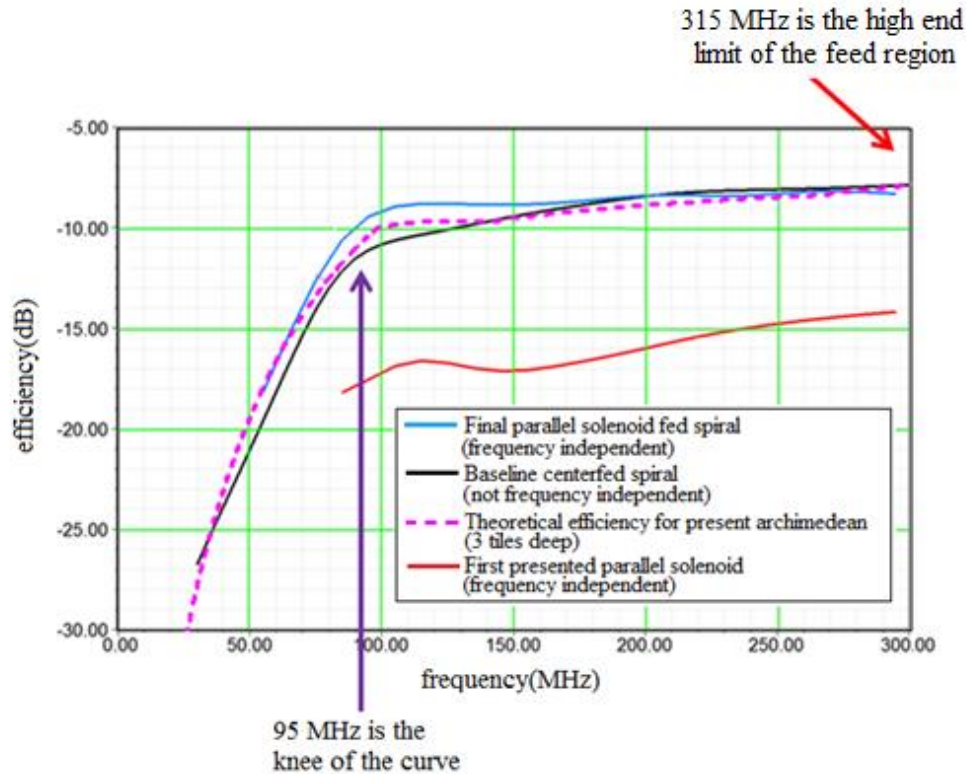


Fig. 6-20 Plot of the Efficiency of the Final Parallel Solenoid Fed Antenna, the Theoretical Efficiency of an Archimedean Antenna with a Height of 18mms, and the Spiral Fed with a Single Loop and the Antenna When the Solenoid Is Touching the Surface.

6.5 Archimedean Spiral Antenna Built Using CZN Laminates Instead of NiZn Tiles

In this section we show the gain results that would be obtained using CZN ferromagnetic laminates instead of the tiles. If we can find a way to use the laminate material we expect to have a much higher efficiency at a specific bandwidth but there is a risk of lower gain and efficiency at lower frequencies because the μ_{DC} of the laminates are much lower than the tiles. Another important fact is that we no longer need to have a 4inch \times 4inch cross section and we can have a smaller thickness (if needed).

We know that both material volume and hesitivity are important to get a high efficiency. The Hesitivity of NiZn is about 35,000 ohms per meter and the Hesitivity of the laminates is 350,000 ohms per meter which is much higher . In order to model the laminate material in HFSS we have to take note that this material is anisotropic and the mu tensor has different values for different directions. In order to solve this problem we model the spiral antenna as seen below.

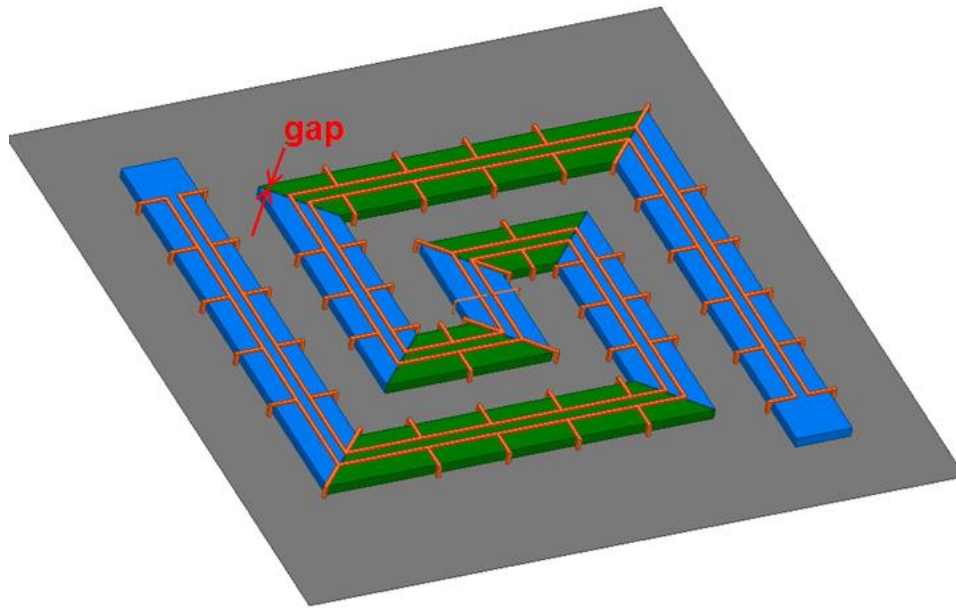


Fig. 6-21 Model of the Spiral Antenna Using CZN Laminates. The Different Regions, Due to the Anisotropic Material, Are Shown in Green and Blue.

In Fig. 6-23 we see the x-directed sections shown in green and the y directed sections shown in blue. Since the CZn laminate is an anisotropic material each of these sections had to be defined with their own tensors shown as μ_x and μ_y below.

$$\mu_x = \begin{bmatrix} \mu_{CZn}(\omega) & & \\ & 1 & \\ & & 1 \end{bmatrix} \quad \mu_y = \begin{bmatrix} 1 & & \\ & \mu_{CZn}(\omega) & \\ & & 1 \end{bmatrix}$$

This model includes a 2mm gap at the mitered corners and yet the parallel solenoid prevents the flux from escaping at those corners. The figure below shows a comparison between the peak gain of the ferrite tile antenna and the CZN laminate antenna which shows that the laminate antenna has much higher gain.

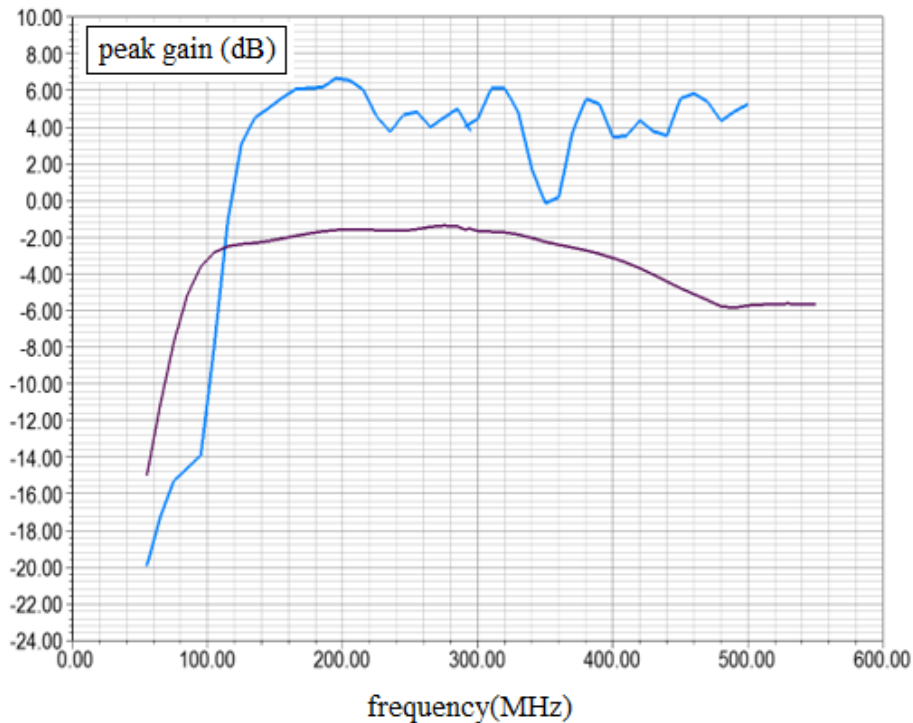


Fig. 6-22 Peak Gain of the Ferrite Tile Antenna (Purple) and the CZN Laminate Antenna(Blue).

6.6 Conclusion

In the previous chapters, we had shown that using the new concept of parallel solenoid feed system for permeable antennas instead of the conventional feeds resulted in higher gain and better impedance properties. In this chapter, we have demonstrated the importance of using the parallel solenoid feed mechanism for a magnetic Archimedean

spiral antenna. We have proved that by adding the parallel solenoid feed to the magnetic spiral antenna we could get high gain and efficiency and frequency independent behavior, good axial ratio, and a bandwidth of 11:1 (only limited by the dimensions of the spiral) which shows the necessity of using the parallel solenoid feed for these types of antennas.

The next logical evolution of this work would be to design a much more general magnetic flux channel in which source excitation, flux binding, tailoring of the frequency response of the guiding surface are all attained. As we will see in full detail in the next chapter, by pushing the magnetic material inside the ground in a trough like structure, this will be possible and the structure will be completely conformal to the outer platform. The metalized trough channel will be introduced in the next chapter in full detail as an evolution to the work done in the previous chapters with the goal of obtaining analytic model with design rules that can be used by engineers to design optimum flux channels for practical applications.

CHAPTER 7

Comprehensive Study on Metalized Magnetic Flux Channel Antenna

“The significant problems we face today cannot be solved at the same level of thinking we were at when we created them.”

Albert Einstein

7.1 Introduction

In our previous chapters, we have addressed the unexpectedly high Efficiency-Bandwidth Product (EBWP) of conformal antennas constructed from existing realistic (dispersive, lossy) magneto-dielectric materials (such as ferromagnetic metal films and ferrites) [2, 27, 28]. For instance, the toroidal magnetic antenna, constructed from a high permeability (and low permittivity) dispersive material and used as an electrically thin conformal antenna, exhibits a radiation efficiency up to two orders of magnitude higher than metal conformal antennas constrained to the same volume. This is an instance of the general principle that permeable antennas have an advantage over metal (and dielectric) antennas in low impedance environments, such as: conformal to a metal surface, adjacent or inside the human body, immersed in water, or inside the earth.

One of the most important factors in designing a magneto dielectric antenna with a large bandwidth is making sure that the antenna can guide the wave along the structure with a speed close to the speed of light. When this is the case, we are assured by the duality of Maxwell’s equations that the permeable antenna conformal to a metal ground

plane will behave exactly (in a complementary sense) like conventional metal antennas suspended in free space.

The success of the parallel solenoid feed must therefore be attributable in part to this phenomenon. The two-wire transmission line that carries the excitation from the feed to all the loops by definition carries a TEM-like wave that must travel close to the speed of light. However, we have also found out that there are limits to the performance of the parallel solenoid feed whereby using too many loops appears to over-bind the wave, trap it at high frequencies, and therefore lead to sub-optimal performance. We therefore need an explicit design technique and apparatus that can allow us to control the propagation of the magnetic current wave in these permeable antennas in such a way that near-light-speed propagation can be obtained over the widest frequency band possible.

Figure below shows the toroidal magnetic antenna [28] and the Archimedean spiral magnetic antenna using the parallel solenoid feed as the flux binding method.

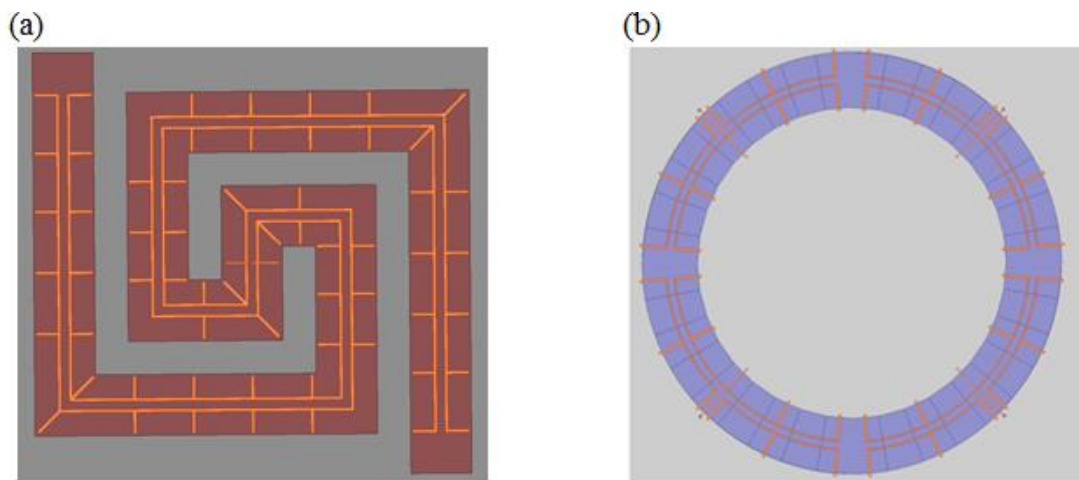


Fig. 7-1 (a) Magneto Dielectric Archimedean Spiral and a (b) MD Toroid Fed with a Multiloop Solenoid

Feed

We can recognize that the parallel solenoid is simply an approximate, discrete, instance of the more general concept of an admittance surface surrounding the magneto-dielectric flux channel. The trough geometry, seen below, is the most convenient way to implement this tailored-admittance surface concept. We will explain the effect of the trough with the spiral antenna as an example.

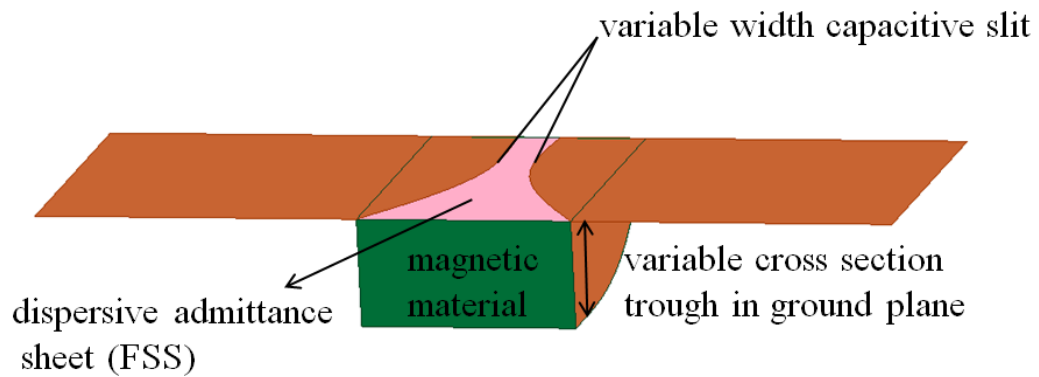


Fig. 7-2 The Generalized Magneto Dielectric Trough Antenna

The Spiral antenna seen below and explained in detail in the previous chapter is an example of an antenna that uses the parallel solenoid to help contain the magnetic flux inside the material and make the dB/dt magnetic current as uniform as possible over a broad band. As previously mentioned, This Spiral was built using 123 NiZn tiles each with a 4inch \times 4inch cross section and 6mm thickness we started with using only 4 loops.

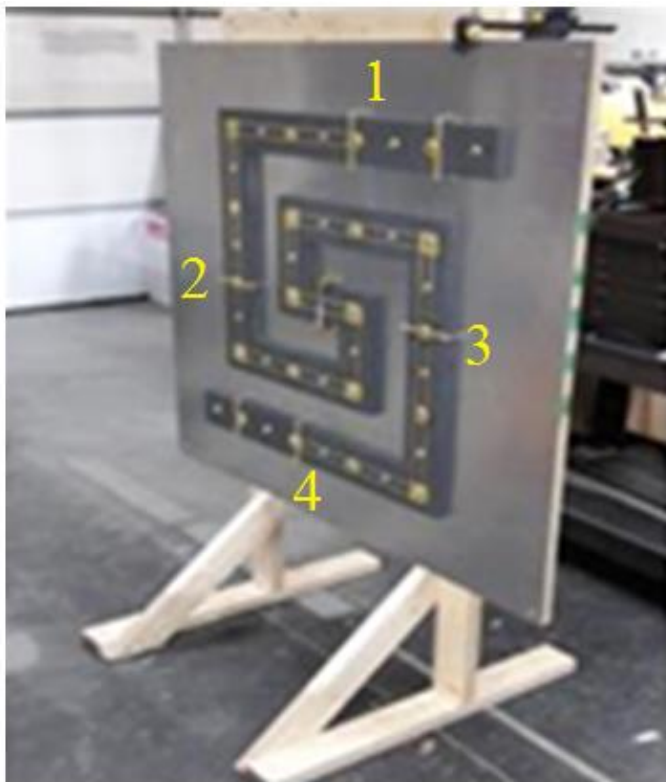


Fig. 7-3 Spiral Antenna with a 4 Loop Solenoid Feed

We have seen many times that the number of loops in the solenoid is a very important factor in flux binding therefore a simulation was done using 30 loops instead of 4 loops. The resulting gain using a 30 loop solenoid compared to a 4 loop solenoid can be seen below. We repeat this so we could use this as a comparison to the more generalized flux channel in the trough form.

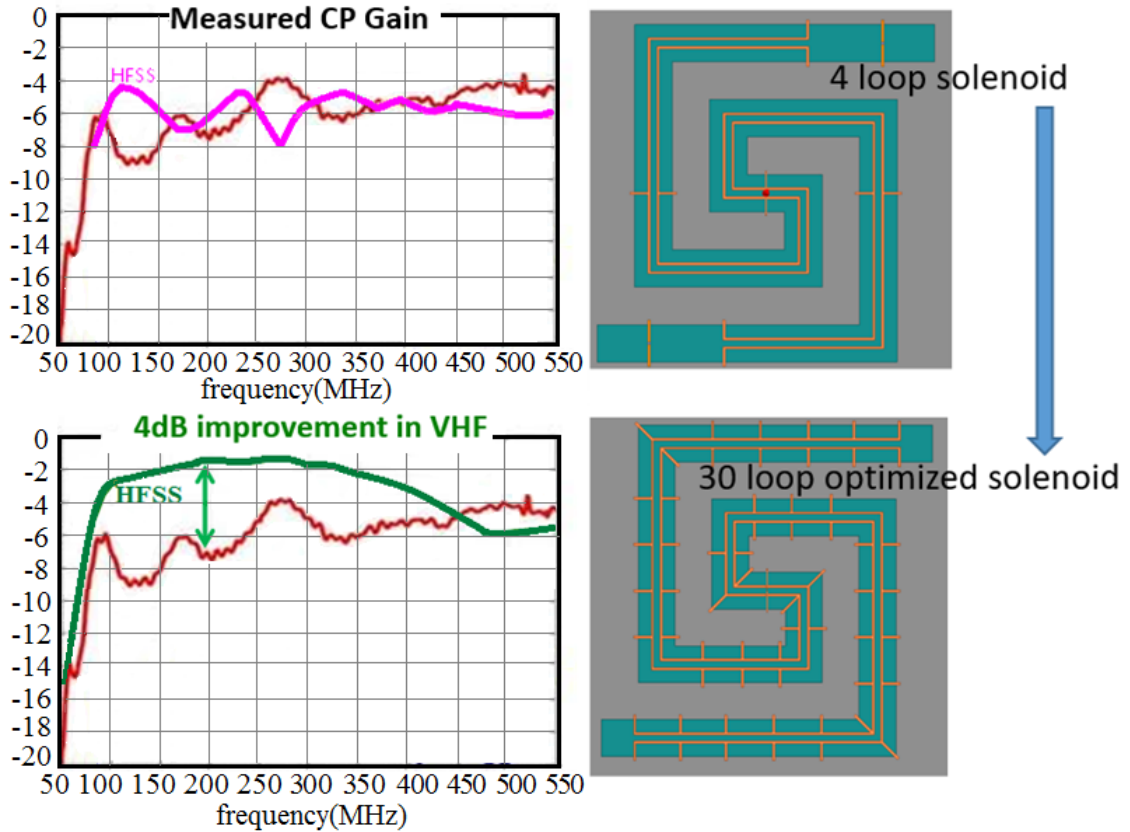


Fig. 7-4 Comparison of the Gain of a Spiral Antenna Using Different Number of Loops in the Solenoid Feed.

The figure above shows more than 4dB improvement in VHF gain by increasing the number of loops. The next logical step is to see if we can improve the results using the trough structure instead of the parallel solenoid. The figure below shows the spiral antenna buried inside the trough with the material surface having a 6mm distance from the metal surface and the parallel solenoid implemented as thin metal bars connected to the surrounding ground plane.

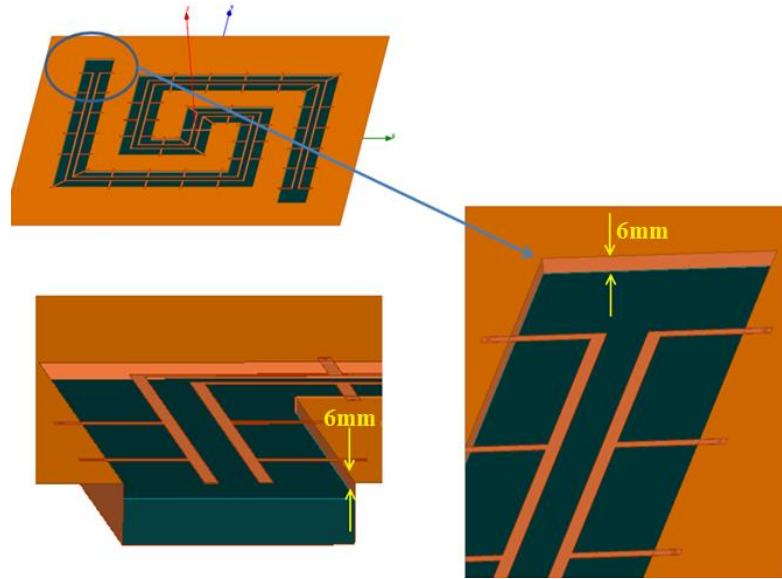


Fig. 7-5 Different Views of the Magnetic Trough Spiral Antenna

The peak gain and efficiency of the solenoid fed antenna and the trough antenna can be seen in figure 7-6. It shows that the trough geometry has resulted in a significant increase in both gain and efficiency and now we can put those antennas conformal to any conducting surface.

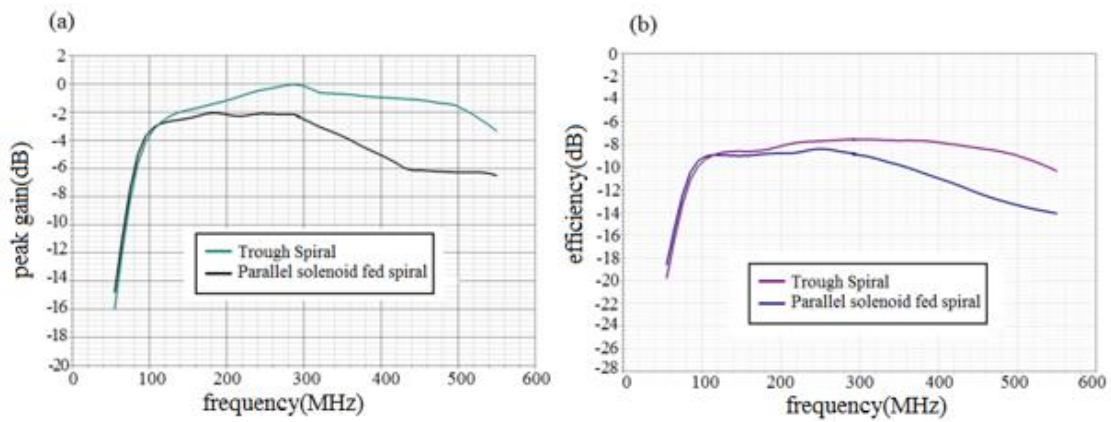


Fig. 7-6 (a) Peak Gain (b) Efficiency of the Spiral Antenna with the Solenoid and with the Trough

Now that the effect of the trough on the antenna parameters is obvious we will follow with studying the trough structure in detail. Our goal in proposing and studying the trough has been to create a structure where source excitation, flux binding, and tailoring of the frequency response of the guiding surface can be tuned and controlled. To make these results most useful to the engineer we seek to develop them in closed form, not by repeated fullwave simulation. Thus, when we wish to incorporate the surface admittance on the mouth of the trough the simplest implementation is a slitted plane, a well-known capacitive boundary that also admits of a closed form solution.

In this chapter, we develop the theory of the magneto dielectric open trough and the trough having a slit. We will see how the geometry (cross section) of the open trough and the dimensions of the slit affect its.

The ultimate purpose of this work is to lay down the foundation for the next generation of magneto dielectric antennas attained by giving the structure these additional degrees of freedom. In the same way that the magneto dielectric antenna can be viewed as a revisiting of the ferrite rod antenna of AM radio days and taking it to its logical extreme, the process of deriving the new structures in this paper can be viewed as the result of revisiting the classic leaky antennas studied by Oliner and others [31, 32] and taking them to their logical extreme.

Because the performance of the new antenna will be compared to that of the magneto-dielectric rod, we recap the approach to the solution and results for the infinite MD rod in Appendix B. The approach is to solve the Green function problem of the structure excited by a current band with the only limitation that we assume the current

band and the fields it excites are uniform in the direction of the current (that is no ϕ dependence for the rod geometry and only TE_{0n} modes excited inside the trough.)

In section 2 we will see how the phase and amplitude of the magnetic current distribution changes as a function of distance from the feed for these antennas. The slope of the current amplitude plot (*named the α plot*) and the slope of the current phase (*named the β plot*) will be studied as a measure of wave decay and wave velocity respectively. Later we will calculate the total power dissipated using the induced EMF method and the radiated power from the Poynting vector and show the formation of the modes and the bandwidth.

Section 3 will cover the theory of the open magneto dielectric trough. The fields of this geometry will be examined and both the amplitude and phase of the magnetic current of the open magneto dielectric trough will be plotted. Similar to what had been done for the MD rod, the α plot and the β plot will be obtained for the open trough and the total power and the radiated power will also be shown for this geometry

In section 4, the slitted trough geometry will be introduced and all the parameters mentioned in previous sections will be calculated for this case in order to be used as a means of comparing the behavior of the three proposed geometries

Section 5 will serve as a comparison study to show which geometry has more degrees of freedom and how these degrees of freedom can be used to design the best magneto dielectric antenna.

7.2 Theory of the infinite magneto dielectric rod

The Magneto-Dielectric Antenna is obtained by replacing the electric conductor of the conventional metal antennas with a penetrable permeable material. Appendix B contains the details of the derivation

7.2.1 Phase and amplitude plots of the magnetic current of the MD rod

Fig.7-7, shows the amplitude and phase of I_m as a function of the distance from the feed multiplied in units of (z/λ) for a magneto-dielectric rod with a 2 inch radius and a material with $\mu = 80$ and $\varepsilon = 2$. The 2" rod serves as an example to study the behavior. The light line is the line of 2π radians phase shift per wavelength.

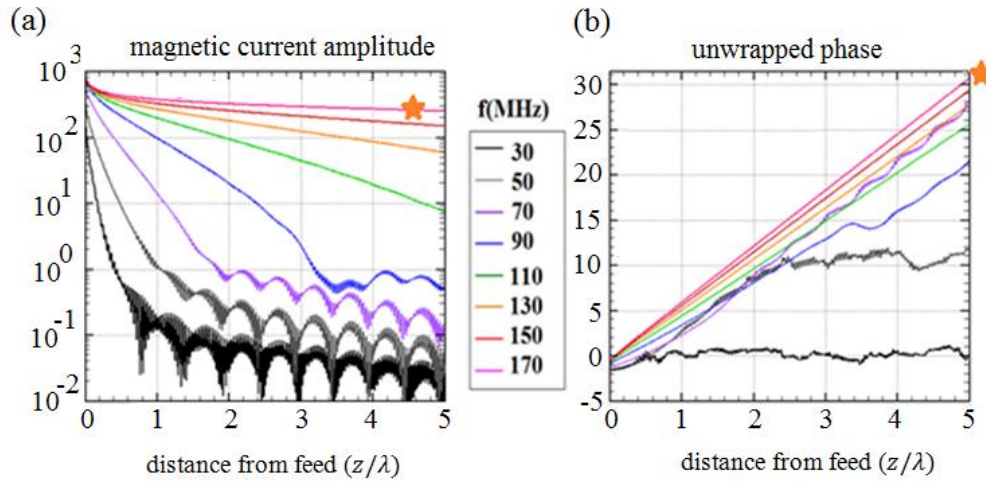


Fig. 7-7 Amplitude (a) and Phase (b) of the Current as a Function of the Distance From the Feed Multiplied by the Wavelength (z/λ) for a Magneto-Dielectric Rod With a 2 Inch Radius and a Material with $\mu = 80$ And $\varepsilon = 2$. Frequencies Go From 30 MHz to 170 MHz In 20 MHz Steps. The Star Symbol Shows the Current Wave Approaching the Light Line.

By looking at both the amplitude and the phase plots we see that at very low frequencies the waves are fast (below the light line) and the amplitude decays precipitously away from the feed. These are leaky waves. As we get closer to 170MHz, the approaching surface wave onset tends to flatten the amplitude of the current wave and brings its speed close to light, thus the MD rod behaves more and more like a PMC metal antenna as it approaches onset. The star symbol in the phase plot highlights these conditions. At this point it would be interesting to see what happens as we go higher in frequency and cross the onset therefore we will examine another set of 8 frequencies

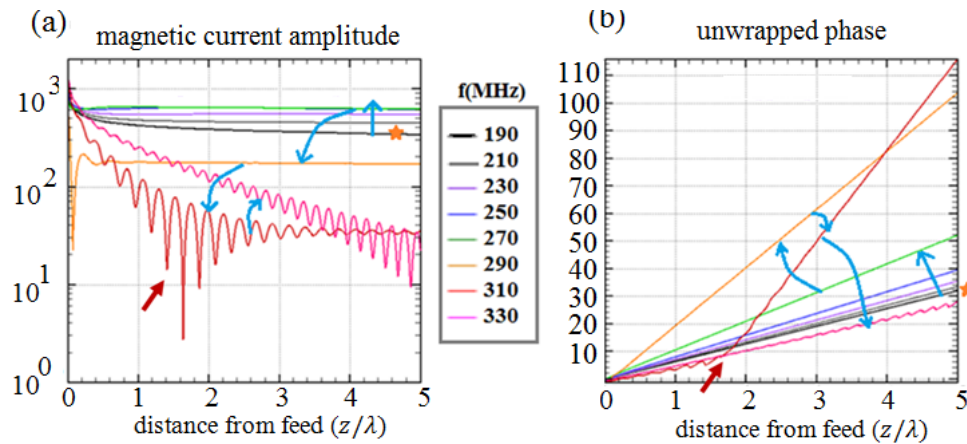


Fig. 7-8 Amplitude (a) and Phase (b) of the Current as a Function of the Distance From the Feed Multiplied by the Wavelength (z/λ) For a Magneto-Dielectric Rod with a 2 Inch Radius and a Material with $\mu = 80$ and $\epsilon = 2$. Frequencies Go From 190 MHz to 330 MHz in 20 MHz Steps. The Star Symbol Shows the Current Wave Approaching the Light Line. The Blue Arrows Shows the Current Wave Going from One Mode to Another Mode and the Red Arrow Shows the Plateau That's the Indication of the New Mode Starting to Appear

Starting to Appear

Fig.7-8 shows the amplitude and phase of I_m versus distance from the feed in wavelengths for frequencies from 190MHz to 330MHz with 20MHz frequency steps. In Fig.7-7 we saw that in the 170MHz frequency we are close to the speed of light and the

amplitude started to get flat. Now by looking at Fig.7-8, as shown by the start symbol, we see that at 190 MHz, the phase is very close to $(5 \times 2\pi = 31.41)$ which means we are just above onset of the guided wave shows amplitude behavior very much like the PMC with decay close to $\log(1/|z|)$. It also shows a phase velocity very close to that of light.

As we go from 190 MHz to higher frequencies up 270 MHz which is shown in green we see that the slope of the phase increases and the amplitude keeps getting flatter (more uniform). In this region, we have started to guide the TE01 mode and we will see that since the slope of the phase is more than the light-line we have waves that are slower than light and all of these show a guided wave.

As we follow the blue arrows and go higher than 270 MHz (starting from the orange line), we see a sudden change in both phase and amplitude. This means that the next mode which is the TE02 is beginning to appear and as shown with the red arrow, we have a fast wave with a large attenuation constant near the feed. The plateau shown in both phase and amplitude curve reveals a very slow wave, probably the last time we can excite the TE01 mode from the surface of the rod. After 310 MHz we are at a frequency that TE02 has not reached onset and similar to the lower frequencies we again start with the leaky fast waves.

Fig.7-9 shows the same plots from 350 MHz to 490 MHz. Around 410 MHz (blue curves) the amplitude becomes much like the PMC antenna's and the phase velocity crosses the light line. Above that the wave continues to become better bound again, this time as TE02, but in complete analogy to what we saw above already.

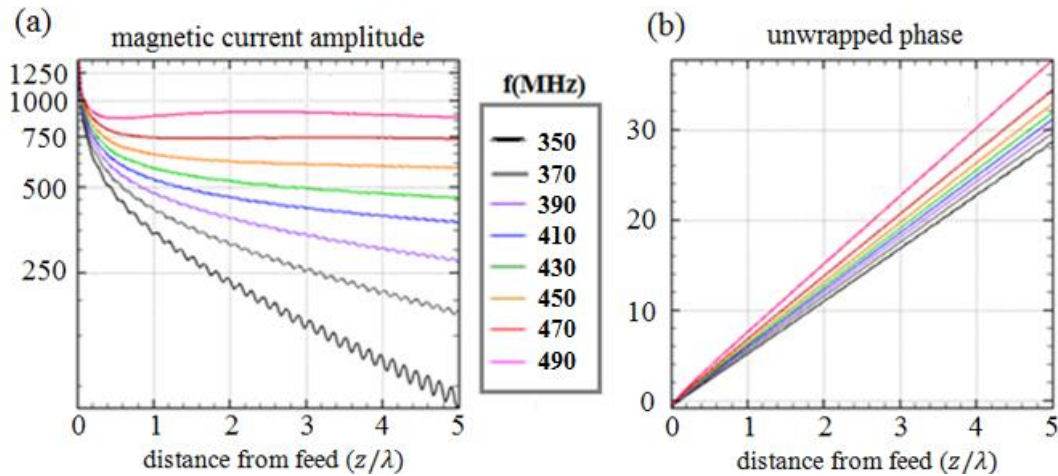


Fig. 7-9 Amplitude (a) and Phase (b) of the Current as a Function of the Distance From the Feed Multiplied by the Wavelength (z/λ) for a Magneto-Dielectric Rod with a 2 Inch Radius and a Material with $\mu = 80$ And $\epsilon = 2$. Frequencies Go from 350 MHz to 490 MHz in 20 MHz Steps.

In this sub-section we have plotted the phase and amplitude plots of the magnetic current and found out that as we approach the onset frequency the amplitude tends to get flatter and the slope of the phase reaches the value of 2π per wavelength at onset. This leads us to use the slope of the phase and amplitude plot as parameters that describe the wave velocity and attenuation respectively. As we will see in the next subsection we will name the slope of the amplitude plot versus frequency the α -plot and the slope of the phase plot versus frequency the β -plot

7.2.2 Using Savitzky-Golay filters to smooth data and obtaining α and β plots for MD rod

In this subsection, we briefly explain how the Savitzky-Golay filters work and we describe the procedure of obtaining the required slopes to plot the α -plots and β -plot. By looking at Fig.7-10, we see that it is important to decide which values of (z/λ) are

chosen for slope estimation. Starting with the magneto dielectric rod, we see in Fig.7-10 that the lower values of (z/λ) have been chosen for the estimation of the slope.

As seen in Fig.7-10 we have chosen the amplitude data that is closer to the feed. For some frequencies, we might have some deviation (similar to the 30MHz in the picture or even more deviation for different geometries) which makes finding a linear fit somewhat difficult. Therefore, we need a proper lowpass filter to smooth the data and give the closest linear fit and the slope. The lowpass filter that has been chosen is the Savitzky-Golay filters which we will briefly introduce in this subsection.

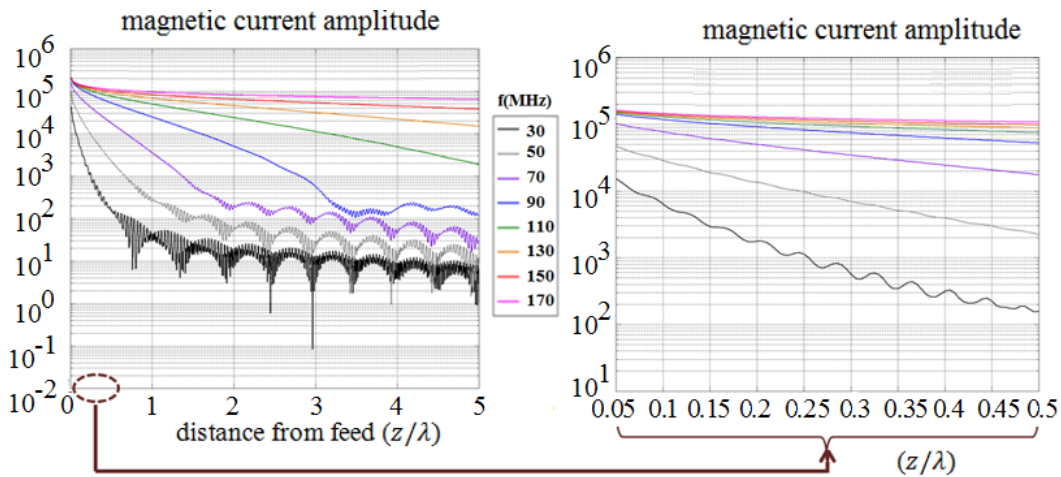


Fig. 7-10 Amplitude of the Current as a Function of the Distance from the Feed Divided by the Wavelength (z/λ) for a Magneto-Dielectric Rod with a 2 Inch Radius and a Material with $\mu = 80$ and $\epsilon = 2$.

Frequencies Go from 30 MHz to 170 MHz in 20 MHz Steps.

What is interesting about Savitzky-Golay filters is that Savitzky and Golay's paper, published in 1964, was described in 2000 by editors of the journal *Analytical Chemistry* as number five among the top ten papers ever published in that journal.

In the mentioned paper, they proposed a method of data smoothing based on local least-squares polynomial approximation. They showed that fitting a polynomial to a set

of input samples and then evaluating the resulting polynomial at a single point within the approximation interval is equivalent to discrete convolution with a fixed impulse response. They were interested in smoothing noisy data obtained from chemical spectrum analyzers, and they demonstrated that least squares smoothing reduces noise while maintaining the shape and height of waveform peaks.

The original paper showed that at each position, the smoothed output value obtained by sampling the fitted polynomial shown with the red circle is identical to a fixed linear combination of the local set of input samples shown with the blue circles. This means that the set of $2M+1$ input samples (In the example figure, we have $M=2$ so we have a set of 5 samples) within the approximation interval are effectively combined by a fixed set of weighting coefficients, shown with green x's, that can be computed once for a given polynomial order N and approximation interval of length $2M+1$.

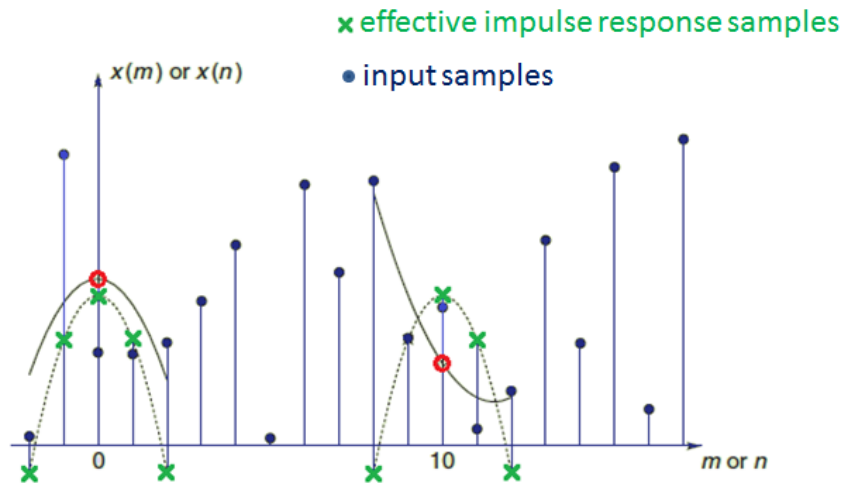


Fig. 7-11 Demonstration of Least-Squares Smoothing by Locally Fitting a Second-Degree Polynomial (Solid Line) to Five Input Samples. Blue Dots Show the Input Samples, Red Circles Show the Smoothed Output Sample, and Green X's Show the Effective Impulse Response Samples (Weighting Constants).

To clarify this smoothing technique, as seen in Fig.7-11, a set of $(2M+1+5)$ points and a polynomial of the order $N=2$ have been chosen as the best fit to the 5 points (the polynomial is shown with the black line). The value of the polynomial at the center point (shown as zero) is the smoothed value. Then the 5 points are shifted to the right and the next smoothed value will be obtained. What Savitzky and Golay proved is that there is no need to do this since a discrete convolution with a fixed impulse response can give you the same results which is much more efficient. This means that the output samples can be computed by a discrete convolution of the form

$$y[n] = \sum_{m=-M}^M h[m]x[n-m] = \sum_{m=-M}^M h[m]x[n-m] \quad (7-1)$$

Tables of convolution coefficients, calculated for m up to 25, were published for the Savitzky–Golay smoothing filter in 1964 but it is not necessary use the Savitzky–Golay tables since the values can be obtained in closed form.

As seen below we will find the slope of the amplitude plot of the magneto dielectric rod with a 2” radius in the following steps:

Step1) We choose small values of (z/λ) from the amplitude plot

Step2) We use the Savitzky–Golay lowpass filtering technique on the data

Step3) A least square method gives the approximate slope of the lowpassed data

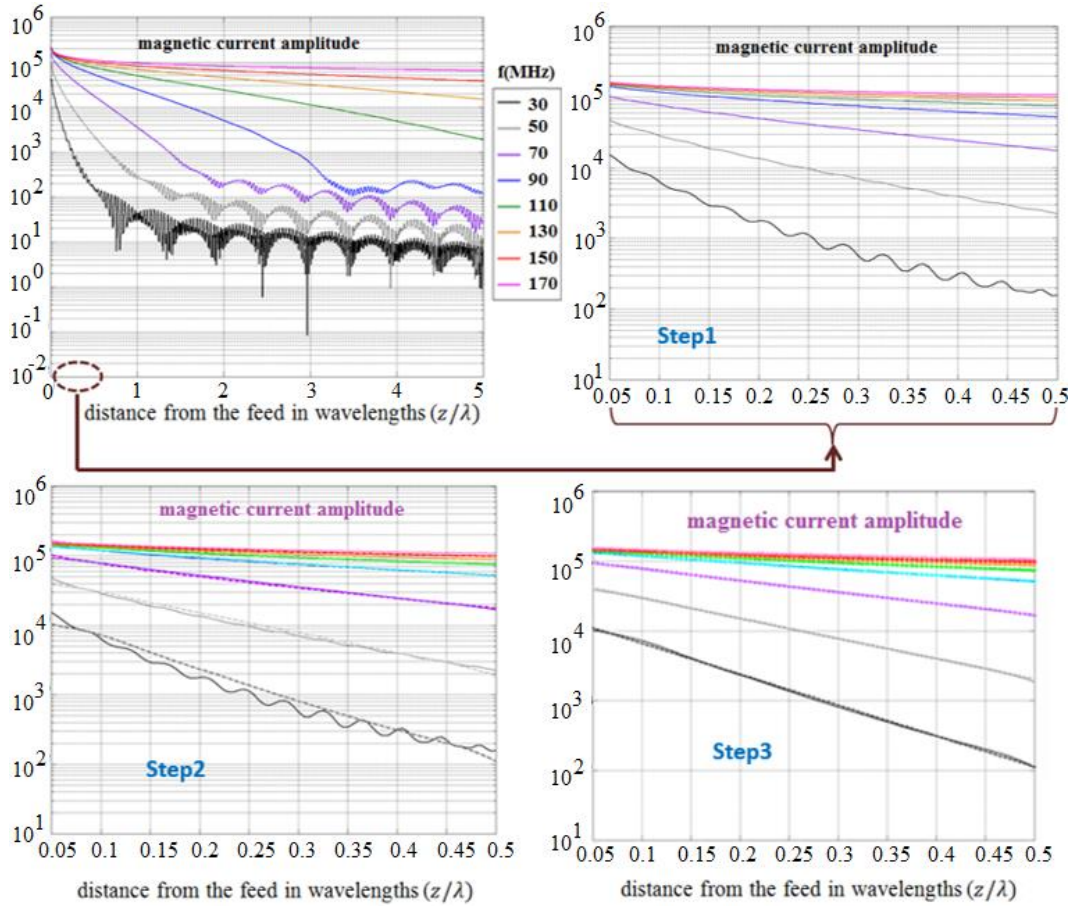


Fig. 7-12 Showing the Steps of Obtaining the Slope of the Amplitude of a 2" Magneto Dielectric Rod.

At this point we have the slopes of the amplitude plot at different frequencies so we can plot them as a function of frequency and obtain the α -plot as seen in the figure below.

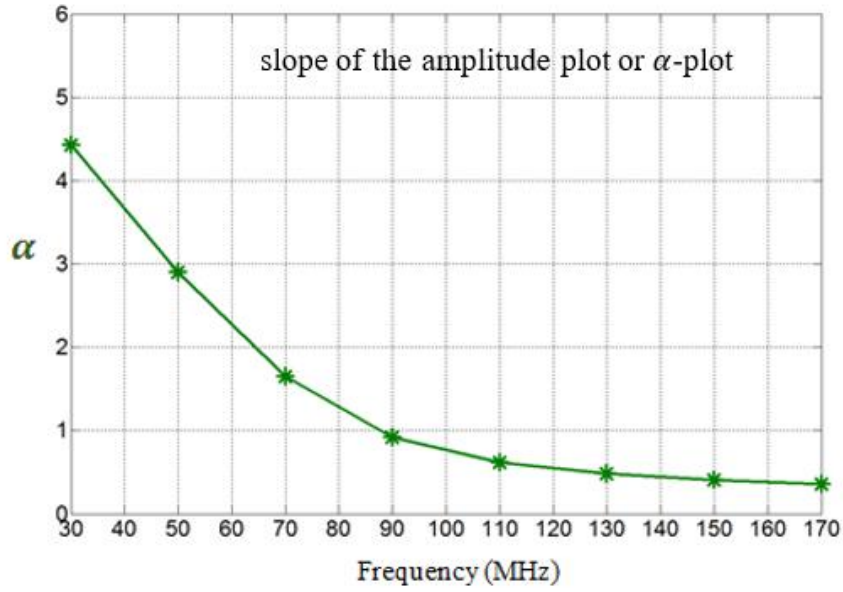


Fig. 7-13 Slope of the Current Amplitude of a 2" Magneto Dielectric Rod or the α -Plot in Nepers Per Wavelength.

The next step is doing the same for the phase plot of the rod. We use the same three steps to obtain the slope of the phase plot versus frequency (β -plot).

Step1) We choose small values of (z/λ) from the phase plot

Step2) We use the Savitzky–Golay lowpass filtering technique on the data

Step3) A least square method can give the approximate slope of the lowpassed data

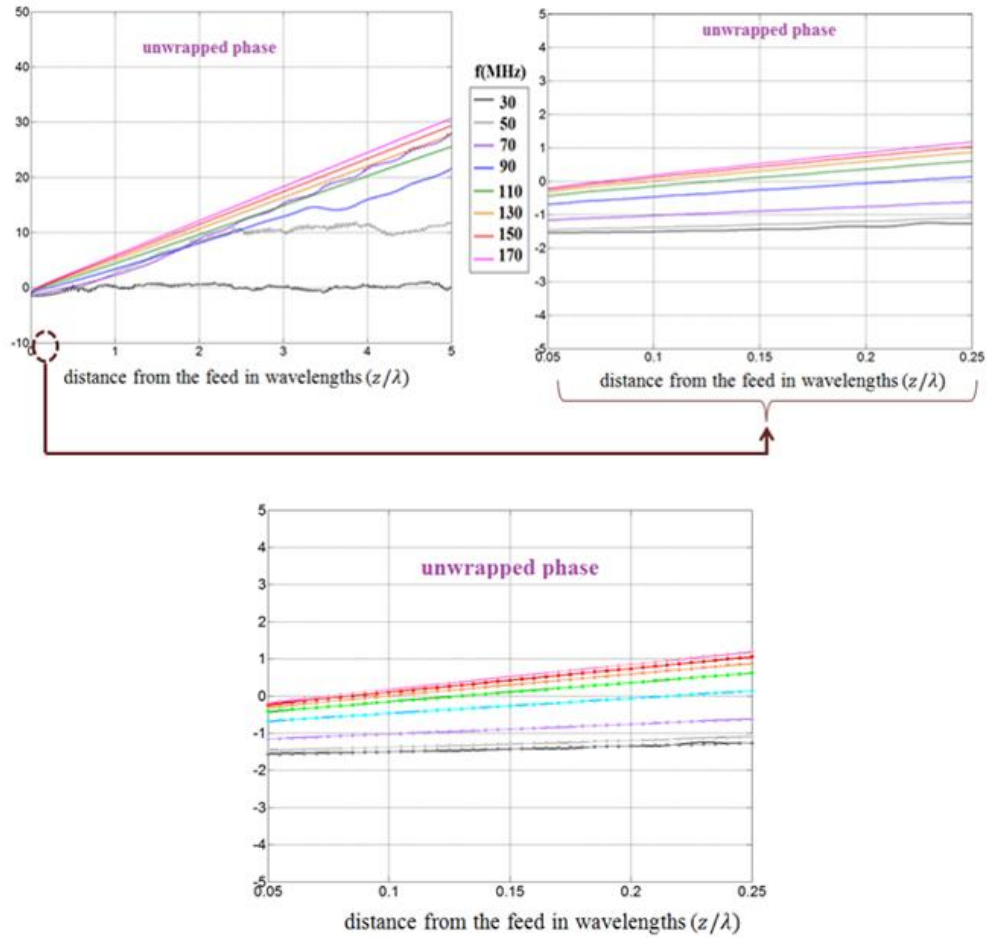


Fig. 7-14 Showing the Steps of Obtaining the Slope of the Phase of a 2" Magneto Dielectric Rod

At this point we have the slopes of the phase plot at different frequencies so we can plot them as a function of frequency and obtain the β -plot as seen in the figure below.

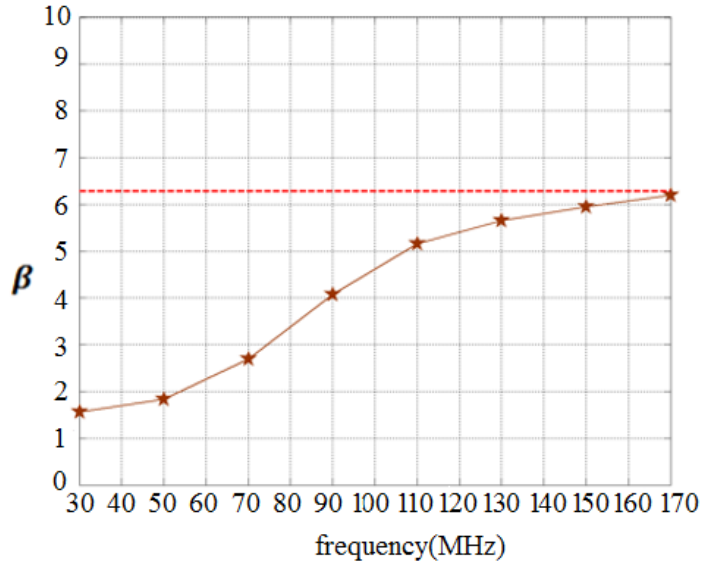


Fig. 7-15 Slope of the Current Phase of a 2" Magneto Dielectric Rod or the β -Plot in Radians Per Wavelength

Here we see that the β -plot gets close to the light line at 170 MHz which means that in the case of the rod with a 2" inch radius we don't pass the lightline at 170 MHz. Another example is a rod with a 1.6" radius the phase and amplitude plots of the magnetic current can be seen below and we can see a comparison between the two rods. We can see that the rod with more material (more volume) approaches the lightline at lower frequencies than the rod with less material.

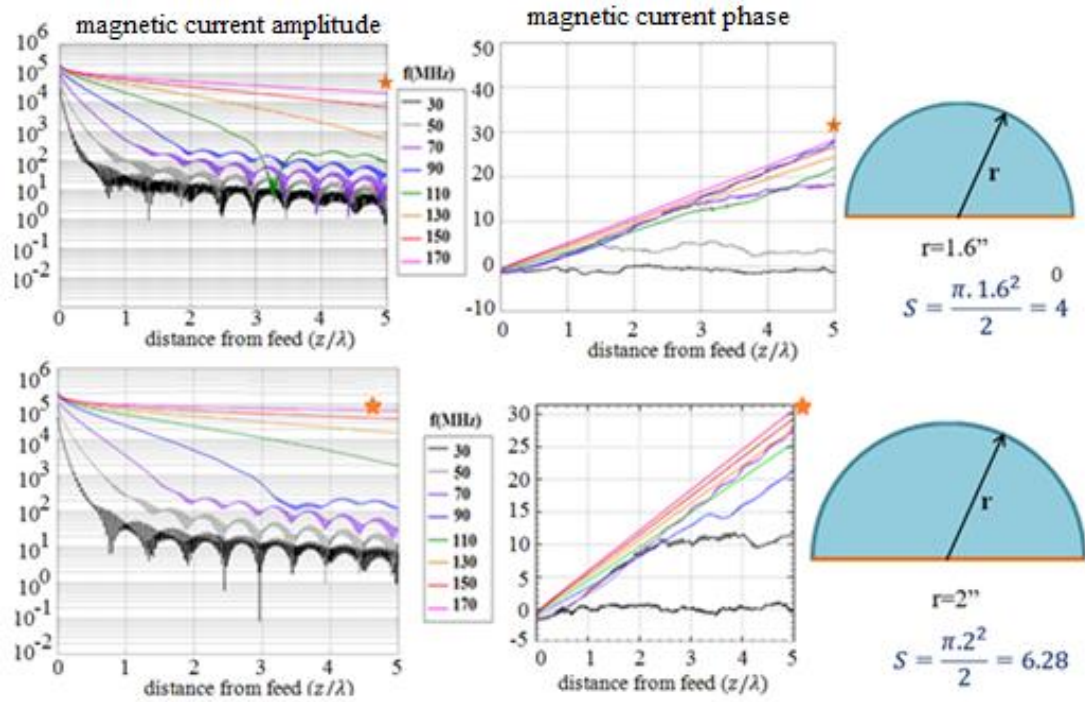


Fig. 7-16 Current Phase and Amplitude Plots of Rod with Different Radii

For the next step, we will go to frequencies higher than 170 MHz for the 1.6'' rod so that the rod passes the lightline. The phase and amplitude plots can be seen below. Somewhere between the pink line (210 MHz) and the brown line (230MHz) we are passing the light line

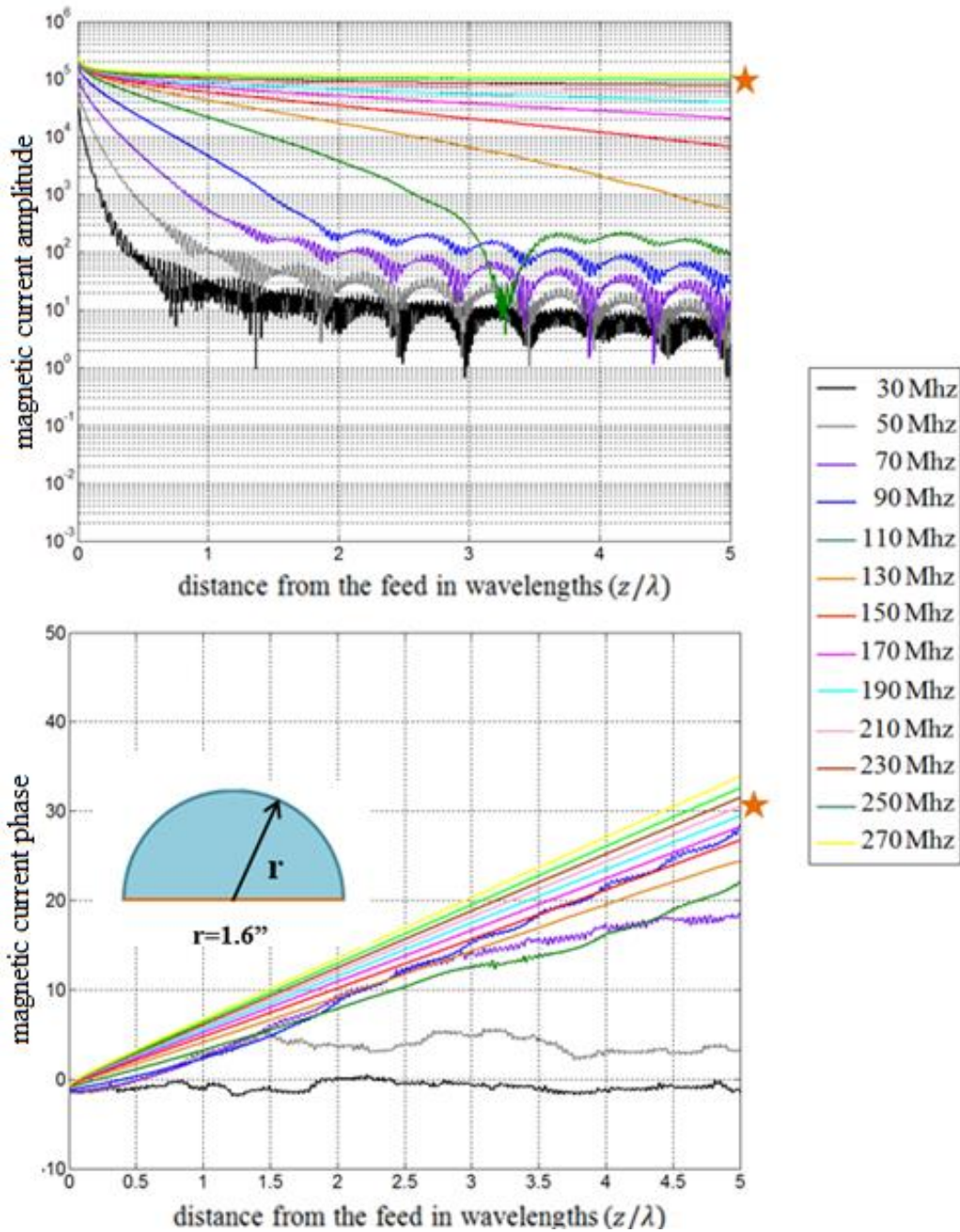


Fig. 7-17 Current Phase and Amplitude Plots of the 1.6" Rod at Higher Frequencies and Passing the Light-Line

Similar to what we did before we will plot the α -plot and β -plot for the rod and see the passing of the light line.

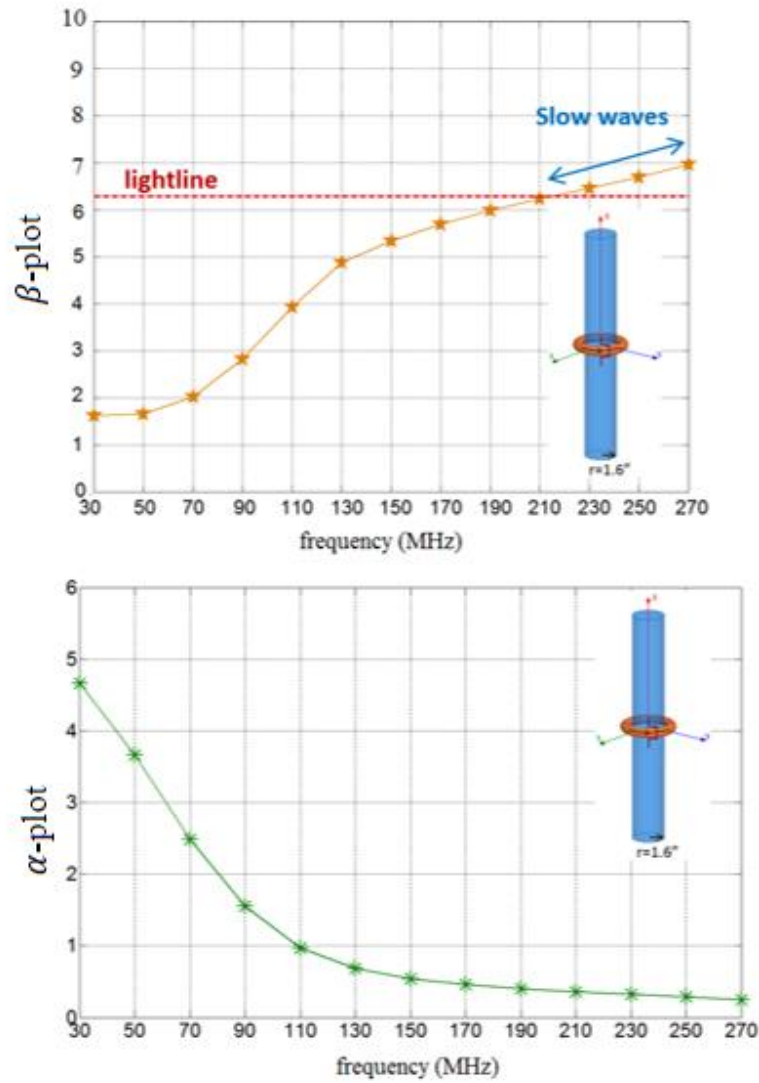


Fig. 7-18 Current Phase and Amplitude Plots of the 1.6" Rod at Higher Frequencies and Passing the Light-Line

In the phase plot, higher slopes mean lower wave speed (slow waves) and when the curve passes 2π we have passed the lightline. Another useful figure is to plot

$2\pi/(\text{slope of phase curves})$ to show the velocity of the wave compared to light. This plot can be seen below.

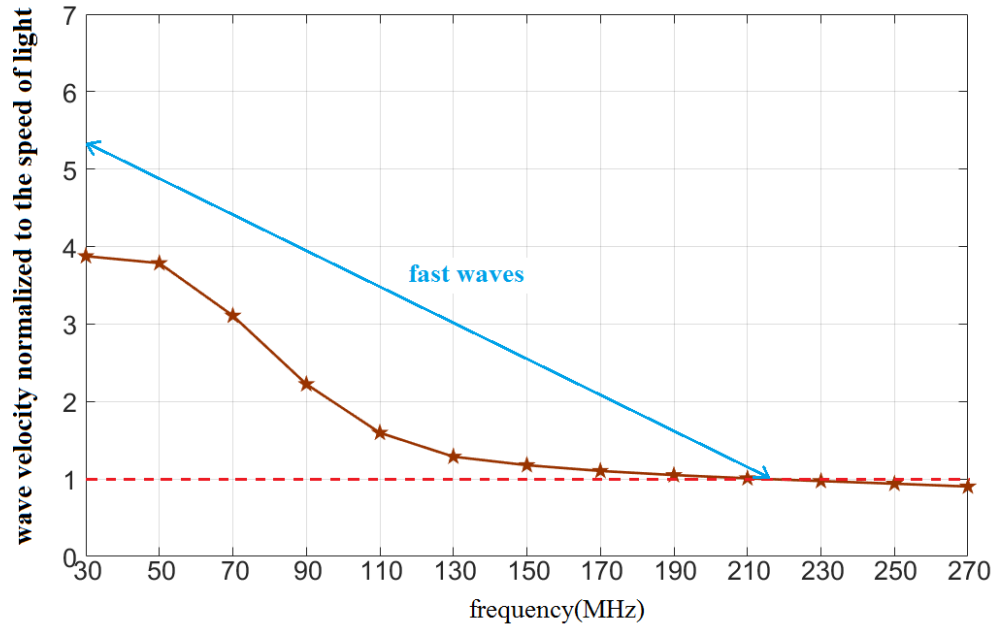


Fig. 7-19 Phase Velocity Plot for the 1.6'' Rod at Higher Frequencies and Passing the Light-Line

7.2.3 Radiated power of the antenna obtained from the Poynting vector

In this section, we will obtain the radiated power of the antenna from the Poynting vector. By plotting the radiated power, we can have a measure of the bandwidth and a new way of studying the antenna behavior.

From the theory of antennas, we know that the Integration of the complex Poynting vector over a surface enclosing the antenna results in a complex number with the real part being identified as the radiated power. In this section we will obtain the Poynting vector and radiated power of the magneto dielectric rod.

The figure below shows the infinite magneto dielectric rod. The first step to finding the pointing vector and the radiated power is to write the fields of this antenna for the outside medium.

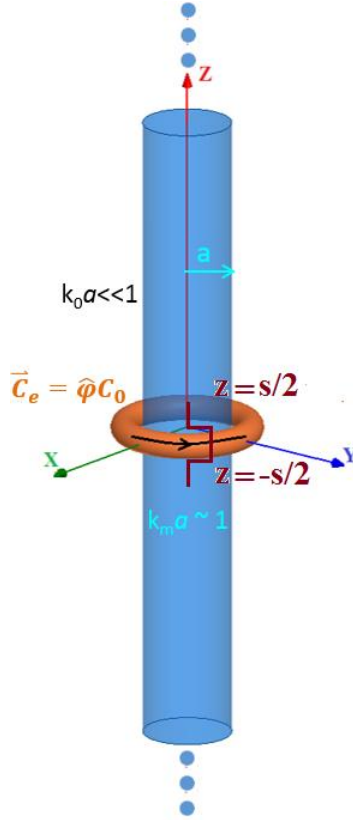


Fig. 7-20 Infinite Magneto Dielectric Rod

The fields in the outside medium of the magneto dielectric rod are as follows:

$$\begin{aligned}
 E_{\varphi} &= \frac{-j\omega I \mu_0 a}{2\pi} \int_{-\infty}^{\infty} \frac{\mu_r J_1(k_{\rho 1} a) H_1^{(2)}(k_{\rho 0} \rho) e^{-jk_z z} dk_z}{\mu_r (k_{\rho 0} \rho) J_1(k_{\rho 1} a) H_0^{(2)}(k_{\rho 0} \rho) - (k_{\rho 1} a) J_0(k_{\rho 1} a) H_1^{(2)}(k_{\rho 0} \rho)} \\
 H_{\varphi z} &= \frac{I a}{2\pi} \int_{-\infty}^{\infty} \frac{\mu_r k_{\rho 0} J_1(k_{\rho 1} a) H_0^{(2)}(k_{\rho 0} \rho) e^{-jk_z z} dk_z}{\mu_r (k_{\rho 0} \rho) J_1(k_{\rho 1} a) H_0^{(2)}(k_{\rho 0} \rho) - (k_{\rho 1} a) J_0(k_{\rho 1} a) H_1^{(2)}(k_{\rho 0} \rho)}
 \end{aligned} \tag{7-2}$$

$$H_\phi = \frac{Ia}{2\pi} \int_{-\infty}^{\infty} \frac{\mu_r k_z J_1(k_{\rho 1} a) H_0^{(2)}(k_{\rho 0} \rho) e^{-jk_z z} dk_z}{\mu_r (k_{\rho 0} \rho) J_1(k_{\rho 1} a) H_0^{(2)}(k_{\rho 0} \rho) - (k_{\rho 1} a) J_0(k_{\rho 1} a) H_1^{(2)}(k_{\rho 0} \rho)}$$

The Poynting vector is defined as:

$$P = \frac{\vec{E} \times \vec{H}^*}{2} = \frac{E_\phi \hat{a}_\phi \times H_z^* \hat{a}_z}{2} \quad (7-3)$$

As expected the Poynting vector is a radial vector and in order to obtain the radiated power we should integrate the pointing vector over a cylindrical surface enclosing the antenna.

$$\text{radiated power} = \int_{\phi=0}^{\phi=2\pi} \int_{z=-\infty}^{z=\infty} P_\rho \hat{a}_\rho \cdot \rho d\phi dz \hat{a}_\rho \quad (7-4)$$

The resulting radiated power for a rod with $\mu = 80$ and a 2" radius is shown below. In the figure we have also shown a 0.5 dB bandwidth edge which is where the radiated power drops to 90% and the relative 0.5dB bandwidth is also shown for all modes. Obviously there can be different bandwidths defined, like a 3dB bandwidth, but this was our choice for demonstration. The bandwidth values showed are relative bandwidths which are defined as follows:

$$BW = \frac{f_c - f_{0.5dB}}{f_c} \quad (7-5)$$

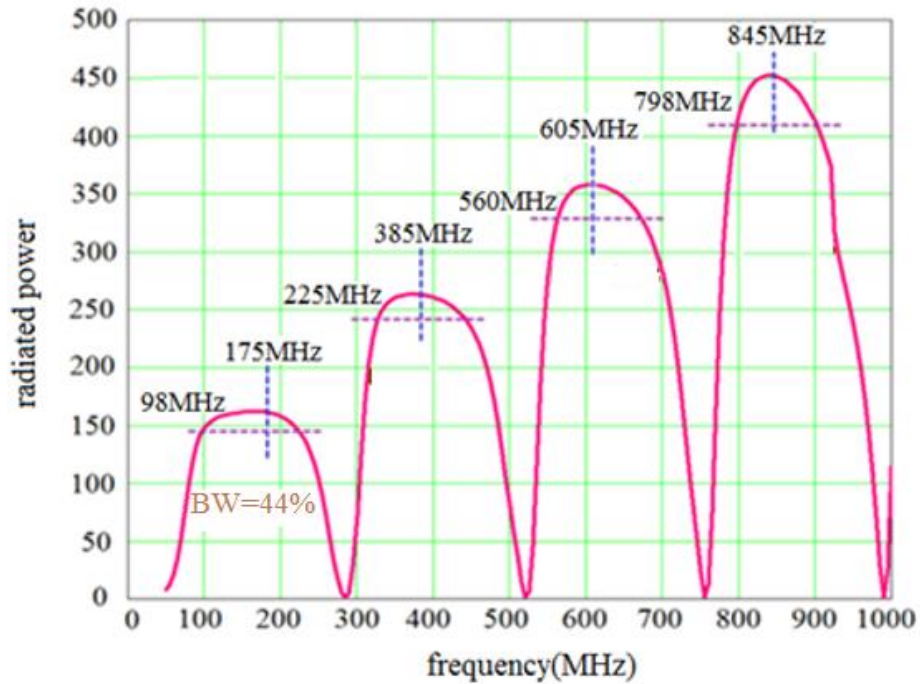


Fig. 7-21 Radiated Power of a Magneto Dielectric Rod with $r=2''$ and $\mu = 80$ with the 0.5db Bandwidth Edges and Relative Bandwidths Shown in the Figure

A reasonable sanity check would be to compare the frequency of the peak of the radiated power to the cutoff frequency of each mode. We expect the peak to happen near the onset. As we had seen before the onset can be obtained from the phase plot of the magnetic current and it approximately happens when the phase plot crosses 10π at $z/\lambda = 5$ which is equivalent to the phase plot having a slope of 2π . Figures below show the onset frequency of different modes of the rod with $\mu = 80$ and a 2'' radius and it also shows that the location of the peak of the radiated power happens close to the onset frequency for all modes.

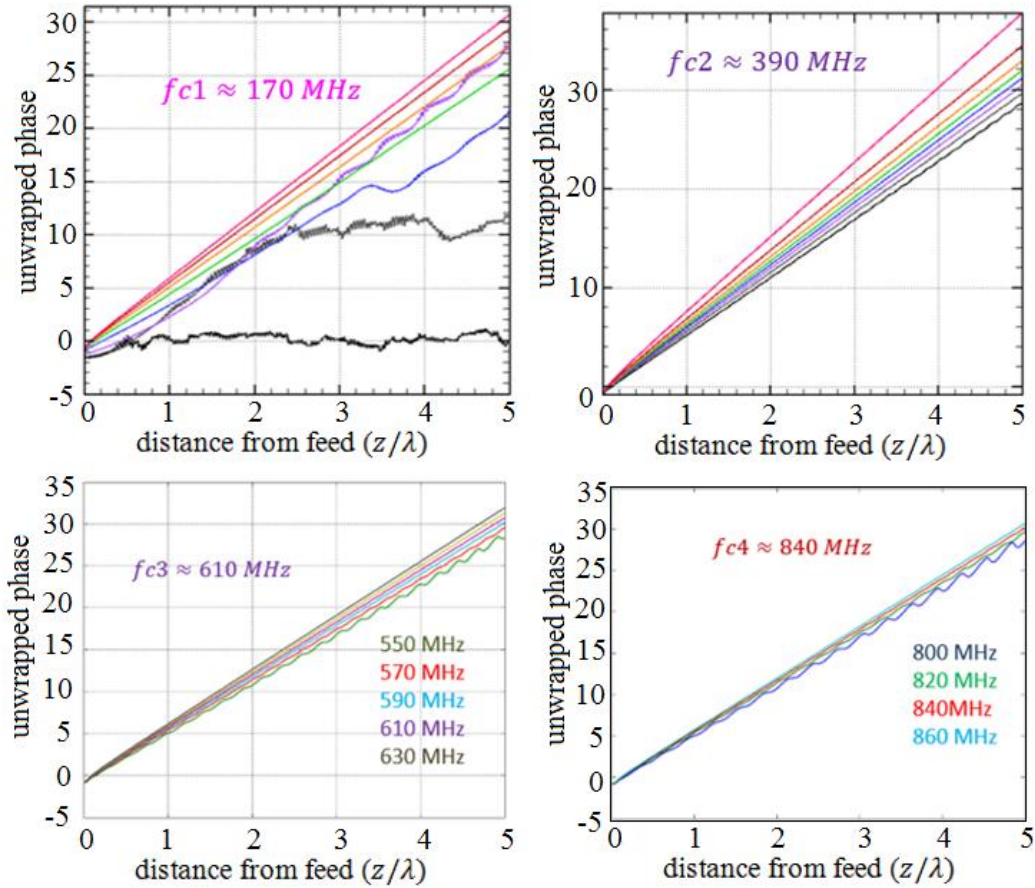


Fig. 7-22 Phase Plots of a Magneto Dielectric Rod With $r=2''$ and $\mu = 80$ Showing the Onset Frequency of Each Mode.

The next step is finding the radiated power for rods with different radii and comparing the bandwidth of different rods using the radiated power. The same fields have been derived and the same calculation has been carried out for a rod with $r=1.6''$ and $\mu = 80$. The following figures show the radiated power for the $r=1.6''$ and $\mu = 80$ magneto dielectric rod and the 0.5dB bandwidth edges and the peak of the radiated power have been shown for each mode.

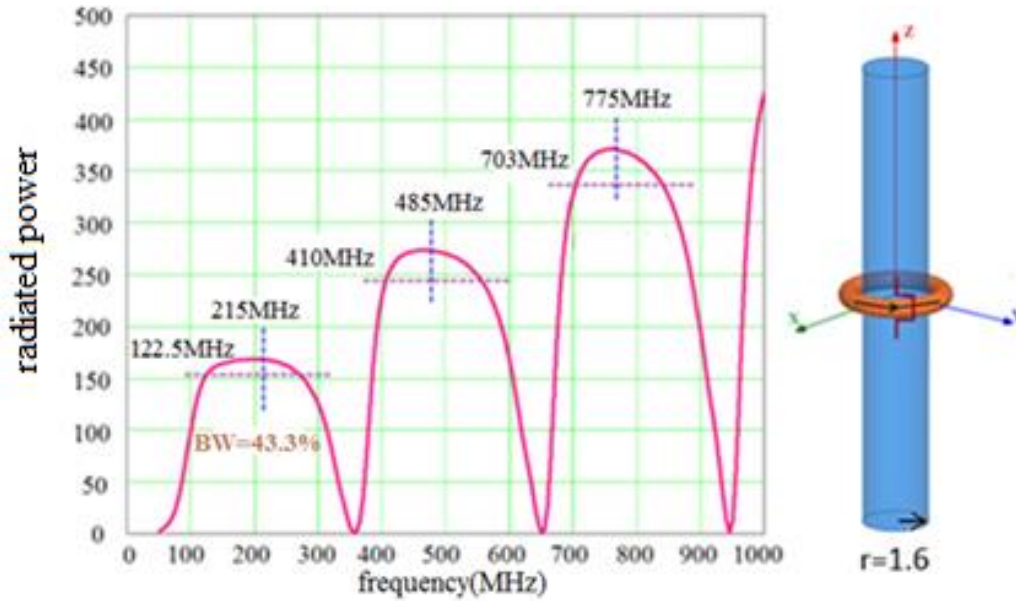


Fig. 7-23 Radiated Power of a Magneto Dielectric Rod with $r=1.6''$ and $\mu = 80$ with the 0.5db Bandwidth Edges and Relative Bandwidths Shown in the Figure

Again, we have shown the phase plots for the different modes to compare the frequency of the radiated power peak to the onset frequency. It can be seen that similar to the $r=2''$ rod, the peak approximately happens at the onset frequency.

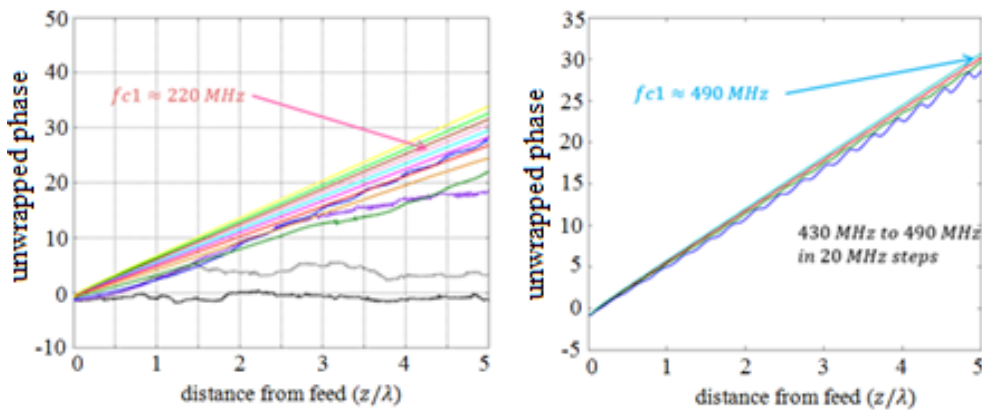


Fig. 7-24 Phase Plots of Magneto Dielectric Rod with $r=1.6''$ and $\mu = 80$ Showing the Onset Frequency of Each Mode

A comparison between the two rods shows that the rod with a larger cross section has almost the same relative bandwidth as the one with smaller cross section which is as expected.

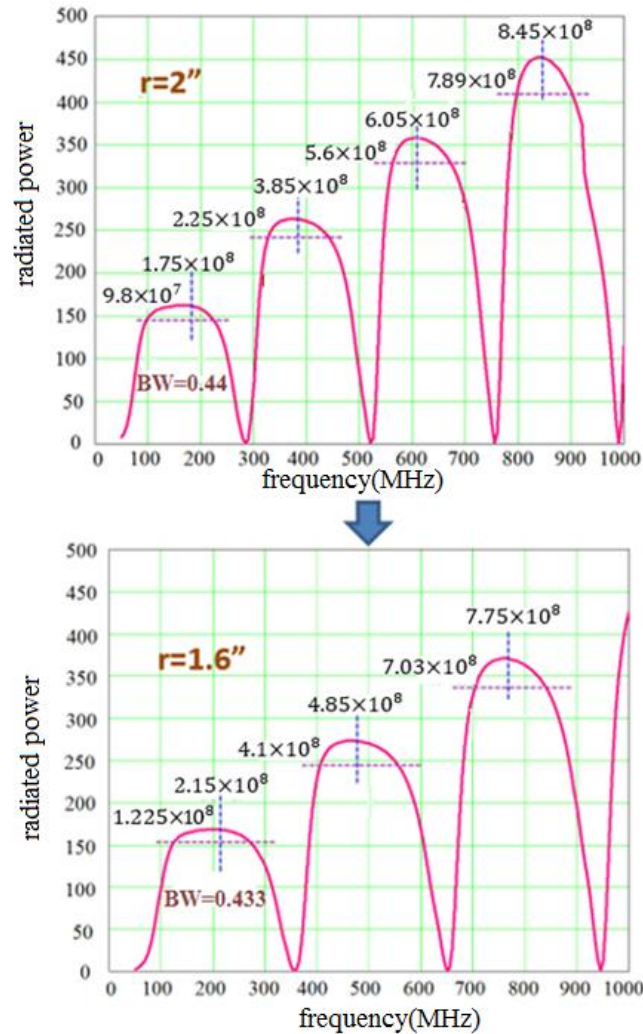


Fig. 7-25 Comparing the Rod with the Larger Cross Section to the Rod with Smaller Cross Section Shows That, as Expected, They Have Almost the Same Bandwidth

Even though the simulations show that the bandwidth of the magnetodielectric rod cannot be designed by changing the radius and the permeability and that the

fractional bandwidth about onset is the same for all rods carrying the TE₀₁ mode, to completely understand this phenomenon and the reason this happens we will provide a proof. We will prove that the permeability and radius can only determine where the onset occurs and the band edges will also change accordingly so that the bandwidth of the trough about onset is constant and not dependent on the radius of the rod or the permeability. This is a problem with the rod which we will later show that our new proposed structures don't have.

To start with the proof we will note that since the rod is an infinite magneto dielectric rod, the bandwidth can be written in terms of radius and material properties as follows:

$$BW \propto (ka)^2 \quad (7-6)$$

We should note that since the magnetodielectric rod is infinite in the z direction the bandwidth has been written in terms of $(ka)^2$ instead of $(ka)^3$ which is what we are familiar with from the Fano-Chu limit. At this point we need to find the dependence of the wavenumber on the radius to see how the bandwidth changes. We can write:

$$\left[\begin{array}{l} k \propto f\sqrt{\mu} \\ f_c \propto \frac{1}{\rho\sqrt{\mu}} \end{array} \right] \rightarrow k \propto 1/\rho \rightarrow BW = const \quad (7-7)$$

Going even further we can show that the quality factor which is the inverse of bandwidth and is the stored energy divided by the radiated energy is also constant.

$$\text{stored energy} = \mu H^2 \times \text{vol} \quad (7-8)$$

$$\frac{\text{stored energy}(1)}{\text{stored energy}(2)} = \frac{[\mu H^2 \times \text{vol}](1)}{[\mu H^2 \times \text{vol}](2)} \quad (7-9)$$

$$\left[\begin{array}{l} \text{vol} \propto \rho^2 \\ \text{Ampere's law: } H \propto 1/\rho \end{array} \right. \longrightarrow \text{stored energy} \propto \mu \quad (7-10)$$

$$\frac{\text{stored energy}(1)}{\text{stored energy}(2)} = \frac{\mu(1)}{\mu(2)} \quad (7-11)$$

Now we will see how the radiated energy changes

$$\begin{array}{l} \text{Im} \propto \mu H \times \text{Area} \times f \\ \frac{\text{rad energy}(1)}{\text{rad energy}(2)} = \frac{\mu(1)}{\mu(2)} \end{array} \quad \frac{\text{Im}(1)}{\text{Im}(2)} \propto \sqrt{\frac{\mu(1)}{\mu(2)}} \quad (7-12)$$

$$Q = \frac{\text{stored energy}}{\text{radiated energy}} = \text{const} \Rightarrow \text{BW} = \text{const} \quad (7-13)$$

This means that the bandwidth of the rod close to onset is not a design parameter that can be tuned with changing the parameters of the rod and even though the permeability and radius can change the onset frequency, the band edges will change so that the bandwidth around onset will stay constant.

7.2.4 Finding the location of bandwidth edge of the rod on α and β plots

In the previous section, we had plotted the radiated power obtained from the integration of the Poynting vector and showed the 0.5dB bandwidth edges. Here we want to see the location of the 0.5 dB bandwidth edge on the α and β plots. The

figure below shows the radiated power and the position of the 0.5dB (or 90% radiated power) bandwidth edge on both the α and β plots. This means that the antenna will radiate 90% of its maximum power at 98MHz which translates to $\alpha = 0.8$ and $\beta = 0.3$. If we see that the 0.5dB power for rods with different radii happens at the approximate same β value we can conclude that we can use the inverse slope of the β plot as a measure of bandwidth. We should note that both beta and alpha are normalized to the wavelength.

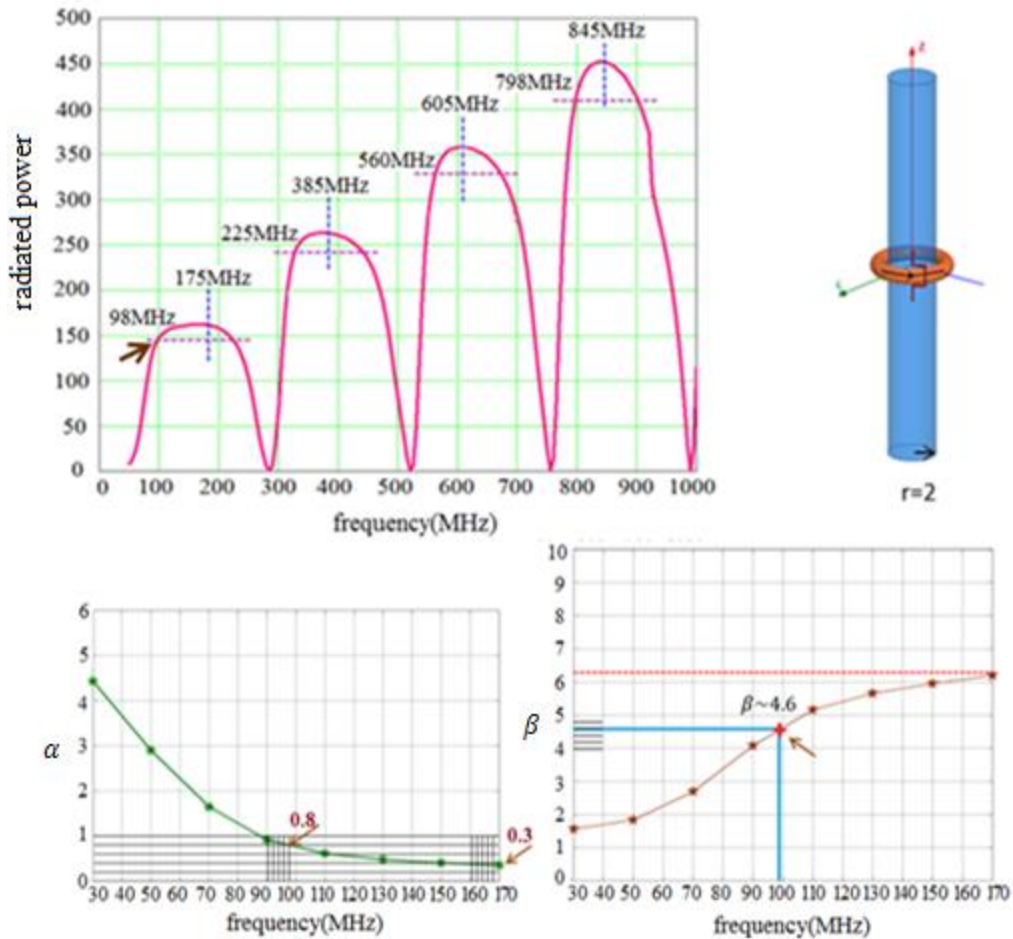


Fig. 7-26 Radiated Power of a Magneto Dielectric Rod with $r=2''$ and $\mu = 80$ and the Location of the 0.5db Bandwidth Edge on the α and β Plots

The wave velocity and the 0.5 dB point can be seen below rod with $r=2''$ and $\mu = 80$. Similar to the beta and alpha plot, it should be mentioned that the wave velocity is normalized to the velocity of light.

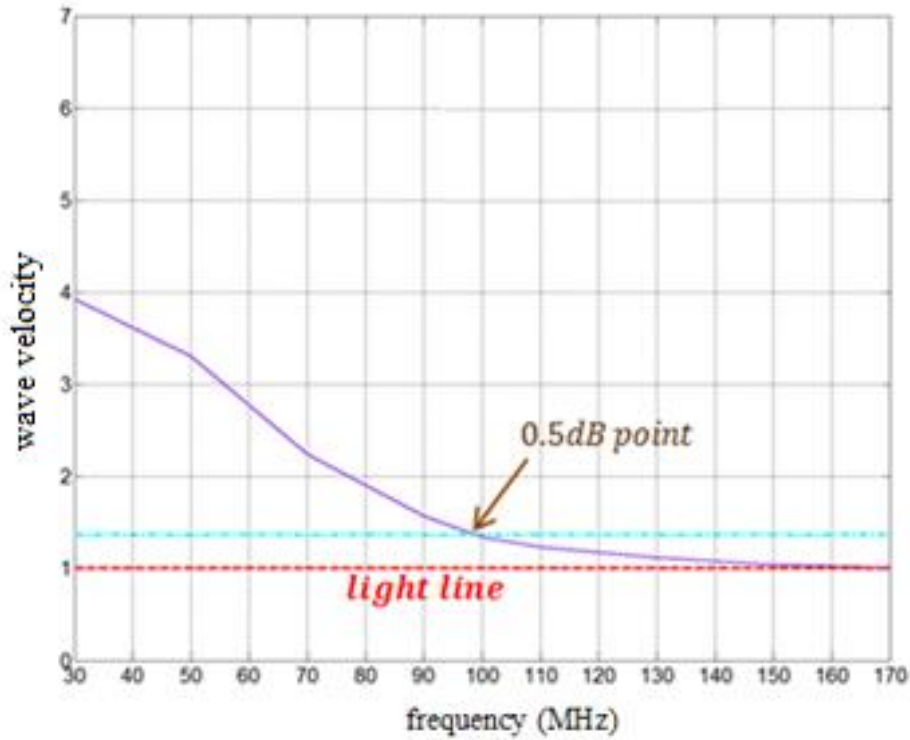


Fig. 7-27 Location of the 0.5dB Bandwidth Edge on the Wave Velocity Plot

In order to see if this happens for different rod radii, we will repeat the same for a rod with radius of 1.6'' and the permeability of $\mu = 80$. The figure below shows the radiated power and the position of the 0.5dB (or 90% radiated power) bandwidth edge on both the α and β plots for a $r=1.6''$ rod.

Again we can see that the value of α and β and the wave velocity at the bandwidth edge is similar to their value for the rod with $r=2''$ and $\mu = 80$

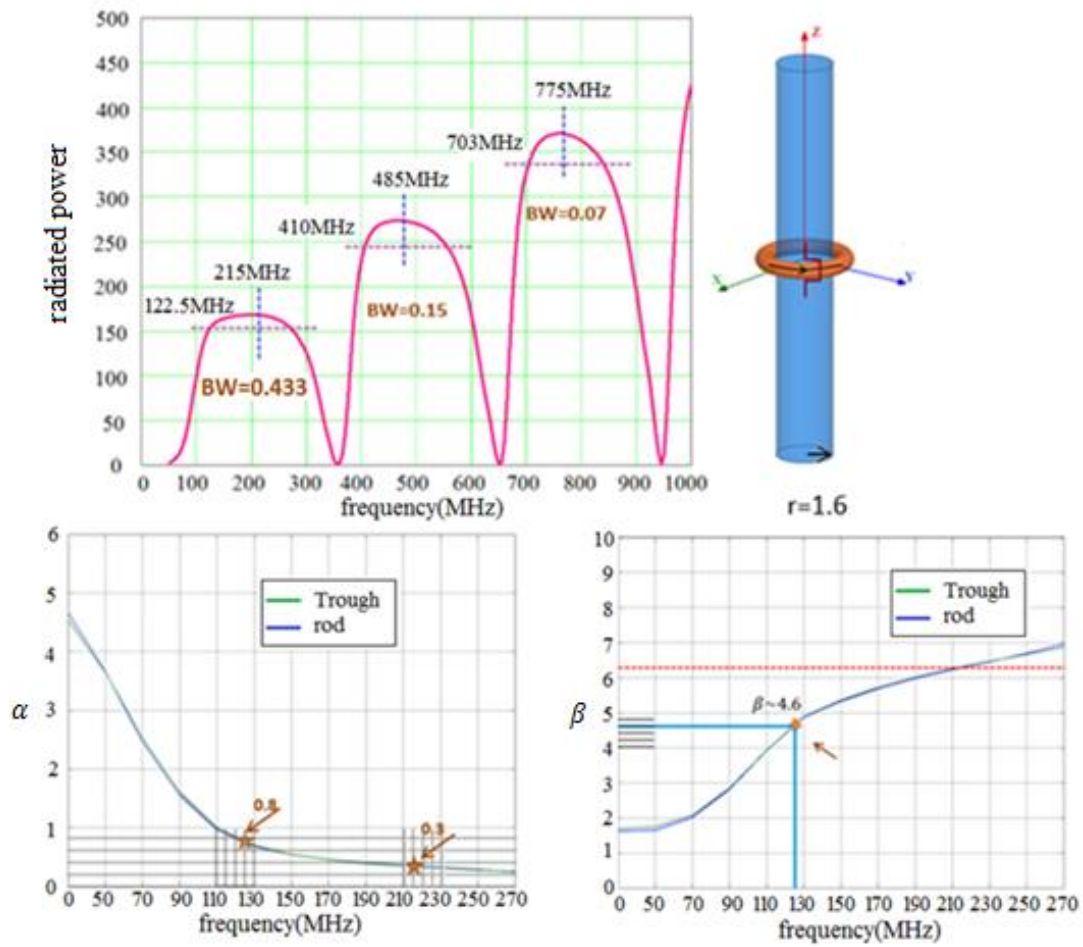


Fig. 7-28 Radiated Power of a Magneto Dielectric Rod with $r=1.6''$ and $\mu = 80$ and the Location of the 0.5db Bandwidth Edge on the α and β Plots

The wave velocity and the 0.5 dB point can be seen below rod with $r=1.6''$ and $\mu = 80$.

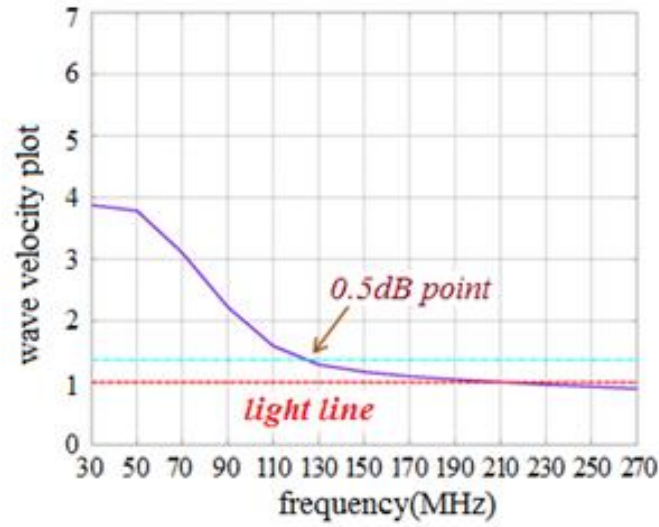


Fig. 7-29 Location of the 0.5dB Bandwidth Edge on the Wave Velocity Plot

As the last example for this case we will plot the radiated power and the position of the 0.5dB (or 90% radiated power) bandwidth edge on the β plot for a $r=2.4''$ rod which shows that the 0.5dB bandwidth edge happens at the same value of β for different rod radii.

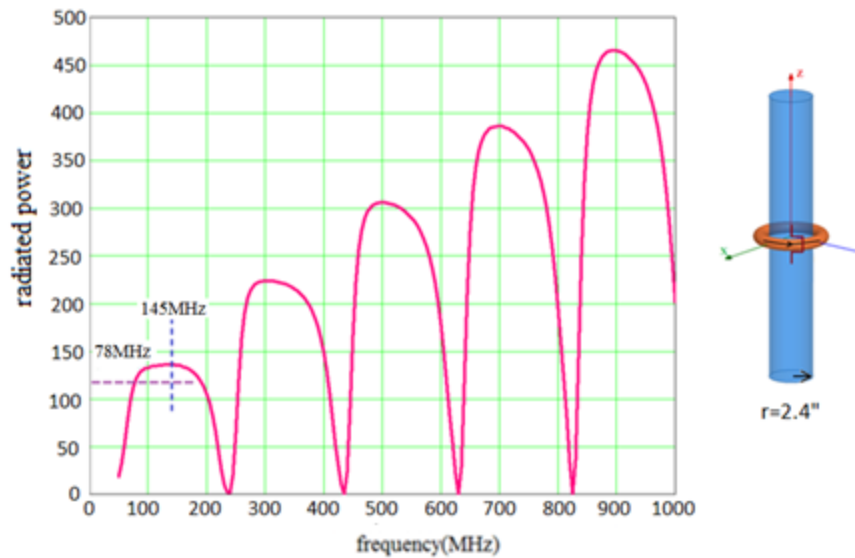


Fig. 7-30 Radiated Power of a Magneto Dielectric Rod with $r=2.4''$ and $\mu = 80$

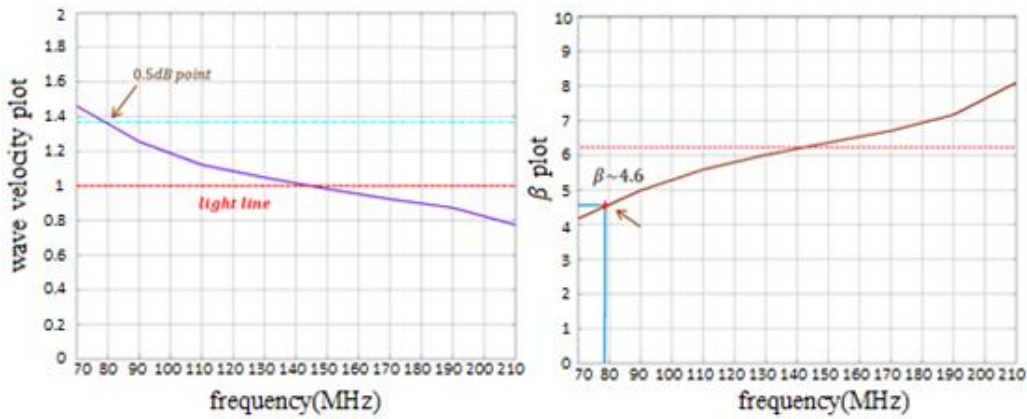


Fig. 7-31 Location of the 0.5dB Bandwidth Edge on the Wave Velocity Plot and the β Plot

Here we can conclude that since the lower 90% band edges happen at 1.36 for all different examples, the slope of the velocity plot can also be used as a measure of bandwidth in addition to the radiation plots.

7.2.5 Obtaining the total power dissipated in the antenna using the induced EMF method

In the previous sections we have found the radiated power of the antenna by integrating the complex Poynting vector over a surface enclosing the antenna which resulted in a complex number with the real part being identified as the radiated power. In this section, we will describe a different way of obtaining the power of the antenna which is called the induced EMF method.

In this method, in order to obtain the antenna power, we will first calculate the voltage around the loop which is as follows:

$$V = \int E \cdot dl = 2\pi a E_{\phi} \quad (7-14)$$

We already know that E_φ of the magneto dielectric loop can be written as follows:

$$E_\varphi = \frac{-j\omega I \mu_0 a}{2\pi} \int_{-\infty}^{\infty} \frac{\mu_r J_1(k_{\rho 1} a) H_1^{(2)}(k_{\rho 0} \rho) e^{-jk_z z} dk_z}{\mu_r (k_{\rho 0} \rho) J_1(k_{\rho 1} a) H_0^{(2)}(k_{\rho 0} \rho) - (k_{\rho 1} a) J_0(k_{\rho 1} a) H_1^{(2)}(k_{\rho 0} \rho)} \quad (7-15)$$

All this is similar to the reaction integral which is $\int J \cdot E dv$ which is the same as $\int K \cdot E ds$ for a current band that is carrying a current K and for our antenna this current band has a width of w and a radius of ρ and the reaction integral gives the power which is the voltage times the current with the voltage being defined as seen in the previous equations. If we calculate the reaction integral in space, then the current band is a step function therefore the current can come out of the integral and we are only dealing with calculating the voltage.

It is obvious that the real part of this voltage times the current will yield the total power of the antenna. However, we have to take note that the power obtained from the EMF method contains both the radiated power and the lost power.

As the next step, we will show that in the case of the perfect PMC rod, the power obtained from the EMF method and the radiated power obtained from the Poynting vector method give the same results. The Poynting vector method and the induced EMF method are obtained from the fields of the PMD rod which are as follows (The details of obtaining the fields can be found in previous sections and will not be repeated here)

$$E_{\varphi PMC} = -j \frac{\omega \mu_0 a}{(k_{\rho 0} a)} \frac{H_1^{(2)}(k_{\rho 0} \rho)}{H_0^{(2)}(k_{\rho 0} a)} K_{e\varphi} \exp(-jk_z z) \quad (7-16a)$$

$$H_{zPMC} = \frac{H_0^{(2)}(k_{\rho 0} \rho)}{H_0^{(2)}(k_{\rho 0} a)} K_{e\varphi} \exp(-jk_z z) \quad (7-16b)$$

$$H_{\rho PMC} = j \left(\frac{k_z a}{k_{\rho 0} a} \right) \frac{H_1^{(2)}(k_{\rho 0} \rho)}{H_0^{(2)}(k_{\rho 0} a)} K_{e\varphi} \exp(-jk_z z) \quad (7-16c)$$

As a sanity check we expect the total radiated power obtained from the EMF method to agree with the radiated power obtained from the Poynting vector method for a PMC rod. The figures below show the results obtained from both methods for different rod radii and we see that they give the exact same results.

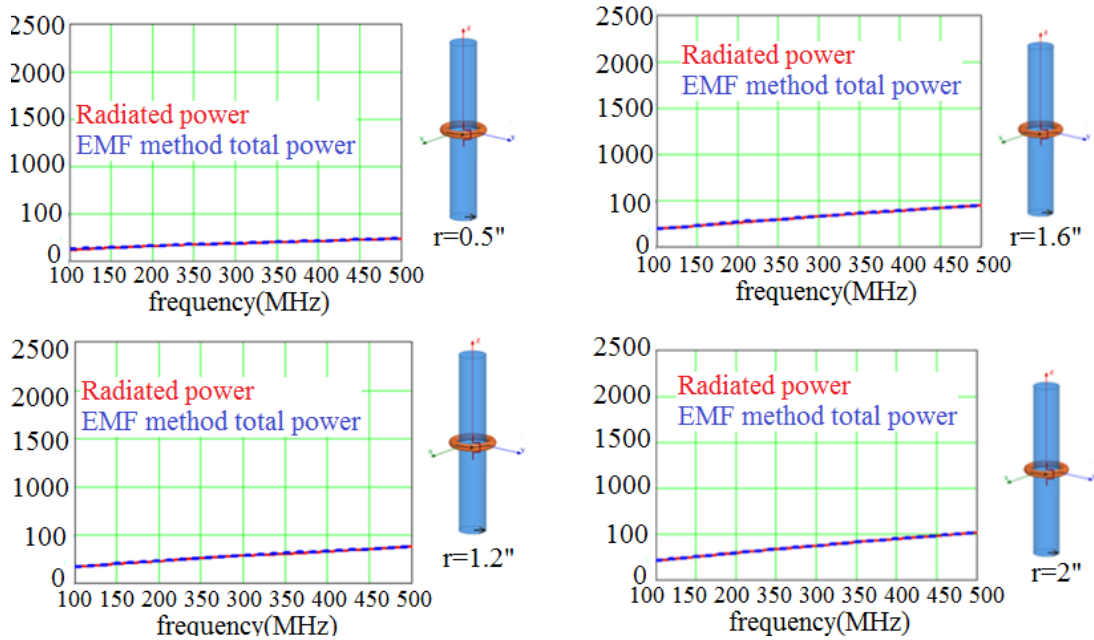


Fig. 7-32 Radiated Power and Total Power of a PMC Rod with Different Radii

The total power of the magneto dielectric rod antenna rod with $r=1.6''$ and $\mu = 80$ has been obtained. This total power is the radiated power and the loss and this is the reason that in the case of the perfect magnetic conductor rod these two plots overlap.

The difference between the power obtained from the EMF method and the radiated power will also be important because it is the power that is lost into the surface waves.

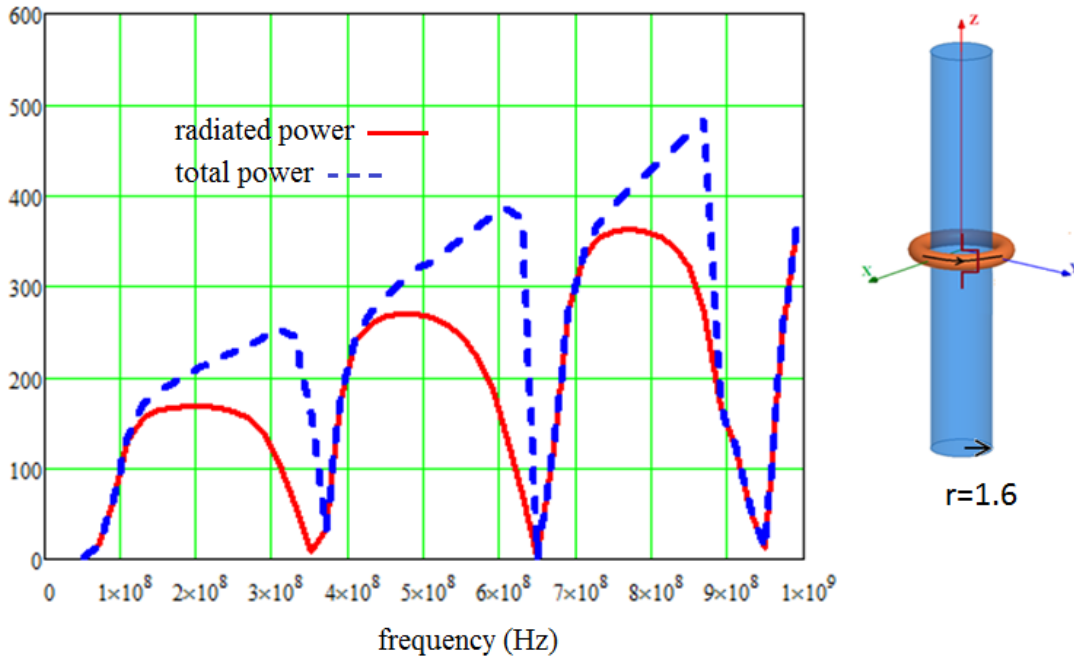


Fig. 7-33 Radiated Power and Total Power of a Magneto Dielectric Rod. The Difference Between Them Is the Power Lost into Surface Waves.

7.3 Theory of the Magneto dielectric open trough

In this section we start with the theory of the magneto dielectric open trough. The magneto dielectric (MD) open trough is obtained by burying the permeable material inside the trough as seen in Fig.7-34

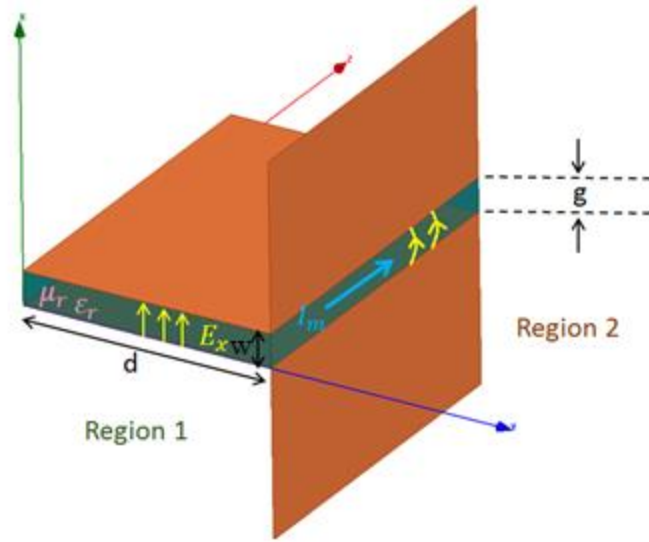


Fig. 7-34 Magneto Dielectric Open Trough with the Fields Shown

In order to obtain the magnetic current, I_m , similar to what we did for the MD rod we will first assume the parallel plane separation is small so that inside Region I we only have \mathbf{E}_x as shown with the yellow arrows. The x directed E field which is arriving from the left side (from inside) will cause a voltage to be formed at the opening that will look to the outside world as a z-directed magnetic current in the opening which is shown by the blue arrow. This z directed magnetic current, will excite cylindrical waves that are purely TEz. By knowing all this we can write the fields in both regions which are as follows:

Fields in region (1)

$$E_x = A(k_z) \sin(k_y y) \exp(-jk_z z) \quad (7-17a)$$

$$H_z = -j \frac{k_y}{\omega \mu_0 \mu_r} A(k_z) \cos(k_y y) \exp(-jk_z z) \quad (7-17b)$$

$$H_y = \frac{k_z}{\omega\mu_0\mu_r} A(k_z) \sin(k_y y) \exp(-jk_z z) \quad (7-17c)$$

With: $k_m^2 = k_y^2 + k_z^2$

Fields in region (2)

$$E_\varphi = -C(k_z) \frac{k_{\rho 0}}{\epsilon_0} H_1^{(2)}(k_{\rho 0} \rho) \exp(-jk_z z) \quad (7-18a)$$

$$H_z = -jC(k_z) \frac{k_{\rho 0}^2}{\omega\mu_0\epsilon_0} H_0^{(2)}(k_{\rho 0} \rho) \exp(-jk_z z) \quad (7-18b)$$

$$H_\rho = C(k_z) \frac{k_{\rho 0} k_z}{\omega\mu_0\epsilon_0} H_1^{(2)}(k_{\rho 0} \rho) \exp(-jk_z z) \quad (7-18c)$$

With : $k_{\rho 0}^2 + k_z^2 = k_0^2 = \omega^2 \mu_0 \epsilon_0$

Similar to what we did for the MD rod we need to know the current to find A and C so we can write the fields. By looking at the previous figure we see that we can assume we have an x-directed electric source current at the interface between the regions at $y=d$. If we look from the outside it seems like we have a $-\varphi$ directed band of current. The rotated figure of the trough shows it better. At this point our goal is to find $A(k_z)$ and $C(k_z)$. In order to do that and to satisfy the jump discontinuity for H_z we first have to write the current Just like what we did for the infinite rod

$$K_x(k_z) = \frac{1}{2\pi} \int_{-\infty}^{+\infty} \left\{ C_0 \left(\text{rect}\left(\frac{z}{s}\right) \right) \right\} e^{jk_z z} dz \quad (7-19a)$$

$$C_0 \left(\text{rect} \left(\frac{z}{s} \right) \right) = \int_{-\infty}^{+\infty} K_x(k_z) e^{-jk_z z} dk_z \quad (7-19b)$$

$$K_x(k_z) = \frac{1}{2\pi} \int_{-\frac{s}{2}}^{+\frac{s}{2}} C_0 e^{jk_z z} dz = \frac{C_0 s}{2\pi} \left[\frac{\sin(k_z s)}{(k_z s)} \right] \quad (7-19c)$$

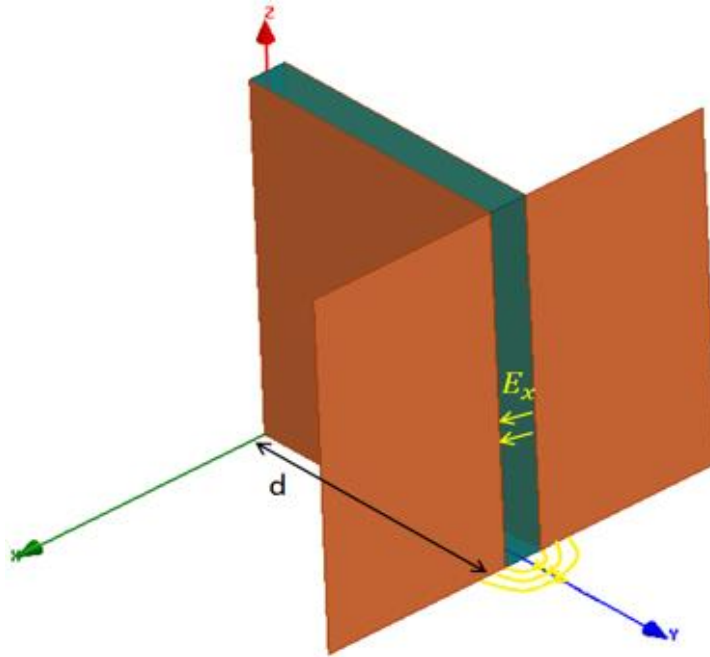


Fig. 7-35 Magneto Dielectric Open Trough with the Fields Shown

The following conditions will give us all the fields (The green term is the contribution from the inside and the brown term is from the outside)

It is important to note that this procedure is due to the method used by Schelkunoff to equate the voltages instead of the tangential field at the boundaries.

$$E_x(\mathbf{y} = \mathbf{d}) \cdot \mathbf{w} = -\pi \frac{a}{2} E_\phi \left(\rho = \frac{a}{2} \right) \quad (7-20a)$$

$$H_z \left(\rho = \frac{a}{2} \right) - H_z(\mathbf{y} = \mathbf{d}) = K_x \quad (7-20b)$$

Now we can find $A(k_z)$ and $C(k_z)$.

$$\begin{cases} E_x(y=d) \cdot W = -\pi \frac{a}{2} E_\varphi \left(\rho = \frac{W}{2} \right) \\ H_z \left(\rho = \frac{W}{2} \right) - H_z(y=d) = K_x \end{cases}$$



$$\begin{cases} A(k_z) \sin(k_y d) = \frac{\pi}{2} C(k_z) \frac{k_{\rho 0}}{\varepsilon_0} H_1^{(2)} \left(k_{\rho 0} \frac{W}{2} \right) \\ -jC(k_z) \frac{k_{\rho 0}^2}{\omega \mu_0 \varepsilon_0} H_0^{(2)} \left(k_{\rho 0} \frac{W}{2} \right) + j \frac{k_y}{\omega \mu_0 \mu_r} A(k_z) \cos(k_y d) = K_x \end{cases}$$

(7-21)

Solving we find:

$$A(k_z) = \frac{\frac{\pi}{2} C(k_z) \frac{k_{\rho 0}}{\varepsilon_0} H_1^{(2)} \left(k_{\rho 0} \frac{W}{2} \right)}{\sin(k_y d)}$$

(7-22a)

$C(k_z)$

$$= \frac{jK_x \frac{\omega \mu_0 \varepsilon_0}{k_{\rho 0}}}{k_{\rho 0} H_0^{(2)} \left(k_{\rho 0} \frac{W}{2} \right) - \frac{\pi k_y}{2 \mu_r} H_1^{(2)} \left(k_{\rho 0} \frac{W}{2} \right) \cotan(k_y d)}$$

(7-22b)

Now we have all the fields but since we are interested in I_m , we write E_φ

$$E_\varphi = -\omega\mu_0 \frac{a}{2} \frac{H_1^{(2)}(k_{\rho 0} \rho)}{H_1^{(2)}\left(k_{\rho 0} \frac{w}{2}\right)} \frac{jK_x \exp(-jk_z z)}{\left(k_{\rho 0} \frac{a}{2}\right) \frac{H_0^{(2)}\left(k_{\rho 0} \frac{w}{2}\right)}{H_1^{(2)}\left(k_{\rho 0} \frac{w}{2}\right)} - \frac{\pi k_y w}{2\mu_r} \cotan(k_y d)} \quad (7-23)$$

Calculating the integral similar to the MD rod will give I_m

$$E_\varphi(z) \pi \frac{a}{2} = I_m(z) = -j\omega\mu_0 \frac{a^2}{8} I_0 \int_{-\infty}^{+\infty} \frac{\left[\frac{\sin\left(k_z \frac{s}{2}\right)}{\left(k_z \frac{s}{2}\right)} \right] \exp(-jk_z z)}{\left(k_{\rho 0} \frac{w}{2}\right) \frac{H_0^{(2)}\left(k_{\rho 0} \frac{w}{2}\right)}{H_1^{(2)}\left(k_{\rho 0} \frac{w}{2}\right)} - \frac{\pi k_y d}{2\mu_r} \left(\frac{w}{d}\right) \cot(k_y d)} dk_z \quad (7-24)$$

Again we have to be careful when we integrate this function because of the poles but adding an imaginary part to the permeability and changing the integration path close to the pole using a smooth curve will solve this problem.

At this point we can calculate the integral for the open trough with dimensions shown below. The trough is made square 2" wide by 2" deep.

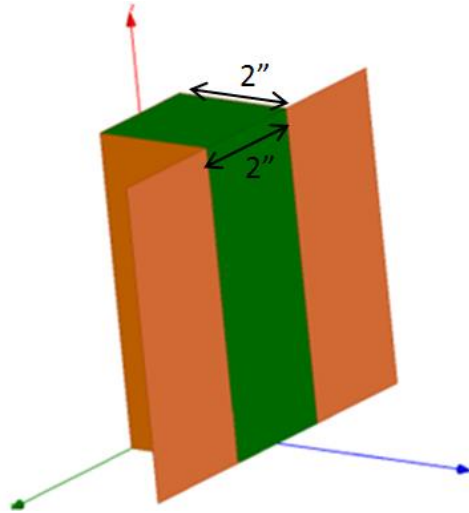


Fig. 7-36 A 2" by 2" Magneto Dielectric Open Trough with $\mu = 80$

Now we can plot the amplitude and phase of the magnetic current

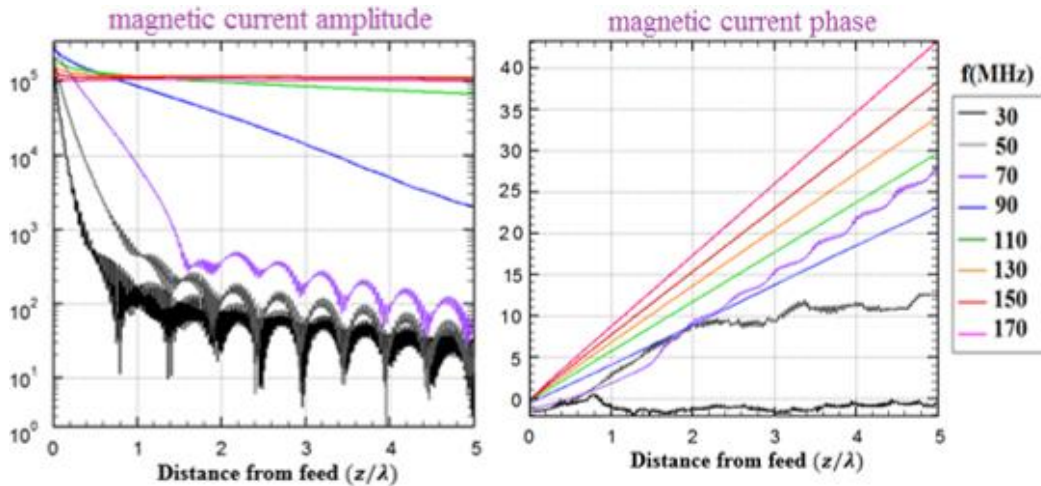


Fig. 7-37 Amplitude and Phase of the Current Wave as a Function of Distance from Feed for a 2" by 2"

Trough Filled with $\mu = 80$ and $\epsilon = 2$, from 30 MHz to 170MHz

Fig 7-38 shows the amplitude and phase from 190MHz to 330MHz which shows behavior similar to the rod with the bound wave eventually getting hard to excite (190 MHz to 250MHz) as it retreats into the trough. Thus, the amplitude drops from the uniform value to an exponential decay and the phase velocity gets very slow and then

suddenly switches to the fast leaky mode behavior above (270 MHz up). Arrows have been added to the plot to guide the eye in following this changing behavior with frequency.

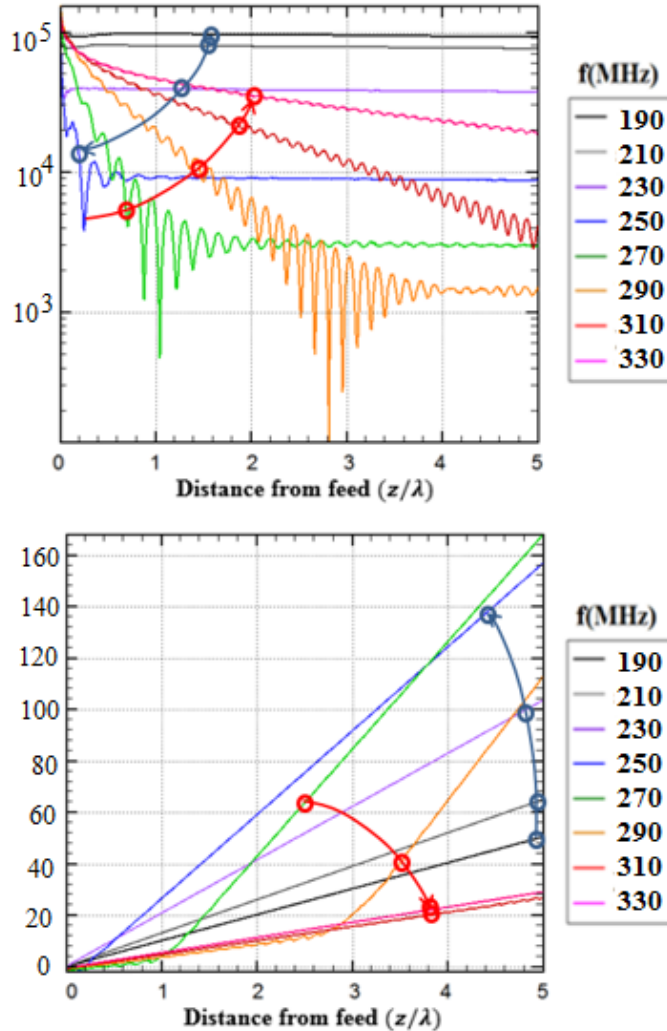


Fig. 7-38 Amplitude (Top) and Phase (Bottom) of the Current Wave as a Function of Distance from Feed for a 2" by 2" Trough Filled with $\mu = 80$ and $\epsilon = 2$, from 190 MHz to 330MHz

Fig. 7-39 shows the results from 350MHz to 490 MHz, very similar to Fig. 7-15 in cycling through the same behavior with the next mode TE₂₀.

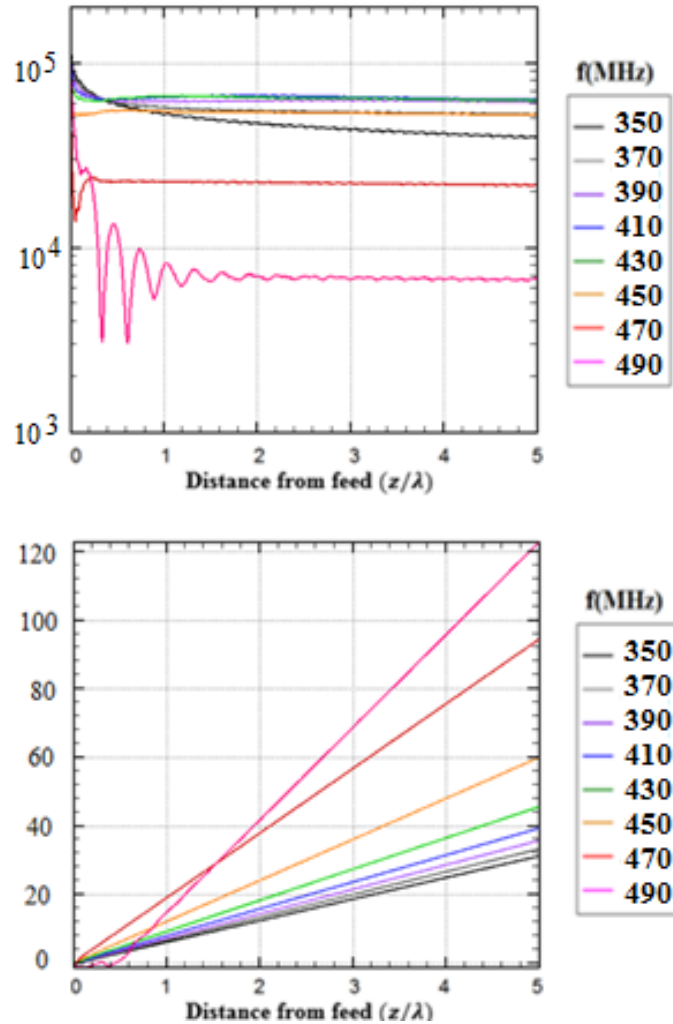


Fig. 7-39 Amplitude and Phase of the Current Wave as a Function of Distance from Feed for a 2'' by 2'' Trough Filled with $\mu = 80$ and $\epsilon = 2$, from 190 MHz to 330MHz

From these results we conclude that the trough filled with the permeable material and the MD rod exhibit analogous behavior. We will study this similarity in more detail later in this section

7.3.1 Magneto dielectric open trough with different cross sections

In this subsection, we study the effect of the dimensions of the cross section of the open through on the amplitude and phase behavior. We see the difference between the

square, the wide, and the deep open trough. Figure below shows the chosen dimensions of the wide trough. In order to have a meaningful comparison we will keep the cross-section constant and only change the width to depth ratio.

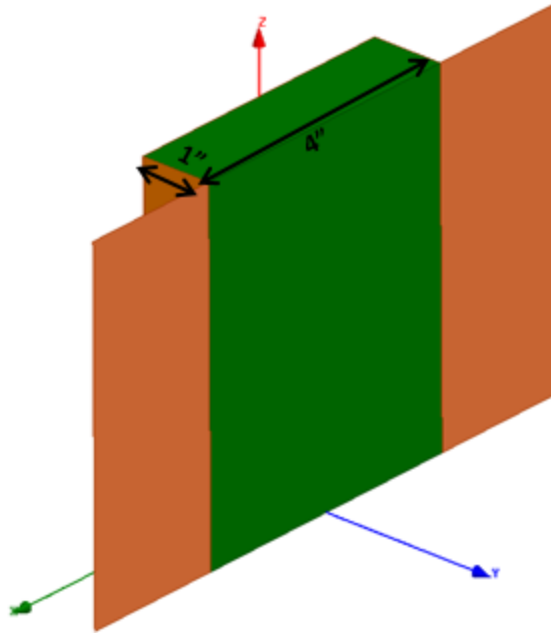


Fig. 7-40 Geometry of 4" by 1" Depth Open Trough Filled with a Material with $\mu = 80$, $\epsilon = 2$

Fig.7-41, shows the amplitude and phase of I_m as a function of the distance from the feed multiplied by the wavelength (z/λ) for the trough geometry shown in Fig.7-47. We see that in this case, in the frequency range shown, we will not reach the onset of the first mode and we have fast waves with phase plots under the light-line and non-uniform amplitude plots. This means that a wider trough pushes the onset frequency to much higher frequencies and that the aspect ratio can be used a tuning parameter for the magneto dielectric trough antenna.

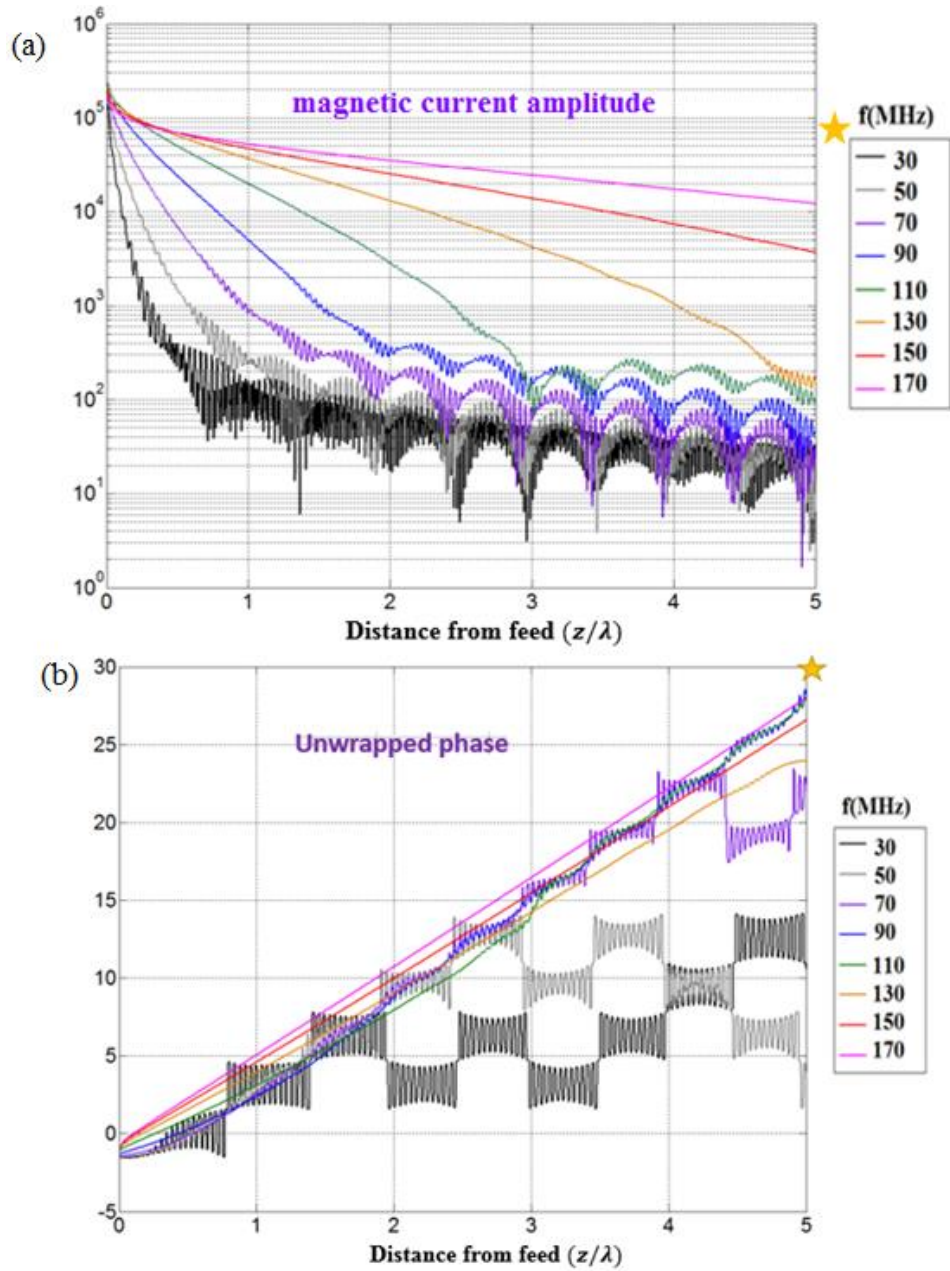


Fig. 7-41 Amplitude (a) and Phase (b) of the Current as a Function of the Distance from the Feed Multiplied by the Wavelength (z/λ) for a Magneto-Dielectric Shallow Open Trough with a 4 Inch by 1 Inch Cross-Section and a Material with $\mu = 80$ and $\varepsilon = 2$. Frequencies Go from 30 MHz to 170 MHz in 20 MHz Steps. The Star Symbol Shows the Current Wave Does Not Reach the Light-Line.

The next logical example is studying the deep trough. Again, we will keep the cross-section constant and just change the aspect ratio. Figure below shows the dimensions of the deep trough

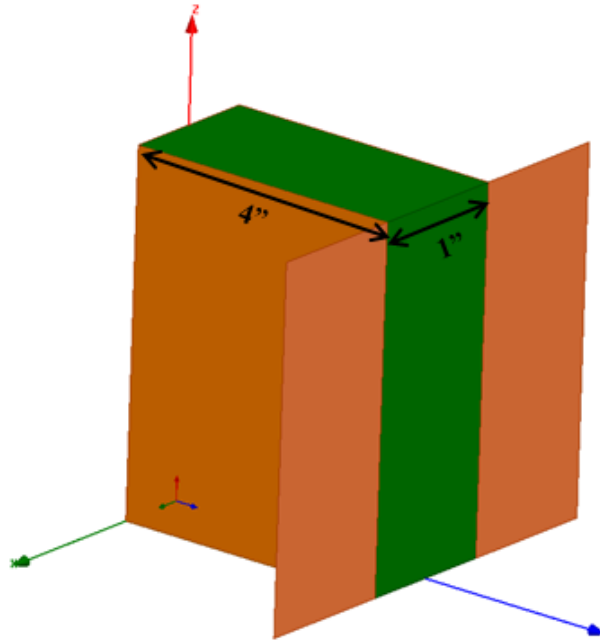


Fig. 7-42 Geometry of a 1" Width by 4" Depth Deep Open Trough Filled with a Material with $\mu = 80$ and $\epsilon = 2$

Fig.7-43, shows the amplitude and phase of I_m as a function of the distance from the feed multiplied by the wavelength (z/λ) for the trough geometry shown in Fig.7-42. We see that from 30MHz to 70 MHz we are getting close to the light-line and at 70 MHz we have already passed it so we are dealing with slower waves (The star symbol shows when we pass the line). Up to 110 MHz we have uniform amplitude. As we go from 130 MHz to higher frequencies we see a sudden change in both phase and amplitude which means that the next mode is beginning to appear and at 190 MHz (magenta), we again have a fast wave with and the next mode has not reached onset.

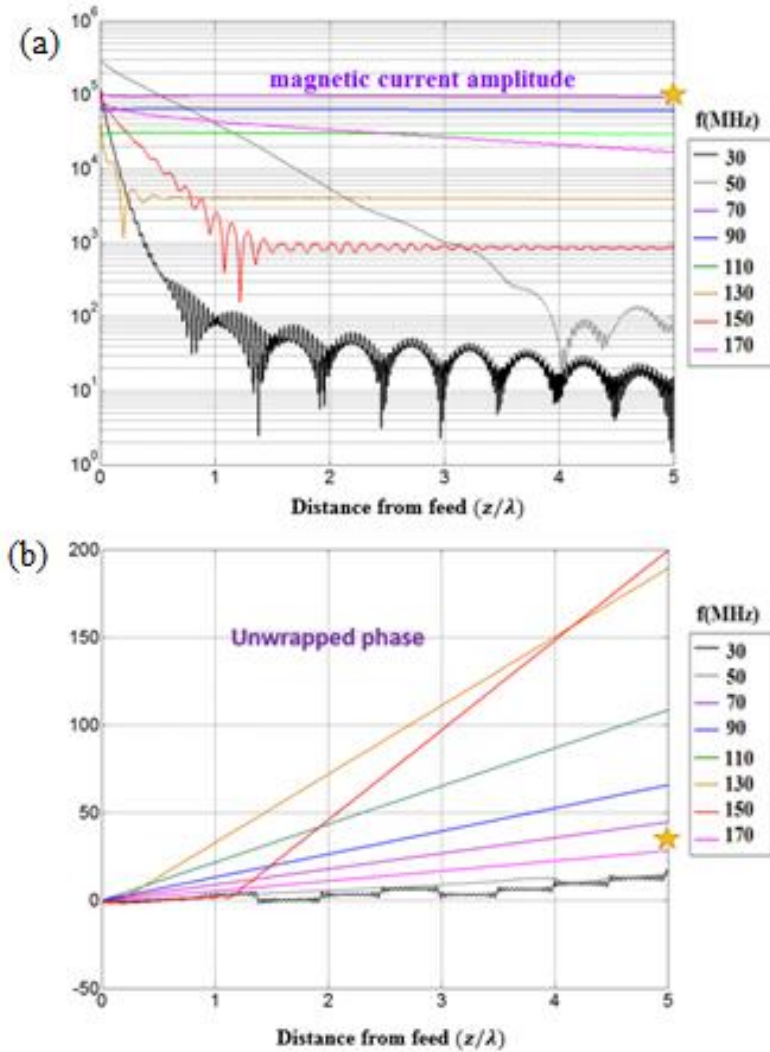


Fig. 7-43 Amplitude (a) and Phase (b) of the Current as a Function of the Distance from the Feed Multiplied by the Wavelength (z/λ) for a Magneto-Dielectric Deep Open Trough with a 1 Inch by 4 Inch Cross-Section and a Material with $\mu = 80$ and $\epsilon = 2$. Frequencies Go from 30 MHz to 170 MHz in 20 MHz Steps. The Star Symbol Shows the Current Wave Reaches the Light Line and Goes to Another Mode Similar to What Happened for the High Frequency Magneto Dielectric Rod.

This means that a deeper trough pushes the onset frequency to much higher lower and again we see that the aspect ratio can be used a tuning parameter for the magneto dielectric antenna.

7.3.2 Using Savitzky-Golay filters to smooth data and obtaining α and β plots for MD open trough

In the previous section we had found the α and β plots for the magnetic rod and we will repeat the same procedure and find the plots for the $2'' \times 2''$ open trough. The figure below shows the magnetic current amplitude of the $2'' \times 2''$ open trough and the same plot for lower values of (z/λ) .

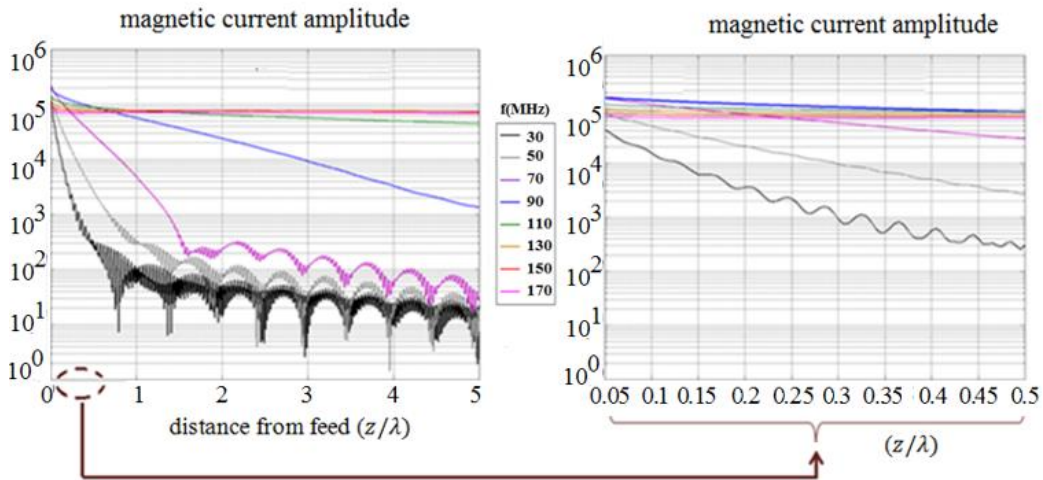


Fig. 7-44 Amplitude of the Current as a Function of the Distance from the Feed Divided by the Wavelength (z/λ) for a Magneto-Dielectric $2'' \times 2''$ Open Trough and a Material with $\mu = 80$ and $\epsilon = 2$ and for Very Small Values of (z/λ) . Frequencies Go From 30 MHz to 170 MHz in 20 MHz Steps.

Similar to the rod, a Savitzky-Golay lowpass filter has been used and a least square linear fit has been obtained for the lowpass filtered data. Fig.7-44 and Fig. 7-45 show the initial data and the linear fit. The next step, as done for the rod, is plotting the slope of the magnetic current amplitude plots as a function of frequency. This plot is

shown in Fig.7-46 which shows that the slope tends to very small values which indicates passing the lightline. Similar to the rod, a study of the phase would show the frequency in which the cutoff happens.

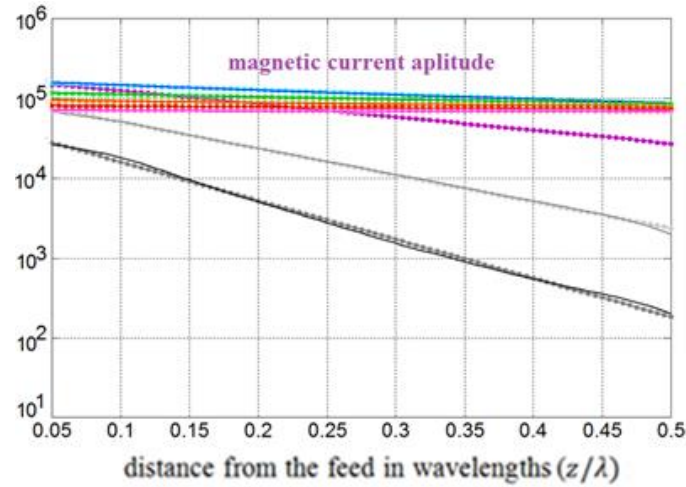


Fig. 7-45 Amplitude of the Current for Very Small Values of (z/λ) for the $2'' \times 2''$ Open Trough. Solid Lines Show the Low Pass Filtered Data and the Dotted Lines Show the Linear Fit. Frequencies Go From 30 MHz to 170 MHz in 20 MHz Steps.

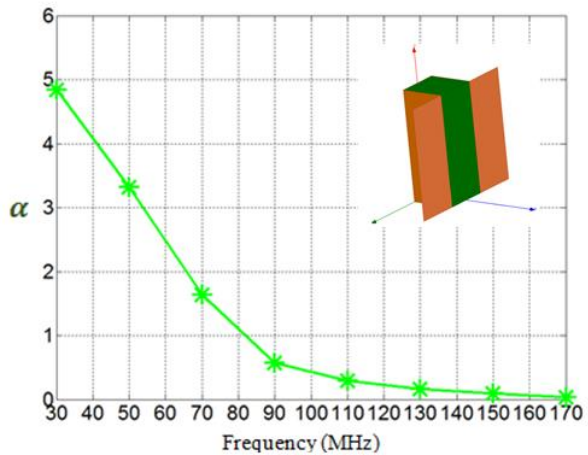


Fig. 7-46 The Slope of the Amplitude Decay or the α Plot of a Magneto-Dielectric Rod with a 1.6 Inch Radius and a Material with $\mu = 80$ and $\epsilon = 2$ Extended to Higher Frequencies

The next step is to repeat the same procedure for the phase of the $2'' \times 2''$ open trough and obtain the β plot. The figure below shows the phase of the magnetic current of the $2'' \times 2''$ open trough and the same plot for lower values of (z/λ) .

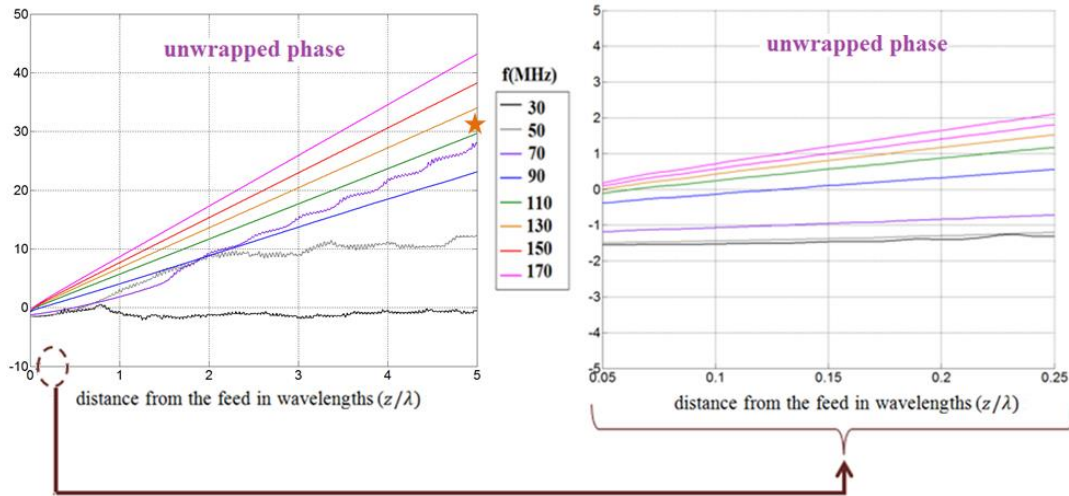


Fig. 7-47 Phase of the Current as a Function of the Distance from the Feed Divided by the Wavelength (z/λ) for a Magneto-Dielectric $2'' \times 2''$ Open Trough and a Material with $\mu = 80$ and $\epsilon = 2$ and for Very Small Values of (z/λ) . Frequencies Go From 30 MHz to 170 MHz in 20 MHz Steps.

After repeating the same procedure for the phase of $2'' \times 2''$ open trough and obtaining the β plot as shown in Fig. 7-48, we see that similar to the rod, as the amplitude gets flatter, the slope of the phase gets higher. When the phase plot in Fig.7-47 reaches $5 \times 2\pi$ at $(z/\lambda)=5$ we have reached the light-line. As seen in Fig.7-47 this happens at somewhere between the green line (110 MHz) and the orange line (130MHz). The slope of the phase is shown in Fig 7-48. We can see that the lightline is crossed at about 118 MHz and after that we will have bounded slower waves.

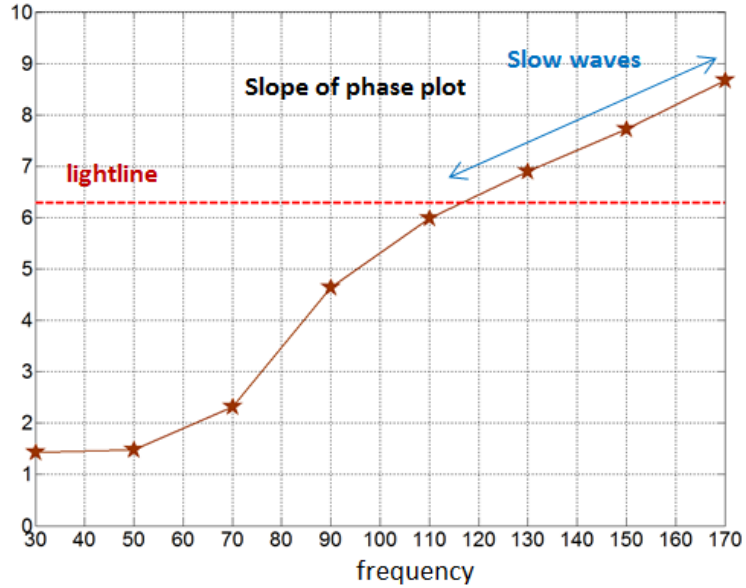


Fig. 7-48 The Slope of the Phase Plot or the β Plot of a Magneto-Dielectric 2" \times 2" Open Trough and a Material with $\mu = 80$ and $\varepsilon = 2$

7.3.3 The effect of the open trough's aspect ratio on the bandwidth and cutoff frequency using the β plots or the velocity plots

We already know that the dimensions of the trough (aspect ratio of the open trough which is ratio of width to depth) gives an extra degree of freedom compared to the rod and that the aspect ratio serves as a tuning parameter that allows us to control the onset frequency. By knowing this, it is important to see how the aspect ratio of the open trough affects the bandwidth and the cutoff frequency.

We expect the cutoff frequency or the onset of guidance for the open trough to occur close to the frequency when the depth is approximately $\lambda_{\text{medium}}/4$ but in order to find how the bandwidth changes we will use the β plots as a measure of bandwidth. Later in this Chapter we will see that the radiated power can also clearly show the bandwidth however the slope of the β plots can also be used as a measure of the bandwidth.

Since we are only showing the effect of the aspect ratio of the open trough we have obtained the phase data of the magnetic current for different open trough geometries all having the same cross section of $4in^2$ and permeability of 80. The reason this is important is that the aspect ratio of the trough give a new degree of freedom compared to the rod and we want to see how we can use this as a parameter to achieve larger bandwidths. Therefore, in this study the only parameter that is changed is the aspect ratio of the open trough. This means that while changing the width(g), we will make sure that all geometries have $depth \times width = 4in^2$ so the important factor of permeability \times volume is kept the same.

In order to see how the antenna behavior changes with changing the aspect ratio, we have changed the width (g) from 2" to 5" in small steps and obtained the β plots for all geometries. The slope of the β plot close to the cutoff can be used as a measure of the bandwidth. It is obvious that same can be said for the velocity plot which is $2\pi/\beta$. We will keep in mind that a larger slope means that the bandwidth in which the wave propagates close to the speed of light is smaller, therefore the inverse of the β plot slope will serve as a bandwidth measure.

We have obtained the β plots for many open trough geometries with widths ranging from 2" to 5" but as an example we have plotted the β plot and velocity plot of only three of the different dimensions which can be seen in the figure below. We should remember that in the ideal case the velocity of the wave stays very close to the light-line therefore in order to have a measure of the bandwidth we find the slope of the plot near the cutoff and the inverse of the slope gives us an idea of the bandwidth. In Section 4 of

this chapter, after we have obtained the radiated power, we will see that the bandwidth can also be directly obtained from the amount of radiated power. By looking at these plots we already expect the structure with higher aspect ratio to have a larger bandwidth

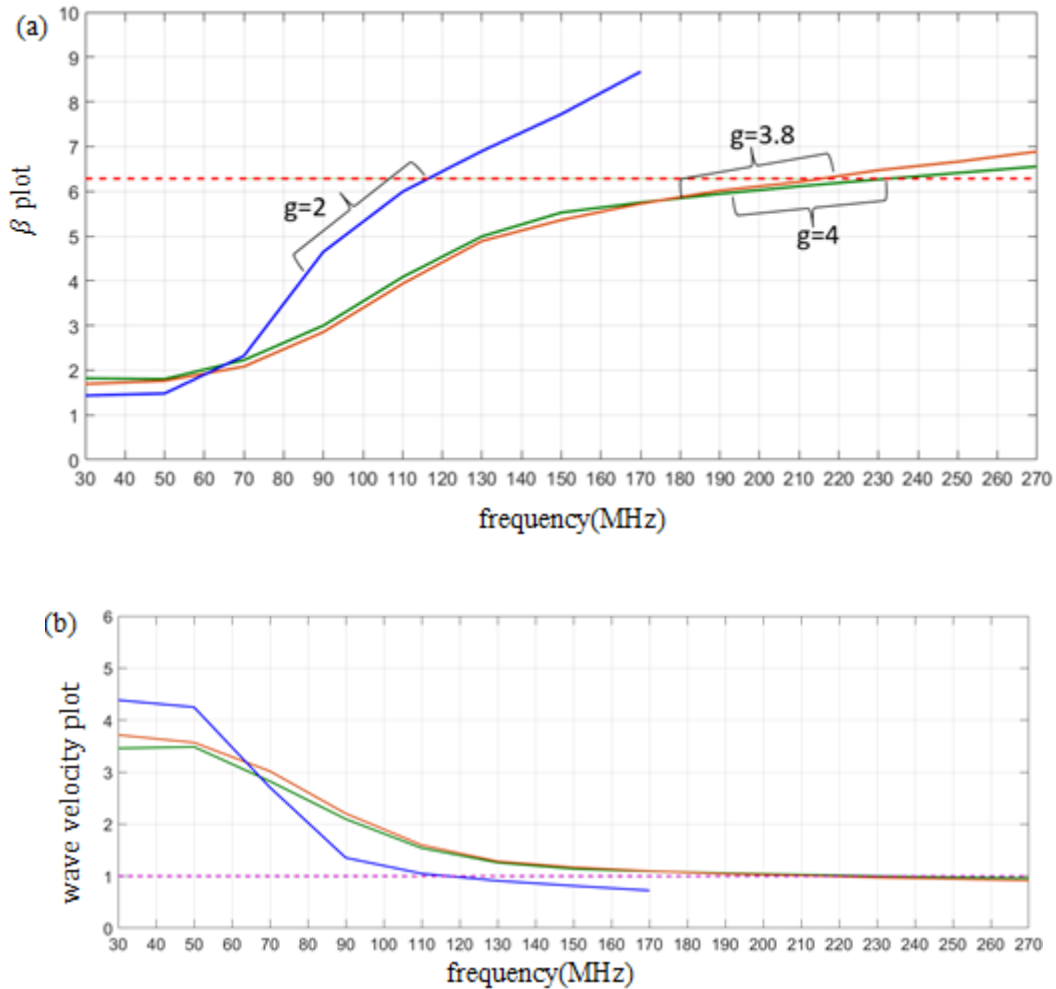


Fig. 7-49 (a) β Plots of Three Structures (b) the Wave Velocity of Three Structures

As previously mentioned and showed in Fig.7-50 , in order to have a measure of the bandwidth, we have obtained the slope of the β plots for a different range of

open trough widths. The inverse of the slopes versus the aspect ratio (width/depth) can be seen below. It should be mentioned that this plot shows the absolute bandwidth and not the relative bandwidth. In order to show the relative bandwidth, we have to divide this by the cutoff frequency which we will get into more detail after we calculate the radiated power. What this plot shows is that as we increase the aspect ratio, even with the same material volume and permeability, we can achieve a larger bandwidth.

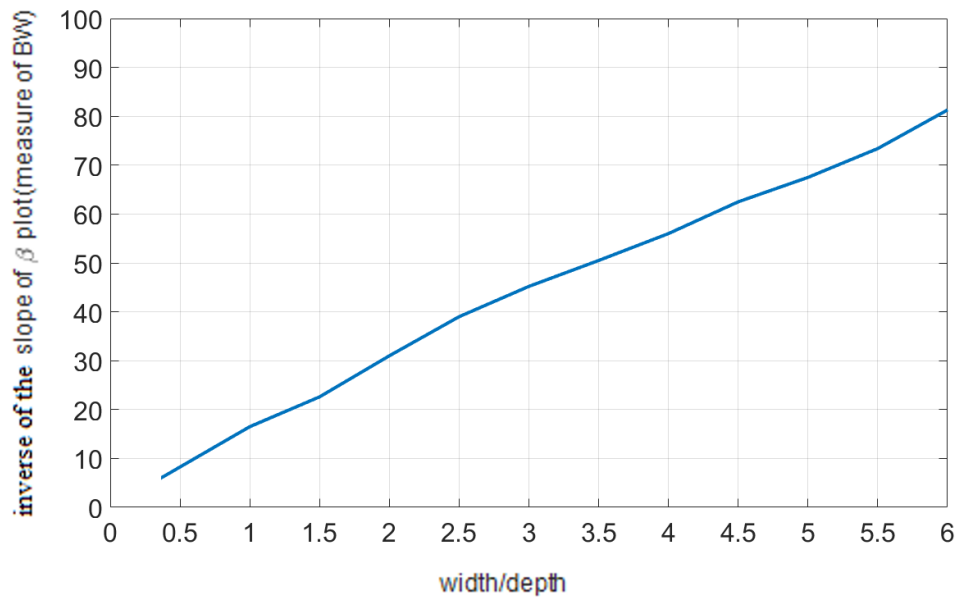


Fig. 7-50 Inverse of the Slope of the β Plots Versus Aspect Ratio

It can be seen that even though we can use the aspect ratio of the trough to push the onset frequency to lower frequencies, we will have a smaller bandwidth of operation.

7.3.4 Calculating the radiated power of the magneto dielectric open trough

In this sub section, similar to what we did for the rod, we will calculate the Integration of the complex Poynting vector of the open trough over a surface enclosing the antenna and store the real part of this complex result as the radiated power of the trough.

The radiated power of the magneto dielectric trough versus frequency can show the formation of different modes and can be a way to define a bandwidth and it can be used to compare the bandwidth of the open trough to the rod. In order to find the radiated power, as explained before, we will write the fields of the open trough in the outside medium and calculate the Poynting vector.

After obtaining the complex Poynting vector, we calculate its integral over a surface enclosing the antenna. This will result in another complex number with the real part being identified as the radiated power.

The fields of the open trough in the outside medium as seen in many previous reports is as follows:

$$E_{\varphi} = -C(k_z) \frac{k_{\rho 0}}{\varepsilon_0} H_1^{(2)}(k_{\rho 0} \rho) \exp(-jk_z z) \quad (7-25a)$$

$$H_z = -jC(k_z) \frac{k_{\rho 0}^2}{\omega \mu_0 \varepsilon_0} H_0^{(2)}(k_{\rho 0} \rho) \exp(-jk_z z) \quad (7-25b)$$

$$H_{\rho} = C(k_z) \frac{k_{\rho 0} k_z}{\omega \mu_0 \varepsilon_0} H_1^{(2)}(k_{\rho 0} \rho) \exp(-jk_z z) \quad (7-25c)$$

$$\text{With : } k_{\rho 0}^2 + k_z^2 = k_0^2 = \omega^2 \mu_0 \varepsilon_0$$

The Poynting vector is defined as:

$$P = \frac{\vec{E} \times \vec{H}^*}{2} = \frac{E_\phi \hat{a}_\phi \times H_z^* \hat{a}_z}{2} \quad (7-26)$$

As expected the Poynting vector is a radial vector and in order to obtain the radiated power we should integrate the pointing vector over a cylindrical surface enclosing the antenna.

radiated power

$$= \text{Re} \left\{ \int_{\phi=0}^{\phi=2\pi} \int_{z=-\infty}^{z=\infty} P_\rho \hat{a}_\rho \cdot \rho d\phi dz \hat{a}_\rho \right\} \quad (7-27)$$

In order to show the radiated power of the trough we have to choose a certain dimension for the magneto dielectric trough. It would be interesting to choose a dimension for the trough that would give us the same cutoff frequency as the 1.6" rod while having the same cross section so that later we could do a comparison. The dimensions that would give the same cutoff is seen below.

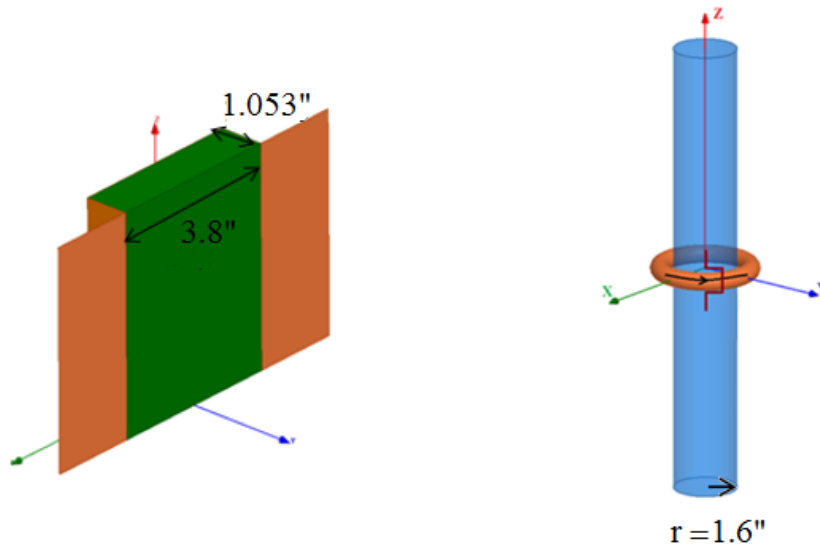


Fig. 7-51 The Open Trough and the Rod Having the Same Cross Section Area and the Same Cutoff

Frequency

We will plot the α and β plots of the MD 3.8" \times 1.053" open trough so we can later compare them to the rod with 1.6" radius. Fig. 7-52 shows the α plot and β plot of the open trough. The wave velocity can also be seen in the figure.

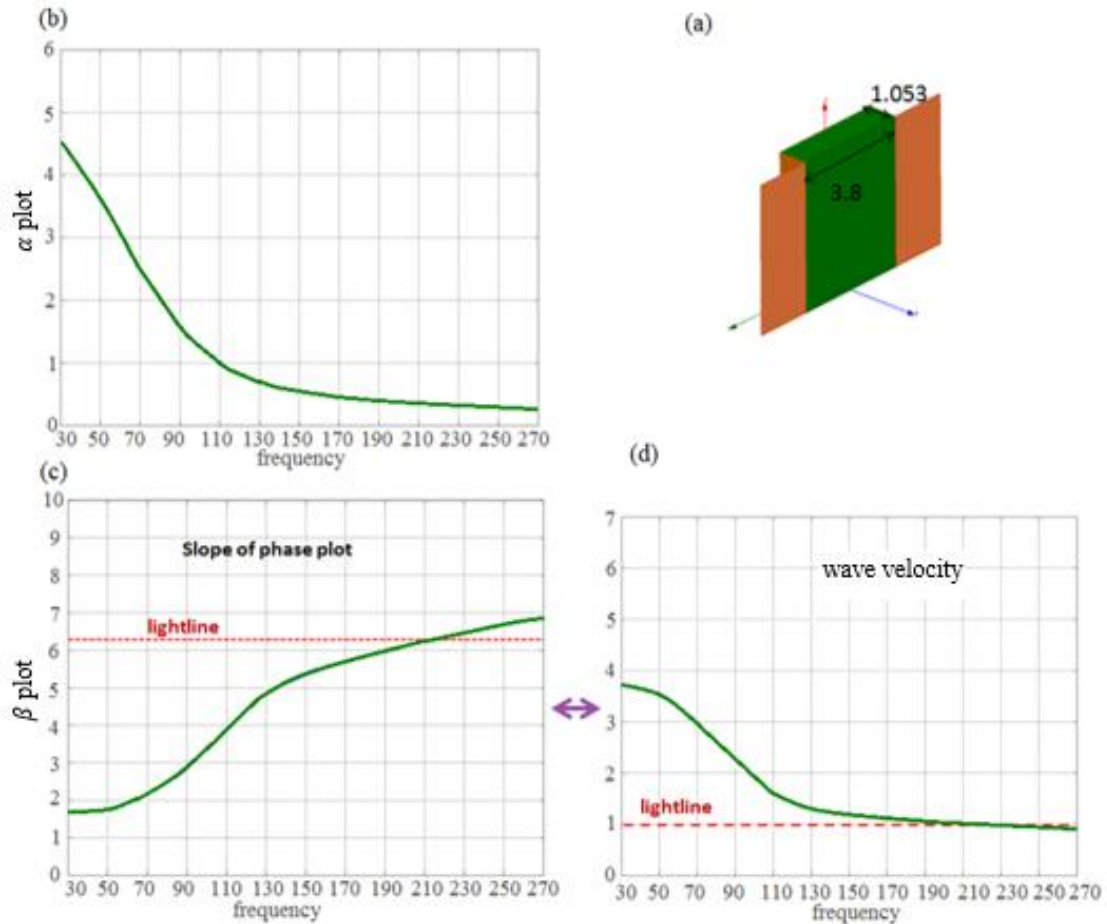


Fig. 7-52 (a) Open Trough with 3.8" \times 1.053" Cross Section (b) α Plot of the Structures (c) β Plots of the Structures (d) the Wave Velocity of the Structure

The radiated power obtained from the Poynting vector of the open trough can be seen below which again shows that the maximum of the radiated power happens close to the cutoff frequency.

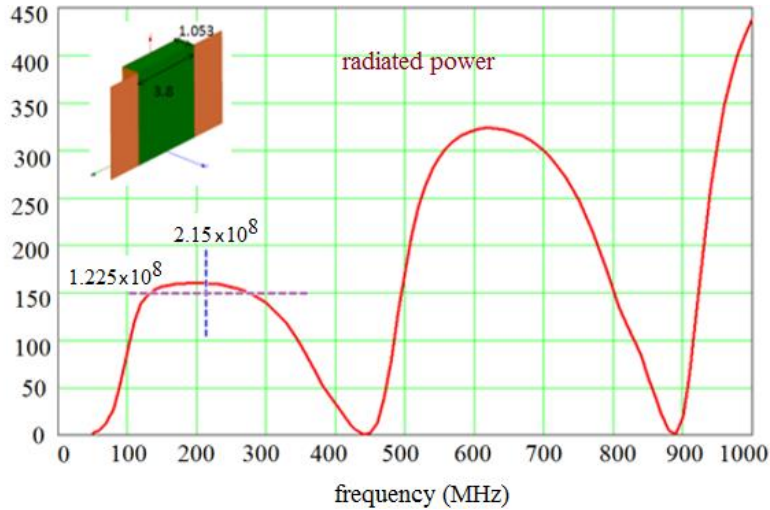


Fig. 7-53 (a) Radiated Power of a Magneto Dielectric Rod with $r=1.6''$ and $\mu = 80$ (b) Radiated Power of a $3.8'' \times 1.053''$ Magneto Dielectric Open Trough with $\mu = 80$

Later in the comparison section we will see in detail that the trough and the rod of identical cutoff and identical permeability times area have the same exact behavior.

7.4 Theory of the magneto-dielectric trough with a slit

In the previous section, we mentioned that a desirable feature of the trough is the additional degree of freedom. We would like to have more degrees of freedom to control the guidance and radiation behavior of the MD trough structure. Therefore, we add a slit to the open trough and we obtain the structure shown in Fig.7-54. Similar to the open trough structure, the permeable material of the MD is buried into a trough but this time a metal slit is added to control the radiating aperture of the trough.

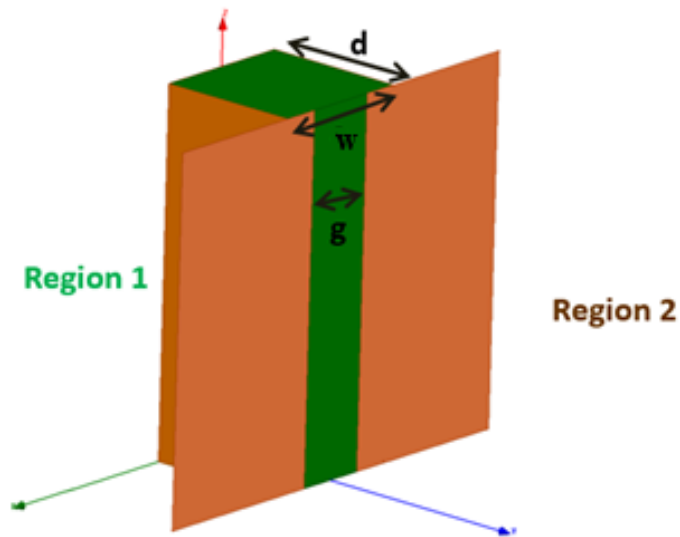


Fig. 7-54 Geometry of the Magneto Dielectric Slitted Trough

At this point we will try to find the fields in the two regions shown in Fig.7-54 with region (1) filled with a material of μ_r and ϵ_r while region (2) is free space. For this case as shown in Fig.7-55, If we assume the slit is an infinitesimal distance inset into the waveguide, the normalized Admittance looking in is that of the short at $y=d$ plus the shunt admittance of the slit as seen in Fig.7-55 below

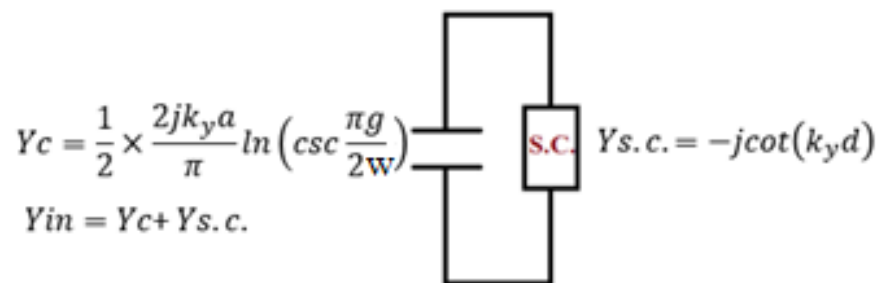


Fig. 7-55 The Normalized Admittance Seen from the Opening of the Slit Looking Inside the Material

The value of the capacitance is obtained from chapter 3-5 of Marcuvitz's waveguide handbook which is half of the angle-dependent admittance of an E-plane slit in a parallel plane waveguide. The reason we have divided this impedance by two is that we are only accounting for the inside fields. Therefore, the input admittance could be written as:

$$Y_{in}(\text{slitted trough}) = -j\cot(k_y d) + jk_y \frac{a}{\pi} \ln\left(\csc \frac{\pi g}{2a}\right) \quad (7-28)$$

The input impedance for an open through only consists of the short circuit term and can be written as:

$$Y_{in}(\text{open trough}) = -j\cot(k_y d) \quad (7-29)$$

According to the calculations in the previous section we had obtained the electric field of the open trough to be as follows:

$$E_\varphi = -\omega\mu_0 \frac{a}{2} \frac{H_1^{(2)}(k_{\rho 0} \rho)}{H_1^{(2)}\left(k_{\rho 0} \frac{a}{2}\right)} \frac{jK_x \exp(-jk_z z)}{\left(k_{\rho 0} \frac{a}{2}\right) \frac{H_0^{(2)}\left(k_{\rho 0} \frac{a}{2}\right)}{H_1^{(2)}\left(k_{\rho 0} \frac{a}{2}\right)} - \frac{\pi k_y a}{2\mu_r} \cot(k_y d)} \quad (7-30)$$

By replacing $j\cot(k_y d)$ for the open trough with $-j\cot(k_y d) + jk_y(a/\pi)\ln(\csc(\pi g/2a))$, we can obtain E_φ for the slitted trough as follows:

$$E_\varphi = -\omega\mu_0 \frac{g}{2} \frac{H_1^{(2)}(k_{\rho 0} \rho)}{H_1^{(2)}\left(k_{\rho 0} \frac{g}{2}\right)} \times \quad (7-31)$$

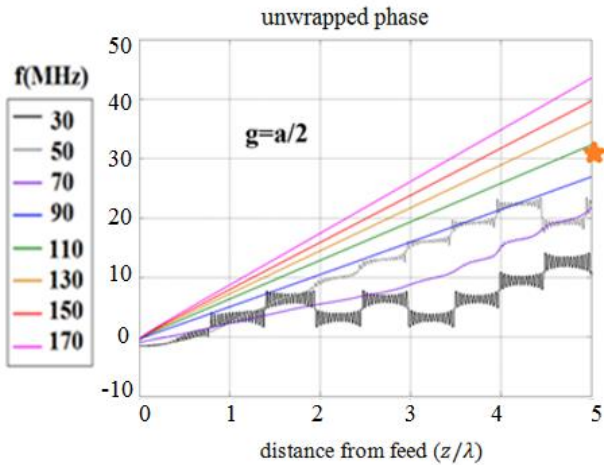
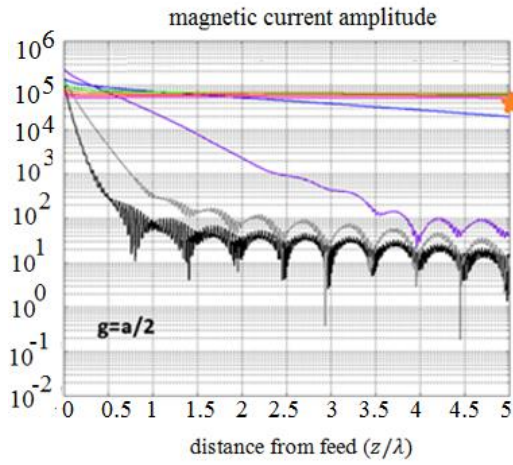
$$\frac{jK_x \exp(-jk_z z)}{\left(k_{\rho 0} \frac{g}{2}\right) \frac{H_0^{(2)}\left(k_{\rho 0} \frac{g}{2}\right)}{H_1^{(2)}\left(k_{\rho 0} \frac{g}{2}\right)} - \left(\frac{\pi g}{2a}\right) \frac{\left(k_y \frac{g}{2}\right)}{\mu_r} \left[\cot(k_y d) - k_y \frac{a}{\pi} \ln\left(\csc \frac{\pi g}{2a}\right)\right]}$$

The next step would be finding the magnetic current by integrating E_ϕ at $\rho = a/2$ which will be as follows:

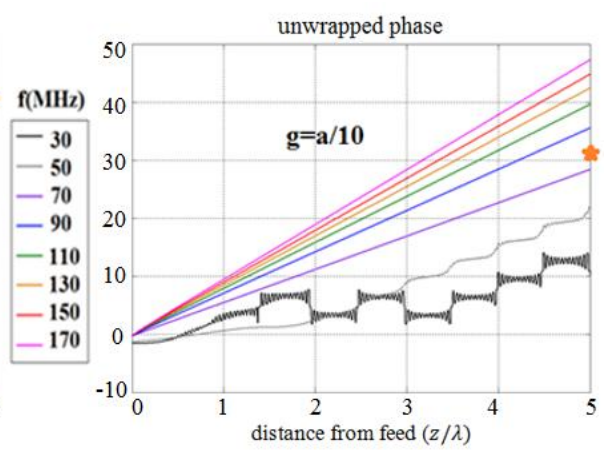
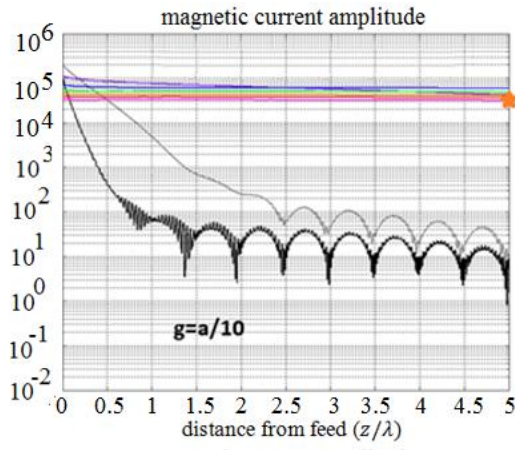
$$E_\phi(z) \pi \frac{g}{2} = I_m(z) = -j\omega\mu_0 \frac{g^2}{8} I_0 \times \int_{-\infty}^{+\infty} \frac{\left[\frac{\sin\left(k_z \frac{s}{2}\right)}{\left(k_z \frac{s}{2}\right)}\right] \exp(-jk_z z)}{\left(k_{\rho 0} \frac{g}{2}\right) \frac{H_0^{(2)}\left(k_{\rho 0} \frac{g}{2}\right)}{H_1^{(2)}\left(k_{\rho 0} \frac{g}{2}\right)} - \left(\frac{\pi g}{2a}\right) \frac{(k_y d)}{\mu_r} \left(\frac{g/2}{d}\right) \left[\cot(k_y d) - k_y \frac{a}{\pi} \ln\left(\csc \frac{\pi g}{2a}\right)\right]} \quad (7-32)$$

Now that we have obtained $I_m(z)$, we can plot it's amplitude and phase for different slit widths.

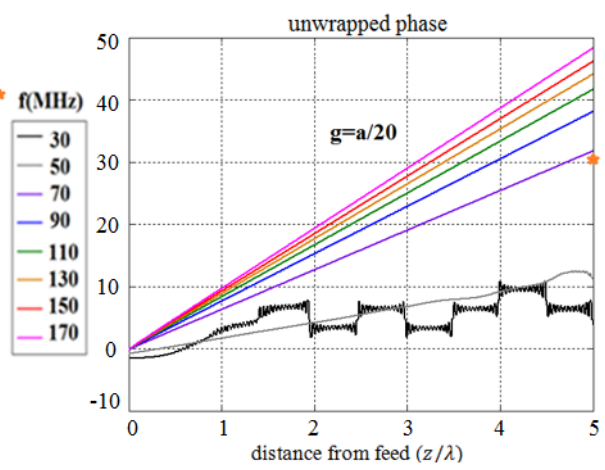
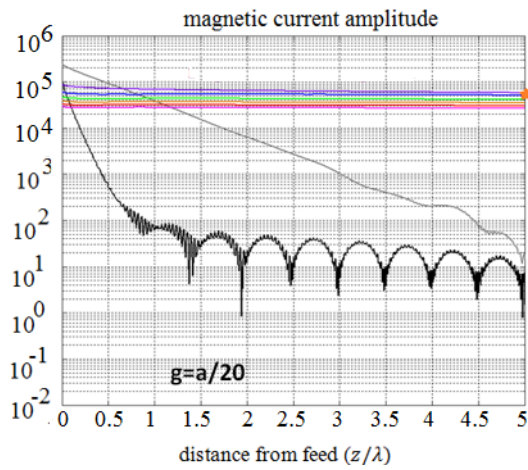
By looking at the plots we see that as the slit gets smaller the cutoff frequency gets lower. In the next report, we will see that by using the open trough and the slitted trough we can achieve lower cutoff frequencies compared to the rod with lower permeabilities.



- 30
- 50
- 70
- 90
- 110
- 130
- 150
- 170



- 30
- 50
- 70
- 90
- 110
- 130
- 150
- 170



- 30
- 50
- 70
- 90
- 110
- 130
- 150
- 170

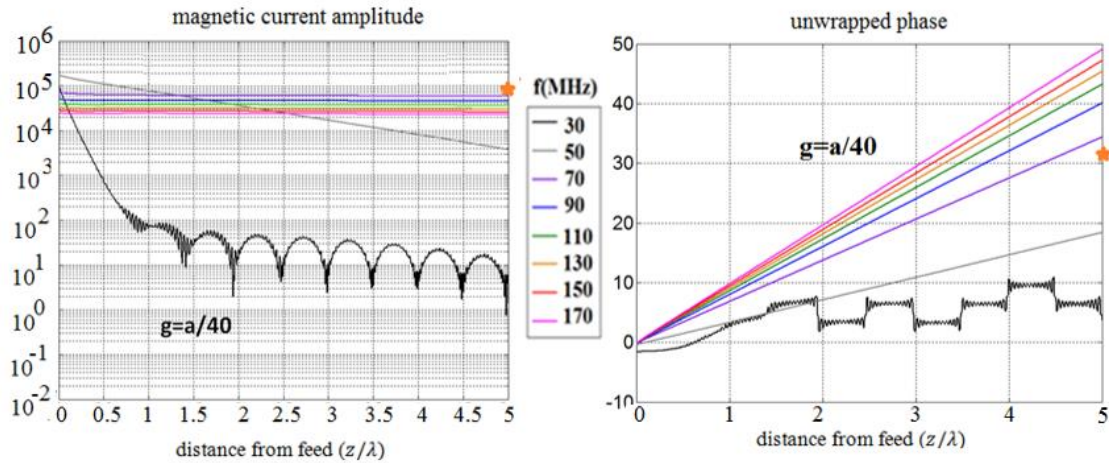


Fig. 7-56 Phase and Amplitude Plots of the Slitted Trough with Different Slit widths

7.4.1 Obtaining the β plots for MD slitted trough and the radiated power using the Poynting vector

By looking at the previous figures we see that by changing the dimensions of the slit we can reduce the cutoff frequency therefore as an example we will use the Savitzky-Golay filters on the following dimensions of the slitted trough to obtain the β plot.

These dimensions have been chosen as an example since with the same cross section area as the rod and the open trough but with $1/4^{\text{th}}$ of the permeability we have been able to obtain the same cutoff frequency as both the open trough and the magneto dielectric rod.

In the next section we will do a comprehensive comparison between these three geometries.

cross section = 4 in^2

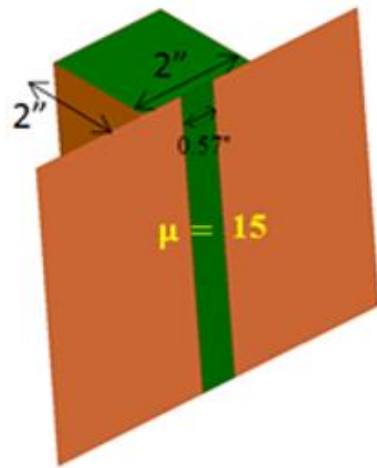


Fig. 7-57 Magneto Dielectric Slitted Trough with Given Dimensions

The figure below shows the β plot obtained from the phase plots using the same steps explained in the previous sections. We have plotted the β plot to show that the cutoff of this structure that has a significantly less permeability and the same cross section area can be tuned to be the same as the open trough and the magneto dielectric rod with the same cross section area but much higher permeability of 80.

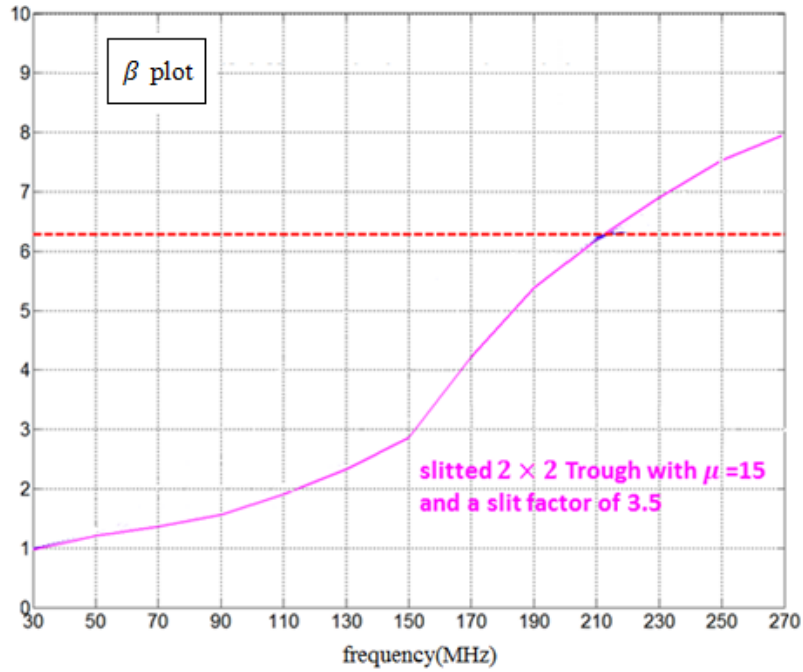


Fig. 7-58 β Plot Which Has Been Obtained from the Phase Plots of the 2'' by 2'' Slitted Trough

The radiated power obtained from the Poynting vector of the slitted trough with the mentioned dimensions can be seen below which again shows that the maximum of the radiated power happens close to the cutoff frequency.

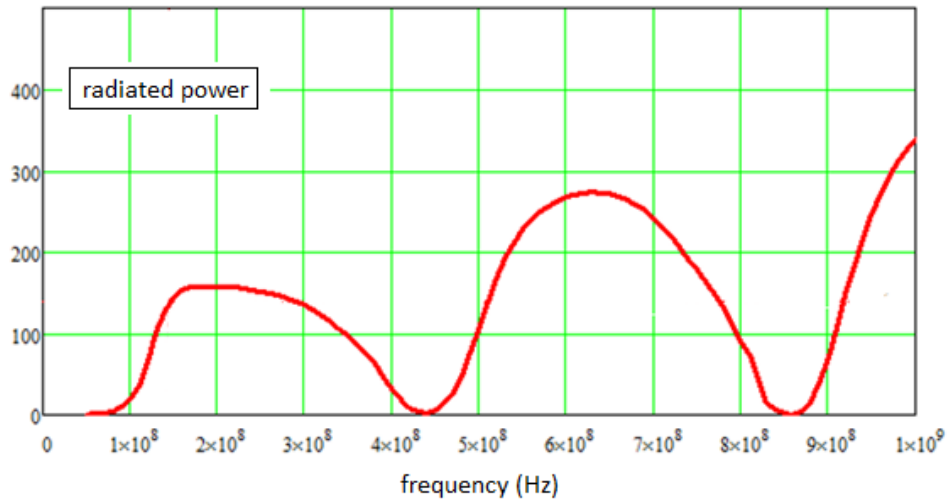


Fig. 7-59 Radiated Power of the 2 by 2 Slitted Trough Showing That the Peak of the Radiated Power

Happens Close to the Onset Frequency

At this point, similar to both the rod and the open trough we will see that the maximum radiation happens at the onset frequency which is a sanity check since we already expect the structure to behave like a PEC radiator at onset.

As has been briefly pointed out after each set of calculations the behavior of these structures obeys certain universal rules. We proceed now to a detailed comparison in order to spell out these rules explicitly.

7.5 Comparison of the MD rod, MD open trough, and the MD slitted trough

7.5.1 Comparing the MD rod and the square open trough with the same volume

The figure below shows the phase plot slopes of the two cases. It is clear that the rod crosses the lightline at a much higher frequency than the trough. Therefore, although the two cases have the same volume (4 inch squared), they do not have the same cutoff.

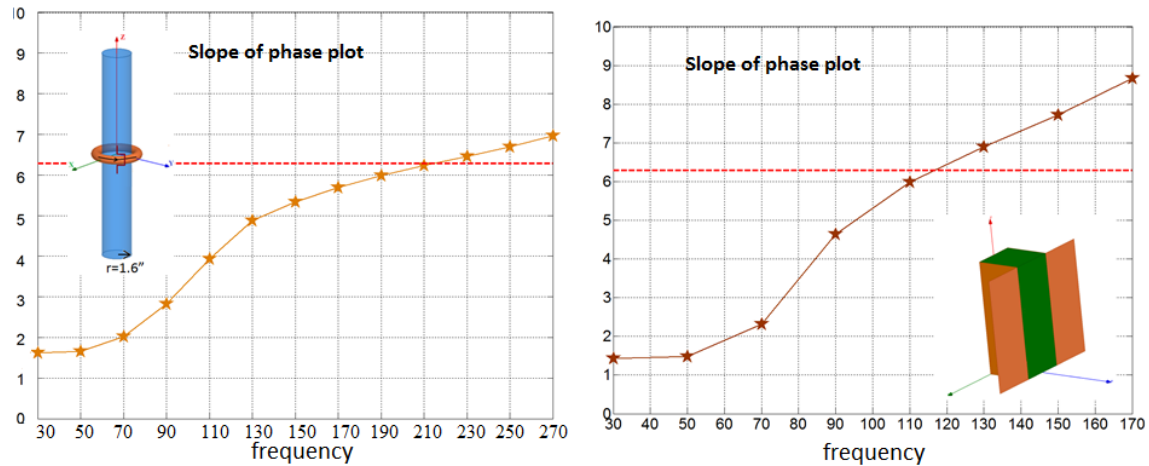


Fig. 7-60 The Slope of the Phase Plot or the β Plot of the Magneto-Dielectric Rod (Left) and the 2" \times 2" Open Trough (Right) Both Having a Material with $\mu = 80$ and $\epsilon = 2$

We have to also note that the phase slope plots are the curve of the phase versus (z/λ) . Higher slopes mean lower wave speed (slow waves) and when the curve passes 2π we have passed the lightline and into the guided wave region. To make the comparison easier, we will plot $2\pi/(\text{slope of the phase curves})$ to show the velocity of the wave compared to light. This plot can be seen below.

The trough, with the lower onset frequency exhibits a higher slope at onset.

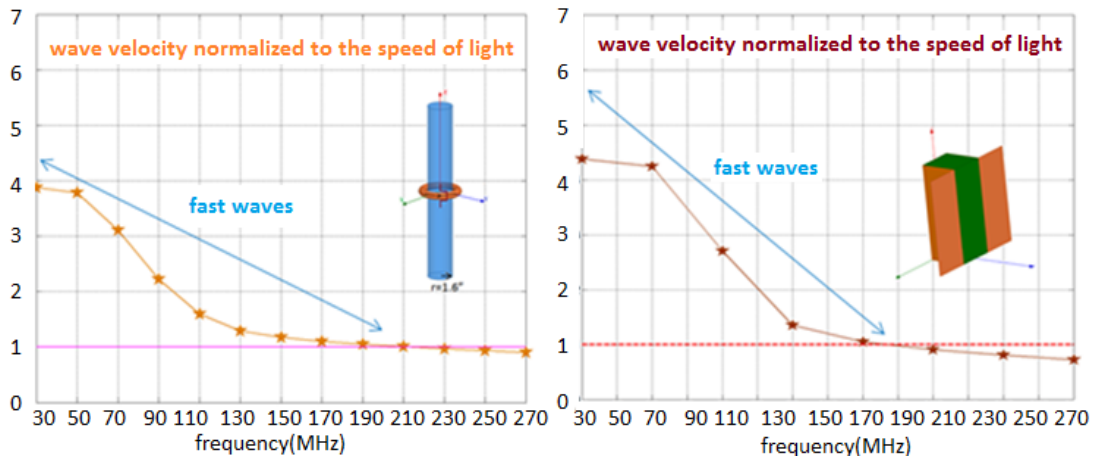


Fig. 7-61 The Wave Velocity of the MD Rod and Trough Normalized to the Speed of Light

7.5.2 Comparison of a MD open trough to the magneto-dielectric rod with both the same volume and the same cutoff frequency

Now we ask, what happens if both the volume and the cutoff frequency are the same? We have seen that for wider shallower troughs, the cutoff happens at higher frequencies. Therefore, we look for a wide trough having a 4 inch squared cross section and the same cutoff frequency as the rod with the 1.6inch radius. This occurs for a 3.8'' by 1.053'' wide trough. Thus, this trough and the 1.6inch radius rod have the same cutoff frequency (215 MHz) and the same material volume.

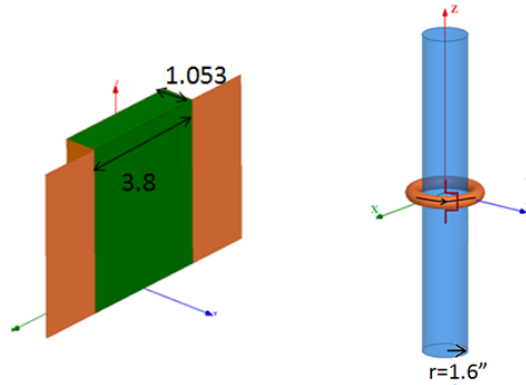


Fig. 7-62 Wide Trough and Rod Having the Same Volume and the Same Cutoff Frequency

In order to show that these two structures have the same cutoff we will plot the phase of the magnetic current for both cases (We have already plotted the phase of the rod shown but we will show it again for comparison). Fig.7-63 shows the two plots side by side. It is clear that both structures pass the light line, at the same frequency.

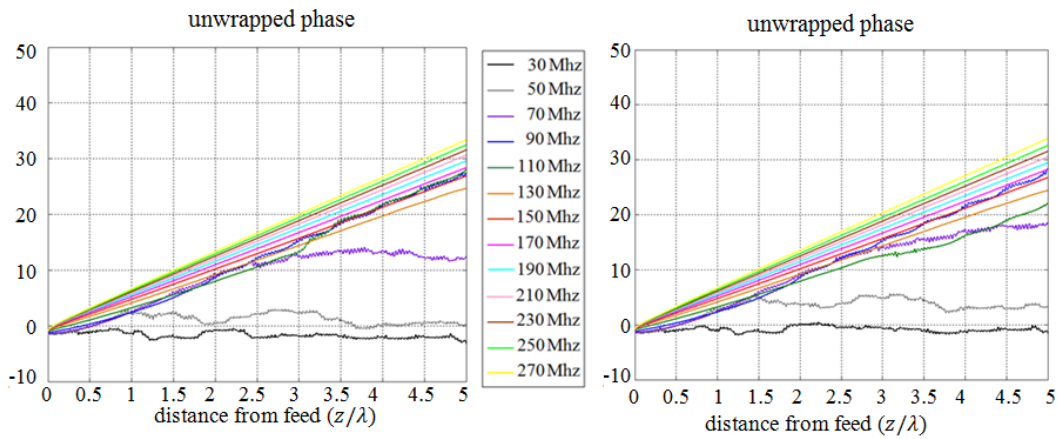


Fig. 7-63 Unwrapped Phase of the Current as a Function of the Distance from the Feed Divided by the Wavelength (z/λ) for a Magneto-Dielectric Wide Trough (Left) and a Rod with a 1.6 Inch Radius (Right) Both Having a Material with $\mu = 80$ and $\epsilon = 2$. Frequencies Go from 30 MHz to 270 MHz in 20 MHz Steps.

For a more clear demonstration, in Fig 7-64, we have plotted the phase of both structures versus (z/λ) on the same figure for frequencies from 110 MHz to 270 MHz.

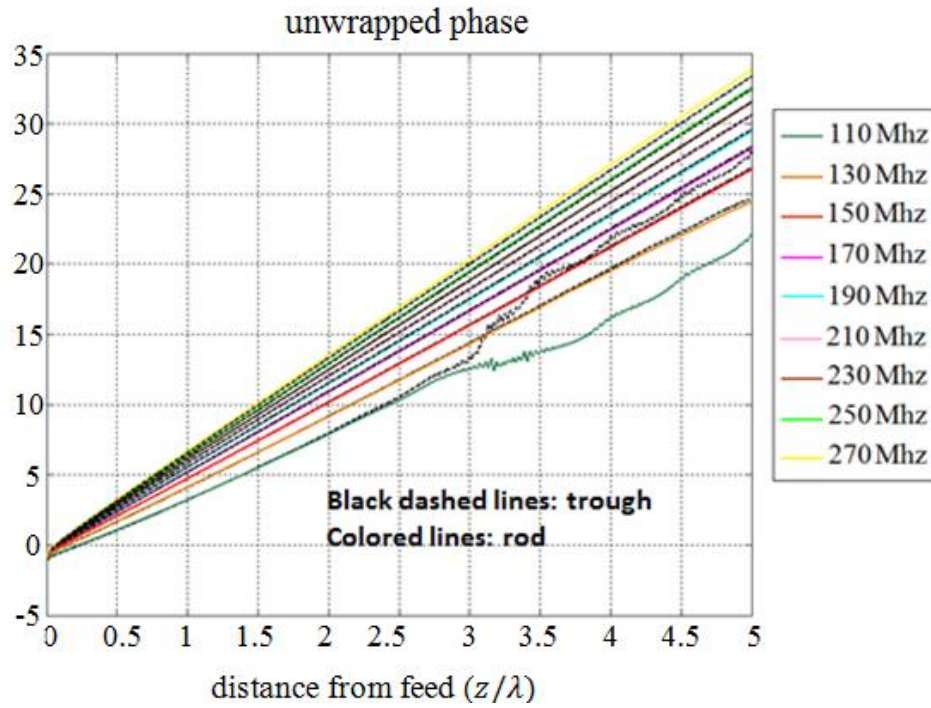


Fig. 7-64 Phase of Both Structures Versus (z/λ) on the Same Figure for Frequencies from 110 MHz to 270 MHz.

In the next figure, we see the amplitude plots of the two cases which show that they are very similar.

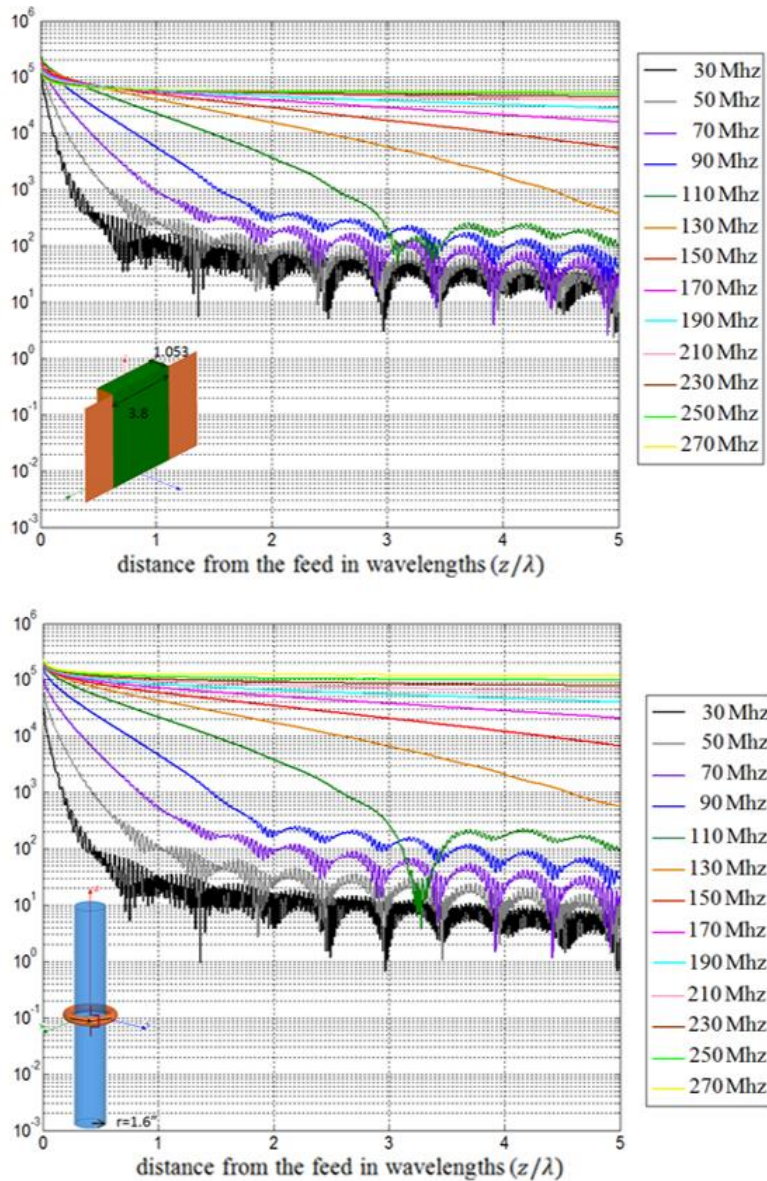


Fig. 7-65 Amplitude of the Current as a Function of the Distance from the Feed Divided by the Wavelength (z/λ) for a Magneto-Dielectric Wide Trough (Left) and a Rod with a 1.6 Inch Radius (Right) Both Having a Material with $\mu = 80$ and $\epsilon = 2$. Frequencies Go from 30 MHz to 270 MHz in 20 MHz Steps.

The next logical step is to compare the α and β plots of the MD $3.8'' \times 1.053''$ open trough with the rod with 1.6'' radius. Fig 7-66 shows the α plot of both structures (up left) and the β plots are shown in the down left plot. The wave velocity can also be

seen. These curves are essentially identical and this proves that we have discovered a universal behavior: For rod and trough flux channels, if permeability and the volume are the same and the onset frequency is the same, the omega beta diagrams will be the same.

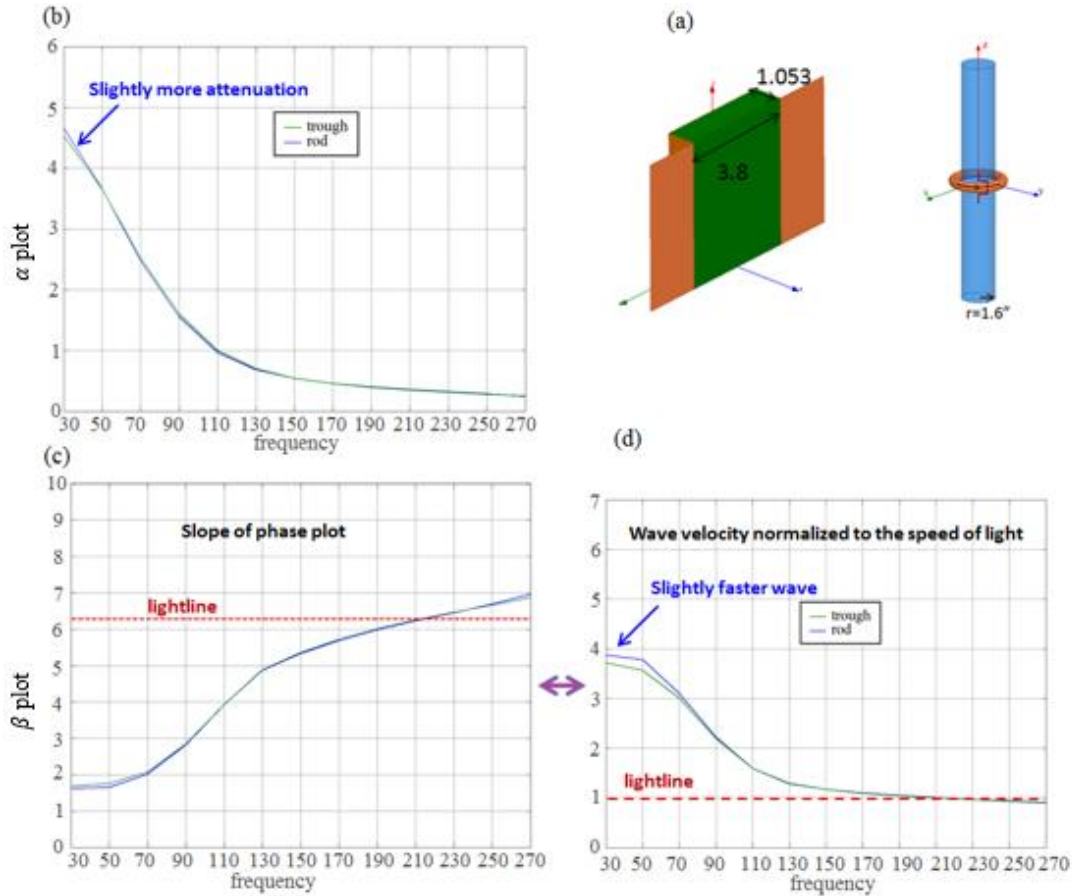


Fig. 7-66 (a) Trough and Rod with the Same Volume and the Same Cutoff (b) α Plot of Both Structures (Blue Shows the Rod and Green Shows the Trough) and (c) the β Plots of Both Structures (d) the Wave Velocity of Both Structures

The next logical step in this section is to see if the universal behavior holds even if we reduce the permeability to lower values. We will first try with a permeability of 40 and compare the wave velocity of the rod to the open trough. Since the cutoff frequency of $\mu = 40$ happens at higher frequencies compared to $\mu = 80$ we have to obtain the

phase plots at even higher frequencies. Figure below shows the phase plots of the two structures with $\mu = 40$ which are very similar. However, we will see the universal behavior much more clear as a velocity plot or a beta plot.

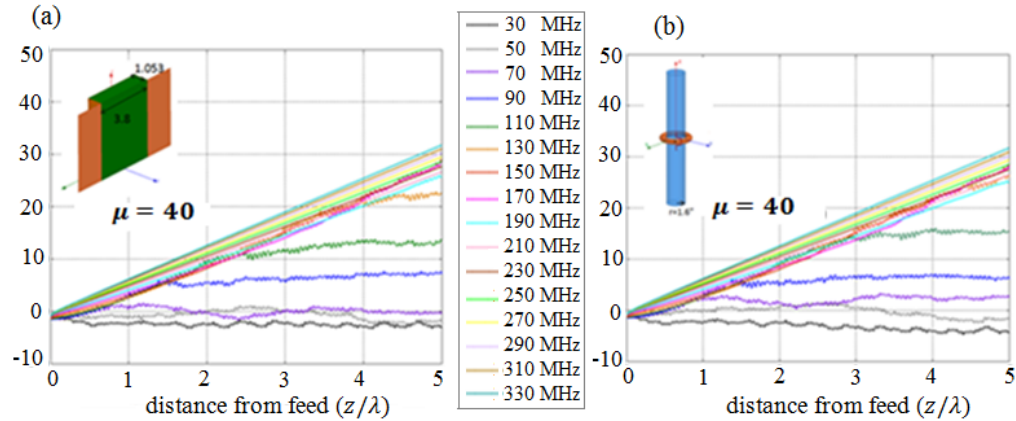


Fig. 7-67 Phase Plots of (a) Trough with the Same Volume as the Previous Figure and Half the Permeability (b) Rod with the Same Volume as the Previous Figure and Half the Permeability

Fig.7-68 shows the attenuation plot, the slope of the phase plot and the wave velocity plot of the same structures shown in Fig.7-68(a). We see that phase slope, amplitude slope and the wave velocity plots are very close which shows that the universal behavior holds even at lower permeabilities.

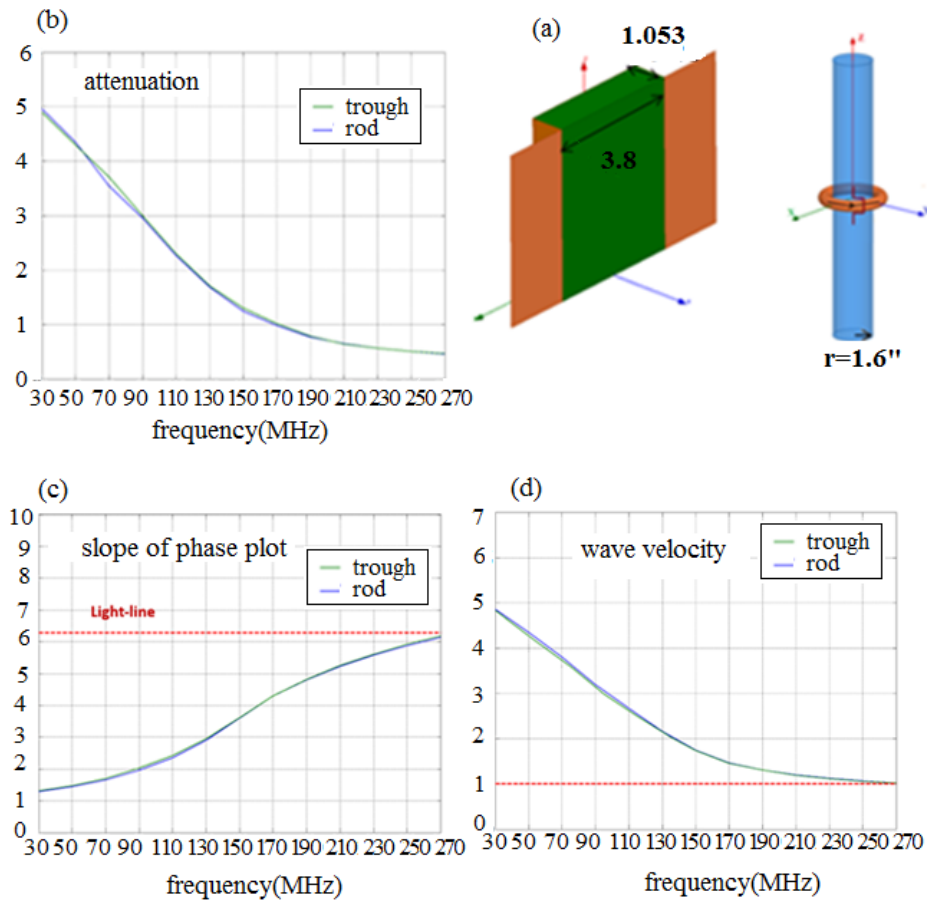


Fig. 7-68 (a) Trough and Rod with the Same Volume and the Same Cutoff (b) α Plot of Both Structures (Blue Shows the Rod and Green Shows the Trough) and (c) the β Plots of Both Structures (d) the Wave Velocity of Both Structures

As the last example to show the effect of permeability on the universal behavior, we will compare the same structures at even lower permeability of 20. Fig. 7-69 shows the phase plot and the wave velocity plot of the two structures having a permeability of 20 which shows that even in lower permeabilities we will still have the universal behavior as long as both the material volume and the cutoff frequency of the magneto dielectric rod and open trough are the same.

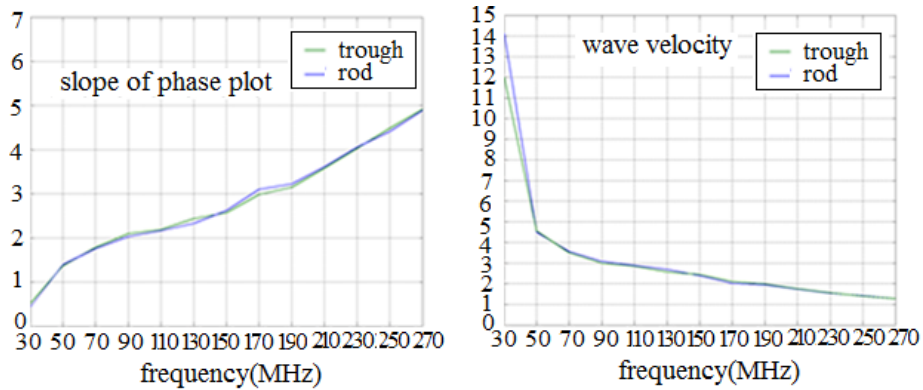


Fig. 7-69 (a) β Plots of Both Structures with the Same Volume as the Previous Figures and $\mu = 20$ (b) the Wave Velocity of Both Structures with the Same Volume as the Previous Figures and $\mu = 20$

We have showed that even at much lower permeabilities we still have the universal behavior. However, we will show that in order to have a universal behavior we don't need the permeability and the volume of the structures to be equal and it is enough to have a rod and an open trough with the same permeability \times volume (that is, permeability times cross sectional area). Figure below shows two structures: The same MD rod as before, having a radius of 1.6" with the permeability of 80 and the other one is a trough with 1/4th of the permeability but 4 times the volume.

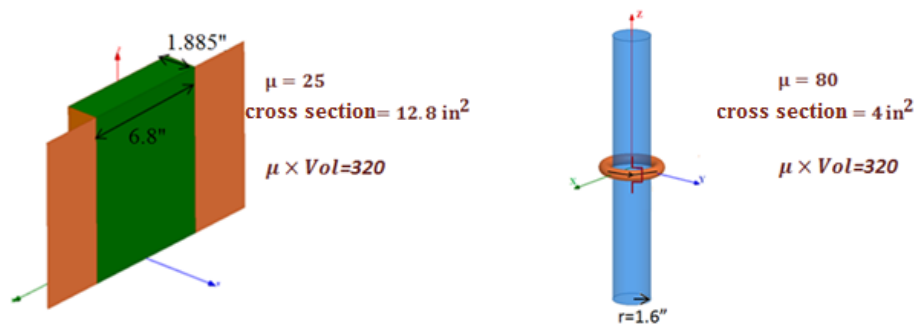


Fig. 7-70 (a) β Plots of Both Structures with the Same Volume as the Previous Figures and $\mu = 20$ (b) the Wave Velocity of Both Structures with the Same Volume as the Previous Figures and $\mu = 20$

In Fig.7-71 the phase plots of the two structures have been plotted which shows that they are very similar. However, in order to show the universal behavior more clearly we will plot them in the same figure.

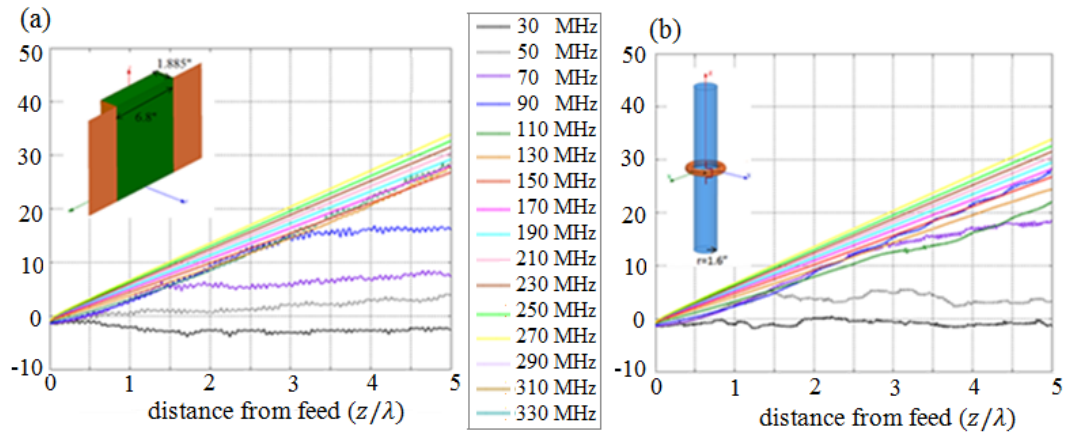


Fig. 7-71 Phase Plots of (a) Trough with 12.8 Inch Squared Cross Section and $\mu = 25$ (b) Rod with the Same Volume as the Previous Figure $\mu = 80$

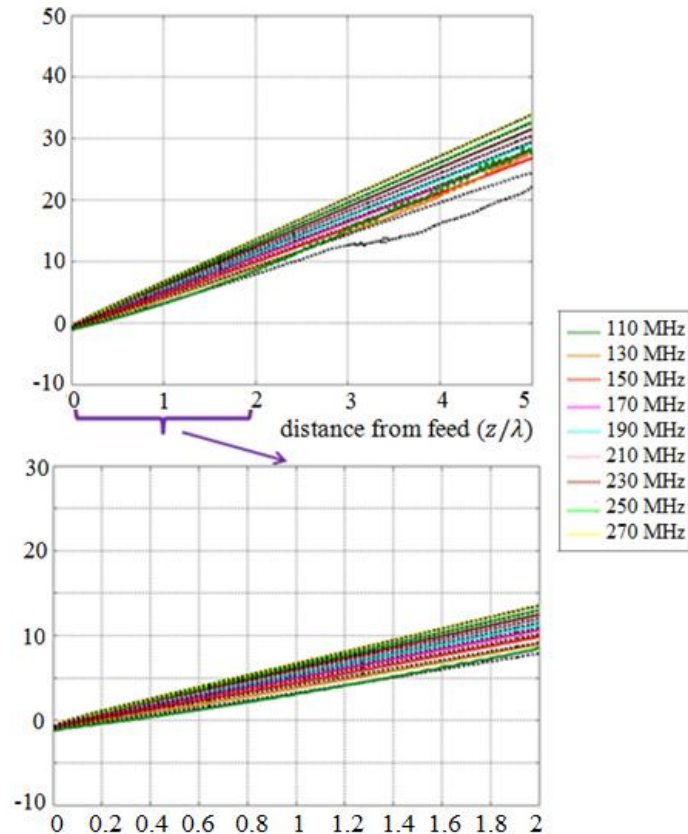


Fig. 7-72 Phase Plots of the Trough with 12.8 Inch Squared Cross Section and $\mu = 25$ Rod with the Same Volume as the Previous Figure and $\mu = 80$ Plotted in the Same Figure. We Can See They Are Overlapping the Colored Lines Show the Trough and the Dashed Black Lines Show the Rod

Similar to what we did before, the slope of the phase plot and the wave velocity plot of the two structures are shown below. This shows that as long as the value of the permeability \times volume (or more precisely permeability times area) for the open trough and the rod are the same, we can find specific dimensions for the trough that would result in the exact same behavior as the rod. The different choices of the dimensions of the trough give us an additional degree of freedom compared to the rod.

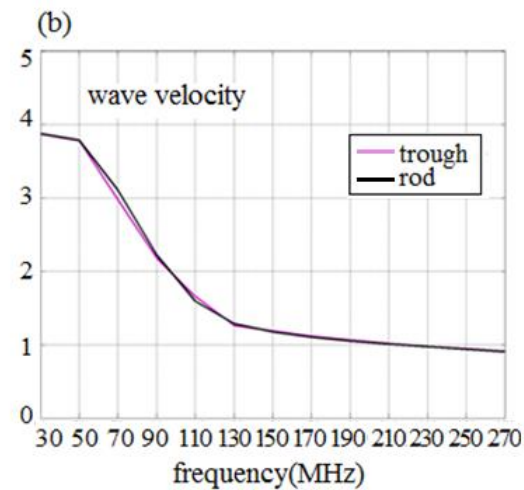
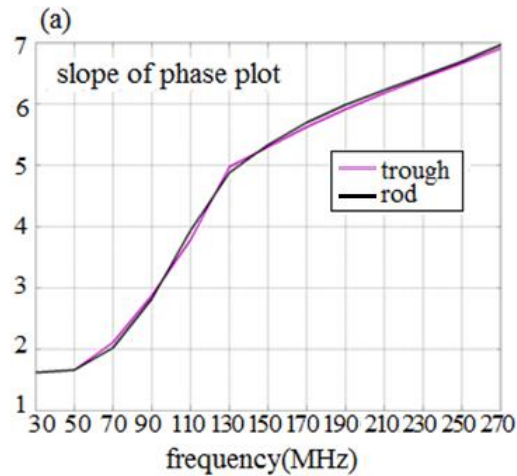


Fig. 7-73 (a) β Plots of the Rod and the Trough Having the Same Permeability \times Volume (b) the Wave Velocity of the Rod and the Trough Having the Same Permeability \times Volume

Another important comparison is the bandwidth of the trough compared to the rod. We had proven that the fractional bandwidth about onset of the rod is constant, independent of the particular rod diameter and permeability, so we will plot the bandwidth of the trough versus aspect ratio for troughs that have the same onset frequency as the rod. The point shown with the star is the aspect ratio that is equivalent to

the rod (from Fig.7-72) so we are normalizing to the bandwidth of the rod. The data is fitted to a line passing zero therefore we can write:

$$BW_{new} = \frac{a_{new}}{a_{base}} \times BW_{base} \quad (7-33)$$

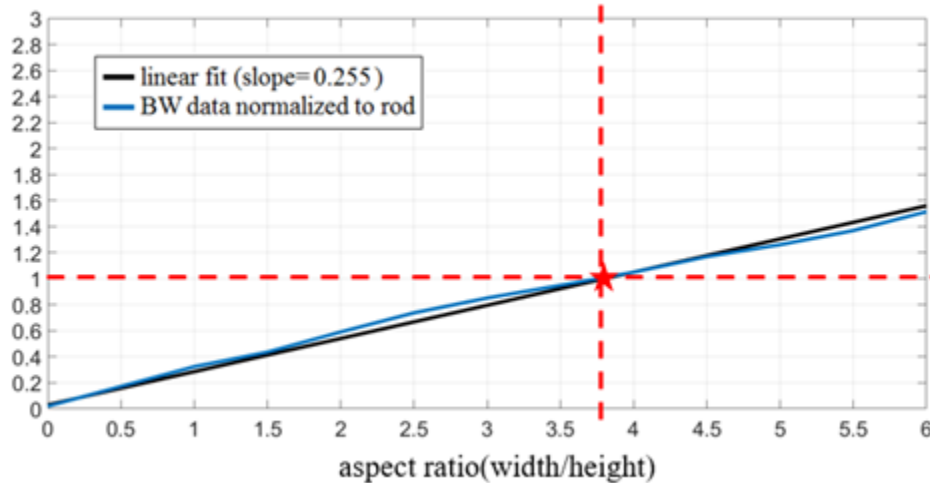


Fig. 7-74 Normalized Bandwidth vs Aspect Ratio of the Trough and Fitted Line

This means that unlike the rod, the bandwidth of the open trough can be tuned by using the aspect ratio. However, increasing the aspect ratio means increasing the volume and makes the antenna more expensive, yet this is part of an engineering trade-off decision because in almost all applications our goal is to maximize the bandwidth.

As a result of comparing the open trough with the magneto dielectric rod we have found out that the open trough gives us an additional degree of freedom compared to the MD rod. The slitted trough gives us even more degrees of freedom. The most general form however would be a designable admittance surface surrounding the magneto-dielectric flux channel. The trough geometry can make all this possible. Before moving to

comparing the slitted trough to the two other structures we will add a flow chart that shows our choices in designing an antenna.

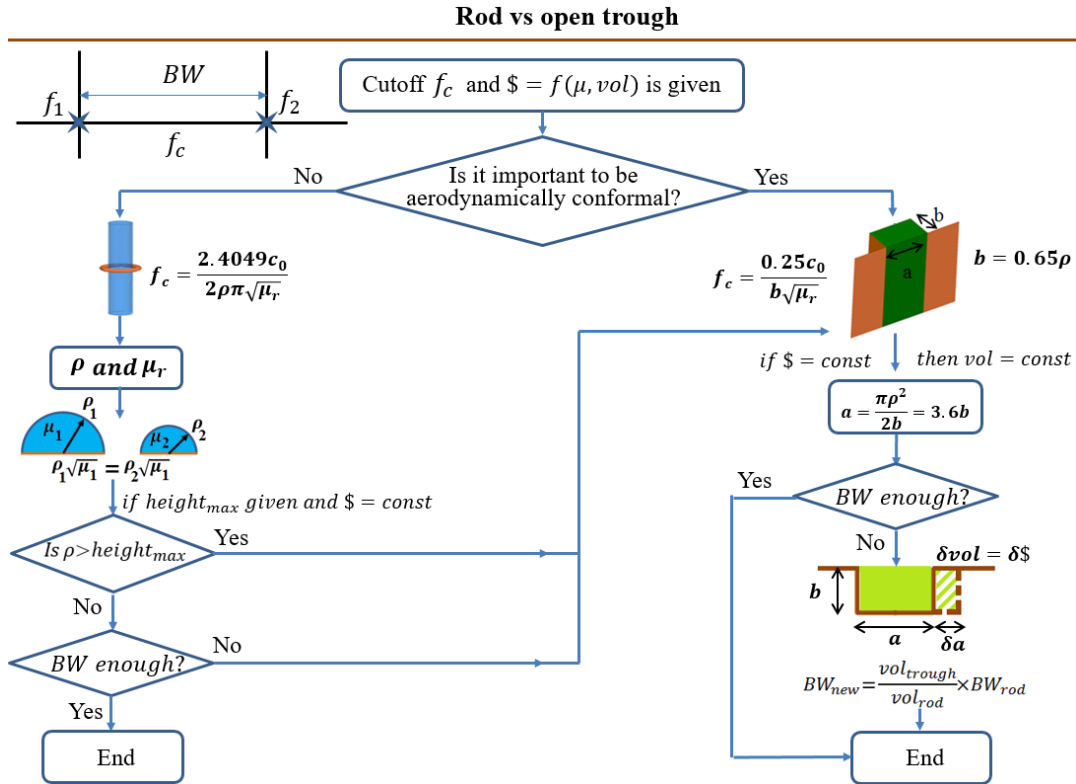


Fig. 7-75 Flow Chart Showing Our Choices in Designing the Rod and the Open Trough Antenna.

What this flowchart shows is that if we have the cutoff and a certain maximum for the permeability and the material volume. The rod radius and the permeability can be set depending on the project specifications. If for a certain permeability we need a lower height for the antenna, we need to use the trough since it is shallower. Also if we need more bandwidth we need to use the trough because the bandwidth of the rod is constant but we can tune the bandwidth of the trough with the aspect ratio. However increasing the

aspect ratio means that we would need more material which makes the structure more expensive. This can be solved with the slitted trough geometry.

In the previous figures we had plotted the slope of the phase plot , or the β plot, and the wave velocity plots. These plots showed that as long as the value of the permeability \times volume (or cross-sectional area) for the open trough and the rod are the same, the extra degree of freedom of the open trough allows us to find specific dimensions for the trough that would result in the exact same behavior as the rod. This means that as long as we are not limited by how wide the trough can get we can achieve the same behavior as the rod by using a material with a much lower permeability.

In general, lower permeability means a less expensive material therefore the importance of this phenomenon is that it is possible to use a much less expensive material (however more volume of it would be needed) and achieve a conformal structure that has the same behavior as a magneto dielectric rod using a much more expensive material. Alternatively, the choice can lead to finding a light weight solution for a particular application. For instance, for frequencies below VHF, high permeability ferrites are available but, being ceramics, they are heavy. Laminated ferromagnetic alloy permeable materials can attain moderate permeabilities with a small amount of metal per unit volume, so that their effective mass density is much lower than a ceramic. Therefore, by designing the antenna based on a lower permeability laminate, the weight can actually be reduced.

Although we have shown that it is possible to achieve the same behavior as the rod with an open trough with much lower permeability, the price we pay is the increase in

the trough's cross section. In this section we will show that we can use the extra degree of freedom of the slitted trough to achieve the same cutoff frequency as the rod with the same cross section and lower permeability. We have to take note that in the cases that will follow, the permeability \times volume of the open trough and the slitted trough is much smaller than the rod therefore we don't expect them to have the exact same behavior in all the frequency range of interest. However, we can achieve the same onset frequency as the rod with much lower permeability and all the interesting behavior occurs precisely near onset. We expect the price we pay to be the bandwidth.

The figure below shows four different geometries; the rod with $r=1.6''$ and $\mu = 80$ as a reference (which had the same results as the open trough with the width of $3.8''$ and depth of $1.053''$ and $\mu = 80$), open troughs with $\mu = 25$ and $\mu = 15$ and a slitted trough with $\mu = 15$. All these structures have the same cross sections and the same cutoff frequency however the permeability \times volumes (cross section) of the four cases are different. This value is shown as $\mu \times S$ in the figure

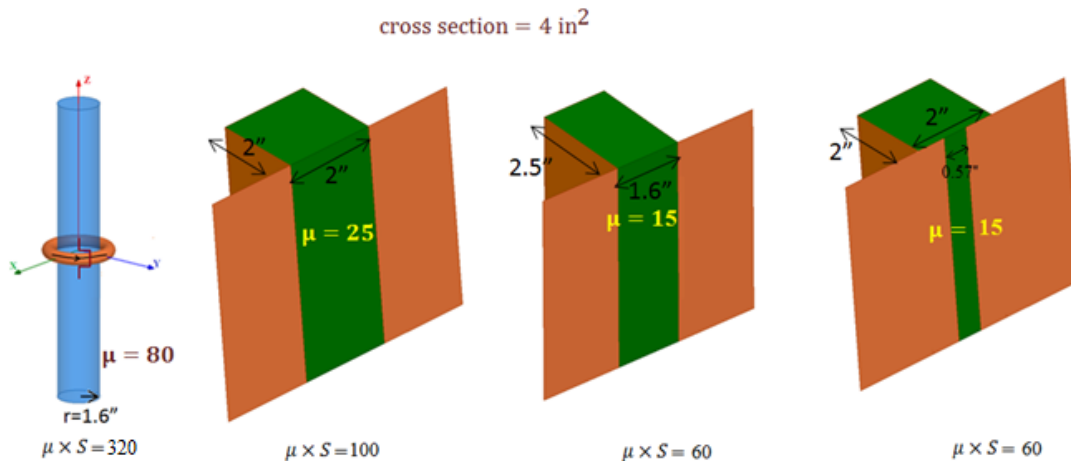
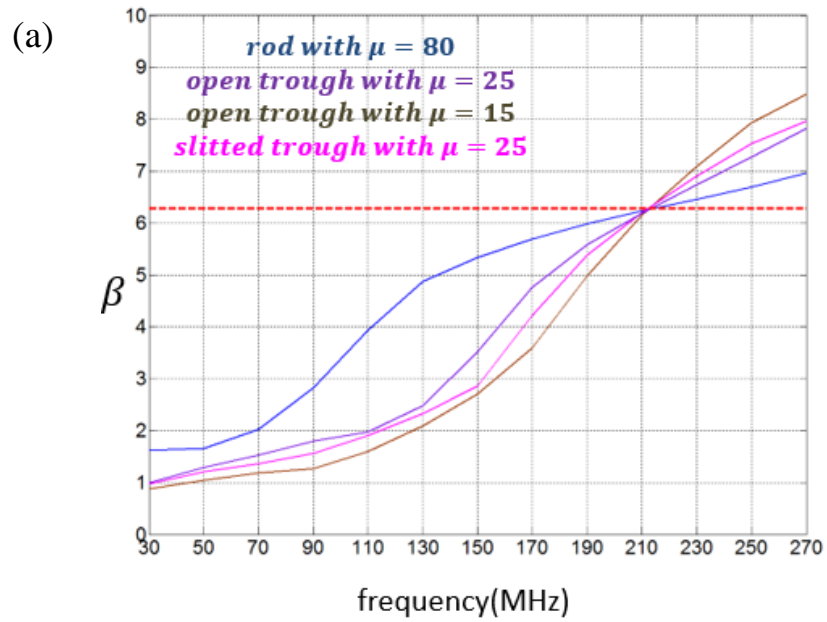


Fig. 7-76 Structures Having the Same Volume (Cross-Section) , and the Same Cutoff Frequency But

Different Values of Permeability \times Cross Section

An important fact that has to be pointed out is that with a specific value for the permeability of the open trough for example ($\mu = 25$), there is only one specific choice of width and depth dimensions for the open trough to get a certain cutoff frequency and keep the same volume. However, the slitted trough has another degree of freedom which is the width of the slit which means that the dimensions of the slitted trough shown is not necessarily the only dimensions that gives the desired cutoff.



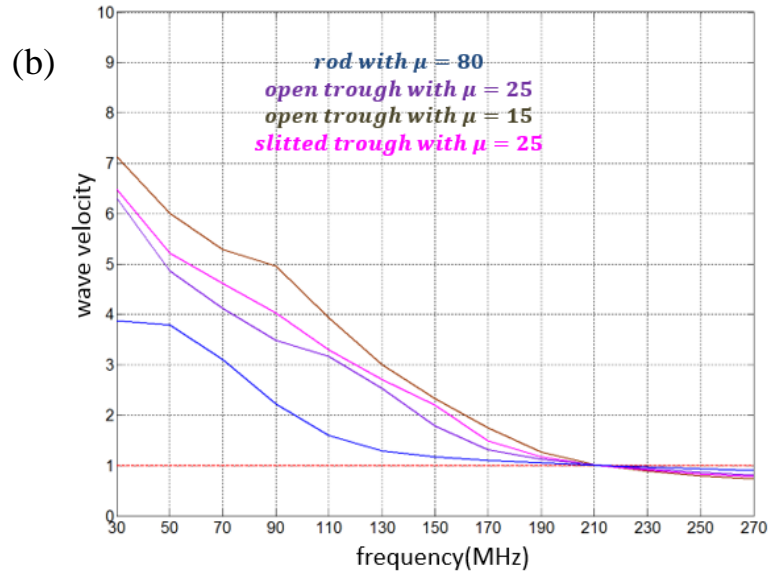


Fig. 7-77 (a) β Plots of Four Structures (b) the Wave Velocity of Four Structures

From the previous figure we can see that although all four cases have the same volume and the same cutoff frequency, the structure with higher permeability \times cross section, which is the rod, has the smallest slope as it passes the light line. This means that although we have the same cutoff frequency we have smaller bandwidth. Another example can be seen in the following figures which shows three different geometries; the rod with $r=1.6''$ and $\mu = 80$ as a reference (which had the same results as the open trough with the width of $3.8''$ and depth of $1.053''$ and $\mu = 80$), an open trough with $\mu = 40$, and a slitted trough with $\mu = 40$. All these structures have the same cross sections and the same cutoff frequency however the permeability \times volumes (cross section) of the three cases are different. This value is shown as $\mu \times S$ in the figure

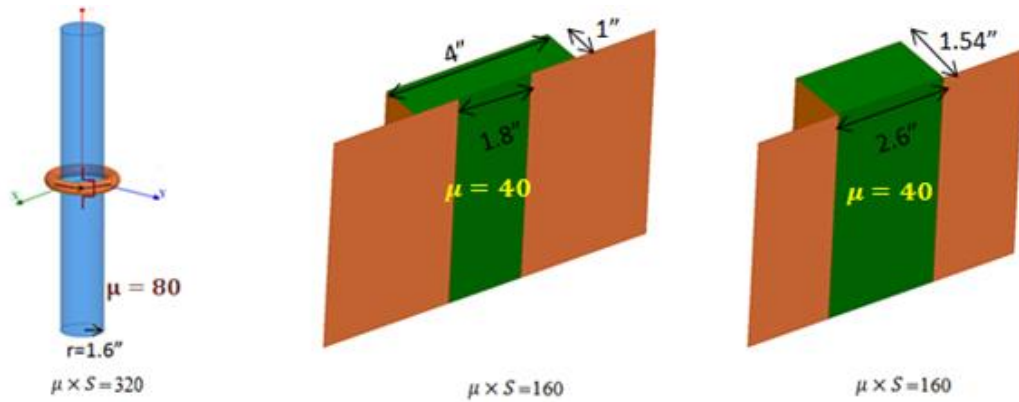
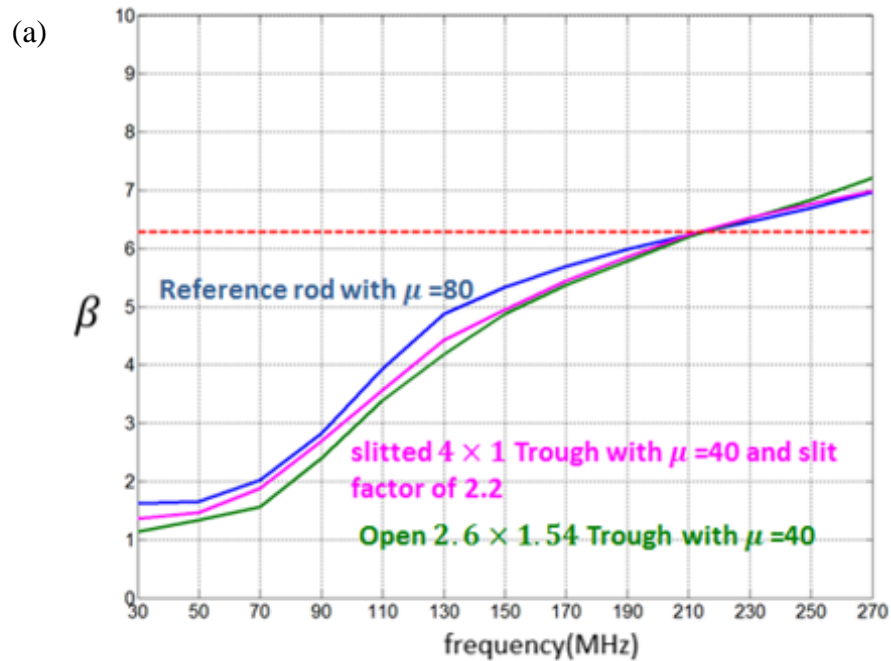


Fig. 7-78 Structures Having the Same Volume (Cross-Section) , and the Same Cutoff Frequency But Different Values of Permeability \times Cross Section

In this case the high permeability rod still has the shallowest slope but only marginally. In fact, for practical purposes all three designs have essentially the same bandwidth. Therefore, the aspect ratio of the trough and the dimension of the slit can be used to improve the bandwidth of the antenna without being wholly constrained by the permeability-cross-sectional-area product.



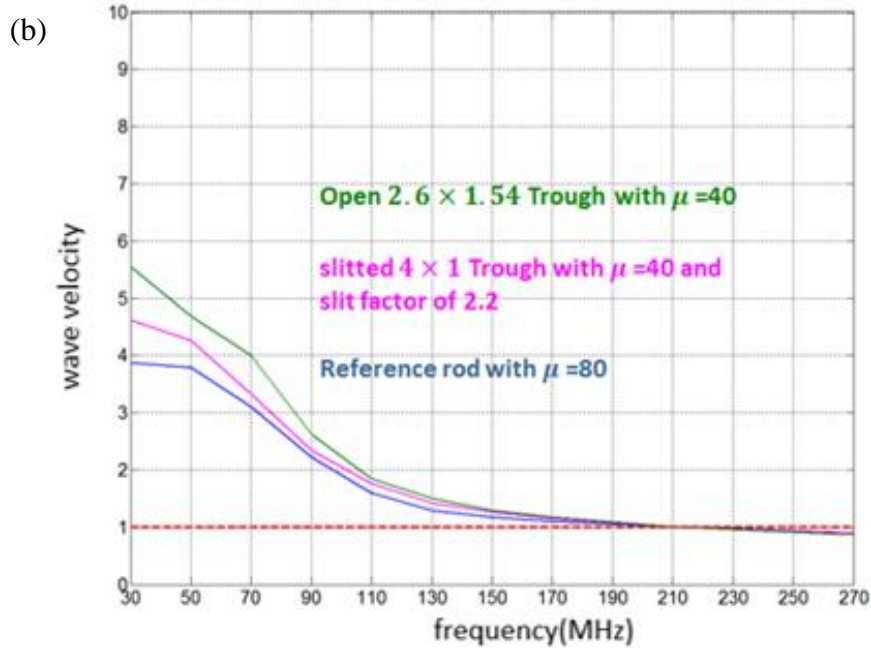


Fig. 7-79 (a) β Plots of Three Structures (b) the Wave Velocity of Four Structures

However, when we use all the degrees of freedom at the same time: permeability \times cross section, trough aspect ratio, and slit width, we can obtain extremely wide bandwidth. A comparison between the slitted trough and the open trough with the same cutoff frequency, volume, and permeability demonstrate this.

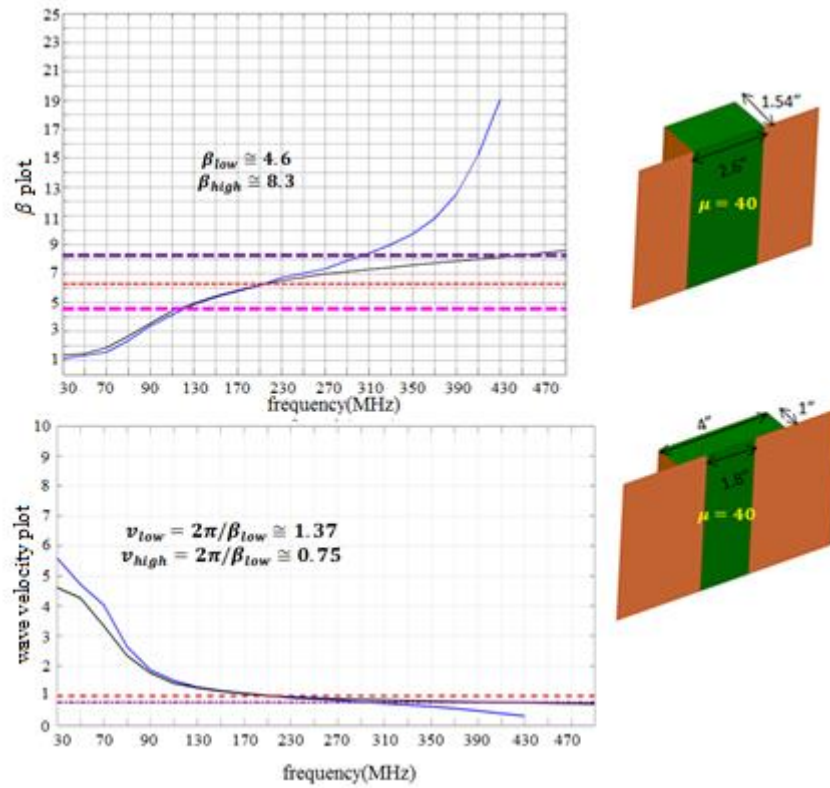


Fig. 7-80 β Plots of and Wave Velocity Plot of the Open Trough and the Slitted Trough with Same Onset Frequency

Fig 7-80 shows that the slit can help to achieve a much larger bandwidth. In order to do a final comparison between the open trough and the slitted trough we will plot the radiated power and compare the bandwidths.

Fig 7-81 shows the radiated power of the open trough and the slitted trough with the same volume, same permeability, and the same cutoff frequency. In this figure it is clear that the slit can help to achieve a much larger radiation bandwidth.

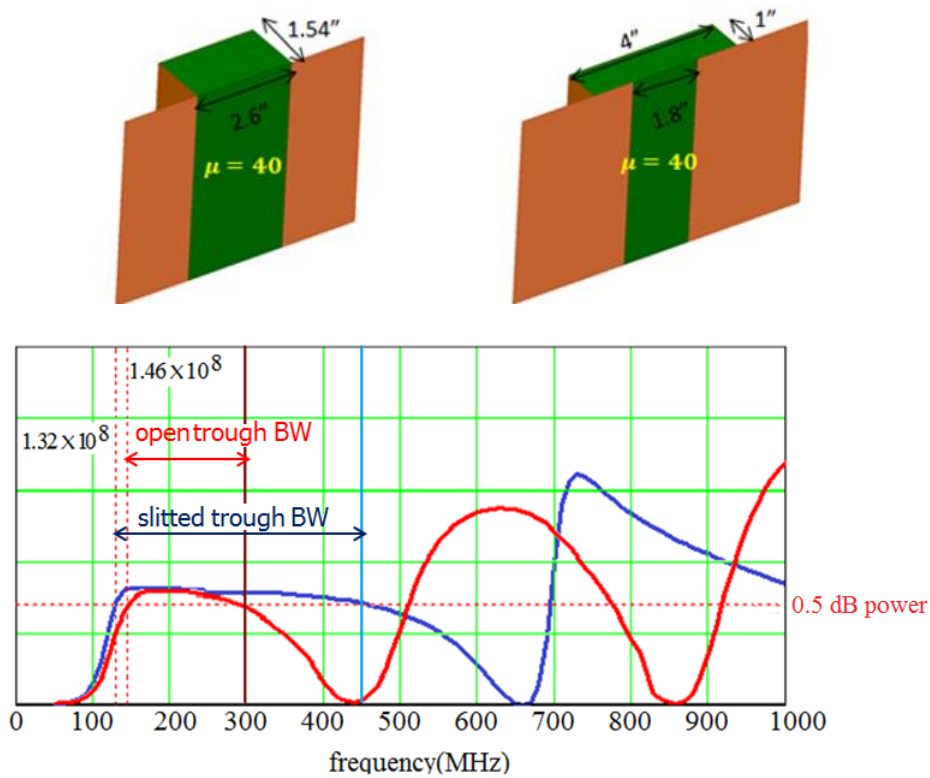


Fig. 7-81 β Plots of and Wave Velocity Plot of the Open Trough and the Slitted Trough Showing Enhanced Radiation Bandwidth

To recapitulate the key results from this investigation, let's compare our initial 1.6" rod, its equivalent open trough and the slitted trough.

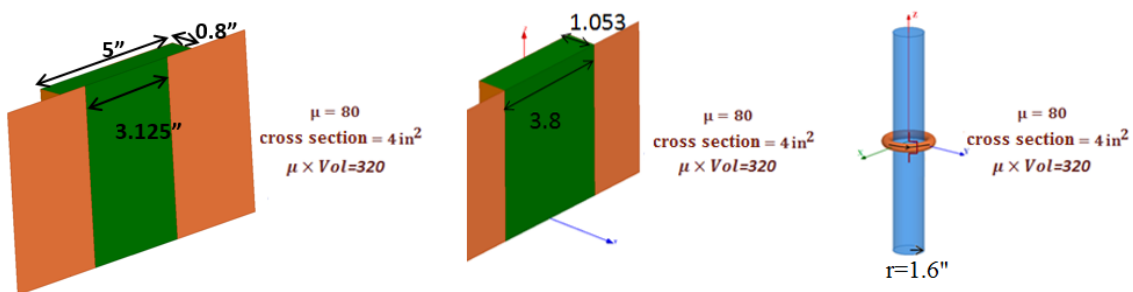


Fig. 7-82 Three Permeable Channels with the Same Onset Frequency and Same Permeability Times Cross Section Product.

Fig 7-83 shows the radiated power of the initial rod, its equivalent open trough and the slitted trough with the same volume, same permeability, and the same cutoff frequency. In this figure it is clear that the slit can help to achieve a larger bandwidth while both the open trough and the slitted trough have additional degrees of freedom.

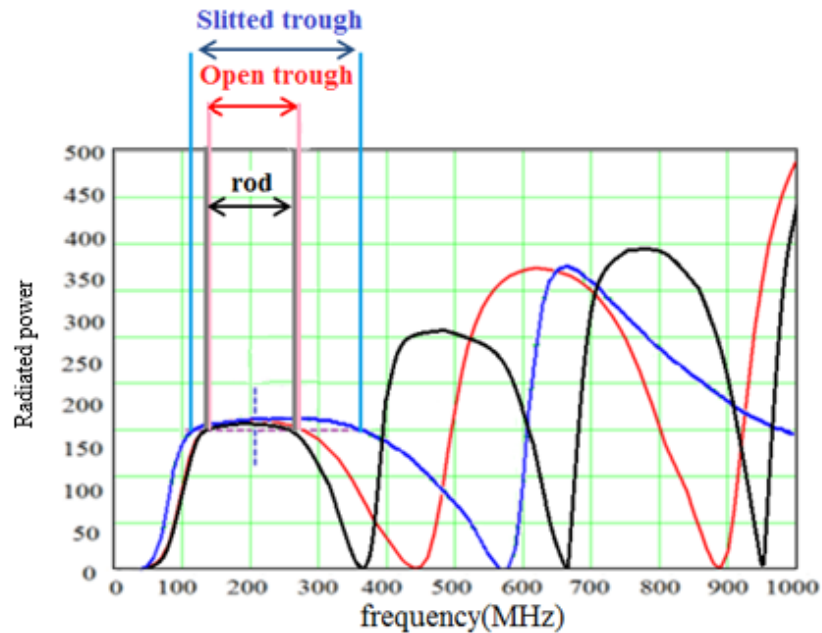


Fig. 7-83 Radiated Power Versus Frequency of the Permeable Channels of Figure 7-82 Showing the Enhanced Bandwidth Available with the Slitted Trough Structure

Before going to the final conclusion, we will add a flow chart that compares all three structures. What this flowchart shows in addition to the previous flowchart is that if we want to increase the bandwidth and not increase the volume, our only choice is the slitted trough. At the same time the slitted trough is shallower and has more degrees of freedom.

An important factor in designing these antennas and ensuring they have a large bandwidth is using a feed mechanism that helps to guide the feed current (and therefore the magnetic current of the antenna) along the structure at nearly the speed of light. This band of frequencies (when the speed of light is within c_0 by +/- 30%) coincides with the band of frequencies where the antenna radiates most efficiently. The parallel solenoid was used as a flux binding mechanism that by the nature of its TEM two-wire line transmission line geometry also had this property of inducing the magnetic current wave near the speed of light. The trough geometry with an admittance surface at its mouth (in the cases demonstrated, a capacitive slit) is the most general manifestation of this concept.

The natural evolution of the previous work on magnetic antennas is the trough metalized channel. The metalized channel geometry has several useful features: First, it enables the antenna to be absolutely conformal to the aerodynamically designed outer mold-line of its platform. The incursion into the inner mold-line is already known to be vastly smaller than any conventional cavity backed antenna. Second, the trough geometry maximizes the strength of the magnetic current in the flux channel by maximizing the number of favorable images of the magnetic current in the surrounding metal. Third, at the same time the trough, and particularly the slit design, pulls the guided TE₀₁ wave at towards the surface of the channel thus extending the frequency band over which the guided wave travels close to the speed of light and maximizing the bandwidth of operation.

The trough structure has enabled us to create a structure where source excitation, flux binding, and tailoring of the frequency response of the guiding surface can be tuned and controlled while the structures can be conformal to any surface.

In addition, we have shown that a fullwave analytic Green function formulation for the trough enables us to rapidly understand the changes induced by variations in materials and dimensions of the flux channel features without having to resort to brute force general purpose computational electromagnetics simulators, such as using ANSYS HFSS.

Although this Green function formulation is much faster than CEM methods, it is still not the simplest closed-form model of the channel. Because engineering rules of thumb are easiest to understand and developed when the theory has been reduced to its simplest form we continue this study in the next chapter. In this next chapter we obtain the $\omega - \beta$ diagram using the simple and readily accessible transverse resonance method and then confirm it (and establish its range of applicability) using a fullwave CEM simulation method. The results obtained from these two methods will be compared to the analytic Green function method, and the leaky wave and guided wave regimes of the antenna structure will be presented and studied in full detail

CHAPTER 8

DISPERSION FEATURES OF THE OPEN TROUGH AND SLITTED TROUGH IN BOTH BOUND-WAVE AND LEAKY-WAVE REGIONS

*“Every word or concept, clear as it may seem to be,
has only a limited range of applicability.”*

Werner Heisenberg

8.1 Introduction

In the previous chapter we introduced the open trough and the slitted trough as the natural evolution of the work done in the previous chapters and as the first step into achieving the optimum permeable flux channel for all magnetodielectric antennas. An analytic Greens function solution had also been obtained in the previous chapter that led to a very detailed understanding of these metalized flux channels. In this chapter, we will go much further into understanding the behavior of the metalized flux channel and present different methods of studying the dispersion diagram of the antennas.

The dispersion features of structures like permeable rods, troughs, and other open electromagnetic waveguides can usually be divided to guided wave regions and leaky wave regions. There have been extensive studies on the guided mode characteristics of many open electromagnetic waveguides however the behavior of the leaky wave region is relatively unknown especially at lower frequencies.

In the previous chapter we studied a trough filled with a permeable material that had μ_r and ϵ_r ($\mu_r \gg \epsilon_r$) and we assumed the material was frequency independent and

homogeneous. In this section, we will present a solution for this structure obtained from fullwave simulation using HFSS. The feed that is defined in HFSS, a coax going from one side of the trough to the other side, will cause a voltage at the top center of the channel which in turn will excite an electric field inside the trough that looks like Fig. 8-1 below.

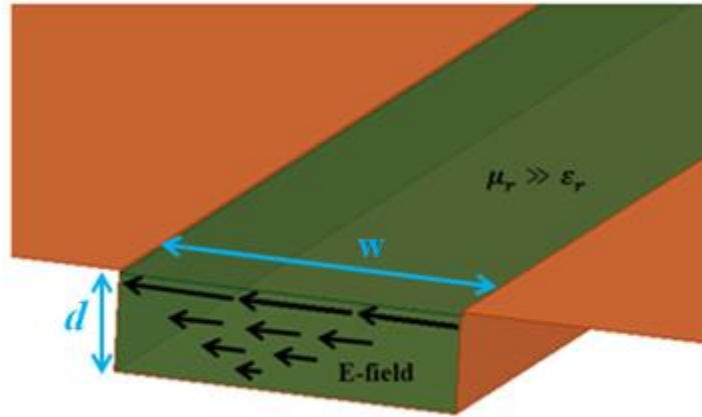


Fig. 8-1 An Open Trough with Isotropic Permeable Material

This lowest order mode is uniform in the transverse direction and has a maximum at the interface of the material and free space, and drops in strength as we go down and get close to the metal at the base of the trough. This mode is essentially half of the TE₀₁ mode of the rectangular waveguide of width w and full height $2d$.

The principal magnetic field then flows along the channel (out of the figure) constituting the radiating magnetic current. In general, the width w is small compared to the wavelength and the surface wave onset frequency is determined only by the depth of the trough and the composition of the material. As we have seen, the radiation band occurs when the flux channel supports its guided wave close to the speed of light (nominally within +/- 30%). The optimized channel would then be one that does this with

minimized loss over a maximized frequency bandwidth. It has already been shown that for a given depth (onset frequency) the wider the trough (the more material is used), the wider the frequency band over which the guided wave in the neighborhood of onset travels close to the speed of light.

When the distance d is approximately a quarter wavelength in the material, this material can guide the wave. If we are at lower frequency in which $d < \lambda/4$ the wave is not truly guided since the wave in space is not decaying exponentially (the wave outside is not evanescent) and therefore the structure radiates. However, if we go to higher frequencies in which $d > \lambda/4$ then we have an exponentially decaying solution outside and the wave is increasingly bound. The guided wave onset frequency is defined as the frequency at which the structure can start guiding waves, it is the boundary between these two regions: Below that frequency we are in the leaky wave region and above that we are in the bound wave region.

As we had seen in the previous chapter, the onset is very important since near onset the wave travels very close to the speed of light, and our goal is to operate in as large a frequency range as possible with near-light speed propagation so that the permeable channel fully emulates the dual of conventional free-space metal antennas. As would be expected, it is in this frequency range that the channel naturally radiates efficiently.

Why is radiation less efficient outside this (+/- 30% band) At higher frequencies, the waves are too tightly bound (too slow to radiate even at discontinuities) and in lower frequencies the wave is a leaky wave with phase velocity higher than the speed of light so

that the energy input into the channel tends to radiate out immediately from the “feed” region, and the antenna does not have maximal length. Beyond these limitations, the other concern common with wide band antennas is the suppression of parasitic higher order modes. By feeding the flux channel at its top center position we are already applying a mode suppression philosophy because such a symmetric feed favors the TE_{0n} modes over TE_{mn} modes with transverse variation.

This ability to increase the operational frequency band without changing the onset frequency (at the expense of adding material) makes the trough implementation of the magnetic flux channel superior to the flux channel that results from simply placing the permeable material on top of the ground plane. (This added degree of freedom arises because the rectangular metal wall geometry constrains more strongly the polarization of the Electric field inside the material, making the lowest order mode inside the trough similar to a Cartesian TE_{01} waveguide mode inside the material as opposed to the more general (cylindrical dielectric-rod like) Bessel function field structure in an open flux channel. The difference is illustrated below:



Fig. 8-2 Difference Between the Electric Field in a Trough and an Open Flux Channel

In order to see this behavior very clearly we simulate a trough with the same homogenous and isotropic material that was seen in the examples of the previous chapter

using HFSS and we will compare the results obtained from HFSS to the results obtained from the transverse resonance method and to the Greens function method and we will keep in mind that the results from HFSS are the most realistic results that take into account all the higher order modes excited at the feed since it is a fullwave simulation. The HFSS method gives the most correct results and takes the most time to analyze. The transverse resonance method code takes a very short time to run but gives the correct dispersion diagram in a smaller frequency range about onset. However, it is a very good engineering design tool because its range of applicability coincides with the operating band we are after. The comparisons will show the use of different methods and when and why they deviate from each other.

Later we will see the effect of adding vertical conducting walls to the homogenous isotropic material inside the open trough and the slitted trough and see how those walls which are modeling an anisotropic material would change the dispersion diagram behavior. At this point the permeability is effectively a tensor. The metal plates turn out to be desirable because they suppress higher order modes with transverse variation that show themselves in higher frequencies.

There have been a number of studies about the different regions of the dispersion diagram however many of them don't discuss the range of frequencies in which the transverse resonance method (TRM) solutions are applicable. Oliner [31, 32], has done studies on bound-wave and leaky-wave ranges for open guiding structures and the dispersion diagrams have been plotted that shows both regions. As an example, [33], the

dispersion diagram for a dielectric-loaded open guiding structure obtained by Oliner can be seen below

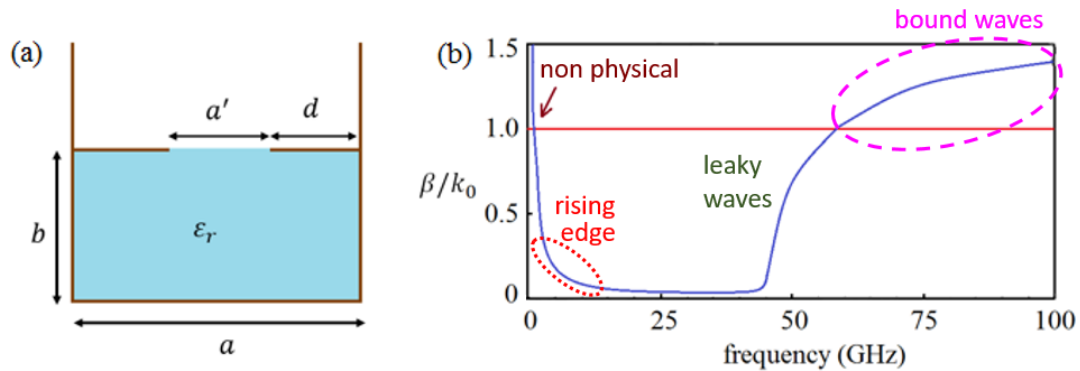


Fig. 8-3 (a) Cross Section of the Partially Dielectric-Loaded Millimeter-Wave Antenna (b) Dispersion Plot Over a Very Wide Frequency Range for the Structure Shown in Fig. 8-3 (a) When $a = 2.20$ mm, $a' = 1.00$ mm, $b = 1.59$ mm, $d = 0.10$ mm, and $\epsilon_r = 2.56$.

The dispersion plot shows that at higher frequencies we have bound waves that travel slower than the speed of light and when it crosses onset, the waves are leaky which travel faster than the speed of light. However, at lower frequencies the β plot turns around and again crosses 1 (indicating slow leaky waves) which is clearly unphysical.

The questions that needs to be answered is: At what frequency does the TRM solution to the dispersion relation become unphysical? An easy answer that has been repeated in publications [34] is the point at which it passes 1. However, a closer look at the dispersion diagram shows a rising edge which is not expected to happen when we are dealing with fast waves.

Another example is the solution given for the guided and leaky waves in a circular dielectric rod waveguides in the dissertation by Kim [34]. In this reference, the author has tried to solve the complex characteristic equation obtained as follows [34] :

$$\left[\frac{\varepsilon_{r1} J'_m(k_1 a)}{k_1 J'_m(k_1 a)} + \frac{\varepsilon_{r2} K'_m(k_2 a)}{k_2 K'_m(k_2 a)} \right] \left[\frac{\mu_{r1} J'_m(k_1 a)}{k_1 J'_m(k_1 a)} + \frac{\mu_{r2} K'_m(k_2 a)}{k_2 K'_m(k_2 a)} \right] \quad (8-1)$$

$$= \left[\frac{m\beta}{k_0 a} \left(\frac{1}{k_1^2} + \frac{1}{k_2^2} \right) \right]$$

Where ε_1 and ε_2 are the dielectric constants of the dielectric and free space regions, respectively, μ_1 and μ_2 are the relative permeability of the dielectric and free space regions, respectively and k_1 and k_2 are the propagation constants in the transverse direction.

As stated in the dissertation, the complex characteristic equation cannot be solved analytically therefore, Davidenko's method has been applied to the dispersion analysis of the rod. The author presents Fig. 8-2 for the normalized phase constant of a dielectric rod waveguide with a dielectric constant of 5 and radius of 5.0 mm. As seen in the figure, the cutoff frequencies for the guided mode were 11.48, 26.36, 41.32, and 56.30 GHz for the TM₀₁, TM₀₂, TM₀₃, and TM₀₄ modes, respectively

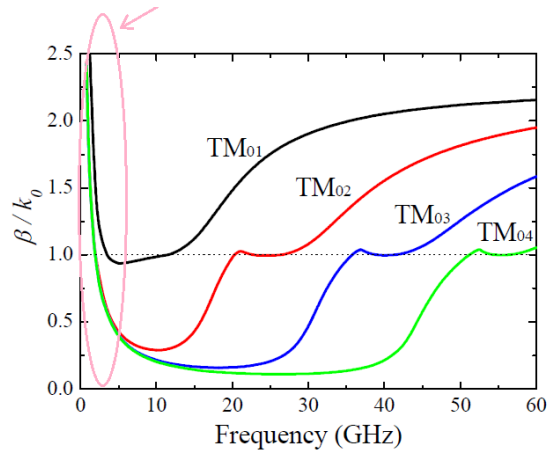


Fig. 8-4 Normalized Phase Constant of Circular Dielectric Rod Waveguide. The Dielectric Constant and Radius of the Rod Were Assumed to Be 5.0 and 5.0 mm, Respectively. [34]

It is obvious that at low frequencies where the normalized phase constants exceed unity, the answer for the leaky wave region has no physical meaning. Crossing unity happens at 3.51, 1.98, 1.95, and 1.94 GHz for the TM01, TM02, TM03, and TM04 modes however we again see the curving of the dispersion diagram at the low frequencies in the leaky wave region before the rising tail that is shown with the arrow.

This increase which happens at much higher frequencies compared to the unity crossing was also present in the article by Oliner which has been shown in Fig.8-3. Yet as will be shown from the fullwave solution and the Green function solution no such curving and rising of the dispersion diagram should exist. This means that the dispersion diagram obtained by the TRM method loses its credibility well before the point at which it crosses unity. The important question that needs to be answered is at what point in the lower frequencies should we stop trusting the solution of the leaky wave region obtained from the transverse resonance method? And second, what is the correct physical answer for the full fast wave region?

In the comparison between the TRM solution and the fullwave solutions we will also show a successive approximation method for obtaining the dispersion diagram that avoids the use of non-linear optimizers (such as Davidenko's complex root finder algorithm). We show that for the leaky wave regime the iterations can be nested inside each other so that a single (messy) equation yields the propagation constant, k_z , to the second approximation, a result good enough to model the behavior around onset.

This expression is then applied to the case of dispersive (frequency dependent) permeable material filling the trough. The permeability and permittivity of the baseline

CZN laminate is used as the example. The result is that the material dispersion, even though it adds loss, flattens the slope of β near onset even more.

8.2 Transverse resonance solution to the trough

According to Marcuvitz [35], with a parallel plane waveguide in TEM mode opening onto an infinite slit on a ground plane and a spacing between the parallel planes equal to b , we have the equivalent circuit parameters as seen below:

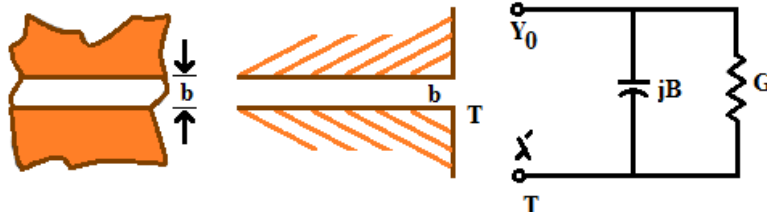


Fig. 8-5 (a)Front View (b) Sideview (c) Equivalent Circuit

The equivalent circuit parameters at reference plane T are as follows:

$$\frac{G}{Y_0} = \int_0^{kb} J_0(x) dx - J_0(kb) \quad (8-2)$$

$$\frac{G}{Y_0} \approx \frac{\pi b}{\lambda'}$$

$$\frac{B}{Y_0} = \int_0^{kb} N_0(x) dx + N_1(kb) + \frac{2}{\pi} \frac{1}{kb} \quad (8-3)$$

$$\frac{B}{Y_0} \approx \frac{2b}{\lambda'} \ln \frac{e\lambda'}{\gamma 2b}$$

Where

$$k = \frac{2\pi}{\lambda'} \quad \lambda' = \frac{\lambda}{\cos\alpha} \quad e = 2.718 \quad \gamma = 1.781 \quad (8-4)$$

The small argument approximation will result in the following equation:

$$Y_T \cong Y_0 \left[\frac{k_x b}{2} + j \frac{k_x b}{\pi} \ln \left(\frac{e\pi}{\gamma k_x b} \right) \right] \quad (8-5)$$

First assuming the medium inside the parallel plate region is free space, we will have:

$$\begin{aligned} Y_T &\cong \frac{1}{\eta} \left[\frac{k_x b}{2} + j \frac{k_x b}{\pi} \ln \left(\frac{e\pi}{\gamma k_x b} \right) \right] \\ &= \frac{k_x}{2\eta} \left[1 + j \frac{2}{\pi} \ln \left(\frac{e\pi}{\gamma k_x b} \right) \right] \\ &= \frac{k_x}{2\eta} \left[1 + j \frac{2}{\pi} \ln \left(\frac{4.795}{k_x b} \right) \right] \end{aligned} \quad (8-6)$$

In the geometries that we are studying, the waveguide is filled and the outside is air therefore we define this terminating admittance in terms of an empty outside region:

$$Y_T = \left(\frac{k_{x0}}{\omega\mu_0} \right) \frac{k_{x0} b}{2} \left[1 + j \frac{2}{\pi} \ln \left(\frac{4.795}{k_{x0} b} \right) \right] \quad (8-7)$$

The transverse resonance problem is seen from the inside therefore, all that is needed is to relate k_{x0} to the k_x inside. With the ultimate goal being to obtain the fast waves below onset in order to compare to Oliner's work, we will go forward with the transverse resonance method.

$$\begin{aligned}\bar{Y}_{left} &= -j \frac{k_x}{\omega \mu_0 \mu} \cot(k_x d) = -\bar{Y}_{rad} \\ &= -\left(\frac{k_{x0}}{\omega \mu_0}\right) \frac{k_{x0} b}{2} \left[1 + j \frac{2}{\pi} \ln\left(\frac{4.795}{k_{x0} b}\right)\right]\end{aligned}\quad (8-8)$$

The constraint equations are

$$\varepsilon \mu k_0^2 - k_x^2 \equiv k_z^2 \equiv k_0^2 - k_{x0}^2 \quad (8-9)$$

By definition, onset occurs when $k_z = k_{z0} = k_0$ so that $k_{x0} = 0$. This means

$$k_x^2 = \varepsilon \mu k_0^2 - k_0^2 \rightarrow k_x = k_0 \sqrt{\mu \varepsilon - 1} \quad (8-10)$$

Since the right hand side of the transverse resonance equation is zero, the left side should also zero also and which means that $k_{xd} = \pi/2$. Therefore

$$k_{0_onset} = \frac{\pi}{2d\sqrt{\mu\varepsilon - 1}} \quad (8-11)$$

Guided waves exist above this k_0 and the leaky waves exist below. The guided waves will be obtained later and at this point we will obtain the leaky waves.

8.2.1 The leaky wave regime solution using successive approximation

Two different methods can be used to obtain the solution to the equation in order to obtain the leaky wave behavior of the structure. One method which will be presented later is a complex root finding optimization method using an unconstrained minimization technique. Another method is an approximation method which will be explained in detail.

For leaky waves, $k_z = \beta_z - j\alpha_z$ with α_z positive since the energy is leaving the trough. It is easy to see from both constraint equations that when the trough is filled with

a lossless material, this forces both k_x and k_{x0} to have negative alphas. The proof is as follows:

$$\begin{aligned} k_z^2 &= \beta_z^2 - \alpha_z^2 - j2\beta_z\alpha_z \\ &\equiv k_0^2 - (\beta_{x0}^2 - \alpha_{x0}^2 \pm j2\beta_{x0}\alpha_{x0}) \end{aligned} \quad (8-12)$$

Since k_0 is purely real, the left hand side imaginary parts must equal each other and this forces k_{x0} to have a sign that is opposite to k_z .

The fact that needs to be further explained is the growing exponential outside which as Oliner pointed out a long time ago can be understood as an “apparent” growth of the signal observed along x, due to the fact that the source wave is decreasing as it travels along z.

For inside, it means that the maximum of the E-field exists at the mouth of the trough and decreases exponentially or as a sine as we travel towards the short circuit. This condition naturally results if we assume a sinh function form to the E field inside but then it wouldn't be clear what it means for the sign of α_x .

So we must have

$$k_z = \beta_z - j\alpha_z; k_x = \beta_x + j\alpha_x; k_{x0} = \beta_{x0} + j\alpha_{x0} \quad (8-13)$$

All alphas are then positive definite.

We are looking for the solution to:

$$\begin{aligned} \left(\frac{k_{x0}}{\omega\mu_0}\right) \frac{k_{x0}b}{2} \left[1 + j\frac{2}{\pi} \ln\left(\frac{4.795}{k_{x0}b}\right)\right] - j\frac{k_x}{\omega\mu_0} \cot(k_x d) \\ = 0 \end{aligned} \quad (8-14)$$

It can be proven that the solution in terms of k_{x0} is located close to

$$\beta_{x_0} = \sqrt{\left(\frac{\pi}{2d}\right)^2 \frac{1}{\mu\varepsilon - 1} - k_0^2} \quad (8-15)$$

With k_{x_0} being easiest to find close to the value that makes the real part of the TRM equation zero. So, we must substitute k_x in terms of k_{x_0}

$$k_0^2(\mu\varepsilon - 1) + k_{x_0}^2 = k_x^2 \quad (8-16)$$

At this point the tangent function needs to be approximated.

It is known that for purely real values, the singularity extraction approximation to the tangent spanning its first Riemann sheet is

$$\tan(x) = \left(1 - \frac{8}{\pi^2}\right)x + \left(\frac{1}{\frac{\pi}{2} - x} - \frac{1}{\frac{\pi}{2} + x}\right) \quad (8-17)$$

That can be analytically continued to complex z more accurately by:

$$\tan(z) = \left(1 - \frac{8}{\pi^2}\right)z + \left(\frac{1}{\frac{\pi}{2} - z} - \frac{1}{\frac{\pi}{2} + z}\right) + 0.0055 \cdot z^3 \quad (8-18)$$

Multiplying the TRM equation by $j\mu d$ we will have:

$$-j\mu \frac{k_{x_0}^2 db}{2} \left[1 + j \frac{2}{\pi} \ln\left(\frac{4.795}{k_{x_0} b}\right)\right] = \frac{k_x d}{\tan(k_x d)} \quad (8-19)$$

Knowing that k_x is mostly real to first order and using the simplest approximation we obtain:

$$\begin{aligned}
& -j\mu \frac{k_{x0}^2 db}{2} \left[1 + j \frac{2}{\pi} \ln \left(\frac{4.795}{k_{x0} b} \right) \right] \\
& = \frac{1}{\left(1 - \frac{8}{\pi^2} \right) + \left(\frac{2}{\left(\frac{\pi}{2} \right)^2 - (k_x d)^2} \right)} \quad (8-20)
\end{aligned}$$

Or

$$\begin{aligned}
& -j\mu \frac{k_{x0}^2 db}{2} + \mu \frac{k_{x0}^2 db}{\pi} \ln \left(\frac{4.795}{k_{x0} b} \right) \\
& = \frac{1}{\left(1 - \frac{8}{\pi^2} \right) + \left(\frac{2}{\left(\frac{\pi}{2} \right)^2 - (k_x d)^2} \right)} \quad (8-21)
\end{aligned}$$

The next step to the solution is by successive approximations. Since the log term changes slowly, we can as a first approximation replace k_{x0} with our first guess of β_{x0} . This makes the log term purely real. Also, we will assume that since the second term in the denominator is infinite at onset, that it will be larger than the first

$$\left(1 - \frac{8}{\pi^2} \right) = 0.189 \quad (8-22)$$

Therefore, we proceed with the first guess

$$\begin{aligned}
& -j\mu \frac{k_{x0}^2 db}{2} + \mu \frac{k_{x0}^2 db}{\pi} \ln \left(\frac{4.795}{\beta_{x0} b} \right) \\
& = \frac{\left(\frac{\pi}{2} \right)^2 - (k_0^2 (\mu \epsilon - 1) + k_{x0}^2) d^2}{2} \quad (8-23)
\end{aligned}$$

$$\begin{aligned}
k_{x0}^2 - j\mu k_{x0}^2 \frac{b}{d} + 2\mu \frac{k_{x0}^2 b}{\pi d} \ln\left(\frac{4.795}{\beta_{x0} b}\right) \\
= \left(\frac{\pi}{2}\right)^2 \frac{1}{d^2} - k_0^2(\mu\varepsilon - 1)
\end{aligned} \tag{8-24}$$

To be solved for the complex k_{x0} we first solve for k_{x0}^2 . That is:

$$k_{x0}^2 = \frac{\left(\frac{\pi}{2d}\right)^2 - k_0^2(\mu\varepsilon - 1)}{\left[1 - j\mu \frac{b}{d} + \frac{2\mu b}{\pi d} \ln\left(\frac{4.795}{\beta_{x0} b}\right)\right]} \tag{8-25}$$

Then we take the square root ensuring that it has the form $\beta_{x0} + j\alpha_{x0}$.

And we have our first approximation for k_{x0} . Then the iteration will be follows:

$$\text{Given } k_0 < k_{0\text{-onset}}; \beta_{x0} = \sqrt{\left(\frac{\pi}{2d}\right)^2 \frac{1}{\mu\varepsilon - 1} - k_0^2} \tag{8-26}$$

$$k_{x0|0} = \beta_{x0}$$

$$\text{Given } k_{x0|n} \rightarrow k_{x|n} = \sqrt{k_0^2(\mu\varepsilon - 1) + (k_{x0|n})^2} \tag{8-27}$$

$$RHS_n = \frac{k_{x|n} d}{\tan(k_{x|n} d)}$$

$$LHSfactor_n = -j\mu \frac{bd}{2} \left(1 + j \frac{2}{\pi} \ln\left(\frac{4.795}{k_{x0|n} b}\right)\right) \tag{8-28}$$

$$k_{x0}|_{n+1} = \sqrt{\frac{RHS_n}{LHSfactor_n}} \quad (8-29)$$

$$Progress = 1 - \frac{k_{x0}|_{n+1}}{k_{x0}|_n} \quad (8-30)$$

Repeat until *Progress* < 0.001 or desired accuracy

The next step is to obtain the solution to the guided wave regime

8.2.2 Guided wave regime solution using successive approximation

Using the same result to the transverse resonance method we proceed:

$$j \frac{k_x}{\mu} \cot(k_x d) = \frac{k_{x0}^2 b}{2} \left[1 + j \frac{2}{\pi} \ln \left(\frac{4.795}{k_{x0} b} \right) \right] \quad (8-31)$$

However, $k_{x0} = -j\alpha_{x0}$ therefore:

$$j \frac{k_x}{\mu} \cot(k_x d) = -\frac{\alpha_{x0}^2 b}{2} \left[1 + j \frac{2}{\pi} \ln \left(\frac{4.795}{-j\alpha_{x0} b} \right) \right] \quad (8-32a)$$

$$j \frac{k_x}{\mu} \cot(k_x d) = -\frac{\alpha_{x0}^2 b}{2} \left[1 + j \frac{2}{\pi} \ln \left(\frac{4.795}{\alpha_{x0} b} \right) + j \frac{2}{\pi} \ln j \right] \quad (8-32b)$$

$$j \frac{k_x}{\mu} \cot(k_x d) = -\frac{\alpha_{x0}^2 b}{2} \left[j \frac{2}{\pi} \ln \left(\frac{4.795}{\alpha_{x0} b} \right) \right] \quad (3-32c)$$

$$j \frac{k_x}{\mu} \cot(k_x d) = -j \frac{\alpha_{x0}^2 b}{\pi} \ln \left(\frac{4.795}{\alpha_{x0} b} \right) \quad (8-32d)$$

$$-\frac{k_x d}{\mu} \cot(k_x d) = \frac{\alpha_{x0}^2 b d}{\pi} \ln\left(\frac{4.795}{\alpha_{x0} b}\right) \quad (8-32e)$$

$$\frac{k_x d}{\tan(k_x d)} = -\mu \frac{\alpha_{x0}^2 b d}{\pi} \ln\left(\frac{4.795}{\alpha_{x0} b}\right) \quad (8-32f)$$

Since we know that $k_x d$ starts at $\pi/2$, solve for the position past $\pi/2$; that is:

$$\frac{\frac{\pi}{2} + \delta}{\tan\left(\frac{\pi}{2} + \delta\right)} = -\mu \frac{\alpha_{x0}^2 b d}{\pi} \ln\left(\frac{4.795}{\alpha_{x0} b}\right) \quad (8-33a)$$

$$\frac{\left(\frac{\pi}{2} + \delta\right) \left(1 - \tan\frac{\pi}{2} \tan\delta\right)}{\tan\left(\frac{\pi}{2}\right) + \tan\delta} = -\mu \frac{\alpha_{x0}^2 b d}{\pi} \ln\left(\frac{4.795}{\alpha_{x0} b}\right) \quad (8-33b)$$

Since the trig identity must always be true and $\tan(\pi/2) = \infty$ we will have:

$$-\left(\frac{\pi}{2} + \delta\right) \tan\delta = -\mu \frac{\alpha_{x0}^2 b d}{\pi} \ln\left(\frac{4.795}{\alpha_{x0} b}\right) \quad (8-34a)$$

$$\left(\frac{\pi}{2} + \delta\right) \tan\delta = \mu \frac{\alpha_{x0}^2 b d}{\pi} \ln\left(\frac{4.795}{\alpha_{x0} b}\right) \quad (8-34b)$$

At this point, if we do the singularity expansion approach we see we don't have $x/\tan(x)$ but $x\tan(x)$. If we do the expansion, we will get a fourth order polynomial which helps us see the dominant term.

$$\begin{aligned} \left(\frac{\pi}{2} + \delta\right) \left[\left(1 - \frac{8}{\pi^2}\right) \delta + \left(\frac{2\delta}{\left(\frac{\pi}{2}\right)^2 - \delta^2}\right) \right] \\ = \mu \frac{\alpha_{x0}^2 b d}{\pi} \ln\left(\frac{4.795}{\alpha_{x0} b}\right) \end{aligned} \quad (8-35)$$

Rearranging to solve for δ

$$\begin{aligned} \left(\frac{\pi}{2} + \delta\right) \left[\left(1 - \frac{8}{\pi^2}\right) \left[\left(\frac{\pi}{2}\right)^2 - \delta^2\right] \delta + 2\delta \right] \\ = \left\{ \mu \frac{\alpha_{x0}^2 b d}{\pi} \ln\left(\frac{4.795}{\alpha_{x0} b}\right) \right\} \left[\left(\frac{\pi}{2}\right)^2 - \delta^2\right] \end{aligned} \quad (8-36a)$$

$$\begin{aligned} A \left[\left(\frac{\pi}{2}\right)^2 - \delta^2\right] \delta \left(\frac{\pi}{2} + \delta\right) + 2\delta \left(\frac{\pi}{2} + \delta\right) \\ = B(\alpha_{x0}) \left[\left(\frac{\pi}{2}\right)^2 - \delta^2\right] \end{aligned} \quad (8-36b)$$

$$\begin{aligned} \left[A \left(\frac{\pi}{2}\right)^2 \delta - A\delta^3 \right] \left(\frac{\pi}{2} + \delta\right) + 2\delta^2 + \delta\pi \\ = B(\alpha_{x0}) \left[\left(\frac{\pi}{2}\right)^2 - \delta^2\right] \end{aligned} \quad (8-36c)$$

$$\begin{aligned} A \left(\frac{\pi}{2}\right)^2 \delta \left(\frac{\pi}{2} + \delta\right) - A\delta^3 \left(\frac{\pi}{2} + \delta\right) + 2\delta^2 + \delta\pi \\ = \left(\frac{\pi}{2}\right)^2 B(\alpha_{x0}) - \delta^2 B(\alpha_{x0}) \end{aligned} \quad (8-36d)$$

$$\begin{aligned} \left[A \left(\frac{\pi}{2}\right)^3 + \pi \right] \delta + \left(2 + B(\alpha_{x0}) + A \left(\frac{\pi}{2}\right)^2 \right) \delta^2 - \frac{\pi}{2} A \delta^3 \\ - A \delta^4 - \left(\frac{\pi}{2}\right)^2 B(\alpha_{x0}) = 0 \end{aligned} \quad (8-36e)$$

This equation can be solved as a fourth order polynomial however, if δ is small the first term dominates and we can start the successive approximations method.

Given $\alpha_{x0} = f \cdot k_{onset}$; f ranging from near 0 to 30

$$B(\alpha_{x0}) = \mu \frac{\alpha_{x0}^2 bd}{\pi} \ln \left(\frac{4.795}{\alpha_{x0} b} \right) \quad (8-37a)$$

$$\delta_0 = \frac{\left(\frac{\pi}{2}\right)^2 B(\alpha_{x0})}{A \left(\frac{\pi}{2}\right)^3 + \pi} ; A = 1 - \frac{8}{\pi^2} \quad (8-37b)$$

But now the TRM equation tells us:

$$\left(\frac{\pi}{2} + \delta\right) \tan\delta = \mu \frac{\alpha_{x0}^2 bd}{\pi} \ln \left(\frac{4.795}{\alpha_{x0} b} \right) \equiv B(\alpha_{x0}) \quad (8-38)$$

So the next step is to substitute δ_0 into one of these deltas and solve for the other and see if that gets better. A quick experiment shows:

$$\left(\frac{\pi}{2} + \delta_0\right) \tan\delta_1 = B(\alpha_{x0}) \quad (8-39)$$

So that

$$\delta_1 = \text{atan} \left[\frac{B(\alpha_{x0})}{\left(\frac{\pi}{2} + \delta_0\right)} \right] \quad (8-40)$$

And to do N iterations we will end up with this nice repeated fraction:

It turns out that for the cases of interest just two iterations are enough to converge on the behavior near onset. This means that we can write a closed form expression for the two approximations by inserting the first approximation directly into the second.

That is, since the constraint equation

$$\varepsilon\mu k_0^2 - k_x^2 \equiv k_z^2 \equiv k_0^2 - k_{x0}^2 \quad (8-43)$$

Tells us that

$$k_x^2 \equiv k_0^2(\varepsilon\mu - 1) + k_{x0}^2 \quad (8-44)$$

Then the TRM equation solves for k_{x0} as:

$$k_{x0}^2 = \frac{\frac{k_x d}{\tan(k_x d)}}{\mu \frac{db}{2} \left[-j + \frac{2}{\pi} \ln \left(\frac{4.795}{k_{x0} b} \right) \right]} \quad (8-45)$$

Furthermore, near onset with very a high index medium in the trough, since k_z is of the order of k_0 , k_x inside the channel is of the order of k_{medium} of the channel. So k_z is of the order of

$$k_z = \sqrt{k_0^2 - k_{x0}^2} \cong \sqrt{k_0^2 - \frac{\frac{k_0 \sqrt{\varepsilon\mu}}{\tan(k_x d)}}{\mu \frac{b}{2} \left[-j + \frac{2}{\pi} \ln \left(\frac{4.795}{k_{x0} b} \right) \right]}} \quad (8-46)$$

Now replace all k_x with functions of k_{x0} and the k_{x0} in the log with functions of k_x from TRM

$$\begin{aligned}
& k_z \\
& \cong \sqrt{k_0^2 - \frac{k_0 \sqrt{\varepsilon \mu}}{\tan \left(d \sqrt{k_0^2 (\varepsilon \mu - 1) + k_{x0}^2} \right)}} \\
& \quad \mu \frac{b}{2} \left[-j + \frac{2}{\pi} \ln \left(\frac{4.795}{b \sqrt{\frac{k_x}{\tan(k_x d)}}} \right) \right] \\
& \quad \mu \frac{b}{2} \left[-j + \frac{2}{\pi} \ln \left(\frac{4.795}{\mu \frac{b}{2} \left[-j + \frac{2}{\pi} \ln \left(\frac{4.795}{k_{x0} b} \right) \right]} \right) \right]
\end{aligned} \tag{8-47}$$

Now replace every k_{x0} with the TRM expression so it is again in terms of k_x and then again

$$\begin{aligned}
& k_z \\
& \cong \sqrt{k_0^2 - \frac{k_0 \sqrt{\varepsilon \mu}}{\tan \left(d \sqrt{k_0^2 (\varepsilon \mu - 1) + \frac{\sqrt{k_0^2 (\varepsilon \mu - 1) + k_{x0}^2}}{\tan \left(d \sqrt{k_0^2 (\varepsilon \mu - 1) + k_{x0}^2} \right)}}} \right)}} \\
& \quad \mu \frac{b}{2} \left[-j + \frac{2}{\pi} \ln \left(\frac{4.795}{b \frac{\sqrt{k_0^2 (\varepsilon \mu - 1) + k_{x0}^2}}{\tan \left(d \sqrt{k_0^2 (\varepsilon \mu - 1) + k_{x0}^2} \right)}}} \right) \right] \\
& \quad \mu \frac{b}{2} \left[-j + \frac{2}{\pi} \ln \left(\frac{4.795}{\mu \frac{b}{2} \left[-j + \frac{2}{\pi} \ln \left(\frac{4.795}{k_{x0} b} \right) \right]} \right) \right]
\end{aligned} \tag{8-48}$$

And now replace k_{x0} with its first guess k_{x0}

k_z

$$\begin{aligned}
 & \frac{k_0 \sqrt{\epsilon \mu}}{\sqrt{k_0^2 - \left[\tan \left(d \sqrt{k_0^2 (\epsilon \mu - 1) + \frac{\tan(d \sqrt{k_0^2 (\epsilon \mu - 1) + \beta_{x0}^2)}{\mu \frac{b}{2} \left[-j + \frac{2}{\pi} \ln \left(\frac{4.795}{\beta_{x0} b} \right) \right]} \right)} \right]^2} \\
 & \cong k_0^2 - \mu \frac{b}{2} \left[-j + \frac{2}{\pi} \ln \left(\frac{4.795}{b \sqrt{k_0^2 (\epsilon \mu - 1) + \frac{\tan(d \sqrt{k_0^2 (\epsilon \mu - 1) + \beta_{x0}^2)}{\mu \frac{b}{2} \left[-j + \frac{2}{\pi} \ln \left(\frac{4.795}{\beta_{x0} b} \right) \right]} \right)} \right) \right]
 \end{aligned} \tag{8-49}$$

Where

$$\beta_{x0} = \sqrt{\left(\frac{\pi}{2d}\right)^2 \frac{1}{\mu \epsilon - 1} - k_0^2} \tag{8-50}$$

Using either method, at this point we can plot k_z versus k_0 diagram in both the leaky wave and the guided wave regimes. As an example, the real and imaginary parts of k_z has been plotted versus k_0 for a 1” by 1” trough filled with a material with $\mu = 40$ and $\epsilon = 3.2$.

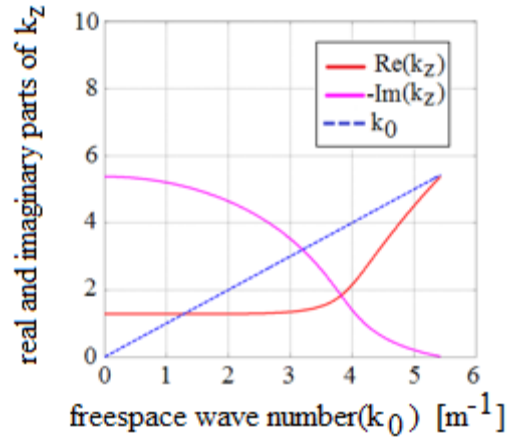


Fig. 8-6 Real and Imaginary Parts of k_z for a 1" by 1" Open Trough Using the Transverse Resonance Method

In the previous figure, it is clearly seen that the real part of k_z is crossing the light-line. The meaning of this crossing in terms of the wave velocity can be seen in the velocity plot below:

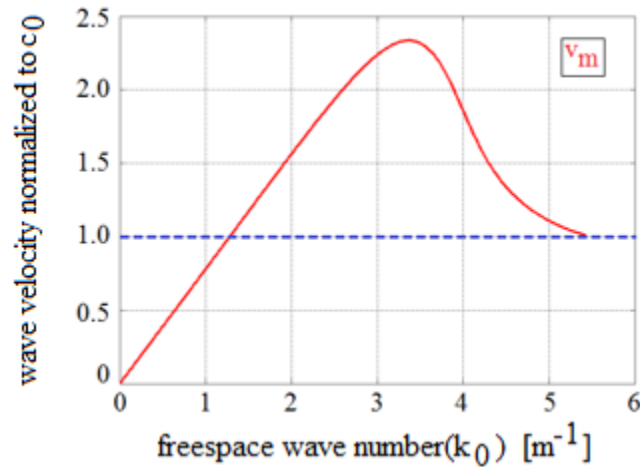


Fig. 8-7 Velocity Normalized to the Speed of Light Versus Free-Space Wavenumber

It can be seen that the phase velocity rises below onset but then its stops rising and turns around until it eventually gets smaller than the speed of light at very low values

of k_0 (smaller frequencies) even though we should still be in the fast wave region. We had seen this before in Oliner's work however before going to the next section we will present the other method of solving the transverse resonance equation that we mentioned before and show that it gives the exact same results as the approximation method.

8.2.4 Transverse resonance equation solution using unconstrained minimization routine

Another way to solve the transverse resonance equation is to use an unconstrained minimization routine to solve the equation. This optimization technique, finds the minimum to the transverse resonance equation and obtains the value of k_z that results in the minimum. The results can be seen in the figure below in the same plot as the results obtained from the approximation method.

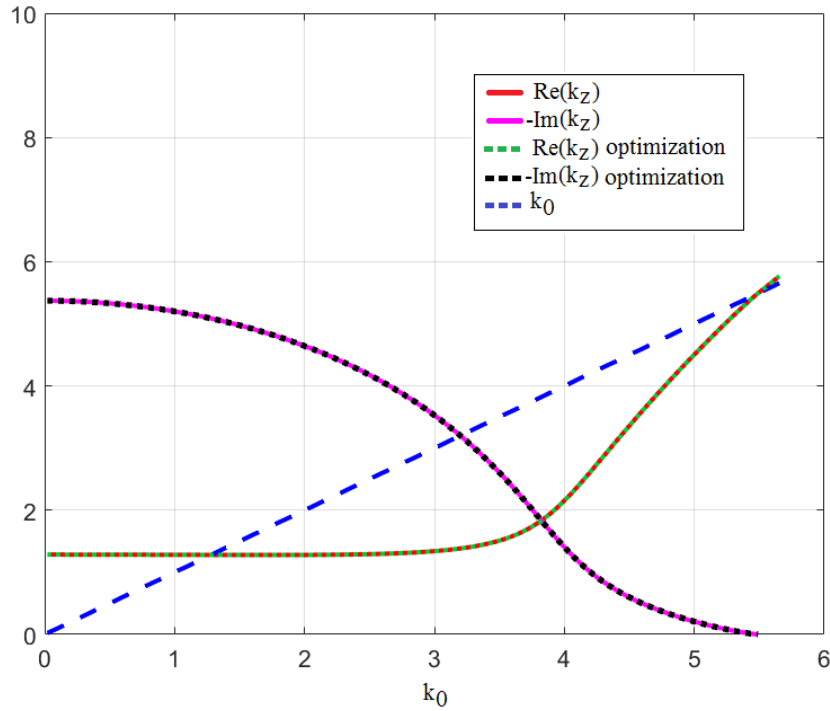


Fig. 8-8 Real and Imaginary Parts of k_z Obtained from Optimization and from the Approximation Method

Even though the perfect agreement of the two solutions shows that the optimization method can be trusted, a sanity check will be to ensure that the solution obtained by the optimization method is unique and the results are correct even with initial values that are not close to the solution. We have picked initial values far from the correct results and plotted contour plots of the inverse of the transverse resonance equation. The reason we are plotting the inverse of the function is that the maximum can be seen with much more clarity on the contour plot compared to the minimum of the transverse resonance function. The plot below shows that the point which gives the minimum value of the transverse resonance function is unique.

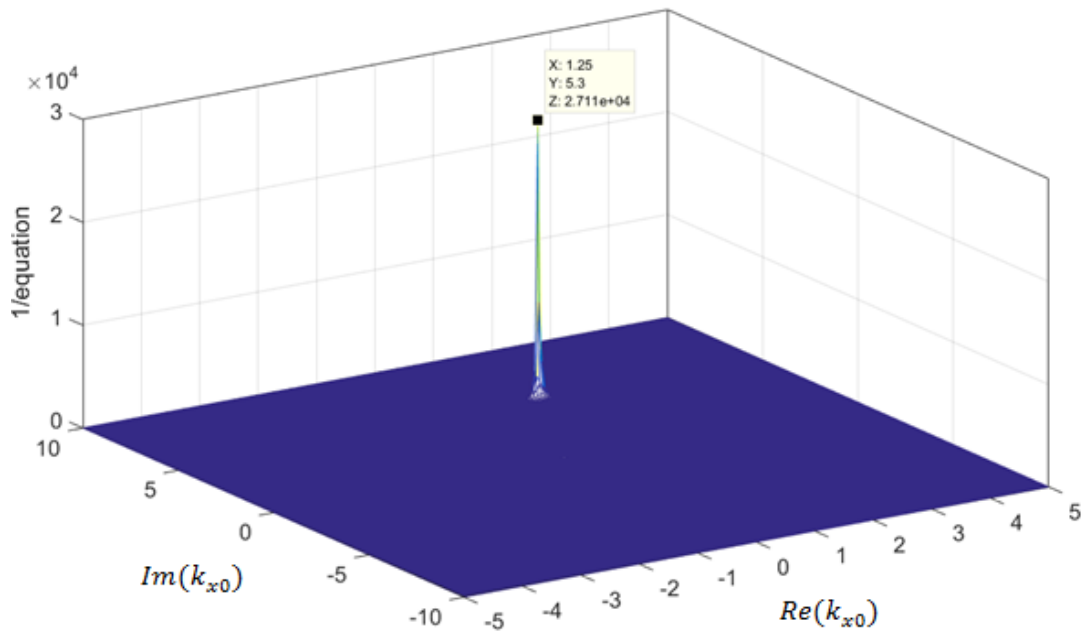


Fig. 8-9 Values of $Re(k_{x0})$ and $Im(k_{x0})$ That Results in the Minimum of the Transverse Resonance

Equation

8.3 Comparing the transverse resonance method to the Greens function method and to full wave simulation

In the previous chapter we had found the Greens function solution to a 3.8” by 1.053” open trough seen in Fig. 8-10

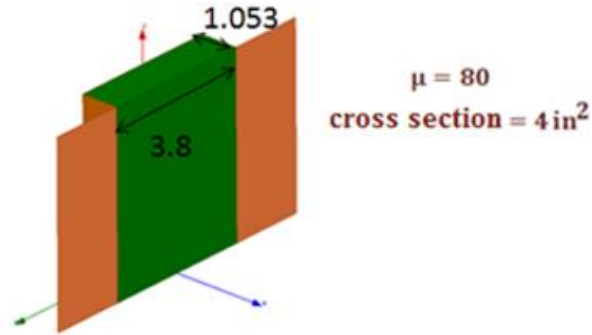


Fig. 8-10 Open Trough Geometry Filled with a Permeable Material

We can also obtain the α and β plots for the mentioned dimensions and the material properties using the transverse resonance method and plot them in the same graph. Another useful comparison would be to use a fullwave simulator to find the slope and amplitude plots of the magnetic current similar to what we did in the Green's function method. The HFSS results take into account every realistic detail of the structure and can be used as a substitute for the Greens function method.

In order to simulate this structure in HFSS, the dimensions of the sides of the computational domain is chosen to be large enough so that the results does not change with increasing the dimensions of the trough sides. As seen below, integration lines have been defined at different distances along the trough and the $\int E \cdot dl$ has been calculated along each path.

Similar to the Green's function method, the slope of the unwrapped phase and the slope of the amplitude plots will result in the β and α plots respectively.

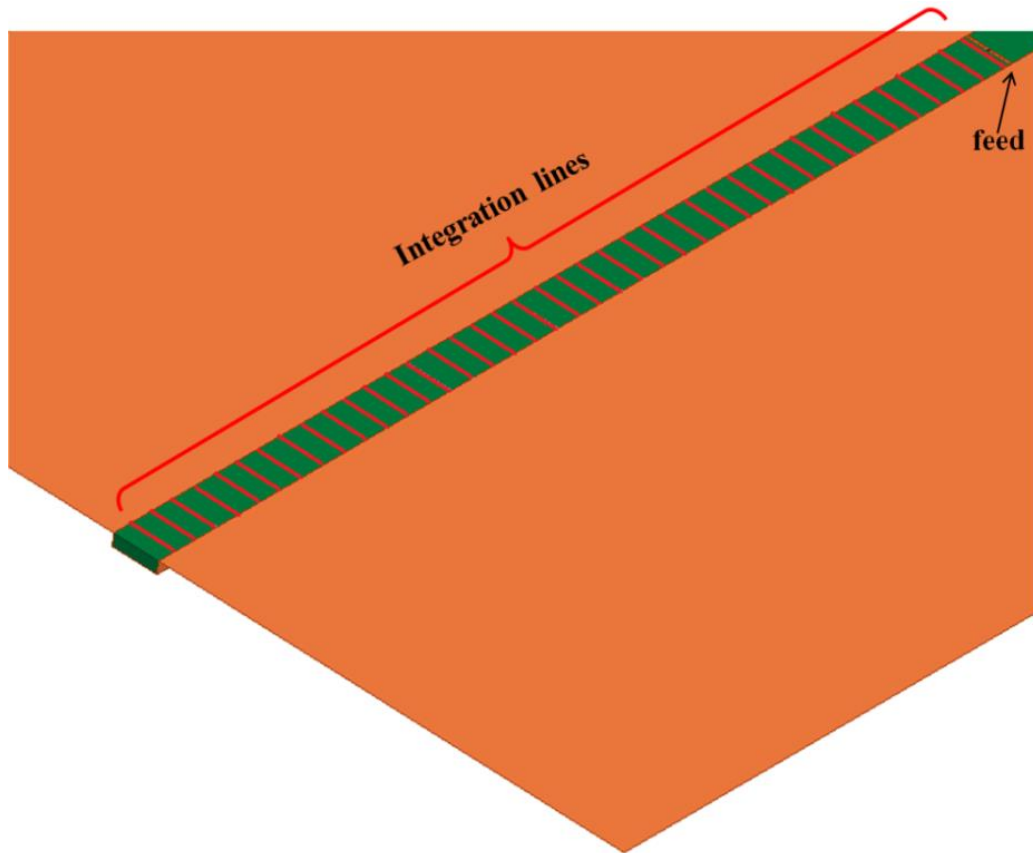


Fig. 8-11 Open Trough Structure Simulation in HFSS Showing the Integration Paths to Obtain the Magnetic Current

The figure below shows the α and β plots obtained from the three different methods

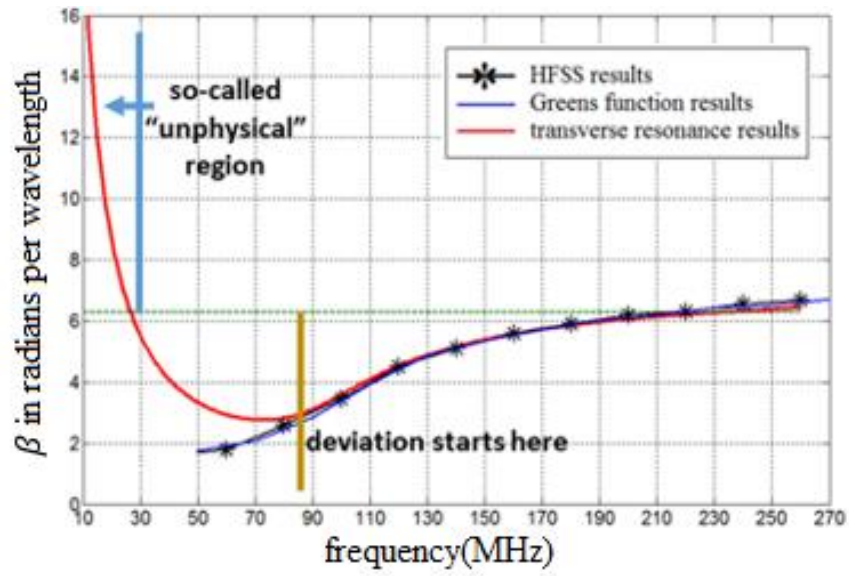


Fig. 8-12 β Plot Obtained from Three Different Methods for a 3.8'' by 1.053'' Open Trough with $\mu = 80, \epsilon = 2$

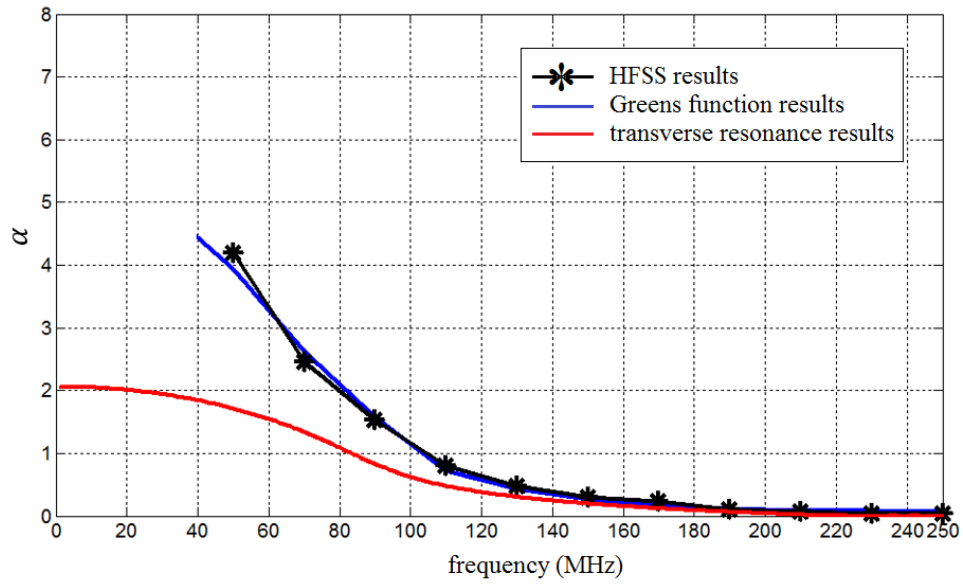


Fig. 8-13 α Plot Obtained Three Different Methods for a 3.8'' by 1.053'' Open Trough with $\mu = 80$ and $\epsilon = 2$

In the previous figures we see that the three methods have a very good agreement in higher frequencies and they deviate as we go lower in frequency. Also we see the curving of the beta plot obtained from the transverse resonance has the same behavior that was present in Oliner's work therefore at lower frequencies it becomes unphysical.

However, the Green's function method and the full wave simulation have a good agreement even in smaller frequencies and the deviation from the transverse resonance method starts at higher frequencies than the "unphysical" point at which the solution crossed the light line again.

As another example, we will compare the transverse resonance solution to the HFSS simulation results of a trough with different dimensions and material properties. The results seen below is for a 1" by 1" trough with the permeability of 40 and permittivity of 3.2.

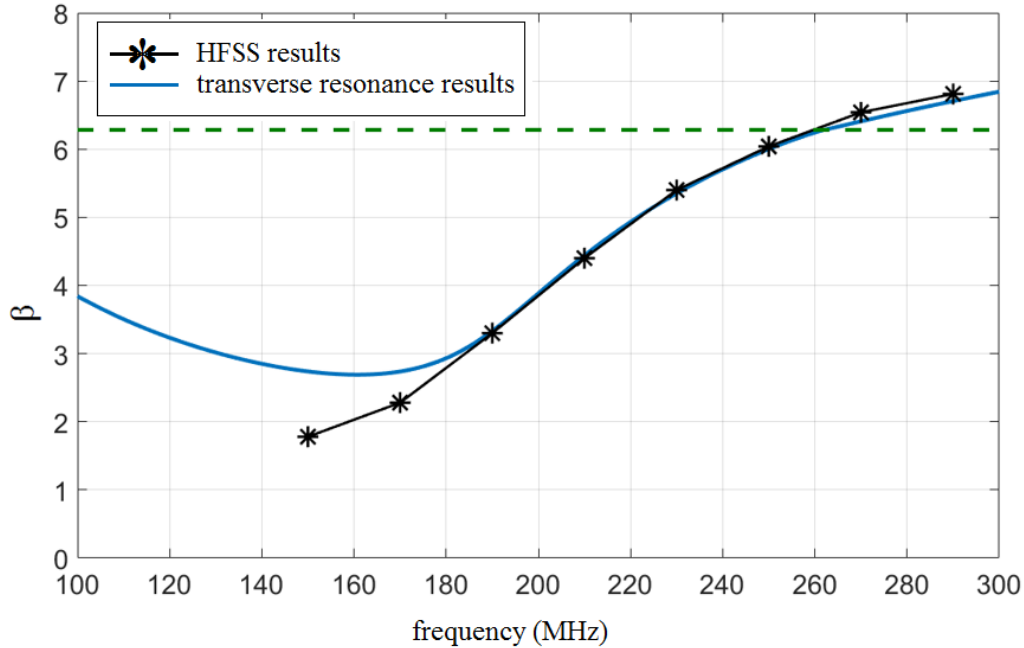


Fig. 8-14 β Plots of a 1”by1” Trough with $\mu = 40$ and $\varepsilon = 3.2$ Using HFSS and Transverse Resonance

Method

In Fig. 8-14 we see that the results from the transverse resonance starts to increase at almost 150MHz which means the waves in the leaky wave region are starting to get slower however as we expect from a physical dispersion behavior and as we had seen in the previous example, the curving of the beta plot does not happen in the HFSS results. We have not gone lower in frequency for the HFSS results since the results were starting to get noisy. However we had seen an agreement with the Green’s function method and the Green’s function method can go to very low frequencies if the data is needed. A question that needs to be answered at this point is, can give an estimation of the frequency in which we can no longer trust the transverse resonance method?

If we go back to the example of the 1.053” by 8.3” inch trough with the permeability of 80 and the permittivity of 20 we can this time plot the β_{x0} and β_{xmed}

obtained from TRM relative to the propagation constants in air and the medium inside the trough. In the following figures, we see that both β_{x0} and β_{xmed} cross 1. That is deep inside the leaky wave regime the solution is telling us that the x-component of the phase constant inside the trough becomes slower than the medium's total propagation constant, which is impossible and has no physical meaning.

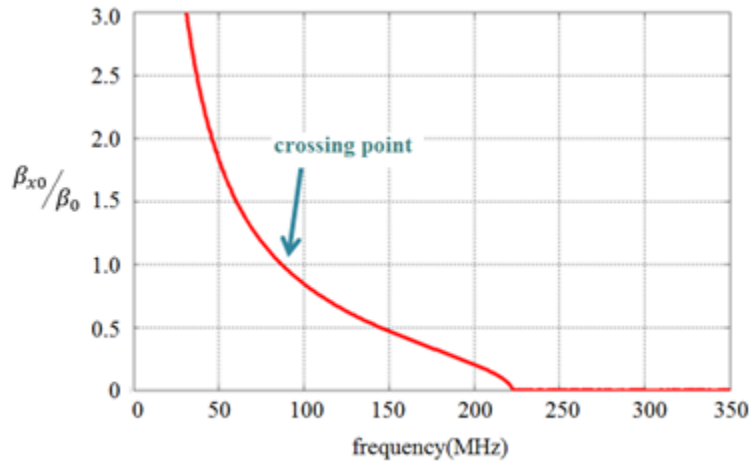


Fig. 8-15 β_{x0}/β_0 Plots of a 1.053'' by 8.3'' Trough with $\mu = 80$ and $\varepsilon = 2$

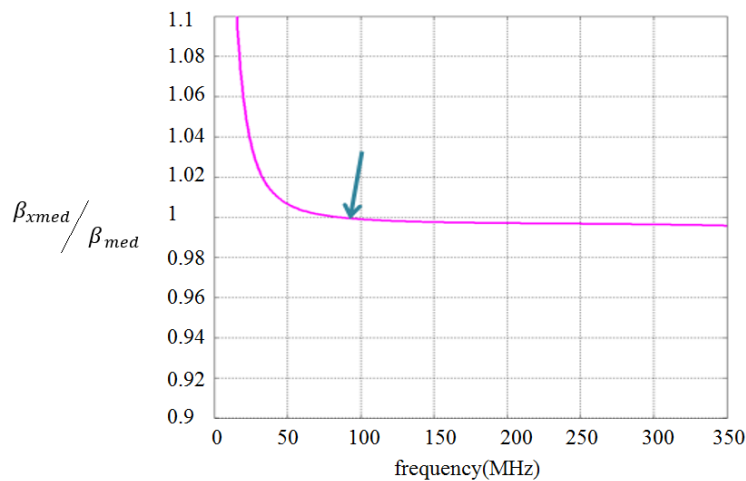


Fig. 8-16 β_{xmed}/β_{med} Plots of a 1.053'' by 8.3'' Trough with $\mu = 80$ and $\varepsilon = 2$

Comparing these figures to Fig.8-12 show that the point in which β_{x0} and β_{xmed} cross one can be an estimation for when the results start to deviate. This is the frequency point in which the β plot experiences an inflection point that changes the character from a downwards bending curve to a curve that eventually bends upwards.. To prove this, we calculate the second derivative for the TRM dispersion curve. Indeed, the second derivative of the β plot becomes zero very close to the point when the x-components of the propagation constants become slower than should be possible.

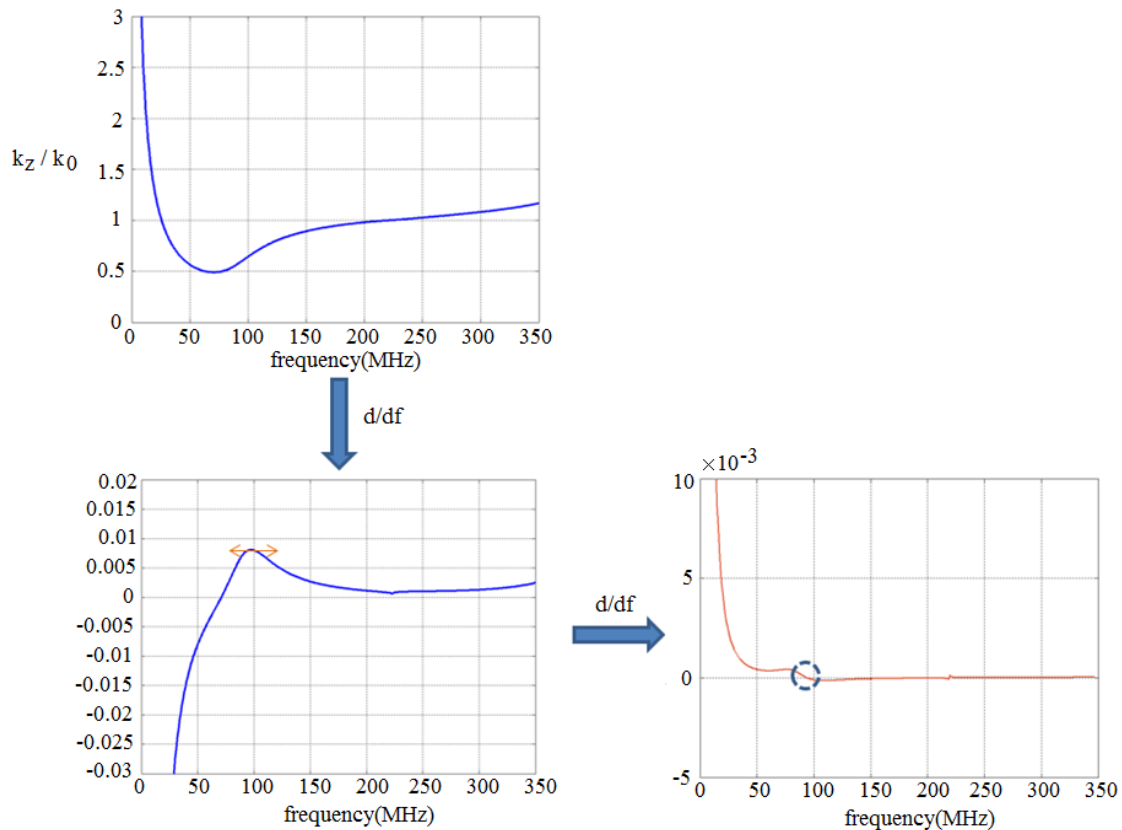


Fig. 8-17 Plot of k_z/k_0 and the First and Second Derivative Showing That the Zero Crossing of the Second Derivative Can Be Used as an Approximate Measure of Defining the Minimum Frequency of Accountability of the Transverse Resonance Method

The calculation is repeated for a 1" by 1" cross section trough to verify this observation.

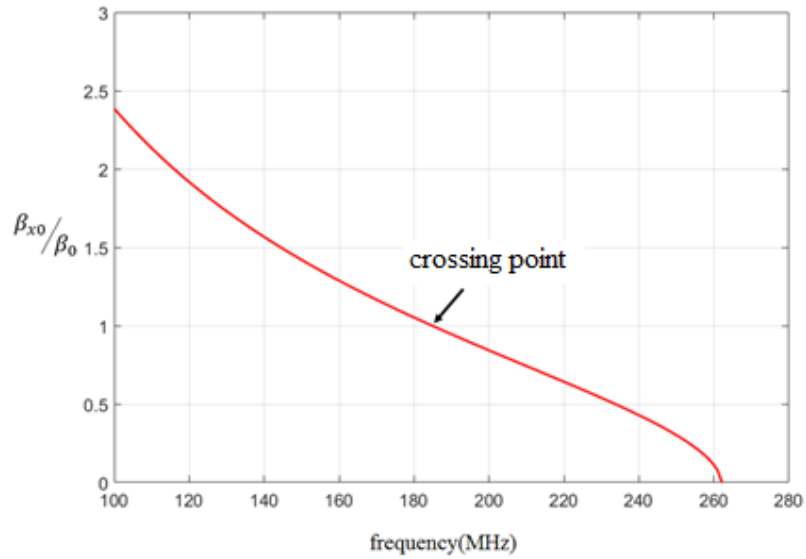


Fig. 8-18 β_{x0}/β_0 Plots of a 1" by 1" Trough with $\mu = 40$ and $\epsilon = 3.2$

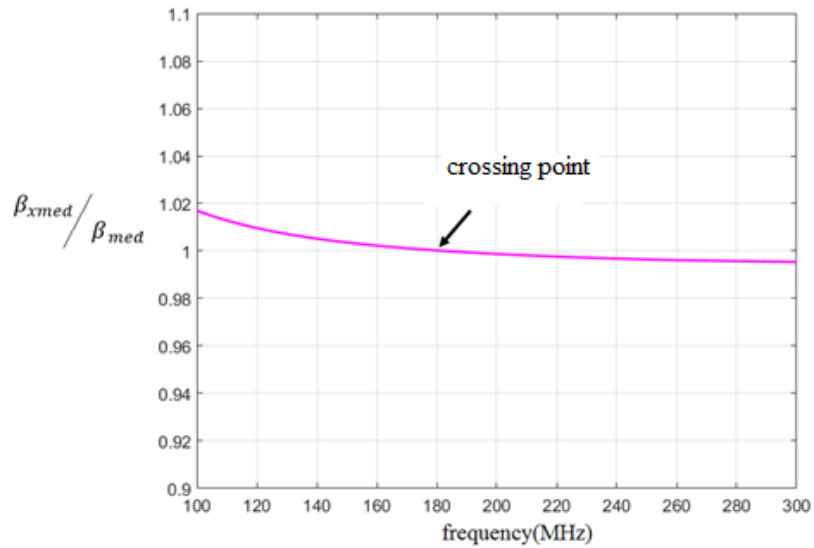


Fig. 8-19 β_{xmed}/β_{med} Plots of a 1" by 1" Trough with $\mu = 40$ and $\epsilon = 3.2$

The second derivative of the beta plot is also shown below which shows that the deviation happens very close to the point where the x-components of the TRM solution become unphysical.

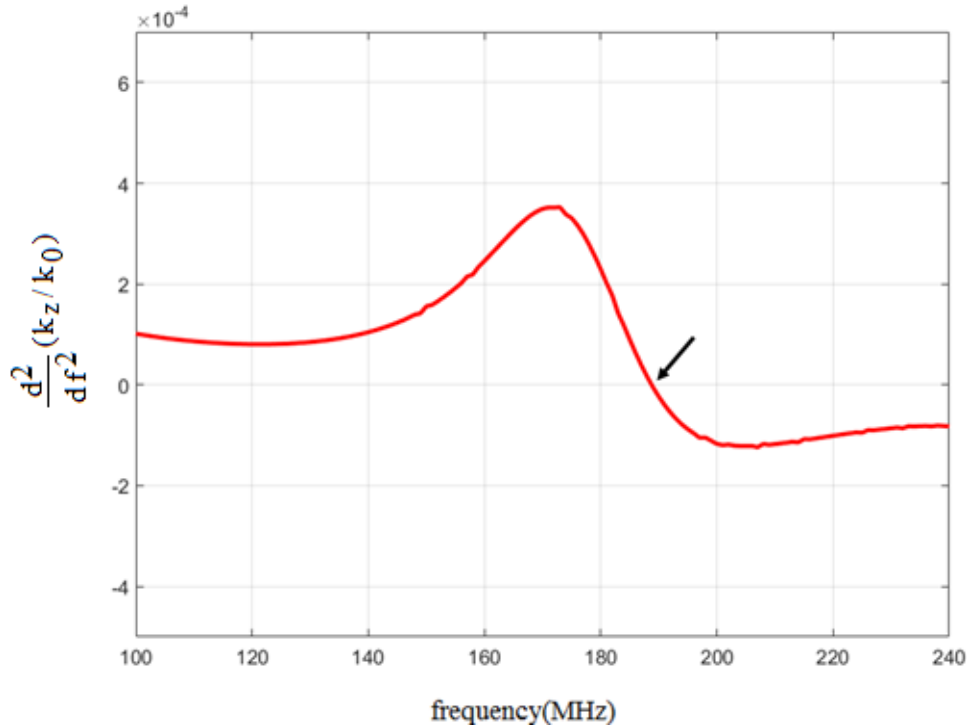


Fig. 8-20 Plot of the Second Derivative of a k_z/k_0 of 1" by 1" Trough with $\mu = 40$ and $\epsilon = 3.2$ Showing That the Zero Crossing of the Second Derivative Can Be Used as an Approximate Measure of Defining the Minimum Frequency of Accountability of the Transverse Resonance Method

Now that we have recognized an approximate lower frequency limit above which we can trust the transverse resonance method, an interesting study would be to check other rules we had found in the Green's function method for example the rule that as long as the cross section area times the permeability is the same for two troughs, then their beta plots will be the same. We will use the same examples as the previous section.

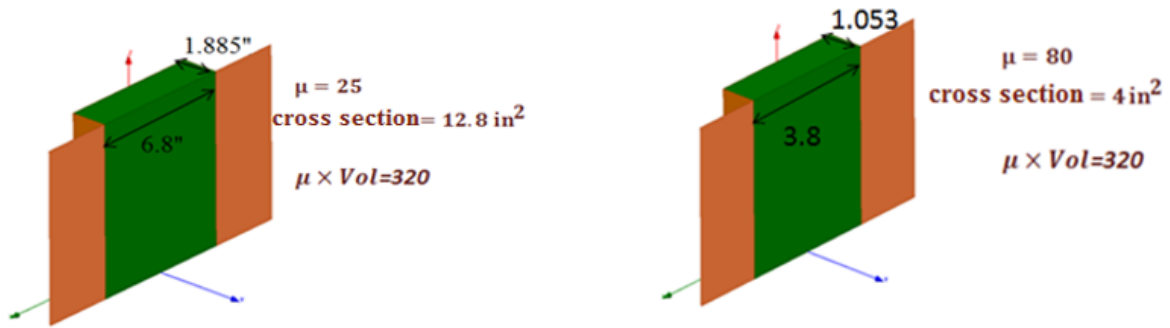


Fig. 8-21 Two Open Trough Structures with Different Permeabilities and Cross Sections While Having the Same Cross Section Area Times the Permeability.

The beta plots obtained from the transverse resonance method are seen below which shows that they are exactly the same until we reach the frequency of the inflection point below which we can no longer trust the transverse resonance method.

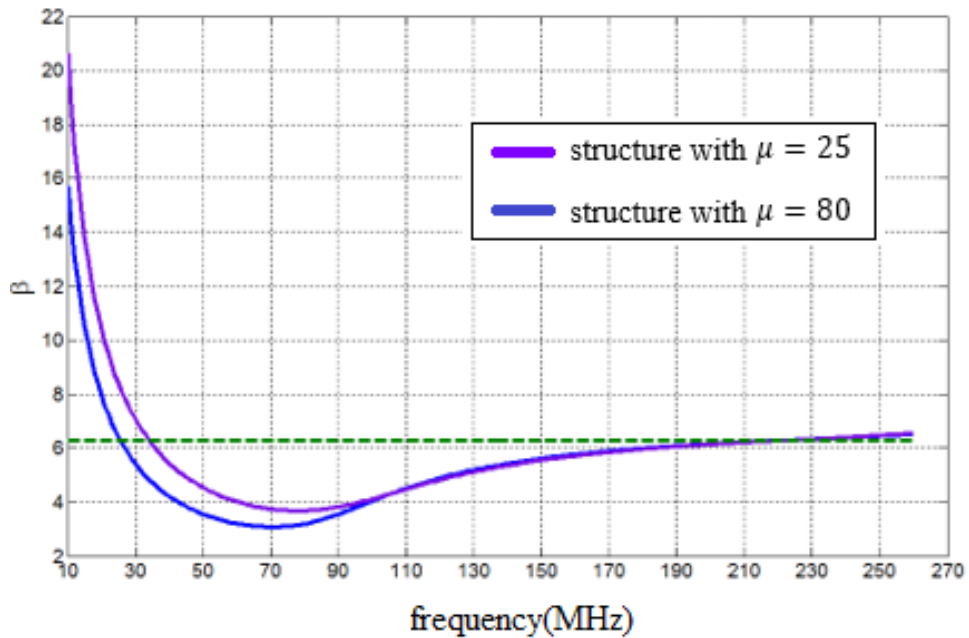


Fig. 8-22 Beta Plots of the Two Geometries with the Same $\mu \cdot vol$ Showing That the Rules Found Before Holds in the Transverse Resonance Method for Frequencies Higher Than the Reliable Frequency

This means that in order to obtain the dispersion features of the trough, we can use the transverse resonance method until the frequency in which the second derivative of the beta plot crosses zero and in order to obtain the dispersion relation of lower frequencies we can either use the Green's function method or a fullwave simulation of the structure.

8.4 Application of transverse resonance method to a slitted trough

As mentioned in detail in the previous chapter, the external admittance is the same as the previous case where b is replaced with g

$$Y_T = \left(\frac{k_{x0}}{\omega\mu_0}\right) \frac{k_{x0}g}{2} \left[1 + j\frac{2}{\pi} \ln\left(\frac{4.795}{k_{x0}g}\right)\right] \quad (8-51)$$

But the internal now has half the capacitance of a slitted plane at the mouth

$$Y_{slit} = \left(\frac{k_x}{\omega\mu_0\mu}\right) j \frac{k_x b}{\pi} \left[\ln\left(\csc\left[\frac{\pi g}{2b}\right]\right)\right] \quad (8-52)$$

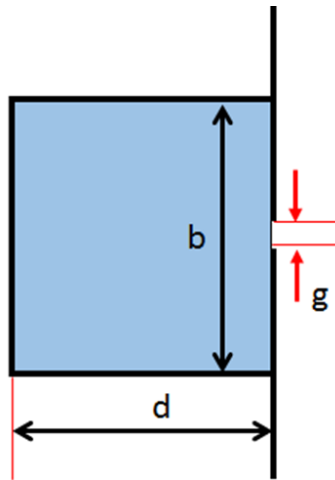


Fig. 8-23 Geometry of the Slitted Trough Where the Slit Adds a Capacitance Term

Then by using the transverse resonance method we will have:

$$\begin{aligned}
\bar{Y}_{left} &= -j \frac{k_x}{\omega \mu_0 \mu} \left\{ \cot(k_x d) - \frac{k_x b}{\pi} \left[\ln \left(\csc \left[\frac{\pi g}{2b} \right] \right) \right] \right\} \\
&= -\bar{Y}_{rad} \\
&= - \left(\frac{k_{x0}}{\omega \mu_0} \right) \frac{k_{x0} g}{2} \left[1 + j \frac{2}{\pi} \ln \left(\frac{4.795}{k_{x0} g} \right) \right]
\end{aligned} \tag{8-53}$$

Probably the easiest way to solve this case given the previous case is to convert the k_x in the new term in the LHS into k_{x0} terms.

$$\begin{aligned}
&-j \frac{k_x}{\omega \mu_0 \mu} \cot(k_x d) + j \frac{k_x^2}{\omega \mu_0 \mu} \frac{b}{\pi} \left[\ln \left(\csc \left[\frac{\pi g}{2b} \right] \right) \right] \\
&= - \left(\frac{k_{x0}}{\omega \mu_0} \right) \frac{k_{x0} g}{2} \left[1 + j \frac{2}{\pi} \ln \left(\frac{4.795}{k_{x0} g} \right) \right]
\end{aligned} \tag{8-54}$$

Then after doing that move it to the RHS

$$\begin{aligned}
&-j \frac{k_x}{\omega \mu_0 \mu} \cot(k_x d) \\
&= - \left(\frac{k_{x0}}{\omega \mu_0} \right) \frac{k_{x0} g}{2} \left[1 + j \frac{2}{\pi} \ln \left(\frac{4.795}{k_{x0} g} \right) \right] \\
&-j \frac{k_0^2 (\varepsilon \mu - 1) + k_{x0}^2}{\omega \mu_0 \mu} \frac{b}{\pi} \left[\ln \left(\csc \left[\frac{\pi g}{2b} \right] \right) \right]
\end{aligned} \tag{8-55}$$

collect

$$\begin{aligned}
& -j \frac{k_x}{\omega \mu_0 \mu} \cot(k_x d) \\
& = - \left(\frac{k_{x0}^2}{\omega \mu_0} \right) \left\{ \frac{g}{2} \left[1 + j \frac{2}{\pi} \ln \left(\frac{4.795}{k_{x0} g} \right) \right] \right. \\
& \quad \left. + j \frac{b}{\mu \pi} \left[\ln \left(\csc \left[\frac{\pi g}{2b} \right] \right) \right] \right\} \\
& \quad - j \frac{k_0^2 (\varepsilon \mu - 1) b}{\omega \mu_0 \mu} \frac{b}{\pi} \left[\ln \left(\csc \left[\frac{\pi g}{2b} \right] \right) \right]
\end{aligned} \tag{8-56}$$

Now collect again and recognize that $\mu \gg 1$ so that $(\varepsilon \mu - 1)/\mu$ is approximately

ε

$$\begin{aligned}
& -j \frac{k_x}{\mu} \cot(k_x d) \\
& \cong -k_{x0}^2 \left\{ \frac{g}{2} \right. \\
& \quad \left. + \frac{j}{\pi} \left[g \cdot \ln \left(\frac{4.795}{k_{x0} g} \right) + \frac{b}{\mu} \cdot \ln \left(\csc \left[\frac{\pi g}{2b} \right] \right) \right] \right\} \\
& \quad - j \frac{k_0^2 b \varepsilon}{\pi} \left[\ln \left(\csc \left[\frac{\pi g}{2b} \right] \right) \right]
\end{aligned} \tag{8-57}$$

As before, multiply both sides times $j\mu d$

$$\begin{aligned}
\frac{k_x d}{\tan(k_x d)} & \cong -j k_{x0}^2 \mu d \left\{ \frac{g}{2} \right. \\
& \quad \left. + \frac{j}{\pi} \left[g \cdot \ln \left(\frac{4.795}{k_{x0} g} \right) + \frac{b}{\mu} \cdot \ln \left(\csc \left[\frac{\pi g}{2b} \right] \right) \right] \right\} \\
& \quad + \frac{k_0^2 b d \mu \varepsilon}{\pi} \left[\ln \left(\csc \left[\frac{\pi g}{2b} \right] \right) \right]
\end{aligned} \tag{8-58a}$$

$$\begin{aligned}
\frac{k_x d}{\tan(k_x d)} &\cong k_{x0}^2 \mu d \left\{ -j \frac{g}{2} \right. \\
&\quad \left. + \frac{1}{\pi} \left[g \cdot \ln \left(\frac{4.795}{k_{x0} g} \right) + \frac{b}{\mu} \cdot \ln \left(\csc \left[\frac{\pi g}{2b} \right] \right) \right] \right\} \\
&\quad + \frac{k_0^2 b d \mu \varepsilon}{\pi} \left[\ln \left(\csc \left[\frac{\pi g}{2b} \right] \right) \right]
\end{aligned} \tag{8-58b}$$

Or making it look like the previous case

$$\begin{aligned}
-j \mu k_{x0}^2 \frac{dg}{2} + \mu \frac{k_{x0}^2 dg}{\pi} \left[\ln \left(\frac{4.795}{k_{x0} g} \right) + \frac{b}{g \mu} \right. \\
\left. \cdot \ln \left(\csc \left[\frac{\pi g}{2b} \right] \right) \right] \\
+ \mu \frac{k_0^2 b d \varepsilon}{\pi} \left[\ln \left(\csc \left[\frac{\pi g}{2b} \right] \right) \right] = \frac{k_x d}{\tan(k_x d)}
\end{aligned} \tag{8-59}$$

Invoking the singularity expansion of the tangent as before

$$\begin{aligned}
-j \mu k_{x0}^2 dg + \mu \frac{2k_{x0}^2 dg}{\pi} \left[\ln \left(\frac{4.795}{k_{x0} g} \right) + \frac{b}{g \mu} \right. \\
\left. \cdot \ln \left(\csc \left[\frac{\pi g}{2b} \right] \right) \right] \\
+ \mu \frac{2k_0^2 b d \varepsilon}{\pi} \left[\ln \left(\csc \left[\frac{\pi g}{2b} \right] \right) \right] \\
= \left(\frac{\pi}{2} \right)^2 - (k_0^2 (\mu \varepsilon - 1) + k_{x0}^2) d^2
\end{aligned} \tag{8-60}$$

Collect

$$\begin{aligned}
k_{x0}^2 \left\{ -j\mu dg + \frac{2\mu dg}{\pi} \left[\ln \left(\frac{4.795}{k_{x0}g} \right) + \frac{b}{g\mu} \cdot \ln \left(\csc \left[\frac{\pi g}{2b} \right] \right) \right] \right\} \\
= \left(\frac{\pi}{2} \right)^2 - (k_0^2(\mu\varepsilon - 1) + k_{x0}^2)d^2 \\
- \mu \frac{2k_0^2bd\varepsilon}{\pi} \left[\ln \left(\csc \left[\frac{\pi g}{2b} \right] \right) \right]
\end{aligned} \tag{8-61}$$

or

$$\begin{aligned}
k_{x0}^2 \left\{ -j\mu dg + \frac{2\mu dg}{\pi} \left[\ln \left(\frac{4.795}{k_{x0}g} \right) + \frac{b}{g\mu} \cdot \ln \left(\csc \left[\frac{\pi g}{2b} \right] \right) \right] \right. \\
\left. + d^2 \right\} \\
= \left(\frac{\pi}{2} \right)^2 - k_0^2d^2(\mu\varepsilon - 1) \\
- \mu \frac{2k_0^2bd\varepsilon}{\pi} \left[\ln \left(\csc \left[\frac{\pi g}{2b} \right] \right) \right]
\end{aligned} \tag{8-62}$$

And solve for k_{x0}^2

$$\begin{aligned}
k_{x0}^2 \\
= \frac{\left(\frac{\pi}{2d} \right)^2 - k_0^2(\mu\varepsilon - 1) - \mu \frac{2k_0^2b\varepsilon}{\pi d} \left[\ln \left(\csc \left[\frac{\pi g}{2b} \right] \right) \right]}{1 - j\mu \frac{g}{d} + \frac{2\mu g}{\pi d} \left[\ln \left(\frac{4.795}{k_{x0}g} \right) + \frac{b}{g\mu} \cdot \ln \left(\csc \left[\frac{\pi g}{2b} \right] \right) \right]}
\end{aligned} \tag{8-63}$$

Now remembering that the ε on the numerator right hand term was really

$(\mu\varepsilon - 1)/\mu$ we collect terms by returning to that form

$$\begin{aligned}
k_{x0}^2 \\
= \frac{\left(\frac{\pi}{2d} \right)^2 - k_0^2(\mu\varepsilon - 1) \left\{ 1 + \frac{2b}{\pi d} \left[\ln \left(\csc \left[\frac{\pi g}{2b} \right] \right) \right] \right\}}{1 - j\mu \frac{g}{d} + \frac{2\mu g}{\pi d} \left[\ln \left(\frac{4.795}{k_{x0}g} \right) + \frac{b}{g\mu} \cdot \ln \left(\csc \left[\frac{\pi g}{2b} \right] \right) \right]}
\end{aligned} \tag{8-64}$$

Whereas for the open trough, before, we had:

$$k_{x0}^2 = \frac{\left(\frac{\pi}{2d}\right)^2 - k_0^2(\mu\varepsilon - 1)}{\left[1 - j\mu\frac{b}{d} + \frac{2\mu b}{\pi d} \ln\left(\frac{4.795}{k_{x0}b}\right)\right]} \quad (8-65)$$

The above is the TRM condition using the singularity extraction approximation for the tangent. Formally the TRM condition is:

$$\begin{aligned} k_{x0}^2 &= \frac{\frac{k_x d}{\tan(k_x d)} - \mu \frac{k_0^2 b d \varepsilon}{\pi} \left[\ln\left(\csc\left[\frac{\pi g}{2b}\right]\right) \right]}{-j\mu \frac{dg}{2} \left[1 + j \frac{2}{\pi} \left[\ln\left(\frac{4.795}{k_{x0}g}\right) + \frac{b}{g\mu} \cdot \ln\left(\csc\left[\frac{\pi g}{2b}\right]\right) \right] \right]} \end{aligned} \quad (8-66)$$

Whereas without the slit it was:

$$k_{x0}^2 = \frac{\frac{k_x d}{\tan(k_x d)}}{-j\mu \frac{db}{2} \left[1 + j \frac{2}{\pi} \ln\left(\frac{4.795}{k_{x0}b}\right) \right]} \quad (8-67)$$

Similar to the previous case we again argue that the log term with k_{x0} is slowly varying and therefore we can put inside it our first guess for k_{x0} , namely β_{x0} from onset. But when does onset occur for the case of the slit?

Onset still occurs when $k_z = k_{z0} = k_0$ so that $k_{x0} = 0$. This means

$$k_x^2 = \varepsilon\mu k_0^2 - k_0^2 \rightarrow k_x = k_0 \sqrt{\mu\varepsilon - 1} \quad (8-68)$$

Since TRM is

$$\begin{aligned}
& -j \frac{k_x}{\omega \mu_0 \mu} \left\{ \cot(k_x d) - \frac{k_x b}{\pi} \left[\ln \left(\csc \left[\frac{\pi g}{2b} \right] \right) \right] \right\} \\
& = - \left(\frac{k_{x0}}{\omega \mu_0} \right) \frac{k_{x0} g}{2} \left[1 + j \frac{2}{\pi} \ln \left(\frac{4.795}{k_{x0} g} \right) \right] \\
& = 0
\end{aligned} \tag{8-69}$$

We must have

$$\cot(k_x d) = \frac{k_x b}{\pi} \left[\ln \left(\csc \left[\frac{\pi g}{2b} \right] \right) \right] \tag{8-70}$$

And so onset occurs earlier than $k_x d = \pi/2$. Assuming we will be close to the original onset (the slit is a perturbation) we write the onset condition as:

$$\cot \left(\frac{\pi}{2} - \delta \right) = \frac{k_x b}{\pi} \left[\ln \left(\csc \left[\frac{\pi g}{2b} \right] \right) \right] \tag{8-71}$$

Where $k_x d = \frac{\pi}{2} - \delta$ so that $k_x = \frac{\pi}{2d} - \frac{\delta}{d}$. We can rewrite then:

$$\begin{aligned}
\tan(\delta) & = \left(\frac{\pi}{2} - \delta \right) \frac{b}{\pi d} \left[\ln \left(\csc \left[\frac{\pi g}{2b} \right] \right) \right] \\
& = \frac{\pi}{2} \frac{b}{\pi d} \left[\ln \left(\csc \left[\frac{\pi g}{2b} \right] \right) \right] \\
& \quad - \delta \frac{b}{\pi d} \left[\ln \left(\csc \left[\frac{\pi g}{2b} \right] \right) \right]
\end{aligned} \tag{8-72}$$

Since we are close to the origin if δ is small, the first guess for δ is

$$\delta_0 = \frac{\frac{b}{2d} \left[\ln \left(\csc \left[\frac{\pi g}{2b} \right] \right) \right]}{1 + \frac{b}{\pi d} \left[\ln \left(\csc \left[\frac{\pi g}{2b} \right] \right) \right]} \tag{8-73}$$

For the next approximation use the next terms in the Taylor series

$$\delta_m = \frac{\frac{b}{2d} \left[\ln \left(\csc \left[\frac{\pi g}{2b} \right] \right) \right] - \frac{\delta_{m-1}^3}{3} - \frac{2\delta_{m-1}^5}{15}}{1 + \frac{b}{\pi d} \left[\ln \left(\csc \left[\frac{\pi g}{2b} \right] \right) \right]} \quad (8-74)$$

Consider the case above where $b=3.8$ inches and $d=1.053$ inches and we make $g=0.5b$, $\delta_0 = 0.447$, $\delta_1 = 0.426$, and $\delta_2 = 0.428$.

So onset occurs at

$$k_{0-onset} = \frac{k_{x-onset}}{\sqrt{\mu\varepsilon - 1}} = \frac{\pi}{2d\sqrt{\mu\varepsilon - 1}} - \frac{\delta_2}{d\sqrt{\mu\varepsilon - 1}} \quad (8-75)$$

And our first guess for k_{x0} is (as before):

$$k_{x00} = \sqrt{k_{0-onset}^2 - k_0^2} \quad (8-76)$$

Therefore since

$$k_x = \sqrt{(\varepsilon\mu - 1)k_0^2 + k_{x0}^2} \quad (8-77)$$

The first approximation

k_{x01}

$$= \frac{\frac{d\sqrt{(\varepsilon\mu - 1)k_0^2 + k_{x00}^2}}{\tan \left(d\sqrt{(\varepsilon\mu - 1)k_0^2 + k_{x00}^2} \right)} - \mu \frac{k_0^2 b d \varepsilon}{\pi} \left[\ln \left(\csc \left[\frac{\pi g}{2b} \right] \right) \right]}{\sqrt{-j\mu \frac{dg}{2} \left[1 + j \frac{2}{\pi} \left[\ln \left(\frac{4.795}{k_{x00}g} \right) + \frac{b}{g\mu} \cdot \ln \left(\csc \left[\frac{\pi g}{2b} \right] \right) \right] \right]}} \quad (8-78)$$

And again

$$\begin{aligned}
& k_{x02} \\
&= \sqrt{\frac{\frac{d\sqrt{(\varepsilon\mu - 1)k_0^2 + k_{x01}^2}}{\tan\left(d\sqrt{(\varepsilon\mu - 1)k_0^2 + k_{x01}^2}\right)} - \mu \frac{k_0^2 b d \varepsilon}{\pi} \left[\ln\left(\csc\left[\frac{\pi g}{2b}\right]\right)\right]}{-j\mu \frac{dg}{2} \left[1 + j \frac{2}{\pi} \left[\ln\left(\frac{4.795}{k_{x01} g}\right) + \frac{b}{g\mu} \cdot \ln\left(\csc\left[\frac{\pi g}{2b}\right]\right)\right] \right]} } \quad (8-79)
\end{aligned}$$

And again

$$\begin{aligned}
& k_{x02} \\
&= \sqrt{\frac{\frac{d\sqrt{(\varepsilon\mu - 1)k_0^2 + k_{x02}^2}}{\tan\left(d\sqrt{(\varepsilon\mu - 1)k_0^2 + k_{x02}^2}\right)} - \mu \frac{k_0^2 b d \varepsilon}{\pi} \left[\ln\left(\csc\left[\frac{\pi g}{2b}\right]\right)\right]}{-j\mu \frac{dg}{2} \left[1 + j \frac{2}{\pi} \left[\ln\left(\frac{4.795}{k_{x02} g}\right) + \frac{b}{g\mu} \cdot \ln\left(\csc\left[\frac{\pi g}{2b}\right]\right)\right] \right]} } \quad (8-80)
\end{aligned}$$

For a meaningful comparison let's make a slit $g=0.5b$ but reduce the depth to keep the onset at 250 MHz like before. This happens for $d=0.67''$ ($\mu = 40$, $\varepsilon = 3.2$, $b=3.8''$). We are therefore reducing the amount (volume) of material used.

Again, similar to the case of the open trough, we can either use this approximation method or to use an unconstrained minimization routine to solve the equation and they will both give the same results.

The red curves are the no slit case and the black are with the slit. Since this is a TRM solution we ignore the "up turn" of the black beta curve below 160MHz since we now this is an unphysical result.

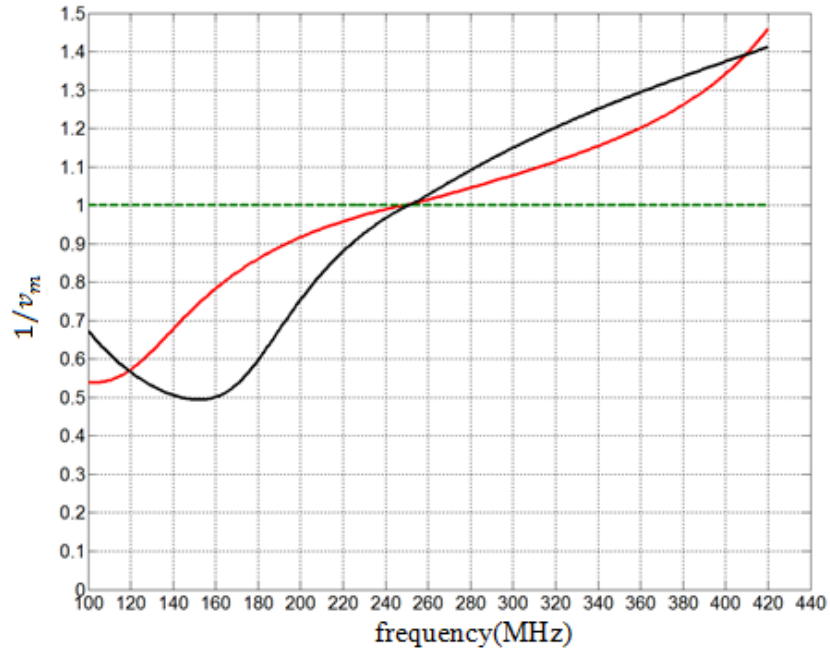


Fig. 8-24 Inverse Velocity ($\beta/2\pi$) Plot for a 1.053" by 3.8" Open Trough with $\mu = 40$, $\epsilon = 3.2$ Shown in Red and the Same Plot for a 0.67" by 3.8" Slitted Trough with the Same Material and a 0.335" Slit Shown in Black

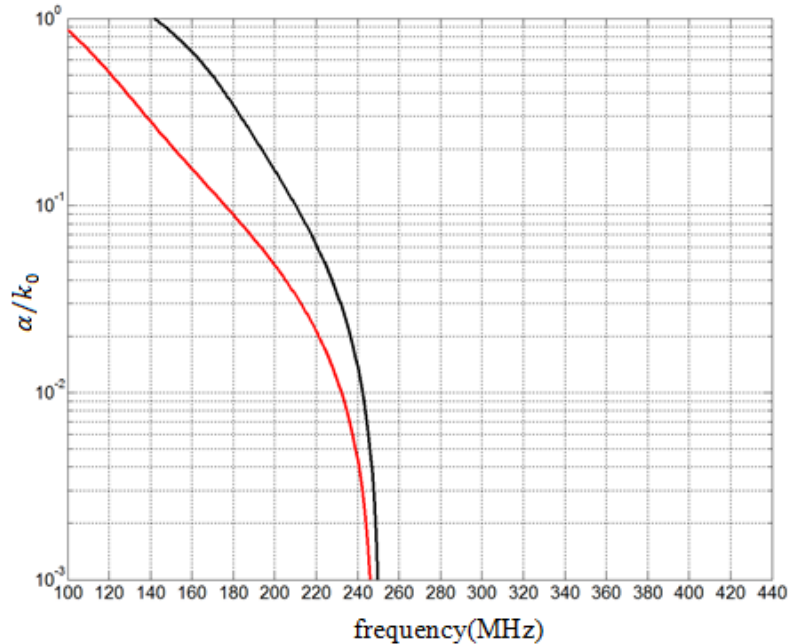


Fig. 8-25 α Plot for a 1.053" by 3.8" Open Trough with $\mu = 40$, $\varepsilon = 3.2$ Shown in Red and the Same Plot for a 0.67" by 3.8" Slitted Trough with the Same Material and a 0.335" Slit Shown in Black

The key result is that in the neighborhood of onset the slope becomes higher (reducing the bandwidth), making the leaky wave attenuation also higher, because we have reduced the amount of material (by 36%) and yet retained the 250 MHz onset.

What happens now if we retain the amount of material, namely increase b ? So, we increase b by the same factor that we have decreased d . Then adjust the slit to get back to 250 MHz to $g=0.595b$ ($b=5.972$, $d=0.67$) .

The results can be seen below.

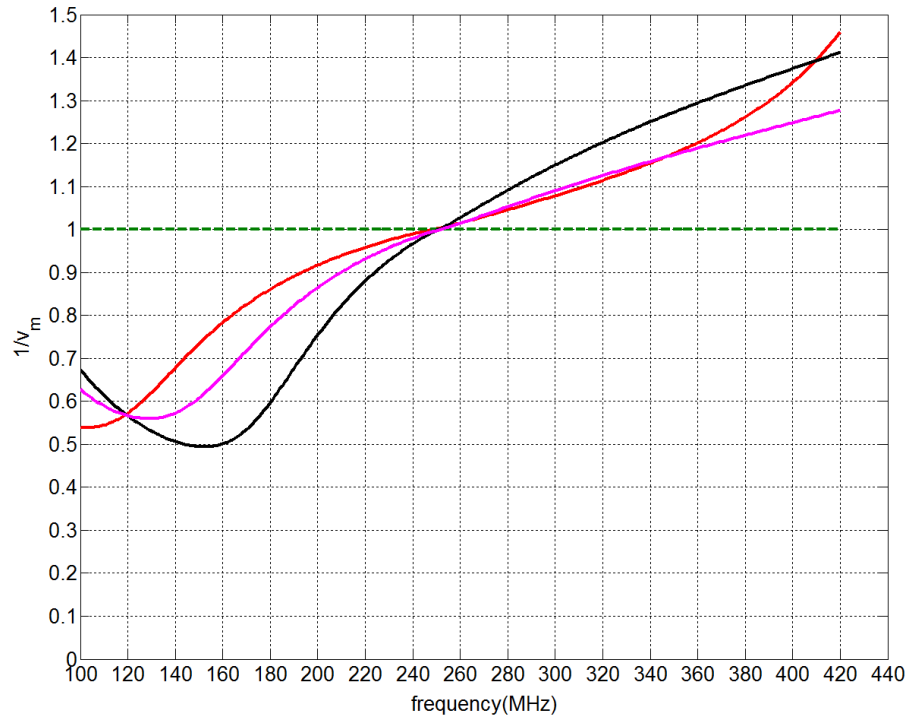


Fig. 8-26 Inverse Velocity ($\beta/2\pi$) Plot for a 1.053" by 3.8" Open Trough with $\mu = 40$, $\epsilon = 3.2$ Shown in Red and the Same Plot for a 0.67" By 3.8" Slitted Trough with the Same Material and A 0.335" Slit Shown In Black and the Same Plot for a 0.67" by 5.972" Slitted Trough with the Same Material and a 0.595" Slit Shown in Magenta

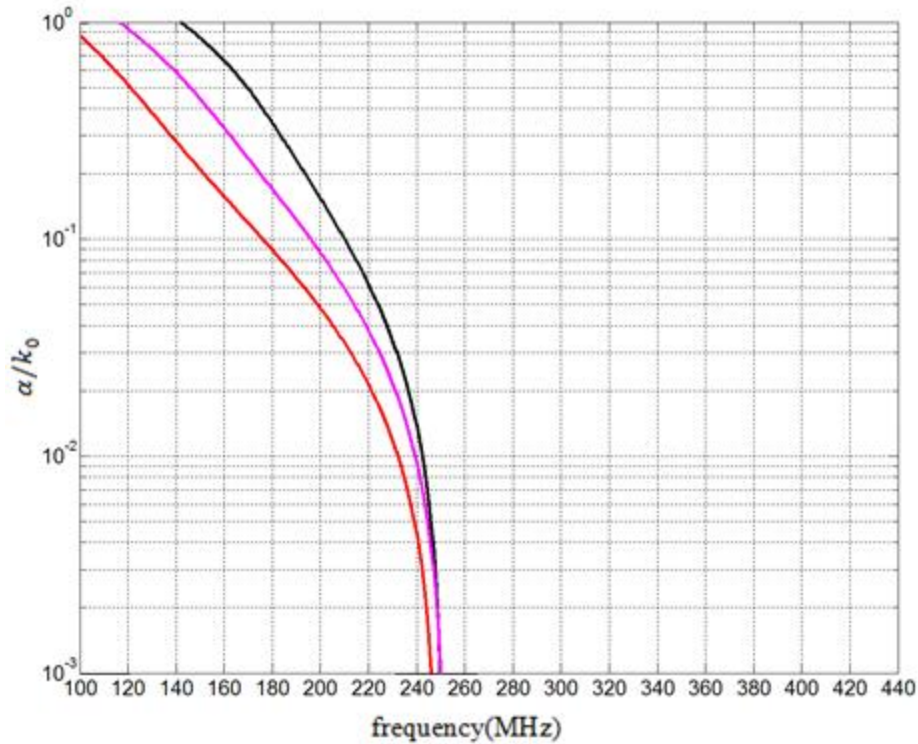


Fig. 8-27 A Plot for a 1.053" by 3.8" Open Trough with $\mu = 40$, $\epsilon = 3.2$ Shown in Red and the Same Plot For a 0.67" by 3.8" Slitted Trough with the Same Material and A 0.335" Slit Shown in Black and the Same Plot for a 0.67" by 5.972" Slitted Trough With the Same Material and a 0.595" Slit Shown in Magenta

The figures show that we recover the beta slope at onset. The slope below onset is higher than for the no slit case and so is the attenuation constant. However, and most importantly, the slope is shallower to higher frequencies because the shallower depth of the trough pushes away the next higher order mode ($d \sim 3/4$ wavelength).

This is exactly what we had seen in the previous chapter when studying the bandwidth, the radiation bandwidth of the Green function solution is widened **upwards** by the slit, all other things remaining constant.

8.5 Full wave simulation results of the slitted trough

As the next step in studying the slitted trough, we have simulated the geometry of the slitted trough in HFSS and we have compared the results to the transverse resonance method obtained in section 8.4. The geometry simulated in HFSS can be seen below which has the same dimensions and material properties as the example demonstrated in chapter 7.

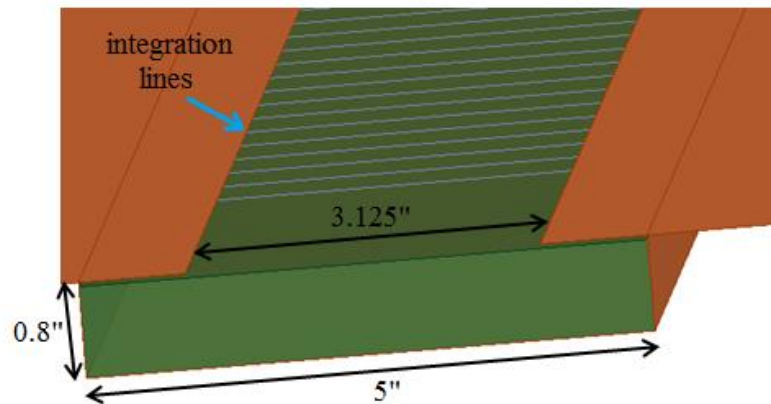


Fig. 8-28 Geometry of a 5”by 0.8” Slitted Trough Simulated in HFSS and Showing the Integration Lines

This structure has the same amount of material as the 3.8” by 1.053” open trough and has the same material properties which are $\mu = 80$, $\varepsilon = 2$. The dimensions of this structure can be seen in the figure and the slit has been chosen to ensure that the onset happens at the same frequency as the open trough. Note that a small air gap has been inserted between the slit planes and the material as was done with the parallel solenoid conductors. The figure below shows the comparison to the results obtained from the transverse resonance method.

Similar to what we saw for the trough, the fullwave simulation and the transverse resonance have a very good agreement but they deviate as we go lower in frequency. Also, we see the curving of the beta plot obtained from the transverse resonance has the same behavior that was present in Oliner's work therefore at lower frequencies it becomes unphysical.

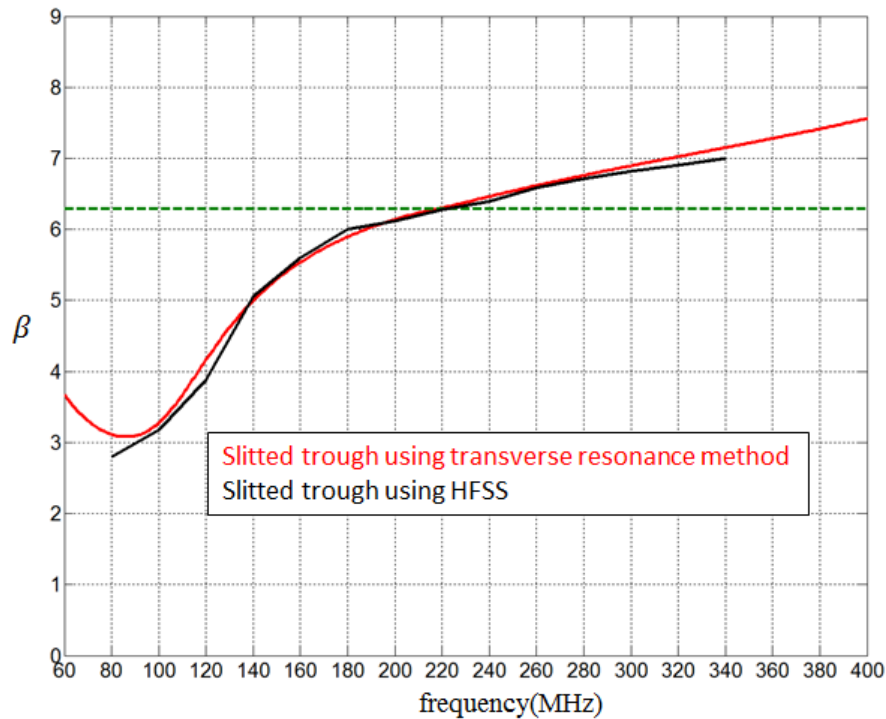


Fig. 8-29 β Plots of a 5"by 0.8" Slitted Trough Obtained Using Fullwave HFSS Simulation and Transverse Resonance Method

8.6 Application of transverse resonance method to dispersive permeable material

At this point it would be interesting to use this solution to study what happens when the material in the trough is dispersive. For instance, let the material filling the trough be the CZN laminate

$$\mu = 1 + \frac{39}{1 + j \frac{f}{1.5 \cdot 10^9} \cdot \frac{1}{0.75} - \left(\frac{f}{1.5 \cdot 10^9} \right)^2} \quad (8-81)$$

$$\varepsilon = 3.2$$

We can use the successive approximation method or the optimization method. However before going forward it should be noted that if we are using the transverse resonance method with a complex material we need to pay attention to an important detail about the α plots that wouldn't cause any trouble in the lossless case but might cause a problem in using the transverse resonance method in the lossy material case.

The difference between a material with a lossless permeability and a lossy permeability is that in the lossless case we know that before onset we have a fast wave with a wave number as $k_z = \beta_z - j\alpha_z$ and from the outside world, we have $k_{x0} = \beta_{x0} + j\alpha_{x0}$ which is a leaky wave. In the guided wave region since $k_z > k_0$ then we have $k_{x0} = -j\alpha_{x0}$ and we have a decaying wave as expected. This means that the solution to the transverse resonance method for a lossless material is unique both in leaky wave and in fast wave regions. The same cannot be said for the lossy material since we don't know the correct solution to α_z since the solution to the transverse resonance method for k_{x0} is no longer unique and can even have a positive or negative answer.

This problem has been seen before in the subject of surface waves on lossy materials in stealth. The question that is always present is does the wave on the lossy material get sucked in so it is slowed down and absorbed or does it get peeled off because it is too lossy to be guided? This is similar to our problem in defining a unique and clear alpha and not being able to make a decision using the eigenvalue problem (that is, TRM).

Therefore, we will obtain the beta plots using the transverse resonance method and leave the alpha plots for a more complete method like the Green's function method. We can also show that after a certain frequency we have more than one answer in the optimizer's zero search for k_{x0} .

Now we will compare the lossless case $\epsilon = 3.2, \mu = 40$ with the dispersive case. The figure below compares the optimization solution of the lossless case $\epsilon = 3.2, \mu = 40$ (black) with the dispersive case (magenta):

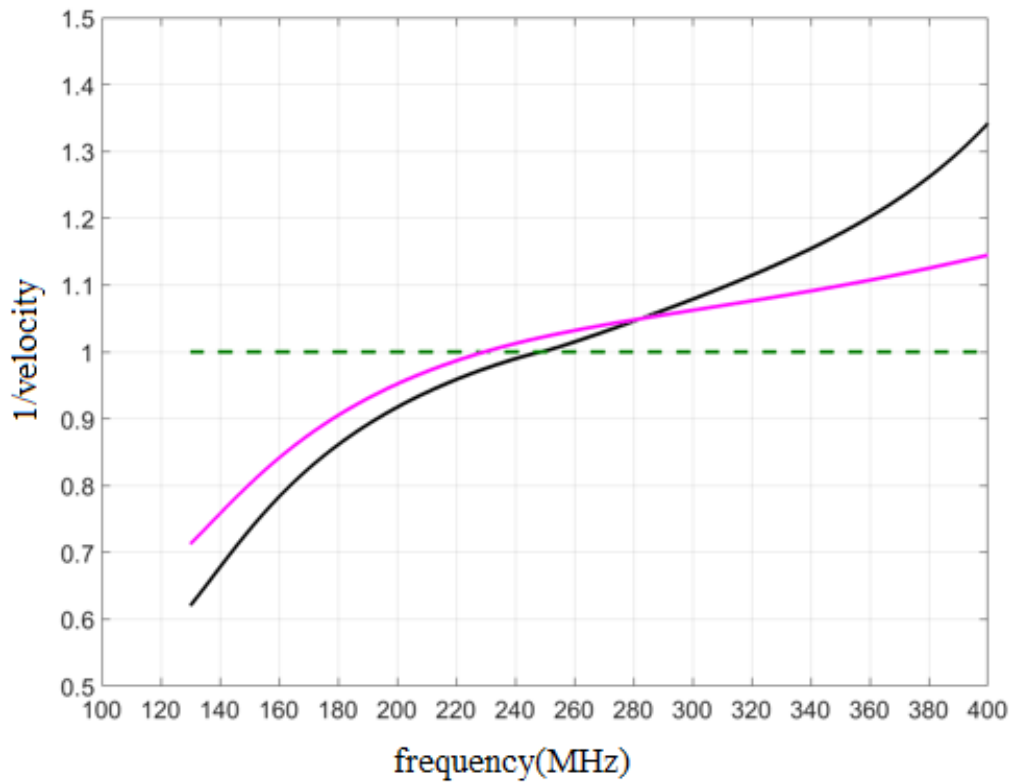


Fig. 8-30 Inverse Velocity ($\beta/2\pi$) Plot for a 1.053" by 3.8" Open Trough with $\mu = 40, \epsilon = 3.2$ Shown in Black and Inverse Velocity ($\beta/2\pi$) Plot for the Same Dimensions and CZN Material Filling

The fact that in the dispersive material there is loss slows the wave down earlier than the original onset (if we define onset as the beginning of slowing down, that is, $v=c_0$). This is surprising: It modifies the onset by moving it from 248 MHz to 232 MHz even though the ferromagnetic resonance is far away, at 1.5GHz.

From the viewpoint of the slope of the beta plot, it is interesting that adding loss flattens the slope. This is because waves guided by a lossy surface have more of their energy in the exterior space and therefore tend to travel close to the speed of light. (e.g. see the solution for a highly lossy half-space in the lossy earth problem).

Now, we know that the efficiency of conformal antennas based on a dispersive permeable flux channel is a function of the hesitivity. Sebastian had pointed out that from the viewpoint of bandwidth, all things (in particular efficiency) being equal it is preferable to place the ferromagnetic resonance in the band of use, thus leading to the final material selection rule. In this case we are looking at operation in the low VHF through UHF (100MHz to 600MHz) but CZN resonates at 1.5GHz. Therefore, we artificially “Snoek” the permeability by raising μ_{DC} by a factor and dropping the resonant frequency by the same factor thus preserving the hesitivity.

The figure below shows the case where the material has been Snoeked by a factor of 2, μ_{DC} at 79 and the resonance at 750MHz, just outside the upper edge of our desired band of operation.

At first glance, the results are startling. As would be expected the “onset” is pushed back because now there is a higher μ but, in addition, because loss tends to guide

a wave, the leaky waves below onset are not as leaky. In other words, we actually reduce the attenuation constant of the low end and bring the propagation speed within 10 percent of lightspeed over a very wide frequency range.

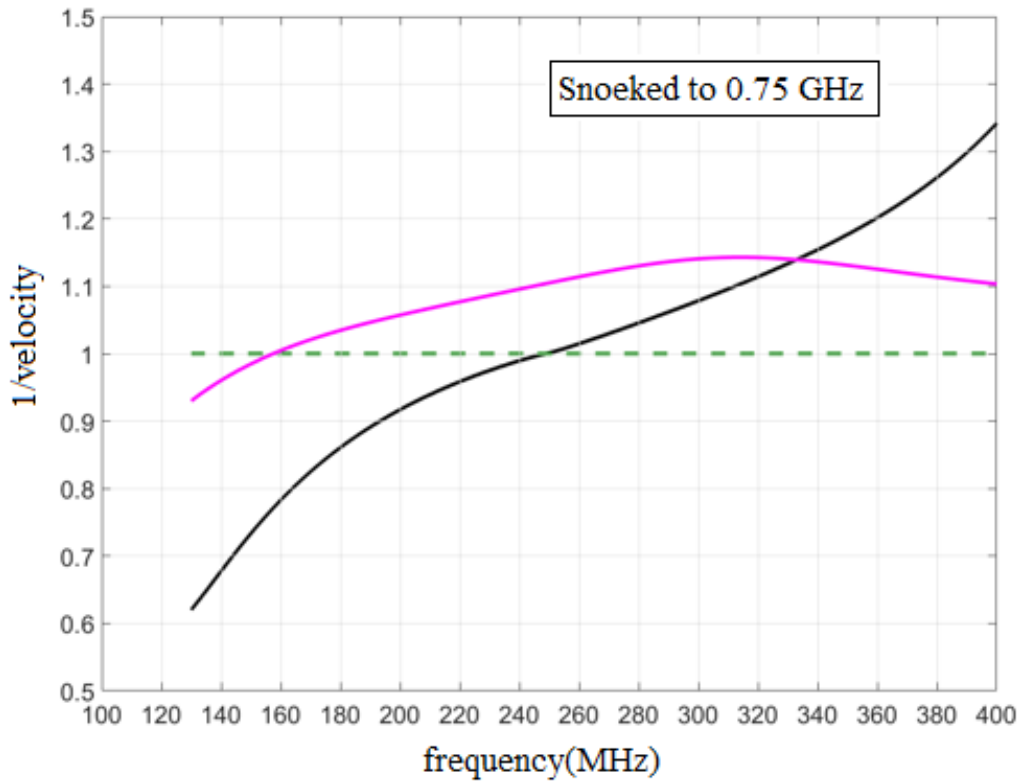


Fig. 8-31 Inverse Velocity ($\beta/2\pi$) Plot for a 1.053” by 3.8” Open Trough with $\mu = 40$, $\epsilon = 3.2$ Shown in Black and Inverse Velocity ($\beta/2\pi$) Plot for the Same Dimensions and CZN Material Snoeked to 0.75GHz

The trend continues when we Snoek by factors of 3 and 4, until we see the approach to the “lossy magnetic conductor” tending to PMC in the figures below:

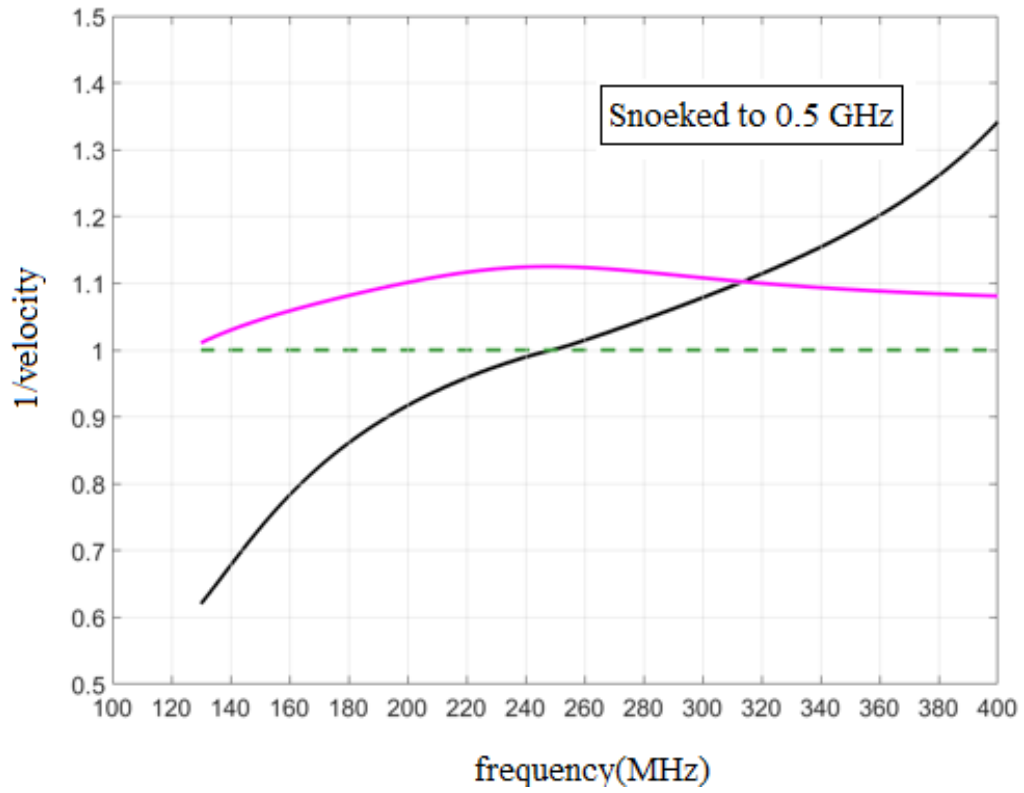


Fig. 8-32 Inverse Velocity ($\beta/2\pi$) Plot for a 1.053" by 3.8" Open Trough with $\mu = 40$, $\epsilon = 3.2$ Shown in Black and Inverse Velocity ($\beta/2\pi$) Plot for the Same Dimensions and CZN Material Snoeked to 0.5GHz

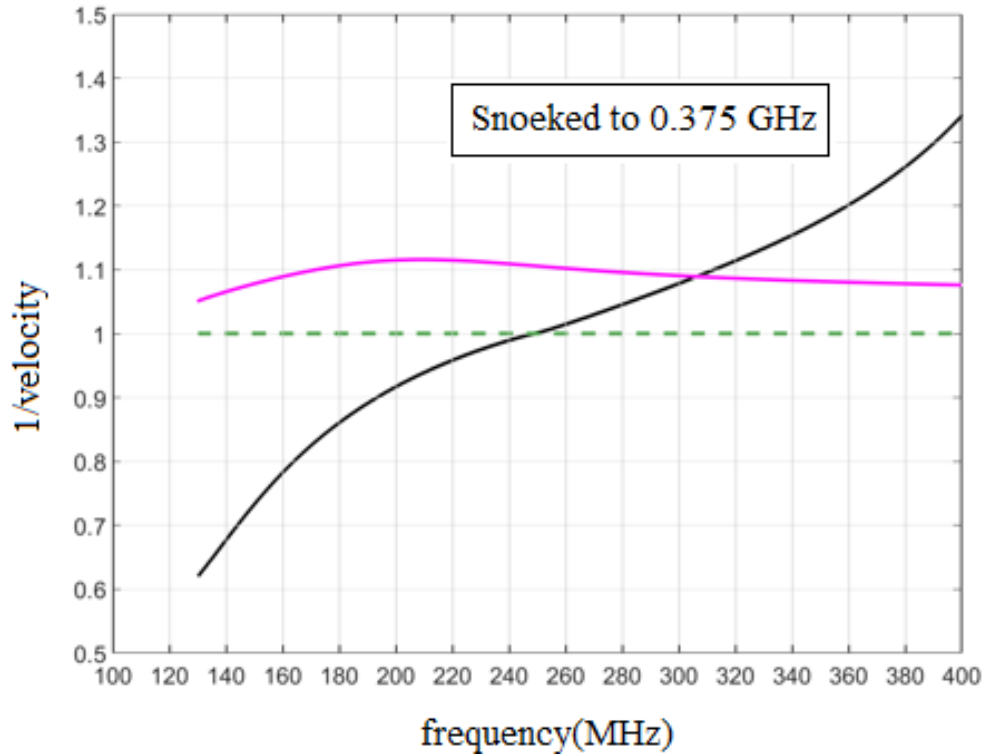


Fig. 8-33 Inverse Velocity ($\beta/2\pi$) Plot for a 1.053" by 3.8" Open Trough with $\mu = 40$, $\epsilon = 3.2$ Shown in Black and Inverse Velocity ($\beta/2\pi$) Plot for the Same Dimensions and CZN Material Snoeked to 0.375GHz

8.7 Full wave simulation results of the trough and the slitted trough filled with metal walls

Electromagnetic materials may possess anisotropic constitutive properties. That is, the permittivity and permeability may depend on the direction of the applied field. In permeable ferromagnetic (metallic) and ferrimagnetic (ceramic) materials this anisotropy may be a result of the manufacturing process but it also can be produced by the method of construction. In particular, ferromagnetic laminates, ferromagnetic artificial materials resulting from alternating thin metal films with thin insulating (non-magnetic) dielectrics, are anisotropic in both effective permittivity and effective permeability.

In the next chapter, we will explain the reason we choose adding vertical metal films (walls) instead of horizontal films inside the magnetic material as one of the methods of obtaining the optimum flux channel and why we expect them to have a mode filtering effect in higher frequencies. However, in this section we proceed to demonstrate results that show the metal walls can help in the ultimate goal of increasing the bandwidth.

In order to prove the mode filtering technique works, the flux channel described in this chapter, 3.8 inches wide, 1.053 inches deep, filled with homogeneous isotropic $\epsilon = 2$, $\mu = 80$ material, and excited by a coax feed at its center was simulated using ANSYS HFSS. The channel was terminated at both ends into the computer code's absorbing boundary conditions which approximately simulate an infinitely long trough. To show the effect of constructed anisotropy, a model of a trough filled with permeable material that has vertical PEC walls inside has been simulated in HFSS. For the sake of completeness, we distinguish between the case where the walls are touching the ground and the case where they are not. Figure below shows the trough with vertical PEC walls that are touching the ground plane.

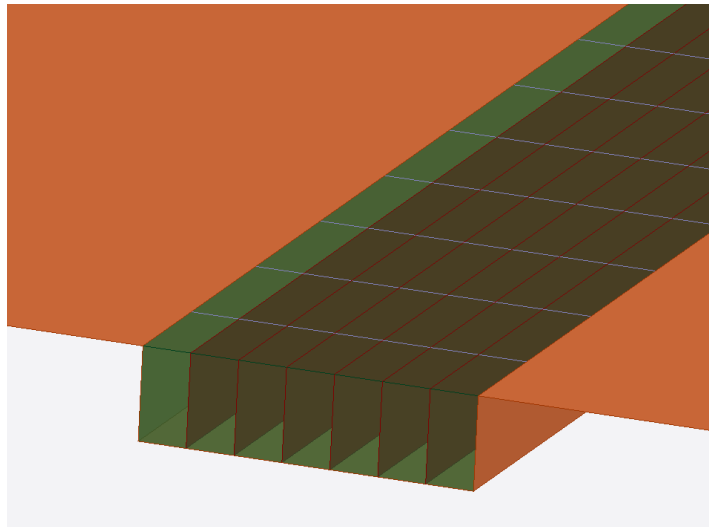


Fig. 8-34 Geometry of a 1.053"by 3.8" Open Trough Simulated in HFSS with Added Vertical Metal Walls Touching the Ground

In order to see how the vertical PEC walls with a gap to ground affects the results, we have included a 1mm gap between the walls and the lower ground plane as seen below.

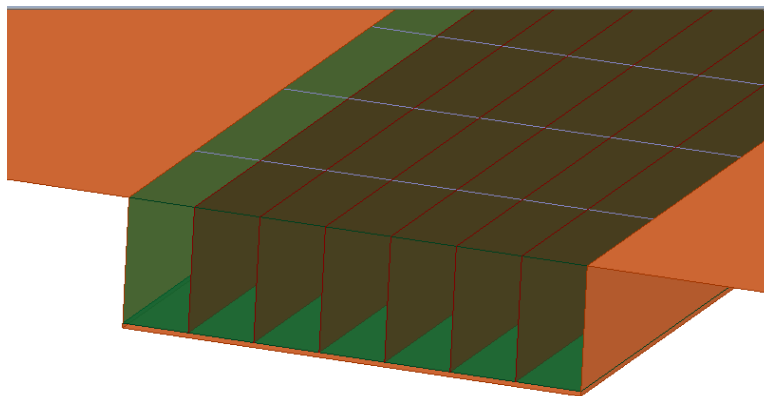


Fig. 8-35 Geometry of a 1.053"by 3.8" Open Trough Simulated in HFSS with Added Vertical Metal Walls and a 1mm Gap from Ground

The beta plots have been compared and since the amount of material used has been kept the same, the onset frequency of the structures happen approximately at the same frequency. And the gap between the conducting walls and the ground unnecessary.

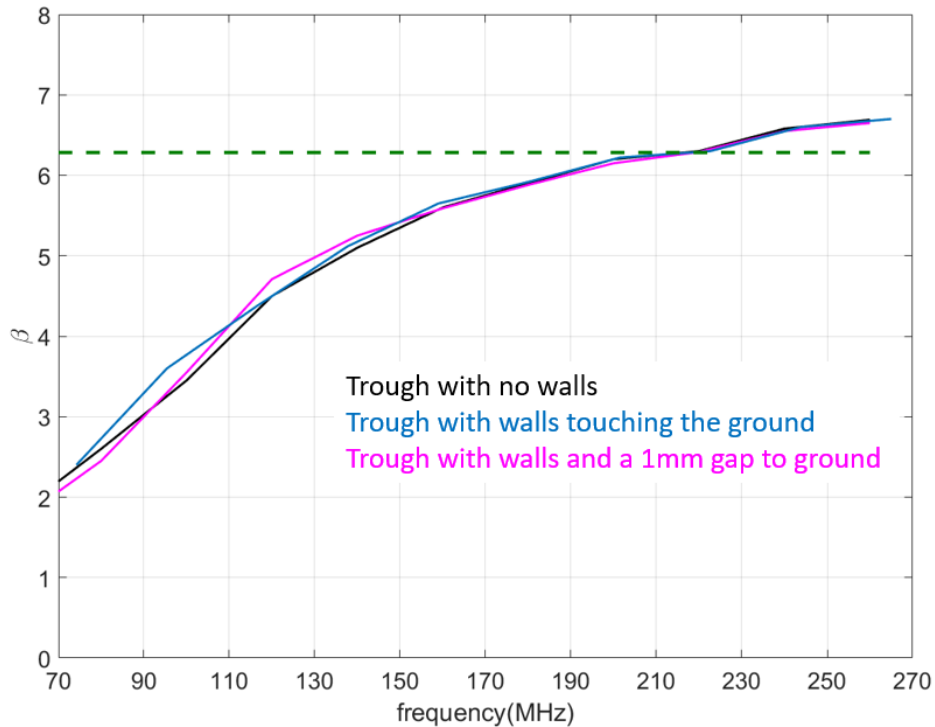


Fig. 8-36 β Plots of a 1.053"by 3.8" Open Trough with Homogenous Material, with Added Walls Touching the Ground and with Added Walls with a Gap to Ground

At first look, it seems like the walls are causing no specific difference however the mode filtering effect shows up later. The figure below shows a plot of the magnetic current amplitude along the channel from the feed to a distance 2.6 wavelengths away at 400MHz. The isotropic material case is the blue curve whereas the material with metal plates added into it to create the desired artificial anisotropy yields the red curve.

The red curve is characteristic of a pure guided mode excited at the feed and propagating outwards from the feed in the “trapped wave” regime. The ten percent “ripple” overlaid on an otherwise smooth amplitude with a slight slope (this slope denoting that the trapped wave is radiating because it is not completely trapped at this frequency) is a result of the imperfect absorbing boundary terminations of the computer code.

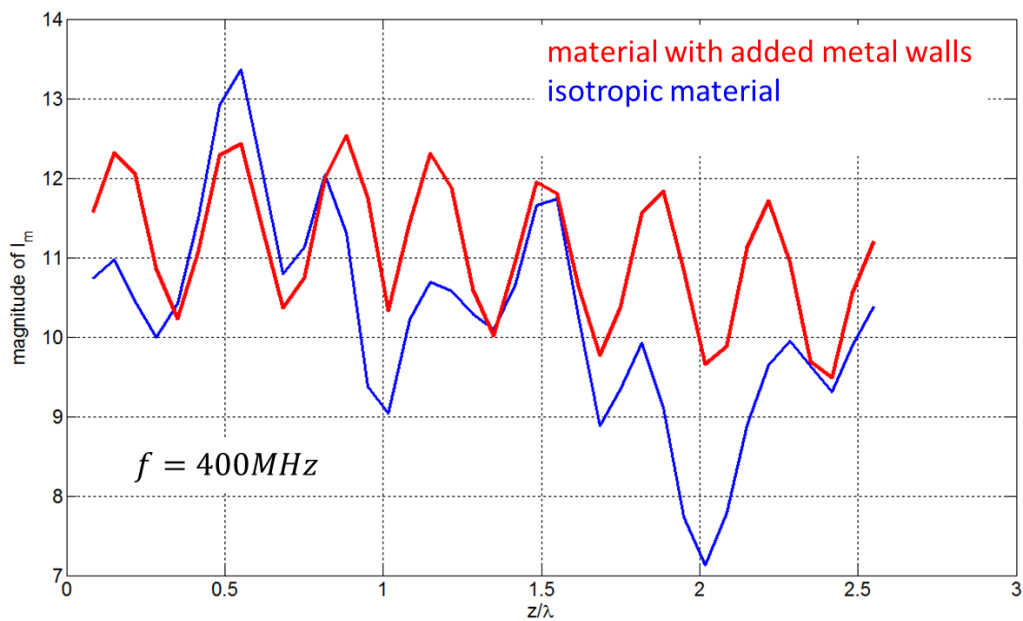


Fig. 8-37 Magnitude of the Magnetic Current Versus Distance from Feed in Wavelengths for the Case of the Open Trough with Walls and the Case of the Open Trough without Walls Showing the Mode Filtering Effect of the Vertical Walls

By contrast the blue curve shows what appears to be a severe beat phenomenon, exactly what would be expected from the co-existence of two traveling modes in the trough at the same time, the intended TE₀₁ mode and the undesired TE₂₁ mode. As is well known in the case of structures supporting more than one propagating mode, the wave injected at a feed-point travels along the structure by transferring its energy back

and forth from one mode to the other along the propagation direction leading to a beat (this is called mode conversion).

8.8 Conclusion

Continuing the work of the previous chapter on the dispersion diagrams of the open trough and the slitted trough, we have presented two additional methods of obtaining these diagrams. We have seen that the transverse resonance method is a very fast and easy method to obtain the dispersion diagram and it is accurate around the onset frequency. An estimation has been given of the minimum frequency that the TRM method can be trusted and it has been shown that below that frequency, we can either use a fullwave simulation to obtain the results or use the Green's function method.

In order to come up with the best way to design a flux channel it is important to know how the dispersion diagram works and it has been shown in this chapter that depending on the frequency range of interest, the amount of memory needed, or the time available for obtaining the dispersion relations there are different methods available. Each method has its benefits and drawbacks however it is crucial to completely understand the dispersion behavior of the demonstrated antenna structures to know how they can be manipulated to have the best functionality.

Since the ultimate goal is to come up with a design methodology for an optimum flux channel, this chapter served as a study on how the geometry and the material properties can be used to flatten the $\omega - \beta$ diagram about onset. From now on we have the tools to design the optimum channel using a change in the cross section geometry,

adding the slit, using a dispersive permeable material, or even adding vertical metal walls to artificially cause anisotropy. The next chapter will contain a detailed discussion and summarize these methodologies and give a full design guideline for an optimum flux channel.

CHAPTER 9

OPTIMAL PERMEABLE ANTENNA FLUX CHANNELS FOR CONFORMAL APPLICATIONS SUMMARY AND DESIGN GUIDELINES

“All of physics is either impossible or trivial. It is impossible until you understand it, and then it becomes trivial.”

Ernest Rutherford

9.1 Introduction

The ultimate goal of all the design and fabrication procedures and technical features of this dissertation was to obtain optimal true magnetic antennas also known as permeable antennas or magnetic flux channel antennas. As mentioned in the previous chapters, these antennas have been recently demonstrated to exhibit extraordinary efficiency in conformal antenna applications. These antennas constitute the most advanced members of a family of antennas that began with the ferrite dipole in the 1950's and includes the mast-clamp antenna, and other ferrite based antennas reported in the technical and patent literature. The advantage of the magnetic flux channel dual antennas is that, in practical implementation, they are conformal to a metallic surface. This metallic surface then acts as the dual of the “open circuit” or perfectly magnetically conducting symmetry plane of their electric metal antenna counterparts.

This chapter is based on our recently filed patent: R. Diaz ,T. Yousefi, “Optimal permeable antenna flux channels for conformal applications”

The advantage of the magnetic flux channel dual antennas is that, in practical implementation, they are conformal to a metallic surface. This metallic surface then acts as the dual of the “open circuit” or perfectly magnetically conducting symmetry plane of their electric metal antenna counterparts. This is important because as mentioned in the previous chapters, electric antennas using metallic conductors to carry radiating electric currents suffer a significant disadvantage when placed conformal to the conducting surface of a platform. This platform can be air, land, or sea vehicle, or even the human body.

The previous chapters and references at the end of this dissertation contains a list of the recent publications that detail the properties of these true magnetic antennas and why they are one to two orders of magnitude more efficient and wider in bandwidth than corresponding metal antennas constrained to the same conformal volume.

In this chapter, we bring together all the key features of a novel implementation of permeable antennas that maximizes efficiency and bandwidth beyond any other current implementation in the literature or disclosed in patents to date, while using realistic (dispersive) materials, as gleaned from the investigations detailed in all previous chapters.

The prototypical magnetic flux channel antenna considered in this dissertation consists of an infinitely long conducting trough in a ground plane – filled with permeable material ($\mu_r > \epsilon_r$). For the purposes of deriving and verifying the design procedure we have shown that the antenna’s electromagnetic behavior can be accurately modelled with a “principal mode” Green function model over the band of interest and approximately

modeled in the neighborhood of the surface wave onset frequency with a Transverse Resonance Method model. The latter method is a very fast design method to obtain the dimensions of the flux channel; and other methods can be used to give correct data as we go far from the onset frequency. This has been verified by comparing the models to full physics simulation using industry standard computational electromagnetics codes (ANSYS HFSS) [20] and ASU's in-house Finite Difference Time Domain code.

The reason the behavior near the surface wave onset frequency is important is that in that frequency range the magnetic flux channel guides an electromagnetic wave over its surface at approximately the speed of light. As seen from the outside, the magnetic field flux lines of this guided wave appear to terminate in the channel and thus this wave is the electromagnetic dual of the wave guided by metal conductors used in conventional antennas. Therefore, in this frequency range the magnetic flux channel behaves most like a magnetic conductor and all presently known antennas implemented with metals can be duplicated with identical antennas made from magnetic flux channels.

9.2 The generalized admittance surface

The onset frequency occurs when the transverse geometry of the trough first satisfies the Transverse Resonance condition. That is, when a quarter wavelength of the guided wave fits in the thickness d , such that the TE₀₁ mode's electric field is zero at the short circuit at the bottom of the trough and a maximum at the open mouth (which behaves as an open circuit.) From the practice of waveguide resonator and filter design

we know we can alter the impedance of the mouth of the trough by adding a shunt admittance; that is, covering the open mouth of the trough with an admittance surface.

In particular if we add a capacitive shunt admittance at the mouth then the thickness d required for the quarter wave resonance is reduced. This means that we can attain a given desired onset frequency by using a shallower trough than is possible with just the open trough. A simple implementation of the capacitive admittance sheet is a slitted metal plane. Since the trough is now shallower, we can keep the same amount of permeable material and make the trough wider. Therefore, we obtain a trough that has a much wider band of operation.

In the figure below, two troughs containing the same amount of material (same cross-sectional area, 4 square inches) of relative permeability 40 (assumed purely real for the sake of simplicity) and relative permittivity 3.2, have been designed to have an onset frequency of 220 MHz. The maximum radiation band (over which 90% of the feed power is radiated) has been determined to occur when the speed of propagation of the guide wave lies between 1.36 times the speed of light and 0.76 times the speed of light, and these are denoted by the dashed lines in the phase velocity plot. The conventional trough crosses these boundaries around 140MHz and 300MHz. By comparison the slope of the slitted trough's curve is much shallower than that for the conventional trough so that it does not cross the upper edge of the maximum radiation band until 450MHz.

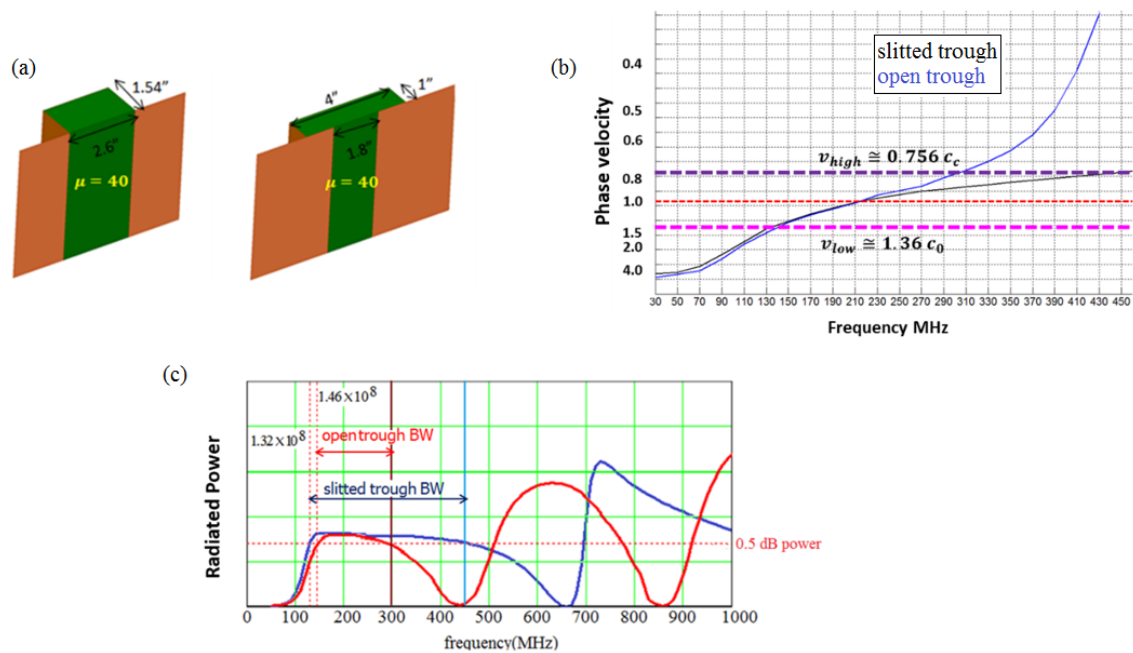


Fig. 9-1 (a) Open and Slitted Troughs Containing the Same Amount of Material of Relative Permeability 40 (b) Phase Velocity of Both Troughs Showing the Slope of the Slitted Trough's Curve Is Much Shallower Than That for the Conventional Trough (c) Radiated Power Versus Frequency for Both Troughs

This is confirmed in the third figure by direct calculation of the total power radiated to the far field. The slitted trough has almost twice the operational frequency bandwidth as the conventional trough.

As is well known in the practice of microwave filters and frequency selective surfaces, there are many ways of implementing a capacitive admittance at a surface. The slitted conducting plane is the simplest one, and one for which a closed form expression of its sheet capacitance is well known. Using it as the exemplary case does not limit the conceived technique to said implementation. Other well-known options include a thin high dielectric constant slab covering the mouth of the trough or a layer of printed circuit capacitive frequency selective surface (such as an array of metal squares, an array of

overlapping metal squares, and so forth, as in the practice of the design of artificial dielectrics).

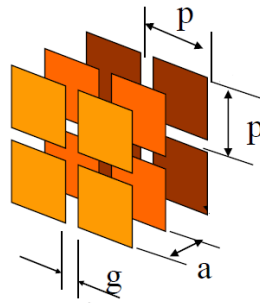


Fig. 9-2 Example of a Frequency Selective Surface

Recognizing that the admittance at the mouth of the trough not only affects the propagation velocity of the guided wave but also the input impedance produced by said wave at the feed, it follows that a purely capacitive admittance is not the only advantageous implementation of this admittance surface. Therefore we recognize that the parallel solenoid feed structure of US Patent Application, US2016/0365642A1, published Dec. 15, 2016, “Parallel Solenoid Feeds for Magnetic Antennas” [36] is a particular implementation of the slitted plane trough and thus constitutes one possible implementation of the generalized admittance surface disclosed in this document.

The figure below from previous chapters and from the cited patent application [36] shows half of a permeable dipole placed on a conducting surface, fed by a coaxial transmission line at its center loop. This center loop is electrically connected by a two-wire transmission line to a series of parallel loops all surrounding the permeable material and terminating on the ground.

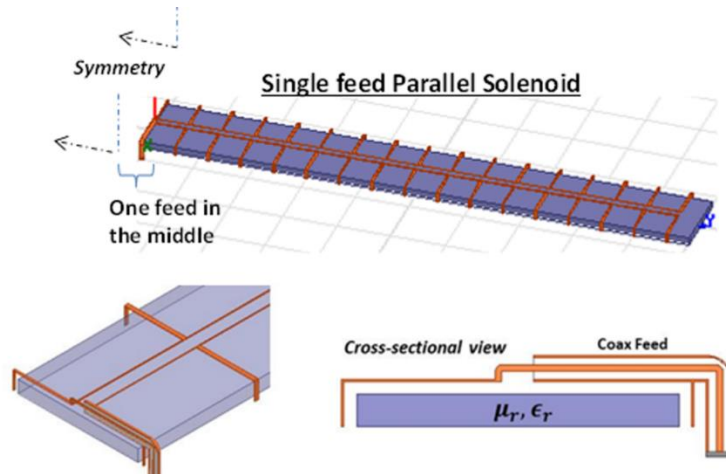


Fig. 9-3 Half of a Permeable Dipole Placed on a Conducting Surface, Fed by a Coaxial Transmission Line at its Center Loop.

As the figure below suggests, if we imagine the spaces between the loops of the parallel solenoid and their connection to the twin-line filled with metal, we see that the permeable material has simply been surrounded by a rectangular metal enclosure with a slit at the top. In other words, this is a variation of the slitted permeable trough where the trough has been moved to be **on top** of the conducting plane. The parallel solenoid then is recognized really as an *inductive grid* version of the slitted plane, where the conducting planes bounding the slit have been replaced by a grid of wires.

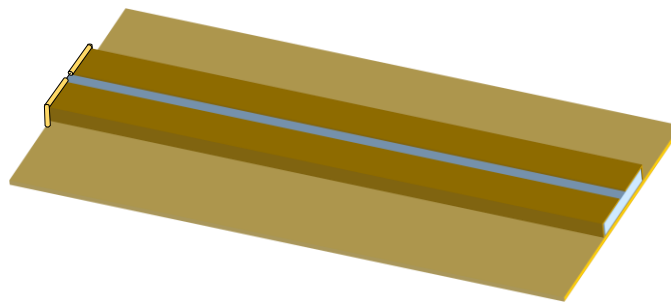


Fig. 9-4 Geometry of an Antenna Consisting of a Permeable Material Surrounded by a Rectangular Metal Enclosure with a Slit at the Top

Such a wire grid construct has long been known in microwave theory, the practice of frequency selective surfaces, and the design of electromagnetic wave polarizers. For example, it is treated in Section 5.19 of the standard reference *Waveguide Handbook* by Marcuvitz [35] and the equivalent circuit parameters have been given in the same chapter for this geometry.

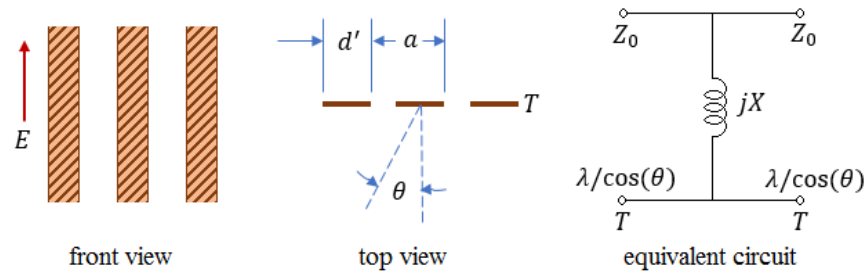


Fig. 9-5 Front View, Top View, and Equivalent Circuit of Inductive Strips which Are Infinitely Extended Plane Grating Formed by Metallic Strips of Zero Thickness with Edges Parallel to the Electric Field and the Plane Wave in Free Space Incident at Angle θ [35]

As an inductive shunt obstacle, the inductive grid presents a short circuit reflecting barrier to low frequency electromagnetic waves that becomes less and less reflective as frequency rises. That is, it is a frequency dependent short circuit. Since the flux channel antenna input impedance is also frequency dependent by nature it is no surprise that tuning the frequency dependence of the conducting path of the slitted plane's admittance surface can be used as a design parameter to optimize the band of operation of magnetic flux channel antennas. The Parallel solenoid patent application shows that this is indeed the case without dwelling on the root cause of why it works.

Based on the subsequent work detailed in the previous chapters we can state that when the parallel solenoid works it does so because it is the appropriate generalized admittance surface required to maximize the radiation bandwidth of the given magnetic flux channel antenna.

From the viewpoint of the transmission line model of the transverse resonance circuit of the flux channel, the parallel solenoid is an instance of terminating the channel with a shunt inductor-capacitor (LC) series circuit (where the inductors are the bars to ground and the capacitor is the gap between the two conductors of the two-wire line connecting the loops). This is as opposed to the nearly pure capacitance of the slitted plane.

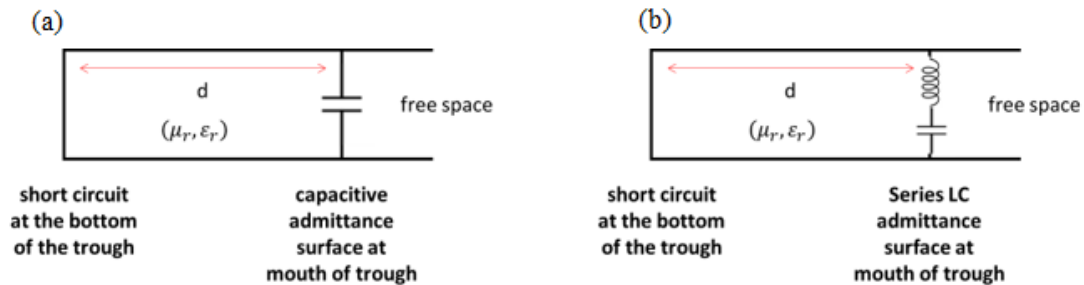


Fig. 9-6 (a) Transmission Line Model of the Nearly Pure Capacitance of the Slitted Plane (b) Parallel Solenoid Modeled as a Shunt Inductor-Capacitor (LC) Series Circuit

The practical use of the parallel solenoid's twin-line-loop construct as an LC shunt admittance surface on the mouth of a trough has already been demonstrated and the first ever frequency independent permeable antenna, using an Archimedean spiral geometry constructed from NiZn ferrite tiles has been designed.

Conventional two-arm spiral antennas attain broad bandwidth of operation because they support a traveling wave along the winding wires that resonates at the active region of the dipole modes of the spherical wave spectrum.

Therefore, to successfully create the electromagnetic dual of a spiral antenna for conformal applications we needed to give the magnetic flux channel constructed from NiZn ferrite tiles the ability to guide the wave along its entire length near the speed of light at all frequencies.

Full wave simulations and experiment show that simply feeding the spiral at its center (as suggested in [37]) does not accomplish this goal. But feeding the ferrite spiral with a parallel solenoid with the correct number of loops to ground does so.

The figure below extracted from our previous chapters shows (top left) a photograph of the first version of the spiral fed by a 4-loop parallel solenoid as illustrated in the CAD drawing on the top right. The measured performance matched the computational simulations within the expected measurement and fabrication uncertainties (middle top). The next iteration of the parallel solenoid is shown in the lower CAD figure and its performance in the second plot in the middle. The design with 30 loops to ground increases the Gain by up to 4dB and smooths out the performance over the band. As the input impedance plots at the bottom show the input impedance is indeed slowly varying with frequency and easily matched to a 50 ohm standard microwave system by simply using a 2:1 transformer. The disclosure on the spiral antennas of US 8847846 B1 does not make either claim or show any evidence for true frequency independent behavior.

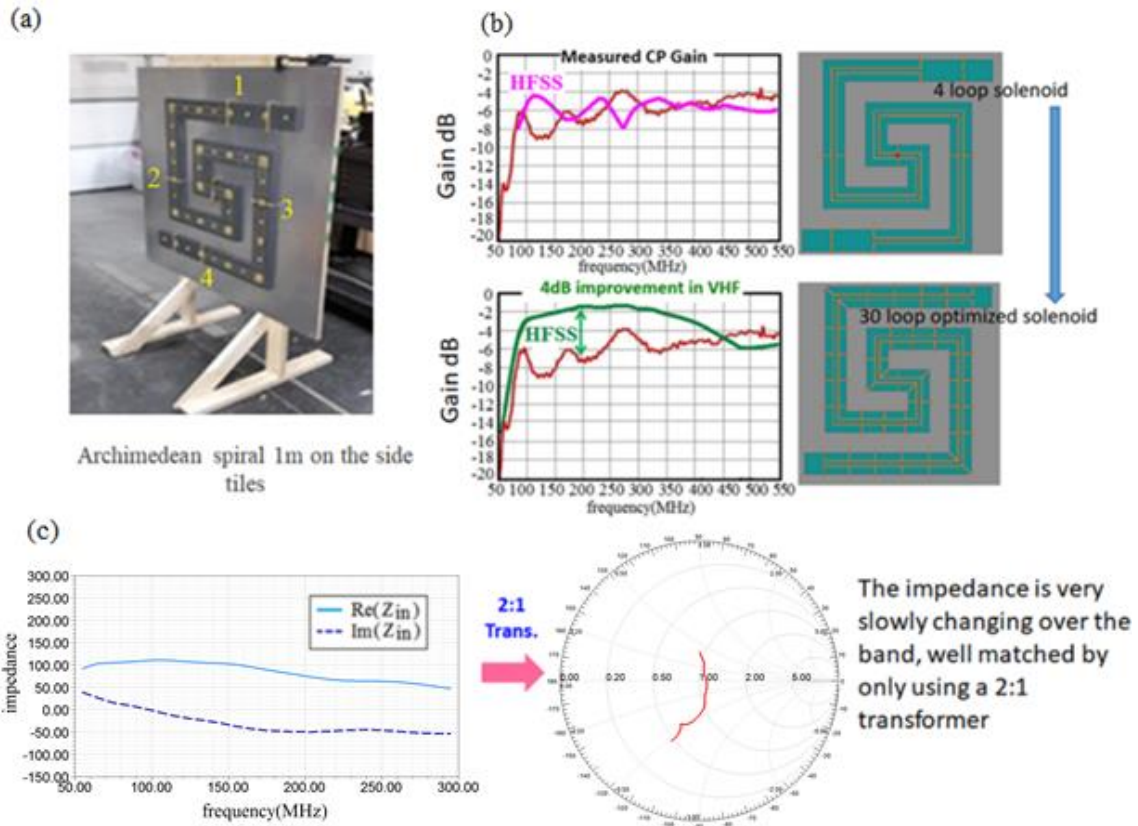


Fig. 9-7 (a) Photograph of the First Version of the Spiral Fed by a 4-Loop Parallel Solenoid (b) HFSS Models of the Same Structure with 4 Loops and 30 Loops and the Measured and Simulated Gain (c) Input Impedance and Smith Chart Representation

This work was continued beyond what is shown in the previous figure to consider the case where the ferrite spiral is buried into a trough and then the parallel solenoid used at its surface. As the next figure shows the performance is even better with higher gain and an operational band from 50MHz to 550MHz.

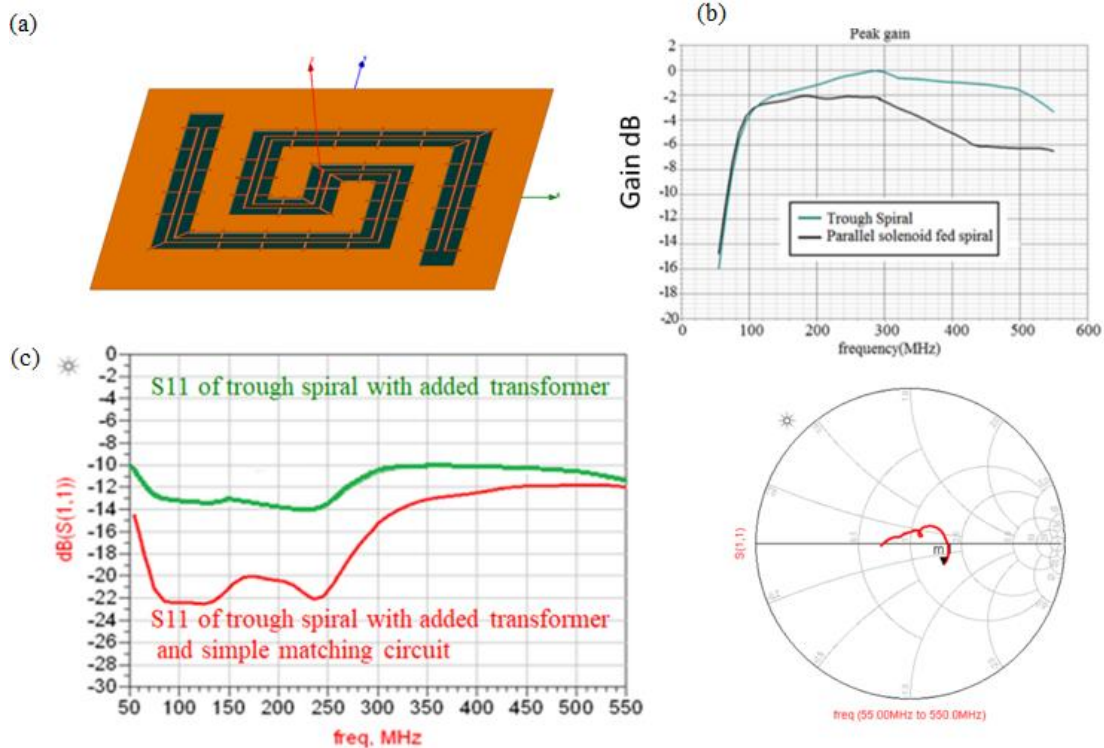


Fig. 9-8 (a) HFSS Models of the 30 Loop Spiral in a Trough Geometry (b) Comparison Between the Peak Gain of the Spiral on Ground and the Spiral in the Trough Geometry (c) S11 of the Trough Spiral and the Smith Chart Representation Showing a Very Large Operational Bandwidth from 50 MHz to 550 MHz

In the figure above, the CAD drawing top left shows the ferrite tiles sunk into a conducting trough in the conducting surface leaving a small (nominally 10 thousandths of an inch) gap between the tile surface and the top edge of the trough. The parallel solenoid structure is then placed across the mouth of the trough, the twin line running as before along the center line of the ferrites and the loops to ground now simply being conducting bars connecting to the edges of the trough. As the plot in the top right shows, the Gain of this configuration is even higher than that of the best one in the previous figure (where the material was placed on top of the conducting ground plane). The Smith Chart plot on the bottom right shows that the antenna can be closely matched to a 50 ohm system with

a simple matching circuit consisting of two capacitors and a transformer. The S11 plot on the lower left (Input match, that is, Reflection coefficient at the feed as a function of frequency) shows that an operational frequency bandwidth from 50MHz to 550MHz (11:1) band is obtained with better than a 2:1 VSWR match (better than -10dB) and better than -20dB from 60MHz to 240MHz proving that true frequency independent permeable antennas can be constructed following the teachings of this dissertation.

The enhanced Gain can be understood as arising in part due to the additional (favorable) images of the magnetic current that are produced on the sidewalls of the channel as opposed to the case when the material is on top of the ground plane. Alternatively, the enhanced Gain can be understood as arising from better confinement of the magnetic current resulting in a stronger flux as is obtained using flux concentrators in the practice of magnetic levitation melting.

Therefore we have shown that a key element of the optimized permeable antenna is the creation of a flux channel in trough form that maximizes the radiation bandwidth of the antenna by (i) selecting the optimal modal structure of the desired Electric field inside the channel (TE01 Cartesian) and then (ii) ***covering the mouth of that trough channel with a generalized admittance surface*** that may be Capacitive (like the slitted plane), series inductive capacitive (like the parallel solenoid) or take the form of any other circuit as learned from the art of frequency selective surfaces that may include also parallel combinations of inductors and capacitors (for instance as in the gapped ring resonator structure) or even circuit constructs including resistive element for, say, terminating the antenna. These circuit constructs in the form of the admittance surface are selected to

modify not only the admittance at the mouth of the trough, and thus its effect on the propagation velocity of the guided wave, but also to optimize the level and bandwidth of the input impedance by compensating for the natural frequency dependence of the antenna resulting from its shape and the frequency dependent properties of its materials of construction.

It should be evident to a person versed in the art of electromagnetic engineering that the generalized admittance surface provides a “tool box” with a large number of degrees of freedom for the engineer to use to optimize a given permeable antenna configuration. The design process can then follow standard approaches of impedance matching and broad-banding or be performed using computational tools and appropriate computational optimizers exploiting these degrees of freedom.

9.3 Enforcing anisotropy in the materials of construction

As mentioned in the previous chapter, the anisotropy of magnetic materials may be a result of the manufacturing process but it also can be produced by the method of construction. In particular, ferromagnetic laminates, ferromagnetic artificial materials resulting from alternating thin metal films with thin insulating (non-magnetic) dielectrics, are anisotropic in both effective permittivity and effective permeability. Here we explain why we had chosen vertical metal films in the previous chapter

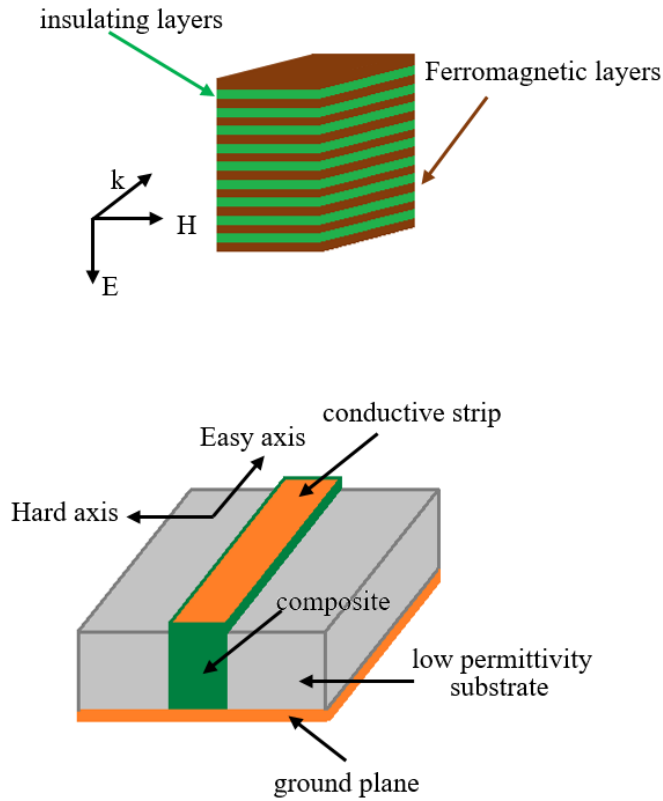


Fig. 9-9 (a) Ferromagnetic Artificial Materials Resulting from Alternating Thin Metal Films with Thin Insulating (b) Composite Material Used as a Substrate

The theory of these materials has been known for decades. For example, Adenot [38, 39] discusses such a ferromagnetic laminate (for a tunable microstrip device shown in Figure 9-9) and points out a simple approximation for the effective permeability parallel to the laminae and effective permittivity perpendicular to the laminae. These being most relevant to his application of placing the material under a microstrip as shown in the figure.

$$\mu_{eff} = q\mu_i + 1 - q \text{ and } \varepsilon_{eff} = \frac{\varepsilon_m}{1 - q} \quad (9-1)$$

Where q is the volume fraction of the metal (ratio of thickness of metal film to the thickness of one period of the periodic arrangement (metal film thickness plus dielectric insulator thickness)).

More accurately the full tensor expressions for the constitutive properties of such a laminated material are given by:

$$\mu_{eff} = \begin{pmatrix} 1 + (\mu_{ix} - 1) \left(\frac{t_m}{t_m + t_d} \right) & 0 & 0 \\ 0 & 1 + (\mu_{iy} - 1) \left(\frac{t_m}{t_m + t_d} \right) & 0 \\ 0 & 0 & 1 \end{pmatrix} \quad (9-2)$$

$$\varepsilon_{eff} \cong \begin{pmatrix} 1 + \frac{(\varepsilon_{ix} - 1)t_d - j \frac{\sigma}{\omega \varepsilon_0} t_m}{t_m + t_d} & 0 & 0 \\ 0 & 1 + \frac{(\varepsilon_{iy} - 1)t_d - j \frac{\sigma}{\omega \varepsilon_0} t_m}{t_m + t_d} & 0 \\ 0 & 0 & \frac{\varepsilon_{iz}}{t_m + t_d} \end{pmatrix} \quad (9-3)$$

Where the x-y plane is the plane of the laminae and z is the direction perpendicular to said plane. And μ_{ix}, μ_{iy} are the intrinsic frequency dependent relative permeability properties of the permeable metal film in the x and y directions and $\varepsilon_{ix}, \varepsilon_{iy}, \varepsilon_{iz}$ are the relative permittivities of the insulating dielectric in the three directions, and σ is the conductivity of the metal films (assumed to be isotropic.)

In practice, the metal films are chosen thinner than the skin depth at the frequencies of use. The insulating dielectrics then prevent circulating currents (in the xz

or yz planes from propagating from one lamina to another. Thus in such a laminate material, magnetic flux can flow unimpeded along the xy plane without being blocked by eddy currents even though the total metal area in the cross section of the material may exceed many times the skin depth.

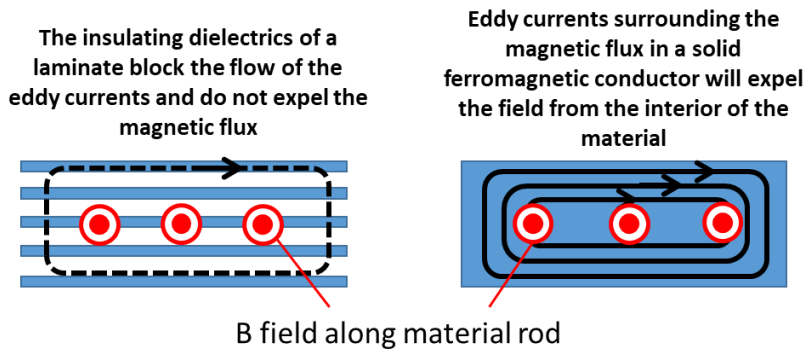


Fig. 9-10 (a) Laminate Material Blocking the Flow of the Eddy Currents (b) Solid Ferromagnetic Material

Allowing the Eddy Current to Flow

An important result of the laminate structure and the tensor properties is that given the very high conductivity of the metal films, the x-y permittivity properties of the laminate material are dominated by the metallic conductivity and therefore the material behaves as a conductor in those two directions. This is why the intrinsic permeability of the ferromagnetic metal in the z direction is unimportant and labeled as 1; in practice the magnetic field inside this composite laminate material cannot penetrate in the z direction. The eddy currents induced in the x-y metal planes completely block any magnetic flux from crossing them.

Many of the thin magnetic metal films used for laminates are intrinsically anisotropic so that, for instance, $\mu_{ix} \gg \mu_{iy}$. Then it is obvious that the flux channel must

be designed such that the magnetic current flux flowing along the channel uses the high permeability orientation of the material.

What is not obvious and does not appear disclosed in the technical or patent literature is that this material anisotropy can be used to advantage to improve the performance of permeable antennas. Consider using a ferromagnetic laminate material as the material of construction for a permeable antenna. When the flux channel is formed by placing the material on the surface of the ground plane, the laminate planes can either be placed perpendicular to or parallel to this ground plane. Even though both flux channels have the same cross sectional area and same permeability in the direction of the desired magnetic current, they are not equivalent in performance. As the figure below shows they support the TE₀₁ magneto-dielectric rod mode differently. The black arrows denote the Electric field while the “arrow heads” seen end-on in red denote the magnetic flux (magnetic current)

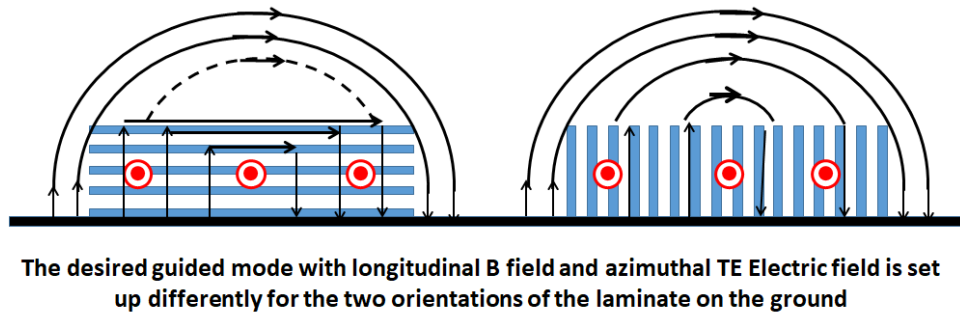


Fig. 9-11 (a) TE₀₁ Mode Fields Shown for the Case of Laminate Plate Parallel to the Ground Plane (b) Fields Shown for the Case of Laminate Plate Perpendicular to the Ground Plane

Because for conformal antennas we want the channel to be as thin as possible, the engineer prefers shallow and wide channels. The problem that arises is that the laminate

structure, in addition to supporting the desired magneto-dielectric-rod-like TE₀₁ field in the space surrounding the channel (as suggested in the figure above) also supports a parasitic parallel plane TEM mode with the electric field terminating on the laminates and traveling parallel to (between) the laminate planes. Because it is always possible to excite this mode at asymmetries in the antenna feed structure or discontinuities in the antenna it is always in danger of being excited.

It is obvious from inspection that the case on the left looks like a stack of microstrip lines capable of carrying such a mode both along the length of the channel and transverse to it. The former would have its magnetic field, not longitudinal as desired for the magnetic current radiator, but transverse. As discussed in the Sebastian dissertation such a mode is the dual not of an antenna but of two wire transmission line and therefore is a very poor radiator. Just based on this fact the configuration with laminate planes parallel to the ground plane is to be avoided. Where manufacturing constraints to force this orientation, it would be necessary to implement a mode filter such as inserting vertical conducting pins through the middle of the channel along its full length to short out the propagating TEM mode.

Following this discussion, it is then obvious that the vertical laminate structure has a built-in mode filter against this traveling TEM wave mode, because the ground plane short circuits the TEM E field and prevents the TEM wave from ever propagating along the channel. As would be expected, at higher frequencies parasitic parallel plane TE (waveguide like) modes could also propagate guided by the laminate plane structure. These would bounce from side to side transversely as they propagate along the channel.

On this account, the vertical laminate placement is to be preferred. As the figure below shows, a shallow wide flux channel could start multi-moding and carrying this parasitic wave at lower frequencies if the laminates are parallel to the ground than if they are perpendicular.

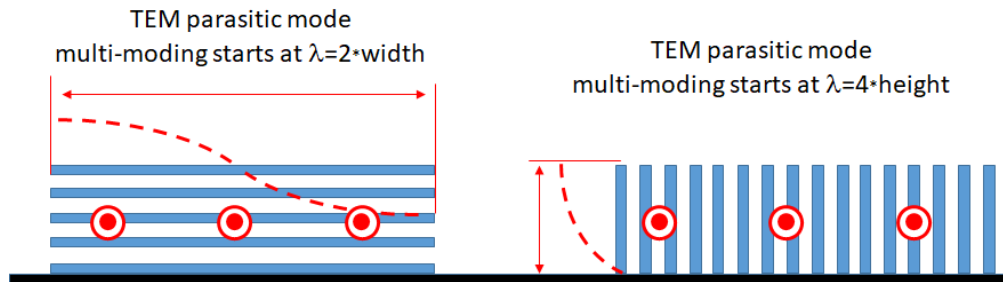


Fig. 9-12 TEM Parasitic Mode Shown in the Horizontal and Vertical Laminates Showing that the Vertical Laminate Structure Has a Built-in Mode Filter Against This Traveling TEM Wave Mode. The Red “Arrow Points” Indicate the Desired Magnetic Field (Magnetic Current).

Furthermore, the fact that the electric field has one full half wavelength variation along the channel for the case on the left again results in a poorly radiating mode since the magnetic current changes direction within the channel. However, the parasitic TE mode on the vertical laminates only has a quarter wave variation, meaning the electric field all points in the same transverse direction and the longitudinal magnetic current also points in only one direction everywhere in the channel cross section.

Therefore, the case on the right with a TE mode traveling within the channel still produces the desired radiation and the mode is not really “parasitic”. It can be surmised that for the flux channel with vertical laminates perpendicular to the ground plane, both the magnetodielectric rod TE₀₁ desired mode and this TE mode coexist and contribute with possibly different strengths to the radiation of the antenna. However, if the two

coexisting modes have different characteristic propagation velocities then interference between them may induce a frequency dependent variation into the electromagnetic properties of the channel.

Therefore, it is concluded that to maximize the bandwidth of operation and radiation efficiency of a magnetic flux channel constructed from laminate structure placed on top of a ground plane, the preferred orientation for the laminates must be perpendicular to the ground plane.

This restriction holds also and even more strongly for the flux channel in the trough configuration. As the figure below shows, the desired propagating mode in the flux channel has a transverse E field (TE₀₁ rectangular mode) that is a maximum at the mouth of the flux channel and minimum (zero) at the bottom of the channel. Clearly for the laminates parallel to the bottom of the trough, the metal laminate surfaces short out this desired Electric field and we would expect it is very difficult to carry the desired mode in preference to a TEM mode trapped between the laminates. This is readily confirmed by full physics simulation of such a flux channel, where the onset frequency is found to occur at an anomalously high frequency and the desired magnetic current is not adequately guided.

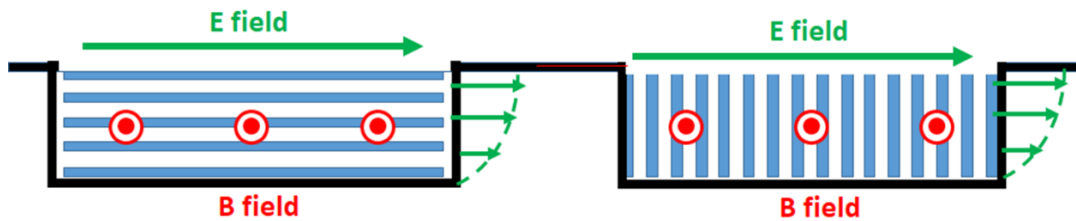


Fig. 9-13 TE₀₁ Rectangular Mode for Horizontal and Vertical Laminates Showing That the Horizontal Laminates Short Out This Desired Electric Field

On the other hand for the laminates vertical, perpendicular to the bottom of the trough, as on the right figure, the mode enforced by the boundary conditions of the trough is exactly the TE mode we mentioned exists on the structure even when it is on the top of the ground. In other words, the trough configuration limits the propagation of the desired mode in the case of the vertical laminates to one unique lowest order mode.

Supporting only one lowest order mode is always preferred whenever broadband electromagnetic structures are desired. (Avoiding any interference between multiple modes.)

So far this discussion has shown that knowledge of the modal structure supported by a laminated permeable material leads to a *design criterion* that dictates the preferred orientation of said laminates. But in addition to dictating this preferred orientation (laminates planes perpendicular to the bottom of the trough) we disclose here that even in the case of a material of construction that is originally, by nature, isotropic, it is advantageous to render it anisotropic by adding conducting planes to enforce the behavior discussed above.

The reason for this becomes apparent when we consider extremely broadband applications like spiral antennas and log periodic antennas. As has been discussed shallow and wide trough magnetic channels are preferred for conformal antennas and offer the widest possible radiation bandwidth. In such applications the width b of the trough will eventually become long enough to exceed one wavelength. For instance consider a trough that is 3.8 inches wide, 1.053 inches deep, filled with a permeable material of $\mu_r = 80$ and $\epsilon_r = 2$. Its onset frequency is 220 MHz. At that frequency the

1.053 inch depth is approximately a quarter wave in the permeable material. This means the trough aperture being almost four times larger than the depth is already almost one wavelength across.

As the figures here suggest, a symmetrically disposed coax feed excites first the TE₀₁ mode E field at the mouth of the trough, and by symmetry suppresses the odd TE₁₁ mode. But the TE₂₁ mode has even symmetry also. This mode with one wavelength variation across the trough will therefore be excited at higher frequencies. But because its electric field changes direction, its corresponding magnetic current also changes direction inside the channel, and it is on the whole a very poor radiator.

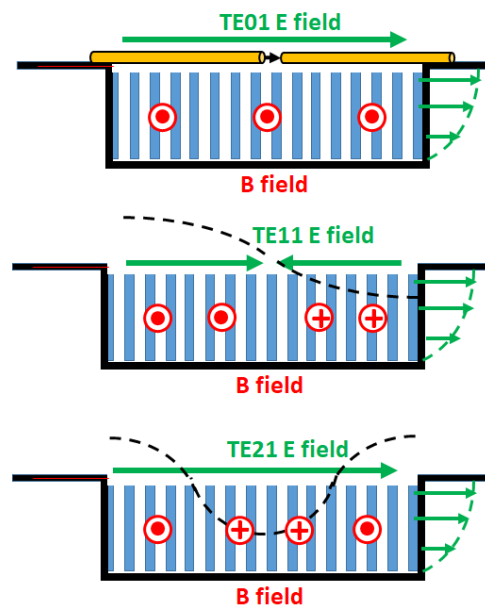


Fig. 9-14 Trough Geometry with the Vertical Metal Plates Showing That the Vertical Metal Plates Suppress the Side to Side Propagation of the Higher Order TE₂₁ Mode

As is known in the practice of waveguide design, whenever a higher order mode is to be suppressed, mode filters are indicated. Fortunately, for the ferromagnetic laminate permeable material, that mode filter is built-in. The vertical metal plates suppress the side to side propagation of the higher order TE₂₁ mode because when that mode travels along the channel it carries a transverse magnetic field in addition to its longitudinal field. That field, perpendicular to the laminate planes, induces strong eddy currents in the planes of the laminates and thus the laminates tend to block it.

Therefore, it follows that when the permeable material available to fill the channel is not a ferromagnetic laminate but a naturally homogenous isotropic material, the mode suppression is to be accomplished by dividing the homogeneous isotropic permeable material into thin segments aligned with the flux channel axis and separating these with thin metal planes. Thus, for instance, in the case of the ferrite tile spiral antenna, if we wish to extend its range of operation into the GHz range we would have the 4 inch-wide tiles sliced into 1 inch wide sections and insert thin copper plates between these (or paint the faces between them with a conducting paint). By this procedure the frequency at which the undesirable TE₂₁-like mode can be excited would be pushed up by at least a factor of 4.

The point is to convert the permeable material filling the channel into an anisotropic magneto-dielectric material with tensor constitutive properties equivalent to those of a ferromagnetic laminate.

9.4 Exploiting the frequency dependent dispersion of realistic permeable materials

All real material are frequency dependent and therefore exhibit complex constitutive parameters (where the real part of the constitutive parameter denotes the energy storage capacity of the material while the imaginary part denotes the dissipation of energy in the material, that is, loss). There is no such thing as a lossless dielectric or lossless permeable material. Recent previous art on this subject of permeable antennas such as the cited “pseudo-conductor antenna” patent US 8847846 B1 [37] and its companion patents [40] assumes that high efficiency permeable antennas require the real part of the material permeability to exceed the imaginary part, and the claims so state it. However, this concept has been demonstrated to be a fallacy as seen in the previous chapters of this dissertation.

It is now known that highly efficient conformal permeable antennas can be designed and implemented where the imaginary part of the permeability of the material of construction is comparable to or greater than the real part. In fact, the NiZn tile material used for the spiral antenna cited earlier in this document, and for a permeable dipole in one of the bibliography references, is sold as an electromagnetic absorber for use in EMC chambers. This material has a Debye-like dispersion (frequency dependence) in its permeability so that its real and imaginary parts are approximately equal at 3MHz and above that frequency the imaginary part becomes increasingly dominant. Yet as shown here the antenna attains Gain comparable to (that is, only 2 to 3dB lower than) a metal spiral in free space. That is, this antenna alone is a counter example to the claims

made in the pseudo-conductor patents cited above that the preferred material for permeable antennas should have $\mu' > \mu''$.

This is extremely important because that means realistic dispersive materials can be used over wide frequency bands and not only over those frequency bands where the real part dominates. Similar statements have been made by wideband phased array designers using permeable material as groundplane covers to implement a high impedance boundary.

We now have proven that the presence of the correct amount of loss, and therefore the correct dispersion in the permeability, can prevent the guided wave from being trapped inside the material at high frequencies and therefore also prevent the excitation of higher order modes inside the channel. Therefore, the statement that the high frequency regime above onset is sub-optimal for these antennas can now be modified.

A judicious amount of loss forces the wave to travel on the surface of the flux channel and prevents it from being trapped inside the material. The result is a permeable flux channel that carries its wave close to the speed of light over a broader frequency range than an identical channel using a low loss material.

Promoting such a true *surface guidance* is also the reason why the slitted plane at the mouth of the trough tends to guide the wave closer to the speed of light over a broad frequency range above onset: the edges of the slit pull the energy of the wave to the surface exposing more fields to the free space above and thus increasing the phase velocity, to bring it closer to the speed of light in free space.

We have illustrated how this technique works using the examples of the 3.8 inches wide trough, 1.053 inches deep filled with homogenous material of DC permeability = 40 compared to a realistic lossy material with dispersive permeability and the Snooked version of the materials in chapter 8 of this dissertation.

It was concluded that this change in material can be used to create a channel that guides waves near the speed of light for an extremely broad range of frequencies, not only because the loss pushes the fields to the surface but because the frequency dependent change in the permeability changes the transverse resonance condition of the channel such that there is no longer a unique (real) onset frequency but instead a continuous distribution of complex onset frequencies over the entire band.

Since as described in the discussion on the spiral antenna, the active region of spirals is one wavelength in circumference, this moderate amount of loss has only a small effect on the performance of the antenna, and this has been demonstrated in our example where the material of construction is an absorbing NiZn ferrite tile.

It now remains to the engineer to decide, based on the requirements of the communication system and the type of antenna being considered, where precisely to place the resonant frequency of the material dispersion. This is a standard trade-off exercise that can be readily performed by using the transverse resonance analysis as disclosed in this dissertation.

These results thus extend the initial discovery that the loss of permeable materials is not a hindrance to their use as conformal antennas. We go beyond that statement to show that such dispersion, inevitable in realistic materials, is in fact desirable and

necessary to enable the creation of magnetic flux channels that approach the ideal electromagnetic dual behavior of conventional metal antennas in free space.

Beyond enabling the electromagnetic engineer to design highly efficient wideband conformal permeable antennas, this result also serves as a guidance to magnetic material development technologists to provide direction on the development of future materials. Even though the trend over the last several decades has been for the development of magnetic materials with increasingly high resonance frequency, even at the expense of the initial permeability, because for many magnetic recording and microwave device applications there is a requirement for low μ'' with increasing operational frequency, that is not the direction to go in for maximizing the performance of permeable antennas. The development for antenna applications should go in the opposite direction, drop the resonance frequency and raise the initial permeability.

9.5 Conclusion

The optimal conformal permeable antenna flux channel is defined as one consisting of antenna elements or sections that behave as closely as possible to the electromagnetic dual of conventional metal antennas in free space. This implies that the flux channel should guide its magnetic current near the speed of light over the widest possible band of frequencies and with the minimum practical loss. The typical approach to the construction of these optimal flux channels is as follows:

Based on the system requirements of operational frequency band and gain, and constraints of available installation area and thickness for the antenna,

- Select the antenna type and shape
- Select a permeable material that will meet the efficiency (Gain) requirements within the Volume constraints
- To the degree that the radii of curvature of the platform surface (and other mechanical constraints such as the composition of the selected material) allow it, implement the permeable material as a laminate structure where conducting planes are to be placed perpendicular to conducting surface of the platform.
- Design the flux channel as a conducting trough in the conducting surface of the platform.
- Design the cross section of the trough such that for the chosen permeable material filling it, the surface wave guidance onset frequency falls within the band of operation near the bottom of the band, nominally such that the bottom of the band is approximately 0.5 the onset frequency.
- Design the cross section of the trough and the admittance surface at its mouth to obtain a phase velocity of propagation as flat as possible, and as close as possible to the speed of light in free space, as a function of frequency, over the band of operation.
- Perform a final engineering trade-off of the features using full physics modeling of the designed structure, trading off as necessary bandwidth, input impedance, and Gain. Fine tune the design, build, and test.

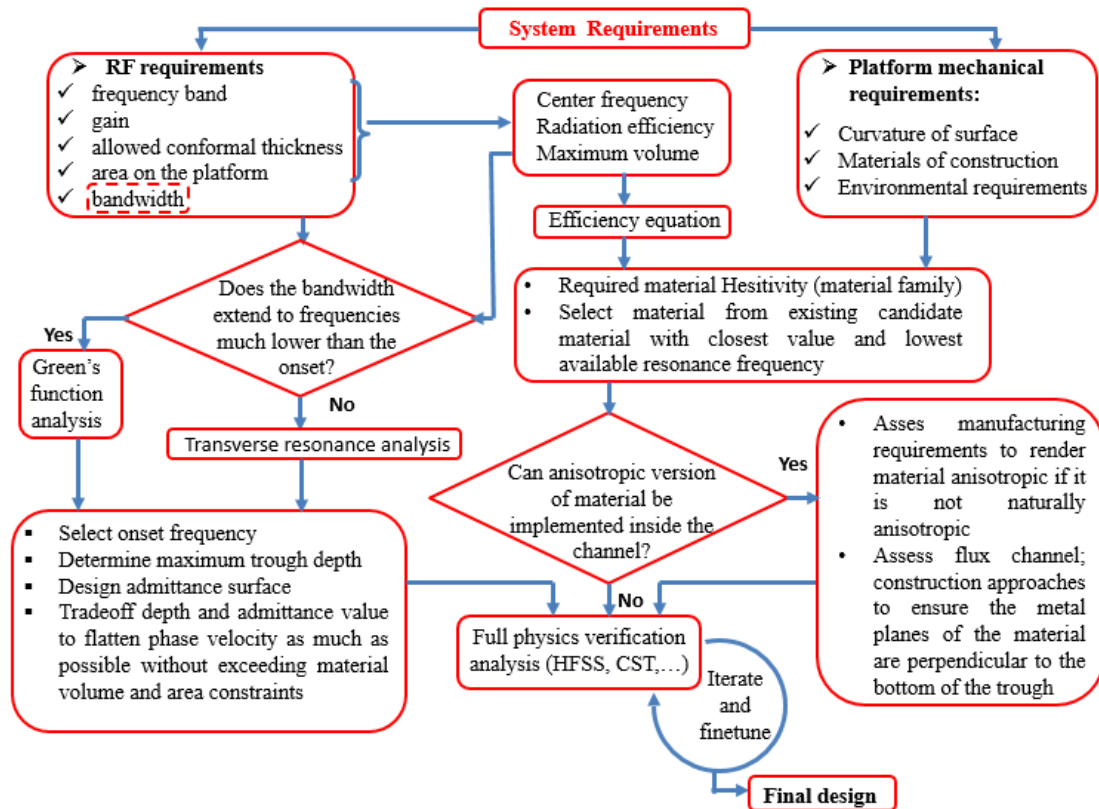


Fig. 9-15 Flow Graph of the Design Procedure of the Optimum Flux Channel

REFERENCES

- [1] T. Yousefi and R. E. Diaz, "Pushing the limits of radiofrequency (RF) neuronal telemetry," *Nature Scientific reports*, vol. 5, no. 10588, 2015.
- [2] T. Sebastian, *Magneto-dielectric wire antennas theory and design*, Tempe. Az: Ph.D. dissertation, Dept. Elect. Eng., Arizona State. Univ., 2013.
- [3] W. Weeks and V. Rumsey, "Electrically small ferrite loaded loop antennas," *IRE Nat. Conv. Rec.*, vol. 4, no. 1, pp. 165-170, 1956.
- [4] R. DeVore and P. Bohley, "The electrically small magnetically loaded multiturn loop antenna," *IEEE Trans. Antennas Propag.*, vol. 25, pp. 496-505, 1977.
- [5] T. V. Hansen, O. S. Kim and O. Breinbjerg, "Electrical properties of spherical dipole antennas with lossy material cores," *Proc. Eur. Conf. on Antennas and Propagation (EuCAP)*, pp. 2474-2478, 2012.
- [6] R. Sutton and J. S. McLean, "An efficient, low-profile antenna employing lossy magneto-dielectric materials," *Proc. IEEE Int. Workshop on Antenna Technology (iWAT)*, p. 261–264, 2012.
- [7] R. E. Diaz and T. Sebastian, "Electromagnetic limits to radiofrequency (RF) neuronal telemetry," *Nature Scientific reports*, vol. 3, no. 3535, 2013.
- [8] S. Schelkunoff and H. Friis, *Antenna theory and practice*, Wiley, 1952.
- [9] R. King, C. Harrison and E. Aronson, "The Imperfectly Conducting Cylindrical Transmitting Antenna," *IEEE Trans. Ant. Propag.*, Vols. AP-14, no. 5, pp. 524-534, 1966.
- [10] J. Toll, "Causality and the Dispersion Relation: Logical Foundations," *Phys. Rev.*,

vol. 104, pp. 1760-1770, 1956 .

- [11] R. Diaz and N. Alexopoulos, "An Analytic Continuation Method for the Analysis and Design of Dispersive Materials," *IEEE Trans. Antennas Propag.*, vol. 45, no. 11, pp. 602-610, 1997.

- [12] J. Smit and H. Wijn, *Ferrites*, New York: Wiley, 1959.

- [13] F. Grant, "Use of Complex Conductivity in the Representation of Dielectric Phenomena," *J. Appl. Phys*, vol. 29, pp. 76-80, 1958.

- [14] R. Diaz, C. Daniel and D. Aukland, "A new type of conformal antenna using magnetic flux channels," *Milcom conference*, 2014.

- [15] R. Diaz and S. Clavijo, "Artificial Magnetic Conductor," in *Encyclopedia of RF and Microwave Engineering*, Wiley, p. EME 551.

- [16] E. Carrubba, S. Genovesi and G. M. A. Monorchio, "AMC-based low profile antennas for 4G communication services," *IEEE Antennas and Propagation Society International Symposium*, p. 3364 – 3367, 2007.

- [17] N. M. Mohamed-Hicho, E. Antonino-Daviu, M. Cabedo-Fabres and M. Ferrando-Bataller, "A Novel Low-Profile High-Gain UHF Antenna Using High-Impedance Surfaces," *IEEE Antennas and Wireless Propagation Letters*, vol. 14, p. 1014 – 1017, 2015.

- [18] A. Foroozesh and L. Shafai, "Investigation Into the Application of Artificial Magnetic Conductors to Bandwidth Broadening, Gain Enhancement and Beam Shaping of Low Profile and Conventional Monopole Antennas," *IEEE Trans. Ant. Propg.*, vol. 59, no. 1, pp. 4-20, 2011.

- [19] S. R. Best and A. D. Yaghjian, "Impedance, bandwidth and Q of antennas," *IEEE Trans. Antennas Propag.*, vol. 44, no. 5, pp. 672-676, 1996.

- [20] ANSYS, *HFSS, Electronics Desktop, 2015.1.*
- [21] T. Sebastian, S. Clavijo, R. Diaz, C. Daniel and D. Auckland, "A new realization of an efficient broadband conformal magnetic current dipole antenna," *IEEE APS Intl. Symp. 2013 (APSURSI)*, p. 1290 – 1291, 2013.
- [22] M. Grudén, M. Jobs and A. Rydberg, "Design and Evaluation of Conformal Patch Antenna Array for Use with Wireless Sensor Network Inside Jet Engines," *7th Eur. Conf. on Ant. Propag. (EuCAP)*, pp. 2100-2102, 2013.
- [23] S. A. Schelkunoff, *Advanced Antenna Theory*, New York: John Wiley & Sons, 1952.
- [24] R. D. Lillo, "Lumped-element quadrature hybrids for wide-band antenna-feed networks," *APS Intl. Symp. AP-S. Digest*, vol. 3, pp. 1840-1843, 1991.
- [25] J. McLean and R. Sutton, "An efficient, low-profile antenna employing lossy magneto-dielectric materials," *Proc. IEEE Int. Workshop on Antenna Technology (iWAT)*, p. 261–264, 2012.
- [26] C. G. Kakoyiannis, T. Zervos, G. Fikioris and M. Pissas, "Efficiency measurements of multiband and circularly polarized magneto-dielectric antennas by the equivalent-circuit wheeler cap," *The 8th European Conference on Antennas and Propagation (EuCAP 2014)*, pp. 372-376, 2014.
- [27] T. Yousefi, T. Sebastian and R. E. Diaz, "Why the Magnetic Loss Tangent Is Not a Relevant Constraint for Permeable Conformal Antennas," *IEEE Trans. Ant. Propag.*, vol. 64, no. 7, pp. 2784-2796, 2016.
- [28] T. Yousefi, R. Diaz, C. Daniel and D. Auckland, "A Wideband Multimode Permeable Conformal Antenna thinner than $\lambda/75$ using advanced ferromagnetic laminate composite materials," *IEEE AWPL Special Cluster on Conformal Antennas and Arrays from New Advanced Materials*, vol. 15, pp. 1931-1934, 2016.

- [29] R. G. Corzine and J. A. Mosko, *Four-Arm Spiral Antennas*, Artech House, 1990.
- [30] S. Darlington, "Synthesis of reactance 4-poles," *Journal of Mathematics and Physics*, vol. XVIII, p. 275–353, 1939.
- [31] L. Goldstone and A. Oliner, "Leaky-wave antennas I: Rectangular waveguides," *IRE Transactions on Antennas and Propagation*, vol. 7, no. 4, pp. 307-319, 1959.
- [32] L. Goldstone and A. Oliner, "Leaky wave antennas II: Circular waveguides," *IRE Transactions on Antennas and Propagation*, vol. 9, no. 3, pp. 280-290, 1961.
- [33] P. Lampariello, F. Frezza and A. A. Oliner, "The transition region between bound-wave and leaky-wave ranges for a partially dielectric-loaded open guiding structure," *IEEE Transactions on Microwave Theory and Techniques*, vol. 38, no. 12, pp. 1831-1836, 1990.
- [34] K. Y. Kim, *Guided and Leaky Modes of Circular Open Electromagnetic Waveguides: Dielectric, Plasma, and metamaterial columns*, Kyungpook National University, 2004.
- [35] N. Waveguide, *Waveguide Handbook*, Iee Electromagnetic Waves Series, 1951.
- [36] R. Diaz, T. Yousefi, T. Sebastian and S. Clavijo, "Parallel Solenoid Feeds for Magnetic Antennas". Patent US Patent Application, US2016/0365642A1, 15 December 2016.
- [37] R. E. Diaz, "Magnetic Pseudo-conductor Spiral Antennas". 2014 Patent US 8847846 B1, 30 September 2014.
- [38] A. Adenot-Engelvin and e. al, "Microwave properties of ferromagnetic composites and metamaterials," *Journal of the European Ceramic Society*, pp. 1029-1033, 2007.
- [39] Adenot-Engelvin and e. al, "Tuneable microstrip device controlled by a weak magnetic field using ferromagnetic laminations," *J. Appl. Phys.*, vol. 87, no. 9, pp.

6914-6916, 2000.

- [40] R. E. Diaz, "Multi-function pseudo-conductor antennas". US Patent US8686918 B1, 2012.
- [41] R. Diaz and T. Sebastian, "Electromagnetic limits to radiofrequency (RF) neuronal telemetry," *Nature Scientific reports*, 2013.
- [42] G. P. Cofer, J. M. Brown and G. Johnson, "In Vivo Magnetic Resonance Microscopy at 5 μm ," *Journal of Magnetic Resonance*, vol. 83, p. 608–616, 1989.
- [43] H. Javaheri, B. Barbiellini and G. Noubir, "Energy transfer performance of mechanical nanoresonators coupled with electromagnetic fields," *Nanoscale Research Letters*, vol. 7, 2012.
- [44] D. B. Suyatin and e. al, "Nanowire-Based Electrode for Acute In Vivo Neural Recordings in the Brain," *PLoS ONE* 8, 2013.
- [45] O. Heaviside, "On the Electromagnetic Effects due to the Motion of Electrification through a Dielectric," *Philosophical Magazine*, vol. 27, p. 324–339, 1889.
- [46] M. Kraichman, "Handbook of Electromagnetic Propagation in Conducting Media," *Headquarters Naval Material Command*, Vols. NAVMAT, P-2302, second printing,, 1976.
- [47] J. L. Chu, "Physical limitations of omnidirectional antennas," *J. Appl.Phys.*, vol. 19, p. 1163–1175, 1948.
- [48] Z. Zhang and R. E. Diaz, "A Novel Simple Anisotropic Effective Medium Method (SAEM) for Modeling Curved Objects in Cartesian FDTD Mesh," *IEEE Intl. Symp. Microwave, Antenna, Propagation and EMC Technologies for Wireless Communications*, vol. Beijing, 2005.
- [49] A. Kyriakou, A. Christ, E. Neufeld and N. Kuster, "Local tissue temperature increase of a generic implant compared to the basic restrictions defined in safety

guidelines," *Bioelectromagnetics*, vol. 33, p. 366–374, 2012.

- [50] A. Borton, M. D. A. Yin and A. Nurmikko, "An implantable wireless neural interface for recording cortical circuit dynamics in moving primates," *J. Neural Eng.*, vol. 10, no. 026010, 2103.

APPENDIX A

OTHER INTERESTING APPLICATIONS OF MAGNETIC ANTENNAS: PUSHING THE LIMITS OF RADIO FREQUENCY (RF) NEURONAL TELEMETRY

“Nothing is more practical than a good theory.”
Ludwig Boltzmann

A.1 Introduction

In previous publications by Sebastian and Diaz [7] it was shown that the channel capacity of an in vivo communication link using microscopic antennas at radiofrequency is severely limited by the requirement not to damage the tissue surrounding the antennas. For dipole-like antennas the strong electric field dissipates too much power into body tissues. Loop-type antennas have a strong magnetic near field and so dissipate much less power into the surrounding tissues but they require such a large current that the antenna temperature is raised to the thermal damage threshold of the tissue. The only solution was increasing the antenna size into hundreds of microns, which makes reporting on an individual neuron impossible. However, recently demonstrated true magnetic antennas offer an alternative not covered in the previous report.

The near field of these antennas is dominated by the magnetic field yet they don't require large currents. Thus they combine the best characteristics of dipoles and loops. By calculating the coupling between identical magnetic antennas inside a model of the body medium we show an increase in the power transfer of up to 8 orders of magnitude higher than could be realized with the loops and dipoles, making the microscopic RF in-vivo transmitting antenna possible.

This chapter is based on our paper: T. Yousefi and R. E. Diaz, "Pushing the limits of radiofrequency (RF) neuronal telemetry," *Nature Scientific reports*, vol. 5, no. 10588, 2015.

In reference [7] the electromagnetic limits to radiofrequency (RF) telemetry from within the brain, have been discussed. By establishing a link budget consistent with picowatts of radiated power at the surface of the head, it was shown that to avoid thermal damage to tissue surrounding the transmitting embedded antenna, and still be able to communicate at 300 Kbps with a reasonable link margin from within the human brain, electric dipoles at least $680 \mu\text{ m}$ in length or magnetic dipoles at least $59 \mu\text{ m}$ in diameter would be required. For the rodent brain case these numbers become $250 \mu\text{ m}$ and $26 \mu\text{ m}$ respectively. In the rodent case, it was estimated that a $14.5 \mu\text{ m}$ diameter loop antenna with a magnetic core (that raised its dipole moment by a factor of 3) could communicate at the reduced rate of 3Kbps. Making the antennas any smaller increases the power dissipated into the proximate tissues above the accepted safety limits [41] . Assuming that the desired size of a sufficiently unobtrusive embedded telemetry node (antenna plus on-board transmitter) is $10 \mu\text{ m}$, these results rendered unfeasible the prospect of using such a microwave RF telemetry system to track neuronal activity in-vivo [42, 43, 44].

The root of the problem is that small electric dipole antennas embedded in lossy dielectric media suffer very large near field loss in the process of radiating a signal and loop antennas suffer excess Ohmic loss in their metal elements. Therefore when these antennas are fed sufficient power to transmit through the brain, the electric dipole would damage the nearby tissue through specific absorption rate (SAR) deposition and the electric loop antenna through heat conduction. But this is not the end of the story.

In the reference paper [41] , the effect of a magnetic core for loop antennas was only modeled as an increase of the antenna's dipole moment thus leading to a slight

benefit in radiated gain. The reality, evident from recent work on magnetic conformal antennas [2, 14, 21] is that the magnetic core of a loop antenna can dramatically alter its input impedance, changing its behavior from that of a metal loop to that of a permeable dipole. In the regime where the magnetic core dominates the behavior, the principal radiating current is not the electric current in the loop but the magnetic polarization current in the core material. Because of the high efficiency properties of these magnetic dipoles, when located in a low impedance environment, have not been reported until recently [2, 14, 21] we describe them below before proceeding with their application to the in vivo neuronal telemetry scenario.

A.2 True Magnetic Antennas

Although in the conventional practice of Antenna Theory and Design a distinction is made between electric dipole antennas (generally metal rods carrying an alternating electric current) and magnetic dipole antennas (generally metal loops carrying an alternating electric current,) in reality both of these antennas are electric current radiators. In the first, the electric current is linear and couples most efficiently to the electric dipole modes of the spherical mode spectrum; in the second the electric current is circumferential and couples most effectively to the magnetic dipole modes of the spherical mode spectrum. Since the work of O. Heaviside [45] in the late 1880's it has been known that Maxwell's equations also admit of the presence of magnetic currents. Therefore behaviors, equivalent to magnetic current radiators exist in principle.

Most antenna practitioners assume that the absence in nature of observed magnetic monopoles precludes the existence of true magnetic currents and therefore

whenever the term magnetic dipole is used, a loop antenna is usually meant, and whenever the term magnetic current is used, a fictitious magnetic current is usually meant. The latter currents arise in Schelkunoff's Equivalence Theorem whenever it is desired to summarize all the sources on one side of a closed mathematical surface by using the tangential electromagnetic fields existing on that surface. Thus the surface fictitious magnetic current, K_m (measured in Volts/meter) is defined as the cross product of the surface normal and the tangential Electric field on that surface.

However, here we are talking about true (as opposed to fictitious) magnetic current radiators. That is, in the same way that electric current density, J_e , (measured in A/m²) flows through a medium with electric conductivity, σ_e (measured in Siemens/meter), as:

$$\vec{J}_e = \sigma_e \vec{E} \quad (\text{A-1})$$

Magnetic current density, J_m , (measured in V/m²) flows through a medium with magnetic conductivity, σ_m (measured in Ohms/meter), as

$$\vec{J}_m = \sigma_m \vec{H} \quad (\text{A-2})$$

Even though magnetic conductivity does not exist at zero frequency (because of the absence of magnetic monopoles), as far as Maxwell's equations are concerned, it exists at any frequency in which a material exhibits a magnetic loss tangent. This is because the imaginary part of the complex permittivity and complex permeability of

materials, $\varepsilon(\omega) = \varepsilon_0(\varepsilon' - j\varepsilon'')$, and $\mu(\omega) = \mu_0(\mu' - j\mu'')$, imply the existence of a corresponding conductivity through the relations:

$$\sigma_e = \omega\varepsilon_0\varepsilon'' \quad (\text{A-3})$$

$$\sigma_m = \omega\mu_0\mu'' \quad (\text{A-4})$$

Thus in Maxwell's curl equations; the terms involving the rate of change of the flux densities imply the existence of magnetic currents as well as electric currents as shown below:

$$\begin{aligned} j\omega D &= j\omega\varepsilon(\omega)E = j\omega\varepsilon_0(\varepsilon' - j\varepsilon'')E \\ &= j\omega\varepsilon_0\varepsilon'E + \omega\varepsilon_0\varepsilon''E = j\omega\varepsilon_0\varepsilon'E + \sigma_e E \\ &= j\omega\varepsilon_0\varepsilon'E + J_e \end{aligned} \quad (\text{A-5a})$$

$$\begin{aligned} j\omega B &= j\omega\mu(\omega)H = j\omega\mu_0(\mu' - j\mu'')H \\ &= j\omega\mu_0\mu'H + \omega\mu_0\mu''H = j\omega\mu_0\mu'H + \sigma_m H \\ &= j\omega\mu_0\mu'H \end{aligned} \quad (\text{A-5b})$$

$+ J_m$

Therefore, whenever a lossy permeable material is used to carry an alternating magnetic field, it behaves exactly as if it were carrying a magnetic current measured in Volts (whereas electric current is measured in Amps) as suggested in Fig.A-1.

Fig.A-1 shows an electric dipole carrying an alternating electric current and its electromagnetic dual which is the magnetic dipole (in this case modeled as rods). Duality requires that since the electric dipole has Perfect Electric Conductor (PEC) feed lines and an electric voltage source load (V_e), the magnetic dipole should have Perfect Magnetic Conductor (PMC) feed lines and a magnetic voltage source (V_m). Since there is no access to PMC feed lines and magnetic voltage sources, a PEC feed loop is used instead to feed the magnetic dipole [2].

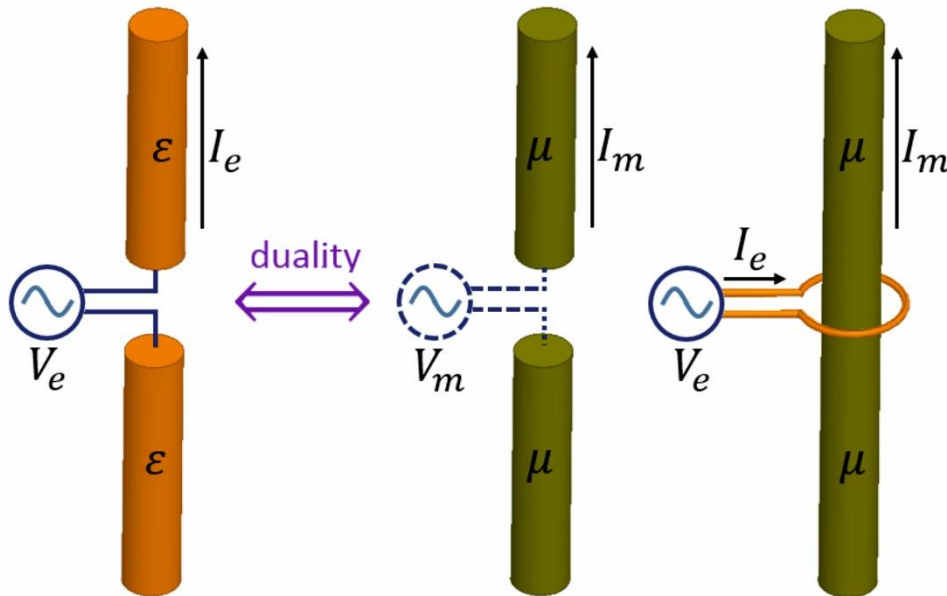


Fig.A-1: Electric Dipole Carrying an Alternating Electric Current and Its Electromagnetic Dual Which Is the Magnetic Dipole (in This Case Modeled as Rods).

Accordingly, throughout this paper the term electric loop refers to a metal loop with no core, electric dipole refers to our copper sphere model of a linear conventional electric dipole, and the true magnetic antennas just defined, will be referred to as magnetic dipoles.

The impact this difference makes in the results of the previous study [7] can be understood in its simplest terms by comparing the two magnetic dipole radiators, one the conventional electric loop antenna, the other, the same loop antenna wrapped around a sphere of dispersive ferromagnetic (or ferrimagnetic) material and comparing their input resistance and radiation efficiency at resonance.

A.3 Comparison of the true magnetic dipole to the conventional loop

To highlight the difference in performance between the true magnetic dipole and a conventional loop antenna it suffices to compare them in free space. The magnetic core will be assumed to be a laminated ferromagnetic material like those used in the magnetic read-head industry. The typical frequency dependent permeability of a single metal layer of such a material (CoZrNb, abbreviated CZN, thin film [39]) is shown Fig.A-2. Heaviside's magnetic conductivity is defined as $\sigma_m = \omega\mu_0\mu''$, where μ_0 is the permeability of free space and μ'' is the imaginary part of the relative permeability.

Assuming the electric loop antenna is a copper loop of conductivity $\sigma_{Cu} = 6 \cdot 10^7 S/m$, radius $a=10 \mu m$ and wire cross sectional radius $\rho = 0.5 \mu m$. The relevant parameters for both antennas can be approximated as shown in Table A-1.

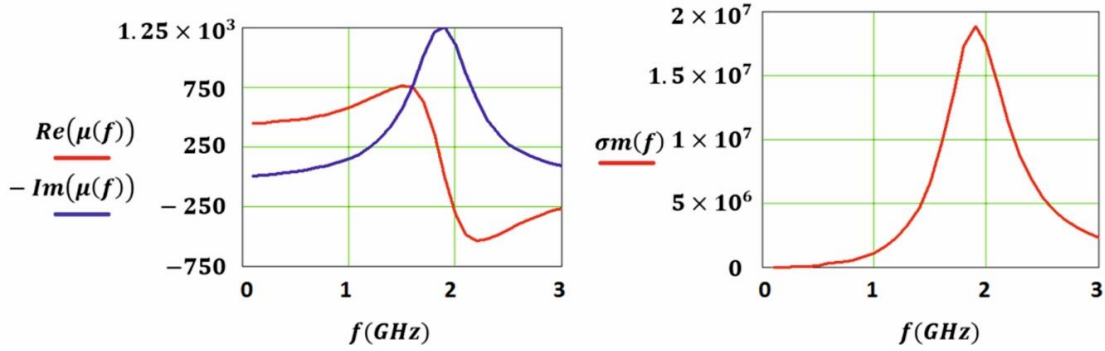


Fig.A-2. Relative Permeability (Left, Unitless) and Corresponding Heaviside Magnetic Conductivity (Right, in Ohms/Meter) of a Typical High Frequency Ferromagnetic Material ($\mu_{initial} = 450$).

Table A-1 Radiation Resistance, Material Resistance, Efficiency and Input Impedance at Resonance of Electrical Loop and Magnetic Dipole Antennas

Antenna	Electric Loop antenna	magnetic dipole
Radiation Resistance (electric or magnetic)	$R_{rad} = 31171 \left(\frac{\pi a^2}{\lambda^2} \right)^2 \Omega$	$R_{radm} = \frac{2}{3\pi\eta} \left(\frac{2\pi a}{\lambda} \right)^2 S$
Material Resistance (electric or magnetic)	$R_{loss} = \frac{2\pi a}{\sigma_{cu}\pi a^2} \Omega$	$R_{lossm} = \frac{2a}{\sigma_m\pi a^2} S$
Efficiency	$efficiency_{electric\ loop}$ $= \frac{R_{rad}}{R_{rad} + R_{loss}}$	$efficiency_{magnetic\ dipole}$ $= \frac{R_{radm}}{R_{radm} + R_{lossm}}$
Input Impedance at resonance (Ω)	$Z_{input_L} = R_{rad} + R_{loss}$	Z_{input_m} $= \frac{1}{R_{radm} + R_{lossm}}$

Since the radiation efficiency of an antenna is the ratio of its radiation resistance to its total resistance, at 1.5GHz (the resonance peak of the permeable core) we find that the efficiencies of the electric loop and the magnetic dipole are:

$$\begin{aligned} \text{efficiency}_{\text{electric loop}} &= 1.44 \cdot 10^{-12} \\ \text{and efficiency}_{\text{magnetic dipole}} &= 9.69 \cdot 10^{-9} \end{aligned} \tag{A-6}$$

As expected the efficiencies of these microscopic antennas are very small, but that of the magnetic dipole is over 6500 times greater than that of the electric loop antenna. At the same time, $Z_{\text{input}_L} = 1.33\Omega$ while $Z_{\text{input}_m} = 174\Omega$. The magnetic dipole has a much higher input impedance than the electric loop. Therefore, while the electric loop must draw a large current to radiate its signal (and thus gets very hot), this magnetic dipole instead develops a high voltage while radiating its signal (much like conventional electric dipoles).

Since we know from the previous study that near field SAR deposition into the surrounding tissue is not a concern for magnetic dipoles the only damage risk here comes from raising the antenna temperature. But because the true magnetic dipole has a much higher impedance than the conventional loop antenna it follows that to radiate equivalent power it will draw a much lower current and thus dramatically reduce the risk of damage through heat conduction.

The end result of these considerations is that the link budget calculation performed in the original report must be redone for this new type of antennas. However, that calculation will be left to a future third report in this series because there is a more

important development that results from choosing microscopic magnetic dipoles as candidate in-vivo RF telemetry antennas. The benefits highlighted by the calculations above in free space, pale in comparison to the benefits derived inside the dielectric lossy medium of the body *especially* if we also assume that the receiving antenna is a magnetic dipole itself.

In the first report, it was seen that the best case human subject scenario requires the receiving antenna to be located just outside the head. Of course any antenna in close proximity to the head will still be affected by the lossy properties of the brain, given the extent of penetration of the antenna's near field. This point was not belabored in that report because accurate modeling of reasonable external antenna configurations would not have changed the essence of the pessimistic results obtained. However, in light of the potentially optimistic results that magnetic dipoles might bring, it is important to consider this effect. And we do so as the worst case scenario where the receiving antenna is itself assumed to be completely immersed in the same lossy dielectric medium as the transmitting antenna.

Therefore, for the balance of this report we concentrate on calculating the signal received from a microscopic antenna by a second microscopic antenna of the same kind in the same medium. The calculation is simplified by assuming (as in the first report) reasonable simple models of the antennas that allow the derivation of a closed-form expression for the mutual coupling between the antennas. The efficiency of signal transmission is then simply expressed as the ratio of the current induced on the receiving antenna to the current driving the transmitting antenna. Since received power is

proportional to the square of the antenna current, the gain in efficiency is proportional to the square of this ratio.

A.4 The case of the insulated Electric Dipole

Before proceeding with this comparison, it is worth mentioning the case of the insulated electric dipole, a case also not addressed in the original report [7]. Long linear electric dipoles are commonly used for communication under sea water, an extreme case of a low impedance medium. Because of the obvious conductivity of seawater medium, it is to be expected that these dipoles should be insulated from the medium to prevent the medium from shorting them out. And the question then arises, should not electric dipoles inside the body also be insulated? The answer can be found in Kraichman's monograph [46]. Although under seawater electric dipoles are insulated for most of their length, they only attain maximum gain if their ends are electrically connected to the conducting medium. If they are completely insulated, instead of an antenna we have a center fed coaxial cable, with the antenna as the inner conductor and the seawater boundary as the outer conductor. The wave injected at the feed of the dipole remains trapped in this coaxial line, reflecting back and forth between its ends.

The same effect arises in the case of our model spherical antenna immersed in the lossy body dielectric, except in our case the ends of the dipole are the conducting hemispheres and the insulated length is the assumption that the feed region itself is insulated from the medium. That is, our closed-form model of the electric dipole as a spherical antenna already behaves as if a narrow strip of insulator were wrapped around the equator where the voltage is applied to the hemispheres. If we were to insulate any

portion of the hemispheres themselves the result would be to add a shunt capacitance at the feed that diverts part of the feed current back to the source, thus reducing the amount of radiating current and therefore the gain. At the same time, the loss resistance presented to the antenna by the outer medium, contacting through a smaller area of the hemispheres, would be increased.

If we suppose that the entire antenna was insulated by a very thin dielectric layer of thickness of t_L , then it is true that we have removed a layer of thickness t_L from the near field ohmic loss integration because now the integral does not extend from a to ∞ but instead from $a + t_L$ to ∞ . However, this would happen automatically if we had increased the radius of the dipole by the same thickness t_L . So the change in near field loss due to a change in radius is not a relevant comparison.

Suppose we keep the outer radius constant and decrease the metal sphere's radius by inserting the insulating layer. The biggest impact of the insulating layer is that we have effectively placed the dipole at the center of an insulating dielectric cavity inside the conducting body medium. Now the input impedance of the small spherical dipole is given by putting in series with the external capacitance, the capacitance of the insulating layer. This capacitance reduces the antenna's total capacitance, therefore raising its capacitive reactance, and requiring now a larger inductor to resonate it. But that's not the main problem. Some flux lines from the upper hemisphere do terminate on the cavity wall while some flux lines terminate on the lower hemisphere. Only those flux lines terminating on the wall induce charges on the surface of the body boundary and it is only those oscillating charges that constitute the dipole moment radiating into the body. The

field lines not terminating on the wall simply constitute a shunt capacitance. Thus for a given input voltage we end up reducing the radiated power and increasing the stored energy. The only thing this accomplishes is decreasing the bandwidth of the antenna, and all the near field loss from a to ∞ is still there.

Thus, the original conclusion from the first report [7] still holds: antennas operating in the magnetic dipole mode have a decided advantage. We show in this contribution that two identical microscopic true magnetic dipole antennas can communicate inside the lossy dielectric body medium with an efficiency that is over 8 orders of magnitude greater than could be attained by conventional electric dipoles or electric loop antennas of the same size. It appears that microscopic RF telemetry inside the brain is now feasible.

A.5 RESULTS

It is known that micron sized antennas store much more energy in their near field per cycle than the power they can radiate to the far field by a ratio called the Quality factor of the antenna. The Fano-Chu limit sets a lower limit [19, 47] for this ratio which can be approximated by $Q \approx 1/(ka)^3$, where k is the propagation constant of the medium and a the radius of the smallest sphere that can enclose the antenna. For example if the body were considered a lossless dielectric, a 20micron antenna inside the body at 2GHz, would have a minimum Q of 40million and an 80micron antenna at the same frequency would have a Q of the order of 600,000. Since the body is a lossy dielectric, these Q values are reduced in actuality but they still serve to gauge the amount of energy

per cycle stored in the near field, energy that is then consumed as heat. Therefore to produce a reasonable radiated power outside the head (in the picowatts range) it was found in our previous analysis that microscopic antennas must be supplied with microwatts of power.

The baseline assumption made in the analysis of reference [7] is that one isolated antenna tries to communicate to the outside world by direct radiation of its signal. Furthermore, in that analysis the effect of adding a magnetically permeable core to a loop antenna was only modeled as an increase in the dipole moment of the loop by at most a factor of 3. The effect on the input impedance of the loop antenna and the possibility that the main radiating current could be the polarization current of the core and not the electric current of the loop were not considered. Yet, recent developments in the theory and practice of magnetically permeable antennas [2, 14, 21] have shown that such antennas exhibit unprecedented gain and efficiency in the presence of a low impedance environment. The result is that a conformal magnetic antenna (constructed from a lossy ferrite) only 1.5 inches thick, lying directly on the conducting roof of a High Mobility Multipurpose Wheeled Vehicle (HUMVEE), was shown to outperform an eight-foot-tall conventional metal monopole antenna on the same vehicle [21]. Since complete immersion in a lossy dielectric also presents a low impedance medium to an antenna, it can be expected that microscopic magnetic antennas inside the body dielectric will also show unprecedented gain and efficiency. This is demonstrated by calculating the mutual coupling between two identical electric dipole antennas, magnetic dipole antennas and electric loops antennas immersed in the body dielectric.

From the impedance point of view, electric loops and electric dipoles are the two fundamental types of antennas. According to Schelkunoff [8] although in order to calculate the impedance of an antenna we might have to solve Maxwell's equation subject to the specific boundary conditions of the antenna, we can obtain some of the important general properties of the impedance from much more basic considerations. An interesting fact is that these properties are not limited to antennas or electrical systems. They are common to all dynamic systems (for example mechanical and acoustical) and they don't even depend on the form of the dynamical equations as long as those equations are linear. A brief consideration of these general properties of impedance will help to understand the reason for the difference in the antennas' behavior.

For any transmitting antenna, the voltage and current at the input terminals can be written as a function of a complex variable which can be called "p" where $p = j\omega$ and ω is the frequency of oscillation. The ratio of the functions $V(p)$ and $I(p)$ is called the input impedance $Z(p)$ of the antenna and the inverse is called the input admittance $Y(p)$.

The schematic in Fig.A-3 shows a network with two accessible terminals and in order to introduce the two fundamental antenna types we can write the impedance and admittance as stated in the figure without being interested in their interior structure.

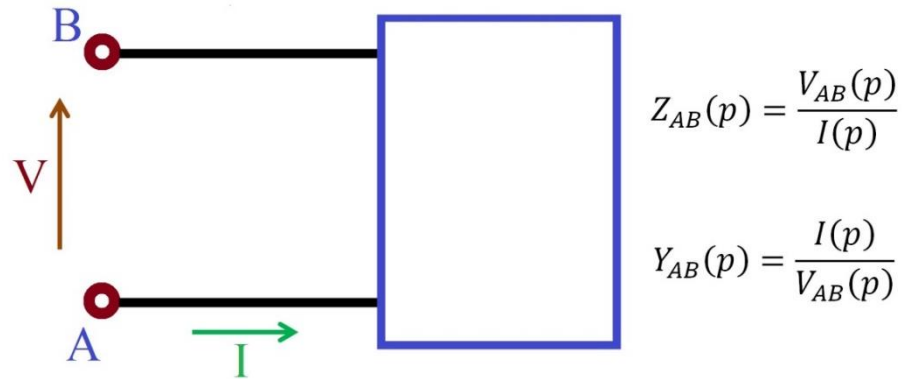


Fig. A- 3. A Schematic of a Network with Two Accessible Terminals.

The roots of the equation $Z(p) = 0$ are called the zeros of the input impedance which are the case for which the voltage across the input impedance vanishes while the current does not. The poles of the impedance are the zeros of the admittance and are roots of the equation $Y(p) = 0$ and it is obvious that in this case the input current goes to zero while the voltage does not which means that the terminals of the antenna are floating or the antenna is an open circuit.

If the terminals of an antenna are open circuited conductors, we can place opposite charges on these conductors and create a voltage across the input impedance and the current will be zero therefore having $p=0$ as a pole of its input impedance. These antennas are called dipole antennas. On the other hand, an antenna consisting of a single perfect conductor having a steady current flowing in it would not have loss. These antennas are called electric loops and $p=0$ is a zero of the impedance of a perfectly conducting electric loop. Fig. A-4, shows the electric dipole and the electric loop as the two general types of antennas.

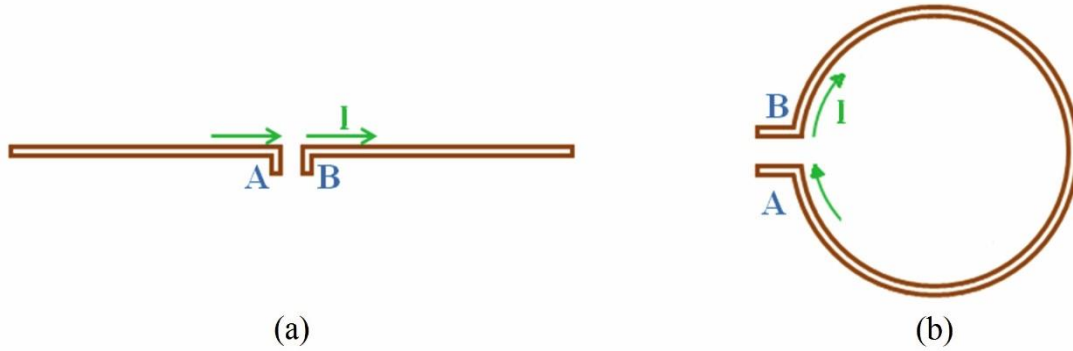


Fig. A-4. Two General Types of Antennas. (a) Dipole Antenna (b) Loop Antenna

This fundamental difference between electric dipole antennas and electric loop antennas is carried through to the case of realistic imperfect environments and materials. The open circuit nature of an electric dipole immersed in a lossy conducting dielectric means that the large voltage developed between its opposite terminals drives a current directly in the medium surrounding it, following the field lines of its near electric field and depositing power into the medium. The short circuit nature of the electric loop means that it cannot drive a current directly in the surrounding medium. Instead currents are induced via electromagnetic induction of eddy currents by its magnetic near field. As shown in reference [41] this results in the loop dissipating much less power into the surrounding medium; but the fact that copper is not a perfect conductor means that the current in the electric loop will cause it to heat up and dissipate power into its own materials. Given these two different behaviors we could ask if there is another kind of antenna that can combine the best features of these, one whose near field is dominated by a magnetic field and yet does not behave as a short circuit to draw large currents. This is precisely what permeable magnetic dipoles do.

For the sake of the computational examples we assume spherical antennas $10 \mu m$ in radius. (The derivations are included in the Methods section to enable the reader to replicate these results.) Fig.A-5 is a sketch of the idealized antenna models represented by these dipoles. We have chosen the sphere geometry as a convenient form for the dipole antennas for many reasons. The spherical geometry of the dipoles makes the radiated field and the mutual coupling calculations straight forward because they can be written in a self-consistent closed form. As we will see later, by using spherical dipoles, we can normalize the radiated field to the field on the surface of the spheres and we can also normalize the induced current to the source current, thus enabling us to compare electric and magnetic antennas on equal footing.

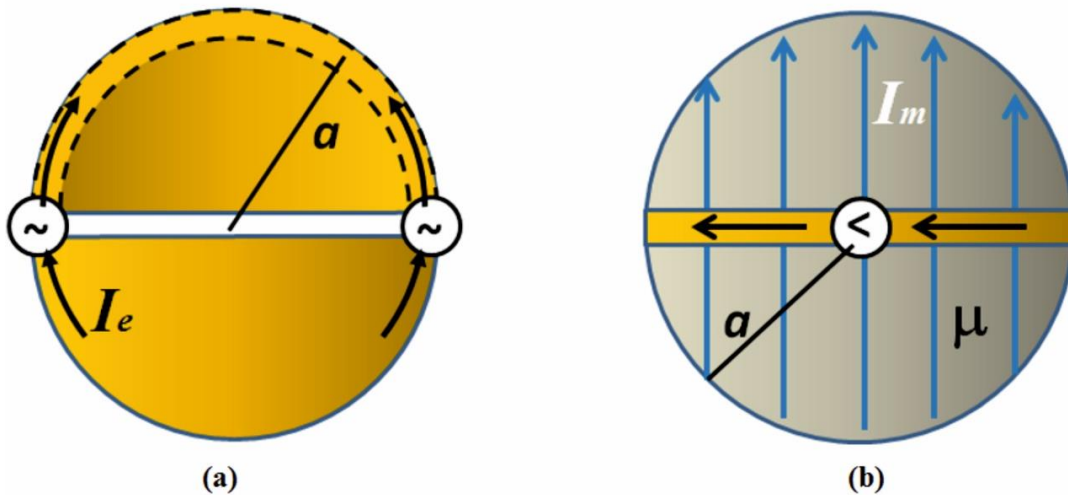


Fig. A-5. Sketch of the Idealized Antennas Considered in This Analysis. (a)Electric Dipole Antenna
(b)Magnetic Dipole Antenna

The electric dipole can be imagined as a hollow sphere cut in half and fed by a distributed electric voltage source, V_E , at the equator such that the total electric current

flowing depends on the self-impedance of the antenna (measured in Ohms) according to equation(A-6).

$$I_E = \frac{V_E}{Z_{E\ self}} ; \text{current moment} = I_E \sqrt{\frac{8}{3}} a \quad (\text{A-6})$$

The magnetic dipole can be imagined as a solid permeable sphere with a conducting belt around its equator, said belt fed by a current source. The current flowing through the belt in Amps is the magnetic Voltage, V_M , and the total magnetic current flowing depends on the magnetic self-impedance of the antenna (measured in Siemens) according to equation (A-7).

$$I_M = \frac{V_M}{Z_{M\ self}} ; \text{current moment} = I_M \sqrt{\frac{8}{3}} a \quad (\text{A-7})$$

The complete duality in Maxwell's equations that is evident once magnetic currents were introduced by O. Heaviside, allow the engineer to translate conventional results of electrically conducting antennas driven by an electric voltage at a gap into the results for magnetically conducting antennas driven by a current flowing in a metal feed loop surrounding the permeable material.

Conventional metal antennas have an Impedance given by the ratio of the applied Voltage, V , to the current that flows in the metal, Z_e measured in Ohms. The current, I , can be measured by performing the circulation integral of Ampere's law around the metal wire, that is

$$I = \oint \vec{H} \cdot d\vec{l} \quad (\text{A-8})$$

In the same way, permeable antennas have a dual magnetic impedance, Z_m measured in Siemens, given by the ratio of the applied Current, I , in the feed loop to the electromotive force around the permeable rod

$$V = \oint \vec{E} \cdot d\vec{l} \quad (\text{A-9})$$

This is why Z_m has the inverse units of Z_e . In the referenced dissertation [2], it is shown that Z_m is nothing but the electric admittance, Y_e in Siemens, measured by the source driving the current in the permeable antenna's feed loop.

In an ensemble of spheres, the mutual coupling between spheres is represented by the mutual impedance. For electric and magnetic dipoles located on the same x-y plane, all polarized along the z-axis, these are given by equations (A-10) and (A-11).

$$Z_{E_{mn}} = \frac{\frac{8}{3}a^2 \frac{\eta_0}{\sqrt{\epsilon_r(\omega)}} e^{-jkr}}{4\pi r} \left(jk + \frac{1}{r} + \frac{1}{jkr^2} \right) \quad (\text{A-10})$$

$$Z_{M_{mn}} = \frac{\frac{8}{3}a^2 e^{-jkr}}{\frac{\eta_0}{\sqrt{\epsilon_r(\omega)}} 4\pi r} \left(jk + \frac{1}{r} + \frac{1}{jkr^2} \right) \quad (\text{A-11})$$

Z_{mn} is the mutual impedance between the m^{th} and n^{th} sphere. Setting $r=a$ (the radius of the sphere) yields Z_{mm} , the self -impedance. (See the Methods section for the details.) With this formulation it is straight-forward to solve self-consistently the problem of the excitation of an ensemble of spheres by any incident field or in particular by one

member of the ensemble. Focusing on the simplest case of two spheres, the Voltage at the feed of each antenna depends on the currents on itself and the other antenna, satisfying an equation of the form:

$$V_1 = I_1 Z_{11} + I_2 Z_{12} \quad (\text{A-12})$$

Thus, under the assumption that the two spheres share the same equatorial plane, the problem of an array of two spheres is represented by a matrix equation of equation (A-13), where all the terms of the Impedance matrix, \bar{Z} , are known from equations (A-10) and (A-11).

$$\bar{Z} \cdot \mathbf{I} = \mathbf{V} \rightarrow \begin{pmatrix} Z_{11} & Z_{12} \\ Z_{21} & Z_{22} \end{pmatrix} \begin{pmatrix} I_1 \\ I_2 \end{pmatrix} = \begin{pmatrix} V_1 \\ V_2 \end{pmatrix} \quad (\text{A-13})$$

To maximize the power transfer from the source to the antenna (and from the antenna to its receiver) we assume that the antennas have been tuned to resonance at the operating frequency either by aid of a matching circuit or the natural resonance of its constitutive materials. This simply means that the self-reactance has been cancelled.

$$Z_{self_tuned} = Z_{mm} \rightarrow Re(Z_{mm}) \quad (\text{A-14})$$

To illustrate how the materials of construction can be used to tune the antenna requires a brief digression. In reference [21] it is shown that, to first order, the input impedance of an electrically small material antenna (as opposed to the idealized perfectly conducting antenna) can be obtained by simply adding in series with the conventional antenna model, the internal Impedance of the material. R. W. P. King and T. T. Wu use a similar argument to analyze the imperfectly conducting antenna.

In the simplest case of a small metal dipole (our spherical dipole antenna) we can approximate its external impedance by the capacitance of its external near field in series with its radiation resistance. In a lossy dielectric medium, the near field capacitance is complex and thus adds extra resistance to the antenna. To resonate (that is to tune) such an antenna the common practice is to add a series inductor such that the series sum of the added inductive reactance and the external capacitive reactance equals zero.

In the same sense a small spherical permeable antenna of radius a , has an external impedance dominated by the magnetic capacitance of its near field. Thus, its dual magnetic input impedance is approximately

$$Z_m \approx \frac{1}{j\omega C_{m_{ext}}} + R_m = \frac{1}{j\omega\mu_0 \frac{3\pi}{2} a} + R_m \quad (\text{A-15})$$

Where R_m is the magnetic dipole's (dual) radiation resistance. Now, assuming the flux inside the permeable sphere is uniform, the internal capacitance can be roughly approximated by a term of the form:

$$C_{m_{int}} = \mu_0\mu_r(\omega) \frac{\pi a^2}{2a} \quad (\text{A-16})$$

Therefore the total impedance of the material antenna is:

$$\begin{aligned}
Z_m &\approx \frac{1}{j\omega\mu_0 \frac{3\pi}{2} a} + R_m + \frac{1}{j\omega\mu_0\mu_r(\omega) \frac{\pi a^2}{2a}} \\
&= R_m + \frac{1}{j\omega\mu_0 \frac{\pi}{2} a} \left(\frac{1}{3} + \frac{1}{\mu_r(\omega)} \right)
\end{aligned} \tag{A-17}$$

In this last equation we see that the internal and external capacitances add in series and it is clear that when the real part of the relative permeability of the material, $\mu_r(\omega)$, gets close to the value -3, the reactance is cancelled and the antenna is resonant. At resonance the input impedance of the antenna is purely resistive, consisting of the radiation resistance, the loss resistance of the antenna metal components and the body dielectric, and the loss contributed by the permeable material's imaginary part of the permeability. Because a ferromagnetic material having a strong Lorentz-like resonance exhibits negative permeability values just past that resonance it is clear that choosing using such a material for the magnetic dipole's permeable core can result in an antenna that is automatically tuned by its materials of construction.

Returning now to the calculation of mutual coupling between antennas, in the most general case where the m^{th} sphere of an array is excited and the rest are passive, the currents on all antennas are obtained by setting $V_m = 1$, all other $V_{n \neq m} = 0$ and inverting the matrix:

$$\bar{Y} = \bar{Z}^{-1} \therefore I = \bar{Y}V \tag{A-18}$$

The case of the electric loops is solved similarly and the details of the derivation can be found in the methods section. The final step before solving the case of interest is

to define the medium in which the antennas are immersed. As in reference 1, a good approximation below 3 GHz to the FCC accepted model for the human head is the a medium of unity relative permeability and relative permittivity given by the following multi-Debye relaxation model including a DC conductivity of 0.68 S/m (with the frequency written in GHz):

$$\begin{aligned}
\varepsilon_r(f) &= \varepsilon' - j\varepsilon'' \\
&= 8 + \frac{18}{1 + j\frac{f_{\text{GHz}}}{0.185}} + \frac{7}{1 + j\frac{f_{\text{GHz}}}{9}} \\
&\quad + \frac{18}{1 + j\frac{f_{\text{GHz}}}{12}} - j\frac{0.68}{0.056f_{\text{GHz}}}
\end{aligned} \tag{A-19}$$

The propagation constant and medium impedance appearing in equations (A-10) and (A-11) become:

$$\begin{aligned}
k_0 &= \frac{2\pi}{\lambda_0} \rightarrow k_{\text{med}} = k_0\sqrt{\varepsilon_r(f)}, \\
\eta_0 &= 377 \rightarrow \eta_{\text{med}} = \eta_0/\sqrt{\varepsilon_r(f)}
\end{aligned} \tag{A-20}$$

The mutual impedances are then:

$$\begin{aligned}
Z_{\text{mutual}}^{\text{electric}} &= \frac{8}{3} \frac{a^2 \eta_{\text{med}} e^{-jk_{\text{med}}r}}{4\pi r} \left(jk_{\text{med}} + \frac{1}{r} \right. \\
&\quad \left. + \frac{1}{jk_{\text{med}}r^2} \right) \text{ electric dipoles}
\end{aligned} \tag{A-21}$$

$$Z_{mutual}^{magnetic} = \frac{Z_{mutual}^{electric}}{(\eta_{med})^2} \quad \text{magnetic dipoles} \quad (\text{A-22})$$

$$Z_{mutual}^{electric} = \frac{j\eta_{med}k_0(\pi a^2)e^{-jk_{med}r}}{4r} (k_{med}a)^2 \left(1 - \frac{j}{k_{med}r} - \frac{1}{(k_{med}r)^2} \right) \text{electric loops} \quad (\text{A-23})$$

These closed form equations are easy to use and have the pleasing feature that to get the self-impedance we simply set $r = a$. However, as explained above, for the magnetic dipole case the self-impedance has an additional series term⁶ due to the material properties of the core.

$$Z_{m \text{ internal}} \cong \frac{1}{j\omega\mu_0(\mu(\omega) - 1) \frac{\pi a^2}{2a}} \quad (\text{A-24})$$

So that for the magnetic dipoles the total self- impedance at resonance is given by equation (9-25).

$$Z_{m \text{ self}} = \text{Re} \left[\frac{1}{j\omega\mu_0(\mu(\omega) - 1) \frac{\pi a^2}{2a}} \right] + \text{Re} [Z_{mutual}^{magnetic}(r = a)] \quad (\text{A-25})$$

The first term on the left, the real part of the internal impedance, represents the loss inside the permeable core. This turns out to be inversely proportional to the Heaviside magnetic conductivity of the material ($R_{lossm} = \frac{2a}{\sigma_m \pi a^2}$) and thus is minimized when the material has a very large initial permeability (500 in our example) and when the operating frequency is chosen as the resonant frequency of the material. This choice also maximizes the input impedance.

Having defined all the relevant parameters, we can calculate the current induced on a second antenna as a function of the current in the source antenna and the separation between them. For example, assuming there are two spheres (or loops) each of radius $a = 10\mu m$, separated from each other by a distance d , we let the distance d range from 5mm to 4 cm in steps of 5mms. The results, plotted as the ratio of the induced current to the source current, are shown as the symbols in Fig.A-6. The advantage of the magnetic dipole antenna by about 4 orders of magnitude is startling. This corresponds to an 8 order of magnitude increase in power transmission, that is, +80 dB gain over the conventional alternatives.

To emphasize that the nature of the receiving antenna is as important as that of the transmitting antenna, we have also plotted in Fig.A-6, as curves, the ratio of the principal field at the distance $r=d$ to the maximum value of that field at the surface of the antenna $r=a$.

$$E_{\theta}(r) = \frac{\eta_0}{\sqrt{\epsilon_r(\omega)}} \frac{I_e \sqrt{\frac{8}{3}} a}{4\pi r} e^{-jkr} \left(jk + \frac{1}{r} + \frac{1}{jkr^2} \right) \sin\theta \quad \text{electric dipoles} \quad (\text{A-26})$$

$$H_{\theta}(r) = \frac{\sqrt{\epsilon_r(\omega)} I_m \sqrt{\frac{8}{3}} a}{\eta_0 4\pi r} e^{-jkr} \left(jk + \frac{1}{r} + \frac{1}{jkr^2} \right) \sin\theta \quad \text{magnetic dipoles} \quad (\text{A-27})$$

$$H_{\theta}(r) = \frac{-(ka)^2 I_e}{4r} e^{-jkr} \left(1 + \frac{1}{jkr} - \frac{1}{(kr)^2} \right) \sin\theta \quad \text{electric loops} \quad (\text{A-28})$$

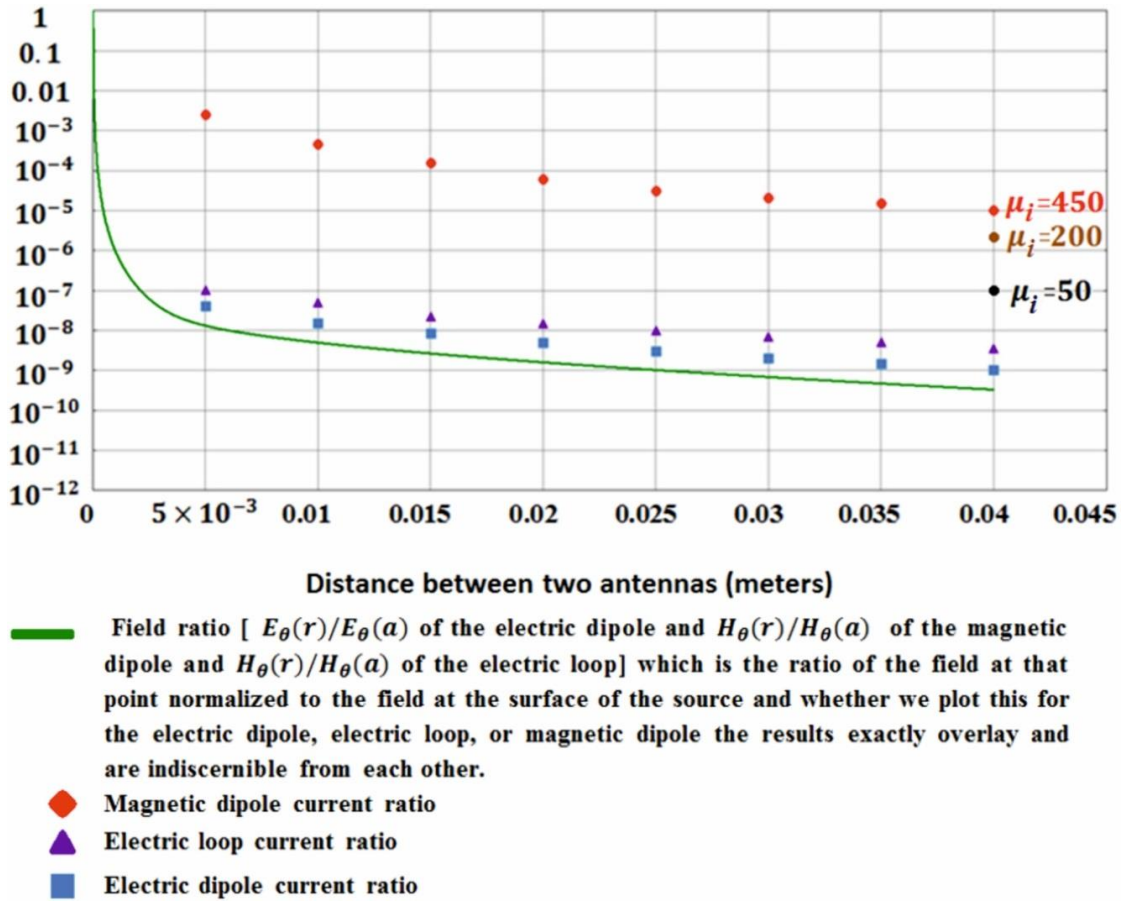


Fig. A- 6. The Fields of the Electric Dipole Antenna, Magnetic Dipole Antenna and the Loop Antenna Normalized to the Fields on Their Surface Is Plotted in the Same Figure as the Induced Current in Each of These Antennas Normalized to the Source Current. The Distance Between the Antennas Has Been Change from 5mm to 40 mm with 5mm Steps. The Normalized Fields of the Three Different Antennas are the Same But Using a Pair of Magnetic Dipole Antennas Results in a Four Order of Magnitude Improvement in the Mutual Coupling, Eight Order of Magnitude Improvement on Power Transfer, When Compared to the Conventional Electric Dipoles and Loops.

By examining this graph we again see the significance difference in the behavior of the mutually coupled magnetic dipoles. All the normalized fields lie on top of each other and 4 centimeters away the normalized field has dropped down by a factor of

3×10^{-10} compared to the field at the surface: -190 dB down. Electric dipole to electric dipole mutual coupling follows this same trend being slightly larger by a factor of 3, while the electric loop to electric loop coupling follows the same trend but stronger by about a factor of 10. The magnetic dipole coupling exceeds the field ratio by almost 5 orders of magnitude.

The efficiency of the magnetic dipole antennas are much higher than the other two alternatives (the electric dipole antenna and the electric loop antenna) because the magnetic material used for these antennas changes contributes to both the dipole moment and the input impedance. The material used for the magnetic dipole antenna calculations was assumed to have the permeability shown in Fig.A-2. These magnetic materials already exist, and having a high $\mu_{initial}$ is an important factor which will result in having a strong magnetic conductivity. To illustrate the importance and role of the high permeability material, we have added two more data points at the distance of 4cms showing that for $\mu_{initial} = 50$ and $\mu_{initial} = 200$ (with the same assumed resonant frequency) the advantage is not as significant as the $\mu_{initial} = 450$.

An additional lesson from these calculations is that only looking at the rate of drop of a field component does not tell us the whole story because the field distribution in this space is dominated by the spherical spreading of the source field and the attenuation due to the medium whereas the way a receiving antenna can harvest energy out of this field is dominated by its self and mutual impedance properties.

A.6 METHODS

Throughout this derivation we exploit the principle of duality inherent in Maxwell's equations where to every conventional electric measurable (Voltage, Current) there is a dual magnetic measurable related through the transformations $E \rightarrow H, H \rightarrow -E, \mu \leftrightarrow \varepsilon, Z_m = Z_e / \eta^2$. The principal polarization fields radiated by electric and magnetic spherical dipoles of radius a , at a distance r , in terms of the current at the feed are respectively:

$$E_\theta = \frac{\eta_0}{\sqrt{\varepsilon_r(\omega)}} \frac{I_e \sqrt{\frac{8}{3}} a}{4\pi r} e^{-jkr} \left(jk + \frac{1}{r} + \frac{1}{jkr^2} \right) \sin\theta$$

(A-29)

$$H_\theta = \frac{\sqrt{\varepsilon_r(\omega)}}{\eta_0} \frac{I_m \sqrt{\frac{8}{3}} a}{4\pi r} e^{-jkr} \left(jk + \frac{1}{r} + \frac{1}{jkr^2} \right) \sin\theta$$

The quantity $a\sqrt{8/3}$ is known as the antenna height, h , for the spherical dipole that defines the voltage impressed across its feed by an incident electric field as $V_{feed} = E_{inc}h$ (and it is also the moment arm of its dipole moment.) For the electric dipole the current I_e is in Amps and is the conventional total current that would be crossing the equator of the sphere. For the magnetic dipole the current I_m is in Volts and is equal to the total polarization current crossing the equator of the sphere

$$\begin{aligned}
I_m &= \int_0^{2\pi} \int_0^a \frac{\partial}{\partial t} \vec{P}_m \cdot \hat{z} R dR d\varphi & (A-30) \\
&= \int_0^{2\pi} \int_0^a \frac{\partial}{\partial t} [\mu_0(\mu_r(\omega) - 1)H_z] R dR d\varphi
\end{aligned}$$

For simplicity we assume that the input impedance of the spherical antennas is closely modelled by the modal impedance of the first spherical wave mode (TM₁₀ for the electric dipole and TE₁₀ for the magnetic dipole.) For the small electric dipole this is given by equation (9-31) .

$$Z_{e1} = \frac{1}{Y_1} ; Y_1 = \frac{jka}{80 \sqrt{\frac{1}{\epsilon_r}}} \left[\frac{1 - j(ka)^3}{1 - (ka)^2 + (ka)^4} \right] \quad (A-31)$$

And for the magnetic dipole by its dual

$$Z_{m1} = \frac{Z_{e1}}{\left(\frac{\eta_0}{\sqrt{\epsilon_r}} \right)^2} \quad (A-32)$$

Then a self-consistent definition of the mutual Impedance is given by equation 33 where the numerator is the Reaction Integral between the two currents, that is, the inner product of the current in antenna 1 times the field antenna 2 produces on it. By the reciprocity of the Reaction Integral $Z_{12}=Z_{21}$.

$$Z_{e12} = - \frac{\iiint_1 \vec{J}_{e1} \cdot \vec{E}_2 dV_1 = \iint_1 \vec{K}_{e1} \cdot \vec{E}_2 dS_1}{I_{e1}I_{e2}} \quad (A-33)$$

Where \vec{J}_{e1} is the volumetric current and \vec{K}_{e1} is the surface current and the numerator is showing both the volumetric current version and the surface current version of the reaction theorem.

Again, by duality:

$$Z_{m12} = \frac{Z_{e12}}{\left(\frac{\eta_0}{\sqrt{\epsilon_r}}\right)^2} \quad (\text{A-34})$$

Assuming the spheres are small and far from each other the Reaction Integral simplifies by assuming a uniform field over the uniform current of the dipole and we get:

$$\begin{aligned} Z_{e12} &= \frac{\frac{8}{3}a^2 \frac{\eta_0}{\sqrt{\epsilon_r(\omega)}} e^{-jkr}}{4\pi r} \left(jk + \frac{1}{r} + \frac{1}{jkr^2} \right); Z_{m12} \\ &= \frac{\frac{8}{3}a^2 e^{-jkr}}{\frac{\eta_0}{\sqrt{\epsilon_r(\omega)}} 4\pi r} \left(jk + \frac{1}{r} + \frac{1}{jkr^2} \right) \end{aligned} \quad (\text{A-35})$$

In practice when the second sphere is farther than one diameter from the surface of the first sphere, the field is uniform enough that it can be extracted from the reaction integral as previously mentioned. Even though by definition the field wouldn't be uniform closer than the mentioned distance, using this mutual impedance equation and

coming exactly to the surface of the source antenna gives an answer that converges on the correct self-impedance. This convenient behavior is a result of the variational properties of the Reaction Integral in equation (A-33).

The mutual impedance of the electric loop has been obtained using two different methods. The first method is finding the mutual inductance and the second method which also serves as a verification check is calculating the reaction integral ($\int E \cdot J dl$) by replacing the loop with a curvilinear square of equal area to make the calculation of the integral very easy.

The mutual inductance found from the first method and the mutual impedance are as follows, where 'r' is the distance between the antennas. (As alluded to above, the mutual impedance tends to the self impedance at $r=a$.)

$$\begin{aligned}
 M_{mutual}(r) & \qquad \qquad \qquad (A-36) \\
 &= -\frac{\mu_0(\pi a^2)}{4r} e^{-j[k_0\sqrt{\epsilon_r}]r} [k_0\sqrt{\epsilon_r}a]^2 \left(\frac{1}{([k_0\sqrt{\epsilon_r}]r)^2} \right. \\
 & \left. + \frac{j}{[k_0\sqrt{\epsilon_r}]r} - 1 \right)
 \end{aligned}$$

$$Z_{12} = j\omega M_{12} \qquad \qquad \qquad (A-37)$$

$$Z_{mutual}(r) = j \frac{\eta_0 k_0 (\pi a^2)}{4r} e^{-j[k_0 \sqrt{\epsilon_r}]r} [k_0 \sqrt{\epsilon_r} a]^2 \left(1 - \frac{j}{[k_0 \sqrt{\epsilon_r}]r} - \frac{1}{([k_0 \sqrt{\epsilon_r}]r)^2} \right) \quad (\text{A-38})$$

For the second method we will perform the reaction integral of E_φ times the circulating current in the loop and that would give us the mutual impedance. A good approximation is to replace the the loop with a curvilinear square of equal area. Now the reaction integral is trivial.

$$Z_{mutual_{loop}} = - \frac{\{E_\varphi(r-a) \cdot I_{e_{loop}}(r-a)\zeta - E_\varphi(r+a) \cdot I_{e_{loop}}(r+a)\}}{I_{e_{loop}} I_{source}} \quad (\text{A-39})$$

After simplifying we will have:

$$Z_{mutual_{loop}} = \frac{\omega \mu_0 \pi a^2}{4\pi} k \frac{\pi a}{2r} \left\{ \left(\frac{e^{-jk(r-a)}}{r-a} + \frac{e^{-jk(r-a)}}{jk(r-a)^2} \right) (r-a) - \left(\frac{e^{-jk(r+a)}}{r+a} + \frac{e^{-jk(r+a)}}{jk(r+a)^2} \right) (r+a) \right\} \quad (\text{A-40})$$

And the final result is as follows:

$$\begin{aligned}
Z_{mutual_{loop}} = \frac{\omega\mu_0\pi a^2}{4\pi} k \frac{\pi a}{2r} \left\{ \left(1 \right. \right. \\
\left. \left. + \frac{1}{jk(r-a)} \right) e^{-jk(r-a)} \right. \\
\left. - \left(1 + \frac{1}{jk(r+a)} \right) e^{-jk(r+a)} \right\}
\end{aligned} \tag{A-41}$$

The results obtained from the two different methods are very close.

A.7 Finite difference time domain (FDTD) simulation approach

The results shown in Fig. A-6, show a dramatic advantage in the case of true magnetic antennas. Even though the closed-form expressions for analyzing this problem have been derived following classic approaches in antenna theory, the results are almost “too good to be true.” Therefore, it is appropriate to spot check the result by an alternate method. The alternative to the analytic formulation is a numerical simulation approach. Such an approach is not without its own difficulties.

In many ways, the problem addressed here resembles the problem of the scattering of light from plasmon resonant sub-wavelength particles. In that case, for particles of the order of 10 nm in diameter the scatterer is of the order of two hundredths of a wavelength. In our case an antenna 20 microns across at 2GHz in the body dielectric is less than one thousandth of a wavelength. To faithfully model such small particles and correctly simulate the resonant behavior with frequency domain Volume Integral Equation methods or Finite Element methods requires an extremely fine mesh and the

inversion of a matrix that at resonance has a nearly zero determinant. Special methods for dealing with this sub-wavelength problem have been devised but are not usually implemented in the commercially available software.

Because all we want to do is spot check the result, a reliable brute force approach is to solve the problem using the Finite Difference Time Domain (FDTD) method. By recognizing that the advantage of the magnetic antenna occurs for every separation distance considered, we can choose a case where two antennas are relatively close and thus examine the case of strong near field coupling. A best case for the electric dipole antenna is chosen where the average body dielectric is more heavily biased towards fat, thus assuming a dielectric constant near 2GHz of 56 and an equivalent conductivity of 1.07 S/m. The antennas are 10 μm in radius, 56 μm center to center apart. The closed form expressions for this case yield the induced magnetic current on the second particle to be of the order of 0.67 (-3.47dB) that of the first whereas for electric dipoles it is 0.06 (-24 dB) of the first.

We choose an FDTD domain discretized uniformly with $dx=dy=dz=ds=4\mu\text{m}$, and dimension 70 ds by 70 ds by 70 ds. This domain is small enough to run 2.5 million time steps in 2 hours on a 16 core CPU. Such a small domain ($\lambda/100$ on the side) could not be used to calculate far field radiation from these antennas. However since it is 14 antenna diameters across it is large enough to accommodate the quasi-static near field that dominates the behavior of these antennas. Even at this small size, the discretization is coarse as illustrated in Fig A-7 where the two antennas are shown as seen from above.

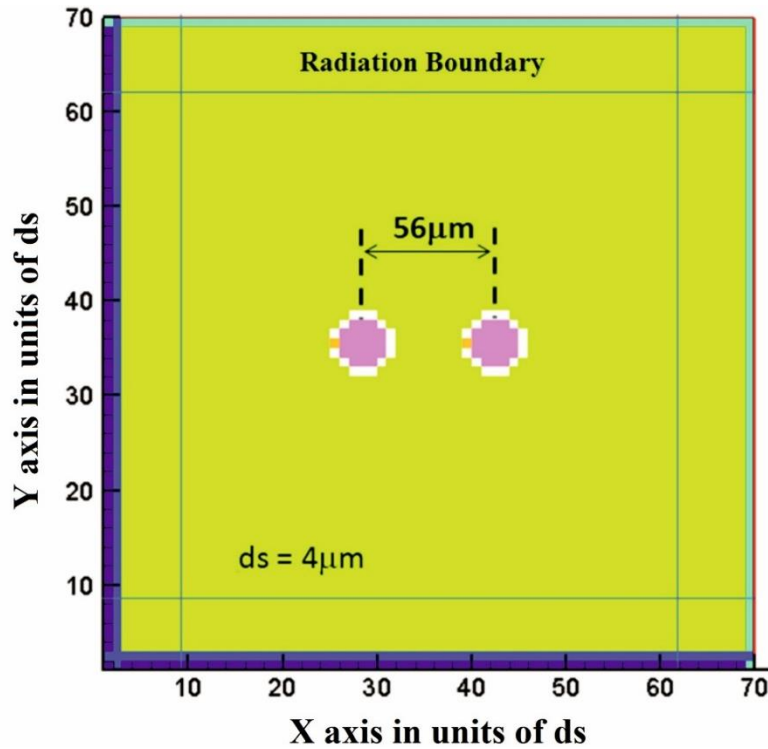


Fig. A-7. Top View of the FDTD Domain Used to Analyze Two Coupled Micro-Antennas

A closed flux path formulation has been employed to maximize symmetry; as in the PEC blocks mentioned in the work done by Z. Zhang and R. E. Diaz [48]. Because of the coarse discretization, even though the antennas are spheres $2.5 ds$ in radius their actual physical size may appear to be larger by one discretization cell (24 microns rather than 20 Microns). Similarly, it is evident that since the conducting bands have been made thick for the same reason, the actual equivalent separation between the antennas for near field coupling may be one cell shorter or 52 microns instead of 56 microns. Such deviations of up to 20% in linear dimension are considered to be slight for the purpose of this computation because the difference in coupling between these antennas according to the closed form model is of the order of 20dB, that is, a factor of ten in induced current. Since we have mentioned that the actual physical sizes may appear to vary by one

discretization cell we have found the closed form expressions for different sizes and distances and the results are very close ranging from -3.75dB to -3.29dB for the magnetic dipoles and -23.1 dB to -24.6 dB for the electric dipoles, showing that the deviations in size are in fact too small to make a significant difference in the coupling.

Since the principal loss mechanism for the case of the magnetic antennas is the permeable material, the spherical core is assumed to have a relative permeability of $300-j300$. That would be the equivalent of using a laminate of $0.75\mu\text{m}$ CZN ferromagnetic alloy layers alternating with $0.5\mu\text{m}$ layers of insulator (SiO_2). In the case of the electric antennas the principal loss mechanism is the current induced in the body medium; thus the core for that case was assumed to be a perfect electric conductor. The core is shown as the pink region in the center of each sphere.

The antennas are made to resonate by wrapping them around the equator with a perfectly conducting “belt” (electrically conducting for the magnetic dipole, magnetically conducting for the electric) that has a gap of one discretization cell on one side of the antenna (the white region surrounding the core). The gap (orange squares in the figure) is filled with a low loss material of high permittivity (magnetic antenna) or permeability (electric antenna) such as to induce resonance close to 2GHz. Although this construction is less realistic than that assumed in the paper it ensures that the comparison between electric antennas and magnetic antennas is as fair as possible by minimizing their differences.

The antenna on the left is excited by driving a time domain field impulse from one end of the gap in the belt to the other. In the case of the magnetic antenna this is an

electric field impulse. In the case of the electric antenna this is a magnetic field impulse. Using a magnetic field impulse on a perfectly magnetically conducting belt as the source for the electric antenna also eliminates any question about whether or not the electric antenna source at its feed could be short circuited by the body dielectric. Fig.A-8 shows the results of the time domain simulation.

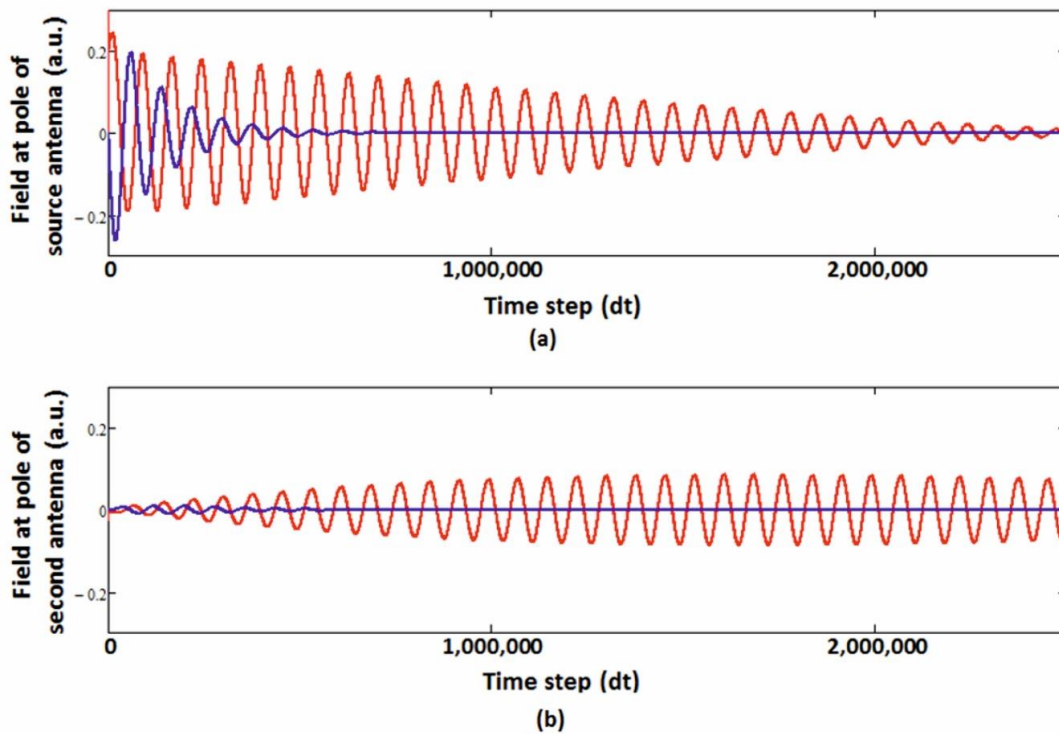


Fig. A-8. Time Domain History of the Interaction Between the Antennas When the First One Is Excited by an Impulse. (a) Current in the Source Antennas Where Blue Shows the Electric Dipole and Red Shows the Magnetic Dipole. (b) Current in the Second Antennas Where Blue Shows the Electric Dipole and Red Shows the Magnetic Dipole.

The field produced just above the pole of the antennas is measured as a function of time. Because of the continuity of the total Maxwell current density this field value is a

direct measure of the current “flowing” through the antenna. The upper figure shows the current in the source antenna while the lower figure shows the current in the second antenna. The difference between a magnetic antenna and an electric antenna in the body medium is evident. The source antenna current dies off exponentially for the electric antenna (blue in the figures) whereas for the magnetic antenna (red in the figures) the drop at the source is a combination of a weak exponential attenuation and attenuation due to the transfer of energy to the second antenna.

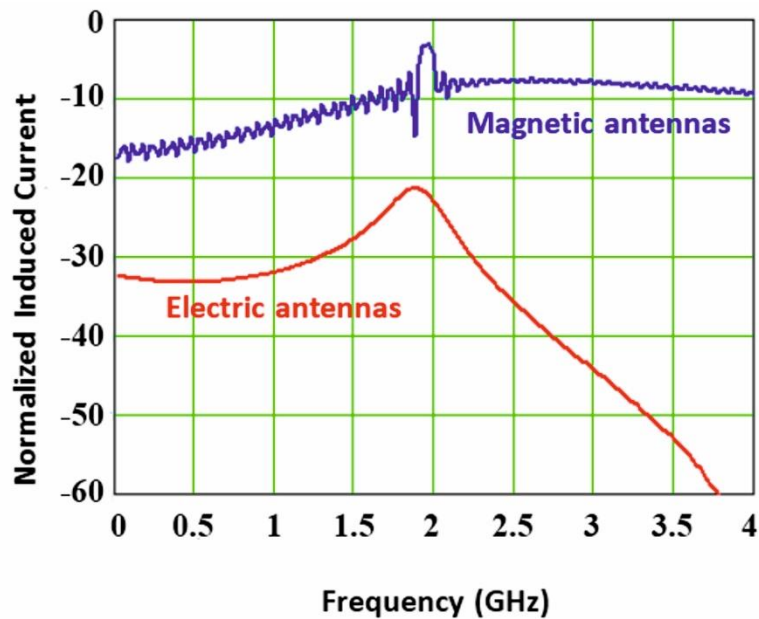


Fig. A-9. Frequency Domain Induced Current on the Second Antenna

That this is what is happening is evident from the second antenna current where we see that for the magnetic antenna the oscillation is still going strong after 2.5 million time steps (only 17 ns of real time has been simulated). Taking the Fourier Transform of these currents and expressing the current in the second antenna relative to the first we obtain the result shown in Fig. A-9. The current induced on the magnetic antenna is -3dB

down from the source whereas the current induced on the electric antenna is -21dB down which shows results similar to those obtained from the closed form calculations.

A.8 Discussion and conclusions

In reference [7] the best antenna considered was the electric loop. The Fig.A-6 plot of the induced current in the electric loop shows that the normalized induced current in the electric loop at 4 cm (far enough to get to the surface of the head from almost everywhere inside the brain) is stronger than the normalized induced current in the electric dipole and, at 3×10^{-9} , it is about an order of magnitude stronger than the normalized field. But the current induced in the magnetic dipole is 2×10^{-5} , almost five orders of magnitude larger than the field ratio. Why is this so?

The time domain response of an antenna to an ambient driving field depends on the quality or the “Q” of its resonance. Since the Q is inversely proportional to the damping, a very low Q antenna is strongly damped. This means that when driven by an ambient field such an antenna will respond, one to one, in direct proportion to the field strength it receives from the very beginning. However, a high Q antenna under the same ambient field will experience an ever-increasing amplitude of oscillation until it reaches a steady state where the power dissipated matches the power input by the field.

The Electric dipoles at the considered size are strongly damped because of the near field direct loss in the body, and similarly, at this size, electric copper loops are also very much damped because of the required large current that dissipates a large amount of energy into their own conductivity. Therefore, the response of electric dipoles and

electric loops follow the field without any resonant amplification. But since true magnetic dipoles induce low body currents and require low metal currents to radiate they are much less damped and therefore develop a much higher current at resonance in response to the applied field.

Alternatively, we can say that the excess loss of the metal antennas results in reduced receiving and transmitting cross sections when compared to the more efficient magnetic dipoles.

In summary, although the magnetic dipole antenna is fed by a loop, the effect of the permeable core is to change the character of the antenna from the short circuit of the electric loop, which has a high current, to an antenna that tends to an open circuit at resonance which as mentioned before is typical of dipoles, since dipoles are open circuits. Therefore, its damping is dominated not by the copper loss but by the constitutive properties of its core. The ferromagnetic metals developed for the magnetic read-head industry on purpose combine high permeability with low damping and this is evidenced in the Lorentz line shape of their frequency dependent permeability; they are by design high Q materials.

As a “verification check” we performed an additional set of calculations in which we set the surrounding medium to free space. This change must remove the advantage of the magnetic dipoles. Indeed, in that case we find that all of the antennas showed the exact same induced current.

Although the materials needed for the magnetic antennas already exist, the results obtained points out the importance of developing magnetic materials with high

permeability and high resonant frequency. Given the small size of the antennas involved and the level of maturity of magnetic read-head industry it can be anticipated that the development and production cost of these materials would not be an obstacle to their use. Magnetic read-head industry materials include multi-layers of “Permalloy” or other alloys with transition metals that have permeabilities in the hundreds and resonance frequencies as high as a few GHz. The magnetic properties of these materials can further be controlled by patterning their layers to control the formation of domains and alter the magnetic anisotropy [49]. Typical dimensions for these design features are in the $0.2 \mu\text{m}$ range [50] fully compatible with an antenna structure in the assumed $10 \mu\text{m}$ size.

We have come to the conclusion that using coupled magnetic dipole antennas as microscopic links in an in-vivo telemetry system is a solution to the tissue damage problem caused by electric dipole antennas through SAR deposition and the electric loop antennas through heat conduction. If we model the head as a sphere of approximately 5cm radius, communication between a transmitting microscopic antenna anywhere inside the brain and an identical one used as a repeater node located just under the skull would derive the +80dB in gain seen in Fig. A-6 as compared to conventional antenna alternatives. Although full re-evaluation of the link budget for a telemetry system exploiting these antennas is yet to be performed we can state that microscopic neuron-by-neuron RF telemetry from within the brain is feasible to the extent that the antennas are no longer the bottleneck.

APPENDIX B
DETAILS AND CALCULATIONS ON THE THEORY OF THE INFINITE
MAGNETO DIELECTRIC ROD

The figure below shows the infinite magneto dielectric rod. The first step to solving this problem is writing the fields of this antenna for both the inside and outside medium.

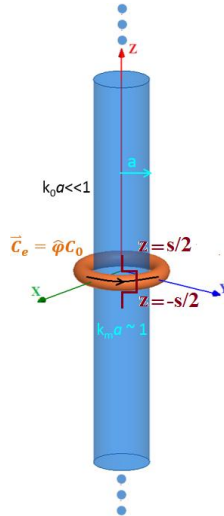


Fig. B-1 Infinite Magneto Dielectric Rod Showing the Current Band at the Origin

Inside the material:	Outside the material:
$E_{\phi} = -A_{0n} \frac{k_{\rho 1}}{\epsilon_1} J_1(k_{\rho 1} \rho) \exp(-jk_z z)$	$E_{\phi} = -C_{0n} \frac{k_{\rho 0}}{\epsilon_0} H_1^{(2)}(k_{\rho 0} \rho) \exp(-jk_z z)$
$H_z = -jA_{0n} \frac{k_{\rho 1}^2}{\omega \mu_1 \epsilon_1} J_0(k_{\rho 1} \rho) \exp(-jk_z z)$	$H_z = -jC_{0n} \frac{k_{\rho 0}^2}{\omega \mu_0 \epsilon_0} H_0^{(2)}(k_{\rho 0} \rho) \exp(-jk_z z)$
$H_{\rho} = A_{0n} \frac{k_{\rho 1} k_z}{\omega \mu_1 \epsilon_1} J_1(k_{\rho 1} \rho) \exp(-jk_z z)$	$H_{\rho} = C_{0n} \frac{k_{\rho 0} k_z}{\omega \mu_0 \epsilon_0} H_1^{(2)}(k_{\rho 0} \rho) \exp(-jk_z z)$

The next step is to expand the current band at the origin into an infinite sum of current waves traveling along the z-axis as follows:

$$\begin{aligned}
& K_\varphi(k_z) \\
&= \frac{1}{2\pi} \int_{-\infty}^{+\infty} \left\{ C_0 \left(\text{rect} \left(\frac{z}{s} \right) \right) \right\} e^{jk_z z} dz; C_0 \left(\text{rect} \left(\frac{z}{s} \right) \right) \\
&= \int_{-\infty}^{+\infty} K_\varphi(k_z) e^{-jk_z z} dk_z
\end{aligned} \tag{B-1}$$

Resulting in:

$$K_\varphi(k_z) = \frac{1}{2\pi} \int_{-\frac{s}{2}}^{+\frac{s}{2}} C_0 e^{jk_z z} dz = \frac{C_0 s}{2\pi} \left[\frac{\sin(k_z s)}{(k_z s)} \right] \tag{B-2}$$

Now, using the fields, we can write (the terms shown in blue are the contribution of the inside fields):

$$\begin{aligned}
\mathbf{H}_z &\rightarrow jC_{0n} \frac{k_{\rho 0}^2}{\omega \mu_0 \varepsilon_0} H_0^{(2)}(k_{\rho 0} a) + jA_{0n} \frac{k_{\rho 1}^2}{\omega \mu_1 \varepsilon_1} J_0(k_{\rho 1} a) \\
&= K_\varphi
\end{aligned} \tag{B-3}$$

$$\mathbf{E}_\varphi \rightarrow C_{0n} \frac{k_{\rho 0}}{\varepsilon_0} H_1^{(2)}(k_{\rho 0} a) = A_{0n} \frac{k_{\rho 1}}{\varepsilon_1} J_1(k_{\rho 1} a)$$

Without getting into the calculation details, both A_{0n} and C_{0n} are obtained as follows:

$$\begin{aligned}
& C_{0n}(k_z) \\
&= \frac{jK_\varphi(k_z) dk_z}{\frac{k_{\rho 0}^2}{\omega \mu_0 \varepsilon_0} H_0^{(2)}(k_{\rho 0} a) \left\{ 1 - \frac{k_{\rho 1} \mu_0 H_1^{(2)}(k_{\rho 0} a) J_0(k_{\rho 1} a)}{k_{\rho 0} \mu_1 H_0^{(2)}(k_{\rho 0} a) J_1(k_{\rho 1} a)} \right\}}
\end{aligned} \tag{B-4a}$$

$$\begin{aligned}
& A_{0n}(k_z) \\
&= \frac{\frac{k_{\rho 0} \varepsilon_1 H_1^{(2)}(k_{\rho 0} a)}{k_{\rho 1} \varepsilon_0 J_1(k_{\rho 1} a)} (jK_\varphi(k_z) dk_z)}{\frac{k_{\rho 0}^2}{\omega \mu_0 \varepsilon_0} H_0^{(2)}(k_{\rho 0} a) \left\{ 1 - \frac{k_{\rho 1} \mu_0 H_1^{(2)}(k_{\rho 0} a) J_0(k_{\rho 1} a)}{k_{\rho 0} \mu_1 H_0^{(2)}(k_{\rho 0} a) J_1(k_{\rho 1} a)} \right\}} \quad (\text{B-4b})
\end{aligned}$$

We see that when the part shown in red in the denominator goes to zero, we will have a pole and later we will need to take this pole into account while integrating to obtain the magnetic current. The next step is rewriting the fields with the obtained $A_{0n}(k_z)$ and $C_{0n}(k_z)$. The fields for the inside and outside medium are as follows:

The fields inside the material are:

$$\begin{aligned}
E_\varphi(\rho, z) &= - \int_{-\infty}^{+\infty} j\omega \mu_0 a \\
&\quad \frac{\left[\frac{1}{k_{\rho 0} a} \frac{H_1^{(2)}(k_{\rho 0} a)}{H_0^{(2)}(k_{\rho 0} a)} \right] K_\varphi(k_z) \exp(-jk_z z) dk_z}{\left(1 - \frac{1}{\mu_r} \left[\frac{1}{k_{\rho 0} a} \frac{H_1^{(2)}(k_{\rho 0} a)}{H_0^{(2)}(k_{\rho 0} a)} \right] \frac{(k_{\rho 1} a) J_0(k_{\rho 1} a)}{J_1(k_{\rho 1} a)} \right)} \quad (\text{B-5a})
\end{aligned}$$

$$\begin{aligned}
& H_z(\rho, z) \\
&= \int_{-\infty}^{+\infty} \frac{k_{\rho 1} a J_0(k_{\rho 1} \rho)}{\mu_r J_1(k_{\rho 1} a)} \frac{\left[\frac{1}{k_{\rho 0} a} \frac{H_1^{(2)}(k_{\rho 0} a)}{H_0^{(2)}(k_{\rho 0} a)} \right] K_\varphi(k_z) \exp(-jk_z z) dk_z}{\left(1 - \frac{1}{\mu_r} \left[\frac{1}{k_{\rho 0} a} \frac{H_1^{(2)}(k_{\rho 0} a)}{H_0^{(2)}(k_{\rho 0} a)} \right] \frac{(k_{\rho 1} a) J_0(k_{\rho 1} a)}{J_1(k_{\rho 1} a)} \right)} \quad (\text{B-5b})
\end{aligned}$$

$$\begin{aligned}
H_\rho &= \int_{-\infty}^{+\infty} j \\
&\cdot \frac{k_z a J_1(k_{\rho 1} \rho) \left[\frac{1}{k_{\rho 0} a} \frac{H_1^{(2)}(k_{\rho 0} a)}{H_0^{(2)}(k_{\rho 0} a)} \right] K_\varphi(k_z) \exp(-jk_z z) dk_z}{\mu_r J_1(k_{\rho 1} a) \left(1 - \frac{1}{\mu_r} \left[\frac{1}{k_{\rho 0} a} \frac{H_1^{(2)}(k_{\rho 0} a)}{H_0^{(2)}(k_{\rho 0} a)} \right] \frac{(k_{\rho 1} a) J_0(k_{\rho 1} a)}{J_1(k_{\rho 1} a)} \right)}
\end{aligned} \tag{B-5c}$$

And the fields outside are as follows:

$$\begin{aligned}
E_\varphi &= - \int_{-\infty}^{+\infty} j \cdot \omega \mu_0 a \frac{H_1^{(2)}(k_{\rho 0} \rho)}{H_1^{(2)}(k_{\rho 0} a)} \\
&\cdot \frac{\left[\frac{1}{k_{\rho 0} a} \frac{H_1^{(2)}(k_{\rho 0} a)}{H_0^{(2)}(k_{\rho 0} a)} \right] K_\varphi(k_z) \exp(-jk_z z) dk_z}{\left(1 - \frac{1}{\mu_r} \left[\frac{1}{k_{\rho 0} a} \frac{H_1^{(2)}(k_{\rho 0} a)}{H_0^{(2)}(k_{\rho 0} a)} \right] \frac{(k_{\rho 1} a) J_0(k_{\rho 1} a)}{J_1(k_{\rho 1} a)} \right)}
\end{aligned} \tag{B-6a}$$

$$\begin{aligned}
H_z &= \int_{-\infty}^{+\infty} k_{\rho 0} a \frac{H_0^{(2)}(k_{\rho 0} \rho)}{H_1^{(2)}(k_{\rho 0} a)} \\
&\cdot \frac{\left[\frac{1}{k_{\rho 0} a} \frac{H_1^{(2)}(k_{\rho 0} a)}{H_0^{(2)}(k_{\rho 0} a)} \right] K_\varphi(k_z) \exp(-jk_z z) dk_z}{\left(1 - \frac{1}{\mu_r} \left[\frac{1}{k_{\rho 0} a} \frac{H_1^{(2)}(k_{\rho 0} a)}{H_0^{(2)}(k_{\rho 0} a)} \right] \frac{(k_{\rho 1} a) J_0(k_{\rho 1} a)}{J_1(k_{\rho 1} a)} \right)}
\end{aligned} \tag{B-6b}$$

$$\begin{aligned}
H_\rho &= \int_{-\infty}^{+\infty} j \cdot k_z a \frac{H_1^{(2)}(k_{\rho 0} \rho)}{H_1^{(2)}(k_{\rho 0} a)} \\
&\cdot \frac{\left[\frac{1}{k_{\rho 0} a} \frac{H_1^{(2)}(k_{\rho 0} a)}{H_0^{(2)}(k_{\rho 0} a)} \right] K_\varphi(k_z) \exp(-jk_z z) dk_z}{\left(1 - \frac{1}{\mu_r} \left[\frac{1}{k_{\rho 0} a} \frac{H_1^{(2)}(k_{\rho 0} a)}{H_0^{(2)}(k_{\rho 0} a)} \right] \frac{(k_{\rho 1} a) J_0(k_{\rho 1} a)}{J_1(k_{\rho 1} a)} \right)}
\end{aligned} \tag{B-6c}$$

We note that all fields have in common the following term in the denominator:

$$\left\{ 1 - \frac{k_{\rho 1} \mu_0 H_1^{(2)}(k_{\rho 0} a) J_0(k_{\rho 1} a)}{k_{\rho 0} \mu_1 H_0^{(2)}(k_{\rho 0} a) J_1(k_{\rho 1} a)} \right\} \tag{B-7}$$

When this is zero we have a pole. Rearranging the terms:

$$H_0^{(2)}(k_{\rho 0} a) J_1(k_{\rho 1} a) \frac{\mu_r}{k_{\rho 1}} = \frac{1}{k_{\rho 0}} H_1^{(2)}(k_{\rho 0} a) J_0(k_{\rho 1} a) \tag{B-8}$$

We recognize this as precisely the transcendental equation for the propagation constant of the TE01 mode in a permeable rod. Thus during the calculation of the Fourier Transform to reconstruct the spatial fields we will have to deal with these surface wave poles as is well known.

These poles can only arise in the range:

$$k_0 < k_z < k_1 \tag{B-9}$$

Because in this range $k_{\rho 0} = \sqrt{k_0^2 - k_z^2} = -jk_0 \sqrt{k_z^2 - k_0^2}$; $k_{\rho 0}$ is a negative imaginary number while $k_{\rho 1} = \sqrt{k_1^2 - k_z^2}$ is a positive number. Now since:

$$K_\alpha(x) = \frac{\pi}{2} (-j)^{\alpha+1} H_\alpha^{(2)}(-jx) \quad (\text{B-10})$$

We can write $H_0^{(2)}(-jx)$ and $H_1^{(2)}(-jx)$ in terms of $K_0(x)$ and $K_1(x)$

$$K_0(x) = \frac{\pi}{2} (-j)^{0+1} H_0^{(2)}(-jx) = \frac{-j\pi}{2} H_0^{(2)}(-jx) \quad (\text{B-11})$$

$$K_1(x) = \frac{\pi}{2} (-j)^{1+1} H_1^{(2)}(-jx) = \frac{-\pi}{2} H_1^{(2)}(-jx) \quad (\text{B-12})$$

Therefore we can write:

$$\frac{H_1^{(2)}(-jx)}{H_0^{(2)}(-jx)} = j \frac{K_1(x)}{K_0(x)} \quad (\text{B-13})$$

At this point it is instructive to see how this surface wave pole enters the integrand as a function of frequency. Thus we study the term in common among all these fields responsible for the pole versus k_z for the case of a rod of $\mu_r = 80$ and $\epsilon_r = 2$ and radius = 2 inches from HF (30MHz) into the UHF range (350MHz). The common term is shown in the following equation:

Common(kz)

$$= \frac{\left[\frac{1}{k_{\rho 0} a} \frac{H_1^{(2)}(k_{\rho 0} a)}{H_0^{(2)}(k_{\rho 0} a)} \right]}{\left(J_1(k_{\rho 1} a) - \frac{1}{\mu_r} \left[\frac{1}{k_{\rho 0} a} \frac{H_1^{(2)}(k_{\rho 0} a)}{H_0^{(2)}(k_{\rho 0} a)} \right] (k_{\rho 1} a) J_0(k_{\rho 1} a) \right)} \quad (\text{B-14})$$

The quantity

$$\frac{H_1^{(2)}(-jx)}{(-jx) \times H_0^{(2)}(-jx)} = \frac{-K_1(x)}{xK_0(x)} \quad (\text{B-15})$$

is purely real and is shown in figure below for $0.08 < x < 0.6$

$$\frac{1}{(-jx)} \frac{H_1^{(2)}(-jx)}{H_0^{(2)}(-jx)} \quad (\text{B-16})$$

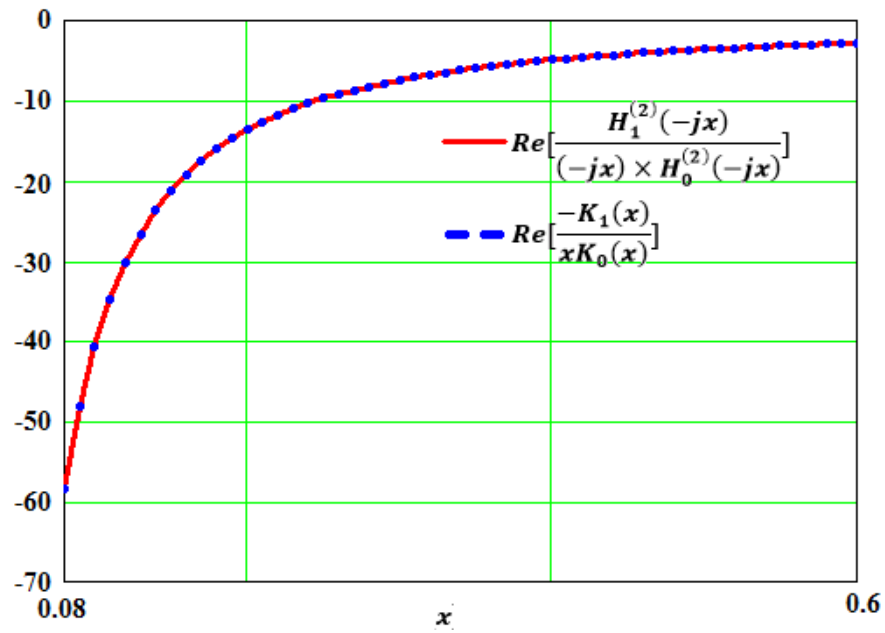


Fig. B-2 A Plot of the Real Part of $-K_1(x)/xK_0(x)$

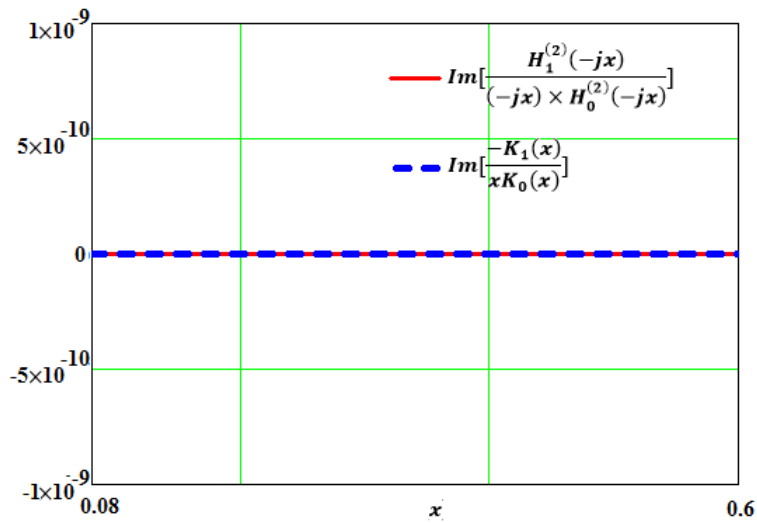


Fig. B-3 A Plot of the Imaginary Part of $-K_1(x)/xK_0(x)$

The reason we have chosen to plot $0.08 < x < 0.6$ is that if we plot $k_{\rho 0}a$ versus k_z normalized to k_1 (k_z/k_1) we will see that $k_{\rho 0}a$ will be purely imaginary starting from 0.08

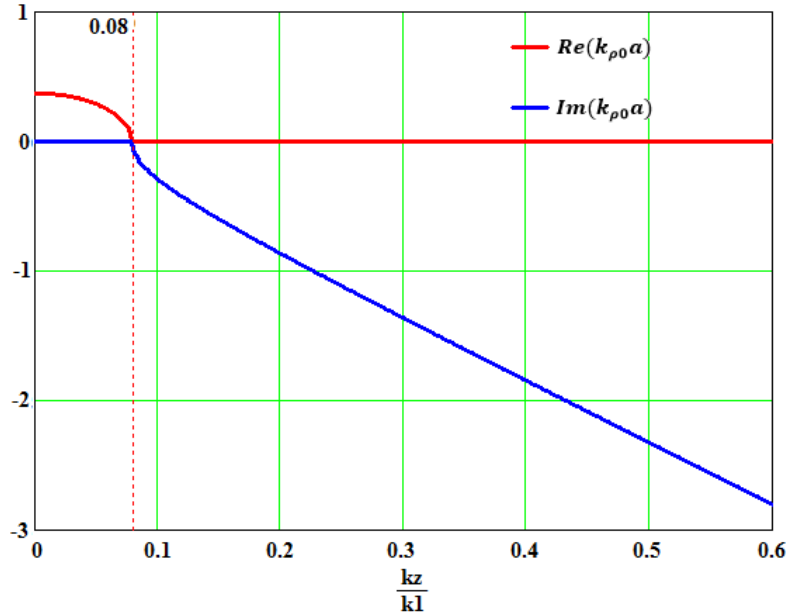
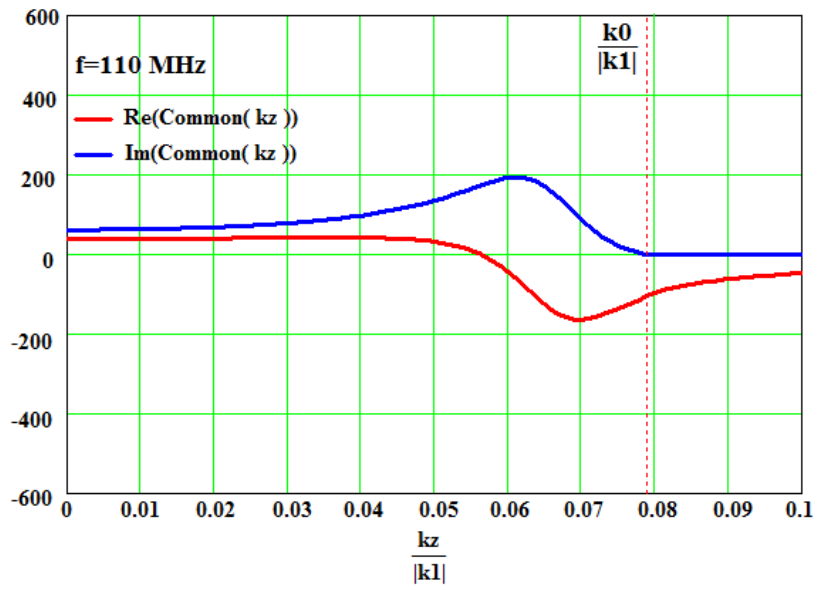
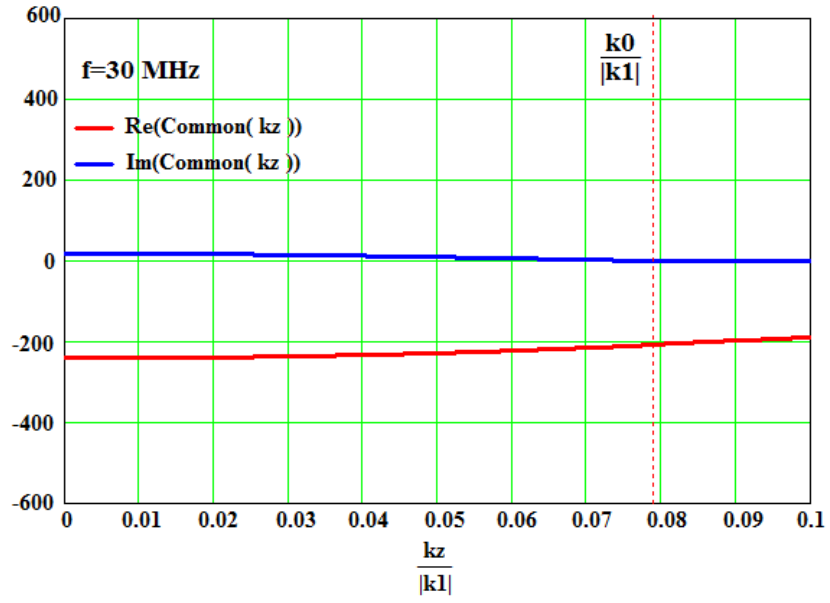


Fig. B-4 A Plot of $k_{\rho 0}a$ Versus Normalized k_z

Now looking back at the common term we can see that the nominator is purely real and negative and the denominator can be zero at a certain values of k_z/k_1 where

$$J_1(k_{\rho 1}a) - \frac{1}{\mu_r} \left[\frac{1}{k_{\rho 0}a} \frac{H_1^{(2)}(k_{\rho 0}a)}{H_0^{(2)}(k_{\rho 0}a)} \right] (k_{\rho 1}a) J_0(k_{\rho 1}a) = 0 \quad (\text{B-17})$$

We also know that since both the nominator and the denominator have real values after $k_z/k_1 = 0.08$ then we will only have a real part which shows the pole. Fig. B-11. shows the common term before the pole appears for $k_z > k_0$ at a few different frequencies.



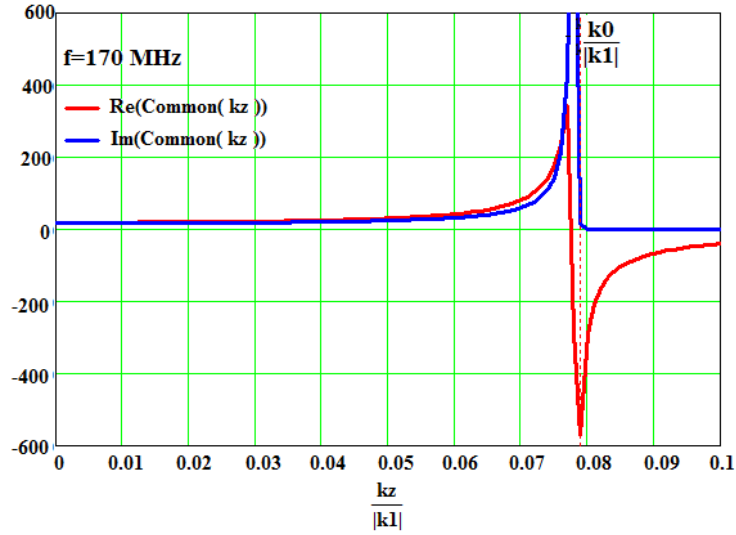
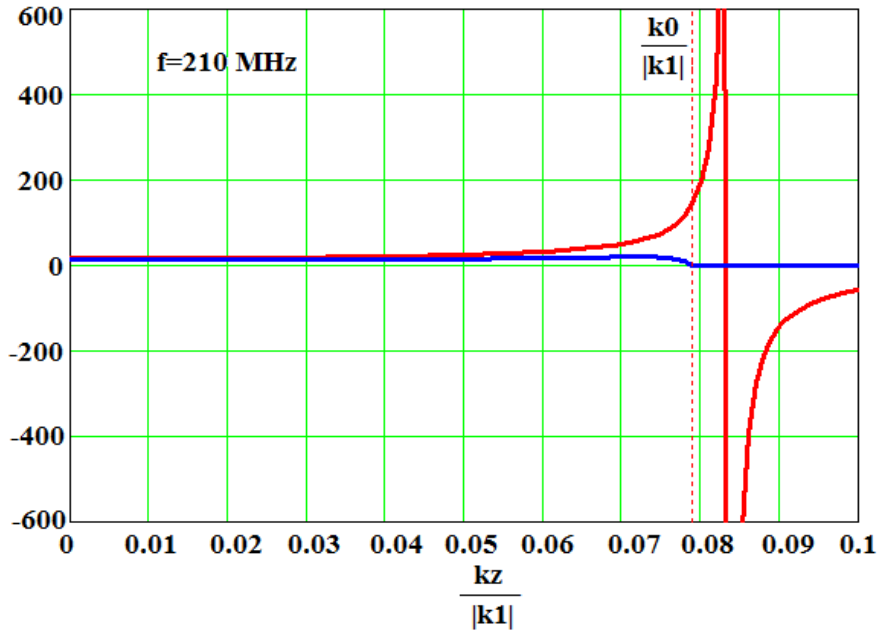


Fig. B-5 Plot of the Common Term Before the Pole Appears for $k_z > k_0$ at 30 MHz, 110MHz, and 170MHz

At this point, since we have no loss in the material, the imaginary part will stay at zero and the pole will move as seen below



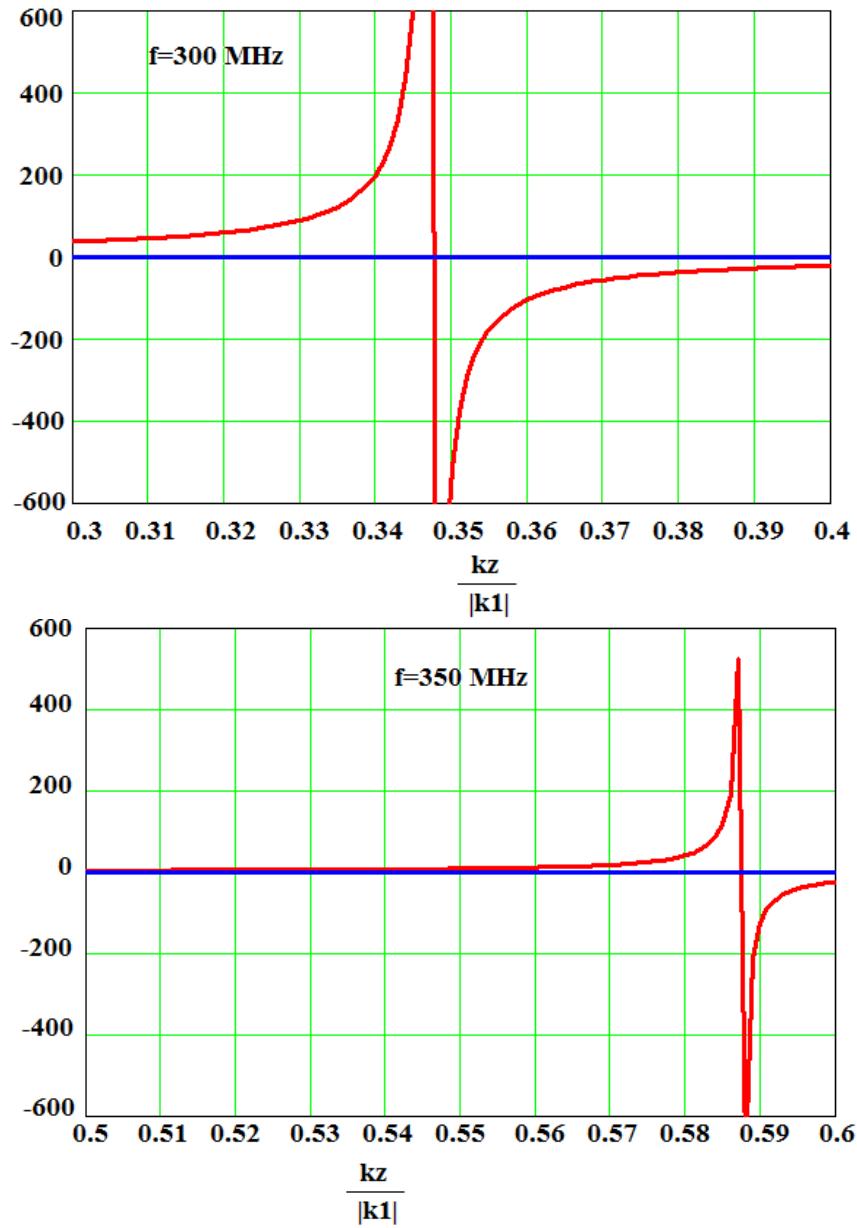
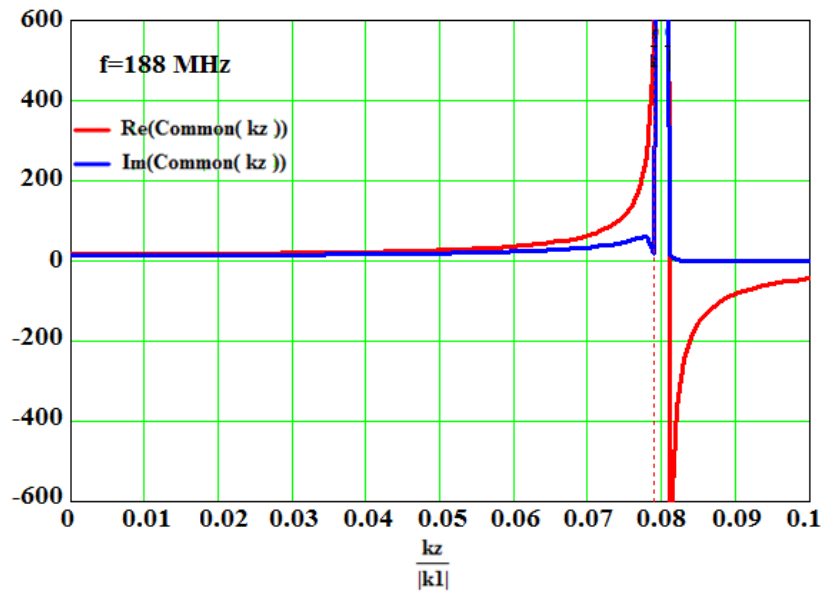


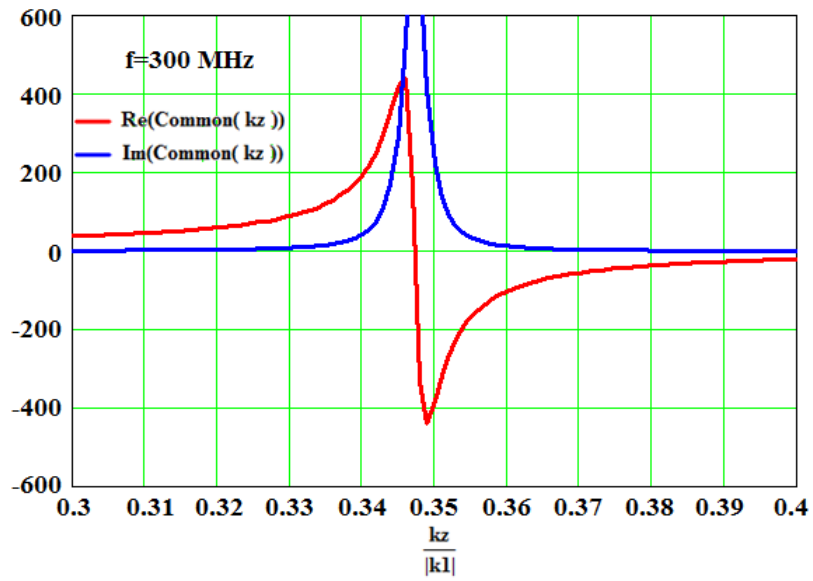
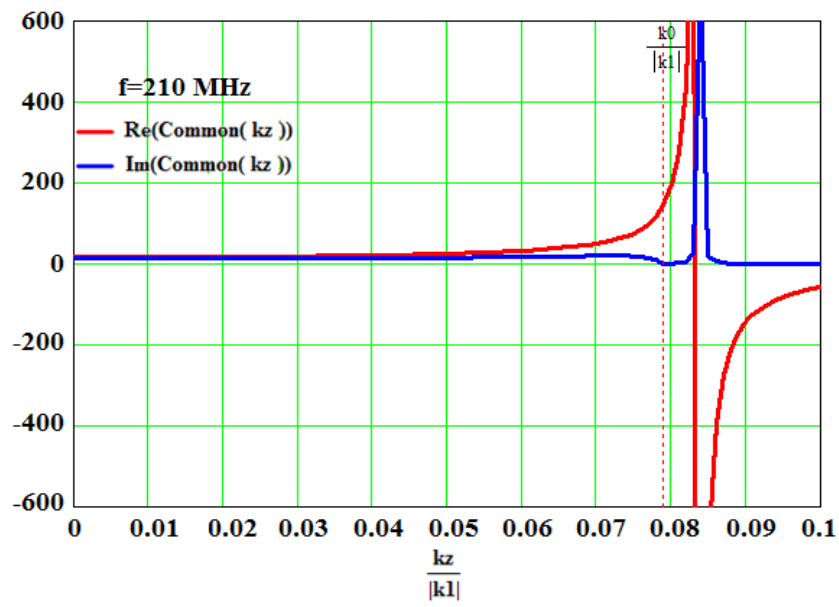
Fig. B-6 Plot of the Common Term After the Pole Appears for $k_z > k_0$ at 210 MHz, 300 MHz, and 350MHz

By adding some loss and changing μ_r from 80 to 80-j0.1 we will see that the surface wave pole first appears at 188 MHz. As the Figures below show, the analytic continuation of the pole arises in the $k_z < k_0$ range (fast wave range) and as the onset

frequency is approached it becomes stronger and migrates towards the horizon $k_z = k_0$, until it is the full-fledged singularity at onset. After onset it continues to travel past $k_z = k_0$ towards k_1 and eventually shrinks.

This is important because these singularities tend to dominate the k-spectrum. The fact that the pole becomes strongest around $k_z = k_0$ may explain the dominance of that region in the spatial domain. A wave guided near the speed of light is what we would tend to see in the spatial domain. This is the principal wave we are after if we want the rod to act similar to a conventional metal antenna.





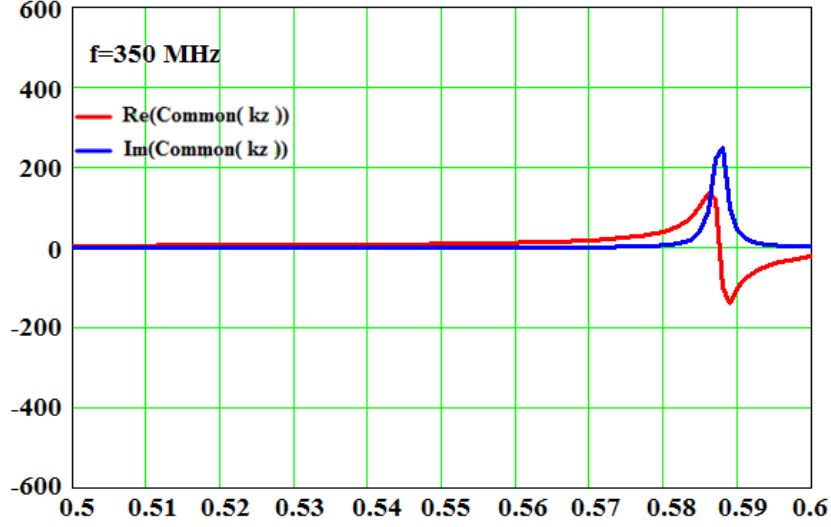


Fig. B-7 Plots of the Common Term at 188MHz, 210MHz, 300 MHz, and 350 MHz, After Adding Some Loss and Changing μ_r from 80 to $80-j0.1$, to See the Appearance of the Surface Wave Pole and Its Behavior at Higher Frequencies

From the results in the previous figures it is clear that at frequencies when the surface wave is guided, the k-space integral will have to account for the location of the pole. In the case of a perfectly magnetically conducting (PMC) rod (the dual of the metal antenna case), the only singularity lies at the horizon. Since this case is of interest as the limiting case of the permeable rod, we write its fields immediately:

$$E_{\varphi PMC} = -j \frac{\omega \mu_0 a}{(k_{\rho 0} a)} \frac{H_1^{(2)}(k_{\rho 0} \rho)}{H_0^{(2)}(k_{\rho 0} a)} K_{e\varphi} \exp(-jk_z z) \quad (\text{B-18a})$$

$$H_{z PMC} = \frac{H_0^{(2)}(k_{\rho 0} \rho)}{H_0^{(2)}(k_{\rho 0} a)} K_{e\varphi} \exp(-jk_z z) \quad (\text{B-18b})$$

$$H_{\rho PMC} = j \left(\frac{k_z a}{k_{\rho 0} a} \right) \frac{H_1^{(2)}(k_{\rho 0} \rho)}{H_0^{(2)}(k_{\rho 0} a)} K_{e\varphi} \exp(-jk_z z) \quad (\text{B-18c})$$

In this case, at the horizons ($k_z = \pm k_0$) $k_{\rho 0} = 0$, and the expression below tends to infinity which is the well-known branch point.

$$\frac{1}{(k_{\rho 0} a)} \frac{H_1^{(2)}(k_{\rho 0} \rho)}{H_0^{(2)}(k_{\rho 0} a)} \quad (\text{B-19})$$

At this point we will calculate the integrals to obtain the fields of the MD rod

For $\rho < a$

$$E_\varphi(\rho, z) = - \int_{-\infty}^{+\infty} j\omega\mu_0 a \frac{\left[\frac{1}{k_{\rho 0} a} \frac{H_1^{(2)}(k_{\rho 0} a)}{H_0^{(2)}(k_{\rho 0} a)} \right] K_\varphi(k_z) \exp(-jk_z z) dk_z}{\left(1 - \frac{1}{\mu_r} \left[\frac{1}{k_{\rho 0} a} \frac{H_1^{(2)}(k_{\rho 0} a)}{H_0^{(2)}(k_{\rho 0} a)} \right] \frac{(k_{\rho 1} a) J_0(k_{\rho 1} a)}{J_1(k_{\rho 1} \rho)} \right)} \quad (\text{B-20a})$$

$H_z(\rho, z)$

$$= \int_{-\infty}^{+\infty} \frac{k_{\rho 1} a J_0(k_{\rho 1} \rho)}{\mu_r J_1(k_{\rho 1} a)} \frac{\left[\frac{1}{k_{\rho 0} a} \frac{H_1^{(2)}(k_{\rho 0} a)}{H_0^{(2)}(k_{\rho 0} a)} \right] K_\varphi(k_z) \exp(-jk_z z) dk_z}{\left(1 - \frac{1}{\mu_r} \left[\frac{1}{k_{\rho 0} a} \frac{H_1^{(2)}(k_{\rho 0} a)}{H_0^{(2)}(k_{\rho 0} a)} \right] \frac{(k_{\rho 1} a) J_0(k_{\rho 1} a)}{J_1(k_{\rho 1} a)} \right)} \quad (\text{B-20b})$$

H_ρ

$$= \int_{-\infty}^{+\infty} j \frac{k_z a J_1(k_{\rho 1} \rho)}{\mu_r J_1(k_{\rho 1} a)} \frac{\left[\frac{1}{k_{\rho 0} a} \frac{H_1^{(2)}(k_{\rho 0} a)}{H_0^{(2)}(k_{\rho 0} a)} \right] K_\varphi(k_z) \exp(-jk_z z) dk_z}{\left(1 - \frac{1}{\mu_r} \left[\frac{1}{k_{\rho 0} a} \frac{H_1^{(2)}(k_{\rho 0} a)}{H_0^{(2)}(k_{\rho 0} a)} \right] \frac{(k_{\rho 1} a) J_0(k_{\rho 1} a)}{J_1(k_{\rho 1} a)} \right)} \quad (\text{B-20c})$$

In this form we can see that for $\rho < a$, the only singularity arises at the surface wave poles when the denominator of the form $1-f(x)$ becomes zero.

For $\rho > a$:

$$\begin{aligned}
E_\phi &= - \int_{-\infty}^{+\infty} j \cdot \omega \mu_0 a \frac{H_1^{(2)}(k_{\rho 0} \rho)}{H_1^{(2)}(k_{\rho 0} a)} \\
&\cdot \frac{\left[\frac{1}{k_{\rho 0} a} \frac{H_1^{(2)}(k_{\rho 0} a)}{H_0^{(2)}(k_{\rho 0} a)} \right] K_\phi(k_z) \exp(-jk_z z) dk_z}{\left(1 - \frac{1}{\mu_r} \left[\frac{1}{k_{\rho 0} a} \frac{H_1^{(2)}(k_{\rho 0} a)}{H_0^{(2)}(k_{\rho 0} a)} \right] \frac{(k_{\rho 1} a) J_0(k_{\rho 1} a)}{J_1(k_{\rho 1} a)} \right)}
\end{aligned} \tag{B-21a}$$

$$\begin{aligned}
H_z &= \int_{-\infty}^{+\infty} k_{\rho 0} a \frac{H_0^{(2)}(k_{\rho 0} \rho)}{H_1^{(2)}(k_{\rho 0} a)} \\
&\cdot \frac{\left[\frac{1}{k_{\rho 0} a} \frac{H_1^{(2)}(k_{\rho 0} a)}{H_0^{(2)}(k_{\rho 0} a)} \right] K_\phi(k_z) \exp(-jk_z z) dk_z}{\left(1 - \frac{1}{\mu_r} \left[\frac{1}{k_{\rho 0} a} \frac{H_1^{(2)}(k_{\rho 0} a)}{H_0^{(2)}(k_{\rho 0} a)} \right] \frac{(k_{\rho 1} a) J_0(k_{\rho 1} a)}{J_1(k_{\rho 1} a)} \right)}
\end{aligned} \tag{B-21b}$$

$$\begin{aligned}
H_\rho &= \int_{-\infty}^{+\infty} j \cdot k_z a \frac{H_1^{(2)}(k_{\rho 0} \rho)}{H_1^{(2)}(k_{\rho 0} a)} \\
&\cdot \frac{\left[\frac{1}{k_{\rho 0} a} \frac{H_1^{(2)}(k_{\rho 0} a)}{H_0^{(2)}(k_{\rho 0} a)} \right] K_\phi(k_z) \exp(-jk_z z) dk_z}{\left(1 - \frac{1}{\mu_r} \left[\frac{1}{k_{\rho 0} a} \frac{H_1^{(2)}(k_{\rho 0} a)}{H_0^{(2)}(k_{\rho 0} a)} \right] \frac{(k_{\rho 1} a) J_0(k_{\rho 1} a)}{J_1(k_{\rho 1} a)} \right)}
\end{aligned} \tag{B-21c}$$

In this case, if $J_1(k_{\rho 1}a)$ and $k_{\rho 1}a$ go to zero in the denominator, they take care of each other and if $J_1(k_{\rho 1}a)$ goes to zero the denominator goes to infinity and all we have is a net zero. The only thing here in the denominator is an $H_1^{(2)}$ but outside the origin it never goes to pure zero (being always complex). And Hankels in the numerator outside the origin are always finite. Therefore there are no other singularities in the entire range of k_z except the surface waves in the range between k_0 and k_1 .

In the case of magneto dielectric rod we have a guided displacement current which is $d\vec{B}/dt$ and since we are interested in the guided current we will obtain this by integrating the circulating E-field at the surface of the rod:

$$\oint \vec{E} \cdot \vec{dl} = \int -\frac{\partial \vec{B}}{\partial t} \cdot d\vec{S} = I_m \quad (\text{B-22})$$

The resulting I_m is as follows:

$$I_m(z) = -j\omega\mu_0 a^2 I_0 \int_{-\infty}^{+\infty} \frac{\left[\frac{1}{k_{\rho 0} a} \frac{H_1^{(2)}(k_{\rho 0} a)}{H_0^{(2)}(k_{\rho 0} a)} \right]}{\left(1 - \frac{1}{\mu_r} \left[\frac{1}{k_{\rho 0} a} \frac{H_1^{(2)}(k_{\rho 0} a)}{H_0^{(2)}(k_{\rho 0} a)} \right] \frac{(k_{\rho 1} a) J_0(k_{\rho 1} a)}{J_1(k_{\rho 1} a)} \right)} \exp(-jk_z z) dk_z \quad (\text{B-23})$$

Now we are ready for the integration but we have to also be careful about the pole. We have different ways of dealing with the poles and choosing either way will give the same results. We can add an imaginary part to μ_r or indent the integration path when crossing the poles.